ICFO
Institut
de Ciències
Fotòniques

Quantum simulations with ultracold atoms: beyond standard optical lattices

Philipp Hans-Jürgen Hauke

Advisor: Prof. Dr. Maciej Lewenstein
Co-advisor: Dr. Fernando Cucchietti

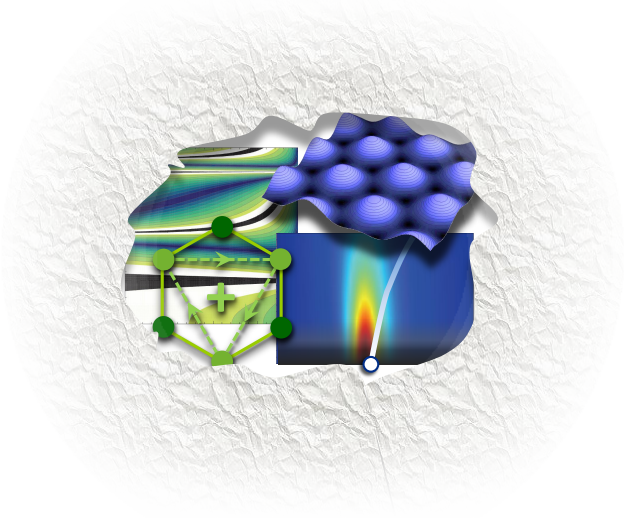

Castelldefels 2012

Quantum simulations with ultracold atoms: beyond standard optical lattices

Philipp Hans-Jürgen Hauke

PhD thesis

at the

ICFO – Institut de Ciències Fotòniques
Castelldefels

and the

Universitat Politècnica de Catalunya
Barcelona

presented by
Philipp Hans-Jürgen Hauke
from Munich

Castelldefels 2012

Thesis committee:	Prof. Dr. Tilman Esslinger
	Prof. Dr. J. Ignacio Cirac
	Prof. Dr. Patrik Öhberg
Substitute members:	Prof. Dr. Anna Sanpera
	Prof. Dr. Darrick Chang

Abstract

Many outstanding problems in quantum physics, such as high-T_c superconductivity or quark confinement, are still – after decades of research – awaiting commonly accepted explanations. One reason is that such systems are often difficult to control, show an intermingling of several effects, or are not easily accessible to measurement. To arrive at a deeper understanding of the physics at work, researchers typically derive simplified models designed to capture the most striking phenomena of the system under consideration. However, due to the exponential complexity of Hilbert space, even some of the simplest of such models pose formidable challenges to analytical and numerical calculations. In 1982, Feynman proposed to solve such quantum models with experimental simulation on a physically distinct, specifically engineered quantum system [Int. J. Theor. Phys. **21**, 467]. Designed to be governed by the same underlying equations as the original model, it is hoped that direct measurements on these so called *quantum simulators* (QSs) will allow to gather deep insights into outstanding problems of physics and beyond.

In this thesis, we identify four requirements that a useful QS has to fulfill, *relevance*, *control*, *reliability*, and *efficiency*. Focusing on these, we review the state of the art of two popular approaches, digital QSs (*i.e.*, special purpose quantum computers) and analog QSs (devices with always-on interactions).

Further, focusing on possibilities to increase control over QSs, we discuss a scheme to engineer quantum correlations between mesoscopic numbers of spinful particles in optical lattices. This technique, based on quantum polarization spectroscopy, may be useful for state preparation and quantum information protocols.

Additionally, employing several analytical and numerical methods for the calculation of many-body ground states, we demonstrate the variety of condensed-matter problems that can be attacked with QSs consisting of ultracold ions or neutral atoms in optical lattices. The chosen examples, some of which have al-

ready been realized in experiment, include such diverse settings as frustrated antiferromagnetism, quantum phase transitions in exotic lattice geometries, topological insulators, non-Abelian gauge-fields, orbital order of ultracold Fermions, and systems with long-range interactions. The experimental realization of all of these models requires techniques which go beyond standard optical lattices, *e.g.*, time-periodic driving of lattices with exotic geometry, loading ultracold atoms into higher bands, or immersing trapped ions into an optical lattice. The chosen models, motivated by important open questions of quantum physics, pose difficult problems for classical computers, but they may be amenable in the near future to quantum simulation with ultracold atoms or ions.

While the experimental control over relevant models has increased dramatically in the last years, the reliability and efficiency of QSs has received considerably less attention. As a second important part of this thesis, we emphasize the need to consider these aspects under realistic experimental conditions. We discuss specific situations where terms that have typically been neglected in the description of the QS introduce systematic errors and even lead to novel physics. Further, we characterize in a generic example the influence of quenched disorder on an analog QS. Its performance for simulating universal behavior near a quantum phase transition seems satisfactory for low disorder. Moreover, our results suggest a connection between the reliability and efficiency of a QS: it works less reliable exactly in those interesting regimes where classical calculations are less efficient.

If QSs fulfill all of our four requirements, they may revolutionize our approach to quantum-mechanical problems, allowing to solve the behavior of complex Hamiltonians, and to design nano-scale materials and chemical compounds from the ground up.

Resumen

Tras varias décadas de investigación, algunos problemas fundamentales de la física cuántica, como la superconductividad de alta temperatura, o el confinamiento de los quarks, carecen de una explicación comúnmente aceptada. Esto se debe en parte a la dificultad existente para controlar y medir estos sistemas. Para lograr una comprensión más profunda, los investigadores han desarrollado modelos simplificados, diseñados para contener los fenómenos de mayor interés en el sistema considerado. Sin embargo, debido a la complejidad exponencial del espacio de Hilbert, incluso la resolución de algunos de los modelos cuánticos más simples plantea grandes retos para el cálculo computacional o analítico. En 1982 [Int. J. Theor. Phys. 21, 467], Feynman propuso resolver estos modelos mediante su simulación experimental en otros sistemas cuánticos. Diseñados para regirse por las mismas ecuaciones que presentaba el modelo original, se espera que la medición directa de estos llamados simuladores cuánticos (SC) lleve a profundizar en la comprensión de algunos de los grandes problemas de la mecánica cuántica.

En la presente tesis doctoral, identificamos cuatro requisitos que debe cumplir un SC para que sea útil: relevancia, controlabilidad, fiabilidad, y eficiencia. Centrándonos en estos, examinaremos lo mas puntero de dos enfoques distintos: SC digitales y analógicos.

Considerando posibilidades de aumentar la controlabilidad sobre los SC, proponemos un sistema para establecer, via espectroscopía cuántica de polarización, correlaciones cuánticas entre un número mesoscópico de partículas con espín en redes ópticas. Esta técnica podría ser útil en la generación de estados, o en protocolos de información cuántica.

Por otra parte, mostraremos la gran variedad de problemas en materia condensada que se pueden atacar mediante SCs de átomos en redes ópticas o iones atrapados, calculando estados fundamentales de sistemas de muchos cuerpos mediante varios métodos analíticos y numéricos. Los ejemplos escogidos, al-

gunos ya realizados experimentalmente, incluyen escenarios diversos como el antiferromagnetismo frustrado, las transiciones de fase cuánticas en geometrías exóticas, los aislantes cuánticos, las redes gauge no abelianas, el orden orbital de fermiones ultrafrios y sistemas con interacciones de largo alcance. La realización experimental de estos modelos requiere técnicas más allá de las estándar en redes ópticas empleando, por ejemplo, modulaciones periódicas en el tiempo de redes de geometría exótica, átomos ultrafríos en bandas excitadas, o iones atrapados sumergidos en redes ópticas. Los modelos considerados, sugeridos por importantes problemas abiertos en física cuántica, a pesar de ser difícilmente resolubles para los ordenadores clásicos, podrían ser fácilmente simulables a nivel cuántico en un futuro cercano, usando átomos ultrafríos o iones.

Pese a que el grado de control alcanzado sobre modelos importantes ha incrementado de forma dramática en los últimos años, la fiabilidad y eficiencia de los SCs ha gozado significativamente de menos atención. Para la segunda parte importante de esta tesis subrayaremos la necesidad de considerar los aspectos mencionados bajo condiciones experimentales realistas. En este contexto, estudiaremos situaciones específicas donde algunos términos que habían sido pasados por alto en la literatura previa pueden cobrar importancia. Posteriormente, caracterizaremos en un ejemplo genérico la influencia del desorden en los resultados de un SC analógico. Más aún, nuestros resultados sugieren una conexión entre la fiabilidad y la eficiencia en un SC: es menos fiable exactamente en aquellos regímenes donde las simulaciones clásicas son menos eficientes.

Si pudieran satisfacer nuestros cuatro requisitos, SCs podrían revolucionar el enfoque a problemas en mecánica cuántica, permitiéndonos calcular el comportamiento de hamiltonianos complejos así como diseñar nano materiales y compuestos químicos de gran versadilidad.

Acknowledgements

This PhD thesis would not have been possible without the assistance of a large number of people. Above all, I want to thank Maciej Lewenstein for his great scientific support, for the many things he has taught me, but also for the fatherly way he leads his group. I also would like to thank Fernando Cucchietti, who has been a great co-supervisor. His cheerful personality has always been motivating and I have learned a lot from him, not only scientifically, but also in terms of presentation and writing skills. A particular thanks also goes to Luca Tagliacozzo, Roman Schmied, Tobias Schätz, and Diego Porras for insightful comments on the manuscript of this thesis.

Also, I want to thank all the inspiring people with whom I have collaborated during the past years or whom I have met at various conferences. The scientific discussions have been very stimulating, but more important are the friendships I gained. Apart from the people already mentioned, these are in particular (in alphabetical order) Mari-Carmen Bañuls, Christoph Becker, Andreas Bick, Alessio Celi, J. Ignacio Cirac, Gabriele de Chiara, Ivan Deutsch, Omjyoti Dutta, André Eckardt, Krittika Goyal, W. Vincent Liu, Michał Maik, Boris Malomed, Leonardo Mazza, Georg Meineke, Morgan Mitchell, Alexander Müller-Hermes, Valentin Murg, Christoph Ölschläger, Wiebke Plenkers, Matteo Rizzi, Tommaso Roscilde, Klaus Sengstock, Rob Sewell, Juliette Simonet, Parvis Soltan-Panahi, Tomasz Sowiński, Julian Struck, Olivier Tieleman, Malte Weinberg, Patrick Windpassinger, Jakub Zakrzewski, and Erhai Zhao.

Special thanks also goes to the rest of the QOT group for stimulating (and often hilarious) discussions, in particular to Alejandro Zamora, Sybille Braungardt, and Christian Trefzger. Further, I want to thank the thesis committee for taking the time for reading the thesis and coming to Barcelona for its defense. I am also grateful to the ICFO administration, who – in their competent and efficient way – always achieve to make things as easy as possible.

Finally, I want to thank all the wonderful friends I made during these years

in Barcelona, above all Federica, Gonzalo, Michela, Mariale, and Joaquim, but also many many more. And, maybe most importantly, I want to express my deep gratitude to my family, especially my parents, my brother, my sister in law, and Nadia. Your support and love have been a great source of motivation and happiness during these past years.

Contents

Published articles

This list provides the references to the articles from the material of which this thesis has been composed, sorted in peer-reviewed articles, preprints, and other papers, and ordered roughly by date of appearance. Below, we indicate the numbers of the chapters to which each article is especially relevant.

Peer-reviewed articles

Non-Abelian gauge fields and topological insulators in shaken optical lattices
Ph. Hauke, O. Tieleman, A. Celi, Ch. Ölschläger, J. Simonet, J. Struck, M. Weinberg, P. Windpassinger, K. Sengstock, M. Lewenstein, and A. Eckardt
Phys. Rev. Lett. **109**, 145301 (2012)
Chapter 5

Tunable gauge potential for neutral and spinless particles in driven optical lattices
J. Struck, Ch. Ölschläger, M. Weinberg, Ph. Hauke, J. Simonet, A. Eckardt, M. Lewenstein, K. Sengstock, and P. Windpassinger
Phys. Rev. Lett. **108**, 225304 (2012)
Chapter 5

Dipolar molecules in optical lattices
T. Sowiński, O. Dutta, Ph. Hauke, L. Tagliacozzo, and M. Lewenstein
Phys. Rev. Lett. **108**, 115301 (2012)
Chapter 10

Can one trust quantum simulators?
Ph. Hauke, F. Cucchietti, L. Tagliacozzo, I. Deutsch, and M. Lewenstein
Rep. Prog. Phys. **75**, 082401 (2012)
Review article, Chapters 1 and 11

Quantum spin models with long-range interactions and tunnelings: A quantum Monte Carlo study
M. Maik, Ph. Hauke, O. Dutta, J. Zakrzewski, and M. Lewenstein
New J. Phys. **14** 113006 (2012)
Chapter 7

Multi-component quantum gases in spin-dependent hexagonal lattices
P. Soltan-Panahi, J. Struck, Ph. Hauke, A. Bick, W. Plenkers, G. Meineke, C. Becker, P. Windpassinger, M. Lewenstein, and K. Sengstock
Nature Phys. **7**, 434 (2011)
Chapter 4

Orbital order of spinless fermions near an optical Feshbach resonance
Ph. Hauke, E. Zhao, K. Goyal, I. H. Deutsch, W. V. Liu, and M. Lewenstein
Phys. Rev. A **84**, 051603(R) (2011)
Chapter 6

Modified spin-wave theory with ordering vector optimization: Spatially anisotropic triangular lattice and J1J2J3 model with Heisenberg interactions
Ph. Hauke, T. Roscilde, V. Murg, J. I. Cirac, and R. Schmied
New J. Phys. **13**, 075017 (2011) (Special issue: Focus on Quantum Simulation)
Chapter 14

Bose–Hubbard model with occupation dependent parameters
O. Dutta, A. Eckardt, Ph. Hauke, B. Malomed, and M. Lewenstein
New J. Phys. **13**, 023019 (2011)
Chapter 9

Frustrated quantum antiferromagnetism with ultracold bosons in a triangular lattice
A. Eckardt, Ph. Hauke, P. Soltan-Panahi, C. Becker, K. Sengstock, and M. Lewenstein
Europhys. Lett. **89**, 10010 (2010)
Chapter 3

Complete devil's staircase and crystal–superfluid transitions in a dipolar XXZ spin chain: A trapped ion quantum simulation
Ph. Hauke, F. Cucchietti, A. Müller-Hermes, M.-C. Bañuls, J. I. Cirac, and M. Lewenstein
New J. Phys. **12**, 113037 (2010)
Chapter 7

Modified spin-wave theory with ordering vector optimization: frustrated bosons on the spatially anisotropic triangular lattice
Ph. Hauke, T. Roscilde, V. Murg, J. I. Cirac, and R. Schmied
New J. Phys. **12**, 053036 (2010)
Chapters 3 and 14

Preprints

Quantum control of spin-correlations in ultracold lattice gases
Ph. Hauke, R. J. Sewell, M. W. Mitchell, and M. Lewenstein
arXiv:1208.1861v1 [quant-ph]
Chapter 8

Quantum disorder in the spatially completely anisotropic triangular lattice II: frustrated hard-core bosons
Ph. Hauke
arXiv:1205.1958 [cond-mat.quant-gas]
Chapters 3 and 14

Quantum disorder in the spatially completely anisotropic triangular lattice I: Heisenberg $S = 1/2$ antiferromagnet
Ph. Hauke
arXiv:1205.1955 [cond-mat.str-el]
Chapter 14

In preparation

Ultracold bosons in a driven triangular lattice: Quantum simulation of frustrated antiferromagnetism
Ph. Hauke, R. Schmied, K. Sengstock, M. Lewenstein, and A. Eckardt
Chapter 3

Other

Speeding up quantum field theories
Ph. Hauke, L. Tagliacozzo, and M. Lewenstein
Science **336**, 1122 (2012)
Perspective article, Chapters 1 and 11

Theoretical pathways towards experimental quantum simulators
A. Niederberger, S. Braungardt, U. Ebling, T. Grass, Ph. Hauke, A. Kubasiak, A. Zamora, R. Augusiak, O. Dutta, E. Szirmai, M. Ciappina, F. M. Cucchietti, A. Eckardt, J. K. Korbicz, G. J. Lapeyre, G. Szirmai, L. Tagliacozzo, M. Rodrǵuez, P. Massignan, M. Lewenstein
Opt. Pura Apl. **44**, 333 (2011)
Review article, Chapter 1

Part I

Quantum Simulators – Background and Foundations

In a vast variety of different contexts, simulations have been used to learn something that otherwise would be unaccessible to human knowledge. Important examples include factory building, product design, complex networks of computers or social agents, national economies, and even entire societies. But even certain aspects of such ordinary things as using training wheels on a bicycle can be understood as a simulation – in this case, a simulation of actually riding a bicycle, but under better-controlled and safer conditions. In general terms,

> *Simulation is the process of designing a model of a real or imagined system and conducting experiments with that model. The purpose of simulation experiments is to understand the behavior of the system or evaluate strategies for the operation of the system.*
>
> — Encyclopedia of Computer Science [1]

For the simulation to be useful, it should be more practical than the real system. Often it offers a safer experimental environment, as for example when letting a pilot train on a land-based device before operating a real airplane (Fig. 1a). In other cases, the simulator permits to reduce costs in terms of capital or time, as happens for example when using wind tunnel measurements on a model plane (Fig. 1b) to decide the necessary dimensions and shape before building a real airplane. In the case of quantum mechanics, simulations deliver, *e.g.*, solutions to problems from high-energy physics, where experiments on real systems typically require huge accelerators, and they widen our understanding of extraterrestrial objects such as neutron stars, which would be impossible to investigate under laboratory conditions.

However, since the simulation should simplify things, by its very definition it has to be an approximation. This implies that for all practical implementations, one first has to derive a model which describes the system to sufficient accuracy, as is already expressed in the definition given above. Finding the relevant aspects of the system that have to be included in the model is an art, as the simulator can only answer the questions it is built for, and precisely what "relevant" means depends on which properties of the simulated system one is interested in. For instance, for the purpose of simulating a low-gravity environment, a water tank is adequate (Fig. 1c), but not to reproduce the low-pressure aspects of space. As an important example in the context of quantum mechanics, the Standard Model of particle physics has been extremely successful since the mid 1970s. In particular, the experimental discovery of various predicted particles, such as the W and Z bosons, several quarks, the tau neutrino, and – very recently – possibly the Higgs boson [2, 3] have confirmed its great predictive

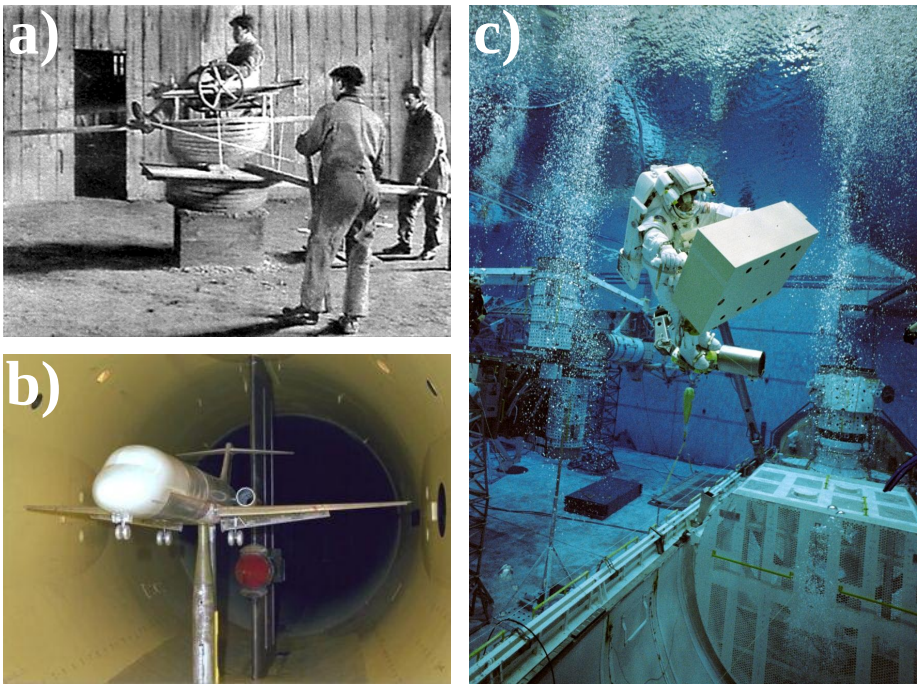

Figure 1: **Simulators for problems from aviation and aeronautics. (a) The first known flight simulator.** In this simulator for the Antoinette monoplane from 1909, two wheels allowed a would-be pilot to familiarize him-/herself with the steers for pitch and roll. Assistants outside would move the device in response to the pilot's use of the steers. **(b) Modern NASA wind tunnel with the model of a plane.** Wind tunnels are based on the insight that an object flying through air is physically the same as the air flowing around the object. Using, *e.g.*, the relationships between their Reynolds numbers, experiments made on small model planes can thus be translated to real-scale airplanes. **(c) Water tank simulator for low-gravity environments.** The buoyant force of water reduces the effects of gravity, such that astronauts can train for the difficult environment outside of a space shuttle or space station. (Pictures from http://en.wikipedia.org.)

power. It does not, however, contain satisfactory explanations for dark matter and dark energy, which amount to 96% of the mass-energy of the known universe. Eventually, its range of validity can only be determined by experiment, which thus remains the final arbiter.

From the practical point of view, the simplest possible model (*i.e.*, which still displays the phenomenon one is interested in) is easiest to implement. Finding this "optimal model" has, however, also fundamental implications; with it one often has also identified the necessary ingredients for a given phenomenon. For instance, if it can be confirmed that the Fermi–Hubbard model shares the superconducting properties of cuprates [4, 5], one may assume that one has discovered the mechanism behind high-T_c superconductivity.

In physics, these abstract models are expressed in the language of mathematics, and the task of simulation reduces to solving the equations describing the model. When thinking about such a simulation, at least as a scientist sitting for large periods in front of a computer screen, one tends to immediately think about "computer simulation." However, wind tunnels, flight simulators, or low-gravity water tanks (Fig. 1) are only some examples for simulation devices which are not based on a classical computer but on a physical system. Such physical implementations are used if a human operator has to be present because he needs to learn how to act in a new situation; in that case mathematical descriptions may not be necessary, but the simulator has still to be a model *setup* of some sort. A physical implementation can also be advantageous if the model is too hard to be solved on a classical computer, as is the case in airplane design due to the difficulty of solving the equations of fluid dynamics. This problem also occurs in quantum mechanics, where the exponential complexity of Hilbert space makes exact calculations practically impossible for all but the simplest systems.

To solve the complex models appearing in quantum many-body physics, Richard Feynman suggested in his 1982 foundational article [6] to use specially-designed physical devices, which have now become known under the name *quantum simulator* (QS). His fundamental insight was that, in order to tackle the complexity of quantum-mechanical problems, the simulator itself has to be governed by the laws of quantum mechanics. Following this idea, by designing a well-controlled system from the bottom up, one could create a computer whose constituent parts are governed by quantum dynamics generated by a desired Hamiltonian. Measuring the properties of this nano-engineered system would then reveal some unknown or difficult to compute properties of a quantum many-body model, such as the nature of quantum phase diagrams. This way, insight may be gathered into many outstanding problems in physics and beyond, such as

high-T_c superconductivity or quark confinement, which are still not completely understood after decades of research (and in the case of high-T_c superconductivity, more than 100,000 publications). Under these prospects, scientists are envisioning a world where special-purpose QSs are readily available at research facilities, allowing to solve complex Hamiltonians or design nano-materials from the ground up.

In the rest of this preparatory part, we describe the general idea of quantum simulation and propose a concise definition (Sec. 1.1), consisting of four parts – relevance, control, efficiency, and reliability. In particular, this definition identifies an important (and only recently recognized) stepping stone that quantum simulation has to reach, namely the assurance of its reliability and possibilities for its validation. We will later discuss this issue in more detail on a few concrete examples (Part III). In Secs. 1.2 and 1.3, we review two different conceptual approaches for QSs, namely digital and analog ones. In Chapter 2, we describe possible implementations of analog quantum simulators with trapped ions and ultracold atoms in optical lattices. The latter are to date maybe the best-developed quantum-simulation architecture. In Part II, we will discuss some of our recent proposals for quantum simulations relying on these architectures. Here, we focus in particular on new avenues opened by techniques that go beyond standard optical lattices. Technical details of our calculations are largely delegated to Part IV. The examples discussed in Part II are intended to give an overview of the wealth of exotic effects which may be amenable to quantum simulation.

Chapter 1

Theoretical considerations

Fueled by the prospect of solving a broad range of long-standing problems in strongly-correlated systems, the tools to design, build, and implement quantum simulators (QSs) [6–8] have rapidly developed and are now reaching sophisticated levels, to such an extent that the journal Science appreciated the recent evolution of QSs as a scientific breakthrough of the year 2010 [9]. Researchers are making ground-breaking advances in quantum control of a variety of systems, including ultracold atoms and molecules (see Sec. 2.1), ions (see Sec. 2.2), photons, circuit quantum electrodynamics (CQED) and polaritons, artificial lattices in solid state, nuclear magnetic resonance (NMR) systems, and superconducting qubits. Some references for recent reviews and current breakthroughs, illustrating the progress in the field, can be found in Table 1.1. At the current pace, it is expected that we will soon reach the ability to finely control many-body systems whose description is outside the reach of a classical computer. For example, modeling interesting physics associated with a quantum system involving 50 spin-1/2 particles – whose general description requires $2^{50} \approx 10^{15}$ complex numbers – is out of the reach of current classical supercomputers, but perhaps within the grasp of a QS.

In a field brimming with excitement, it is important to critically examine such high expectations, as we pointed out in Refs. [61, 62]. Real-world implementations of a QS will always face experimental imperfections, such as noise due to finite precision instruments and interactions with the environment. Feynman's QS is often considered as a fundamentally *analog* device, in the sense that all operations are carried out continuously. However, while in a digital device external perturbations have to achieve a certain strength to introduce an er-

QS architecture	current breakthroughs	recent reviews
ultracold atoms and molecules	[10–23]	[24–26]
ions	[27–33]	[34–36]
photons	[37–41]	[42]
CQED and polaritons	[43–47]	[48]
artificial lattices in solid state	[49]	
NMR systems	[50–53]	
superconducting qubits	[54, 55]	[56–59]

Table 1.1: **Common QS architectures with references for recent breakthroughs and reviews.** For a general overview see the strategic report [60].

ror (for example, to flip a classical bit typically a mesoscopic magnetization or charge has to be changed), errors in an analog device, even small ones, can propagate and multiply uncontrollably [63]. Indeed, Landauer, a pioneer of the physics of information, questioned whether quantum coherence was truly a powerful resource for computation because it required a continuum of possible superposition states that were "analog" in nature [64].

This contrasts with the operation of a universal *digital* quantum computer as envisioned by David Deutsch, in which all operations are digitized into a finite set of logic gates and measurements [65].[1] The invention of quantum-error-correcting codes showed that a quantum computer is in some sense *both* analog and digital. Through a discrete set of unitary transformations, we can get arbitrarily close to any superposition, and imperfections can always be projected on a discrete set and thus can be corrected [66]. When such a digital quantum simulation operates with fault-tolerant quantum error correction [67], we can trust its output to a known finite precision.

Universal digital quantum computers may serve as digital QSs (DQSs) that mimic dynamics of some quantum many-body system of interest. While in such a case error correction and fault tolerance is guaranteed, the question of

[1] We use the notion of digital QS in this sense, *i.e.*, the digitization of operations, not in the sense of digits of precision. In particular, the outcome of an analog QS will also yield only a finite digital precision, but its operations are performed continuously.

efficiency of such a device is highly non-trivial. The number of resources needed for precise simulation of continuous-time dynamics of a many-body system by stroboscopic digital applications of local gates might be enormous [68]. One can also consider DQSs that are experimental systems that have at their disposal only a limited, non-universal set of gates. In such a situation, the error correction and fault tolerance are not guaranteed and the question of efficiency is even more pertinent.

This raises one central problem of this thesis: can we trust the results obtained with a real-world QS, and under what conditions are they *reliable* to a known degree of uncertainty? Although this thesis concentrates on analog QSs (AQSs), we report also on the state of art of DQSs.

The rest of this chapter is organized as follows. Section 1.1 develops the general concept of QSs. In the spirit of the DiVincenzo criteria for quantum computing [69], we present one of the main points of this chapter, a definition of the QS based on four indispensable properties: relevance, controllability, reliability, and efficiency. Section 1.2 is devoted exclusively to DQSs. It contains several subsections in which we review various proposals for DQSs, classify them, and discuss the present state of knowledge concerning their controllability, reliability, and efficiency. Section 1.3 is organized similarly, but focused on AQSs.

The considerations of this chapter, together with the numerical results of Chapter 11, which serve to illustrate the need for a careful analysis of the influence of imperfections in a real-world QS, can be found in the article [61].

1.1 Definition of a quantum simulator

Before proceeding, we must establish a clear definition of a QS. Following the considerations on p. 3*f*, we consider here a QS to be a device which, when measured, reveals features of an ideal mathematical model, *e.g.*, the phase diagram for the Bose–Hubbard model on a specified lattice with specified interactions. A QS may be a special purpose device that simulates a limited class of models, *e.g.*, the Bose–Hubbard model simulated by atom transport in an optical lattice [70–72] (see Sec. 2.1), or a universal machine that is capable, in principle, of simulating any Hamiltonian on a finite-dimensional Hilbert space.

In the spirit of the DiVincenzo criteria for quantum computing [69], we formulate the following "working" definition of a QS, consisting in its core of a few minimal conditions a QS should fulfill. We will provide some more detailed explanations below (see also the recent book [8]):

Definition

A quantum simulator is a *quantum-mechanical, experimental system* that *mimics a simple model,* or a family of simple models of quantum mechanical origin, such as from condensed matter physics, high energy physics, or quantum chemistry.
A useful quantum simulator should fulfill the following four requirements:

- **(a)** ***Relevance:*** The simulated models should be of some relevance for applications and/or our understanding of challenges in physics and related fields.
- **(b)** ***Controllability:*** A QS should allow for broad control of the parameters of the simulated model, for control of initialization and evolution of the system, and for detection of the relevant observables.
- **(c)** ***Reliability:*** Within some prescribed error, one should be assured that the observed physics of the QS corresponds faithfully to that of the ideal model whose properties we seek to understand.
- **(d)** ***Efficiency:*** The QS should solve problems more efficiently than is practically possible on a classical computer. (Although it may be of interest to have a QS realizing a model that is classically computable but not accessible or realized in nature.)

In the next two sections, we characterize the state-of-the-art knowledge concerning these four points of our definition for different types of QSs. But before that, we would like to add a few general remarks. These will in particular show that the requirements (c) and (d), which have been largely neglected until recently, have strong connections to each other and the other requirements.

The requirements (a) to (c) are general and can be demanded of any simulator. For the examples of Fig. 1 on p. 4: (a) Direct tests on airplanes or in space are expensive and dangerous, making simpler system necessary that can be manipulated without risk and at reduced cost. (b) Flight simulators allow relevant operations such as adjusting speed and height, and similar considerations hold for the simulation of outer space in water tanks. Wind tunnels allow to simulate different air speeds and measurement of flow (visualized with smoke) as well as forces and moments (for these, the model plane is typically mounted on a force

balance). (c) In the wind tunnel, error bars on air speed, force measurements, and the dimensions of the model plane have to be precisely known. For the flight simulator or the water tank, the conditions in the simulator have to be realistic enough to prepare the operator adequately (although in these cases the lack of a mathematical model does not allow to give precise error bars).

For the QS, we only made two additions to these requirements. First, in order to solve quantum-mechanical problems, the QS has to be of quantum-mechanical origin. Second, per requirement (d), it has to be more efficient than what can be done on a classical computer. Else, we cannot justify the experimental effort and the large cost for building the QS. Hence, (d) is also a necessary condition for (a): demanding that the mimicked models solve open problems also implies that these cannot be solved by other means, *i.e.*, they should be computationally hard for classical computers.

This notion of "computationally hard for classical computers" may have several meanings: *(i)* an efficient (scalable, with polynomial growth in resources as a function of problem size) classical algorithm to simulate the model might not exist, or might not be known; *(ii)* the efficient scalable algorithm is known, but the required size of the simulated model is too large to be simulated under reasonable time and memory restrictions. However, there might be exceptions to the general rules. For instance, it is desirable to realize QSs to simulate and to observe novel phenomena that so far are only theoretically predicted, even though it might be possible to simulate these phenomena efficiently with present computers. Simulating and actually observing in the lab is more than just simulating abstractly on a computer.

To understand better under which situations a QS may work more efficiently than a classical computer, we now discuss shortly which systems can be simulated efficiently classically and which ones cannot. Generally speaking, an important set of tasks for a QS includes

1. Statics of the mimicked system at zero temperature; this implies simulation of ground states and their properties.

2. Statics at thermal equilibrium, *i.e.*, Hamiltonian dynamics at low energies or thermodynamics at non-zero, typically low, temperatures.

3. Continuous-time dynamics of the system, in particular Hamiltonian dynamics out of equilibrium.

4. Dissipative or open-system continuous-time dynamics.

Classical simulations of quantum systems are currently performed using one of the following numerical methods (see also Part IV of this thesis or the book by Lewenstein, Sanpera, and Ahufinger [8]):

- Quantum Monte Carlo (QMC)
- Systematic perturbation theory
- Exact diagonalizations
- Variational methods, such as mean field methods, density-functional theory (DFT), dynamical mean-field theory (DMFT), tensor-network states (TNS), density-matrix renormalization group (DMRG), tree tensor network states (TTN), multiscale entanglement-renormalization *Ansatz* (MERA), projected entangled-pairs states (PEPS), ...

Each of these methods has its limitations. Let us first focus on points 1 and 2 of the previous list of possible QS tasks. In those cases, QMC works for various large systems, but fails for Fermi or frustrated systems due to the famous sign problem [73]. Perturbation theory works only if there exists a small expansion parameter. Exact diagonalization (ED) works only for small systems (see Chapter 12.1). In the case of 1D systems, there are special cases which can be solved exactly via the Jordan–Wigner transform (see Chapter 12.3) or the Bethe *Ansatz* [74]. For the other one-dimensional cases, DMRG, MERA, and TTN techniques (see Chapter 12.2) scale favorably and can, in principle, treat very large systems [75–77]. In 2D the situation is more complex – similar to ED, DMRG and TTN work only for reasonably small systems [78–80], whereas 2D tensor-network methods (PEPS, MERA) in principle work for arbitrarily big systems (bosonic, and even fermionic [81] or frustrated [82]) but are biased towards slightly entangled states. Mean field [83] (see Chapter 13), DFT [84, 85], or DMFT [86], finally, have other limitations. For instance, they are essentially designed for weakly-correlated systems.

As a side remark, in part due to this computational complexity, 2D is often the most interesting case. In 1D, many systems can be solved efficiently numerically, and often there are even no phase transitions (which happens if the "lower critical dimension" is 1D). For large dimension (*i.e.*, larger than or equal to the "upper critical dimension", which can be as low as 4D) mean-field theories become exact in the thermodynamic limit. It is only between these critical dimensions that "interesting" physics happens, and since many parameters scale as the inverse of the dimension, 2D is often the most interesting situation. For

this reason, the systems treated further on in this thesis will be mainly in two dimensions.

Which are then the models that are computationally hard for points 1 and 2 in the previous task list? Generally speaking, computationally hard are "strongly entangled" models in more than 1D such as

- Fermionic models, with paradigmatic examples being the Fermi–Hubbard [87] or $t-J$ models for spin 1/2 fermions [4].
- Frustrated models, with paradigmatic examples being antiferromagnetic (AFM) Heisenberg or XY models on a kagome or anisotropic triangular lattice (Chapter 3).
- Disordered models, with paradigmatic models being quantum, or even classical spin glasses [88].

For points 1 and 2, currently available QSs are typically not yet able to outperform classical computations. For example, in the temperature regimes of current experiments, the Fermi–Hubbard model can be simulated classically by high-temperature expansion [13]. However, as soon as experiments achieve lower temperatures, this will cease to work and problems of fermionic simulations (such as the sign problem in QMC [73]) will become relevant. In this light, we may hope that soon QSs will be able to outperform classical computers for points 1 and 2 of the tasks list, although recent efforts in variational Monte Carlo [89] and fermionic tensor networks [90–94] are rapidly providing ever better variational approximations.

When we move to points 3 and 4 of the task list, *i.e.*, studying dynamics, we can safely state that

- Quantum dynamics on a long time scale is generally computationally hard.

The latter statement implies that while it might be possible to simulate with classical computers short-time dynamics in a restricted class of 1D models, such attempts will nearly always fail at longer time scales. This fact is related to correlation and entanglement spreading according to the Lieb–Robinson theorem that states that, after a sufficiently long evolution, states can become strongly entangled ([95–100], see also the review [101]). Recently, this complexity led to the demonstration that a QS can outperform even the most sophisticated, state-of-the-art classical algorithms: in an experiment based on ultracold bosonic atoms, the controlled dynamics ran for longer times than present classical algorithms based on DMRG could efficiently keep track of [19].

Finally, the requirement of efficiency is interrelated with the reliability of a quantum simulator. In fact, we could try to improve the precision of a QS by averaging more experiments, but in hypersensitive regimes (like close to quantum phase transitions) the necessary number of repetitions can grow rapidly, possibly bringing the overall efficiency of the QS down to the level of classical computers. A connection between (c) and (d) could also be relevant for cross validation [102]. In this popular approach, it has been proposed to compare the results of two different physical realizations performing a quantum simulation of the same model. From this, one hopes to find universal features which then would be ascribed to the simulated model. It may be, however, that the universal features shared by multiple platforms are robust only because they could have been predicted efficiently with some classical algorithm. Or, even worse, because they are associated to imperfections which affect the different QSs in the same way (such as the emergence of Griffith's phases [103] or the change of the order quantum phase transitions [104] due to disorder).

The necessity of validation also connects requirement (c) to (d). In fact, one would like to require sufficient control over model parameters to be able to set them in a regime where the model becomes tractable by classical simulations. Comparing the results from both approaches provides an elementary instance of validating the QS. Furthermore, an important idea proposed and analyzed in Ref. [61] (see also Ref. [62]) is a more sophisticated manner of validation, namely the checking of the sensitivity of the quantum simulation with respect to addition of noise and/or disorder. Such a consistency check, which is only possible with sufficient control over the system, may allow to provide error bounds and in some cases even an extrapolation of relevant observables to the ideal, imperfection-free case.

Note, however, that there are alternative possibilities for a partial validation, as pointed out to us by Z. Hadzibabic [105]. Namely, in some situations where it is impossible to simulate the system classically, it might still be possible to test by classical means the sensibleness of the quantum-simulation results. As a trivial example, the measured ground-state energy should fulfill all known bounds, such as variational ones, and others.

Up to here, our remarks concerning the four requirements (a-d) of our definition were of quite general nature, without invoking a specific implementation of the QS. In the following two sections, we explore – first for digital, then for analog QSs – the state of the art concerning (b-d) in more detail.[2]

[2]Since the relevance (a) depends on the concrete model (and, indeed, the individual taste), we do not go into much detail here.

1.2 Digital quantum simulators (DQS)

In this section, we classify DQSs, discuss their general properties, various protocols for implementing such devices, and summarize state-of-the-art knowledge concerning their controllability, reliability, and efficiency.

1.2.1 Universal digital quantum simulators (UDQS)

While the concept of QSs should be traced back to the proposal by Feynman [6], these ideas were made concrete by Seth Lloyd who showed that any local many-body unitary evolution governed by a local Hamiltonian could be implemented by the control afforded by a universal digital quantum computer [106]. For this reason, in the following we will term Lloyd's DQS a "universal DQS" (UDQS). In order to realize it in a laboratory, an experimentalist has to have to his/her disposal a universal set of unitary quantum gates.

The task of a UDQS is to simulate the unitary time-evolution operator of a desired quantum system, which can then be employed to extract quantities like energy gaps and ground-state properties. The action of the global, unitary, continuous-time evolution operator is mimicked by appropriate stroboscopic applications of various quantum gates. The mathematical basis for such a digitalization is given by the Trotter–Suzuki formula. Let us list below some possible realizations and properties of UDQSs:

Realizations: While implementation of a fully-functioning large-scale digital quantum computer is still in development, there are several physical systems for which universal sets of quantum gates are available, and for which proof-of-principle UDQSs exist. These systems include ultracold ions [36], ultracold trapped atoms interacting via cold collisions [26] or the Rydberg-blockade mechanism [107], CQED [108], and superconducting qubits. The first concrete proposals for realizations of UDQSs where given in Refs. [109, 110], and first experiments were performed in NMR systems [50–52]. Using a digital trapped-ion architecture with a stroboscopic sequence of gates, the quantum simulation of Ising, XY, and XYZ spin models in a transverse field was recently demonstrated in a proof-of-principle experiment with up to six ions [30].

Controllability: In accordance with Lloyd's pioneering work [106], with the help of a universal set of gates a UDQS is perfectly controllable. This control allows for simulation of practically any local Hamiltonian evolution, as well as for the preparation, manipulation, and detection of relevant states and observ-

ables of the system in question. Recently, Preskill's group has also proven that the scattering amplitudes in simple relativistic quantum field theories can be efficiently (in polynomial time) simulated by UDQSs [111, 112] (see also the Perspectives article [62]). Note, however, that not much is known about the possibility to quantum simulate, using UDQSs, systems with long-range interactions like Coulomb or dipole–dipole interactions.

Reliability: A UDQS is the only DQS which has guaranteed access to error correction and fault tolerance [113, 114] (for the first proof-of-principle experiments see Refs. [55, 115–119]).

Efficiency without errors: So far, the community has mostly focused on developing requirement (b), control, for suitable relevant models, both theoretically and experimentally. The conditions (c), reliability, and (d), efficiency, have received considerably less attention, especially their interrelation. Most work that has been done is focused on efficiency in the absence of errors. For this case, Lloyd showed that a Trotter–Suzuki decomposition of a time-evolution operator is efficient in the sense that each logic gate acts on a scalable Hilbert space associated with a small subset of qubits and the total number of gates N_g scales polynomially, $N_g \sim \tau^2/\epsilon$, where τ is the time of evolution to be simulated and ϵ is the error in the result [106]. Aharanov and Ta-Shma showed that a UDQS is efficient when the Hamiltonian is "sparse," *i.e.*, the number of nonzero entries in any row is at most poly(log(D)), where D is the dimension of the many-body Hilbert space [120]. In the absence of errors, the computational complexity of such a simulation has been well studied [121, 122].

Efficiency in the presence of errors: In the presence of errors, however, ensuring reliability to a desired precision has profound implications for efficiency even in a UDQS on a fault-tolerant quantum computer [68, 123]. In the digital approach with a finite universal gate set, one applies error-correction schemes that can make the whole computation fault-tolerant when the error per operation is below a certain threshold – thus UDQSs fulfill the reliability requirement (c). The Trotter expansion, however, can scale poorly when error correction is included, as emphasized by Brown *et al.* [68]. For a given error ϵ, associated to $b = -\log_2(\epsilon)$ bits of precision, the number of gates in the expansion scales as $\sim 1/\epsilon$, which corresponds to a scaling as $\sim 2^b$. Hence, in terms of the required degree of precision b, in the presence of errors fault-tolerant implementation of this Trotter expansion grows *exponentially* in the number of gates and the time to perform the simulation. Moreover, Brown *et al.* showed that

for a small number of qubits where one might avoid error correction, analog control errors on the logic gates can lead to faulty results, negating requirement (c), and robust control pulses become essential. In a similar vein, Clark *et al.* [124] performed a careful analysis of the resources necessary to implement the Abrams–Lloyd algorithm [125] to calculate the ground-state energy of the 1D transverse Ising model on a state-of-the-art fault-tolerant ion-trap quantum computer. Again, the overhead in the number of time steps to fault-tolerantly implement the quantum-phase estimation algorithm grows exponentially with the degree of precision required. Assuming realistic values for gate times and failure probabilities, they found that for 100 spins, in order to achieve $b \geq 10$ bits of precision, at least two levels of concatenated error correction are necessary, requiring at least 100 days of run time on the ion-trap quantum computer; for $b \geq 18$, three levels are necessary, requiring at least 7.5×10^3 years! On the up-side, for a fixed precision, the growth of the number of resources with system size is only weak.

1.2.2 Non-universal digital quantum simulators (nUDQS)

A non-universal DQS (nUDQS) is in many aspects similar to a UDQS, except that it is a special-purpose quantum computer with a restricted, non-universal set of unitary quantum gates. This may appear, for example, in situations where it is experimentally simpler to design a setup for a specific quantum simulation which does not require a full universal set of gates. The task of a nUDQS is the same as that of a UDQS: to simulate real- or imaginary-time quantum many-body dynamics of a certain quantum system described by a certain Hamiltonian. Let us list below some properties and possible realizations of such a nUDQS:

Realizations: In all systems in which the universal sets of quantum gates are available, one can also restrict the set of gates and realize a nUDSQ. For example, in some of the recent experiments of the Blatt group [30], only a necessary subset of the available set of universal gates was used. All of the systems discussed above (atomic, superconducting, etc.) are potentially platforms for implementing nUDQSs. A seminal example of this approach goes back to the so-called "Average Hamiltonian Theory" in NMR [126, 127].

Controllability: nUDQSs are typically not perfectly controllable. Still, in most experimental realizations they should allow for a wide control of parameters, which in turn should allow for simulations of wide families of Hamiltonians

of interest.

Error correction: For nUDQSs, it is not guaranteed that error correction and fault-tolerant computing is possible.

Efficiency and reliability: All of the above discussion concerning UDQSs applies also to nUDQSs. But there are many novel, open problems associated specifically with nUDQSs, since, *e.g.*, sometimes giving up on universality may result in substantial efficiency gains. For example, universality could be sacrificed in favor of a highly precise and fast gate (a simple example is an external homogeneous field such as used in the experiments of Lanyon and coworkers [30], which in a UDQS might have to be applied as a sequence of one-qubit gates). In particular, it is possible that for some classes of nUDQSs the problems of Trotterization are not as severe as in the case of UDQSs [107].

1.2.3 Open-system digital quantum simulators (OSDQS)

An open-system DQS (OSDQS) is quite a new concept. In contrast to DQSs aimed at Hamiltonian evolutions, OSDQSs are designed to simulate open-system, dissipative dynamics described in the simplest situation by a Markovian Lindblad master equation for the density matrix of a many-body system of interest. OSDQSs can be aimed at continuous-time simulation of open-system dynamics, or at a designed dissipative dynamics toward a specific stationary state, in particular a pure, highly-entangled state [128–130].

The experimentalist who realizes an OSDQS, in contrast to a Hamiltonian DQS, needs to have at his/her disposal some non-unitary, dissipative quantum gates, which mathematically correspond to Lindblad super-operators acting on the density matrix in the master equation. This fact opens a plethora of new questions. For example, while the conditions for controllability of an open quantum systems are under exploration [131], it remains an open question what the universal sets of gates for this type of evolution are. In the case of unitary computing, the universal set of gates allows for realization of arbitrary unitary transformations acting on the (pure) state of the system. In the case of open-system dynamics, a universal set of gates should allow for the realization of an arbitrary completely positive map (CPM) acting on the density matrix of a system. The problem of error correction in this context is unsolved as well. As these examples indicate, in the area of OSDQSs there are more open questions

than answers.

Realizations: In all systems in which the universal sets of quantum gates are available, typically one can also realize dissipative gates by tracing out ancillas and realize in this way an OSDQS. While the first concrete proposals for open-system DQS concerned Rydberg gates [107], the first experimental realizations have been achieved with trapped ions [31]. Good alternatives seem to be atomic ensembles or NMR [132].

Controllability: OSDQSs are typically not universal in the sense of achieving an arbitrary quantum map. Nevertheless many experimental realizations should allow for a wide control of parameters, which in turn should allow for simulations of open-system (Markovian) evolutions for wide families of open systems. As pointed out in Refs. [129, 130], due to the purely dissipative nature of the process, this way of doing quantum information processing exhibits some inherent robustness and defies some of the DiVincenzo criteria for quantum computation. In particular, there is a natural class of problems that can be solved by open-system DQSs or AQSs: the preparation of ground states of frustration-free quantum Hamiltonians.

Error correction: For OSDQSs, it is not known if error correction and fault-tolerant computing is possible as for a UDQS. In fact, the standard schemes for error correction assume that the quantum computer (*i.e.*, DQS) follows a unitary evolution, *i.e.*, dissipation and decoherence are considered as sources of errors, which the error correction is supposed to remove. To our knowledge, there are no works where these are considered as desired, so that error correction is supposed to restore imperfect implementations of them. However, due to the purely dissipative nature of the process, this type of simulation has a certain intrinsic robustness and built-in "error correction." An example can be found in the OSDQS implementation of Kitaev's toric code [31, 107].

Efficiency and reliability: All of the above discussion concerning (n)UDQSs applies also to OSDQSs. However, to date most of these general aspects concerning OSDQSs have not yet been investigated systematically. First results in the Rydberg OSDQS for Kitaev's toric code [107] show that errors in the gates result in effective heating. For the case of approaching the stationary (ground) state of frustration-free Hamiltonians as in Refs. [128–130], the efficiency depends on the size of the gap between the ground state and the excited states, or more precisely, on the real part of the first non-zero eigenvalue of the Lindblad

equation, which determines the rate of approaching the stationary state.

1.3 Analog quantum simulators (AQS)

Similar to the previous section, we now classify AQSs with respect to the four requirements of our definition. AQSs, as DQSs designed to mimic the quantum dynamics of interesting quantum many-body models, typically rely on "always on" inter-particle interactions that are augmented by fast local unitary control. By definition they operate in continuous time, and thus Trotterization problems do not concern them. On the other hand, standard error-correction methods cannot be applied.

1.3.1 Universal analog quantum simulators (UAQS)

Sometimes known as "Hamiltonian simulation," the goal of a universal AQS (UAQS) is to transform – through a well-designed control sequence – a given Hamiltonian acting on a fixed Hilbert space into an arbitrary target Hamiltonian. While not conceived as a practical AQS device, the concept explores an abstract quantum-information-processing system capable of simulating unitary evolution for all (or at least all local) Hamiltonians.

Realizations: To our knowledge there are no concrete proposals for experimental realizations of UAQSs.

Controllability: While for UDQSs the issue is the access to the universal set of quantum gates, for UAQSs the question is what the necessary resources are (not necessarily quantum gates) that allow for the simulation of all Hamiltonian evolutions of interest. Universal control sets (as opposed to universal digital logic gates) that generate an arbitrary Hamiltonian evolution have been studied [133, 134]. Typically, such an approach using "always on" interactions is associated with more limited control than is available in a universal digital quantum computer.

Reliability: UAQSs do not allow for standard error correction and fault tolerance such as holds for UDQSs.

Efficiency and Reliability: Dür *et al.* studied a hybrid construction of always-on interactions with stroboscopic digital control to achieve a universal Hamiltonian simulator via the Trotter construction [135]. They found that

decoherence and analog timing errors can make such a device inefficient. Other issues concerning UAQSs are essentially the same as for non-universal AQSs, so we leave their discussion to the next section. The only difference is that UAQSs, by definition, are capable of performing tests of robustness of the quantum simulations that we propose in the following section. These tests are based on adding disorder or noise in a controlled manner to the simulated Hamiltonian, which for non-universal AQSs may require additional resources.

1.3.2 Non-universal analog quantum simulators (nUAQS), or simply AQS

Non-universal AQSs (nUAQS, or simply AQS) constitute the most popular class of QSs, but despite this fact there is little known about their reliability and efficiency. Therefore, we focus on them in the remainder of this thesis. AQSs are experimental systems that can mimic continuous-time unitary Hamiltonian evolution for a given family of quantum many-body models. Their characteristics are as follows:

Realizations: The most advanced experiments with AQSs have been with ultracold atoms in optical lattices (see Chapter 2.1). The degree of quantum control is maybe even better in trapped-ion systems (see Chapter 2.2). Although so far these are limited to few ions, the first step toward large-scale QSs was recently achieved [136]. In the last years, there has also been substantial progress with other possible candidates for AQS, such as photonic systems [37–41], photonic and polariton systems [43–47], or artificial lattices in solid-state systems [49, 137].

Controllability: Most, if not all, of the proposals and realizations of AQSs allow for at least partial controllability. The paradigm examples are AQSs employing ultracold atoms in optical lattices. Here, the typical controls involve optical lattice parameters (*e.g.*, laser intensity or wavelength), lattice geometry (see Chapters 3 and 4), lattice dimensionality, temperature, and other thermodynamical control parameters, as well as atomic interaction strength and nature (van der Waals interactions are controlled via Feshbach resonances, while dipole interactions by the strength of the dipoles, lattice-site-potential shape, etc.). Further, tunneling can be laser or shaking assisted and can mimic artificial Abelian or even non-Abelian gauge fields (cf. Chapter 5). Moreover, dipolar interactions may lead to non-standard terms in Hubbard models, such as occupation-dependent tunneling (see Chapter 10), and orbital physics can also

be quantum simulated (see Chapters 6 and 9). For more details, see Sec. 2.1 of this thesis and Chapter 4 of the book by Lewenstein, Sanpera, and Ahufinger [8].

Error correction: AQSs do not allow for standard error correction and fault tolerance as applied to DQS.

Efficiency: The issues of reliability and efficiency are essential for the usefulness of any QS. In the context of AQSs, however, there has been little analysis of these problems. Firm criteria on computational complexity and efficiency for AQSs are in general difficult to address and have not yet been established. First of all, they require that for the considered quantum models the classical computational complexity of the static or dynamical properties is known. Unfortunately, in the realm of classical computation, there are few proofs that a given computational problem is outside the class P or not, or even if there is a clear delineation between certain complexity classes.[3]

Reliability: So far, there exists no perfect and rigorous way to assess the reliability of AQSs. There are, however, several complementary approaches. One proposal is to cross validate a variety of different physical systems (*e.g.*, atoms in optical lattices, trapped ions, and superconducting qubits) [102]. The hope is that since every platform has its own set of imperfections, they will agree on the universal properties of the ideal quantum many-body model being simulated. While it remains to be seen whether such universal features would emerge, this approach has a number of shortcomings. For example, there may be models that have only one known implementation, or different implementations may suffer in the same way from imperfections, hence consistently exhibiting features associated with noise rather than with the ideal model.

A more systematic approach is to validate the results of a QS against analytical and numerical predictions in the regime of parameters where such comparison is possible. This was recently demonstrated in experiments with ultracold bosonic and fermionic atoms [11–13]; amazingly, in one case numerical simulations helped to correct the expected experimental temperature by up to 30%. Relying solely on validation from classical calculations, however, would restrict QSs to models in regimes where these efficient classical algorithms exist – that means contradicting the relevance and usefulness requirement, point (a) of our definition of a QS. In general, we desire to operate QSs in regimes whose prop-

[3] As described on p. 12*f*, in recent years there has been considerable progress in understanding that the ground states of 1D gapped systems can be efficiently simulated by classical methods [138–140], and that quantum dynamics is in general computationally hard [100, 101].

erties are difficult to deduce by classical methods, *e.g.*, near or at the critical point of a QPT, or in genuine *terra incognita* regimes. In these regimes, however, many relevant models become *hypersensitive* to perturbations [141, 142], and even small levels of noise may spoil completely the results of the quantum simulation. For example, the capability of an analog quantum-information processor whose dynamics is characterized by quantum chaos (*i.e.*, well described by random matrix theory) can be severely impacted by imperfections [143, 144]. More importantly, this also means that successfully validating a QS in a classically accessible regime does not give certainty about its robustness in regimes which are classically not accessible.

1.3.3 Open-system analog quantum simulators (OSAQS)

Finally, let us mention open-system AQS (OSAQSs). Similar to OSDQSs, OSAQSs are supposed to simulate dissipative dynamics for the density matrix of a many-body system of interest, aimed at a simulation of open-system dynamics or at a designed dissipative dynamics toward a stationary state of interest. Many-body Lindblad master equations relevant for this approach have been studied in the context of evaporative, laser, and sympathetic cooling of degenerate atomic gases. Recently, there has been a revival of interest in such systems due to the prospect of using them for the preparation of interesting pure, highly-entangled states [128–130].

The experimentalist who realizes an OSAQS, in contrast to an AQS has to have to his/her disposal some non-unitary, dissipative quantum mechanism. In a sense, all designed cooling or entropy-reduction methods are of this sort.

Realizations: All AQS systems can, in principle, be used as OSAQSs.

Controllability: OSAQSs are typically not universal in a sense similar to OSDQSs; they allow neither for the simulation of arbitrary (local) Markovian dynamics nor for the preparation of arbitrary states. Nevertheless, in most of the proposals [128–130] or experimental realizations they allow for a wide control of parameters, which in turn allows to simulate open-system (Markovian) evolutions for wide families of open systems.

Error correction: For OSAQSs, it is not known in how far error correction and fault-tolerant computing is possible, similarly to OSDQSs.

Efficiency and reliability: All of the above discussion concerning AQSs ap-

plies also to OSAQSs. But, as in the case of OSDQSs, due to the purely dissipative nature of the process, this type of simulation has a certain amount of intrinsic robustness and built-in "error correction." Still, again as in the case of OSDQSs, most of these general aspects have not yet been investigated systematically.

1.4 Summary

In Tables 1.2 and 1.3, we summarize to which extent digital and analog QSs fulfill the requirements (b-d) of our definition. From our discussion, it becomes clear that currently these aspects are best-studied for UDQSs and nUAQSs.

All of the above considerations clearly lead to the fundamental question: *Can we trust quantum simulators?* One can hope that they are at least more robust than full-fledged quantum computers, since very often the amount of output information required from a QS may be significantly smaller than what one could demand from a universal quantum computer. QSs should provide information about phase diagrams, correlation functions, order parameters, perhaps even critical exponents or nonlocal hidden order parameters. But a common assumption is that these quantities are more robust than what is required for a universal quantum computer. In fact, quantum computer algorithms will typically need to form correlations in a basis unrelated to the physical implementation (qubits). For example, Shor's algorithm [145] develops a wavefunction where the peaks of high probability are equally spaced in the computational basis. In contrast, a QS needs to form correlations that are, in general, physically related to the elementary components of the simulator.

Before we can address the issue of robustness of QSs in more detail, we need to provide some background about the QS architectures considered in this thesis, including their advantages and shortcomings. This forms the subject of the next two chapters. The issue of robustness will also be an recurring leitmotif in Part II, where we present – exemplified on several proposals and experimental realizations – an overview of the current trends in optical-lattice QSs. From these, we can acquire a deeper understanding of these architectures for analog quantum simulation, which will be useful in the discussion of their robustness, which we postpone until Part III.

	digital quantum simulators		
	universal	**non-univ.**	**open**
Realizations	trapped ions, ultracold neutral or Rydberg atoms, CQED, superconducting qubits, ...	same as UDQS	as UDQS (especially trapped ions, ultracold neutral or Rydberg atoms)
Control	full (long-range interactions difficult ?)	partial	partial
Error correction (EC)	with exponential overhead (Trotterization issues)	not known	not known
Reliability	full	not guaranteed	not guaranteed
Efficiency	efficient without EC (for general class of models); much less efficient with EC (Trotterization issues)	at least as UDQS, but may not be provable	can be better than UDQS

Table 1.2: **Classification of DQSs** (universal *vs.* non-universal, Hamiltonian *vs.* open) focusing especially on the requirements (b) to (d) of our definition (Sec. 1.1). Particularly well studied are UDQS. Detailed descriptions are provided in Sec. 1.2.

	analog quantum simulators		
	universal	**non-univ.**	**open**
Realizations	?	many (trapped ions, ultracold atoms, photon and polariton systems, artificial solid-state lattices, ...)	same as nUAQS
Control	full	partial (but long-range interactions "easy")	partial
Error correction (EC)	no standard EC	no standard EC	no standard EC
Reliability	?	? (partial validation schemes available)	? (partial validation schemes available)
Efficiency	?	?	?

Table 1.3: **Classification of AQSs** (universal *vs.* non-universal, Hamiltonian *vs.* open) focusing especially on the requirements (b) to (d) of our definition (Sec. 1.1). Detailed descriptions are provided in Sec. 1.3. Control over a large number of realizations has been achieved for nUAQS. Error-correction, reliability, and efficiency, however, are badly studied for all types of AQSs (question marks).

Chapter 2

Ultracold atoms and ions as analog quantum simulators

There are currently various distinct architectures which are used as AQSs (see Table 1.3, realizations), each with its own advantages and disadvantages. In this thesis, we are concerned with ultracold atoms in optical lattices [26] and trapped ions [34–36], which we describe now in a non-technical manner.

2.1 Ultracold atoms in optical lattices

In 1998, Jaksch *et al.* recognized the possibilities for many-body quantum simulation offered by the recently produced Bose–Einstein condensates (BECs) of atomic gases [70]. As they pointed out, by introducing the BEC in an optical lattice, the Bose–Hubbard model can be simulated. This model accurately describes Cooper pairs tunneling between superconducting grains, and in the limit of strong interaction it can be mapped to an XY quantum magnet.

Perhaps even more important is its fermionic variant, which describes – in the most simplified way – the interplay between kinematics and interactions of electrons in crystal lattices. It has been suggested that this so called Fermi–Hubbard model [87] contains the physics relevant for high-temperature superconductivity [4]. For over three decades, the hope of achieving room-temperature superconductors, which would allow to losslessly conduct electrical current in everyday situations, has driven intense efforts aimed at a thorough understanding of this effect. However, this understanding has not yet been achieved, in part because

we do not know of any efficient way to solve generic fermionic models in more than one dimension. A reliable quantum simulation of such models may, hence, be of extreme practical relevance.

Here, we explain briefly how optical lattices are realized experimentally, and we show why atoms loaded into one are well described by Hubbard models. We also explain the possibly most common measurement technique in these setups, namely time-of-flight imaging. After that, we discuss current research directions as well as the main advantages of optical-lattice experiments as compared to other QS setups. A pedagogical introduction to optical-lattice QSs can be found in the book [8].

2.1.1 Experimental realization of optical lattices

An optical lattice (sketched in Fig. 2.1) is a standing wave of light, created by counter-propagating laser beams which are off-resonant to an atomic transition. The AC-Stark shift leads to an intensity-dependent potential for the atoms, which can be repulsive or attractive, depending on the sign of the detuning between the light wave-length and the atom transition. Using three pairs of counterpropagating beams, one can create a three-dimensional, periodic potential for the atoms. Since in the far field of the laser the only spatial dependence is longitudinal and monochromatic, the resulting periodic potential forms an essentially perfect lattice structure, where the constant distance between two lattice minima is given by the laser wavelength.

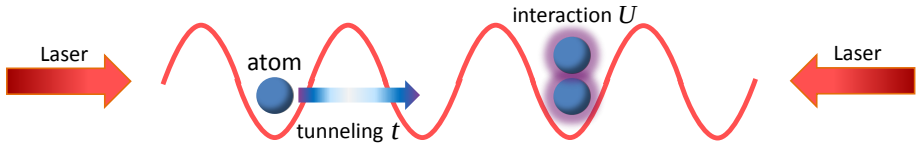

Figure 2.1: **Sketch of an optical lattice.** For not too shallow lattices, atoms are confined to the lattice minima, and the kinetics is exhausted by tunneling processes between these (t). In the most standard scenario, interactions are only important between (bosonic) atoms on the same site (U). This constitutes the famous Bose–Hubbard model, Eq. (2.1).

The time scales achievable in optical-lattice experiments are essentially limited by heating, which can appear due to phase instabilities of the lasers forming the lattice or spontaneous emission following absorption of lattice-laser photons by the atoms [146]. Other sources of noise include fluctuations of the amplitudes

of the lasers, which, however, may be possible to avoid using a dressed optical lattice that is created with the help of an auxiliary excited atomic state [147].

2.1.2 Derivation of the Bose–Hubbard model

The motion of the atoms in the periodic optical lattice is effectively governed by the Hubbard model. Therefore, nowadays it is possible to realize almost perfectly (*i.e.*, under well-controlled approximations) a model which was introduced in the 1960s as an extreme abstraction to describe electrons in solid-state crystals, retaining only the most essential effects [148]. Here, we give a short derivation for the standard version of the bosonic variant of this model. Afterwards, we point out various possibilities for non-standard extensions and improvements, which we will treat later in the thesis.

The Hamiltonian governing the bosonic atom-field operators $\hat{\Psi}(\boldsymbol{r})$ in the optical lattice reads in second quantization

$$\begin{aligned}\hat{\mathcal{H}} &= \int \mathrm{d}^3 r\, \hat{\Psi}^\dagger(\boldsymbol{r}) \left(-\frac{\hbar^2 \nabla^2}{2M_{\mathrm{at}}} + V_{\mathrm{lat}}(\boldsymbol{r}) + \mu + V_{\mathrm{trap}}(\boldsymbol{r}) \right) \hat{\Psi}(\boldsymbol{r}) \\ &+ \frac{1}{2} \int \mathrm{d}^3 r \int \mathrm{d}^3 r' \hat{\Psi}^\dagger(\boldsymbol{r}) \hat{\Psi}^\dagger(\boldsymbol{r}') V_{\mathrm{int}}(\boldsymbol{r} - \boldsymbol{r}') \hat{\Psi}(\boldsymbol{r}') \hat{\Psi}(\boldsymbol{r}) \,. \end{aligned} \tag{2.1}$$

Here, M_{at} is the atom mass, $V_{\mathrm{lat}}(\boldsymbol{r})$ the optical-lattice potential, μ the chemical potential for the atoms, and $V_{\mathrm{trap}}(\boldsymbol{r})$ is an external confinement, typically harmonic, preventing the atoms from laterally escaping the lattice. In the standard scenario, it is sufficient to approximate the interaction between the ultracold bosonic atoms by contact interactions

$$V_{\mathrm{int}}(\boldsymbol{r} - \boldsymbol{r}') = \frac{4\pi a_s \hbar^2}{M_{\mathrm{at}}} \delta(\boldsymbol{r} - \boldsymbol{r}') \,, \tag{2.2}$$

where a_s is the s-wave scattering length, $\hbar$ the reduced Planck constant, and $\delta(\boldsymbol{r} - \boldsymbol{r}')$ the Dirac delta function.

In the presence of the periodic potential, it is convenient to express the field operators $\hat{\Psi}(\boldsymbol{r})$ in terms of the lowest-band Wannier functions $w_i(\boldsymbol{r})$, which form a basis consisting of states that are exponentially localized at the lattice minima i. That is, we expand

$$\hat{\Psi}(\boldsymbol{r}) = \sum_i w_i(\boldsymbol{r}) \hat{b}_i \tag{2.3}$$

with $\hat{b}_i$ the annihilation operator for a boson at site i. It is sufficient to consider only the lowest band if all energy scales are small compared to the excitation

energy to the second band, which in the most typical experimental situations is the case. Expanding the field operators in Hamiltonian (2.1) according to Eq. (2.3), we obtain the Bose–Hubbard model,

$$\hat{\mathcal{H}}_{\mathrm{BH}} = -\sum_{i,j} \frac{t_{ij}}{2} \left(\hat{b}_i^\dagger \hat{b}_j + \mathrm{h.c.}\right) + \sum_i \frac{U_i}{2} \hat{n}_i(\hat{n}_i - 1) - \sum_i \mu_i \hat{n}_i \tag{2.4}$$

where $\hat{b}_i$, $\hat{b}_i^\dagger$ are bosonic annihilation and creation operators, and $\hat{n}_i = \hat{b}_i^\dagger \hat{b}_i$ is the corresponding number operator. The matrix elements U_i and t_{ij}, denote, respectively, on-site interactions and tunneling between sites i and j, and $\mu_i = \mu - V_i^{\mathrm{trap}}$ captures the combined effects of the chemical potential μ and the confining potential. We have the local trap potential

$$V_i^{\mathrm{trap}} = \int \mathrm{d}^3 r \, w_i^\star(\boldsymbol{r}) V_{\mathrm{trap}} w_i(\boldsymbol{r}) \,, \tag{2.5}$$

and the on-site interactions

$$U_i = \frac{4\pi\hbar^2 a_s}{M_{\mathrm{at}}} \int \mathrm{d}^3 r \, |w_i(\boldsymbol{r})|^4 \,. \tag{2.6}$$

Here, we took only same-site contributions into account. In most situations, this is sufficient due to the exponential localization and the resulting small overlap of Wannier functions associated to different sites. The hopping matrix elements read

$$t_{ij} = -\int \mathrm{d}^3 r \, w_i^\star(\boldsymbol{r}) \left(-\frac{\hbar^2 \nabla^2}{2M_{\mathrm{at}}} + V_{\mathrm{lat}}(\boldsymbol{r})\right) w_j(\boldsymbol{r}) \,. \tag{2.7}$$

For shallow lattices, nearest-neighbors matrix elements of t_{ij} can be large, but the strong localization of the Wannier orbitals typically allows to neglect hopping between sites at larger distances.

These terms constitute the standard Bose–Hubbard model, which – although strikingly simple – is already difficult to solve in many situations (see also the discussion on p. 12*f*), making its experimental quantum simulation very useful.

In its derivation, we made a number of (well-controlled) approximations. Consistency with the lowest-band approximation requires a large energy separation from the first excited band, which is achieved if the width of the Wannier functions ζ is small compared to the lattice spacing d, *i.e.*, $\zeta \ll d$. Further, to avoid excitations to the higher bands, the interaction energy $Un_i(n_i - 1)/2$

has to be smaller than the band gap.[1] Additionally, the approximation of the interaction potential as point-like requires $a_s \ll \zeta$.

While in typical situations these conditions can be readily fulfilled, we will discuss in this thesis various scenarios beyond standard cubic optical lattices where the simple Bose–Hubbard model has to be extended, opening the possibility to observe novel phenomena. For example, for large scattering lengths $a_s \sim d$, the Wannier functions are broadened by interaction effects, leading to an admixture of higher bands. This situation can be captured by an effective single-band Hamiltonian with occupation-dependent parameters, as discussed in Chapter 9. There, we also address the situation, where higher-band effects become important due to a large $Un_i(n_i-1)/2$ (while a_s remains small). Higher bands can also be purposefully occupied, which allows to quantum simulate orbital physics and models similar to color models from quantum chromodynamics. We discuss this situation in Chapter 6. We also consider cases where the interaction potential $V_{\mathrm{int}}(\boldsymbol{r}-\boldsymbol{r}')$ is dominated by strong dipolar interactions, extending the Bose–Hubbard model by non-negligible off-site interactions (Chapter 7) and correlated tunneling terms (Chapter 10). Finally, in Chapter 4, we discuss an example where an exotic lattice geometry renders next-to-NN tunneling important.

Already in its most simple formulation, the Bose–Hubbard model shows interesting physics. Most strikingly, it harbors a quantum phase transition between two qualitatively very different regimes. These can be accessed by adjusting the ratio t_{ij}/U_i which is achieved simply by changing the strength of the laser beams forming the optical lattice. Namely, increasing the lattice depth typically *decreases* the tunneling matrix elements t_{ij} exponentially (due to the decreasing overlap of the Wannier functions at neighboring sites i and j), while it *increases* the on-site interactions U_i slowly (*i.e.*, as a power law; this is due to the stronger confinement of the Wannier functions in deeper optical lattices and the resulting stronger on-site overlap).

If the optical lattice is weak ($t_{ij}/U_i \gg 1$), the atoms are free to tunnel between different potential wells, and they retain the long-range coherence that they had in the free BEC cloud. The resulting state is a *superfluid* (SF) with long-range phase coherence and considerable particle-number fluctuations. In the opposite limit of a strong optical lattice ($t_{ij}/U_i \ll 1$), for integer filling, the atoms cannot overcome the barriers between the potential wells and localize

[1] For deep lattices, one can obtain a good estimate for the gap by approximating the lattice sites as harmonic potentials. The gap is then given by the frequency of the associated harmonic oscillator, which is roughly $\sqrt{4E_{\mathrm{rec}}V_0}/\hbar$, where E_{rec} is the recoil energy and V_0 the depth of the optical lattice [70].

at the lattice minima. Coherence between sites is lost and the atoms enter an insulating state, a so called *Mott insulator* (MI). In this state, the particle number at each site has almost no fluctuations and is fixed to an integer value. This SF-to-MI transition has been observed in a ground-breaking experiment [72] only a few years after the theoretical proposal [70].

2.1.3 Time-of-flight imaging of the atom momentum distribution

A typical and well-developed measurement technique allowing to observe the SF–MI transition is the so called time-of-flight (ToF) imaging [24, 149, 150] of the atom momentum distribution. The main idea for this is to abruptly remove the optical lattice and the external confinements holding the atoms, and to let the atoms expand freely. The absorption images of the atom density distribution after a sufficiently large expansion time hold then information about the in-trap off-diagonal correlations, as we show now.

After switching off all confinements, the cloud becomes very dilute very rapidly, so that interactions play only a minor role during the expansion and the cloud expands almost ballistically. Further, after long enough expansion times τ_{ToF} the cloud is spread out sufficiently such that the initial in-trap distribution of the atoms does not play any role and can be approximated as point-like. Then, the atom distribution at time $\tau = \tau_{\mathrm{ToF}}$ is solely given by the initial momentum distribution at time $\tau = 0$,

$$n_b(\boldsymbol{r})\Big|_{\tau=\tau_{\mathrm{ToF}}} = n_b\left(\boldsymbol{k} = \frac{M_{\mathrm{at}}\boldsymbol{r}}{\hbar\tau_{\mathrm{ToF}}}\right)\Big|_{\tau=0} . \tag{2.8}$$

In other words, an atom with initial momentum $\boldsymbol{k}$ moves during time τ_{ToF} from $\boldsymbol{r} \approx 0$ to $\boldsymbol{r} = \hbar\boldsymbol{k}\tau_{\mathrm{ToF}}/M_{\mathrm{at}}$. The in-trap momentum distribution can be expressed in atom-field operators $\hat{\Psi}(\boldsymbol{r})$ as

$$n_b(\boldsymbol{k})\Big|_{\tau=0} = \langle\hat{\Psi}^\dagger(\boldsymbol{k})\hat{\Psi}(\boldsymbol{k})\rangle = \int \mathrm{d}^3r \int \mathrm{d}^3r' \mathrm{e}^{i\boldsymbol{k}\cdot(\boldsymbol{r}-\boldsymbol{r}')} \langle\hat{\Psi}^\dagger(\boldsymbol{r})\hat{\Psi}(\boldsymbol{r}')\rangle . \tag{2.9}$$

In the lowest-band approximation, one can again expand the field operators in Eq. (2.9) in terms of the Wannier functions, Eq. (2.3), yielding for a translationally invariant system with $w_i(\boldsymbol{r}) = w(\boldsymbol{r} - \boldsymbol{r}_i)$,

$$n_b(\boldsymbol{k})\Big|_{\tau=0} = |w(\boldsymbol{k})|^2 \sum_{i,j} e^{-i\boldsymbol{k}\cdot(\boldsymbol{r}_i-\boldsymbol{r}_j)} \langle\hat{b}_i^\dagger\hat{b}_j\rangle , \tag{2.10}$$

where

$$w(\boldsymbol{k}) = \int \mathrm{d}^3 r \, \mathrm{e}^{i\boldsymbol{k}\cdot\boldsymbol{r}} w(\boldsymbol{r}) \tag{2.11}$$

is given by the Fourier transform of the Wannier orbitals. The Wannier envelope $|w(\boldsymbol{k})|^2$ has *a priori* nothing to do with the Hubbard model, but is a non-universal feature reflecting the form of the lattice-site potentials.

Equations (2.10) and (2.8) map the in-trap correlations $\langle \hat{b}_i^\dagger \hat{b}_j \rangle$ onto the real-space distribution $n_b(\boldsymbol{r})$ after free expansion. The resulting distribution can be understood as the interference pattern of elementary partial waves originating from all lattice sites. $n_b(\boldsymbol{r})$ can be measured in a straightforward manner by shining resonant light through the expanded atom cloud. The light, which can be observed by a CCD camera, will be attenuated corresponding to the density of atoms. This technique requires a sufficiently large number of atoms for good absorption pictures and sufficient space in the vacuum chamber for reaching large expansion times. Also, the ToF measurement is destructive. It has, however, the huge advantage that the resolution of standard imaging systems is sufficient to observe the expanded atom cloud.

The off-diagonal correlations $\langle \hat{b}_i^\dagger \hat{b}_j \rangle$ measured in this way have proven an important observable, as they allow to distinguish the primary phenomenon occurring in typical optical lattices, namely the MI–SF quantum phase transition [72]: In the MI phase there are no off-diagonal correlations, and the images reveal a smeared-out cloud with no particular features (Fig. 2.2b).[2] In the SF phase, on the other hand, the atoms condense at certain $\boldsymbol{k}$ vectors and the resulting off-diagonal long-range correlations appear as strong peaks at the corresponding positions (modulo reciprocal lattice vectors) in the momentum distribution (Fig. 2.2a and c). The contrast of the resulting ToF interference patterns is an important observable for quantifying long-range coherence.

2.1.4 Advantages and future directions

One huge advantage of optical-lattice experiments is the large number of atoms which can be controlled, reaching several thousands. Until recently, however, a big handicap was that only global measurements were possible, such as the ToF images described above. However, a few years ago single-site manipulation and readout has been achieved [11, 152–154], allowing *in-situ* measurements of many-body states. These give access to the diagonal correlations, thus yielding

[2] Except the features given by the Wannier envelope. In most cases, these are trivial, but in Chapter 6.3 we show that they can allow to distinguish different quantum phases of fermions in the p-band of an optical lattice.

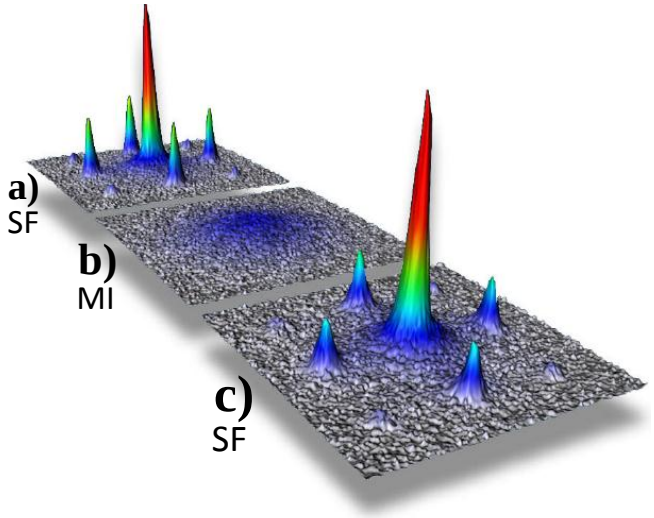

Figure 2.2: **Typical experimental time-of-flight images** (from the cover of the PhD thesis of Markus Greiner [151]). **(a) At low lattice depths,** the system is in a SF with coherence between sites. The atoms are condensed at specific $\boldsymbol{k}$ vectors, resulting in strong peaks in the momentum distribution. **(b) For strong lattices,** tunneling is suppressed, and the atoms enter a Mott-insulating phase. Correlations between sites are lost, and the atoms are localized at individual lattice minima, resulting in a broad, featureless momentum distribution. **(c) Ramping back to low lattice depths** re-establishes a SF state, and the characteristic peaks associated to long-range correlations are restored. This panel demonstrates that the loss of coherence is not due to experimental imperfections but to a quantum phase transition.

important information complementary to the off-diagonal correlations recorded in ToF measurements.

Another feature of optical lattices is their extreme cleanness and regularity. This goes so far that effects of disorder can only be observed if they are introduced "by hand." The control over disorder has now achieved very sophisticated levels [155], which has allowed to observe for the first time Anderson localization of matter waves [156–158], an effect which had been predicted theoretically almost fifty years before [159].

A further advantage is that the dimensionality of optical lattices can be tuned easily. By ramping up the strength of one of the counter-propagating laser pairs, large potential barriers along 2D plains can be created, prohibiting tunneling along this direction, and the system becomes effectively two-dimensional. Increasing similarly the strength of one of the other pairs renders the system effectively one-dimensional. Further, the concept can be easily extended to more exotic geometries than the standard, simple cubic optical lattice. To this, the angle between the laser beams and their polarization has merely to be chosen appropriately. Current research effort focuses in particular on triangular [160] (see Chapter 3), hexagonal [161, 162] (see Chapters 4 and 5), and kagome lattices [163] (see also Chapter 5).

Since the early stages, optical lattice experiments have achieved a considerable maturity, making it to date possibly the most versatile QS architecture. For a pedagogical derivation and a description of the manifold of models simulatable in optical lattices, see the recent book [8]. The Hubbard model is perhaps the simplest lattice model capturing the interplay between interactions and kinetics, but in recent years, it has been extended in many different directions. These include quantum simulation of quantum magnetism [16, 164, 165] (see Chapter 3), the study of higher-band effects [166] (see Chapters 6 and 9), or the trapping of atoms or molecules with permanent dipole moments [167], allowing the investigation of long-range interacting systems (see Chapter 10 and also Chapter 7). Further, neutral atoms do not feel the effect of a real magnetic field as electrons do, requiring clever schemes to create "artificial" magnetic fields [10, 20]. Taking this even further, also artificial (Abelian and non-Abelian) gauge fields can now been implemented [22, 23], see Chapter 5. Other recent developments include experiments on Fermionic atoms [13, 15, 18, 87, 154, 168–171] or dynamics [19, 21, 172], which also demonstrated effects similar to the Kibble–Zurek mechanism [173]. In all of these arenas, exciting progress can be expected in the next years.

2.2 Trapped ions

Another promising architecture for quantum simulations are trapped ions. The corresponding technology has been developed for several decades, mostly for precision metrology such as for mass spectroscopy or atomic clocks. In the mid-1990's, it experienced an important boost due to the increasing interest in quantum computing, and in particular to the first proposal for a universal quantum computer based on trapped ions, the famous Cirac–Zoller article [174]. In 2004, Porras and Cirac proposed to use this technological know-how for quantum simulations of quantum spin models [175]. In a different context, similar spin models were derived earlier by Mintert and Wunderlich [176], who studied the possibility of individual ion addressing using inhomogeneous magnetic fields.

2.2.1 Trap setups for ultracold ions

To appropriately manipulate the ions, they have to be held stably within a predefined experimental area. But how can an ion trap be realized, when Earnshaw's theorem forbids to create a stable potential minimum for charged particles through electrostatic forces? One way to circumvent this obstacle was found by Paul and Steinwedel in the 1950's; they demonstrated that an *effective* potential minimum for charged particles can result as the time-average of quickly-oscillating, *time-dependent* electric fields. For this work, Paul received the Nobel prize in physics in 1989. The trapping device relying on this idea, known under the name "Paul trap," is currently the standard setup for trapped-ion QSs (although alternative trapping devices such as Penning traps or surface traps are making giant advances in recent years, see below).

A Paul trap typically consists of four parallel rods; in one realization, one applies an ac current on two opposing rods, while the other two are grounded (see Fig. 2.3a). As explained in Fig. 2.3b, this can create a stable trapping potential, confining the ions to a tube parallel to the rods. To prevent an escape of the ions along the longitudinal direction, one adds end caps at a static voltage. In a strong enough trap, and at sufficiently low temperatures, the repulsive interactions between ions in combination with the trapping potential will arrange them in a periodic structure, a so called Coulomb crystal. Large enough crystals are sufficiently homogeneous to allow quantum simulation of periodic lattice models, where the ion positions act as lattice sites. Natural lattice structures arising this way are linear chains (indicated by red bullets in Fig. 2.3a), zig-zag chains [177], helical structures and disk-shaped triangular lattices [178], and even more complex patterns in three dimensions [179].

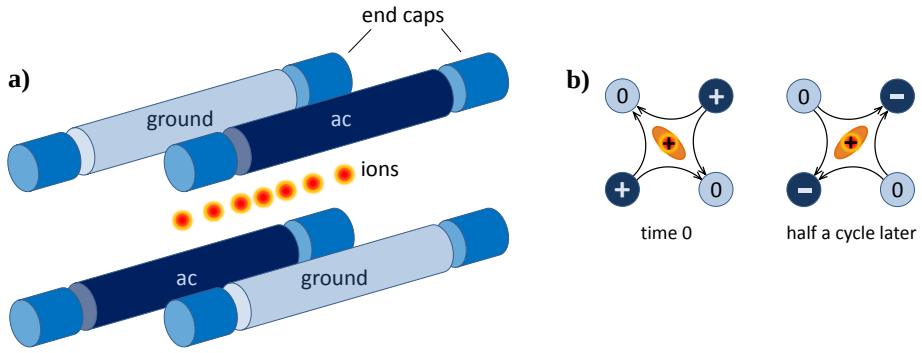

Figure 2.3: **(a) Sketch of a Paul trap.** It typically consists of four rods, with two opposing ones at ac voltage (dark) and the other two grounded (light color). End caps at dc voltage prevent longitudinal escape of the ions. **(b) Cut through the central rods, explaining the trapping principle.** The alternating voltage leads to a periodic repetition of focusing and anti-focusing forces (indicated by the orange ellipsoid). If the frequency is high enough, the ions (sketched for positive charge) cannot follow the force and get trapped in the center due to their inertia. The black lines exemplify field lines.

2.2.2 Advantages, disadvantages, and current directions

Trapped ions have a number of advantages. Control over state preparation, manipulation, and read-out can exceed the one achieved in typical setups consisting of ultracold neutral atoms. In particular, single-site addressability is straight-forward, since – due to the strong electro-static repulsion – the distance between ions is on the order of micrometers. For neutral atoms in optical lattices, this requires considerable additional effort involving sophisticated optical instruments [11, 152–154]. Moreover, because of the long-range nature of Coulomb-interactions, long-range interactions are achieved easily [175, 180, 181] (see Chapter 7), without the large experimental effort necessary in ultracold-atom setups.

Unfortunately, Paul traps cannot be easily scaled to large numbers of ions, and current experiments are typically carried out with on the order of 10 ions. A related drawback is that currently it is difficult to extend the quantum simulation ideas to simple, regular three dimensional systems. To reach the large numbers necessary for a useful quantum simulation, novel technologies are under development, where QSs are profiting enormously from the efforts aimed at

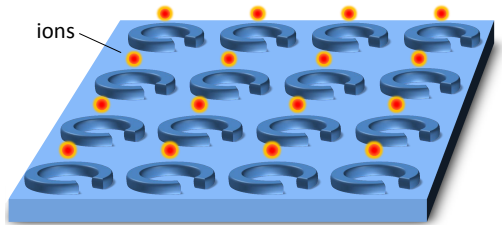

Figure 2.4: **Sketch of a surface microtrap array.** Engineering an electrode design on a surface (here sketched as individual microcoils à la Chiaverini *et al.* [182]), can allow to reach scalable trapping architectures of arbitrary geometry.

scalable quantum computers. A particularly promising approach is the use of micro-fabricated surface traps [182] (see Fig. 2.4), which could allow to reach practically arbitrary lattice geometries in a scalable manner [183]. Another promising trapping technology is Penning traps [184], where recently the first step has been done towards quantum simulation with trapped ions on large scales [136]. Further, recent developments in trapping ions solely by optical means [185, 186] open a whole new avenue, including the possibility of bringing neutral atoms and trapped ions together in a single setup, thus amongst others allowing the study of charge-transfer processes.

To date, a large variety of quantum simulations employing trapped ions has been proposed, some of which have been implemented experimentally (see the reviews [34–36]). The list includes neural networks [187, 188], controlled disorder [189], the Frenkel–Kontorova model [190], the Kibble–Zurek scenario [191], relativistic effects related to the Dirac equation [32, 33, 192, 193], Hawking radiation [194, 195], or unitary random quantum walks [196]. Further, the ion vibrations can simulate Bose–Einstein condensates [197], SF–MI transitions and the Tonks–Girardeau gas [198], and non-Abelian gauge fields [199]. Also, new proposals have extended the initially basic spin models, amongst others, to spin–boson models [200], models with spins larger than $S = 1/2$ [201], strongly frustrated models [202, 203] (see also Chapter 3), and models with long-range interaction [180, 181, 204] (see also Chapter 7). And, indeed, the quantum spin models that sparked the interest in trapped-ion quantum simulation [175] have been realized in proof-of-principle experiments [27–29].

While this thesis focuses on AQSs, important breakthroughs are currently being achieved on the front of trapped-ion implementations of DQSs. Perhaps most noteworthy are the experimental implementations of a universal [30] and of an open-system DQS [31].

Part II

Quantum Simulators – Calculation and Experiment

In this part of the present thesis, we discuss several new directions of quantum simulations which go beyond standard optical lattices. Our aim is not so much to treat each subject exhaustively, but rather to give an overview of the extremely diverse and rich physics attainable in ultracold-atom and trapped-ion quantum simulators. The presented models have in common that they pose considerable challenges for analytical or numerical methods, thus making them relevant targets for quantum simulation.

In particular, we describe	Chapter
how frustrated lattice geometries may lead to exotic quantum-disordered phases,	3
how spin-dependent lattices allow to tune the many-body behavior of spin mixtures, including forced antiferromagnetic and supersolid states,	4
how combining exotic lattice geometries with time-periodic driving generates topological and quantum spin Hall insulators as well as non-Abelian gauge fields,	5
how fermions in higher bands achieve ground states which break time-reversal symmetry,	6
how combining trapped ions and optical lattices permits to quantum simulate long-range interactions, and	7
how one can engineer spin correlations in optical lattices, in particular in arrays of atomic micro-ensembles, using quantum non-demolition measurements.	8

The last chapter is an exception, as it does not describe how to realize a specific model. Instead, it rather presents a generally applicable method to manipulate quantum correlations in optical lattices. As such, it may be useful for engineering states appearing in the models of the other chapters. We delegate technical details to Part IV, so that the chapters contained here can focus on presenting the considered system, its relevance in a wider context, and our results.

Chapter 3

Frustrated quantum magnetism with ultracold bosons in a triangular lattice

As described in Chapter 2.1, ultracold neutral atoms, confined in optical lattices allow the quantum simulation of a large variety of strongly-correlated systems. A particularly appealing perspective in this arena is the study of lattice-boson models with *frustration*, because, as mentioned in Chapter 1.1, from a theoretical point of view, bosonic frustration in the presence of strong interparticle interactions on a lattice represents a very hard problem in dimensions $d > 1$. Indeed, controlled perturbative expansions are not available in the strongly correlated regime, semiclassical methods break down in the presence of strong quantum fluctuations enhanced by frustration, and in QMC simulations the so called sign problem occurs. Hence, the implementation of bosonic frustration in optical-lattice experiments would represent a fundamental instance of a relevant quantum simulation.

In general, one calls a system frustrated if not all constraints (in our case, for the energy) can be optimized at the same time. In the standard situation, bosons in an optical lattice, described by the simple Bose–Hubbard model (2.4) are not frustrated. Geometrical frustration can arise, however, if the hopping

matrix elements are, contrary to the usual case, *positive*, $-t_{ij} > 0$,

$$\hat{\mathcal{H}}_{\mathrm{BH}} = \sum_{\langle i,j \rangle} \frac{\tilde{t}_{ij}}{2} \left(\hat{b}_i^\dagger \hat{b}_j + \mathrm{h.c.} \right) + \frac{U}{2} \sum_i \hat{n}_i (\hat{n}_i - 1) \tag{3.1}$$

where we defined $\tilde{t}_{ij} = \left| \tilde{t}_{ij} \right| = -t_{ij}$. Further, $\hat{b}_i$, $\hat{b}_i^\dagger$ are bosonic operators, $\hat{n}_i = \hat{b}_i^\dagger \hat{b}_i$ the corresponding number operator, and $\langle i, j \rangle$ represents pairs of NN sites.

To illustrate how the sign change in the Bose–Hubbard model leads to frustration of the kinetic energy, consider the state of a single boson spread over two sites, i and j, $|\psi\rangle = \left(|1_i, 0_j\rangle + \mathrm{e}^{i\varphi} |0_i, 1_j\rangle \right) / \sqrt{2}$. The interaction terms in the Bose–Hubbard Hamiltonian (3.1) are unaffected by the relative phase φ, but the tunneling term depends on it, $\langle \psi | \tilde{t}_{ij} \left(\hat{b}_i^\dagger \hat{b}_j + \hat{b}_j^\dagger \hat{b}_i \right) | \psi \rangle = \tilde{t}_{ij} \cos\varphi$. For the standard situation of ferromagnetic tunneling, $\tilde{t}_{ij} < 0$, the energy is minimized if the relative phase between all sites vanishes, leading to Bose-condensation in the zero mode. For antiferromagnetic (AFM) tunneling, $\tilde{t}_{ij} > 0$, on the other hand, the energy of each bond is minimal if the relative phase is $\varphi = \pi$.[1] As illustrated in Fig. 3.1a, on a triangle, *e.g.*, this cannot be fulfilled for all bonds, because the single-valuedness of the wave function demands that the phase around a plaquette be a multiple of 2π. If, *e.g.*, the wave function collects a phase of π along the diagonal bonds (dashed), the phase along the horizontal bond (solid) is 0, which is energetically maximally disfavored. Hence, the ground-state wavefunction has to find a compromise, which in extended lattices can lead to novel phases with spiral order properties or even quantum-disordered phases. On the other hand, simple square lattices with only nearest-neighbor (NN) tunneling are not frustrated (along every bond a phase of π can be picked up, leading to a total phase around a plaquette of 4π). The study of frustration effects requires more exotic lattice geometries than that.

In an optical-lattice experiment, frustration in the intersite hopping amplitudes (*i.e.*, inversion of the sign of the hopping matrix elements) can be created, for instance, by coupling the bosons to a (artificial) magnetic field via Raman schemes [205, 206], where fundamental steps have recently been taken experimentally [10, 20, 23]. This is formally equivalent to a description of the system in a rotating reference frame, which implies that the system is subject to the spontaneous appearance of vortices. Such vortices can form ordered arrays (vortex crystals) coexisting with Bose condensation, which consequently takes place

[1] A generalization to an arbitrary number N_b of bosons is straightforward. In that case, the SF state for two sites can be written as $|\Psi_{N_\mathrm{b}}\rangle \propto \left(\hat{b}_i^\dagger + \mathrm{e}^{i\varphi} \hat{b}_j^\dagger \right)^{N_\mathrm{b}} |0_i, 0_j\rangle$. The expectation value of the tunneling operator $\tilde{t}_{ij} \left(\hat{b}_i^\dagger \hat{b}_j + \hat{b}_j^\dagger \hat{b}_i \right)$ is also for this wave function $\propto \tilde{t}_{ij} \cos\varphi$.

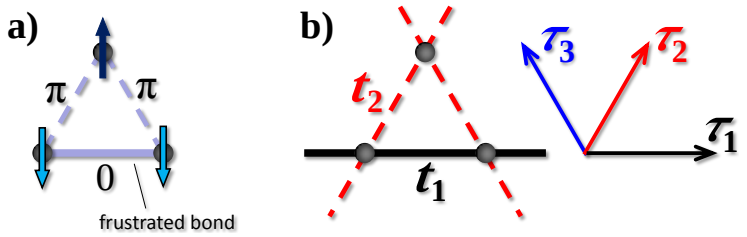

Figure 3.1: **(a) Illustration of frustration.** If the bosons pick up a phase of π along the dashed bonds (the energetically optimal case for positive hopping matrix elements), the relative phase along the horizontal, solid bond has to be 0, which is energetically least favored. Therefore, not all three bonds of a triangle can minimize their energy simultaneously. (Phases are illustrated by blue arrows, sites by gray bullets.) **(b) The geometry of the SATL** is an extrapolation of the triangle to an extended lattice, with two different bond strengths, $\tilde{t}_{\boldsymbol{\tau}_1} = t_1$ along $\boldsymbol{\tau}_1 = \boldsymbol{e}_x$ and $\tilde{t}_{\boldsymbol{\tau}_{2,3}} = t_2$ along $\boldsymbol{\tau}_{2,3} = \left(\boldsymbol{e}_x \pm \sqrt{3}\boldsymbol{e}_y\right)/2$ (the lattice spacing is set to 1). This strongly frustrated lattice exhibits quantum disorder.

in a macroscopic wavefunction sustaining persisting circulating currents (see Ref. [207] and references therein); or they can even disrupt condensation completely, and lead to a disordered insulating state [208]. Such disordered states are notoriously difficult to study theoretically, which makes them relevant targets for quantum simulators (QSs).

Alternatively, and experimentally maybe more straightforward, one can employ a periodical shaking of the optical lattice to invert the sign of the hopping matrix elements [22, 209–211]. Using this, the group of K. Sengstock has already realized frustrated hoppings [17] (although in the weakly-interacting, classical regime). We will describe in the next section, how such a lattice shaking can achieve the desired sign change. A similar model as Eq. (3.1) can also be realized in ion traps with anharmonicities in the local trapping minima [202]. Hence, we can expect exciting progress in this respect in the near future.

In the following, we will in particular analyze the frustrated model (3.1) in the extreme quantum limit of infinite repulsion $U \to \infty$ and half filling $\langle \hat{n}_i \rangle = 1/2$. In this limit, the Holstein–Primakoff transformation

$$\hat{n}_i \;\to\; S_i^z + 1/2\,, \tag{3.2a}$$

$$\hat{b}_i^\dagger \;\to\; S_i^+\,, \quad \hat{b}_i \;\to\; S_i^- \tag{3.2b}$$

maps the Bose–Hubbard model to the $S = 1/2$ XY Hamiltonian [212]

$$\hat{\mathcal{H}}_{\mathrm{S}} = \sum_{\langle i,j \rangle} \tilde{t}_{ij} \left(S_i^x S_j^x + S_i^y S_j^y \right) , \tag{3.3}$$

where S_i^μ is the μ^{th} component of the $S = 1/2$ spin operator acting on site i. In two dimensions, frustrated spin models such as Eq. (3.3) exhibit ground states with spiral order, the magnetic counterpart to the aforementioned Bose-condensed states with vortex arrays. In special circumstances, the interplay between quantum fluctuations and frustration may lead to disordered *spin-liquid* states, which correspond to bosonic insulating phases. XY antiferromagnets can also describe the physics of Cooper pairs in arrays of ultra-small Josephson junctions [213], and they can be regarded as the limiting case of AFM Hamiltonians with planar anisotropy in the couplings, relevant to the description of frustrated AFM materials.[2]

In the next section, we explain how the sign change and thus the frustration of the hopping matrix elements in Eq. (3.1) can be achieved in optical-lattice experiments simply by shaking the lattice. Then, as an example for the exotic quantum effects expected due to frustration in the strongly interacting regime, we discuss in Sec. 3.2 the ground-state phase diagram of the XY quantum antiferromagnet on the spatially anisotropic triangular lattice (SATL). There, we find several candidate regions for exotic quantum-disordered behavior. In Sec. 3.3, we study the experimentally relevant finite-temperature phase diagram, on which the ground-state phases clearly imprint their properties. In Sec. 3.4, we show that a generalization of the model to the spatially *completely* anisotropic triangular lattice (SCATL) can give valuable insight into the physics and stability of the putative quantum-disordered phases. We summarize our findings for these frustrated quantum spin models in Sec. 3.5. The prospect of observing these exotic phases makes the considered models important targets for QSs. Finally, we discuss in Sec. 3.6 the SATL in the limit of weak interactions, which is relevant to current experiments with ultracold atoms. In that section, we also provide some concluding remarks for this chapter.

[2] For a discussion of magnetic materials with Heisenberg interactions, see Chapter 14.2.

3.1 Realizing the positive-hopping Hubbard model via shaking

As we explain now, a simple periodical driving of the optical lattice can invert the negative sign typically associated with hopping matrix elements in optical-lattice experiments, leading to the Bose–Hubbard model (3.1) with frustrated hopping. A publication of this discussion is in preparation [214].

3.1.1 The shaken lattice system

Consider a gas of ultracold neutral atoms subjected to an optical lattice potential $V_{\mathrm{lat}}(\boldsymbol{r})$ as well as to a uniform force $\boldsymbol{F}_\omega(\tau)$ that for times $\tau \geq 0$ is time periodic,[3]

$$\boldsymbol{F}_\omega(\tau + T) = \boldsymbol{F}_\omega(\tau)\,, \tag{3.4}$$

with $T = \frac{2\pi}{\omega}$, and that averages to zero over a period,

$$\frac{1}{T}\int_0^T \mathrm{d}\tau\, \boldsymbol{F}_\omega(\tau) = 0. \tag{3.5}$$

The force has been switched on before $\tau = 0$ in some way, after the system had been prepared at time τ_p, $\tau_p < 0$.

If the lattice is sufficiently deep, such that its band gap is large compared to any other energy scale such as temperature, chemical potential, or frequency and strength of the periodic forcing, it is justified to describe the system within a Wannier-type basis comprising a single localized state i at each lattice minimum $\boldsymbol{r}_i$. Following the steps in Chapter 2.1 leading to the Bose–Hubbard model (2.4), we can arrive at the driven Hubbard-type Hamiltonian [70]

$$\hat{\mathcal{H}} = -\sum_{\langle ij\rangle} t_{ij}\hat{b}_i^\dagger \hat{b}_j + \sum_i \frac{U}{2}\hat{n}_i(\hat{n}_i - 1) + \sum_i v_i^\omega(\tau)\hat{n}_i. \tag{3.6}$$

Here, we assume bosonic particles described by annihilation and number operators $\hat{b}_i$ and $\hat{n}_i = \hat{b}_i^\dagger \hat{b}_i$, respectively, acting on the lattice site i.[4] For deep lattices, the kinetics is exhausted by tunneling between pairs $\langle ij\rangle$ of neighboring lattice sites, described by negative tunneling matrix elements $-t_{ij} < 0$. The second term of the Hamiltonian comprises on-site interactions with strength U. Finally,

[3] We use τ for the time variable to avoid confusion with the hopping matrix elements t_{ij}.

[4] The restriction to bosons is not crucial and the results of this section can easily be generalized to the case of fermions or mixtures of different particle species or spin states.

the last term describes the time-periodic force in terms of the time-dependent potential

$$v_i^{\omega}(\tau) = -\boldsymbol{F}_{\omega}(\tau)\cdot\boldsymbol{r}_i = M_{\mathrm{at}}\ddot{\boldsymbol{x}}(\tau)\cdot\boldsymbol{r}. \tag{3.7}$$

A convenient way to realize such a situation experimentally is to "shake" an optical lattice along a time-periodic orbit $\boldsymbol{x}_{\omega}(\tau)$, $\boldsymbol{x}_{\omega}(\tau+T)=\boldsymbol{x}_{\omega}(\tau)$, such that in the laboratory frame of reference the particles are subjected to the potential $V_{\mathrm{lat}}(\boldsymbol{r}-\boldsymbol{x}(\tau))$ [215]. As a consequence, in the reference frame co-moving with the lattice, particles of mass M_{at} are subjected to the uniform inertial force[5]

$$\boldsymbol{F}_{\omega}(\tau) = -M_{\mathrm{at}}\ddot{\boldsymbol{x}}_{\omega}(\tau). \tag{3.8}$$

We are interested in lattice shaking with frequencies on the order of the recoil energy (up to a few kilo Hertz) and amplitudes on the order of a lattice constant (a micron or less). Such a lattice motion can be achieved, *e.g.*, via acousto-optical modulators to control in a time-dependent fashion the detuning between the different laser beams creating the optical lattice [17, 22, 216]. If the lattice is created by retroreflecting laser beams at a mirror, the lattice motion can also be achieved by mounting the mirror on a Piezo actuator and moving it back and forth [215].

The Hubbard description (3.6) is possible only in the reference frame moving with the lattice. This simplification relies on the fact that the particles are dragged with the minima of the deep lattice while the lattice is translated. Particles can move relative to the lattice only via tunneling between the minima of the deep lattice.

3.1.2 Tunnel modification by off-resonant shaking

To avoid undesired excitations and associated heating effects, we consider the regime of off-resonant forcing, with the frequency large compared to the energy scales given by both kinetics and interactions,

$$\hbar\omega \gg |t_{ij}|, |U|, \tag{3.9}$$

[5] For a single particle described by the wave function $\psi(\boldsymbol{r},\tau)$ and the Hamiltonian $h(\boldsymbol{r},\tau) = \frac{\boldsymbol{p}^2}{2M_{\mathrm{at}}} + V_{\mathrm{lat}}(\boldsymbol{r}-\boldsymbol{x})$, the transformation to the co-moving frame, $\psi \to u\psi$ and $h \to uhu^{\dagger} - i\hbar u\dot{u}^{\dagger} = \frac{\boldsymbol{p}^2}{2M_{\mathrm{at}}} + V_{\mathrm{lat}}(\boldsymbol{r}) - M_{\mathrm{at}}\ddot{\boldsymbol{x}}\cdot\boldsymbol{r}$, is accomplished by the unitary operator $u = \exp\big(-\frac{i}{\hbar}\int_{-\infty}^{t}\mathrm{d}\tau'\,\frac{M_{\mathrm{at}}\ddot{\boldsymbol{x}}^2(\tau')}{2} + \frac{i}{\hbar}M_{\mathrm{at}}\dot{\boldsymbol{x}}(\tau)\cdot\boldsymbol{r}\big)\exp\big(\frac{i}{\hbar}\boldsymbol{x}(\tau)\cdot\boldsymbol{p}\big)$, with $\boldsymbol{p} = -i\hbar\nabla_{\boldsymbol{r}}$. The interactions between many particles, depending on relative coordinates only, are not altered when transforming to the co-moving frame.

while still being lower than the band gap, $\hbar\omega \ll E_{\mathrm{G}}$. At the same time, we allow for strong forcing, with amplitudes $K_{ij} \sim \hbar\omega$ that can be much larger than $|U|$ and $|t_{ij}|$. Here, K_{ij} is defined as the amplitude of the potential modulations

$$v_{ij}^{\omega}(\tau) \equiv v_i^{\omega}(\tau) - v_j^{\omega}(\tau) = M_{\mathrm{at}}\ddot{\boldsymbol{x}}(\tau)\cdot\boldsymbol{r}_{ij} \tag{3.10}$$

between two neighboring sites i and j, with $\boldsymbol{r}_{ij} = \boldsymbol{r}_i - \boldsymbol{r}_j$.

At this point, it is instructive to perform a unitary transformation. If the state $|\psi(\tau)\rangle$ describes the time-evolution of the system as it is determined by the Hamiltonian (3.6), we can transform to a Dirac picture and "split off" the time evolution as it would be generated solely by the forcing. Namely,

$$|\psi(\tau)\rangle = \hat{U}_{\omega}(\tau)|\psi'(\tau)\rangle\,, \tag{3.11}$$

with $\hat{U}_{\omega}(\tau) = \exp\big(-\frac{i}{\hbar}\int_{\tau_p}^{\tau}\mathrm{d}\tau'\hat{\mathcal{H}}_{\omega}(\tau')\big)$, where $\hat{\mathcal{H}}_{\omega}(\tau)$ denotes the driving term $\sum_i v_i^{\omega}(\tau)\hat{n}_i$ of the Hamiltonian (3.6). We introduce

$$\boldsymbol{A}_{\omega}(\tau) = -\int_{\tau_p}^{\tau}\mathrm{d}\tau'\,\boldsymbol{F}_{\omega}(\tau') = M_{\mathrm{at}}\dot{\boldsymbol{x}}_{\omega}(\tau)\,, \tag{3.12}$$

where to evaluate the integral, we have used that, before the shaking has been switched on, the lattice had been at rest, $\dot{\boldsymbol{x}}_{\omega}(\tau_p) = 0$. Further, we define

$$\chi_i^{\omega}(\tau) = \frac{1}{\hbar}\boldsymbol{r}_i\cdot\boldsymbol{A}_{\omega}(\tau)\,. \tag{3.13}$$

With this, we can write

$$\hat{U}_{\omega}(\tau) = \exp\left(-i\sum_i \hat{n}_i\chi_i^{\omega}(\tau)\,.\right) \tag{3.14}$$

The time-evolution of $|\psi'(\tau)\rangle$ is then governed by the Hamiltonian

$$\begin{aligned}\hat{\mathcal{H}}'(\tau) &= \hat{U}_{\omega}^{\dagger}(\tau)\hat{\mathcal{H}}(\tau)\hat{U}_{\omega}(\tau) - i\hbar\hat{U}_{\omega}^{\dagger}(\tau)\big[\mathrm{d}_{\tau}\hat{U}_{\omega}(\tau)\big] &(3.15)\\ &= -\sum_{\langle ij\rangle} t_{ij}\mathrm{e}^{i\chi_{ij}^{\omega}(\tau)}\hat{b}_i^{\dagger}\hat{b}_j + \sum_i\frac{U}{2}\hat{n}_i(\hat{n}_i-1)\,, &(3.16)\end{aligned}$$

with phases

$$\chi_{ij}^{\omega}(\tau) = \chi_i^{\omega}(\tau) - \chi_j^{\omega}(\tau)\,. \tag{3.17}$$

The operator $\hat{U}_\omega(\tau)$ has a clear physical interpretation. Namely, it translates, in a time-dependent oscillatory fashion, all particles in quasimomentum by $\Delta p_\omega(\tau) = -\boldsymbol{A}_\omega(\tau)$. Since

$$\frac{1}{T}\int_\tau^{\tau+T} \mathrm{d}\tau'\, \boldsymbol{A}_\omega(\tau') = 0\,, \tag{3.18}$$

[use the definition of $\boldsymbol{A}_\omega(\tau)$, Eq. (3.12), and $\boldsymbol{x}_\omega(\tau+T) = \boldsymbol{x}_\omega(\tau)$] the induced momentum shift averages to zero in time. Equation (3.18) is a consequence of the fact that the forcing is created inertially by time-periodic lattice shaking, starting from a lattice initially at rest, since we used the condition $\dot{\boldsymbol{x}}_\omega(\tau_p) = 0$ to arrive at Eq. (3.12). The property (3.18) turns out to be quite convenient. Evaluating it for $\tau = 0$, and again using the definition (3.12), we can rewrite the integral appearing in Eq. (3.18) as

$$-\int_{\tau_p}^{0} \mathrm{d}\tau' \boldsymbol{F}_\omega(\tau') = \frac{1}{T}\int_0^T \mathrm{d}\tau \int_0^\tau \mathrm{d}\tau' \boldsymbol{F}_\omega(\tau')\,. \tag{3.19}$$

We can incorporate this to be able to work without integrating over the switching history ($\tau_p \le \tau \le 0$) and without specifying the way the force $\boldsymbol{F}_\omega(\tau)$ is created, simply by defining the unitary transformation (3.14) through [164]

$$\boldsymbol{A}_\omega(\tau) = -\int_0^\tau \mathrm{d}\tau'\, \boldsymbol{F}_\omega(\tau') + \frac{1}{T}\int_0^T \mathrm{d}\tau \int_0^\tau \mathrm{d}\tau'\, \boldsymbol{F}_\omega(\tau')\,. \tag{3.20}$$

Under the assumption of off-resonant forcing, Eq. (3.9), we can now apply a simple approximation to the dynamics generated by $\hat{\mathcal{H}}'(\tau)$. The rate at which the state $|\psi'(\tau)\rangle$ changes in time (defined as the rate at which occupations and phases at a site i change) is determined by the amplitudes of the terms of $\hat{\mathcal{H}}'(\tau)$ and, thus, of the order of $|t_{ij}|/\hbar$ or $|U|/\hbar$. If the frequency ω of the periodic forcing is large compared to these rates, as assumed initially through Eq. (3.9), one can approximately integrate out the rapid oscillations of the hopping phase factors $\mathrm{e}^{i\chi_{ij}^{\omega}(\tau)}$ by averaging $\hat{\mathcal{H}}'(\tau)$ over a period in time,

$$\hat{\mathcal{H}}'(\tau) \approx \frac{1}{T}\int_\tau^{\tau+T} \mathrm{d}\tau\, \hat{\mathcal{H}}'(\tau) = \frac{1}{T}\int_0^T \mathrm{d}\tau\, \hat{\mathcal{H}}'(\tau) \equiv \hat{\mathcal{H}}_{\mathrm{eff}}\,. \tag{3.21}$$

One finds

$$\hat{\mathcal{H}}_{\mathrm{eff}} = -\sum_{\langle ij\rangle} t_{ij}^{\mathrm{eff}} \hat{b}_i^\dagger \hat{b}_j + \sum_i \frac{U}{2}\hat{n}_i(\hat{n}_i - 1)\,; \tag{3.22}$$

the dynamics is described by an effective *time-independent* Hamiltonian that possesses the form of the undriven Hubbard model, with modified tunneling matrix elements

$$t_{ij}^{\text{eff}} = t_{ij} \frac{1}{T} \int_0^T \mathrm{d}\tau \, \mathrm{e}^{i\chi_{ij}^{\omega}(\tau)} \,. \tag{3.23}$$

Within this approximation, the time evolution of $|\psi(\tau)\rangle$ is described by

$$|\psi(\tau)\rangle \approx \hat{U}_{\omega}(\tau) \exp(-i\hat{\mathcal{H}}_{\text{eff}}\tau/\hbar)|\psi'(0)\rangle \,. \tag{3.24}$$

In Eq. (3.24), we have achieved to separate the dynamics of the system on short and long time scales. The state evolves slowly, on time scales determined by tunneling t_{ij}^{eff} and interaction U, according to the modified Hubbard Hamiltonian $\hat{\mathcal{H}}_{\text{eff}}$. Superimposed to this non-trivial slow dynamics is the simple rapid oscillatory translation of all particles in quasimomentum described by $\hat{U}_{\omega}(\tau)$.

For sinusoidal forcing, the effective modification of tunneling as in Eq. (3.23) has been pointed out in Refs. [217–219]. The derivation presented here takes into account also the interactions among the particles, which are allowed to be strong compared to the tunneling kinetics. The effective tunneling modification through rapid forcing as presented here, can be derived in a more systematic fashion using quantum Floquet theory [220]. The Floquet approach gives a transparent account also for processes beyond the effective hopping approximation that become relevant when $\hbar\omega$ becomes comparable to t_{ij} or U [221]. Moreover, it allows to study the response of the system to slow parameter variations.

Considering the special case of sinusoidal forcing of frequency ω obtained by shaking the lattice along the elliptical orbital

$$\boldsymbol{x}_{\omega}(\tau) = \boldsymbol{x}_c \cos(\omega\tau) + \boldsymbol{x}_s \sin(\omega\tau), \tag{3.25}$$

Eq. (3.23) gives

$$t_{ij}^{\text{eff}} = t_{ij} \mathcal{J}_0\big(\tfrac{K_{ij}}{\hbar\omega}\big). \tag{3.26}$$

In deriving Eq. (3.26), we have used the relation $\exp(iz\sin(\alpha)) = \sum_{\ell=-\infty}^{\infty} \mathrm{e}^{i\ell\alpha} \mathcal{J}_{\ell}(z)$ involving Bessel functions $\mathcal{J}_{\ell}$. Moreover, from Eq. (3.10) we get $v_{ij}^{\omega}(\tau) = M_{\text{at}} \dot{\boldsymbol{x}}(\tau) \cdot \boldsymbol{r}_{ij} \equiv K_{ij} \cos(\omega t - \varphi_{ij})$, with

$$K_{ij} = M_{\text{at}} \omega^2 \sqrt{(\boldsymbol{x}_c \cdot \boldsymbol{r}_{ij})^2 + (\boldsymbol{x}_s \cdot \boldsymbol{r}_{ij})^2} \tag{3.27}$$

and

$$\varphi_{ij} = \operatorname{atan}\big(\boldsymbol{x}_s \cdot \boldsymbol{r}_{ij} / \boldsymbol{x}_c \cdot \boldsymbol{r}_{ij}\big) \,. \tag{3.28}$$

Equation (3.26) predicts a strong modification of tunneling if the amplitude of the forcing K_{ij} becomes comparable to $\hbar\omega$. Because of the off-resonance condition (3.9) this is the regime of strong driving, $K_{ij} \gg |U|, |t_{ij}|$; accordingly, the Bessel-type dependence of t_{ij}^{eff} on the amplitude K_{ij} reflects the non-perturbative influence of the forcing. The Bessel function $\mathcal{J}_0(z)$ possesses its first zero at $z \approx 2.4$. Ramping up the strengths of the forcing $K_{ij}/\hbar\omega$ towards this value, the tunneling can be strongly suppressed. For even stronger forcing, crossing the first zero, the hopping matrix element changes sign. Defining $\tilde{t}_{ij} = -t_{ij}^{\text{eff}}$ (> 0), this allows the promised generation of a Bose–Hubbard with frustrated hoppings, Eq. (3.1).

The experimental control over this technique has increased considerably in recent years. The Bessel-type modification of tunneling (3.26), including the sign change, has first been probed successfully via the coherent expansion dynamics of a BEC in a sinusoidally-shaken, one-dimensional optical lattice [216]. It has also been observed with single particles in a shaken double well [222]. The tunnel suppression described by Eq. (3.23) has, moreover, been successfully used as a tool to enter the regime of strong coupling and, in that way, to dynamically control the transition of a bosonic SF to a Mott insulator [220, 223]. In the context of frustrated magnetism, in the weakly-interacting regime of a triangular optical lattice, the sign change allowed observation of Bose condensation at finite quasimomentum, spontaneously breaking time-reversal symmetry [17]. In the next section, we will discuss the exotic quantum behavior that can appear – due to the sign change and resulting frustrated hoppings – in a triangular optical lattice at strong interactions.

Finally, one can also interpret the unitary transformation $\hat{U}_\omega(\tau)$ as a gauge transformation from a description in terms of the scalar potential $V_\omega(\boldsymbol{r}, \tau)$, represented by the discrete potential $v_i^\omega(\tau)$ in the Hamiltonian (3.6), to a description of the forcing by the vector potential $\boldsymbol{A}_\omega(\tau) = \int_{\tau_p}^{\tau} \mathrm{d}\tau' \nabla_{\boldsymbol{r}} V_\omega(\boldsymbol{r}, \tau')$, represented by the Peierls phase factors $\mathrm{e}^{i\chi_{ij}^\omega(\tau)}$ attached to the hopping matrix elements in the new Hamiltonian (3.16). We will exploit this interpretation in Chapter 5, where we show that the associated Peierls phase can be used to quantum simulate topological insulators and non-Abelian SU(2) gauge fields. A first step towards the quantum simulation of gauge fields via lattice shaking has been done in recent experiments in Hamburg [22].

3.2 The quantum spatially anisotropic triangular lattice (SATL) at $T = 0$

A particularly interesting model in the arena of frustrated hard-core bosons, governed by Hamiltonian (3.3), is the spatially anisotropic triangular lattice (SATL) with NN XY interactions (see Fig. 3.1b). This model is – besides being a paradigmatic model for frustrated quantum antiferromagnetism – relevant to the experiments in Hamburg [17]. In this section, we employ Takahashi's modified spin-wave theory (MSWT) [224] with ordering-vector optimization, supplemented by ED and PEPS data, to compute the ground-state phase diagram of this model, which all give a consistent qualitative picture.[6] We find that the zero-temperature phase diagram includes a 1D quasi-ordered phase, a 2D Néel-ordered phase, and a 2D spiraling-ordered phase. Most notably, we also find strong indications that the various ordered or quasi-ordered phases are separated by spin-liquid phases with short-range correlations, in analogy to what has been predicted for the Heisenberg model on the same lattice (see Chapter 14.2.1). In Sec. 3.3, we will extend our results to the phase diagram at low but finite temperatures which is relevant for realistic experiments. As we will see, it is dominated by the ground-state behavior.

For coherence with the technique used – spin-wave theory – and for a better comparison with existing results in the literature, this section will be generally expressed in the language of spin physics, but guidance will be provided on how to translate the magnetic observables into bosonic ones.

The rest of this section is organized as follows. In Sec. 3.2.1, to form intuition, we present the classical phase diagram and known results on the quantum XY SATL at zero temperature. The following sections are devoted to analyzing this model using MSWT, ED, and PEPS. First, in Sec. 3.2.2, we discuss various indicators from MSWT for quantum-disordered behavior. In Sec. 3.2.3 we propose a complementary observable to distinguish ordering and spin-liquid behavior using the ED spectra of small clusters. Then, in Sec. 3.2.4, we characterize the properties of the ordered phases in more detail. We connect the description in terms of spin language to the original hard-core boson systems in Sec. 3.2.5, where we also present MSWT predictions for time-of-flight pictures. Finally, in Sec. 3.2.6, we summarize our findings on the ground-state phase diagram of the SATL. The results presented here have been published in Ref. [225].

[6] See Chapters 12.1, 12.2, and 14.1 for explanations of these methods.

3.2.1 Classical phase diagram and previous results

The frustrated quantum spin model (3.3) on the SATL is characterized by the parameter $\alpha \equiv t_2/t_1$, where $t_1 = \tilde{t}_{\boldsymbol{\tau}_1}$ denotes the bond strengths along the chains and $t_2 = \tilde{t}_{\boldsymbol{\tau}_{2,3}}$ the bond strengths along the diagonals (black and red bonds, respectively, in Fig. 3.1). This parameter interpolates between various qualitatively different regimes, namely an ensemble of decoupled one-dimensional chains at $\alpha = 0$, the isotropic triangular lattice at $\alpha = 1$, and the square lattice for $\alpha \to \infty$.

A good indicator for the potential ordered phases appearing in the quantum SATL is given by the classical phase diagram. It can be obtained by replacing the quantum-XY spins in Eq. (3.3) by classical rotors in the xy-plane. These classical spins show LRO at an ordering vector $\boldsymbol{Q}^{\mathrm{cl}} = \left(Q_x^{\mathrm{cl}}, Q_x^{\mathrm{cl}}\right)$, which is found as the $\boldsymbol{k}$-vector that minimizes the Fourier transform of the coupling strengths. It fixes the direction of each spin (up to a global phase) as $\boldsymbol{S_i} = S\left(\cos(\boldsymbol{Q}^{\mathrm{cl}} \cdot \boldsymbol{r}_i), \sin(\boldsymbol{Q}^{\mathrm{cl}} \cdot \boldsymbol{r}_i)\right)$, where in the SATL $Q_y^{\mathrm{cl}} = 0$ and

$$Q_x^{\mathrm{cl}} = \begin{cases} 2\arccos\left(-\frac{\alpha}{2}\right), & 0 \le \alpha \le 2 \\ 2\pi, & \alpha > 2 \end{cases} \tag{3.29}$$

If we assume the spins to behave classically, the 2D-Néel order, present for $\alpha \geq 2$, starts to continuously deform into spiral order at $\alpha \leq 2$ (compare Fig. 3.2a). This spiral phase extends down to $\alpha = 0$ where the chains decouple.

In Fig. 3.2b, we reproduce the quantum-mechanical phase diagram as predicted from PEPS calculations by Schmied *et al.* [202]. According to this study, both the square lattice limit ($\alpha \to \infty$) and the most frustrated case, the isotropic triangular lattice ($\alpha = 1$), display magnetic long-range order (LRO). In the limit of decoupled chains ($\alpha = 0$) the system displays quasi-LRO with algebraically decaying correlations. However, similarly to what has been found in the Heisenberg model (see Chapter 14.2.1), the system seems to feature spin-liquid phases with exponentially decaying correlations that intervene between different types of order or quasi-order. Other distinct features of the quantum model due to quantum fluctuations are the shift to considerably smaller values of α of the transition between 2D-Néel and spiral order, and the extension of the quasi-ordered 1D-like state over a broad region in the phase diagram.

In the following, we compute the MSWT ground-state phase diagram of Hamiltonian (3.3), and compare its predictions with PEPS results and ED. The following system geometries are considered for the three different methods:

- PEPS: a rhombic lattice of $20 \times 20 = 400$ spins with open boundary conditions. PEPS is a generalization of the concept of MPS to higher di-

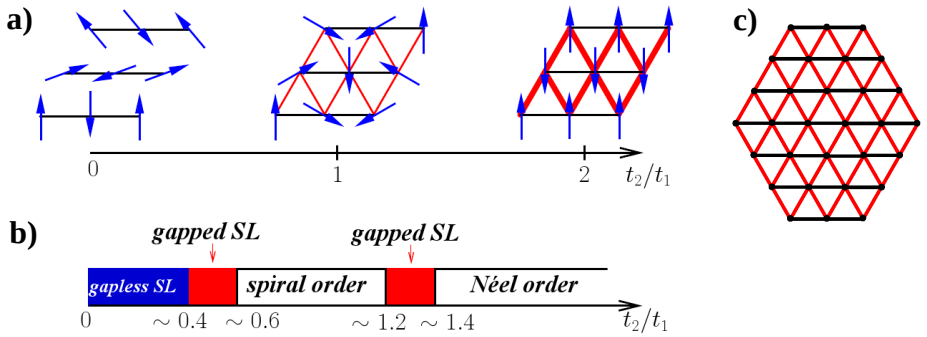

Figure 3.2: **(a) Classical ground-state phase diagram** of the SATL with sketches of the 1D state at $\alpha = 0$, the spiral state at $\alpha = 1$ and the 2D-Néel state for $\alpha \geq 2$. **(b) Quantum mechanical phase diagram** from Schmied *et al.* [202], hosting spin liquids (SLs). **(c) Cluster of 30 spins used for ED.** The 24-spin system is equivalent, only with the top and bottom rows removed. The clusters are chosen for large symmetry with respect to reflection on the axes and for a ratio of t_2- (red) to t_1-bonds (black) close to 2.

mensions. It has a refinement parameter controlling the precision of the *Ansatz*, the bond dimension D. PEPS is a powerful numerical tool which goes beyond mean-field theory, but for small D it accounts only partially for the entanglement in the ground state (see also Chapter 12.2). This limitation becomes particularly serious close to quantum phase transitions. However, Schmied and coworkers demonstrated that $D = 2$, which we use here, is already accurate enough to effectively capture the most relevant physics of the system [202].

- ED: Lanczos diagonalization [226] of clusters of 24 and 30 spins (the latter is shown in Fig. 3.2c), again with open boundary conditions (these are necessary to allow for the accommodation of arbitrary ordering vectors). More details can be found in Chapter 12.1.

- MSWT: rhombic lattices of $32 \times 32 = 1024$ and $64 \times 64 = 4096$ spins as well as in the infinite-lattice (thermodynamic) limit under periodic boundary conditions. We find that at these lattice sizes all quantities have essentially reached the infinite lattice limit except, as it can be expected, in the one-dimensional limit and at critical points. Although MSWT dresses a classically ordered state with quantum fluctuations, as is usual for a spin-wave

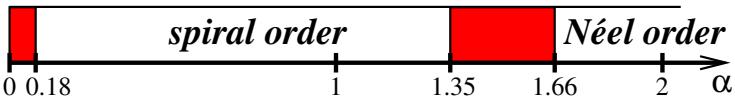

Figure 3.3: **Parameter regions where MSWT breaks down (red)** due to the appearance of imaginary modes. These are candidate regions for quantum disorder in the true ground state.

Ansatz, it formulates good predictions also for states with low ordering tendencies such as quasi-ordered states. MSWT relies on a self-consistent minimization of the free energy, which we improved by an optimization of the ordering vector. Technical details can be found in Chapter 14.

3.2.2 Distinction of spin-liquid candidate regions

As a first step in our analysis, we discuss in which parameter regions MSWT suggests LRO and in which quantum disorder. To this, we first investigate if there appear imaginary modes in the dispersion relation, which would indicate instabilities. Afterwards, we study the order parameter M_0 and the spin stiffness.

Imaginary frequencies and breakdown of convergence

Convergence in the self-consistent equations of MSWT with ordering vector optimization, Eqs. (14.11–14.13) and (14.16–14.19), cannot be achieved in selected regions of the ground-state phase diagram, namely for $\alpha \lesssim 0.18$ and for $1.35 \lesssim \alpha \lesssim 1.66$, as summarized in Fig. 3.3. (Interestingly, convergence is restored in the pure 1D limit, $\alpha = 0$, for which the theory formulates surprisingly good predictions.)

This breakdown of convergence corresponds to the appearance of an imaginary part in the spin-wave frequencies, Eq. (14.13), signaling an instability of the ordered ground state. The breakdown of a self-consistent description of the system in terms of an ordered ground state is strongly suggestive of a quantum-disordered ground state in the exact behavior of the system. Hence, one can interpret these parameter regions as candidates for the spin-liquid phases predicted by PEPS calculations [202] (compare Fig. 3.2b).

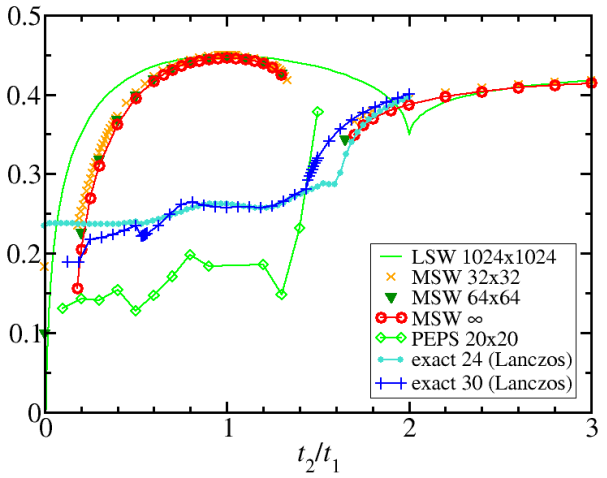

Figure 3.4: **Order parameter.** The MSWT order parameter M_0, Eq. (14.15), shows little size dependence (system sizes are given in the labels). The agreement to ED and PEPS results [$\sqrt{S(\boldsymbol{Q})/N}$ from Eq. (3.30)] for $\alpha \approx 1.66$ indicates that MSWT captures well the influence of quantum fluctuations in that region. Here, it improves considerably over the order parameter from LSWT. A large value indicates strong LRO, with the theoretical maximum being 0.5.

Order parameter and spin stiffness

A fundamental indication for the validity of spin-wave theories is generally given by the order parameter for the magnetization M_0, Eq. (14.15), and the spin stiffness, Eq. (14.21). The influence of quantum fluctuations is strong where these observables are small, and in such a case the primary assumption that the system can be described by a semi-classical spin-wave state begins to falter. Since MSWT only takes quantum fluctuations partially into account, a small order parameter and/ or spin stiffness also suggests that the true quantum ground state could be completely disordered. We display these quantities in Figs. 3.4 and 3.5.

To check the validity of MSWT, we compare the order parameter with results from ED and PEPS calculations. In both cases, we can extract the ordering vector $\boldsymbol{Q}$ as well as the order parameter M from the Fourier transform of the spin–spin correlations, the static structure factor. For XY interactions, it is

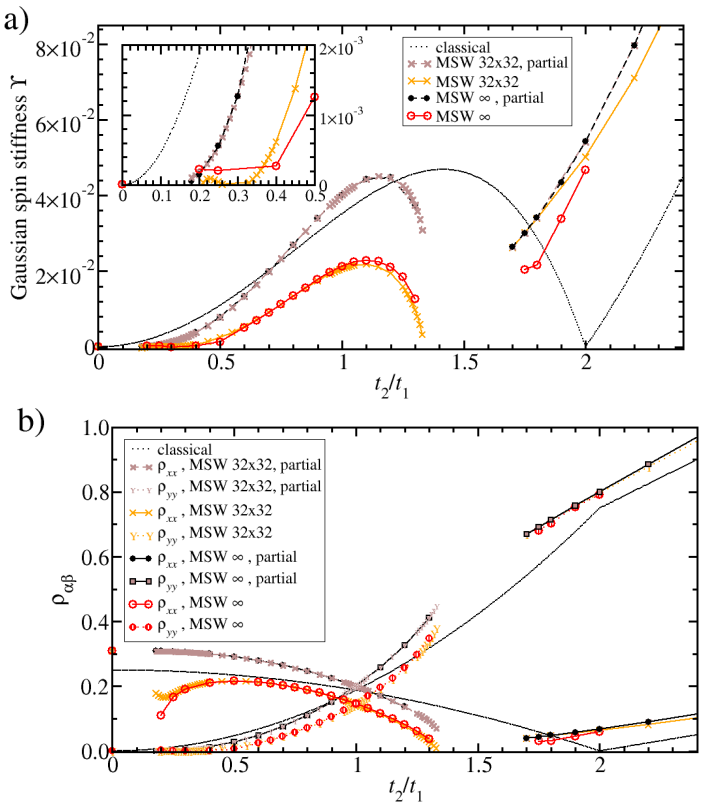

Figure 3.5: **(a) Gaussian spin stiffness Υ. (b) Components of the spin-stiffness tensor.** The mixed second derivative ρ_{xy} vanishes for symmetry reasons. The inset in (a) is a zoom on the region of small α, showing the smallness of Υ for $\alpha \lesssim 0.35$. The low values at $\alpha \lesssim 0.35$ and upon approaching the region $1.35 \lesssim \alpha \lesssim 1.66$ may indicate quantum disordered behavior in the true ground state. The numbers behind the labels give the system sizes. The curves labeled 'partial,' obtained by Eq. (14.23), provide upper bounds on the spin stiffness.

defined as

$$S(\boldsymbol{k}) = \frac{1}{N} \sum_{i,j} e^{-i\boldsymbol{k}\cdot(\boldsymbol{r}_i - \boldsymbol{r}_j)} \langle S_i^x S_j^x + S_i^y S_j^y \rangle \,, \tag{3.30}$$

The ordering vector $\boldsymbol{Q}$ is the vector which maximizes $S(\boldsymbol{k})$, and the order parameter M is given by $M = \sqrt{S(\boldsymbol{Q})/N}$, which in the thermodynamic limit defines the magnetization of the system.

In the square lattice limit $\alpha \to \infty$, the order parameter attains the value $M_0 = 0.435$ in the thermodynamic limit, which is very close to $M = 0.437$ as extrapolated from quantum Monte Carlo calculations [227]. For the spin stiffness, Sandvik and Hamer [227] obtained $\rho_\parallel/\alpha = 0.270$; MSWT returns the only slightly larger value $\rho_\parallel/\alpha = 0.272$. It appears that in this special case the main quantum corrections are correctly captured by MSWT. The large values of the order parameter (around 87% of the theoretical maximum) and of the spin stiffness support the assumption that the classical picture remains essentially valid in the large-α limit. Indeed, as the comparison to ED shows (Fig. 3.4), MSWT is quantitatively reliable in the entire Néel phase ($\alpha \gtrsim 1.66$).

In the spiral phase, the comparison is more problematic. While ED and PEPS confirm the existence of an ordered spiral region for α around 1, the magnitude of the order parameter appears to be largely overestimated by MSWT. It seems implausible that the frustrated spiral phase ($0.18 < \alpha < 1.35$) has an order parameter which can be larger than that of the unfrustrated case of the square lattice ($\alpha \to \infty$). In fact, around $\alpha \approx 1$, MSWT only moderately improves upon LSWT for what concerns the order parameter. This discrepancy could be due to corrections to the spin-wave expansion of third-order in the boson operators which our approach neglects, and which can become important in spiral configurations [228]. Interestingly, in both regions of largest spatial isotropy of the interactions, *i.e.*, at large α (isotropic square lattice) and around $\alpha = 1$ (isotropic triangular lattice), the order parameter M_0 coincides with that of linear spin-wave theory (LSWT).

In the 1D-limit ($\alpha \to 0$), LRO disappears due to the Mermin–Wagner theorem [229]. This is reflected in the breakdown of the order parameter M_0. Within MSWT, the breakdown occurs already at a finite value of the inter-chain coupling, $\alpha \approx 0.18$ (note that within LSWT the order parameter vanishes only for $\alpha \to 0$). This coincides with the appearance of imaginary spin-wave energies as discussed in the previous section. At small but finite α the spin stiffness ρ_{yy} essentially vanishes, which is characteristic of a 1D-like state that consists of effectively decoupled chains. This finding suggests that the physics becomes basically independent of the y-component of $\boldsymbol{Q}$ for $\alpha \lesssim 0.35$.

A single XY chain can be solved exactly by Bethe-*Ansatz* equations, and by use of twisted boundary conditions one can obtain the exact solution for the spin stiffness $\rho_{xx} = 1/\pi \approx 0.318$ [230]. Our MSWT result of $\rho_{xx} \approx 0.308$ lies surprisingly close. For one-dimensional models it is known that a non-zero spin stiffness is accompanied by quasi long-range correlations with power-law decay. The critical nature of the state in the 1D-like phase reflects itself also in the fact that finite-size effects play an important role.

In summary, from the MSWT order parameter M_0 we can derive a loss of LRO at $\alpha \lesssim 0.18$, and the spin stiffness suggests a strong weakening of inter-chain correlations already at $\alpha \lesssim 0.35$. The spin-stiffness also decreases strongly upon approaching the parameter region $1.35 \lesssim \alpha \lesssim 1.66$. Together with the appearance of imaginary spin-wave frequencies for $\alpha \lesssim 0.18$ and $1.35 \lesssim \alpha \lesssim 1.66$, this strongly indicates the appearance of disordered phases in these regions. The breakdown region of MSWT at $1.35 \lesssim \alpha \lesssim 1.66$, is only roughly consistent with the one where PEPS calculations [202] indicate the appearance of a short-ranged spin-liquid phase, namely $1.2 \lesssim \alpha \lesssim 1.4$. Nonetheless, it is tempting to associate the breakdown of MSWT to this quantum-disordered phase. In the rest of parameter space, magnetic LRO order seems to survive quantum fluctuations.

3.2.3 Signatures of ordering and spin-liquid behavior in the ED spectra of a small cluster

Before characterizing in detail the nature of the ordered phases, we derive now, from the ED energy spectra of small clusters, a complementary signature for the division of the SATL ground-state phase diagram into ordered and disordered phases. The system Hamiltonian (3.3) commutes with the total magnetization along the z axis, $S_z^{\mathrm{tot}} = \sum_i \langle S_i^z \rangle$, so that excited states can be classified on the basis of this quantum number.

Figure 3.6 shows (for a 24-spin cluster as described in Fig. 3.2c) the excitation energies of the first excited states in each S_z^{tot} sector (up to $S_z^{\mathrm{tot}} = 11$) with respect to the minimum energy in each sector, $E_0(S_z^{\mathrm{tot}})$. The absolute ground state is located at $E_0(S_z^{\mathrm{tot}} = 0)$. Upon varying α, we observe a significant evolution of the low-energy spectrum of the system, which points at the widely different regimes explored by the system. In particular, in the spirally and Néel ordered phases – exemplified in Fig. 3.6 by $\alpha = 1$ and $\alpha = 2$, respectively – in each S_z^{tot} sector there are a few states close to the minimum energy, and separated from the other excited states by a large gap. According to a standard 'tower-of-states' argument [231], these low-lying states are expected

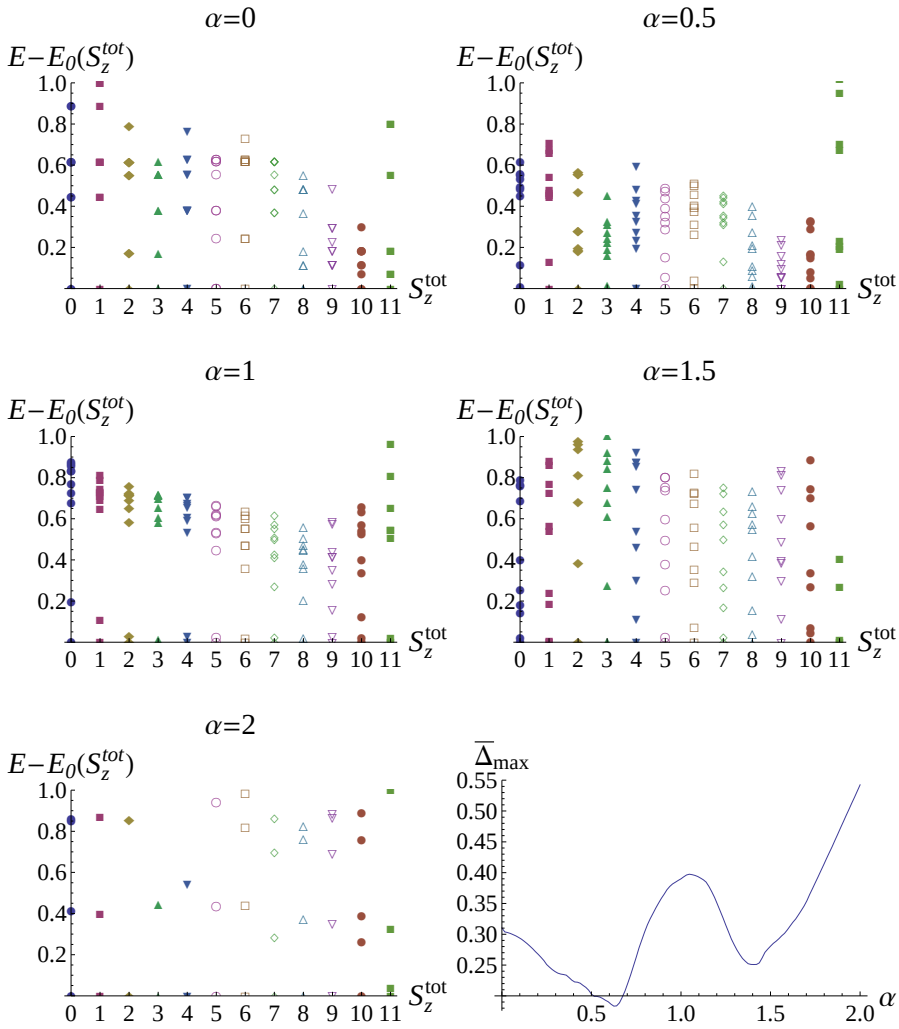

Figure 3.6: **Spectra from ED on a 24-site cluster.** For large α (exemplified by $\alpha = 2$), the spectrum in all magnetization sectors displays a low-lying state that is well separated from the excited states. This behavior is typical of phases that are ordered in the thermodynamic limit, where the low-lying states of different S_z^{tot} collapse to the Néel-ordered ground state, and the higher-energy states constitute spin-wave excitations. Similarly, around $\alpha = 1$, two closely-spaced low-lying states are separated from the higher-energy states. Around $\alpha \approx 1.5$ and below $\alpha \approx 0.7$, the states are approximately equally spaced, suggesting quantum disorder. **Lower-right panel: the average maximal level spacing,** Eq. (3.31), can be used to quantify this behavior. The low values around $\alpha \approx 0.6$ and $\alpha \approx 1.4$ suggest disordered phases.

to collapse to the ground state in the thermodynamic limit, giving rise to degenerate superpositions of all S_z^{tot} sectors, each breaking the U(1) rotational symmetry of the Hamiltonian and displaying spiral or Néel order, respectively. The higher-energy states instead will in the thermodynamic limit reproduce the true excitation spectrum.

This tower-of-states feature is on the contrary absent in other regions of the phase diagram, in which the energy levels in each S_z^{tot} sector are more homogeneously spaced. The absence of a low-lying multiplet of states separated from the higher energy states is observed in models whose ground state is generally considered to be a spin liquid [232]. We therefore introduce an observable aimed at quantifying the extent to which the spectrum exhibits the expected features in presence of spontaneous symmetry breaking in the thermodynamic limit. We consider the *average maximal level spacing* $\bar{\Delta}_{\mathrm{max}}$, defined as

$$\bar{\Delta}_{\mathrm{max}} = \frac{1}{N_S+1} \sum_{S_z^{\mathrm{tot}}=0}^{N_S} \max_i \left[E_{i+1}(S_z^{\mathrm{tot}}) - E_i(S_z^{\mathrm{tot}}) \right] , \tag{3.31}$$

i.e., the maximal level spacing in each S_z^{tot} sector, averaged over the $N_S+1 = 12$ sectors considered. To extract it, we consider the lowest 10 levels $E_i(S_z^{\mathrm{tot}})$, which captures the behavior of the low-energy part of the spectrum. The definition of $\bar{\Delta}_{\mathrm{max}}$ is chosen so that it will be maximal in presence of a large separation between the low-lying tower of states and the higher-energy spectrum, while it will be minimal for homogeneously spaced levels in each sector.

As a function of α (see Fig. 3.6), $\bar{\Delta}_{\mathrm{max}}$ has two pronounced minima, at $\alpha \approx 0.6$ and $\alpha \approx 1.4$. Remarkably, these correspond to the regions in parameter space where PEPS calculations predict a spin-liquid phase [202] (see Fig. 3.2b). Hence, the lack of the tower-of-states feature in the spectra of this small cluster is consistent with the PEPS prediction for disordered phases.

3.2.4 Analysis of the ordered phases

To characterize the long-range ordered phases in more detail, we use the ordering vector, which is a measure for the predominant ordering tendencies, and the chiral correlations, which witness spiral LRO. After introducing these observables, we will describe the different ordered phases in detail. As we will see, MSWT indeed reproduces the main features of the phase diagram of Fig. 3.2b quite accurately.

In MSWT with ordering-vector optimization, the ordering vector $\boldsymbol{Q}$ (plotted in Fig. 3.7, where without loss of generality $Q_y = 0$) is a direct result of the self-

consistent optimization. In ED and PEPS, it corresponds to the peak-position of the static structure factor, Eq. (3.30). Three limiting values are known. Intra-chain AFM order as occurring at $\alpha = 0$ is described by $\boldsymbol{Q} = \pi \boldsymbol{e}_x$. Square-lattice Néel order (as at large α) is described by $\boldsymbol{Q} = 2\pi \boldsymbol{e}_x$. In the isotropic lattice ($\alpha = 1$), the threefold symmetry[7] leads to an ordering vector of $\boldsymbol{Q} = \frac{4\pi}{3} \boldsymbol{e}_x$. The importance of optimizing the ordering vector is apparent in Fig. 3.7 when comparing MSWT to the classical (and LSWT) curve.

Spiral phases carry not only a magnetic, but also a chiral order parameter. In particular, a vector chirality [233] can be defined on an upwards pointing triangle Δ and a downwards pointing triangle ∇ with counter-clockwise labeled corners (i, j, k) and (i, l, j), respectively, as

$$\kappa_\Delta = \frac{2}{3\sqrt{3}} \left[\boldsymbol{S}_i \times \boldsymbol{S}_j + \boldsymbol{S}_j \times \boldsymbol{S}_k + \boldsymbol{S}_k \times \boldsymbol{S}_i \right]_z \tag{3.32a}$$

$$\kappa_\nabla = \frac{2}{3\sqrt{3}} \left[\boldsymbol{S}_i \times \boldsymbol{S}_l + \boldsymbol{S}_l \times \boldsymbol{S}_j + \boldsymbol{S}_j \times \boldsymbol{S}_i \right]_z . \tag{3.32b}$$

Chirality correlations are then defined as [234]

$$\psi_- = \left\langle \left(\kappa_\Delta - \kappa_\nabla \right) \left(\kappa_{\Delta'} - \kappa_{\nabla'} \right) \right\rangle , \tag{3.33}$$

where (Δ, ∇) and (Δ', ∇') denote two pairs of neighboring triangles that share a $\boldsymbol{\tau}_1$ edge. In Fig. 3.8, we plot the average chirality correlation of the central plaquette with all other plaquettes, normalized to the theoretical maximum 4/9. The MSWT data have been obtained by expanding the chiral correlation up to the fourth order in the Dyson–Maleev boson operators [for technical details see Eq. (14.3)], which is consistent with the truncation of the spin-wave Hamiltonian (14.4) to the same order. Including higher orders might change the result in regions where M_0 is small. In particular, the unphysical negative values for small α are an artifact of this truncation.

Transition from 2D-Néel to spiral order

Coming from the large-α limit, for all methods (MSWT, ED, and PEPS), the wavevector associated with the dominant correlations (see Fig. 3.7) jumps from $\boldsymbol{Q} = 2\pi \boldsymbol{e}_x$, which is characteristic of the Néel phase, to a continuously varying $\boldsymbol{Q}$, which is characteristic of a spiral phase: for PEPS this occurs at $\alpha \approx 1.4$, for ED at $\alpha \approx 1.44$, and for MSWT when traversing the breakdown region, *i.e.*, between

[7] The ED and PEPS results deviate at $\alpha = 1$ because the shape of the simulation clusters (Fig. 3.2c) breaks the threefold symmetry.

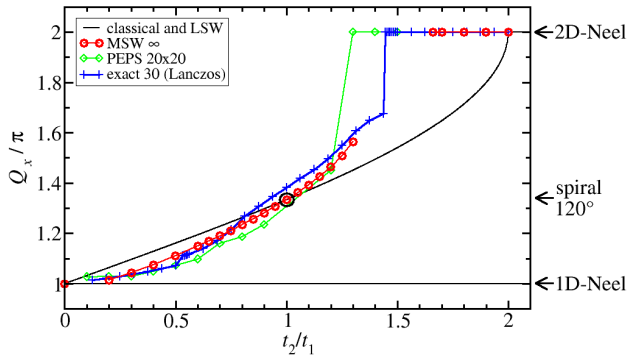

Figure 3.7: **x-component of the ordering vector, Q_x.** MSWT (red) compares well to ED (blue) and PEPS (light green), improving considerably upon the LSWT values (black), which are equal to the classical ones. In particular, MSWT reproduces the strong shift of the transition between spiral and Néel LRO, and the weak dependence on α close to the 1D limit. The numbers in the labels are the respective system sizes. The black circle marks the isotropic spiral ordering vector, $Q_x = 120°$, at $\alpha = 1$.

$\alpha = 1.35 - 1.66$. Notably, in all three approaches Néel order persists to much lower α than classically ($\alpha_c = 2$), since – due to order-by-disorder phenomena [235] – quantum fluctuations generally stabilize states where spins are ordered collinearly (see, *e.g.*, Refs. [235, 236]). The onset of strong chiral correlations (Fig. 3.8) confirms that the new phase shows, indeed, spiral order.

The overlap $|\langle\psi_\alpha|\psi_\infty\rangle|$ of the ground state with the 2D-Néel ordered state of $\alpha = \infty$, as extracted from ED and plotted in Fig. 3.9, lends further support to the stabilization of Néel order due to quantum fluctuations: it remains at large values down to the transition Néel–spiral at $\alpha \approx 1.44$, where it drops to essentially 0.

Persistence of 1D quasi-LRO up to finite inter-chain couplings

As discussed above, within MSWT the magnetic order parameter breaks down at $\alpha \approx 0.18$ (see Fig. 3.4) and the spin-stiffness component ρ_{yy} practically vanishes for $\alpha \lesssim 0.35$ (see Fig. 3.5b). These findings indicate a transition, occurring at finite inter-chain couplings, to a non-magnetic phase such as the one reproduced in the one-dimensional limit $\alpha \to 0$. This is consistent with the ground-state

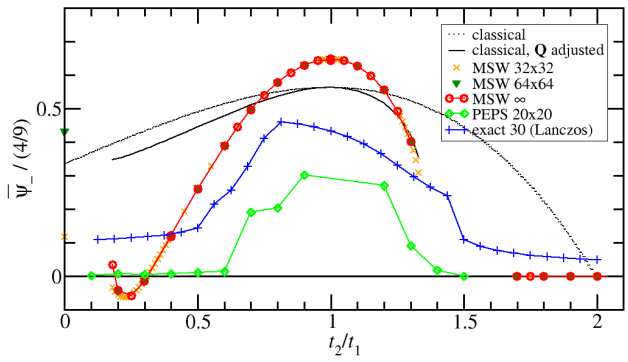

Figure 3.8: **Averaged chiral correlation** normalized to the theoretical maximum 4/9. ED (blue), PEPS (light green), and MSWT (orange, dark green, and red) consistently predict chiral LRO in a broad (but smaller than classical) region around $\alpha = 1$. The black dotted line is the classical result and the black solid line is the classical chiral correlation that is obtained if for a given α the $\boldsymbol{Q}$ of the MSWT calculation rather than $\boldsymbol{Q}^{\mathrm{cl}}$ is used.

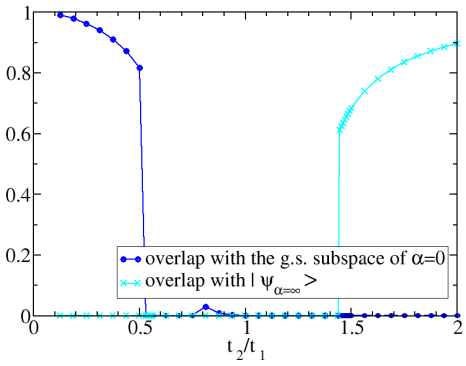

Figure 3.9: **The overlap of the ground state** at α with the 2D-Néel ground state of $\alpha = \infty$, $|\Psi_{\alpha=\infty}\rangle$, is large for $\alpha \gtrsim 1.44$, indicating Néel order. The overlap with the six-dimensional ground-state subspace of $\alpha = 0$ is large for $\alpha \lesssim 0.5$, indicating a 1D-like phase. Values from ED of the 30-spin cluster.

overlap $\sqrt{\sum_{i=1}^{6} |\langle\psi_\alpha|\psi_0^i\rangle|^2}$ to the subspace spanned by the six-fold degenerate[8] ground-states of $\alpha = 0$, computed in ED, which remains very large (almost 80 percent) up to $\alpha \approx 0.5$ (Fig. 3.9).

Other observables lend further support a quasi-1D phase at finite inter-chain couplings. For example, the ground-state energy and spin–spin correlations (not shown) approach the value of decoupled chains, and the chiral correlations (Fig. 3.8) drop strongly. Further, the ordering vector (Fig. 3.7) shows a very weak α-dependence in the quantum case, contrary to classical results, which exhibit a linear dependence on α. We note also that in the limit $\alpha = 0$, MSWT produces surprisingly good results. For example, the spin–spin correlations deviate from the exact results from a Jordan–Wigner transformation (see Sec. 12.3) only by 7.5%.

As we discuss in Chapter 14.2, in the same lattice with Heisenberg interactions, recent works found the persistence of spiral order for all finite inter-chain couplings $\alpha > 0$ [237, 238]. Since quantum fluctuations are more effective for disrupting order in the Heisenberg model, we would expect *a fortiori* that also in the XY spiral order persists for all $\alpha > 0$. However, the findings of Refs. [237, 238] are disputed [239–242]. In particular, our results presented in Chapter 14.2.1 suggest otherwise. Still, these considerations show that the existence of such a quasi-1D phase is a subtle issue.

3.2.5 Momentum distribution of the hardcore bosons

We now wish to make contact with possible experimental observation of the ground-state phases described above. In the introduction to this chapter, the $S = 1/2$ spin Hamiltonian (3.3) resulted as a convenient description of a system of infinitely repulsive bosons at half filling. Hence, it is important to match spin observables with their physical bosonic counterparts. To this, one simply has to invert the Holstein–Primakoff transformation (3.2).[9]

The most important observables can now be translated as follows. A nonzero magnetic order parameter M_0 implies the appearance of off-diagonal LRO

[8] This degeneracy is due to the particular geometry of the 30-spin system (Fig. 3.2c). At $\alpha = 0$, the even chains are in a singlet while the four odd chains may each be in a state with total spin $\pm 1/2$, leading to a degeneracy of 2^4. Restriction to the (physical) states with total magnetization $\sum_i \langle S_i^z \rangle = 0$ reduces this degeneracy to a six-fold one.

[9] For comparison with spin-wave results, one has to take note that the lowering and raising operators appearing in the Holstein–Primakoff transformation are defined with respect to the z axis, in contrast to the raising and lowering operators used in the spin-wave calculations (see Chapter. 14.1) which act with respect to the quantization axis of a twisted coordinate system, Eq. (14.2).

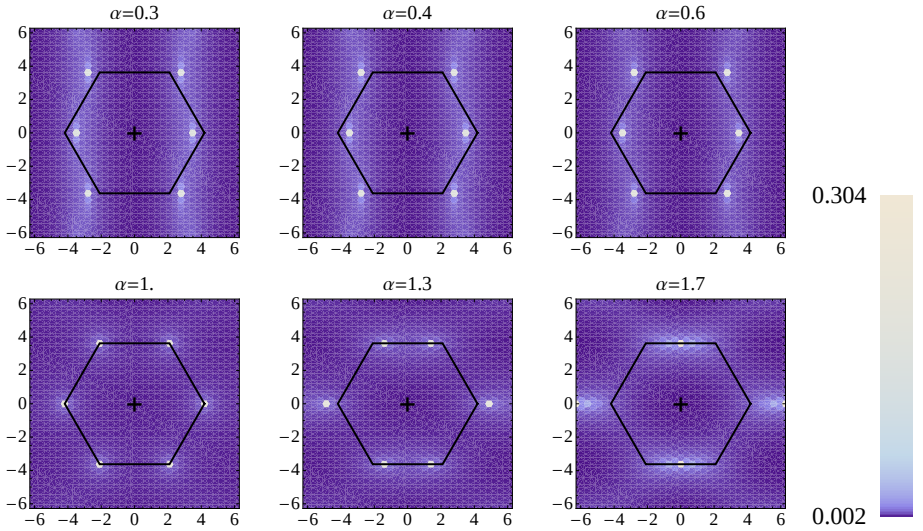

Figure 3.10: **Momentum distribution of a half-filled gas of frustrated hardcore bosons** [corresponding to the spin structure factor $S(\boldsymbol{k})$], marking the crossover from 1D-like behavior (small α) to spiral LRO ($\alpha \approx 1$), and to square-lattice Néel order ($\alpha > 1.66$). The data (on a logarithmic color scale, scaled to the number of sites) result from a MSWT calculation on an 18×18 lattice. The black hexagon marks the first Brillouin zone and the black cross its origin.

in the bosonic one-body density matrix,

$$\langle \hat{b}_i^\dagger \hat{b}_j \rangle \overset{|\boldsymbol{r}_{ij}|\to\infty}{\longrightarrow} M_0^2 \cos\left(\boldsymbol{Q}\cdot\boldsymbol{r}_{ij}\right) . \tag{3.34}$$

The ordering vector $\boldsymbol{Q}$ corresponds to the momentum at which condensation occurs. The condensed state in the spiral phase is characterized by a pattern of persistent currents forming a crystal of vortices, whose geometrically correlated structure is captured by the spin chirality. Finally, the parallel spin stiffness $\rho_\parallel \equiv \left(\rho_{xx} + \rho_{yy}\right)/2$ corresponds to the superfluid density of the bosons, $\rho_s = \rho_\parallel / S$.

The most common observable in cold-atom experiments is the momentum distribution, measurable, *e.g.*, in time-of-flight (ToF) images as explained in Chapter 2.1. Neglecting the trivial Wannier envelope, Eq. (2.10) becomes

$$\frac{n_b\left(\boldsymbol{k}\right)}{N} = \frac{1}{N}\sum_{i,j} e^{-i\boldsymbol{k}\cdot\left(\boldsymbol{r}_i - \boldsymbol{r}_j\right)} \langle \hat{b}_i^\dagger \hat{b}_j \rangle = S\left(\boldsymbol{k}\right) , \tag{3.35}$$

i.e., for hard-core bosons, the ToF momentum distribution measures the static structure factor (3.30) of the associated $S = 1/2$ spins. Figure 3.10 shows the MSWT prediction for the momentum distribution at various α values, spanning all the condensation regimes of the bosons at zero temperature. At $\alpha = 0$ (not shown), the system displays quasi-condensation at finite momenta along the uncoupled chains, resulting in vertical ridges at $Q_x = \pm\pi$ in the momentum distribution. These ridges corrugate as the interchain coupling increases, and true condensation peaks emerge in reciprocal space, corresponding to a condensate state which supports a crystalline vorticity pattern. As seen by combining Eqs. (3.34) and (3.35), the peak height (normalized to the number of sites) is given by the square of the order parameter M_0. For $\alpha = 1$, these peaks are located at the six corners of the first Brillouin zone. For $\alpha < 1$, the peaks are elongated in the y direction, while for $\alpha > 1$ they are elongated in the x direction, witnessing the spatial anisotropy of the lattice. This situation persists up to the breakdown of MSWT at $\alpha = 1.35$; after recovery of the theory at $\alpha = 1.66$, the momentum distribution shows condensation at the four corners of the Brillouin zone of a (deformed) square lattice, defined by the dominant diagonal bonds of the SATL.

3.2.6 Summary

Before proceeding to the finite-temperature analysis, let us summarize the main features of the zero-temperature phase diagram obtained via MSWT with $\boldsymbol{Q}$-vector optimization. The region where the system behaves like an ensemble of decoupled chains is extended to considerable inter-chain interactions. The order parameter indicates that inter-chain correlations set in at $\alpha \approx 0.18$; the spin stiffness suggests that an effective decoupling of the chains may even persist up to $\alpha \approx 0.35$. At larger α, the system crosses over to a spirally-ordered phase that persists up to $\alpha \approx 1.35$, where MSWT breaks down, suggesting a quantum disordered ground state. At $\alpha \approx 1.66$, MSWT finds again a self-consistent solution, this time corresponding to a 2D-Néel state.

These results are consistent with the PEPS phase diagram of Fig. 3.2b and ED calculations. Especially the persistence of 1D behavior to surprisingly large values of α, the stability of spiral LRO against quantum fluctuations, and the extension of 2D-Néel LRO to much smaller values of α than classically are reproduced. Further, the indications for quantum disordered behavior are consistent with the PEPS results and signatures from ED, which suggest several spin-liquid phases. However, there are some deviations, which are generally to be expected from a spin-wave approach. In particular, MSWT appears to overestimate the range of the ordered phases.

Two improvements to MSWT have proven to be crucial: First, the minimization of the free energy with respect to $\boldsymbol{Q}$ in the self-consistent equations has enabled us to describe to a surprisingly satisfactory level the considerable shift of the ordering vector by quantum effects. Second, the Gaussian spin stiffness, detecting regions with weak ordering tendencies, serves to detect parameter values where spin-liquid behavior may appear in the true quantum ground state. While MSWT cannot determine the properties of such disordered phases, it provides a fast and clear method for finding candidates for disordered behavior. This method can therefore serve as a guide in our search for interesting quantum-mechanical lattice models which require an experimental QS for further study of their phase diagram.

3.3 Finite-temperature phase diagram

Since real-world experiments are never carried out at exactly zero temperature, we now investigate how the phase diagram of the XY SATL translates to finite temperatures. To do this, we make use of MSWT in the thermodynamic limit.

At finite temperatures, continuous symmetries cannot be spontaneously broken in two dimensions [229, 243]. Therefore, in agreement with Berezinskii–Kosterlitz–Thouless (BKT) theory, we find for the XY SATL that zero-temperature long-range-ordered phases turn into quasi-ordered phases (up to a BKT transition temperature), while zero-temperature quasi-ordered phases become short-range correlated at finite temperature. At the BKT temperature T_{BKT}, the system undergoes a topological phase transition from quasi-LRO to an exponential decay of correlations, involving the unbinding of vortex–antivortex pairs [244–246]. The existence of a BKT transition in the XY model is in contrast to the Heisenberg model, where vortex excitations are not topologically stable [246], precluding a BKT transition.

The possibility of observing the BKT transition is a particular advantage of MSWT. In contrast, LSWT predicts a stable BKT phase with algebraic order at arbitrary temperatures. The non-linearities contained in MSWT allow the disruption of quasi-LRO and the transition to the short-range-ordered phase. However, vortex–antivortex excitations are not explicitly present in the theory, preventing an accurate estimation of T_{BKT}.

3.3.1 Spin–spin correlations

An important observable for the analysis of a temperature-dependent phase diagram is the two-point correlation function

$$C_{ij} \equiv \langle S_i^x S_j^x + S_i^y S_j^y \rangle \,/\, \cos\left(\boldsymbol{Q} \cdot \boldsymbol{r_{ij}}\right) . \tag{3.36}$$

In our analysis, we focus on $C_{m\boldsymbol{\tau}_1}$ and $C_{m\boldsymbol{\tau}_2}$ where m is a positive integer, and $\boldsymbol{\tau}_1 = (1,0)$ and $\boldsymbol{\tau}_2 = \left(1/2, \sqrt{3}/2\right)$ are the lattice vectors. The behavior of $C_{m\boldsymbol{\tau}_1}$ captures the intra-chain correlations, while that of $C_{m\boldsymbol{\tau}_2}$ describes inter-chain correlations.

To locate the BKT transition, we calculate the residual sum of squares $R = \sum_m \left[C_{m\boldsymbol{\tau}_{1,2}} - f(m\boldsymbol{\tau}_{1,2})\right]^2$ for an exponential $f(r) = Ae^{-r/\xi}$, where ξ is the correlation length, and an algebraic fit $f(r) = A/r^{\eta}$. We fit these functions to correlations over distances of $m = 3 \ldots 15$ lattice spacings. (The increasing computational time with distance between spins limits the distances reasonably reachable.) We identify a BKT transition where the R's of the exponential and the algebraic fit become equal. This gives a rough estimate of the transition temperature. Where we give numerical values, these are from averages of the fits to $C_{m\boldsymbol{\tau}_1}$ and $C_{m\boldsymbol{\tau}_2}$.

Figure 3.11 shows representative log–log plots of the correlation function $C_{m\boldsymbol{\tau}_1}$ at $\alpha \equiv t_2/t_1 = 0.7$ and $\alpha = 100$ (where the ground states show spiral and 2D-Néel order, respectively) for several temperatures. In these plots, algebraically decaying correlations correspond to straight lines. In the entire parameter range of the spiral phase, a clear transition from algebraic to exponential decay occurs at the computed BKT temperature. On the contrary, at $\alpha = 100$ we cannot find such a clear transition. Rather, the curves acquire a curvature fairly continuously. To check how the suggested BKT line changes when taking correlations to more distant spins into account, we exemplarily computed spin–spin correlations for $\alpha = 100$ up to distances of 64 lattice spacings. The transition temperature of $T_{\mathrm{BKT}}/(t_1 + 2t_2) = 0.134$, is lowered by approximately 15% from what is obtained if distances only up to 15 lattice spacings are considered. In light of the approximate nature of MSWT, we find that this level of precision is satisfactory. In the spiral phase, due to the more abrupt change in the behavior, one can expect the change in the transition temperature when including larger distances to be even smaller.

Further, we can find from the correlations the temperature at which the MSWT formalism breaks down. This temperature is characterized by the complete loss of all correlations, even to the NN. This behavior, occurring at temperatures on the order of the coupling strength, is clearly an artifact of the

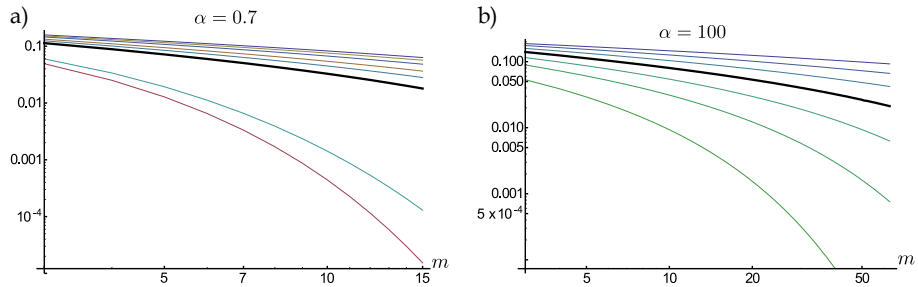

Figure 3.11: **Intra-chain correlations** $C_{m\boldsymbol{\tau}_1}$, **(a)** for $\alpha = 0.7$, and **(b)** for $\alpha = 100$ (on a log–log scale). From top to bottom, the lines correspond to the normalized temperatures (a) $T/(t_1 + 2t_2) = 0.064 \ldots 0.078$ in steps of 0.002, and (b) $T/(t_1 + 2t_2) = 0.068 \ldots 0.164$ in steps of 0.016. The line closest to T_{BKT} calculated from MSWT data is bold. Above the bold line (lower temperatures), the curves are approximately linear, witnessing algebraic correlations, while the downwards curvature at higher temperatures indicates exponential decay. In (b), the maximal distance m has been increased to 64 to check how the estimated transition temperature depends on it. The change of only about 15% is a satisfactory level of precision.

method, since in real systems the complete loss of correlations occurs only at extremely large temperatures where spin–spin interactions become negligible. Interestingly, in the domain α close to 1, where frustration is largest, it occurs at the lowest temperatures.

3.3.2 The phase diagram

In this section, we present the finite-temperature phase diagram of the SATL obtained via MSWT with ordering vector optimization.[10] Our calculations encounter convergence problems for too low temperatures (when the chemical potential becomes smaller than the accuracy of our numerical integrations). Depending on the parameter region, the lowest temperatures for which proper convergence could be achieved vary from less than one-tenth of a percent to several percent of the coupling strengths. This pathology is not observed at $T = 0$ (as calculated in section 3.2), because there the chemical potential vanishes exactly, allowing a special treatment of the zero-mode [see Eqs. (14.16) and (14.17)]. We typically calculated down to $T/(t_1 + 2t_2) = 0.025$, which seems

[10] In the following, we set the Boltzmann constant k_{B} to unity.

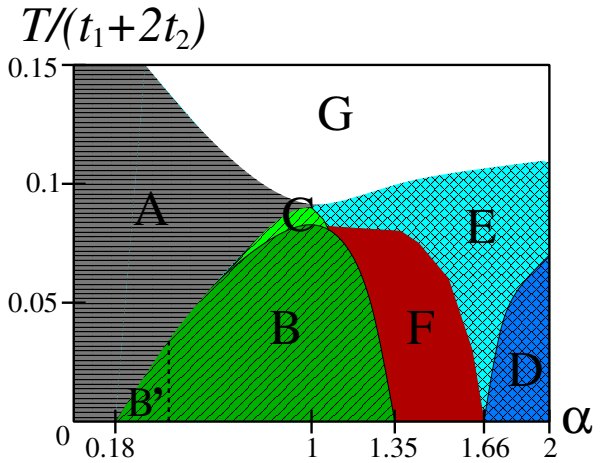

Figure 3.12: **Schematical temperature-dependent phase diagram of the XY SATL.** The different regions are listed along with their main characteristics in Table 3.1. Horizontal lines mark 1D-Néel order, diagonal lines spiral order, and cross-hatches 2D-Néel order.

sufficiently low to connect the results smoothly to the zero-temperature phase diagram. The breakdown of the calculations for too low temperature can be clearly seen in Fig. 3.13, which displays the phase diagrams obtained from several observables.

Before discussing these results, we first present a summarizing sketch of the phase diagram in Fig. 3.12, where we introduce labels for the occurring phases for reference in the following discussion. Table 3.1 lists the main properties of these phases. In short, at small α, there is a phase with properties similar to the algebraic 1D-Néel-like state found at $T = 0$ but with exponential decay of intra-chain correlations (phase A). Further, the phase diagram contains two quasi-LRO regions: a region at intermediate α corresponding to spiral quasi-LRO (phase B), and another region at large α which is characterized by Néel quasi-LRO (phase D). These phases undergo BKT transitions to similar phases with short-range order, phases C and E, respectively. Moreover, between them lies a region where imaginary frequencies occur in the spin-wave dispersion, which can be interpreted as an indication for an extremely short-range-ordered phase (phase F). This general structure of the phase diagram is supported by all the observables we investigate. At large T, MSWT breaks down and does not allow any interpretation (region G).

A natural starting point for an analysis of the temperature-dependent phase diagram is given by the respective ground-state phases. We proceed from small to large α.

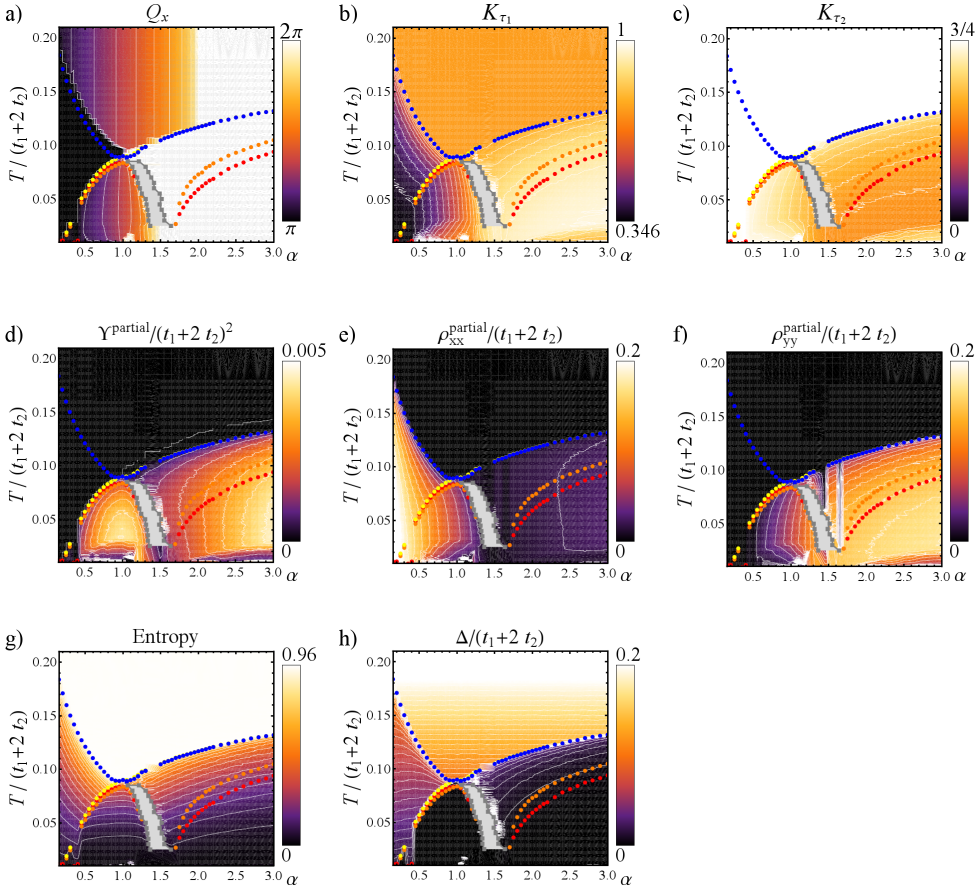

Figure 3.13: **Observables characterizing the finite-temperature phase diagram.** **(a)** Q_x, **(b)** intra-chain correlation $K_{\boldsymbol{\tau}_1}$, **(c)** inter-chain correlation $K_{\boldsymbol{\tau}_2}$, **(d)** partial Gaussian spin stiffness $\Upsilon^{\text{partial}}$, and **(e)** and **(f)** partial spin stiffnesses $\rho_{xx}^{\text{partial}}$ and $\rho_{yy}^{\text{partial}}$, respectively. The mixed component of the spin stiffness $\rho_{xy}^{\text{partial}}$ vanishes for symmetry reasons. Figures **(g)** and **(h)** show the entropy and the gap Δ. All plots are in linear color scale in dependence of α and $T/(t_1+2t_2)$. Points mark the BKT transition for $\boldsymbol{\tau}_1 = (1,0)$ (red) and for $\boldsymbol{\tau}_2 = \left(1/2, \sqrt{3}/2\right)$ (orange), identifying the transition from quasi-LRO to SRO (computed through the two-point correlations $C_{m\,\boldsymbol{\tau}_{1,2}}$); also shown are the temperature where inter-chain correlations disappear, witnessing a transition to a 1D-like phase (yellow), and the breakdown temperature (blue). In the gray region, imaginary frequencies appear in the spin-wave dispersion.

Phase		Q_x	decay of correlations
(A)	1D-like SRO	π	intra-chain: exponential inter-chain: uncorrelated
(B)	Spiral quasi-LRO	$\pi < Q_x < 2\pi$	algebraic
(C)	Spiral SRO	$\pi < Q_x < 2\pi$	exponential
(D)	2D-Néel quasi-LRO	$Q_x = 2\pi$	algebraic
(E)	2D-Néel SRO	$Q_x = 2\pi$	exponential
(F)	Unstable (imaginary modes)	—	—
(G)	Breakdown of theory	—	no correlations

Table 3.1: **Parameter regions of the finite-temperature phase diagram** of Fig. 3.12. We distinguish mainly between phases with quasi-LRO, *i.e.*, algebraic decay of correlations, and phases with SRO, *i.e.*, exponential decay of correlations. Moreover, two regions are listed where the MSWT formalism ceases to be applicable, (F) and (G).

(A) 1D-like phase

At finite temperature, the 1D-like quasi-ordered ground-state phase for which we found strong indications below $\alpha \approx 0.18$ becomes a short-range-ordered phase. It is characterized by the ordering vector $(\pi, 0)$ (Fig. 3.13a) and vanishing correlations between neighboring chains already at low temperature (Fig. 3.13b). Nearest-neighbors on the same chain are anti-correlated (Fig. 3.13c), and the finite gap for all $T > 0$ (Fig. 3.13h) implies exponentially decaying intra-chain correlations [247], consistent with the expected finite-temperature behavior above a ground state with quasi-LRO. In this phase the inter- and intra-chain correlations behave qualitatively differently. In the rest of the phase diagram they follow the same pattern, since in a truly two-dimensional structure the correlations in one direction typically cannot disappear without affecting the correlations in the other one.

The assumption that this low-α phase really describes decoupled chains is reinforced by the component $\rho_{yy}^{\text{partial}}$ of the spin stiffness (Fig. 3.13f), which vanishes in this region, implying that the order properties along the y-direction are arbitrary.

It is remarkable that, with increasing temperatures, this phase is preferred over the quasi-ordered spiral phase. In the ground-state phase diagram, we have seen that quantum fluctuations stabilize 1D-Néel quasi-order. The same mech-

anism is at work here: collinear spin correlations are stabilized by fluctuations, in this case thermal ones.

(B and C) Spiral phases

At intermediate inter-chain couplings, $0.18 \lesssim \alpha \lesssim 1.35$, and low temperature we find a spiral phase with magnetic quasi-LRO (phase B). It can be seen as the finite-temperature continuation of the spirally-ordered ground-state phase. At larger temperatures, a BKT transition to a phase with a spiral ordering vector but with an exponential decay of correlations occurs (phase C). At large α, phase B is delimited by region F, where imaginary spin-wave frequencies appear. For α slightly smaller than one, there appears a transition from phase B to a narrow strip of phase C, almost immediately followed by a transition to phase A. For smaller α, the transition between B and A may actually be direct, since the extent of phase C becomes extremely small in temperature, but the finite resolution of our data does not allow us to unambiguously identify this.

At the isotropic point $\alpha = 1$, the BKT transition from B to C is approximately located at $T_{\mathrm{BKT}}/(t_1 + 2t_2) = 0.0836$. Quantum effects lower the transition temperature considerably from the classical value $T^{\mathrm{cl}}_{\mathrm{BKT}}/(t_1 + 2t_2) = 0.165$ (from classical Monte Carlo simulations [248]). A pure-quantum self-consistent harmonic approximation, developed by Capriotti and coworkers [249], gives $T_{\mathrm{BKT}}/(t_1 + 2t_2) = 0.0625$. The fact that MSWT produces a significantly higher estimate is not surprising given that the method of Capriotti *et al.* [249] takes vortex–antivortex excitations explicitly into account while MSWT does not. Also, it is well known that mean-field theories typically overestimate transition temperatures [83].

We note also a strong drop of the BKT transition temperatures around $\alpha \approx 0.4$. In Fig. 3.12, this is marked by a dashed line which separates phase B from a phase B' with similar properties. We believe that this behavior is a numerical artifact and that in fact B and B' constitute a single phase.

(F) Spin-liquid candidate region

At the large-α side of the spiral phases, we find a region where the spin-wave dispersion acquires imaginary modes. With increasing temperature, the width in α of this region stays approximately constant, but it moves to smaller α, leaving space to the collinear short-range-ordered phase (E). The spin-stiffness decreases upon approaching this region, which could be interpreted as a further precursor of a short-range-ordered phase.

This region where MSWT predicts an instability extrapolates well down to the suspected $T = 0$ spin-liquid phase at $1.35 \lesssim \alpha \lesssim 1.66$. Given that at $T = 0$ MSWT breaks down at a putative spin-liquid phase due to its lack of order, *a fortiori* one can expect MSWT to break down in the same parameter range at finite temperatures, because in that case the theory would be required to describe not only the ground state but also the excitations on top of it.

(D and E) 2D-Néel states

As expected from BKT theory, with increasing temperature the 2D-Néel ground state first changes into a low-T quasi-long-range ordered phase (phase D), which at a temperature T_{BKT} undergoes a transition into a high-T short-range-ordered phase (phase E). Both are characterized by an ordering vector at the 2D-Néel value $\boldsymbol{Q} = (2\pi, 0)$. Furthermore, neighboring spins which share a diagonal bond are strongly anticorrelated whereas neighboring spins which lie on the same chain are positively correlated.

The square XY lattice, which is reached as $\alpha \equiv t_2/t_1 \to \infty$, has been extensively studied in the past. The classical BKT-temperature $T^{\mathrm{cl}}_{\mathrm{BKT}}/t_2 = 0.695$ (classical Monte Carlo simulations [250]) is in the quantum limit significantly lowered to $T_{\mathrm{BKT}}/t_2 \approx 0.35$ (QMC [251, 252]). Our MSWT results yield a BKT temperature of $T_{\mathrm{BKT}}/t_2 \approx 0.27$ at $\alpha = 100$, where the system has practically reached the square lattice limit.[11] Once again, this disagreement is not surprising, given that MSWT does not account properly for vortex–antivortex excitations. In particular, the BKT line for $\alpha \gtrsim 1.6$ is not very distinct, as explained in the discussion of Fig. 3.11b. Therefore, its quantitative value should be interpreted with caution. However, the qualitative behavior of the phase diagram seems to be described correctly.

3.3.3 Observables distinguishing between LRO and SRO

In the following, we turn to observables which help to distinguish between different *strengths* of order (*i.e.*, quasi-LRO *vs.* SRO), in particular the partial Gaussian spin stiffness $\Upsilon^{\mathrm{partial}}$, the entropy, and the gap Δ.

The interpretation of these observable is as follows. The entropy, which can be computed via Eq. (14.5), is large in phases with strong tendencies towards order. The partial Gaussian spin stiffness, in contrast, is large in phases with strong order, as it measures the resistance of the system towards deformation

[11] At this value of α we computed the correlations to spins as far as 64 lattice sites away, contrarily to the rest of the phase diagram, see Sec. 3.3.1.

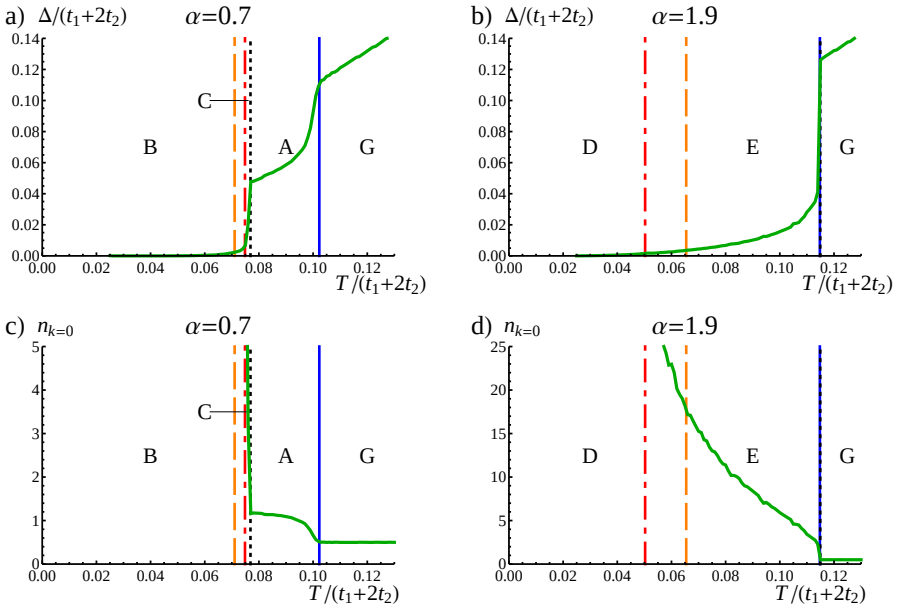

Figure 3.14: **(a-b) Gap Δ. (c-d) Occupation of the zero mode $n_{\boldsymbol{k}=0}$.** A large Δ and small $n_{\boldsymbol{k}=0}$ mean fast decay of correlations. The vertical lines denote the BKT transitions computed from the decay of correlations $C_{m\boldsymbol{\tau}_1}$ (red dot-dashed) and from $C_{m\boldsymbol{\tau}_2}$ (orange long-dashed). The breakdown temperature is represented by a solid blue vertical line, and the temperature where inter-chain correlations disappear by a dotted, black one [in (b) and (d), these coincide]. Capital letters refer to the phases of Fig. 3.12.

of the ordering vector. Indeed, as can be seen in Fig. 3.13g, the entropy is smallest in the low-temperature spiral and 2D-Néel phases (B and D), a behavior consistent with the quasi-ordered character of these phases. Correspondingly, $\Upsilon^{\text{partial}}$ (Fig. 3.13d) is large in these regions.

The gap $\Delta = \omega_{\boldsymbol{k}=0}$ of the spin-wave dispersion is another useful measure for the strength of order. It is directly imposed by the chemical potential μ [see Eqs. (14.12) and (14.13)], and its magnitude determines the rapidity of the decay of correlations: a finite (vanishing) gap leads to exponential (algebraic) correlations [247]. Hence, in principle, the onset of a gap at finite temperatures corresponds to the occurrence of a BKT transition. In reality, within MSWT,

we observe typically a very gradual thermal onset of the gap, and it does not provide a clear identification of the transition, as can be seen in Figs. 3.14a and b, where we report the gap for two representative values of α. This observation can be understood on the basis of a well-known fact: the chemical potential of the half-filled Dyson–Maleev boson gas, which determines the existence of a gap, cannot vanish at finite temperature because of the absence of Bose–Einstein condensation in two dimensions. As a consequence, we find a finite gap at any finite temperature, and the correlations decay exponentially at long distances. This implies that, strictly speaking, MSWT is not able to describe the BKT transition. However, for temperatures much lower than the BKT transition the gap is extremely small, being below our numerical precision. For all practical purposes, such a small gap entails a decay of correlations which is not distinguishable from an algebraical decay. Moreover, in a selected region of the phase diagram (corresponding to the spiral phase) the gap is seen to increase drastically around the estimated BKT transition temperature (Fig. 3.13h and Fig. 3.14a), and correspondingly the correlation function decays much more rapidly above that temperature. Hence, we conclude that MSWT still accounts for one of the most salient features of the BKT transition, namely a discontinuous behavior of correlations as the temperature is increased. Notably, whereas in the spiral phase the gap displays a sharp increase right above the BKT transition (Fig. 3.14a), it evolves smoothly through the BKT transition in the Neel phase (Fig. 3.14b).

We also note that in all phases, Δ increases sharply (accompanied by a sharp drop of $\Upsilon^{\text{partial}}$) at the breakdown temperature, where correlations are completely lost. Finally, in phase A, we find that the gap is almost a linear function of temperature up to very close to the breakdown temperature (this is better visible for smaller of values α than the one shown in Fig. 3.14a). This is typical of critical systems, where the temperature gives the only energy scale.

Neither entropy, spin stiffness, nor gap present a sharp change at the BKT transition. However, the contour lines of all of these seem to be consistent with the shape of the T_{BKT} curve as derived from the correlation functions.

We get further insight into the strength of correlations from the occupation of the zero-mode $n_{\boldsymbol{k}=0}$. It takes the role of the order parameter M_0 of the zero-temperature phase diagram when finite temperature prevents Bose condensation. Since, due to constraint (14.10), the average mode occupation $\sum_{\boldsymbol{k}} n_{\boldsymbol{k}}/N = S$ is fixed by the spin length, all spin-waves which are not in the zero mode have to occupy excited modes. Since these have a finite $\boldsymbol{k}$ vector, their interplay tends to destroy the order of the classical reference state given by the ordering vector. Conversely, a large occupation of the zero mode implies

small occupations of excited modes and, therefore, stronger order.

In Figs. 3.14c and d, we show examples for the evolution of $n_{\boldsymbol{k}=0}$ with temperature for two values of α. Similar to what was seen for the gap, at the transition between phases C and A, $n_{\boldsymbol{k}=0}$ drops from extremely large values to the order of 1 (Fig. 3.14c). After the drop, it changes only slowly with T. The behavior of $n_{\boldsymbol{k}=0}$ is different for the 2D-Néel phase (Fig. 3.14d). At the BKT line that we extracted from the two-point correlation functions $C_{m\boldsymbol{\tau}_1}$ and $C_{m\boldsymbol{\tau}_2}$, $n_{\boldsymbol{k}=0}$ decreases strongly but smoothly. Up to the breakdown point, however, its values are still several times larger than in the 1D-like phase A, indicating stronger order tendencies. The strong decrease supports our identification of the BKT transition; but the smoothness of $n_{\boldsymbol{k}=0}$ also shows the reason why the observables of Sec. 3.3.3 could not point out a sharp transition.

3.3.4 Summary

In summary, the finite-temperature phase diagram is a natural extension of the ground-state phase diagram. Zero-temperature LRO (quasi-LRO) is reflected in finite-temperature phases with quasi-LRO (SRO), and at temperatures below a few percent of the coupling strengths, the main characteristics of the ground-state phase diagram are retrieved. These contain a short-range 1D-like phase (A), and two quasi-ordered phases, one with spiral properties near the isotropic triangular limit (B), and one with 2D-Néel-like characteristics at large values of α (D). These are separated by a potential spin liquid (F). This last phase was identified by *(i)* the lowering of the spin stiffness as it is approached, and *(ii)* the breakdown of MSWT, which indicates that the assumption of an underlying ordered state is invalid.

Further, we have given a rough estimate for T_{BKT}. In our results, the BKT transition is clearer for the spiral phase than for the 2D-Néel phase. Although the results are to be interpreted only semi-quantitatively because MSWT does not explicitly account for vortex-antivortex excitations, we have found agreement in the magnitude where estimations from other methods exist.

3.4 The quantum spatially completely anisotropic triangular lattice (SCATL) at $T = 0$

In the previous sections, we found strong indications for spin-liquid behavior in the SATL. Initially, spin liquids were assumed to appear at strongest frustration, but as we saw, they seem to rather occur at transitions between two

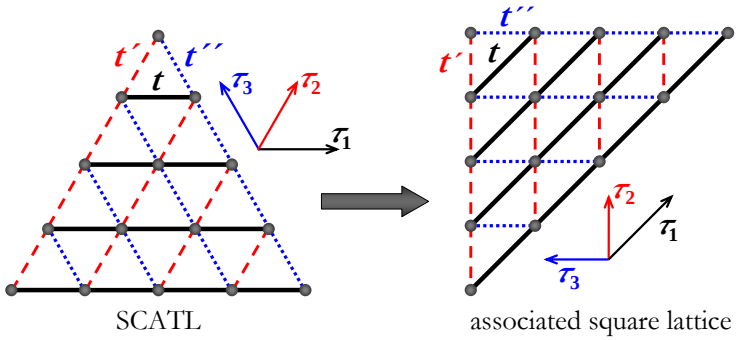

Figure 3.15: **Geometry of the SCATL.** The spins (gray bullets) are coupled to NNs along the lattice vectors $\boldsymbol{\tau}_{1,2,3}$ by the couplings $\tilde{t}_{\boldsymbol{\tau}_1} \equiv t$, $\tilde{t}_{\boldsymbol{\tau}_2} \equiv t'$, and $\tilde{t}_{\boldsymbol{\tau}_3} \equiv t''$, which can all be mutually different. The right part of the figure illustrates the associated square lattice. The shown geometry is the one used in the ED of the 15-site system, chosen for maximal symmetry between all three couplings.

different types of order. It appears plausible that at these points quantum fluctuations are most effective in disrupting classical order. Indeed, in classical statistical physics, thermal fluctuations typically suppress short-range order most effectively just above (*i.e.*, at higher temperature) a transition between a commensurate and an incommensurate phase, a concept which is known under the name *disorder point* [253–256]. To identify if it is a more general behavior that spin liquids appear at the transition between two phases of different order, we analyze now a generalization of the SATL, the spatially *completely* anisotropic triangular lattice (SCATL) with AFM XY interactions. Here, the tunneling matrix elements $\tilde{t}_{ij} = t, t', t''$ [see Eq. (3.3)] along all *three* lattice vectors are different (Fig. 3.15).

The SCATL is interesting for two reasons. First, from an experimental point of view, it is relevant for studying the sensitivity of the spin-liquid phases predicted in the SATL towards imperfect lattice shaking, *i.e.*, shaking which does not create two perfectly equal couplings. Second, from a more fundamental point of view, this model allows to investigate in a more general setting under which circumstances spin liquids appear. As we will show, also in the SCATL spin liquids do not occur at largest frustration but instead intervene in the transition between phases with different type of order, meaning that the spiral phase is completely surrounded (in terms of anisotropy of the couplings) by gapped

spin liquids. This suggests that the two – supposedly different – gapped spin liquids appearing in the SATL (compare Fig. 3.1b) could actually be continuously connected! As these results indicate, the additional anisotropy of the SCATL, allowing to approach spin liquid phases from different angles, can give fundamental insight into the nature of quantum disordered phases.

Ultracold-atom experiments as by Struck and coworkers [17] and trapped-ions implementations after the proposal by Schmied *et al.* [202] can easily be generalized to this situation by choosing an elliptical driving orbit or a preferred direction of ion vibration, respectively, that is not parallel to any of the sides of the triangular plaquettes. In Fig. 3.15, we also sketch the associated square lattice with an interaction along one of the diagonals. We will work in the latter one, to simplify the interpretation of our results. The SATL is retrieved at the lines $t'/t = 1$, $t''/t = 1$, and $t' = t''$.

The rest of this section is organized as follows. First, to give an overview over the ordered phases that one can expect in the quantum SCATL, we discuss the phase diagram of its classical counterpart (Sec. 3.4.1). Section 3.4.2 contains the discussion of the quantum-mechanical ground-state phase diagram of the SCATL, including various observables from MSWT and ED, as well as, for a possible comparison to experiment, the expected boson momentum distributions at selected points of the phase diagram. We will summarize our findings in Sec. 3.5 where we put them in a wider context of frustrated XY models. The $S = 1/2$ AFM SCATL with Heisenberg interactions, motivated by recent experiments on magnetic organic salts, is treated in a similar way in the Chapter 14.2.2. The results presented in this section can be found in the preprint Ref. [257].

3.4.1 Classical phase diagram

The classical phase diagram of the SCATL can serve as a guide to what ordered quantum phases are to be expected, and it allows to appreciate the changes brought about by quantum fluctuations. In the square lattice associated to the SCATL, we obtain the classical ordering vectors

$$Q_x^{\mathrm{cl}} = \begin{cases} \pi & \text{for} \quad -\frac{t}{2t'} - \frac{t'}{2t} + \frac{tt'}{2t''^2} \leq 1 \\ 0 & \text{for} \quad -\frac{t}{2t'} - \frac{t'}{2t} + \frac{tt'}{2t''^2} \geq 1 \\ \arccos\left(-\frac{t}{2t'} - \frac{t'}{2t} + \frac{tt'}{2t''^2}\right) & \text{else} \end{cases} \tag{3.37a}$$

$$Q_y^{\mathrm{cl}} = \begin{cases} \pi & \text{for} \quad -\frac{t}{2t''} - \frac{t''}{2t} + \frac{tt''}{2t'^2} \leq 1 \\ 0 & \text{for} \quad -\frac{t}{2t''} - \frac{t''}{2t} + \frac{tt''}{2t'^2} \geq 1 \\ \arccos\left(-\frac{t}{2t''} - \frac{t''}{2t} + \frac{tt''}{2t'^2}\right) & \text{else} \end{cases} \tag{3.37b}$$

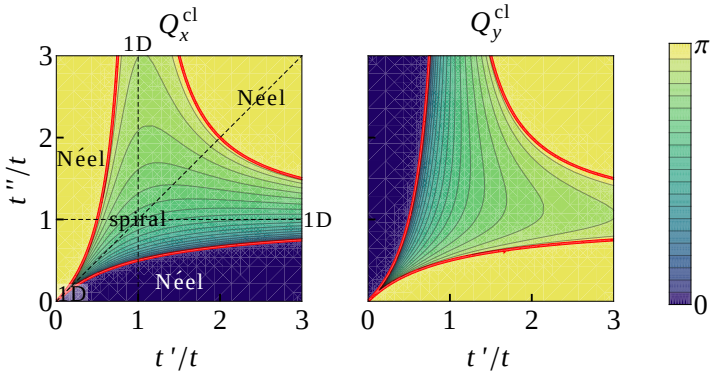

Figure 3.16: **Classical phase diagram of the SCATL, ordering vector.** We find three Néel-ordered and an extended spiral-ordered phase, as indicated by the labels in the left panel. The limits where the system decouples into an ensemble of independent chains are labeled "1D." The thick red lines denote transitions between different kinds of order, and along the dashed black lines the system is in the SATL limit.

The resulting classical phase diagram of the SCATL, plotted in Fig. 3.16, contains several Néel-ordered phases and an extended spiral-ordered phase. The Néel phases spread around the square-lattice limits $(t'/t, t''/t) = (1, 0)$ with $\boldsymbol{Q}^{\mathrm{cl}} = (0, \pi)$, $(t'/t, t''/t) = (0, 1)$ with $\boldsymbol{Q}^{\mathrm{cl}} = (\pi, 0)$, and $t'/t, t''/t \gg 1$ with $\boldsymbol{Q}^{\mathrm{cl}} = (\pi, \pi)$. The spiral phase, with continuously varying ordering vector, connects smoothly to the Néel phases, and occupies the extended region between them. In particular, it extends down to $t'/t = t''/t = 0$ [and, symmetrically, to $(t'/t = 1, t''/t \to \infty)$ and $(t''/t = 1, t'/t \to \infty)$], where the system decouples into an ensemble of 1D chains.

3.4.2 Quantum-mechanical phase diagram

Now, we turn to the quantum-mechanical ground-state phase diagram of the XY SCATL. To compute it, we use the MSWT supplemented with ordering-vector optimization, as explained in Chapter 14, working directly in the thermodynamic limit. We compare these results to ED of a 15-site lattice, the geometry of which, depicted in Fig. 3.15, is chosen for its symmetry between t, t', t'' bonds. As for the SATL, in small lattices it is important to leave the boundaries open to account for incommensurate ordering vectors.

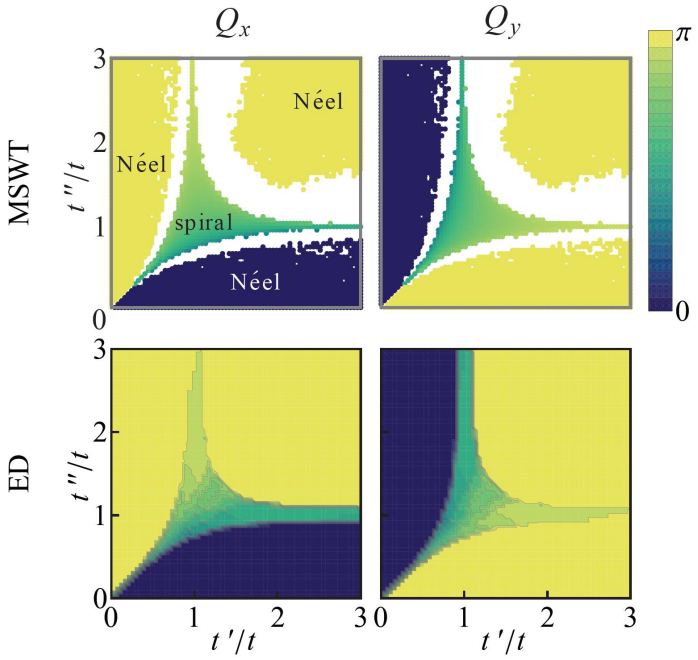

Figure 3.17: **Quantum-mechanical phase diagram of the SCATL, ordering vector. Upper row: MSWT data.** Around $t' = t'' = t$, a part of the classical spiral phase survives quantum fluctuations. **Lower row: ED data.** The growth of the Néel phase and reduction of spiral order, as seen in the MSWT data, can already be appreciated for $N = 15$ sites.

MSWT and ED results – ordering vector and order parameter

In this section, we give a first overview over the phase diagram, as obtained from the ordering vector $\boldsymbol{Q}$ and the order parameter M, followed in the next two sections by more detailed analyses.

As seen in the MSWT and ED ordering vectors, presented in Fig. 3.17, quantum fluctuations stabilize the Néel phases compared to the classical case, as already observed in the SATL. In the central region around $t' \sim t'' \sim t$, the ordering vector indicates spiral order with a broad range of incommensurate ordering vectors. The finite MSWT order parameter (Fig. 3.18, left panel) indicates that in these phases indeed long-range order survives quantum fluc-

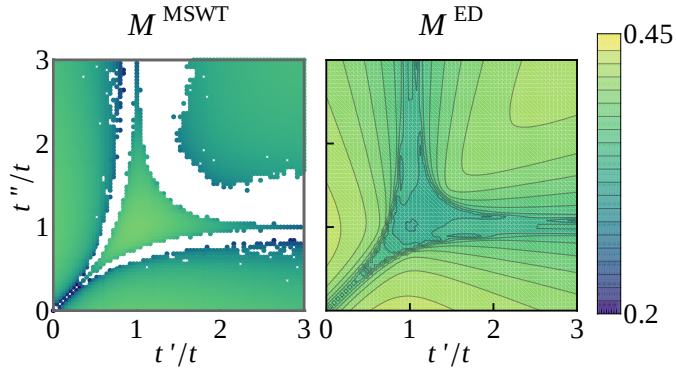

Figure 3.18: **Quantum-mechanical phase diagram of the SCATL, order parameter.** ED results qualitatively confirm the MSWT phase diagram. In particular, the order parameter for both methods decreases rapidly upon approaching the MSWT breakdown regions.

tuations. The self-consistent MSWT calculations become relatively unstable for small order parameters, which results in the ragged boundary lines of the ordered phases.

In the Néel phases, the ED order parameter (Fig. 3.18, right panel) is maximal, giving support to the assumption that here LRO persists. However, it is much smaller in the spiral phase than the MSWT value, a discrepancy already found in the SATL.

Between the ordered regions, we find a broad region where the MSWT theory breaks down, indicating as discussed in the SATL that these regions do not allow a description in terms of an ordered, semi-classical state. This, in turn, hints at quantum spin-liquid phases. Therefore, it appears that it is a quite universal feature of frustrated quantum antiferromagnets that spiral- and collinearly-ordered phases are always separated by quantum disordered phases. This is the main result of this section.

We obtain further support to this interpretation, which we will further corroborate in the next two sections, from the strong decrease of the MSWT and ED order parameters upon approaching this region (Fig. 3.18). Note also that both the ED and MSWT order parameter seems to disappear relatively smoothly when approaching the putative 1D-like spin liquid (consider, *e.g.*, in the range $2 \lesssim t'/t \lesssim 3$, $t''/t \to 1^-$). Upon approaching the putative large-α spin liquid

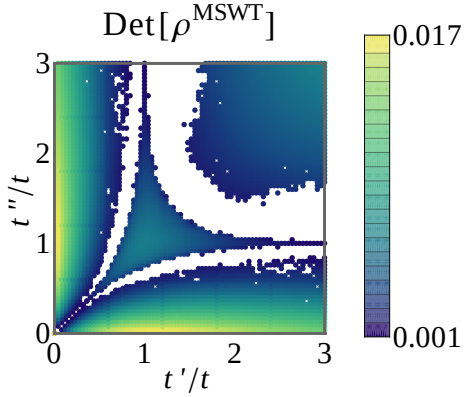

Figure 3.19: **The partial spin stiffness** (normalized to the coupling strengths $1 + t' + t''$) decreases upon approaching the MSWT breakdown region, suggesting the disruption of magnetic LRO.

dividing spiral from Néel LRO, on the other hand, for ED, the order parameter decreases more sharply (consider, *e.g.*, the line $t'/t = 1$, $t''/t \to 1^-$). Here, for MSWT, the breakdown occurs abruptly at finite order parameters. This may point at a difference in the type of phase transition upon approaching the large-α spin liquid and the spin liquid at the decoupled-chains limit.

The rest of this section is devoted to fleshing out our main finding, the appearance of a disordered region encircling the spiral phase.

Supporting observables from MSWT – spin stiffness and spin-wave velocities

In the SATL, the spin stiffness (14.21) has proven a valuable consistency check of our MSWT calculations. Even if the order parameter is finite, a small spin stiffness suggests that taking further quantum fluctuations into account than within MSWT could disrupt the remaining order and lead to disordered phases.

In Fig. 3.19, we show the determinant of the partial spin-stiffness tensor, $\det(\rho)$, normalized to the coupling strengths $1 + t' + t''$.[12] As we should expect [258], $\det(\rho)$ decreases upon approaching the phase transitions, especially from the Néel-ordered side. At large t' (t''), this decrease is due to a softening of the stiffness in x (y) direction, and at small $(t'/t, t''/t)$ in the direction perpendicular to $\boldsymbol{\tau}_1$, *i.e.*, in the direction perpendicular to the dominating chain, as we also saw in the SATL.

[12] Since for our purposes it is enough to extract an upper bound for the spin stiffness, we use the partial spin stiffness as defined in Eq. (14.23).

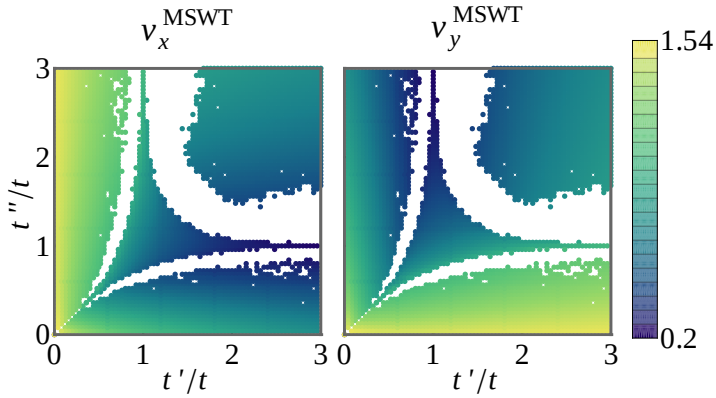

Figure 3.20: **Lower panels: The spin-wave velocities** (normalized to the coupling strengths $1+t'+t''$) soften in the 1D limits in the direction perpendicular to the dominating coupling strength. Differences in the spin-wave velocities might allow to measure the anisotropy of the SCATL.

Another indicator for approaching disordered phases is given by the spin-wave velocities $v_{x,y}$, which are connected to the spin stiffness via the susceptibility [259]. Since the spin-wave velocities are defined as the leading order of an expansion of the spin-wave dispersion relation, Eq. (14.13), around small $|\boldsymbol{k}|$, *i.e.*,

$$v_x = \lim_{k_x \to 0} \omega_{\boldsymbol{k}}/k_x \Big|_{k_y=0}, \tag{3.38a}$$

$$v_y = \lim_{k_y \to 0} \omega_{\boldsymbol{k}}/k_y \Big|_{k_x=0}, \tag{3.38b}$$

they can be measured directly from the excitation spectrum, allowing an experimental check of our findings.

As seen in Fig. 3.20, close to the 1D breakdown region, they, too, soften in the direction perpendicular to the dominating coupling. On the other hand, when approaching the putative large-α spin liquid dividing the spiral from the Néel phase, both spin-wave velocities remain finite. This is another (besides the different behavior of the order parameter) indication that the large-α spin liquid may be qualitatively different from the spin liquid found in the limit of decoupled chains.

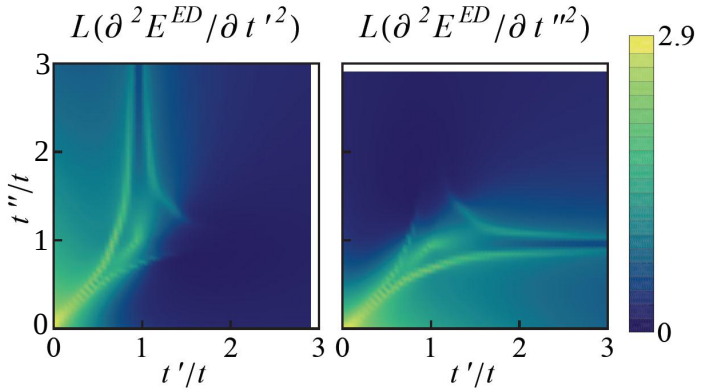

Figure 3.21: **Second derivative of ED ground-state energy** for the $N = 15$ system. For clarity, we plot the logarithm after a shift to positive values larger than one, $L(\partial^2(E/N)/\partial t^{\gamma 2})$, where t^γ is t' or t'', and $L(x) = \log(1+\max(x)-x)$. Strong peaks clearly mark the phase transitions from the Néel phases. The peak around $(t'/t, t''/t) = (1, 1)$ might be an indication of an additional phase separating the Néel phases from the spiral one.

Supporting observables from ED – energy derivative, gap, and chiral correlations

The ED observables investigated above (ordering vector and order parameter) allowed to interpret the predominant ordering behavior, but did not yield clear evidence if within ED really QPTs exist, and if yes, where their boundaries lie. The second derivative of the ED ground-state energy, which we plot in Fig. 3.21, can provide such an indicator. In fact, in the thermodynamic limit, it should diverge at a QPT.

Indeed, there are clear peaks along lines similar to where in MSWT the Néel order breaks down. Also, a peak appears around $(t', t'') = (1, 1)$. This might be interpreted as the precursor of a QPT away from the spiral state, and possibly to the spin liquid that is supposed to exist in this system.

We get further support for this phase diagram from the ED energy gap between ground and first excited state, Fig. 3.22. In the well-known limiting cases of the SCATL, it behaves as expected: There is no gap close to the decoupled-chains limits, since the system is then in a critical phase. In the Néel ordered phases, there is a large gap which separates the ground state from closely-spaced

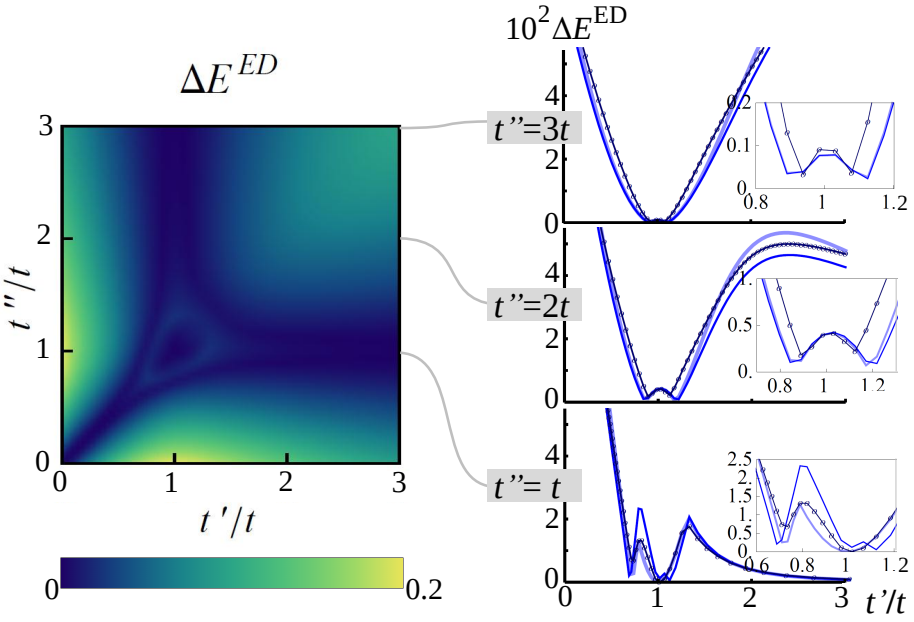

Figure 3.22: **Left panel: The singlet gap from ED** gives support to the MSWT phase diagram. A finite gap separates in the Néel phases spin-wave excitations from the ground state. In the spiral phase, the ground state is doubly degenerate due to the ambiguity in choice of chirality. The finite gap surrounding the degenerate region could be a precursor of a gapped, disordered phase. At the transitions to the Néel phases, the gap closes again. **Right panels: cuts** at fixed $t''/t = 1, 2, 3$ for triangles with increasing N (from light to dark and thick to thin: 6,10,15). There is little size dependence in the central gapped phase ($t'' = 2, 3t$ with $t' \approx t$, as well as $t'' = t$ and $t'/t \gtrsim 1.5$).

excitations, which in larger lattices become the spin waves, collapsing slowly towards the ground state [231] (for an example of the excitation spectrum in a Néel phase, see also the panel for $\alpha = 2$ of Fig. 3.6). This is consistent with the considerable size dependence found in our calculations, as can be seen in the right panels of Fig. 3.22, where we plot cuts of ΔE^{ED} at fixed $t''/t = 1, 2, 3$ for triangular systems (similar to the one in Fig. 3.15) with $N = 6, 10, 15$.

On the contrary, there is no gap in the spiral-ordered phase, because the ambiguity in the choice of chirality leads to a ground-state degeneracy.[13] We find that the vanishing of the gap depends strongly on the system geometry, but it occurs consistently for all triangular systems considered.

Interestingly, the gapless spiral phase is surrounded by a region where the gap attains considerable values. The very small dependence on system size indicates that here it is stable towards the thermodynamic limit. A finite gap is not consistent with a spiral-ordered phase. On the other hand, the predominant order in this region is at incommensurate wave-vectors. Hence, the finite gap is clearly not due to square-lattice Néel-like physics. Optimistically, these findings could therefore be interpreted as the precursors of a gapped spin-liquid phase. This gapped region completely encircles the spiral phase, suggesting that the low- and large-α gapped spin liquids found in the SATL could actually be continuously connected via the additional anisotropy of the SCATL.

The gap closes again upon approaching the Néel phases, indicating a quantum phase transition.

From the gap, it seems that there is support for the assumption of an extended gapped phase separating spiral and Néel LRO. Still, it would be desirable to be able to exclude for this region spiral LRO in the thermodynamic limit. To do this, we now study where chiral correlations persist, because in a spiral phase they have to remain finite. For the small systems used in our ED, we generalize the chiral correlations (3.33) to

$$\Psi_{-} = \frac{4}{N_{\Delta}} \langle \sum_{c} s_c \kappa_c \sum_{a} s_a \kappa_a \rangle \ . \tag{3.39}$$

Here, to minimize boundary effects, the sum over c runs only over the central triangles, while a runs over all triangles of the lattice. The factors $s_{a,c}$ weight the vector chiralities defined in Eq. (3.32) with a + (−) sign if the triangle points upwards (downwards). The prefactor including N_{Δ}, the number of summands, is chosen such that the chiral correlation has the same theoretical maximum of $\frac{9}{4}$ as the usual definition for large lattices, Eq. (3.33) [234].

[13] We checked that in the spiral phase there is a gap, similar to the spin-wave gap found in

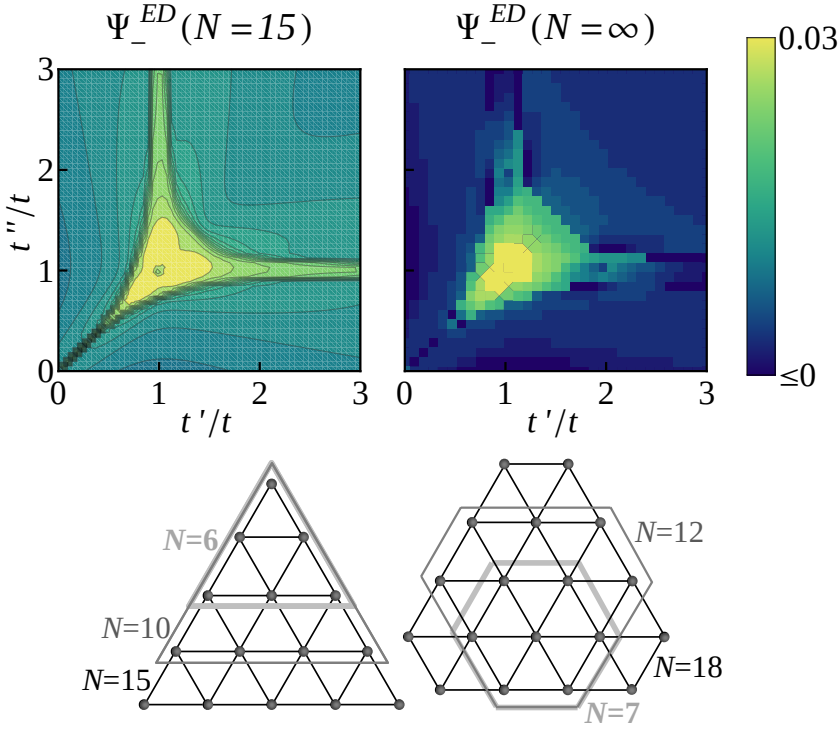

Figure 3.23: **Chiral correlations from ED. Upper left:** Already for small systems (N = 15), the chiral correlations are appreciably smaller in the Néel phases than in the rest of the phase diagram. **Upper right:** From an extrapolation to large lattices, it appears that chiral LRO only survives in a small central region around $(t'/t, t''/t) = (1, 1)$, lending support to an extended disordered phase close to the 1D limits. **Below:** The geometries used in the extrapolation are chosen for symmetry upon rotation by 60° and equal number of t, t', and t'' bonds.

As can be seen from the ED results of the $N = 15$ lattice (Fig. 3.23, left panel), the chirality is relatively small in the Néel phases. However, at this lattice size, there are still appreciable chiral correlations in the rest of the parameter regime. In particular, in the 1D limit, the chiral correlations are only a little smaller than in the spiral phase around $(t'/t, t''/t) = (1, 1)$. Therefore, we also plot in Fig. 3.23, right panel, an extrapolation to large lattices by $\Psi_-(N) = \Psi_-(N = \infty) + \frac{c_1}{N^{3/2}} + \frac{c_2}{N^2}$, where we use the known form for the leading finite-size behavior [260] but also include the first subleading correction due to the small systems under consideration (our data comes from lattices with $N = 7, 10, 12, 15, 18$, all chosen to have the same number of t, t', and t'' bonds, as sketched at the bottom of Fig. 3.23). While this can not be seen as a rigorous finite-size analysis, which is difficult for the small systems studied, it shows a clear trend, namely that the chiral correlations only survive in the central region around $(t'/t, t''/t) = (1, 1)$. From this data, it appears that while chiral order disappears in an extended region close to the limit of decoupled chains, it extends all the way to the Néel phases, contrary to the MSWT and PEPS results on the SATL (see Sec. 3.2). Further studies on larger lattices or with complementary methods seem necessary to settle this question.

With this, we have several independent observations from ED indicating the existence of a magnetically disordered phase, some of which indicate that it completely surrounds the spiral phase: the increase of the gap when leaving the central region around $(t'/t, t''/t) = (1, 1)$ suggests that there is no spiral LRO in this region. We could corroborate this with a vanishing chirality close to the decoupled chains. On the other hand, the predominant order is at incommensurate ordering vectors, indicating that this phase is also not Néel ordered. Therefore, it seems natural to assume that this region could host a spin-liquid phase, possibly gapped far away from the 1D limit and gapless close to it.

MSWT predictions for the hard-core boson momentum distribution

Finally, we wish to connect our predictions to experiment. As explained in Chapter 2.1 and Sec. (3.2.5), a well-established experimental technique for the observation of the quantum phases of ultracold atoms is time-of-flight (ToF) imaging of the atom momentum distribution, Eq. 3.35. In Fig. 3.24, we present ED predictions (for $N = 15$) for ToF images at various values of anisotropy, where the uppermost row shows parameter values from the SATL, and the other rows show from top to bottom results for increasing additional anisotropies in

---

the Néel phases, between the *second* and the *third* energy level.

steps of 10%. The black lines denote the first Brillouin zone (1st BZ).

Commensurate spiral order appears as peaks at the corners of the 1st BZ (as in the first panel of the second row), while peaks at the center of two opposing sides of the 1st BZ mark Néel order (as in the lower two panels of the second row). Incommensurate spiral order is characterized by peaks lying between these two limiting cases (as in the second panel of the second row). Close to the 1D limit, the peaks decrease in magnitude and smear strongly out along a straight line (as seen in the first panel of the first row).

In large systems, disordered phases are characterized by a sub-extensive growth of the peak height, but for the small system considered here it is difficult to draw such conclusions. However, the influence of the additional anisotropy on the predominant order properties (be they of long or short range) can be seen clearly already for the small systems considered in Fig. 3.24. In particular, the additional anisotropy can shift the system from one phase to a qualitatively different one. For example, the momentum distributions in the first row pass from an almost 1D-like spiral state to an adjacent Néel phase. Similar behavior is found for other values of $(t'/t, t''/t)$. Such ToF pictures, therefore, would allow to observe the influence of the additional anisotropy in experiment.

3.5 Summary for the frustrated quantum models

In this chapter, we have provided a thorough analysis of the ground-state phase diagrams of the quantum XY SATL and its generalization, the SCATL (that has not been considered before in the literature). To this purpose we investigated various observables from MSWT, PEPS, and ED.

We found two main recurrent features for strongly frustrated quantum magnets in two dimensions. First, collinear order is considerably stabilized by quantum fluctuations against spiral order. Extending our results for the SATL to finite temperatures, we found that thermal fluctuations have a similar effect. Second, (quasi-)ordered phases characterized by different forms of order (collinear *vs.* spiral) do not continuously connect to each other, but they rather seem to be separated by quantum disordered phases. In the SATL, this behavior possibly leads to the appearance of one gapless and two gapped spin liquids. This effect was also more recently found by Varney *et al.* in a frustrated XY model on the honeycomb lattice [261].

As a consequence, in the SCATL, the spiral phase seems to be entirely sur-

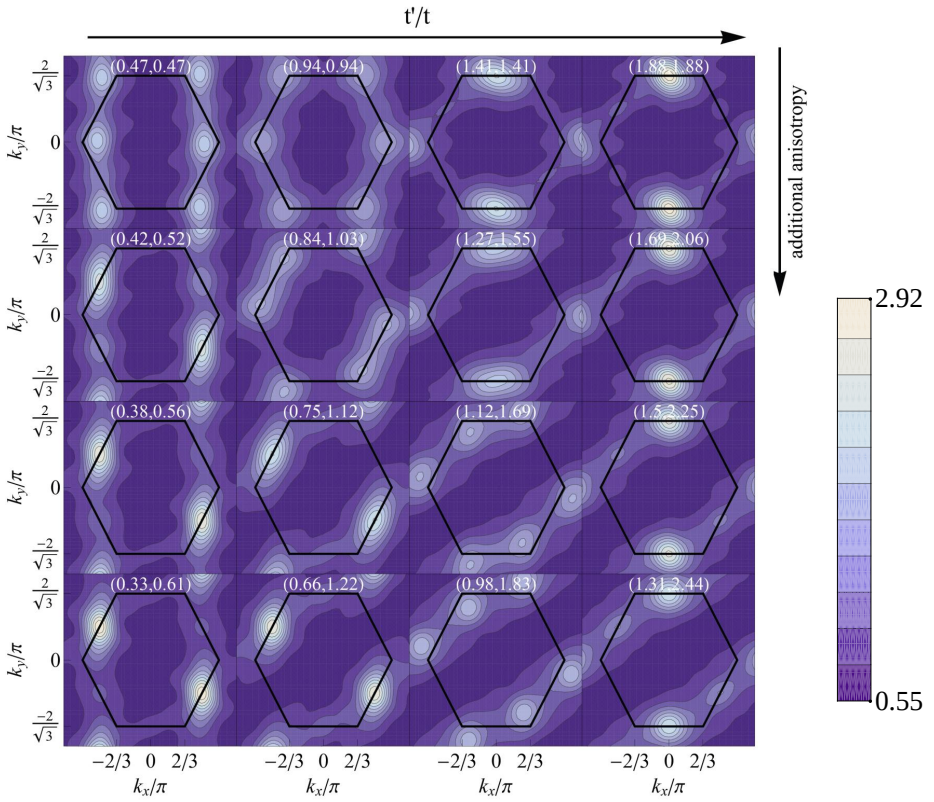

Figure 3.24: **ToF predictions** (corresponding to the static structure factor) allow comparison to typical experimental results. The additional anisotropy of the SCATL increases from top to bottom in steps of 10%, showing that it can shift the system to phases with different qualitative order. Data from ED of $N = 15$ spins.

rounded by a quantum disordered region. This result, which constitutes one of the main findings of this chapter, is supported by the breakdown of MSWT theory, together with the strong decrease of the order parameter and the spin stiffness. It is further corroborated by ED data, where a finite gap makes spiral LRO seem unlikely, while the location of the structure-factor peak at incommensurate wave vectors seems to preclude Néel LRO. Also, the strong decrease of the ED structure-factor peak appears to support this interpretation. Our ED data remains inconclusive, however, as an extrapolation of chiral correlations to large lattices seems to predict a breakdown of chiral order only close to the limit of decoupled chains.

A complete encircling of the spiral phase by disordered phases could naturally explain the succession of a gapped and a gapless spin liquid at the low-α limit of the SATL (as presented in Fig. 3.2b). The gapless spin liquid would be continuously connected to the limit of decoupled chains, while the additional anisotropy of the SCATL would adiabatically connect the gapped spin liquids at small and large α. This consideration shows the great potential of the additional anisotropy to deliver new insights into the nature of these phases. Further, it allows to approach the small-α spin liquids not only from the spiral phase, but also from the Néel phase. We found, indeed, some indications that very close to the 1D limit the transition from the Néel phase to the putative disordered region could be qualitatively different from what happens at larger α.

Finally, we provided ED predictions for the boson momentum distribution in time-of-flight pictures, a comparison to which might allow to test our findings in upcoming experiments with ultracold atoms.

3.6 Connection to current experiments and summarizing remarks

Before concluding this chapter, we wish to more precisely place our results into the context of current cold-atom experiments. Currently, heating effects prevent reaching the strongly-interacting regime so that experiments are carried out not in the limit of infinite inter-boson repulsion, but rather at weak interactions [17]. In this regime, the system behaves almost classical. To see in how far frustration effects play a role in this case, we now address briefly the phase diagram of the SATL at weak inter-particle repulsion.

For small on-site interactions U, we can compute the ground-state behavior of the frustrated Bose–Hubbard model (3.1) via an expansion in condensate fluc-

tuations. This becomes possible since quantum fluctuations in this regime are typically small, and the ground state is Bose-condensed, showing strong ordering tendencies. Normally, the behavior of the system in this case is well captured by a Bogolioubov–deGennes expansion, which replaces operators by (global) mean values dressed with small fluctuations around them. However, as described in the previous sections, in the extreme quantum limit of $U \to \infty$, geometrical frustration can disrupt order and lead to quantum-disordered states. We can expect to find precursors of this physics in the weakly-interacting regime, such as reduced LRO of the condensate phase. In this case, a standard Bogolioubov–deGennes expansion is not an adequate approach, because it is based on the assumption that the phase fluctuations remain small on a global scale (*i.e.*, from one side of the sample to the other). To circumvent this limitation, we employ a Mora–Castin expansion [262] as explained in Chapter 13.3. This type of expansion only relies on the assumption that the variation of the phase is slow on the order of the lattice spacing, but it may be strong on larger distances. This generalization makes this method also applicable to systems with reduced degrees of order. We extend the expansion of the original article [262] to include terms up to fourth order in the fluctuations, and solve the resulting equations self-consistently. This improvement proves crucial to capture the change of the order properties with increasing U (*i.e.*, with increasing "quantumness"). Our findings are presented in Fig. 3.25a. Technical details can be found in Chapter 13.3. The results presented here have been published in Ref. [164] without detailed derivations. A publication including these is in preparation [214].

To characterize the phases of the weakly-interacting limit of the SATL, we employ the ordering vector, Eq. (13.41). As it shows, the shift of the transition between Néel and spiral order, observed in the $U \to \infty$ limit of the SATL (Sec. 3.2), seems to set in immediately and smoothly with increasing U.

Further, to judge the strength of quantum fluctuations, and as a fundamental self-consistency check of the Mora–Castin formalism, we also compute the phase fluctuations and the condensate fraction, using Eqs. (13.43) and (13.46), respectively. Where the phase fluctuations become too large or the condensate fraction too low, the initial assumption in the Mora–Castin formalism that quantum fluctuations are small is no longer valid and the theory cannot be applied. In Fig. 3.25a, we include lines where the condensate fraction falls below 0.75 and where phase fluctuations along the bonds $\boldsymbol{\tau}_1$ and $\boldsymbol{\tau}_2$ rise above $\pi/4$. We identify these lines with the onset of strong tendencies towards quantum disorder. The values chosen are arbitrary, but they show a clear trend: order is disrupted more easily close to the transition between Néel and spiral LRO. This is consistent with our results from Sec. 3.2, which suggest that in this param-

eter region a gapped spin liquid appears at large U. Considering the limit of weakly-coupled chains, from the ordering vector, we do not find the extension of a gapless 1D-like spin liquid to finite inter-chain couplings as should happen for strong U. However, the condensate fraction and inter-chain phase order are less stable at small t_2/t_1, indicating weaker ordering tendencies. It appears that the putative spin-liquid regions imprint precursors of their properties also on the weakly-interacting regime.

We can tentatively interpolate our findings between the regime of weak interactions and the extreme quantum limit from Sec. 3.2. The result is sketched in Fig. 3.25b. While the shift of the transition between Néel and spiral LRO seems to increase smoothly with U, the various quantum disordered phases (gapped or gapless spin liquids) seem to set in only at finite interaction strengths.

Although the theoretical tools that we have at our disposal all have their shortcomings, we were able to considerably narrow down the parameter regions where quantum spin liquids may occur. To study such exotic quantum states with all their intriguing properties and possible applications, an experimental quantum simulation seems indispensable, which could be realized via lattice shaking as explained.

As we have seen in this chapter, the lattice geometry plays a crucial role for the physics of ultracold atoms systems. In the examples above, a triangular lattice induces geometrical frustration, leading to new quantum phases. The particular triangular optical lattice used in the experiments of the Hamburg group [160, 165] offers, however, the intriguing possibility to also explore another geometry: simply by changing the polarization of the laser beams creating the lattice, it can be transformed into a honeycomb lattice [161]. A lattice of such a geometry, loaded with Fermions [162], may be used for mimicking graphene physics. The first experiment in an optical honeycomb lattice together with comparison to theoretical results is the subject of the next chapter.

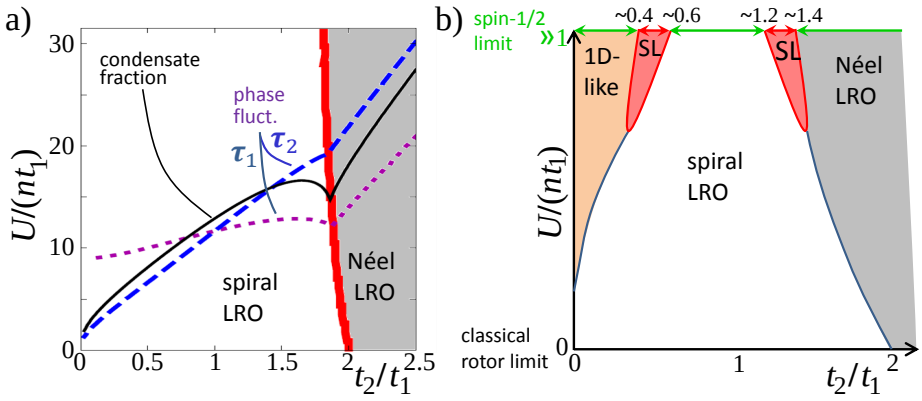

Figure 3.25: **(a) Phase diagram of the SATL for weak interaction U,** from a Mora–Castin expansion with mean occupation number $n = 3.5$. Quantum fluctuations, quantified by $U/(n\,t_1)$, shift the Néel–spiral transition to lower values of t_2/t_1 (thick red line). The purple dotted (blue dashed) line marks where NN phase fluctuations along the lattice vector $\boldsymbol{\tau}_1$ ($\boldsymbol{\tau}_2$) reach $\pi/4$, and the thin solid line where the condensate fraction has dropped to 0.75. Phase fluctuations and reduction of the condensate fraction are stronger at the Néel–spiral transition and close to the 1D limit, indicating a stronger instability towards disorder. **(b) Putative phase diagram of the SATL for all interaction regimes,** combining the results from panel (a) with those of Sec. 3.2 and Schmied *et al.* [202]. While the shift of the transition Néel–spiral can already be observed at arbitrarily small U, the extension of a gapless phase with 1D-like quasi-LRO seems to happen at finite interactions. At larger U, gapped spin-liquids (SLs) should emerge.

Chapter 4

Multi-component quantum gases in spin-dependent honeycomb lattices

The geometry of a system fundamentally defines its properties. Hence, to be generally applicable, quantum simulators have to be able to treat various geometries with widely different properties. However, so far, most experiments with ultracold quantum gases have been carried out in lattices of cubic symmetry. Optical lattices allow, however, much more than this. Due to the prospect of realizing a variety of novel phenomena with possible applications in quantum information and spintronics, a strong current theoretical development [211, 263–267] aims especially at the quantum simulation of systems with a honeycomb geometry. This direction of research is especially spurred by the rapid development in the last years of graphene technology [268], which has a vast spectrum of potential applications, ranging from transistors [269] over chemical sensors [270] to – perhaps most promising – graphene photonics [271], optoelectronics [272], and plasmonics [273–278]. Mastering the honeycomb geometry would allow access to the fascinating effects encountered in graphene, carbon nanotubes [279], and a large number of other carbon-based compounds, including topological and spin-Hall insulating phases [280, 281] (see Chapter 5).

In this chapter, we discuss the first experiments on ultracold quantum gases in a spin-dependent optical honeycomb potential, realized by Prof. Sengstocks group in Hamburg. The experimental results have been published together

with our theoretical analysis in Ref. [161]. Previously, different types of spin- and/or state-dependent lattices have been implemented to study transport and magnetic properties of ultracold lattice gases [10, 282–286]. Exotic geometries have more recently also been achieved by other groups, such as the tunable honeycomb lattice in the group of T. Esslinger [162] or the kagome lattice in the group of D. Stamper-Kurn [163].

We demonstrate how the spin-dependent honeycomb lattice can be used to tailor quantum phases and dynamics of spin-mixtures. We show that the combination of interactions between different spin-states and the spin-dependent lattice potential leads to novel quantum phases: a *forced antiferromagnetic* (AFM) Néel order when two spin-components localize in different sublattices, and a pronounced interaction-induced modulation of the SF density, when one spin-component is localized in one sublattice and imposes an interaction-induced lattice on the other SF spin-component. This can be understood as a *forced supersolid*. Examining the influence of the spin state on the SF to MI transition, we demonstrate furthermore that the mobility of particles in the lattice can be adjusted by immersing the SF particles into a well-localized spin-crystal. We present the phase diagrams from the Gutzwiller mean-field *Ansatz* (GMFA, see Chapter 13.1), where we find good agreement with the experimental results. Our studies show the strong influence of the lattice geometry on effects like the SF–MI transition. The realization of honeycomb lattices is a first step towards the quantum simulation of graphene-like physics in an optical-lattice architecture. As our results show, optical-lattice setups go even beyond a pure mimicking of solid-state effects, opening possibilities that are not realizable in solid-state systems.

4.1 Experimental setup

The basic structure of the spin-dependent optical honeycomb lattice used by the Hamburg group is illustrated in Fig. 4.1. It generalizes the basic idea of optical lattices described in Chapter 2.1. Three laser-beams derived from a Ti:Sapphire laser running at $\lambda = 830\,\mathrm{nm}$ intersect under an angle of 120°, with each beam linearly polarized in the plane of intersection. This leads to the formation of local potential minima in a honeycomb structure. A perpendicular one-dimensional lattice with a different frequency restricts the motion of the atoms to two-dimensional planes. Typical potential depths of this 1D-lattice are $V_{1\mathrm{D}} = 44 E_{\mathrm{rec}}$. The resulting two-dimensional honeycomb lattice potential is

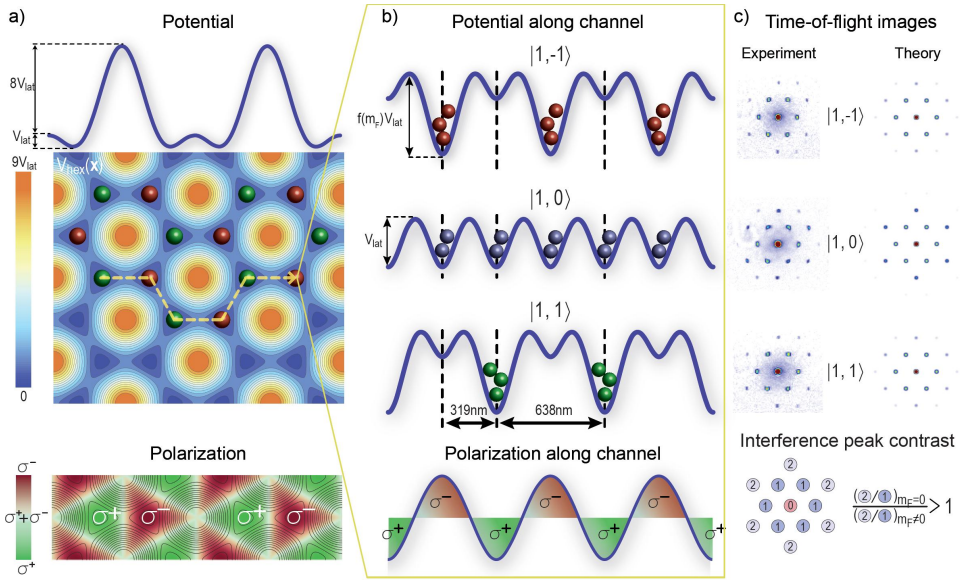

Figure 4.1: **Spin-dependent honeycomb lattice. (a) The lattice** with alternating σ^+ (green bullets) and σ^- (red bullets) polarization structure. The upper plot shows a cut through the 2D potential (center). The lowest graph shows the polarization distribution in the lattice ranging from fully σ^+(green) to σ^-(red) polarized. **(b) The potential along the orange dashed line** in panel (a) for particles in different Zeeman states $|F, m_F\rangle$. The modulation depth of the potential depends on the m_F-state. The lower part shows the corresponding light polarization. For large lattice depth, atoms in the different substates will localize as indicated by the red, blue, and green bullets. **(c) Time-of-flight images** of SF samples prepared in different Zeeman substates (left) and the corresponding calculated momentum distributions (right). The second- to first-order interference peak ratio (depicted at the bottom) differs between $|1, \pm 1\rangle$ atoms (which assume a *triangular* configuration) and $|1, 0\rangle$ atoms (which assume a *honeycomb* configuration).

given by

$$V(\boldsymbol{x}) = -2V_{\mathrm{lat}}\Big\{3-\cos\left[(\boldsymbol{b}_1-\boldsymbol{b}_2)\cdot\boldsymbol{x}\right]+\cos\left(\boldsymbol{b}_1\cdot\boldsymbol{x}\right)+\cos\left(\boldsymbol{b}_2\cdot\boldsymbol{x}\right)\Big\} \qquad (4.1)$$
$$-2\sqrt{3}V_{\mathrm{lat}}\alpha\, m_F\Big\{\sin\left[(\boldsymbol{b}_1-\boldsymbol{b}_2)\cdot\boldsymbol{x}\right]+\sin\left(\boldsymbol{b}_1\cdot\boldsymbol{x}\right)-\sin\left(\boldsymbol{b}_2\cdot\boldsymbol{x}\right)\Big\}$$

where g_F is the Landé g-factor, μ_{B} is the Bohr magneton, m_F labels the different atomic Zeeman substates, $\boldsymbol{b}_1 = \sqrt{3}/2k\boldsymbol{e}_x + k/2\boldsymbol{e}_y$ and $\boldsymbol{b}_2 = \sqrt{3}k\boldsymbol{e}_x$ (with $k = 2\pi/\lambda$) are the reciprocal vectors of the honeycomb lattice, and V_{lat} gives the strength of the lattice. The constant α depends on the detuning of the lattice laser from the atomic resonance; in the experiments of the Hamburg group, $\alpha = 0.13$.

4.1.1 Basic behavior of atoms in the spin-dependent lattice

In the experiments of Prof. Sengstock's group, this lattice is loaded with typically several 10^5 atoms of ^{87}Rb. To achieve this, initially Bose–Einstein condensates in the hyperfine state $|F, m_F\rangle = |1,-1\rangle$ are prepared in an optical dipole trap. From these, pure hyperfine- and magnetic Zeeman-states or specific compositions of different such states can then be prepared with the aid of radio-frequency and/or microwave sweeps. After these preparatory steps, the lattice is ramped up, during which coherence between different spin states is lost.

The atoms experience a potential composed of the honeycomb lattice and the perpendicular 1D-lattice, *i.e.*, $V(\boldsymbol{x}) + V_{\mathrm{1D}}\sin^2(kz)$. For neighboring intensity maxima of the honeycomb lattice, the local polarization alternates between σ^+ and σ^- (for example, when following the dashed line in Fig. 4.1a, center; see also Fig. 4.1a, bottom). Since atoms in a light field experience a polarization-dependent ac Stark shift [287], the potential at σ^+ and σ^- polarized potential wells differs for different atomic Zeeman substates. According to the local polarization, we denote the two triangular sublattices constituting the bi-atomic basis of the honeycomb lattice by σ^+ and σ^-.

Mapping the polarization of the light field $\mathcal{P}(\boldsymbol{x})$ (+1 for pure σ^+ and −1 for pure σ^- polarizations) onto a pseudo-magnetic field $B_{\mathrm{eff}}(\boldsymbol{x}) \propto -V_{\mathrm{hex}}(\boldsymbol{x})\,\mathcal{P}(\boldsymbol{x})/\mu_{\mathrm{B}}$, the potential $V(\boldsymbol{x})$ can be written in the compact form

$$V(\boldsymbol{x}) = V_{\mathrm{hex}}(\boldsymbol{x}) + m_F g_F \mu_{\mathrm{B}} B_{\mathrm{eff}}(\boldsymbol{x})\,. \qquad (4.2)$$

This potential consists of a spin-independent part $V_{\mathrm{hex}}(\boldsymbol{x})$ of honeycomb geometry and a state-dependent potential due to the local pseudo-magnetic field

$B_{\text{eff}}(\boldsymbol{x})$ that acts in opposite ways for the two sublattices. Due to this energy bipartition of the honeycomb lattice, atoms with $m_F \neq 0$ are preferably confined to either the σ^+ or the σ^- triangular sublattice. In contrast, for atoms in the $m_F = 0$ state, the B_{eff} term vanishes, so that they will distribute homogeneously over both the σ^+ and the σ^- sublattice (Fig. 4.1b).

For typical experimental parameters, tunneling of the atoms follows predominantly along channels connecting neighboring local minima of $V_{\text{hex}}(\boldsymbol{x})$, because the large central peak maxima ($9V_{\text{lat}}$) reduces a diagonal tunneling across honeycomb plaquettes. One such nearest neighbor (NN) tunneling channel is indicated in Fig. 4.1a by a dashed line. Figure 4.1b illustrates the spin-dependent lattice potentials along the dashed line for the $F = 1$ hyperfine ground-state manifold of ^{87}Rb. The potential along this line corresponds to a sinusoidal potential with 319 nm period, modulated by a cosine function with 638 nm period. The modulation depth $f(m_F)V_{\text{lat}}$ along this line depends, due to Eq. (4.2), on the m_F-state and is given by $\{1,1.7,2.5\}V_{\text{lat}}$ for $m_F = \{0, \pm 1, \pm 2\}$ and $\lambda = 830$nm.

4.1.2 Experimental measurement methods

Due to the pseudo-magnetic field term in the potential (4.2), the preferred distribution of the atoms over the $\sigma^{\pm}$ sublattices depends on the hyperfine state. The resulting differences in the structure factor were observed in the Hamburg experiments by time-of-flight (ToF) measurements, such as explained in Chapter 2.1. Typical measurement results for states that localize in triangular and hexagonal configurations ($|1, \pm 1\rangle$ and $|1, 0\rangle$, respectively) are shown in Fig. 4.1c together with the corresponding theoretical prediction from a one-particle band structure calculation (also due to Prof. Sengstock's group). The observed second- to first-order interference peak ratio (see Fig. 4.1c bottom) is significantly larger for the hexagonal than for the triangular configurations. It typically ranges between 2 and 4 for the experimental parameters. This fact can be explained by considering the Bloch functions and their quasi-momentum distribution for the corresponding spin-dependent lattice geometry. As explained in Chapter 2.1, the ToF measurement maps the spatial density distribution of the ensemble after a free expansion to the in-lattice momentum spectrum. The height of the observed peaks, quantified by the visibility, is a measure for the coherence of the atoms in the lattice. It serves to distinguish the SF regime (large visibility) from the MI regime (low visibility).

To obtain more precise information about the spatial in-trap distribution, the Hamburg group employed a specialized method for state- and site-selective microwave spectroscopy. It allows for *in-situ* investigations of the spatial spin-

ordering and is suitable for studying different regimes ranging from the SF to the MI phase. Previously, a similar kind of polarization-dependent radio-frequency spectroscopy method was used to study cubic lattices [284]. Here, we sketch the main idea and refer to the publication [161] for more details. In this method, a microwave pulse transfers population from the populated m_F-states to initially non-occupied, auxiliary $m_{F'}$-states. The efficiency of this transfer depends on the detuning of the microwave energy to the energy difference between m_F and $m_{F'}$, $\Delta E_{m_F,m'_F}$. Therefore, this technique is sensitive to the spatial variation of $\Delta E_{m_F,m'_F}$ that is generated by the pseudo-magnetic field B_{eff}, given by

$$\Delta E_{m_F,m'_F} = \Delta V(\boldsymbol{x}) = \mu_{\text{B}} \left(m_{F'} + m_F\right) \left(B_0 + B_{\text{eff}}\left(\boldsymbol{x}\right)\right)/2 + E_{\text{hfs}}\,, \tag{4.3}$$

where B_0 is an additional homogeneous magnetic guiding-field and E_{hfs} is the ^{87}Rb-hyperfine splitting. The spectroscopy signal is obtained by releasing the sample from the lattice and performing Stern–Gerlach separation. Since the transfer efficiency between initial and final state depends on the Franck–Condon overlap, care has to be taken to normalize the signal correspondingly. By counting the fraction of transferred atoms as a function of the microwave frequency, the spectroscopy signal reveals the relative occupations of the two sublattices σ^+ and σ^-.

4.2 Theoretical model

Before discussing the experimental results for the spin-dependent honeycomb geometry, we first explain how we analyze these theoretically. We model the system by the two-species Bose–Hubbard model

$$\begin{aligned}\hat{\mathcal{H}} \;=\; & -\sum_{\langle ij\rangle}\left(t^a \hat{a}_i^\dagger \hat{a}_j + t^b \hat{b}_i^\dagger \hat{b}_j + \text{h.c.}\right) \\ & + \sum_i \left[\sum_{\alpha=a,b}\left(-\mu^\alpha + E_i^\alpha\right)\hat{n}_i^\alpha + U_i^{a,b}\,\hat{n}_i^a \hat{n}_i^b + \sum_{\alpha=a,b}\frac{U_i^\alpha}{2}\hat{n}_i^\alpha\left(\hat{n}_i^\alpha - 1\right)\right],\end{aligned} \tag{4.4}$$

and compute its ground state using the GMFA (see Chapter 13.1 for technical details). This Hamiltonian is a straightforward generalization of the simple Bose–Hubbard model (2.4) to the case of two spin components (a and b) and two sublattices (σ^+ and σ^-). The operator $\hat{a}_i$ ($\hat{b}_i$) annihilates an a (b) boson at site i, and $\hat{n}_i^a$ ($\hat{n}_i^b$) are the corresponding occupation number operators. Angle brackets denote pairs of NNs and $t^\alpha_{\text{NN}} = t^\alpha$ ($\alpha = a, b$) the corresponding tunneling matrix

elements. We will also present results including next-to-NN (NNN) tunneling. We denote the local energy offsets at a $\sigma^{\pm}$ site by $E_i^{\alpha} = E_{\sigma^{\pm}}^{\alpha}$, and $U_i^{\alpha,\alpha'} = U_{\sigma^{\pm}}^{\alpha,\alpha'}$ is the corresponding interaction between the spin-components $|\alpha\rangle$ and $|\alpha'\rangle$. For convenience, we define $U_{\sigma^{\pm}}^{\alpha} \equiv U_{\sigma^{\pm}}^{\alpha,\alpha}$. Similarly we will abbreviate expectation values $\langle \hat{a}_i \rangle = \langle \hat{a}_{\sigma^{\pm}} \rangle$ if $i \in \sigma^{\pm}$, where we make use of translational invariance. For conciseness of notation, we will further index in the following the $|1,-1\rangle$ state by -1 and the $|2,\pm 2\rangle$ state by ± 2. For simplicity, we implement the GMFA in the grand-canonical ensemble, to which we introduce the chemical potentials μ^{α}. To obtain results for fixed particle numbers, we iteratively adjust the chemical potential until the desired particle number is reached. In most situations, this approach works well, but there are cases where convergence is problematic.

To allow a quantitative comparison to experiment, we extract E_{σ}^{α}, $U_{\sigma^{\pm}}^{\alpha,\alpha'}$, and t^{α} from the experimental parameters. The energy offsets E_{σ}^{α} can be computed in a straightforward manner from Eq. (4.1). For the on-site interactions, we have to evaluate the integral Eq. (2.6). To do this, we approximate the optical lattice potential at the bottom of each site as a harmonic oscillator, which allows to replace the Wannier functions by Gaussians. For not too shallow lattices, this approximation works well near the center of a site, from which the integral obtains the largest part of its weight. In shallow lattices, on the other hand, the interaction is weak and the tunneling term dominates, so that small errors in the estimation of the interaction do not play any role. Therefore, also in the case of shallow lattice the approximation of the Wannier functions as Gaussians is acceptable. For consistency, we include also the zero-point energy of the harmonic oscillator in the energy offsets E_{σ}^{α}.

The tunneling matrix elements may be extracted from the overlap between Wannier functions at different sites, using Eq. (2.7). Contrary to the interactions, for the tunneling one has to use the true Wannier functions since these have strong oscillations in their tails. For the interactions, we could use Gaussian functions and neglect these tails, because they are exponentially small. They do have an important influence, however, in the overlap integral defining the tunneling matrix elements. Since the calculation of the Wannier functions for an optical honeycomb lattice is a challenging task, we estimate the tunneling from a simpler approach. Namely, we fit exact one-particle band-structure calculations of the full optical lattice to the band structure of a tight-binding model Hamiltonian (*i.e.*, without interaction terms). This gives a good estimate for the tunneling matrix elements, where the agreement is improved if not only NN tunneling terms but tunneling terms up to some larger distance are included. In our case, the bi-atomic basis of the honeycomb lattice complicates this ap-

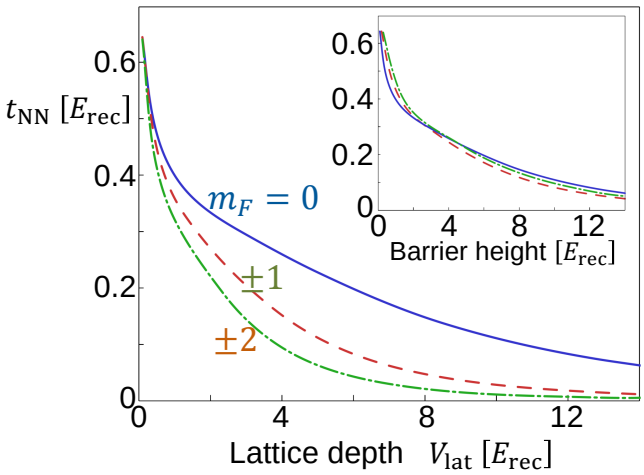

Figure 4.2: **NN tunneling matrix elements for different spin states.** The solid, dashed and dot-dashed lines represent t_{NN} for $m_F = 0, \pm 1$, and ± 2. The inset shows t_{NN} as a function of the spin-dependent barrier height.

proach, because one has to analyze the tunneling not between single sites, but between double wells consisting of a σ^+ and a σ^- site.

The results for the NN tunneling matrix elements t_{NN} are summarized in Fig. 4.2. They decrease from $m_F = 0$ to $m_F = \pm 1$ to $m_F = \pm 2$. This is due to the increasing barrier height between neighboring wells (such as sketched in Fig. 4.1b), as can be seen when plotting the tunneling matrix elements against the barrier height instead of against the absolute strength of the lattice (inset).

4.3 Superfluid to Mott-insulator transition in pure systems

The mobility of particles plays an important role in understanding, for example, the conductivity of solid-state systems. In optical lattices, this property is essentially governed by the interplay of the on-site interaction U with the tunnel matrix element t, and is usually well captured in a Bose–Hubbard model such as Eq. (4.4). As described in Chapter 2.1, in optical lattice experiments, the ratio of t/U is directly adjustable through the power of the lattice beams. The Hamburg group used this to drive the ensemble from the SF to the MI and observed this transition by analyzing the visibility of ToF images. In this section, we describe the experimental results for pure systems, and we explain the findings with the help of the GMFA relying on the experimental parameters as described in

Sec. 4.2. We discuss in the next section how mixtures of different spin states allow tuning the critical point of the SF–MI transition.

The visibility data shown in Fig. 4.3a compares different single-component samples. For the analyzed species, the SF–MI transition as a function of lattice depth occurs in the order $|2,-2\rangle$, $|1,-1\rangle$, and $|1,0\rangle$. The general tendency is qualitatively confirmed by the Gutzwiller calculations. In Fig. 4.3b, we plot our predictions for the superfluid order parameter $|\langle\hat{a}_{\sigma^+}\rangle|+|\langle\hat{a}_{\sigma^-}\rangle|$ for experimentally relevant filling factors between two and four per unit cell. In these calculations we included explicitly only tunneling processes between NNs, but we will see presently that NNN tunneling processes play an important role.

But first, let us explain the general tendency. The deepest optical lattice to drive the system across the SF–MI transition is required for the $m_F = 0$ atoms. Since in this case the optical potential is not modulated by $B_{\text{eff}}(\boldsymbol{x})$, tunneling is resonant to the three NNs, and the delocalization tendencies are strong. The situation changes for $|1,-1\rangle$ and $|2,-2\rangle$ atoms. For these states, $B_{\text{eff}}(\boldsymbol{x})$ leads to an energy difference between the σ^+ and σ^- sublattices, so that resonant tunneling to NNs is not possible. The energy difference increases with $|m_F|$, so that the $|2,-2\rangle$ are stronger localized. Additionally, the barrier height between NNs increases with $|m_F|$, see Eq. (4.2) and the sketches in Fig. 4.1b. Therefore, we expect the SF–MI transition to occur at lower beam powers for increasing values of $|m_F|$, as we indeed find.

As Fig. 4.2, inset, shows, the tunneling matrix elements for all three species are equal, if rescaled to the effective barrier height. If the difference in the transition is purely due to this effect, we can expect the transitions to coincide when they are rescaled accordingly. This is indeed observed in the experimental data, as displayed in the inset of Fig. 4.3a. At second thought, however, this is an unexpected behavior, since the NN hopping for $m_F = 0$ is resonant while the one for $m_F = \pm1, \pm2$ is not. Moreover, the off-resonance is different between $m_F = \pm1$ and $m_F = \pm2$, so that some other effect should be in play. Consistent with these considerations, the GMFA with only NN tunneling does not reproduce the behavior of the experimental data.

We find a simple explanation of the experimental findings when considering, in addition to NN tunneling t_{NN}, also NNN processes t_{NNN} (sketched in the inset of Fig 4.4b). To assess the influence of t_{NNN}, we calculate the SF–MI transition for systems with four particles per unit cell. We estimate t_{NN} from experimental parameters as before and fix t_{NNN} as a given percentage of t_{NN}. As can be expected, the critical point of the SF–MI transition moves to larger lattice depths with increasing t_{NNN} (Fig. 4.4a). The relative shift of the critical point is more pronounced for $m_F = \pm1$ and $m_F = \pm2$, because for these species

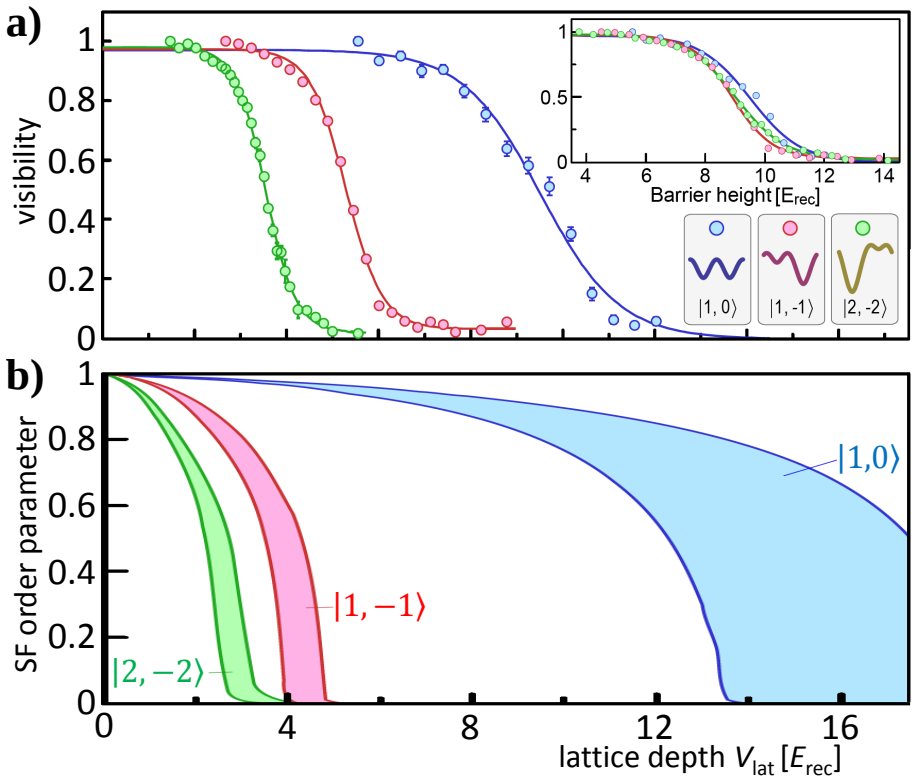

Figure 4.3: **SF to MI transition for pure atomic spin-states. (a) Experimental data.** As the visibility curves show, different pure spin states become insulating at different lattice depths V_{lat}. As demonstrated in the inset, the SF–MI transitions as a function of the effective tunneling barrier (sketched in the lower right; see also Figure 4.1b) nearly coincide. The data are averaged over typically 7-10 experimental runs, and the error bars indicate the standard deviation. The solid lines are guides to the eye. **(b) Theory.** The approach to zero of the SF order parameter (normalized to the occupation number) indicates the position of the SF–MI transition. The qualitative agreement with (a) is satisfactory. The areas represent the results for the experimentally relevant filling factors between two and four per unit cell.

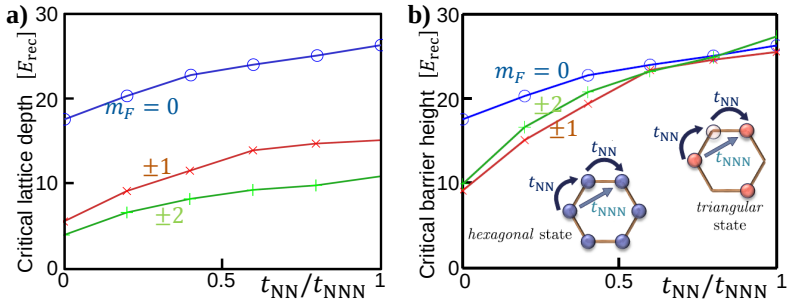

Figure 4.4: **Influence of NNN tunneling processes, GMFA. (a)** The critical lattice depth V_{lat} for the SF-MI transition increases with t_{NNN}. To extract the numerical values for the critical point, we assume that it is reached when the SF density has fallen below 1% of the maximum. **(b)** When plotting against the barrier height, the curves for $m_F = \pm 1$ and $m_F = \pm 2$ roughly coincide for all values of $t_{\mathrm{NNN}}/t_{\mathrm{NN}}$. For $t_{\mathrm{NNN}}/t_{\mathrm{NN}} \gtrsim 0.6$, they also coincide with the $m_F = 0$ curve, as is found in experiment.

the additional t_{NNN} presents a way for direct, *resonant* tunneling. For $m_F = 0$, on the other hand, the NN tunneling is already resonant so that the influence of t_{NNN} is smaller. We can explain the experimental results presented in the inset of Fig. 4.3a, if we find a reasonable NNN tunneling strength t_{NNN} where the critical points for all three species coincide when rescaling to the effective barrier height. Indeed, for $m_F = \pm 1$ and $m_F = \pm 2$ this is roughly the case in the entire considered range of t_{NNN}. However, to make also the critical point for $m_F = 0$ coincide with the one of $m_F = \pm 1$ and $m_F = \pm 2$, a relatively large $t_{\mathrm{NNN}} \gtrsim 0.6 t_{\mathrm{NN}}$ is required. From this analysis it appears that in the spin-dependent honeycomb lattice, NNN tunneling plays an important role. This is in contrast to standard square optical lattices, where NNN tunneling can usually be neglected.

4.4 Tuning the system behavior using spin mixtures

Until now, we were concerned with samples of pure spin states. However, the Hamburg experiments offer exciting new possibilities when loading the spin-dependent lattice with mixtures of different spin states. These are the subject of the present section.

4.4.1 Particle distribution in mixtures and forced supersolid

The different atomic Zeeman species and different mixtures of them arrange spatially different in the spin-dependent honeycomb lattice. As explained in Sec. 4.1, for pure samples, from the form of the lattice potential (4.2), we expect that the density of $m_F = 0$ atoms is distributed homogeneously while $|1,-1\rangle$ ($|1,+1\rangle$) atoms should occupy exclusively σ^- (σ^+) sites for sufficiently deep lattices. These expectations have indeed been confirmed in the Hamburg experiments using the microwave spectroscopy described in Sec. 4.1.2.

Since the experimental setup allows the preparation of arbitrary spin mixtures, this behavior opens intriguing possibilities for the preparation of quantum states. For example, one can actively generate a magnetically-ordered Néel state with predefined magnetization. One possibility to create such a state is to employ a mixture of different spin states, such as $|1,-1\rangle$ and $|1,+1\rangle$, and drive the system into the deep-lattice regime where the spins localize into the $\sigma^\pm$ sublattices in a staggered fashion.

Even more interesting is the case of a mixture of $|1,0\rangle$ and $|1,-1\rangle$ atoms. Namely, the fact that the SF–MI transition occurs at different lattice-beam intensities for different values of $|m_F|$ adds an exciting new dimension to the honeycomb lattice geometry: it opens the possibility to create spin-mixtures where a fully localized component is immersed in a SF bath. In pure systems, the $|1,-1\rangle$ atoms tend to localize in the σ^- sites, while the $|1,0\rangle$ atoms fill the honeycomb lattice homogeneously. In the case of a mixture, however, the repulsive inter-species interaction with the $|1,-1\rangle$ atoms imprints a periodic density modulation on the $|1,0\rangle$ atoms. Comparison of the microwave-spectroscopy signal in such a mixture with the one for pure systems indicates that $(30 \pm 5)\%$ of the $m_F = 0$ atoms sitting at σ^- sites in the pure system are transferred to σ^+ sites.

This crystalline order imprinted onto the $|1,0\rangle$ atoms by the $|1,-1\rangle$ atoms can appear in two qualitatively different scenarios: *(i)* When the lattice is deep enough that the $|1,0\rangle$ atoms are localized on the σ^+ sites, the system forms an alternating MI with $|1,0\rangle$ atoms on σ^+ sites and $|1,-1\rangle$ atoms on σ^- sites. In this case, the mixture resembles a localized alternating spin-ordering, similar to what we discussed above for the $|1,-1\rangle$–$|1,+1\rangle$ mixture. *(ii)* At intermediate lattice depths, one can reach a situation, where the $|1,-1\rangle$ atoms are localized, while the $|1,0\rangle$ atoms remain superfluid. Figure 4.3a suggests that this will be the case at around $V_{\mathrm{lat}} = 7\,E_{\mathrm{ref}}$. In such a situation, the $|1,0\rangle$ atoms retain off-diagonal LRO, as has been demonstrated experimentally by the existence of pronounced

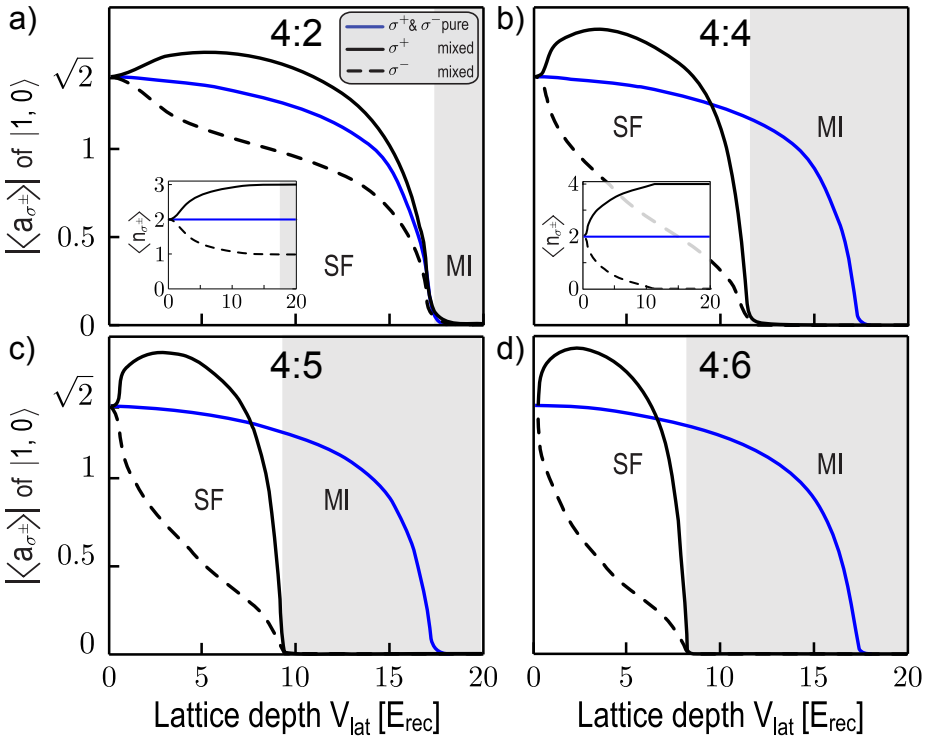

Figure 4.5: **Forced supersolid** behavior of $|1,0\rangle$ atoms under mixture with $|1,-1\rangle$ atoms, illustrated by the SF order parameter $|\langle \hat{a}_{\sigma^\pm}\rangle|$ and occupation number $\langle \hat{n}_{\sigma^\pm}\rangle$ (insets) of $|1,0\rangle$ atoms. We display GMFA results for a pure ensemble of $|1,0\rangle$ atoms (blue line) and increasing admixtures of $|1,-1\rangle$ atoms (black lines) at ratios of **(a)**, $n^{|1,0\rangle}:n^{|1,-1\rangle} = 4:2$, **(b)** 4:4, **(c)** 4:5, and **(d)** 4:6. In a pure system, the values are identical at σ^+ and σ^- sites (blue line). When one admixes $|1,-1\rangle$ atoms, the $|1,0\rangle$ atoms get repelled from σ^- sites (dashed lines), and accumulate at σ^+ sites (solid black line). Also, an admixture of $|1,-1\rangle$ atoms shifts the critical point of the MI–SF transition. These effects become stronger with increasing number of $|1,-1\rangle$ atoms.

interference peaks in the ToF pictures and by the spectroscopy measurements. On the other hand, the $|1,-1\rangle$ atoms induce a density modulation on the $|1,0\rangle$ atoms, so that the system also shows diagonal LRO. This state is very similar to a *supersolid* [288, 289] except that the symmetry breaking for the diagonal order is not spontaneous but forced by the interaction with the localized $|1,-1\rangle$ atoms. Such a supersolid is an exotic quantum phase with crystal and SF behavior at the same time. Until recently, there was only one claim of an experimental realization of a supersolid in ^{4}He [290, 291], which is still disputed [292, 293]. Therefore, it would be interesting to find other systems which show supersolid properties and are cleaner to interpret. Ultracold atoms are an ideal playground in this respect, as shown nicely in the recent experiments at the group of T. Esslinger, where a BEC immersed into an optical cavity displayed *spontaneous* supersolid behavior [14, 294].

In the experiments of the group of K. Sengstock, by varying the depth of the lattice, the $|1,0\rangle$ atoms were driven across the SF to MI transition, and scenarios *(i)* and *(ii)* have both been realized experimentally. We analyze this situation theoretically in Fig. 4.5. In a pure $|1,0\rangle$ system, $|\langle\hat{a}_{\sigma^+}\rangle|$ and $|\langle\hat{a}_{\sigma^-}\rangle|$ as well as $\langle\hat{n}_{\sigma^+}\rangle$ and $\langle\hat{n}_{\sigma^-}\rangle$ coincide for all V_{lat} revealing the expected homogeneous atom distribution. This changes when $|1,-1\rangle$ atoms are admixed to the $|1,0\rangle$ atoms. At already moderate lattice depths, the $|1,-1\rangle$ particles are localized at the σ^- sites. As a consequence, the $|1,0\rangle$ atoms are repelled from these sites, and their occupation number and SF order parameter become spatially modulated, depending on the mixture ratio. In the regime where $|1,0\rangle$ remains superfluid, the system thus, indeed, realizes a supersolid.

We also observe that the critical lattice depth for the $|1,0\rangle$ MI transition is suppressed in the mixture due to the effective blocking of σ^- sites by $|1,-1\rangle$ particles. As for the density modulation, this effect increases with the fraction of admixed $|1,-1\rangle$ atoms. Hence, admixing a second spin-component allows to tune not only a spatial density modulation but also the critical point of the SF–MI transition.

4.4.2 Superfluid to Mott-insulator transition in mixtures

To study how different mixtures allow to engineer SF–MI transitions, the Hamburg group loaded the lattice with $|1,-1\rangle$ atoms and mixed these with an equal number of $|2,-2\rangle$ or $|2,+2\rangle$ atoms. The $|1,-1\rangle$ atoms preferably occupy the σ^- sublattice, as do the $|2,+2\rangle$ atoms, while particles in the state $|2,-2\rangle$ prefer the σ^+ sublattice. It is useful to remember that the $|2,\pm2\rangle$ atoms have stronger localization tendencies than the $|1,-1\rangle$ atoms. The pictograms in Figure 4.6a

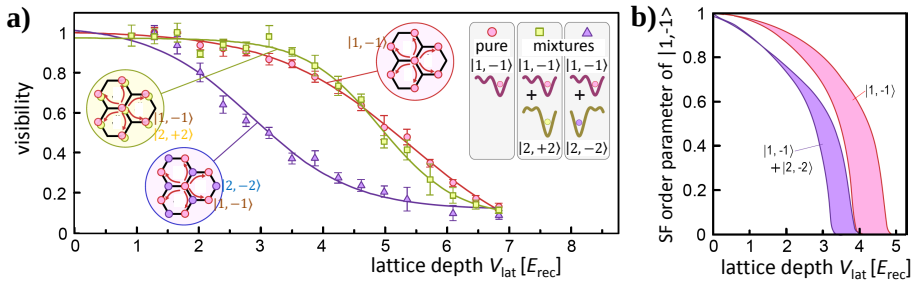

Figure 4.6: **SF to MI transition for mixed atomic spin-states. (a) Experiment.** As the visibility curves for a pure $|1,-1\rangle$ sample and 50%:50% mixtures with $|2,-2\rangle$ or $|2,+2\rangle$ atoms show, the mixture $|1,-1\rangle$—$|2,-2\rangle$ localizes much faster than the other cases. This is explainable by the modification of second-order tunneling processes of $|1,-1\rangle$ between σ^-–σ^+–σ^- sites (little arrows in the pictograms). The presence of $|2,+2\rangle$ blocks the off-resonant σ^+ site (see the pictograms for the preferred atom distributions for the different mixtures). The experimental results are averaged over typically 7-10 runs, and the error bars indicate the standard deviation. Solid lines are guides to the eye. **(b) Gutzwiller calculations** reproduce the shift of the SF–MI transition in a 50%:50% mixture of $|1,-1\rangle$ with $|2,-2\rangle$ as compared to the pure $|1,-1\rangle$ system. Shown is the SF order parameter of the $|1,-1\rangle$ state for filling factors between two and four per unit cell. (Results for a mixture with $|2,+2\rangle$ are not shown because of numerical instabilities.)

illustrate the configurations for these cases as well as for a pure $|1,-1\rangle$ system.

SF–MI transitions at fixed particle number

As the experimental results in Fig. 4.6a show, a considerable shift in the SF–MI transition of the $|1,-1\rangle$ atoms is observed when the admixed atoms are in the $|2,-2\rangle$. On the other hand, the transition remains practically unaltered in the case of $|2,+2\rangle$. The observed suppression of tunneling in the $|1,-1\rangle$–$|2,-2\rangle$ mixture can be ascribed to a modification of second-order hopping processes: At sufficiently deep lattices, the $|1,-1\rangle$ will almost exclusively occupy σ^- sites. Due to the large energy cost for occupying σ^+ sites, they will visit these only in virtual tunneling processes.

To understand the main principle, let us neglect entirely the occupation of $|1,-1\rangle$ on σ^+ sites and of $|2,-2\rangle$ on σ^- sites. Under this assumption, the effective strength of the second-order tunneling process $\sigma^- \to \sigma^+ \to \sigma^-$ is

$$\propto t^2 \Big/ \Big[(E_{\sigma^+}^{(-1)} - E_{\sigma^-}^{(-1)}) + U_{\sigma^+}^{(-1,-2)} n_{\sigma^+}^{(-2)} - U_{\sigma^-}^{(-1)} (n_{\sigma^-}^{(-1)} - 1) \Big] \,. \tag{4.5}$$

This is the typical form for processes from second-order perturbation theory. The numerator is the square of the transition matrix element from the state with low energy ($|1,-1\rangle$ at σ^-) to the excited state ($|1,-1\rangle$ at σ^+); and the denominator comes from the energy difference between the ground-state manifold and the excited, virtual state. In the presence of $|2,-2\rangle$ particles on the σ^+ site, the denominator is enlarged by $U_{\sigma^+}^{(-1,-2)} n_{\sigma^+}^{(-2)}$. Effectively, the repulsive interaction with $|2,-2\rangle$ particles blocks second-order tunneling for $|1,-1\rangle$ and thus shifts the SF–MI transition towards lower lattice-beam intensities. We find this observed shift of the SF–MI transition reproduced in our Gutzwiller computations (see Figure 4.6b). Hence, by changing the relative composition of the mixture, the critical point for the $|1,-1\rangle$ particles can be tuned.

SF–MI transitions in the grand-canonical ensemble

We can gain further insight into the underlying physical processes by considering grand-canonical phase diagrams calculated in the Gutzwiller approximation. This is in contrast to Figs. 4.3b and 4.6b, where we reached a desired particle number by iteratively adjusting μ. In Fig. 4.7a, we show the phase diagram against μ for the same experimental configurations as discussed in Fig. 4.6. Here, we have chosen the chemical potential equal for both components, *i.e.*, $\mu^{(-1)} = \mu^{(\pm 2)}$. In the $|1,-1\rangle$–$|2,-2\rangle$ mixture, this leads to an approximately 50%:50%

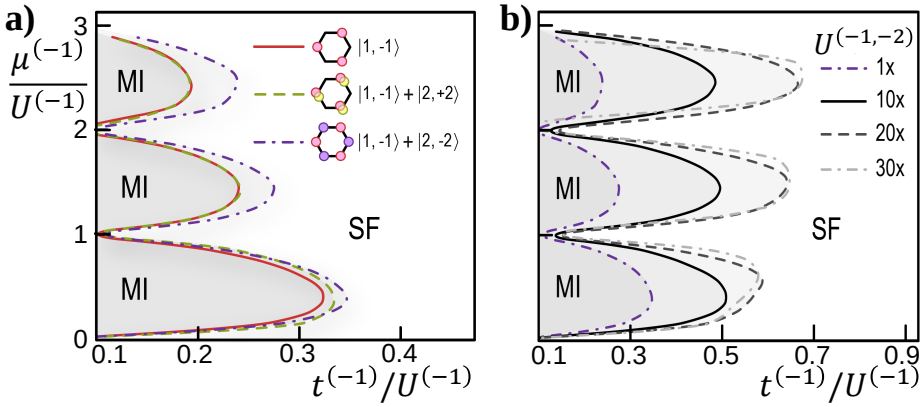

Figure 4.7: **Gutzwiller phase diagram of the multi-component Bose–Hubbard model** (4.4)**. (a) Mott lobes for realistic experimental parameters.** An admixture of $|2,-2\rangle$-atoms (blue dot-dashed line) strongly enlarges the $|1,-1\rangle$ Mott-lobes with respect to the pure system (red solid line) while an admixture of $|2,+2\rangle$-atoms (green dashed line) hardly affects the transition. **(b)** In a $|1,-1\rangle$–$|2,-2\rangle$-mixture, when increasing the interaction strength $U_{\sigma^\pm}^{(-1,-2)}$ between the spin-components, *e.g.*, by a Feshbach resonance [295], the $|1,-1\rangle$ Mott-lobes grow. For large $U_{\sigma^\pm}^{(-1,-2)}$ the standard tendency that Mott-lobes decrease with occupation number can even be inverted.

relationship, while in the $|1,-1\rangle$–$|2,+2\rangle$ mixture the $|1,-1\rangle$ atoms strongly repel the $|2,+2\rangle$ atoms, such that the occupation number can be heavily asymmetric. A clear modification of the MI lobes of $|1,-1\rangle$ can be observed when strongly localized atoms are present in the complementary triangular sublattice, in our case $|2,-2\rangle$. Such a strong modification with respect to the pure case does not occur when both components tend to occupy the same sites, as happens in the mixture $|1,-1\rangle$+$|2,+2\rangle$. This perfectly agrees with the experimental observations displayed in Fig. 4.6a.

Until now, all parameters for the theoretical calculations were drawn from realistic experimental parameters of the Hamburg experiment. However, other interesting effects can be generated by playing with the relative interaction strengths. Consider, for example, a mixture of $|1,-1\rangle$ and $|2,-2\rangle$ atoms. Using the approximation of Wannier functions as Gaussians described in Sec. 4.2, the interspecies interaction strength as for the Hamburg experiments with ^{87}Rb is $U_{\sigma^+}^{(-1,-2)}/U^{(-1)} = 1.1$ and $U_{\sigma^-}^{(-1,-2)}/U^{(-1)} = 0.8$. In this case, as is the standard situation, the Mott-lobes decrease with occupation number. In Fig. 4.7b, we demonstrate what happens when $U_{\sigma^+}^{(-1,-2)}$ is artificially increased, which may be achieved experimentally with the help of Feshbach resonances [296] – for sufficiently large $U^{-1,-2}$ the standard tendency is inverted and the Mott lobes *increase* with occupation number. This implies that the SF–MI transition for higher occupation numbers occurs at finite tunneling, which would allow to observe this transition in the interesting regime that interpolates between the Bose–Hubbard regime (small occupation) and a regime described by a coupled rotor model (large occupation). Such a coupled rotor model can be derived as follows. In the limit of large occupation, the boson-operators in the Bose–Hubbard model (4.4) can be rewritten in the phase representation, substituting $\hat{a}_i^\dagger \to \sqrt{\bar{n}_i^a} e^{i\theta_i^a}$, $\hat{b}_i^\dagger \to \sqrt{\bar{n}_i^b} e^{i\theta_i^b}$, and $\hat{n}_i^\alpha \to \bar{n}_i^\alpha - i\frac{\partial}{\partial\theta_i^\alpha}$. Here, $\bar{n}_i^\alpha = \langle\hat{n}\rangle_i^\alpha$ is the mean occupation number of species $\alpha = a,b$ at site i. In this approximation, the Hamiltonian reads

$$\hat{\mathcal{H}} = \sum_{\alpha=a,b}\Bigg[-2t^\alpha \sum_{\langle i,j\rangle}\sqrt{\bar{n}_i^\alpha}\sqrt{\bar{n}_j^\alpha}\cos\left(\theta_i^\alpha-\theta_j^\alpha\right) - \sum_i \frac{U_i^\alpha}{2}\frac{\partial^2}{\partial\theta_i^{\alpha\,2}} \tag{4.6}$$

$$- i\sum_i\left(U_i^\alpha\bar{n}_i^\alpha - U_i^{ab}\bar{n}_i^{\not\alpha} - \mu^\alpha + E_i^\alpha + \frac{1}{2}U_i^\alpha\right)\frac{\partial}{\partial\theta_i^\alpha}\Bigg] - \sum_i U_i^{ab}\frac{\partial}{\partial\theta_i^a}\frac{\partial}{\partial\theta_i^b} + E_0\left[\bar{n}_i^\alpha\right]$$

where we defined $\not\alpha$ as the species different from α. $E_0\left[\bar{n}_i^\alpha\right]$ is a constant energy depending on the mean occupation numbers. This coupled-rotor model is similar to Hamiltonians encountered in arrays of coupled Josephson junctions [297].

4.5 Summary

To summarize this chapter, qualitative and quantitative agreement between a Gutzwiller mean-field analysis and the comprehensive experimental studies by the group of Prof. Sengstock in Hamburg allowed to explain the physics appearing in ultracold bosons in a spin-dependent honeycomb lattice. In particular, we have analyzed the SF–MI transition for pure samples and spin mixtures. We have shown that the critical point, which for pure ensembles depends only on the Zeeman state m_F, can be tuned when admixing a second spin component. We could explain this effect by considering second-order tunneling processes, which become suppressed if a second atomic species blocks sites that are left empty in the pure system. Controlling the tunneling rate by, *e.g.*, locally switching the spin-states opens perspectives for the implementation of atomtronic transistor circuits [298]. In this context, we have shown that the modification of the Bose–Hubbard parameters t/U arises from the combination of repulsive interaction and the specific honeycomb lattice structure. This situation is clearly different from, *e.g.*, Bose–Fermi mixture experiments [299, 300] where t and U are effectively modified by higher order effects. Further, we have shown that mixtures of different spin-components can lead to forced AFM states or states mimicking supersolid behavior.

In our calculations, we used realistic model parameters. For the interaction and energy differences between the two sublattices, we obtained these by considering Gaussian Wannier functions. To estimate realistic tunneling matrix elements, we fitted the exact band-structure for the single-particle problem to a tight-binding model for the double wells. Comparing our theoretical analysis to experiment, we found that NN tunneling alone is not sufficient to quantitatively describe the experimental data, and – in contrast to standard optical lattices – NNN tunnelings have to be taken into account.

There are many directions to explore with this quantum-simulation setup. For example, in future experiments, one could increase the interspecies interaction via Feshbach resonances, which, as we have demonstrated with the Gutzwiller *Ansatz*, leads to a growth of Mott-lobes with occupation number – contrary to the standard behavior. As promising further directions, entropy effects and entropic cooling [301] can be studied in the honeycomb system. Also, as demonstrated by Soltan-Panahi and coworkers, unconventional multi-orbital superfluidity can arise in this system [302]. Further, by only changing the polarization of the laser beams which create the lattice, a spin-independent triangular lattice can be created [160]. As discussed in Chapter 3, a bosonic gas in the triangular lattice can then be used to mimic frustrated antiferromagnetism by

employing a time-dependent lattice modulation. Particularly interesting, however, is the prospect of studying Fermi gases or Fermi–Bose mixtures in the honeycomb geometry, such as is currently done in the group of T. Esslinger [162]. At half filling, these systems will mimic the physics of graphene [266], *i.e.*, they will exhibit a Dirac dispersion relation and related artificial relativistic effects. Introducing artificial gauge fields in such a situation [10, 20, 303–306] will lead to the occurrence of the anomalous quantum Hall effect and a whole variety of exotic quantum phase transitions (see for instance the work of Bermudez *et al.* [307]). In the next chapter, we show how these artificial gauge fields can be achieved with the shaking techniques described in Chapter 3, and how this allows to generate the anomalous quantum Hall effect, topological insulators, and more.

Chapter 5

Non-Abelian gauge fields and topological insulators via lattice shaking

In this chapter, we show that the time-periodic driving techniques of optical lattices described in Chapter 3 allow much more than "only" the quantum simulation of geometrical frustration. Combining a slightly more elaborate driving scheme with spin-dependent lattices or lattices of exotic geometry (such as discussed in Chapter 4), we obtain an experimentally simple method to explore various topological phenomena in optical-lattice experiments.

Topological order and topological insulators [281] are currently in the center of interest of quantum physics, especially because of their possible applications in quantum information and spintronics [308]. For this reason, there is an ongoing search in- and outside of solid-state physics on ways to realize these in a feasible way. Here, ultracold ground-state atoms provide a very promising playground [8] (although Rydberg-excited atoms [107], trapped ions [31], and photons in nano-structured materials [40, 42] offer interesting alternatives). Typically, topological effects require ultra-strong gauge fields or spin-orbit-like couplings. There are several ways to achieve these with ultracold atoms, from trap rotation [309] to (more efficient) laser-induced Berry-phase imprinting [10, 303, 304]. In optical lattices, combining laser-induced tunneling with superlattice techniques allows for Abelian [205] and non-Abelian [310] gauge-field fluxes of order π per unit plaquette, and for the realization of an en-

tire toolbox for topological insulators [311]. So far, the first lattice experiments led to the creation of staggered flux lattices [20, 305, 306], and other groups follow this direction, employing, *e.g.*, kagome [163] or honeycomb lattices [162].

Recently, there has been a burst of interest in another, experimentally less demanding, approach to manipulate ultracold-atoms QSs, namely periodical lattice shaking, such as described in Chapter 3.1. Simple sinusoidal shaking leads to a change of strength, or even sign of the tunneling [216, 220, 312] and allows to control the Mott-insulator–superfluid transition (for a recent work in honeycomb geometry, see also the work by Koghee *et al.* [313]). While in the square lattice this introduces neither frustration nor synthetic gauge fields, in the triangular lattice a sign-change of the tunneling is equivalent to a π-flux Abelian field [314]. As described in detail in Chapter 3, for weak interactions, such a system mimics frustrated classical antiferromagnetism [165], while in the hard-core boson limit it simulates frustrated quantum antiferromagnetism [164], and is expected to exhibit exotic spin-liquid phases [202, 225, 257]. Moreover, as we have reported on in Ref. [22], by breaking temporal symmetries of the shaking trajectory, arbitrary phases of the tunneling in a 1D lattice have been created in the experiments of K. Sengstock's group. This allowed to shift the band-structure, and, among others, to induce (quasi-)condensation at finite quasi-momentum. Since in that case the resulting tunneling phases can, however, be mapped by a suitable choice of gauge to the standard situation without phases, we will not describe these results in detail, and rather focus in this chapter on the, from a fundamental perspective, more important case of 2D lattices.

In the rest of this chapter, we will describe in detail how time-periodic shaking of 2D lattices allows quantum simulation of (non-Abelian) artificial gauge-fields, topological insulators, and related effects. First, in Sec. 5.1, we describe which symmetries the driving function has to break to create non-trivial tunneling phases. Here, we generalize our discussion from Chapter 3.1 to include AC-induced tunneling (ACT), which permits greatly enhanced control over the generated phases. Then, in Sec. 5.2, we show in different (spin-independent) lattice geometries involving triangular plaquettes how staggered gauge fields arising through homogeneous shaking can control frustration and band structures. However, such homogeneous shaking cannot induce artificial magnetic fluxes in square lattices. In Sec. 5.3, we discuss how the time-periodic modulation of a superlattice added to the square lattice makes this possible. This technique even allows to engineer the form and extent of patches of strong artificial magnetic flux with the same sign. In Sec. 5.4, we demonstrate that homogeneous shaking of spin-dependent honeycomb lattices (see Chapter 4) allows quantum simulating topological and quantum spin Hall (QSH) insulators

(c.f. [267, 281]). Finally, we show in Sec. 5.5 how simple sinusoidal shaking of a spin-dependent square or honeycomb lattice, loaded with two different spin components that are additionally mixed on-site via magnetic or Raman-laser fields, generates non-Abelian SU(2) gauge fields, leading to an anomalous integer quantum Hall effect [315]. We conclude this chapter with some summarizing remarks (Sec. 5.6). The corresponding results can be found in Ref. [211].

5.1 Basic scheme and temporal symmetries

We start by discussing the scheme for the creation of artificial gauge potentials in driven lattices. For this purpose, we generalize the discussion of Chapter 3.1, where we allow for a static energy offset between lattice sites, and consequently ACT created by the driving [316], as it has been observed in recent experiments [317–319]. As we will see below, this facilitates the generation of arbitrary Peierls phases. Such an energy offset can easily be realized in spin-dependent lattices such as the honeycomb lattice discussed in Chapter 4. We generalize the driven, Hubbard-type Hamiltonian (3.6) to encompass bosons and fermions, but we work in the regime of negligible interactions.[1] Further, we include, besides the periodic driving, a constant energy difference between sites.

Then, the system is described by

$$\hat{\mathcal{H}}(\tau) = -\sum_{i,j} t_{ij}\hat{a}_i^\dagger \hat{a}_j + \sum_i \left(v_i^\omega(\tau) + \nu_i \hbar\omega\right)\hat{n}_i \,. \tag{5.1}$$

Here, t_{ij} are the (bare) tunneling matrix elements and $\hat{a}_i$ ($\hat{n}_i$) is the annihilation (number) operator for a particle at site i, which now can be fermionic or bosonic. We choose the constant local energies $\nu_i\hbar\omega$ resonant with the shaking, *i.e.*, they are characterized by integers ν_i. We will see later, that the additional freedom permitted by ACT proves extremely advantageous for the generation of arbitrary artificial fluxes.

Following the reasoning of Chapter 3.1.2, we now apply the gauge transformation (3.14,3.15), but we generalize $\chi_i^\omega(\tau)$, Eq. (3.13), to the situation with constant energy off-sets,

$$\chi_i^\omega(\tau) \to \chi_i(\tau) = \chi_i^\omega(\tau) + \nu_i\omega\tau + \gamma_i \,. \tag{5.2}$$

[1] Inter-particle interactions are not necessary for our purposes of simulating gauge-fields. However, for several of the described effects it is an interesting and open question how the topological effects change under the influence of interactions.

Here, the constants γ_i represent the gauge freedom of choosing the local phase at site i. Using this in the transformation (3.14,3.15) leads to the new Hamiltonian

$$\hat{\mathcal{H}}'(\tau) = -\sum_{ij} t_{ij} \mathrm{e}^{i\chi_{ij}(\tau)} \hat{a}_i^\dagger \hat{a}_j \,, \tag{5.3}$$

Here, we defined the general shorthand $X_{ij} \equiv X_i - X_j$.

For large frequencies, $\hbar\omega \gg t_{ij}$, this Hamiltonian can again be approximated by its period average (3.21), so that we obtain the effective model

$$\hat{\mathcal{H}}_{\mathrm{eff}} \equiv \langle \hat{\mathcal{H}}'(\tau) \rangle_T = -\sum_{i,j} t_{ij}^{\mathrm{eff}} \hat{a}_i \hat{a}_j \,. \tag{5.4}$$

Here, we introduced the time average $\langle \bullet \rangle_T \equiv \int_0^T \bullet \, \mathrm{d}\tau/T$. The time-evolution in $\hat{\mathcal{H}}_{\mathrm{eff}}$ is effectively governed by the modified tunneling parameters

$$t_{ij}^{\mathrm{eff}} = t_{ij} \left\langle \mathrm{e}^{i(\chi_{ij}^{\omega}(\tau) + \nu_{ij}\omega\tau + \gamma_{ij})} \right\rangle_T \,. \tag{5.5}$$

In this treatment, the energy offsets $\nu_i\hbar\omega$ have been absorbed in the time-dependence of the particle operators in $\hat{\mathcal{H}}'(\tau)$, and hence modify t_{ij}^{eff} [compare Eq. (3.23) for the situation without energy offsets]. Therefore, in the absence of periodic forcing v_{ij}^{ω}, a non-zero $\nu_{ij}\hbar\omega$ suppresses tunneling between i and j in $\hat{\mathcal{H}}_{\mathrm{eff}}$, so that $t_{ij}^{\mathrm{eff}} = 0$. Finite driving $v_{ij}^{\omega} \neq 0$ in the case of $\nu_{ij} \neq 0$ generates an ACT, so that effective tunneling matrix elements are finite, $t_{ij}^{\mathrm{eff}} \neq 0$.

The leitmotif of the present chapter is to use this control scheme to induce Peierls-type phases

$$\theta_{ij} = \arg\left(\left\langle \mathrm{e}^{i(\chi_{ij}^{\omega}(\tau) + \nu_{ij}\omega\tau + \gamma_{ij})} \right\rangle_T \right) \tag{5.6}$$

that cannot be eliminated globally by choice of gauge, *i.e.*, by adjusting the constants γ_i. Such non-trivial phases correspond to artificial Abelian gauge fields. The gauge-invariant magnetic flux $\phi \in]-\pi, \pi]$ piercing a lattice plaquette P is (modulo 2π) obtained by summing the θ_{ij} around P.

We identify the following symmetries of the driving which imply trivial $\theta_{ij} = 0$ $\forall i, j$:[2]

(r) *global* reflection symmetry $v_i^\omega(-\tau - \tau^\star) = v_i^\omega(\tau - \tau^\star)$ with respect to a site-independent time $\tau^\star$ (in this case, using the choice $\gamma_i = -\nu_i \omega \tau^\star$ gives $\theta_{ij} = 0$ $\forall i, j$);

or, if ACT is not involved (*i.e.*, $\nu_{ij} = 0$),

(r') *local* reflection symmetry $v_{ij}^\omega(-\tau - \tau_{ij}^\star) = v_{ij}^\omega(\tau - \tau_{ij}^\star)$ for suitable local times $\tau_{ij}^\star$ (since $\nu_{ij} = 0$ implies that $\gamma_{ij} = -\nu_{ij}\omega\tau_{ij}^\star$ can always be fulfilled, independent of $\tau_{ij}^\star$); or

(s) shift antisymmetry $v_i^\omega(\tau - \frac{T}{2}) = -v_i^\omega(\tau)$ (with $\gamma_i = 0$).

These symmetries have to be broken to achieve artificial gauge fields. From these, we see that the driving $v_i^\omega(\tau)$ is subject to less constraints if ACT is involved. This is nicely exemplified by recent proposals where already simple sinusoidal forcing [fulfilling (r') and (s)] leads to magnetic fields when combined with ACT – provided the temporal phase of the driving can be made site dependent [thus breaking (r)] [199, 320]. In the following, we consider experimentally feasible scenarios where the whole system is driven in phase [such that both (r) and (s) are broken].

5.2 Staggered fluxes in triangular plaquettes

In plaquettes that do not have pairwise parallel edges (*e.g.*, triangular ones), artificial magnetic fluxes can be generated simply by a homogeneous time-periodic force $\boldsymbol{F}(\tau)$ [22, 210]. As in Chapter 3.1, we consider an inertial force obtained by shaking the lattice along a periodic orbit $\boldsymbol{x}(\tau)$ in space, resulting in the driving potential $v_i^\omega(\tau) = -\boldsymbol{r}_i \cdot \boldsymbol{F}(\tau)$ with site position $\boldsymbol{r}_i$. Accordingly, for $\nu_{ij} = \text{const}$ the Peierls phases θ_{ij} depend only on the vector $\boldsymbol{r}_{ij} = \boldsymbol{r}_i - \boldsymbol{r}_j$ connecting the two sites i and j, *i.e.*, $\theta_{ij} = f_\theta(\boldsymbol{r}_{ij})$. Here, we consider a unidirectional force $\boldsymbol{F}(\tau) = F(\tau)\boldsymbol{e}_F$ with $\boldsymbol{e}_F = \cos(\varphi_F)\boldsymbol{e}_x + \sin(\varphi_F)\boldsymbol{e}_y$, and – in contrast to Chapter 3.1 – a paused-sine-wave amplitude as depicted in Fig. 5.1a,

$$F(\tau) = \begin{cases} F_0 \sin(\frac{2\pi}{T_1}\tau), & 0 \le \tau \bmod T < T_1 \\ 0, & T_1 \le \tau \bmod T < T \end{cases} \tag{5.7}$$

This form of driving breaks both symmetries (r) and (s).

[2] For the special case $\nu_i = 0$ see also Ref. [22].

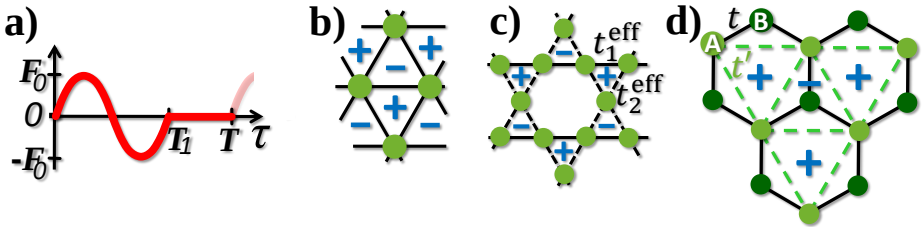

Figure 5.1: **(a) Example for a driving function** breaking symmetries (r) and (s), a paused sine-wave, Eq. (5.7). **(b-d) Lattice geometries** involving triangular plaquettes pierced by an artificial magnetic flux $\phi_{\nabla,\Delta} = \pm\phi$ as indicated by + and − signs. **(b)** Triangular lattice. **(c)** Kagome lattice with effective tunneling $t_1^{\rm eff}$ ($t_2^{\rm eff}$) along the solid horizontal (dashed diagonal) bonds (see Sec. 5.2). **(d)** Honeycomb lattice where NN tunneling between shallow A-sites and deep B-sites is AC-induced (solid lines) and NNN tunneling connects only A-sites (dashed lines). The corresponding undriven matrix elements are t and t', respectively (see Sec. 5.4).

Inserting the relationships (3.13) and (3.20) into Eq. (5.5), and carrying out the time integration, such a driving creates for $\nu_{ij} = 0$

$$\frac{t_{ij}^{\rm eff}}{t_{ij}} = \frac{T_1}{T} e^{-i\gamma_{ij}} \left[-e^{-i\eta_{ij}\frac{T-T_1}{T}} \mathcal{J}_0(\eta_{ij}) + e^{i\eta_{ij}\frac{T_1}{T}} \frac{T-T_1}{T_1} \right] . \tag{5.8}$$

Here, we defined the dimensionless driving amplitude $\eta_{ij} = \boldsymbol{r}_{ij} \cdot \boldsymbol{e}_F F_0 T_1/(2\pi\hbar)$.

For $T_1 = T$, we recover the result (3.26), and for $T_1 = 0$, relationship (5.8) simply expresses the freedom in the choice of gauge. For the special case $T_1 = T/2$ (and choosing the local phases $\gamma_{ij} = 0$), the Peierls phases θ_{ij} are thus

$$\tan\theta_{ij} \equiv \tan f_\theta(\boldsymbol{r}_{ij}) = \frac{1+\mathcal{J}_0(\eta_{ij})}{1-\mathcal{J}_0(\eta_{ij})} \tan\frac{\eta_{ij}}{2} . \tag{5.9}$$

The tunable flux threaded through a triangular plaquette Δ as sketched in Fig. 5.1b-c is then $\phi_\Delta = f_\theta(\boldsymbol{e}_x) + f_\theta(-\boldsymbol{e}_x/2 + \sqrt{3}/2\boldsymbol{e}_y) + f_\theta(-\boldsymbol{e}_x/2 - \sqrt{3}/2\boldsymbol{e}_y)$ (and similarly for Fig. 5.1d, where the triangular plaquette is spanned by next-nearest-neighbor tunneling). It can be non-zero since $f_\theta(\boldsymbol{r}_{ij})$ is a non-linear function of $\boldsymbol{r}_{ij}$. The resulting flux through the inverted plaquette is $\phi_\nabla = -\phi_\Delta$, such that one can create in the triangular or kagome lattice staggered flux patterns as shown in Fig. 5.1b-c.

These fluxes continuously control the degree of frustration from none for zero flux to maximum for π-flux [corresponding to ferromagnetic (FM), $-t_{ij}^{\rm eff} < 0$, and

antiferromagnetic (AFM) coupling, $-t_{ij}^{\text{eff}} > 0$, respectively]. The fully-frustrated regime gives rise to intriguing physics; for example, the flat lowest band of the kagome lattices makes the system extremely susceptible towards interaction-driven physics [321]; moreover, as discussed in Chapter 3, the case of hard-core bosons can be mapped to the spin-1/2-XY antiferromagnet where spin-liquid ground states are predicted to occur for the spatially anisotropic triangular lattice. For the case of the kagome lattice as realized in the experiments at the group of D. Stamper-Kurn [163], the physics of strongly frustrated XY interactions is still unexplored, but since the Heisenberg kagome lattice hosts quantum disordered ground states [322], similar quantum effects may also be expected in the XY case.

The ability to tune continuously between zero and maximum frustration can be a powerful tool for the adiabatic preparation of frustrated quantum phases. In the scenarios involving simple sinusoidal driving described in Chapter 3, the effective tunneling is just the bare tunneling dressed by a zero-order Bessel function, Eq. (3.26). To tune the tunneling from FM to AFM via this simple driving involves, therefore, reducing the tunneling strength to zero before achieving negative values. As long as the driving amplitude remains in the FM regime (*i.e.*, positive values of the Bessel function), the dispersion relation has a unique (although ever shallower) minimum at the origin of the first Brillouin zone. At the first zero of the Bessel function, the tunneling vanishes, the atoms are perfectly localized, and the dispersion relation is completely flat. When reaching the AFM side, new minima at finite $\boldsymbol{k}$ appear. Therefore, when the driving amplitude crosses the zero of the Bessel function, the peak of the atom momentum distribution has to "jump" from $\boldsymbol{k} = 0$ to $|\boldsymbol{k}| > 0$, which can lead to undesired heating. This can be avoided if, instead, the frustration is tuned by the phase. In that case, the dispersion relation never becomes flat, and the minimum can be moved adiabatically from $\boldsymbol{k} = 0$ to the AFM value.

Further, the realization of tunable staggered fluxes gives rise also to interesting physics in its own right. For example, in the bosonic case deviations from π-flux directly map to tunable Dzyaloshinskii–Moriya couplings and thus allow to explore magnetic models with spin-orbit coupling [323]. In Fig. 5.2, we present another possibility, namely to use a finite flux $\phi_\Delta = \phi$ to manipulate the band structure of optical lattices that host triangular plaquettes. We illustrate this on the example of a kagome lattice with an anisotropy in the tunneling couplings, such that $|t_{ij}^{\text{eff}}|$ equal to t_1^{eff} (t_2^{eff}) along the horizontal (other) bonds (see Fig. 5.1c). As our findings suggest, the three bands of the kagome lattice feature a complex band-touching structure whose topology can be controlled by the driving.

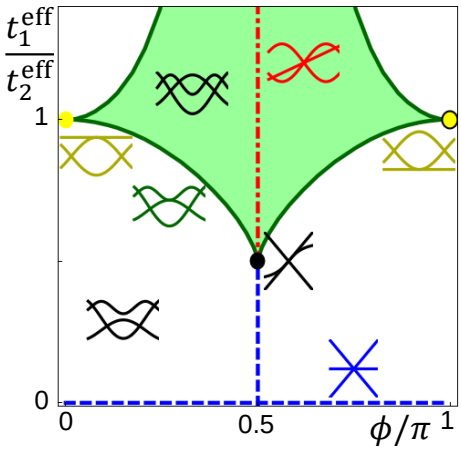

Figure 5.2: **The topology of band touching for the kagome lattice** can be controlled by tunneling anisotropy $t_1^{\rm eff}/t_2^{\rm eff}$ and plaquette flux ϕ. The way and how often the three bands touch is depicted by the icons. In the green (white) region, there are six (four) points where bands touch. Especially interesting is the yellow bullet to the right, where the flat lowest band makes the system extremely susceptible to interaction-driven physics [321].

5.3 Superlattice modulation and flux rectification

In lattices with pairwise parallel bonds, such as square lattices, the homogeneous driving discussed so far cannot create artificial magnetic fluxes. To generate them, one can, however, employ inhomogeneous forcing, which can be achieved by adding to the square lattice an oscillating superlattice like

$$V(\boldsymbol{r},\tau) = f(\tau)V_0(\boldsymbol{r}) = f(\tau)\sum_\alpha \frac{V_\alpha}{2}\cos(\boldsymbol{q}_\alpha\cdot\boldsymbol{r}-\varphi_\alpha)\,, \tag{5.10}$$

where $V_0(\boldsymbol{r})$ may be incommensurate with the host lattice. To arrive at non-trivial Peierls phases, the driving function $f(\tau) = f(\tau+T)$ has to break symmetries (r) and (s). To achieve a vanishing mean, $\langle f(\tau)\rangle_T = 0$, each component α of the lattice can be created by two non-interfering standing waves such that

$$f(\tau)V_\alpha\cos(\boldsymbol{q}_\alpha\cdot\boldsymbol{r}-\varphi_\alpha) = V'_\alpha(\tau)\cos(\boldsymbol{q}_\alpha\cdot\boldsymbol{r}-\varphi_\alpha)+V''_\alpha(\tau)\cos(\boldsymbol{q}_\alpha\cdot\boldsymbol{r}-\varphi_\alpha+\pi)\,, \tag{5.11}$$

with $V'_\alpha, V''_\alpha > 0$. The resulting on-site energies read $v_i^\omega(\tau) = V(\boldsymbol{r}_i,\tau)$, and the Peierls phases θ_{ij} will be a function $\theta(\eta_{ij})$ of the amplitude η_{ij} of $(v_i^\omega - v_j^\omega)/\hbar\omega$.

In Fig. 5.3, we show – on the example of a square lattice with a paused sine-wave shaking function as in Fig. 5.1a (with $T_1/T = 0.8$) – that, using different superlattice structures, various configurations of plaquette fluxes can be engineered, including stripes or extended patches where the magnetic field is approximately constant.

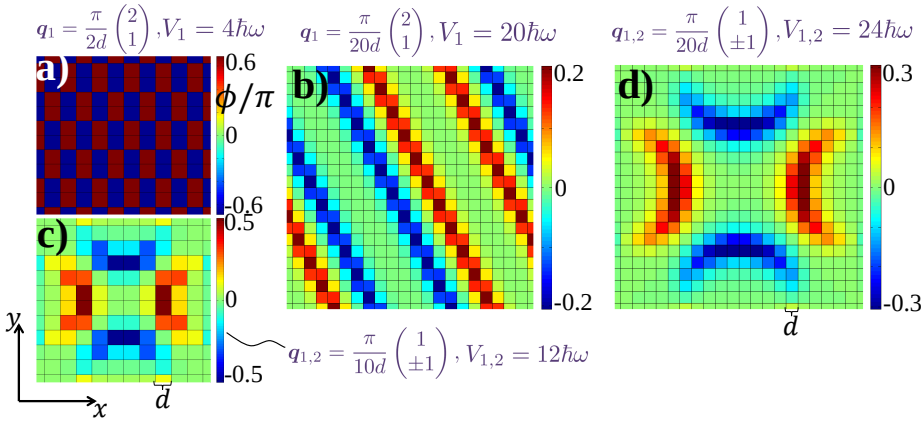

Figure 5.3: **Modulation of the amplitude of a superlattice** can generate strong artificial magnetic fluxes ϕ that point in the same direction within stripes or larger patches, even in lattices with pairwise parallel bonds such as square lattices. The examples show that various spatial patterns are possible. We show magnetic plaquette fluxes for superlattices V_α of **(a-b)** one component ($\alpha = 1$), and **(c-d)** two components ($\alpha = 1, 2$), and the parameters given in purple [see Eq. (5.10); in all cases, the modulation phase $\varphi_\alpha = 0$]. To provide scale, the lattice constant d of the square lattice is also indicated.

In the long-wave-length regime ($|\boldsymbol{q}_\alpha d| \ll \pi$, valid for Figs. 5.3b-d) these plaquette fluxes are approximately given by

$$\phi(\boldsymbol{r}) \simeq \frac{1}{2} w_{xy}(\boldsymbol{r}) \left[\frac{\partial\theta\left(w_y(\boldsymbol{r})\right)}{\partial w_y(\boldsymbol{r})} - \frac{\partial\theta\left(w_x(\boldsymbol{r})\right)}{\partial w_x(\boldsymbol{r})} \right], \tag{5.12}$$

where $w_{xy}(\boldsymbol{r}) = d^2\partial_x\partial_y V(\boldsymbol{r})/(\hbar\omega)$ and $w_\mu = d\,\partial_\mu V(\boldsymbol{r})/(\hbar\omega)$, with $\mu = x, y$, are the scaled curvature and gradient, respectively. Therefore, roughly larger superlattice-wave-lengths imply larger patches of quasi-constant flux.

As these consideration show, superlattice modulation can generate strong magnetic fluxes through square plaquettes, which is not possible by homogeneous shaking schemes. Even more, it can create not only staggered fluxes, but also large regions with approximately constant magnetic field. In these regions, strong-field quantum Hall-type physics can be studied. Their inhomogeneity and finite extent provide a promising test ground for the investigation of robust edge modes.

5.4 Topological and quantum spin Hall insulator

Such plaquette fluxes open also another intriguing possibility: they can be used to engineer topological and QSH insulators [267], which are currently receiving much attention in the quantum physics community [281]. These systems defy ordinary band-structure considerations. They are gapped in the bulk, *i.e.*, they are insulators. Yet, at their boundaries the gap closes and they host currents localized to the edges, *i.e.*, here they are metallic. These edge currents are robust against disorder, which makes these system interesting candidates for novel electronic components. Further, QSH insulators, where the edge modes transport only spin but no charge, are considered as possible elements for spintronic devices. Further, certain topological insulators may also host Majorana edge modes which may be useful as qubits for topological quantum computing [308]. Interestingly, under this novel paradigm, the integer quantum Hall effect with its insulating bulk and localized edge currents can be considered a topological insulator.

5.4.1 Mimicking the dispersion relation of a topological insulator

To create a topological insulator via lattice shaking, we consider a spin-dependent honeycomb optical lattice loaded with two spin components, $\uparrow$ and $\downarrow$. The lattice has a bi-atomic bases, and we consider a situation where sites of the A (B) sublattice are energetically lifted (lowered) by $\Delta E/2$ for $\uparrow$ particles, and vice versa for $\downarrow$ particles. In Chapter 4, we described how such a lattice has been realized in the experiments of the group of K. Sengstock [161]. While there we were interested in the interaction-driven SF–MI transition of bosonic mixtures, we assume for the following discussion that we work in a regime where interactions can be neglected. Further, to quantum simulate topological insulators such as relevant for electronic solid-state systems, the honeycomb lattice should be loaded with ultracold fermionic atoms, where the $\uparrow$ and $\downarrow$ particles could, *e.g.*, be atoms with $m_F = \pm 1/2$ hyperfine states. A tunable honeycomb optical lattice with fermions has recently been realized in the experiments of Tarruell and coworkers [162].

We first focus on a pure system of $\uparrow$-particles. For substantial detuning ΔE we can assume that nearest-neighbor (NN) tunneling (between A and B sites) is energetically suppressed and that next-NN (NNN) tunneling is relevant only between sites of the "shallow" A sublattice as sketched in Fig. 5.1d. Now assume that the system is driven resonantly by a time-periodic homogeneous

force of frequency $\nu_{AB}\hbar\omega = \Delta E$ (with integer ν_{AB}) that both re-establishes NN tunneling by ACT and creates finite artificial fluxes through the triangular NNN plaquettes of the A sublattice ("+" and "−" in Fig. 5.1d).

In this case, the effective Hamiltonian (5.4) becomes

$$\hat{\mathcal{H}}_{\text{eff}} = -\sum_{i\epsilon A}\left(\sum_{\langle i,j\rangle} t_{ij}^{\text{eff}}\,\hat{f}_i^\dagger \hat{f}_j + \sum_{\langle\langle i,j\rangle\rangle} t_{ij}'^{\text{eff}}\,\hat{f}_i^\dagger \hat{f}_j\right) + \text{h.c.}\,. \tag{5.13}$$

Here, $\langle i,j\rangle$ denotes pairs of NN sites, which are connected by $\boldsymbol{\tau}_1 = (\sqrt{3}\boldsymbol{e}_x + \boldsymbol{e}_y)/2$, $\boldsymbol{\tau}_2 = (-\sqrt{3}\boldsymbol{e}_x + \boldsymbol{e}_y)/2$ and $\boldsymbol{\tau}_3 = -\boldsymbol{e}_y$, and $\langle\langle i,j\rangle\rangle$ are pairs of NNNs in sublattice A, connected by $\boldsymbol{\tau}_4 = \boldsymbol{\tau}_1 - \boldsymbol{\tau}_2$, $\boldsymbol{\tau}_5 = \boldsymbol{\tau}_1 - \boldsymbol{\tau}_3$, $\boldsymbol{\tau}_6 = \boldsymbol{\tau}_2 - \boldsymbol{\tau}_3$, and $-\boldsymbol{\tau}_{4,5,6}$.

The topological nature of this Hamiltonian becomes best visible in its momentum representation. To this, we apply the Fourier transform

$$\hat{f}_i = \begin{cases} \frac{1}{\sqrt{N}}\sum_k \mathrm{e}^{-i\boldsymbol{k}\boldsymbol{r}_i}\hat{f}_{A\boldsymbol{k}}\,, & \text{if} \quad i\epsilon A\,, \\ \frac{1}{\sqrt{N}}\sum_k \mathrm{e}^{-i\boldsymbol{k}\boldsymbol{r}_i}\hat{f}_{B\boldsymbol{k}}\,, & \text{if} \quad i\epsilon B\,, \end{cases} \tag{5.14}$$

where N is the number of unit cells of the honeycomb lattice. Defining $\hat{\boldsymbol{f}}_{\boldsymbol{k}}^\dagger = (\hat{f}_{A\boldsymbol{k}}, \hat{f}_{B\boldsymbol{k}})^\top$ and introducing the corresponding Pauli matrices σ for the sublattice degree of freedom, the resulting Hamiltonian can be written in the compact matrix form

$$\hat{\mathcal{H}}_{\text{eff}} = \sum_{\boldsymbol{k}} \hat{\boldsymbol{f}}_{\boldsymbol{k}}^\dagger h(\boldsymbol{k}) \hat{\boldsymbol{f}}_{\boldsymbol{k}}\,, \tag{5.15}$$

where

$$h(\boldsymbol{k}) = \Re\left(g(\boldsymbol{k})\right)\sigma_x - \Im\left(g(\boldsymbol{k})\right)\sigma_y + g'(\boldsymbol{k})\frac{1}{2}\left(\mathbb{I} + s_z\sigma_z\right)\,. \tag{5.16}$$

Here, we defined $s_z = 1$ for $\uparrow$ particles, and the effective NN (NNN) tunnelings t_δ^{eff} ($t_\delta'^{\text{eff}}$) appear in their Fourier transforms,

$$g(\boldsymbol{k}) \;=\; -\sum_{\boldsymbol{\tau}_\delta = \boldsymbol{\tau}_{1,2,3}} t_\delta^{\text{eff}}\,\mathrm{e}^{i\boldsymbol{k}\cdot\boldsymbol{r}_\delta}\,, \tag{5.17a}$$

$$g'(\boldsymbol{k}) \;=\; -\sum_{\boldsymbol{\tau}_{\delta'} = \pm\boldsymbol{\tau}_{4,5,6}} t_{\delta'}^{\text{eff}}\,\mathrm{e}^{i\boldsymbol{k}\cdot\boldsymbol{r}_{\delta'}}\,. \tag{5.17b}$$

Here, we introduced the notation ${t^{(\prime)}}_\delta^{\text{eff}} = {t^{(\prime)}}_{ij}^{\text{eff}}$ for $\boldsymbol{r}_j = \boldsymbol{r}_i + \boldsymbol{r}_\delta$. Diagonalizing $h(\boldsymbol{k})$ gives the dispersion relations

$$\varepsilon_\pm = \frac{1}{2}g'(\boldsymbol{k}) \pm \sqrt{|g(\boldsymbol{k})|^2 + |g'(\boldsymbol{k})/2|^2} \tag{5.18}$$

for the two bands. Under appropriate shaking, this dispersion relation is that of a topological insulator, as we discuss in the next section.

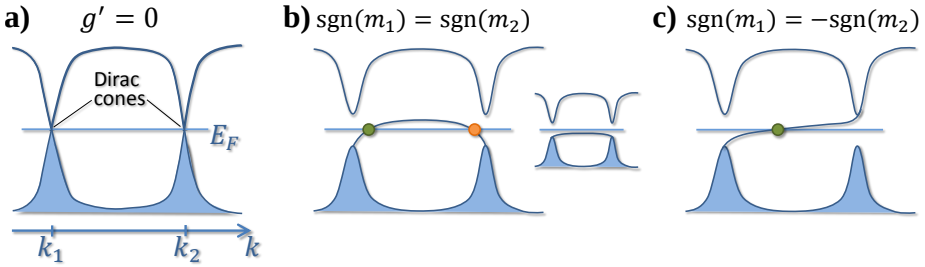

Figure 5.4: **Sketch of dispersion relations. (a) Dirac cones.** At vanishing NNN tunneling, the system can possess Dirac cones at $\boldsymbol{k}_{1,2}$. A finite NNN tunneling splits the bands, and the Dirac cones acquire the masses $m_{1,2} = g'(\boldsymbol{k}_{1,2})$. **(b) Topologically trivial system,** $n_C = 0$. If m_1 and m_2 have the same sign, the resulting edge mode crosses the Fermi energy E_F an even number of times. The number of right-moving (green dot) and left-moving (red dot) edge modes is equal and the edge current vanishes. Inset: Local changes can deform the system into a topologically equivalent one where no edge modes cross E_F. **(c) Topological insulator,** $n_C = \pm 1$. If m_1 and m_2 have opposite sign, the edge modes cross E_F an odd number of times; they are topologically protected and conduct current.

5.4.2 Topological insulators and Haldane model

At vanishing NNN tunneling ($g' = 0$), the system can possess a pair of points where the two bands touch, *i.e.*, $g(\boldsymbol{k}_{1,2}) = 0$. These so-called Dirac points have light-cone-like dispersion relation, see Fig. 5.4a. A finite g' will split the bands at these points and the Dirac-type dispersion relations found near $\boldsymbol{k}_{1,2}$ acquire finite curvatures, *i.e.*, "masses," $m_{1,2} = g'(\boldsymbol{k}_{1,2})$.

Due to the gap created by g', the system is an insulator if the lower band is entirely filled, *i.e.*, if E_F lies within the gap. If the system has a boundary, however, the splitting of the Dirac cones *in the bulk* gives rise to modes localized *to the edge*. These can conduct an effective current if the number of right- and left-moving edge modes is different. For each edge mode, the direction of the localized current associated with it is determined by the group velocity v_F, which is given by the way the dispersion relation of the edge modes intersects the Fermi energy E_F. At a boundary along the μ-direction, with $\mu = x, y$, the group velocity $\hbar v_F = d\epsilon/dk_\mu|_{E_F} > 0$ defines a right-moving edge mode. On the opposite boundary, the corresponding group velocity will have the opposite sign.

In a case where the mass terms $m_{1,2}$ have the same sign, which is the stan-

dard situation, these edge modes cross the Fermi energy an even number of times (Fig. 5.4b). The number of right- and left-moving edge modes is then equal at each boundary and there is no chiral current around the sample. The topological invariant describing the conduction properties of the edge modes, the Chern number, takes the value $n_C = 0$. This vanishing Chern number implies that the system is topologically equivalent to a trivial system without any edge modes. The edge modes are therefore not topologically protected, and a change of the dispersion relation, by adjusting the Hamiltonian locally near the boundary, can entirely remove them (Fig. 5.4b, inset).

If the mass terms have different signs, on the other hand, the edge modes cross the Fermi energy an odd number of times (Fig. 5.4c), which also implies a chiral current around the sample. A local change of the Hamiltonian can still deform the dispersion relation, but it can not entirely remove the edge modes – the difference between the number of right- and left-moving modes is preserved under any such local changes, *i.e.*, it is a topological invariant. In fact, it equals the Chern number difference between the sample and the surrounding medium (the vacuum has $n_C = 0$). This surprising one-to-one relationship between a bulk property (the Chern number) and the conductance at the boundary is known as *bulk-boundary correspondence* [281]. In our case, if the masses $m_{1,2}$ have opposite sign, the lowest band possesses the finite Chern number $n_C = \pm 1$. Then, if the lowest band is filled with $\uparrow$ fermions (this requires that the bands do not overlap in energy), the system is a topological insulator with finite quantized Hall conductivity and robust chiral edge modes.

Even more, repeating the above reasoning for $\downarrow$ particles, for which the role of A and B sites is interchanged, one obtains the same result, but with $s_z = -1$ entering in Eq. (5.16), and inverted Hall conductivity. Filling the lowest band for both $\uparrow$ and $\downarrow$ particles, therefore, leads to a state with vanishing net particle current but finite spin current, since the edge modes have opposite chirality for the two species – the system thus realizes a QSH insulator [324].

It is instructive to compare our proposed setup to the Haldane model [325], where this type of topological insulator was predicted first. The Haldane model is a honeycomb lattice with uniform NN tunnelings t and NNN tunnelings t' that are equal for the two sublattices A and B. A staggered magnetic field induces a phase θ which has the same chirality on both sublattices (*i.e.*, it has for all NNN tunnelings a positive sign if taken clockwise within one plaquette, see Fig. 5.5b). The Hamiltonian matrix describing this situation can be written as

$$h_{\mathrm{Hald}}(\boldsymbol{k}) = \Re\left(g(\boldsymbol{k})\right)\sigma_x - \Im\left(g(\boldsymbol{k})\right)\sigma_y + 2\cos\theta\,\Re\left(g'(\boldsymbol{k})\right)\mathbb{I} + 2\sin\theta\,\Im\left(g'(\boldsymbol{k})\right)\sigma_z\,. \tag{5.19}$$

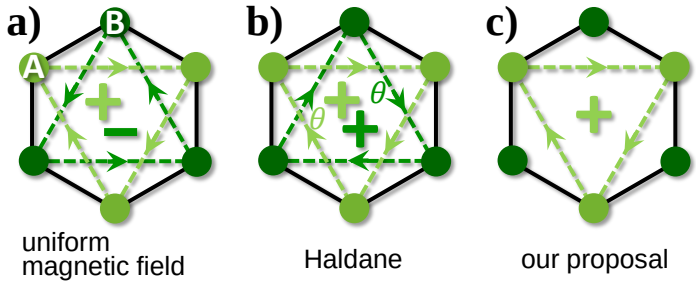

Figure 5.5: **Schematic comparison of Peierls-phase patterns on the honeycomb lattice. (a)** For a *uniform* magnetic field, positive phases θ are picked up along the directions indicated by the arrows. The corresponding phase chiralities (denoted "+" and "–") for the two sublattices A and B cancel each other, leading to $n_C = 0$. **(b)** In the Haldane model, a *staggered* magnetic field leads to same-sign phase chiralities on the two sublattices, thus breaking time-reversal symmetry. The system acquires a non-trivial $n_C = \pm 1$. **(c)** In our proposal, time-reversal symmetry breaking, and the associated non-trivial Chern number, is achieved by canceling the NNN tunnelings for one sublattice (here, B) by making its wells sufficiently deep.

The details of our $h(\boldsymbol{k})$, Eq. (5.16), differ from $h_{\mathrm{Hald}}(\boldsymbol{k})$, but in both cases the term $g(\boldsymbol{k})$ given by NN tunneling creates Dirac cones, and these are split by terms proportional to σ_z generated by the NNN tunneling $g'(\boldsymbol{k})$. Similarly as in our case, given an appropriate phase structure, the resulting mass terms proportional to σ_z can have opposite signs at the two Dirac cones. We compare the lattice and phase structure of the original Haldane model with our proposal in Fig. 5.5. In each case, for such mass terms with opposite sign to be possible, one needs a certain amount of time-reversal symmetry breaking. For this, the chiralities of the phases for the NNN tunnelings associated to the sublattices A and B must not cancel. In the original Haldane model, the chiralities were set equal using the staggered field. Here, we took a different route and turned off completely the NNN tunneling for one sublattice (in our case B). For this, the wells of the B sublattice must be much deeper than the ones of the A sublattice, which implies a strong energy difference $\nu_{AB}\hbar\omega$. However, this energy difference would contribute to $h(\boldsymbol{k})$ a term proportional σ_z. This contribution, therefore, also produces a mass term, but, since it is independent of $\boldsymbol{k}$, with equal sign at both Dirac points. It, hence, counteracts the opposite signs of the mass terms created by the NNN tunneling $g'(\boldsymbol{k})$, and thus works against a non-trivial Chern

number. The ACT, which is employed to tune the Peierls phases of the effective tunnelings, also effectively cancels this energy difference and thus allows to achieve mass terms with opposite signs.

5.4.3 Numerical example

As a concrete example to implement the proposed scheme, we consider unidirectional forcing $\boldsymbol{F}(\tau) = F(\tau)\boldsymbol{e}_F$ with unit vector $\boldsymbol{e}_F = (\cos(\varphi_F), \sin(\varphi_F))^\top$ and $F(\tau)$ as given by the paused sine-wave (5.7) (see also Fig. 5.1a). We use the concrete parameters $\hbar\omega = \Delta E/2$ and $T_1 = T/2$, which yields a NNN tunneling $t'^{\text{eff}}_\delta/t'$ similar to Eq. (5.8). In this case, the NN tunneling is given by

$$\frac{t^{\text{eff}}_\delta}{t} = -\frac{1}{2} i \mathrm{e}^{i\frac{\eta_\delta}{2}} \mathcal{J}_1(\eta_\delta)\,. \tag{5.20}$$

(In the direction $\boldsymbol{r}_\delta$ where $\nu_{ij} = 1$; in the opposite direction $\nu_{ij} = -1$ the phase changes sign.) Here, we introduced the undriven NN (NNN) tunneling matrix elements t (t').

To find Dirac cones for these effective tunnelings, we first compute the dispersion relation (5.18) for $t' = 0$, and find via numerical minimization the points where the gap between the two bands closes. Then, we compute the masses $m_{1,2} = g'(\boldsymbol{k}_{1,2})$ at these Dirac points (if they exist). In Fig. 5.6a, we plot the smaller one of the two mass terms, $|m_<| \leq |m_>|$. As this shows, by varying the angle φ_F and the dimensionless forcing amplitude $\eta = dF_0T_1/(2\pi\hbar)$ (with d the lattice constant), we can access various topologically distinct phases. There are topologically less interesting regions without Dirac points (white), and regions where the forcing is perpendicular to one of the NN bonds (gray), suppressing the corresponding tunneling and rendering the physics effectively one dimensional (when neglecting NNN tunneling). Besides these, there are parameter spaces where the two Dirac points acquire mass terms of the same sign (hatched horizontally and diagonally) and parameter regions where the mass terms have opposite sign (un-hatched), *i.e.*, where the topological insulator is realized. Between these, topological quantum phase transitions occur, marked by a closing of the gap and therefore (at least one) vanishing mass term (dark color).

As Fig. 5.6a demonstrates, changing the driving allows to manipulate the Dirac cones. In Fig. 5.6b, we show in detail for the case of $\varphi_F = -2\pi/15$ how the Dirac cones can be moved and merged, simply by increasing the driving amplitude η. We plot the trajectory for a pair of non-equivalent Dirac points. As can be seen, sometimes a pair of Dirac points splits and merges again at

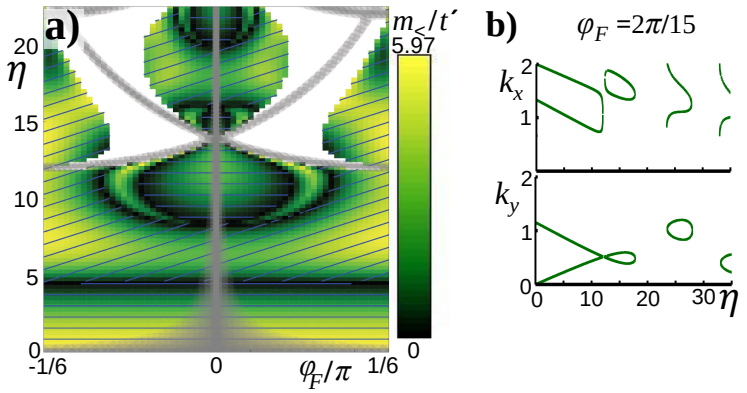

Figure 5.6: **(a) Quantum spin Hall phase diagram.** The honeycomb lattice (as shown in Fig. 5.1d) is subjected to a paused-sine-wave driving with amplitude η and direction $\boldsymbol{e}_F = (\cos(\varphi_F), \sin(\varphi_F))^\top$, leading to a splitting of the two non-equivalent Dirac cones with masses $m_{<,>}$. The color scale denotes the smaller one, $|m_<| \leq |m_>|$. In the diagonally (horizontally) hatched region both masses are positive (negative). In the un-hatched region, they have opposite sign. Here, the system is a topological insulator (or, for two spin states, a quantum spin Hall insulator). In the white (or gray) regions no Dirac points are present (or a small nearest-neighbor tunneling $< 0.02t$ renders the physics effectively 1D). **(b) Position of two Dirac points** in k-space for $\varphi_F = -2\pi/15$, indicating how they move and merge as a function of the driving amplitude η.

some larger η, forming a loop in k-space, while other times they merge with the Dirac points from different pairs, forming open trajectories in k-space.

As a final remark, in the analysis of this section, we assumed negligible atom–atom interactions. Since general results about topological insulators in the presence of strong interactions are limited (see, *e.g.*, Refs. [326–328]), it would be interesting to observe their effects by tuning them – *e.g.*, via a Feshbach resonance – in an ultracold-atom experiment.

5.5 Non-Abelian SU(2) gauge fields

In QSH insulators as described in Sec. 5.4, the two species involved acquire opposite phases, thus realizing a specific non-trivial SU(2) gauge field for the species degree of freedom. The periodic driving permits, however, even more:

it allows the exploration of *arbitrary* non-Abelian SU(2) gauge fields, if the two species additionally are mixed. To show this, we consider two species ↑,↓ with opposite spin (say, hyperfine states $m_F = \pm 1$), which will constitute the degree of freedom for which the SU(2) gauge fields are created.

Quantum simulation of such non-Abelian SU(2) physics is relevant to the electroweak interaction of the Standard Model of particle physics, and an extension to SU(3) may even give insight into phenomena from quantum chromodynamics. Systems with non-Abelian anyonic excitations may also find useful application in topological quantum computing [329]. For these reasons, the prospect of quantum simulating non-Abelian gauge fields has received increased interest in recent years (see, *e.g.*, the works [303, 307, 310, 315, 330–337]), but mostly in the context of artificial gauge fields induced in rotating condensates or by laser-mediated Berry-phase imprinting. Our proposal, based on a simple time-periodic driving of the lattice, appears experimentally more straightforward. (In a similar vein, Bermudez *et al.* [199] considered – among others – how driven on-site potentials can generate non-Abelian SU(2) gauge fields. Although their work is motivated by trapped ions, the main ideas can be translated to neutral atoms in optical lattices.)

5.5.1 Engineering non-Abelian SU(2) tunneling matrices

To illustrate our scheme, we assume that the two species ↑ and ↓ are loaded into a spin-dependent square lattice as depicted in Fig. 5.7a. Such a lattice can be created by two perpendicular pairs of counterpropagating lasers that are polarized in plane and have a phase shift of $\pi/2$ [338]. The result is a bipartite square lattice with alternating σ^- and σ^+ polarized sites, which we denote as A and B. This situation is quite similar to the one explored in Chapter 4 for the honeycomb geometry. We will comment on this situation further on, where, in particular, we will show that in that case a little additional experimental effort is needed in order to create non-Abelian SU(2) gauge fields.

The hyperfine states $m_F = \pm 1$ couple differently to the σ^+ and σ^- polarizations of the bipartite lattice, such that for ↑-particles ($m_F = +1$) the σ^+ wells are shallow and σ^- wells deep, and the other way around for ↓ ($m_F = -1$). In such a situation, the energy of ↑ particles is lifted (lowered) by $\Delta E/2$ on A (B) sites, and vice versa for ↓ particles. These energy shifts are summarized by $\Delta E \sigma_z s_z/2$, if we introduce two sets of Pauli matrices s and σ for spin (↑ or ↓) and sublattice (A or B) degree of freedom, respectively. Due to this energy difference, NN hopping will be off-resonant so that it is realized by ACT only, providing the necessary control for our scheme.

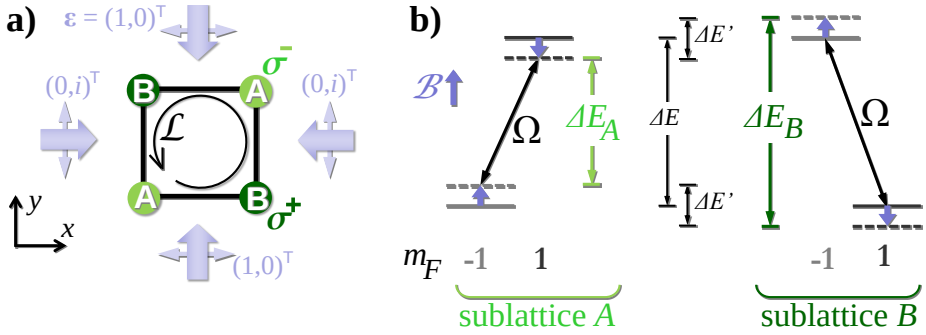

Figure 5.7: **Creation of non-Abelian SU(2) gauge fields. (a) Lattice geometry.** Two standing laser waves with a phase shift of $\pi/2$ and in-plane polarization $\boldsymbol{\varepsilon}$ as denoted in the figure create a bipartite square lattice with alternating σ^- and σ^+ polarized sites (A and B). $m_F = \pm 1$ particles feel an energy difference of $\pm\Delta E$ between A and B sites. **(b) Resulting level scheme.** A constant $\mathcal{B}$-field realizes an additional on-site energy splitting $\Delta E'$ (blue arrow) such that $|\Delta E_{A,B}| = |\pm\Delta E + \Delta E'|$ becomes sublattice dependent. The coupling Ω of both spin states can be realized by magnetic or microwave fields.

Including the NN tunneling t, the Hamiltonian of this system reads

$$\hat{\mathcal{H}} = -\sum_{\langle i,j\rangle} t\,\hat{\boldsymbol{a}}_i^\dagger \mathbb{I}\hat{\boldsymbol{a}}_j + \sum_i \hat{\boldsymbol{a}}_i^\dagger \frac{1}{2}\Delta E \sigma_z s_z \hat{\boldsymbol{a}}_i\,, \tag{5.21}$$

with $\hat{\boldsymbol{a}}_i^\dagger = (\hat{a}_{i\uparrow}, \hat{a}_{i\downarrow})$. At this stage, the tunneling matrix equals the 2×2-identity matrix, which we included in Eq. (5.21) for emphasis. Our aim is to engineer the system in such a way that it can be any arbitrary SU(2) matrix.[3]

For this reason, we need several additional ingredients. First, to realize arbitrary non-diagonal matrices, additional magnetic or microwave fields couple the two species on site with a strength Ω. Further, to realize non-commuting matrices, we will need a stronger distinction between the sublattices than a mere sign difference of the energy splittings $\pm\Delta E$. One way would be a site-dependent coupling strength Ω. For now, we pursue a different possibility,

[3] Our scheme works also for mixtures of species with different absolute value of hyperfine quantum number (*e.g.*, $m_F = 0$ and 1). In that case, however, the two species will have distinct bare tunneling, realizing a tunneling matrix $\neq \mathbb{I}$ in the initial Hamiltonian (5.21). This mingles the non-Abelian physics with a spin-orbit coupling. We do not pursue here this interesting possibility.

namely the creation of site-dependent energy splittings. These can be induced by a constant magnetic field $\mathcal{B}$, which produces the site-independent energy splitting $\Delta E'$. These additions can be summarized in the site-independent term $\Delta E' s_z/2 + \Omega s_x$. The absolute value of the total $\uparrow$–$\downarrow$-splitting $\Delta E_i = \Delta E \sigma_z - \Delta E'$ becomes then sublattice dependent. The resulting level structure is summarized in Fig. 5.7b, where we define $\Delta E_i = \Delta E_{A,B}$ if $i \epsilon A, B$. With these ingredients, the Hamiltonian becomes

$$\hat{\mathcal{H}} = -\sum_{\langle i,j \rangle} t\, \hat{\boldsymbol{a}}_i^\dagger \mathbb{I} \hat{\boldsymbol{a}}_j + \sum_i \hat{\boldsymbol{a}}_i^\dagger \left(\frac{1}{2} \Delta E_i s_z + \Omega s_x \right) \hat{\boldsymbol{a}}_i \,. \tag{5.22}$$

To capture their effect in a single matrix, we diagonalize the on-site Hamiltonian

$$\hat{\mathcal{H}}_i = \hat{\boldsymbol{a}}_i^\dagger \left(\frac{1}{2} \Delta E_i s_z + \Omega s_x \right) \hat{\boldsymbol{a}}_i \,. \tag{5.23}$$

This is achieved with the transformation $\hat{\boldsymbol{b}}_i = u_i^\dagger \hat{\boldsymbol{a}}_i$, where u_i are time-independent unitary 2×2-matrices. Labeling the on-site eigenvalues as $\pm \hbar \lambda_i$, with

$$\hbar \lambda_i = \frac{1}{2} \sqrt{\Delta E_i^2 + 4\Omega^2} \,, \tag{5.24}$$

we arrive at

$$\hat{\mathcal{H}} = -\sum_{\langle i,j \rangle} t\, \hat{\boldsymbol{b}}_i^\dagger u_i^\dagger u_j \hat{\boldsymbol{b}}_j + \sum_i \hat{\boldsymbol{b}}_i^\dagger \hbar \lambda_i s_z \hat{\boldsymbol{b}}_i \,. \tag{5.25}$$

Now, the tunneling matrix is described by $u_i^\dagger u_j$, and it is clear why the sublattice dependence entering through $\Delta E_i/(2\Omega)$ is necessary: it achieves generically $u_i^\dagger u_j \neq u_i^\dagger u_i = \mathbb{I}$.

To achieve genuinely non-Abelian physics, we require a final ingredient. Namely, it is not enough to have two non-commuting tunneling matrices. Instead, one has to demand the stronger condition that their product *around a plaquette*, the so called *Wilson loop* $\mathcal{L}$, not simply yields a phase $\mathrm{e}^{i\phi}\mathbb{I}$ [315]. Namely, if $\mathcal{L} = \mathrm{e}^{i\phi}\mathbb{I}$ is the case, the physics is equivalent to an Abelian magnetic flux ϕ, and one can find a gauge where the tunneling matrices are all individually proportional to the identity. At this point, the Wilson loop describing $\hat{\mathcal{H}}$ as given by Eq. (5.25) is

$$\mathcal{L} = u_A^\dagger u_B \; u_B^\dagger u_A \; u_A^\dagger u_B \; u_B^\dagger u_A = \mathbb{I} \,, \tag{5.26}$$

identifying the physics of this system as Abelian. (Here, we abbreviated $u_{i \epsilon A,B} = u_{A,B}$ and fixed the convention to start at the bottom left corner of a plaquette with sublattice A.)

To arrive at a non-Abelian Wilson loop, we now introduce a non-linear element, namely lattice shaking realized by a simple spin-independent sinusoidal drive $v_i^\omega(\tau) = -\boldsymbol{r}_i \cdot \boldsymbol{F}_0 \cos(\omega\tau)$. The Hamiltonian now becomes

$$\hat{\mathcal{H}} = -\sum_{\langle i,j\rangle} t\,\hat{\boldsymbol{b}}_i^\dagger u_i^\dagger u_j \hat{\boldsymbol{b}}_j + \sum_i \hat{\boldsymbol{b}}_i^\dagger [\hbar\lambda_i s_z + v_i^\omega(\tau)]\hat{\boldsymbol{b}}_i\,. \tag{5.27}$$

As in the derivation preceding Eq. (5.6), the unitary transformation $\exp\big(-i\sum_i \hat{\boldsymbol{b}}_i^\dagger[\lambda_i\tau s_z - \eta_i \sin(\omega\tau)]\hat{\boldsymbol{b}}_i\big)$ with $\eta_i = \boldsymbol{r}_i \cdot \boldsymbol{F}_0/(\hbar\omega)$ leads to a purely kinetic Hamiltonian

$$\hat{\mathcal{H}}'(\tau) = -\sum_{\langle i,j\rangle} t\,\hat{\boldsymbol{b}}_i^\dagger W_{ij}(\tau)\hat{\boldsymbol{b}}_j\,. \tag{5.28}$$

Here,

$$W_{ij}(\tau) = \mathrm{e}^{-i\eta_{ij}\sin(\omega\tau)} \begin{pmatrix} c_{ij}\mathrm{e}^{i(\lambda_i-\lambda_j)\tau} & d_{ij}\mathrm{e}^{-i(\lambda_i+\lambda_j)\tau} \\ -d_{ij}^\star \mathrm{e}^{i(\lambda_i+\lambda_j)\tau} & c_{ij}^\star \mathrm{e}^{-i(\lambda_i-\lambda_j)\tau} \end{pmatrix}, \tag{5.29}$$

if we parametrize $u_i^\dagger u_j$ as

$$u_i^\dagger u_j = \begin{pmatrix} c_{ij} & d_{ij} \\ -d_{ij}^\star & c_{ij}^\star \end{pmatrix}. \tag{5.30}$$

For $\hbar\omega \gg t_{ij}$, we can approximate $\hat{\mathcal{H}}'(\tau)$ by its time average

$$\hat{\mathcal{H}}_{\text{eff}} = \langle \hat{\mathcal{H}}' \rangle_T = -\sum_{\langle i,j\rangle} t_{ij}^{\text{eff}} \hat{\boldsymbol{b}}_i^\dagger M_{ij} \hat{\boldsymbol{b}}_j\,, \tag{5.31}$$

with the effective tunneling matrix elements

$$t_{ij}^{\text{eff}} = t\sqrt{|\det(\langle W_{ij}\rangle_T)|}\,, \tag{5.32}$$

and the matrices

$$M_{ij} \equiv \langle W_{ij}\rangle_T / \sqrt{|\det(\langle W_{ij}\rangle_T)|}\,. \tag{5.33}$$

This choice of normalization ensures $\det M_{ij} = 1$ and allows to separate genuinely non-Abelian effects from a mere driving-induced modification of the overall tunneling amplitude. To achieve finite $t_{ij}^{\text{eff}} \neq 0$ via ACT, we require

$$\lambda_{i\epsilon B} \pm \lambda_{i\epsilon A} = \nu_\pm\,\omega \tag{5.34}$$

with integers $\nu_\pm$. Then, the matrix elements of M_{ij} can be obtained from

$$\langle W_{ij}\rangle_T = \begin{pmatrix} c_{ij}\mathcal{J}_{\nu_-}(\eta_{ij}) & d_{ij}\mathcal{J}_{\nu_+}(\eta_{ij}) \\ d_{ij}^\star \mathcal{J}_{\nu_+}(\eta_{ij}) & -c_{ij}^\star \mathcal{J}_{\nu_-}(\eta_{ij}) \end{pmatrix}. \tag{5.35}$$

Here, the amplitude of the forcing $\eta_{ij} = (\boldsymbol{r}_i - \boldsymbol{r}_j)\cdot\boldsymbol{F}_0/(\hbar\omega)$ depends only on the direction $\boldsymbol{r}_{ij} = \boldsymbol{r}_i - \boldsymbol{r}_j$ of link ij, which depends on the lattice geometry. Further, to ensure unitarity $M_{ij}M_{ji} = \mathbb{I}$, we have to impose the additional condition that the $\nu_\pm$ are either both even or both odd (to see this, use $\nu_-(ji) = -\nu_-(ij)$ and $\eta_{ji} = -\eta_{ij}$).

5.5.2 Analytic calculation of the Wilson loop

Now, we derive an analytical expression for the Wilson loop $\mathcal{L}$ around a fundamental plaquette. First, we show that it is independent of the choice of the local phases of the two states $\uparrow$ and $\downarrow$. For this, it is convenient to write the unitary matrices u_i diagonalizing the on-site Hamiltonian (5.23) as

$$u_i = \mathrm{e}^{\frac{i}{2}\Lambda_i s_y}\mathrm{e}^{i(\varphi_i s_z + \beta_i)}\,, \tag{5.36}$$

where

$$\Lambda_i = \arctan\frac{\Delta E_i}{2\Omega}\,. \tag{5.37}$$

The phases φ_i and β_i generalize the γ_i from Eq. (5.2) to the situation of two species; they attest the freedom in choosing the phases of the two states which form the local basis. As these are arbitrary, physical observables such as the Wilson loop operator $\mathcal{L}$ cannot depend on them. This is immediate in the absence of periodic driving. Indeed, in that case the Wilson loop is the identity whatever choice of the phases we take in u_i, since Eq. (5.26) contains only products of the form $u_i^\dagger u_i = \mathbb{I}$. In presence of periodic driving, the cancellation of the phases is slightly more involved.

From the definition of the M_{ij}, Eqs. (5.33) and (5.35), it can be seen that their matrix elements have the same phases (up to multiples of π) as the elements of $u_i^\dagger u_j$ given in Eq. (5.30). (The moduli of the matrix elements of M_{ij}, on the other hand, are independent of the phases of $u_i^\dagger u_j$.) This implies that for two different choices of the local phases at the sites i and j, say $\{\varphi_i, \beta_i, \varphi_j, \beta_j\}$ and $\{\varphi_i', \beta_i', \varphi_j', \beta_j'\}$, the effective hopping matrices relate as

$$M_{ij}' = \mathrm{e}^{i(\Delta\varphi_i s_z + \Delta\beta_i)} M_{ij} \mathrm{e}^{-i(\Delta\varphi_j s_z + \Delta\beta_j)}, \tag{5.38}$$

where $\Delta\varphi_k \equiv \varphi_k' - \varphi_k$, and $\Delta\beta_k \equiv \beta_k' - \beta_k$. That is, the choice of the phases commutes with the time-average procedure. It follows that, as in the time-independent case, the phases cancel out when the hopping matrices M_{ij} are multiplied in the Wilson loop $\mathcal{L}$. Hence, $\mathcal{L}$ is independent of the choice of local phases, as it should be.

We finally remark that the same happens for more involved choices of the optical lattice, as the actual form of the local Hamiltonian does not play any role (cf. Sec. 5.5.4).

Using this result, we may choose $\varphi_i = \beta_i = 0$, $\forall i$, which, together with Eq. (5.36), implies that

$$u_i^\dagger u_j = \mathrm{e}^{\frac{i}{2}(\Lambda_j - \Lambda_i)s_y} \,. \tag{5.39}$$

From this, we can derive an analytical formula for the Wilson loop, which will us help understand under which circumstances it can be non-Abelian. To do this, we call, in all generality, $\mathcal{M}$ the forcing-induced non-linear map that relates $u_i^\dagger u_j$ to the effective hopping matrix M_{ij}, $M_{ij} = \mathcal{M}[u_i^\dagger u_j]$. As mentioned in the discussion following Eq. (5.35), the energy differences ν_+ and ν_- have to be integers which are either both even ("*even* forcing") or both odd ("*odd* forcing"). It is convenient to characterize the action of $\mathcal{M}$ separately for these two situations.

Even forcing

First, we analyze the action of $\mathcal{M}$ for even forcing, *i.e.*, $\nu_+ = 2n$, $\nu_- = 2n'$. By construction, $\mathcal{M}$ maps *(i)* unitary matrices to unitary matrices, and *(ii)* real matrices to real matrices. From this, it follows, using Eq. (5.39), that

$$\mathcal{M}[u_i^\dagger u_j] = \mathcal{M}[\mathrm{e}^{i\Lambda_{ij}s_y}] = \mathrm{e}^{i\Lambda'_{ij}s_y} \,, \tag{5.40}$$

where

$$\Lambda'_{ij} = \arctan\Big[\frac{\mathcal{J}_{2n'}(\eta_{ij})}{\mathcal{J}_{2n}(\eta_{ij})}\tan\Lambda_{ij}\Big] \,. \tag{5.41}$$

Since this form of $\mathcal{M}[\mathrm{e}^{i\Lambda_{ij}s_y}]$ only involves the s_y Pauli matrices, the hopping matrices $M_{ij} = M_\delta$ commute for different links δ. Further, Eq. (5.41) shows that traveling a link $\langle i,j\rangle$ in its mirror-reflected direction, *i.e.*, starting from the same site, yields $M_{-ij} = M_{ij}$ (since by Eq. (5.37), $\Lambda_{i'} - \Lambda_j = \Lambda_i - \Lambda_j$ $\forall i, i'$ NN of j). On the other hand, traveling on the very same link in opposite direction gives $M_{ji} = M_{ij}^\dagger$ (since $\Lambda_{ji} = -\Lambda_{ij}$). These possibilities are summarized in Fig. 5.8a.

The Wilson loop on the square lattice with lattice vectors $\boldsymbol{r}_{\delta=1,2} = \boldsymbol{e}_{x,y}$, sketched in Fig. 5.8b, is then

$$\mathcal{L} = M_1 M_2 M_{-1} M_{-2} = M_1 M_2 M_1 M_2 = \mathrm{e}^{i(\Lambda'_1 + \Lambda'_2)s_y} \,, \tag{5.42}$$

where we defined $M_{ij} = M_{1,2}$ for $\boldsymbol{r}_{ij} = \boldsymbol{r}_{1,2}$, and similarly for $\Lambda_{1,2}$. This form of the Wilson loop implies that this system can host non-Abelian phenomena.

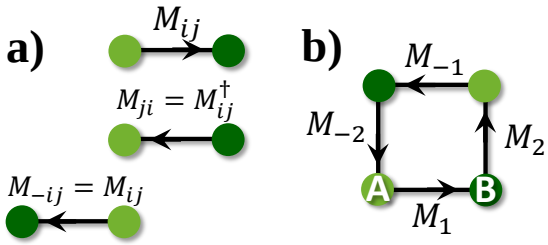

Figure 5.8: **(a) Tunneling matrices along a link,** for even forcing. If we define the tunneling matrix on a given link in a given direction as M_{ij} (top), the tunneling matrix in the mirror reflected direction is the same, $M_{-ij} = M_{ij}$ (bottom). Traveling in opposite direction on the same link, however, gives $M_{ji} = M_{ij}^\dagger$ (center). **(b) The Wilson loop** on the square lattice can be non-Abelian.

Odd forcing

Similarly, for *odd* forcing, *i.e.*, when both ν_+ and ν_- are odd numbers, $\nu_+ = 2n+1$, $\nu_- = 2n'+1$, the time-averaging procedure results in

$$\mathcal{M}[\mathrm{e}^{i\Lambda_{ij}s_y}] = s_z \mathrm{e}^{i\Lambda'_{ij}s_y}\,, \tag{5.43}$$

where

$$\Lambda'_{ij} = \arctan\Big[\frac{\mathcal{J}_{2n'+1}(\eta_{ij})}{\mathcal{J}_{2n+1}(\eta_{ij})}\tan\Lambda_{ij}\Big]\,. \tag{5.44}$$

This implies the relations for the tunneling matrices $M_{ij} = M_{-ij}$ and $M_{ji} = s_z \exp(-i\Lambda_{ij}s_y)$.

To compute $\mathcal{L}$, we note that

$$s_z \mathrm{e}^{i\Lambda'_a s_y} s_z = \mathrm{e}^{-i\Lambda'_a s_y}\,. \tag{5.45}$$

Simple algebra leads then to

$$\mathcal{L} = M_1 M_2 M_1 M_2 = s_z \mathrm{e}^{i\Lambda'_1 s_y} s_z \mathrm{e}^{i\Lambda'_2 s_y} s_z \mathrm{e}^{i\Lambda'_1 s_y} s_z \mathrm{e}^{i\Lambda'_2 s_y} = \mathrm{e}^{i(\Lambda'_2 - \Lambda'_1)s_y}. \tag{5.46}$$

The difference $\Lambda'_2 - \Lambda'_1$ can take any value between zero and 2π, allowing for a non-trivial Wilson loop.

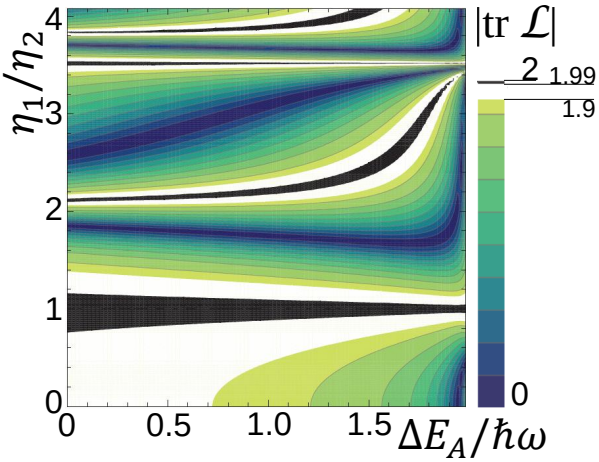

Figure 5.9: **The trace of the Wilson loop** $\mathcal{L}$ (as sketched in Fig. 5.7a), exemplified for $\eta_2 = 1.84$, shows broad regions where it deviates from 2, demonstrating genuinely non-Abelian physics. The effect is especially strong outside of the white (black) regions, where $|\mathrm{tr}\mathcal{L}| < 1.9$ (< 1.99).

On the bipartite square lattice, the configuration of tunneling matrices illustrated in Fig. 5.8a results in a checkerboard configuration of $\mathcal{L}$ and $\mathcal{L}^\dagger$, similar to a staggered flux in the single-species case. Both for even and odd forcing, the traces of $\mathcal{L}$ and $\mathcal{L}^\dagger$, however, are equal, see Eqs. (5.42) and (5.46). Also, this limitation can be circumvented by using other geometries. For instance, as we describe below (Sec. 5.5.4), non-trivial Wilson loops can be achieved in honeycomb lattices, and in that case, the Wilson loops will be homogeneous since the sublattices A and B are located in the same order in every plaquette.

5.5.3 Numerical calculation of the Wilson loop

To demonstrate that the bipartite square lattice as sketched in Fig. 5.7, combined with lattice shaking, can host non-Abelian SU(2) physics, we consider now a concrete numerical example.

We choose odd forcing $\nu_+ = 3$ and $\nu_- = 1$. Due to Eqs. (5.34) and (5.24), this is achieved by setting $\Delta E_B = -\sqrt{12(\hbar\omega)^2 + \Delta E_A^2}$ and $\Omega = \sqrt{(\hbar\omega)^2 - \Delta E_A^2/4}$. This leaves $\Delta E_A/\hbar\omega$, η_1, and η_2 as free parameters (where $\eta_{1,2}$ is the amplitude of the forcing η_{ij} in positive x, y-direction). Further, we fix $\eta_2 = 1.84$, as this lies close to the first maximum of the Bessel function $\mathcal{J}_1(\eta_2)$, ensuring large tunneling $t_{ij}^{\mathrm{eff}} = t\sqrt{|\det(\langle W_{ij}\rangle_T)|}$ in y-direction.

As mentioned above, we have achieved genuinely non-Abelian physics, if the Wilson loop $\mathcal{L}$ yields not just a simple phase $\mathrm{e}^{i\phi}\mathbb{I}$. As shown by Goldman and

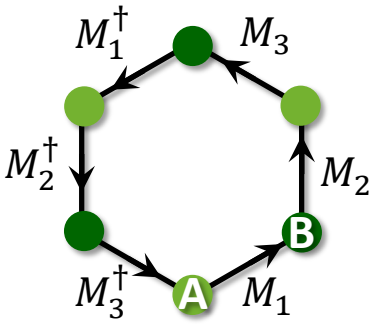

Figure 5.10: **The Wilson loop on a honeycomb plaquette** is always trivial, be it for even or odd forcing, at least if the mixing Ω is site-independent.

coworkers [315], this is equivalent to requiring $|\mathrm{tr}\mathcal{L}| < 2$, a *sine qua non* for the anomalous integer quantum Hall effect and fractional quantum Hall states with non-Abelian anyonic excitations [335]. For the odd driving, we have,

$$|\mathrm{tr}\mathcal{L}| = 2\,|\cos(\Lambda_2' - \Lambda_1')|\,. \tag{5.47}$$

Since the difference $\Lambda_2' - \Lambda_1'$ can take any value between zero and 2π, we can achieve any value between 2 and 0, as can be seen in Fig. 5.9. This proves the presence of a strong artificial non-Abelian gauge field. Moreover, under typical conditions, the system hosts Dirac cones, be it Abelian or non-Abelian.

5.5.4 Achieving non-trivial Wilson loop in honeycomb lattices

For the honeycomb lattice, the setup described above does not suffice to achieve non-trivial Wilson loops. Namely, if we define a plaquette by the lattice vectors $\boldsymbol{r}_1 = (\sqrt{3}\boldsymbol{e}_x + \boldsymbol{e}_y)/2$, $\boldsymbol{r}_2 = \boldsymbol{e}_y$, $\boldsymbol{r}_3 = (-\sqrt{3}\boldsymbol{e}_x + \boldsymbol{e}_y)/2$, and $-\boldsymbol{r}_1$, $-\boldsymbol{r}_2$, $-\boldsymbol{r}_3$, we obtain for even forcing the Wilson loop displayed in Fig. 5.10,

$$\mathcal{L}_{\mathrm{hex}} = M_1 M_2 M_3 M_1^\dagger M_2^\dagger M_3^\dagger\,. \tag{5.48}$$

Using the commutativity of all M_a implied by Eq. (5.40), we immediately obtain

$$\mathcal{L}_{\mathrm{hex}} = M_1 M_1^\dagger\; M_2 M_2^\dagger\; M_3 M_3^\dagger\; = \mathbb{I}\,, \tag{5.49}$$

For odd forcing, simple algebra using Eqs. (5.43) and (5.45) leads equally to $\mathcal{L}_{\mathrm{hex}} = \mathbb{I}$, so that the Wilson loop in the honeycomb lattice implies standard Abelian physics in both situations.

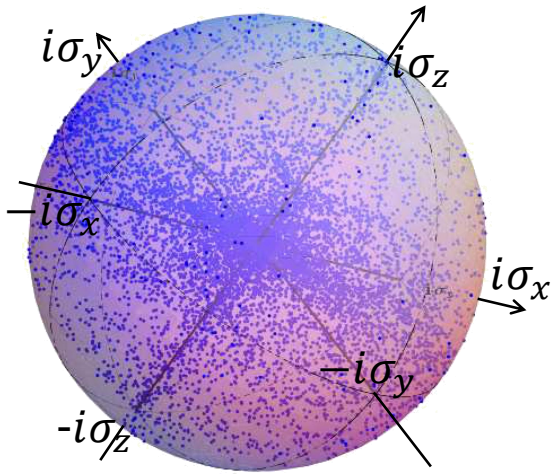

Figure 5.11: **Wilson loop $\mathcal{L}$ under site-dependent mixing of $\uparrow$ and $\downarrow$.** Shown is the Bloch-sphere representation of $\mathcal{L}$ in a honeycomb lattice under odd forcing $\nu_+ = 3$, $\nu_- = 1$ with Raman-laser wavevector $\boldsymbol{q} = d(\cos\theta_q, \sin\theta_q)$. The parameters are chosen randomly in the ranges $\theta_q \in [0, 2\pi[$, $\frac{\Delta E_A}{2\Omega} \in]5, 15[$, and the driving has strengths $\sqrt{\eta_1^2 + \eta_2^2} \in]0, 5[$ and random direction. The resulting $\mathcal{L}$'s can be arbitrary SU(2) matrices, covering the entire Bloch sphere.

The triviality of the Wilson loop in the honeycomb lattice is due to the form of M_{ij}, which is – for a site-independent mixing Ω of $\uparrow$- and $\downarrow$-particles given by Hamiltonian (5.23) – limited to $e^{i\varphi' s_y}$ or $s_z e^{i\varphi' s_y}$. This limitation can be overcome by employing position-*dependent* coupling via Raman-laser mixing, $\Omega \to \Omega_i = \Omega e^{i\boldsymbol{q}\cdot\boldsymbol{r}_i}$, with $\boldsymbol{q}$ the wave-vector difference of the Raman lasers. In this case, the local Hamiltonian (5.23) takes the form

$$\hat{\mathcal{H}}_i = \hat{\boldsymbol{a}}_i^\dagger \left\{ \frac{1}{2}\Delta E_i s_z + \Omega \left[\cos(\boldsymbol{q}\cdot\boldsymbol{r}_i) s_x - \sin(\boldsymbol{q}\cdot\boldsymbol{r}_i) s_y \right] \right\} \hat{\boldsymbol{a}}_i \,, \tag{5.50}$$

The main difference in this case is that, while still depending only on the link direction $\boldsymbol{r}_i - \boldsymbol{r}_j$, the M_{ij} for different link directions do generally not commute. Indeed, in this case the local transformation u_i may be chosen as

$$u_i = e^{i\frac{\boldsymbol{q}\cdot\boldsymbol{r}_i}{2} s_z} e^{\frac{i}{2}\arctan\frac{\Delta E_i}{2\Omega} s_y} \,. \tag{5.51}$$

Hence, the products $u_i^\dagger u_j$ for different link directions are not commuting, and the map $\mathcal{M}$ acts highly non-trivial on them.

Analytical expression for this form of site-dependent species mixing are very involved. To illustrate the additional liberty that it gives, we instead compute the Wilson loop numerically for a number of randomly selected parameters. We parametrize the results on the Bloch sphere, $\mathcal{L} = c_0 \mathbb{I} + \boldsymbol{c}\cdot\boldsymbol{s}$, with the Bloch-vector components $c_\alpha = \mathrm{Tr}(\mathcal{L} s_\alpha)$ and $c_0 = \mathrm{Tr}(\mathcal{L})$. Using $\mathcal{L}^\dagger\mathcal{L} = \mathbb{I}$ and $\det\mathcal{L} = \mathbb{I}$, we can

write $|\mathrm{Tr}\,\mathcal{L}| = \sqrt{1+|\boldsymbol{c}|^2}$. Hence, the trace of the Wilson loop is uniquely defined by the Bloch vector $\boldsymbol{c}$. In particular, $|\boldsymbol{c}| < 1$ implies $|\mathrm{Tr}\,\mathcal{L}| < 2$. The results, plotted in Fig. 5.11, show that $\mathcal{L}$ is in general non-trivial and dense in the Bloch sphere, *i.e.*, we can simulate any designed $\mathcal{L} \in \mathrm{SU}(2)$. Hence, in this way, the M_{ij} as well as $\mathcal{L}$ can be tuned to be a generic ($i\times$) SU(2) matrix, both in square and honeycomb lattices.

Alternatively, in a honeycomb lattice with NNN tunneling, non-trivial Wilson loops can appear around different loops then those around the elementary plaquettes involving only NN tunneling. For example, there is *a priori* no reason for a loop involving two NN tunneling matrices M_{AB} and $M_{BA'}$ and one NNN tunneling matrix $M^{\mathrm{NNN}}_{A'A}$, *i.e.*, $M_{AB}M_{BA'}M^{\mathrm{NNN}}_{A'A}$, to equal the identity. If there exists any loop for which $\mathcal{L} \neq \exp(i\phi)\mathbb{I}$, the system is subject to non-Abelian effects.

5.6 Summarizing remarks and outlook

To summarize this chapter, we proposed a feasible scheme to manipulate artificial non-Abelian gauge fields and various topological effects, and exemplified the possibilities of the method on various lattice geometries (kagome, honeycomb, square). The proposed scheme relies on time-periodic driving of the optical lattice, which is experimentally relatively simple. Further, because it does not make use of internal states of the atoms, it allows greater flexibility than alternative methods. In the case of fermions, *e.g.*, since interaction can only take place between different internal states, having these at one's disposal can be very advantageous for reaching the strongly-correlated regime.

Recently, a variety of techniques to detect topological states of ultracold atoms in optical lattices have been developed, including Bragg-spectroscopy detection of edge states [339–343] or time-of-flight measurement of Chern numbers [267, 344]. Specifically, a feasible way to measure the topological band structure of the topological insulator described in Sec. (5.4) is given by the method of Price and Cooper [345]. It is based on semi-classical wave-packet dynamics and can be applied thanks to the adiabatic principle for Floquet systems [346] [see the work by Eckardt and Holthaus [221] for its application to the effective Hamiltonian (5.15)]. Therefore, the topological phenomena discussed in this chapter should be accessible to observation in near-future experiments. Besides their importance for a fundamental understanding of solid-state physics, these effects may have future applications in quantum information and spintronics.

Until now, we restricted the considerations of this thesis to the *s*-band of

the optical lattice, which is a good approximation at low occupation numbers and if all energy scales are small compared to the excitation energy to the second band. In reality, however, there are situations where higher orbits play an important role (see Chapter 9). For example, for the honeycomb lattice discussed in Chapter 4, Soltan-Panahi and coworkers [302] found unconventional superfluidity that could only be explained as a multi-orbital effect. In the next chapter, we discuss how intentionally exploiting such higher bands allows to quantum simulate orbital physics of spinless fermions.

Chapter 6

Orbital order of spinless fermions near an optical Feshbach resonance

In strongly-correlated solid-state systems, orbital physics of electrons plays an important role in a variety of materials, such as transition metal oxides [347], and orbital effects are needed to understand important material properties, including colossal magnetoresistance, ferroelectricity, unconventional superconductivity, and charge ordering. In particular, novel quantum phases emerge due to the coupling of the orbital degree of freedom to the charge, spin, or lattice degrees of freedom [348, 349]. Such coupling, while generating interesting effects, also complicates the theoretical treatment. It is, therefore, desirable to study simpler systems with the orbital degree of freedom decoupled from all others. Ultracold atoms in higher bands of optical lattices provide an ideal tool for this purpose; they allow to quantum simulate orbital dynamics in a well controlled environment, including orbital-only models of single-species (spinless) fermions.

Traditionally, ultracold-atoms experiments have been concerned with the lowest band (the s-band) of optical lattices, but several groups have now achieved loading and manipulating ultracold atoms in higher (such as p-) bands [350–354]. Observation of orbital physics in optical lattices has exciting prospects (see also the Nature Physics News and Views article by Lewenstein and Liu [166]): For example, p-orbital bosons can form Bose–Einstein condensates at finite momentum, apparently contradicting the conventional wisdom that Bose–Einstein

condensation occurs at zero momentum.[1] Also, using higher bands, one can go beyond the integer quantum Hall effect, which – as discussed in Chapter 5.4 – can be induced in the s-orbitals of an optical honeycomb lattice that is subject to a synthetic gauge field. Namely, in the flat p-bands of such a lattice, exotic incompressible states analogous to the Laughlin *fractional* quantum-Hall liquid can be created [264].

For spinless fermionic atoms, when the chemical potential lies within the p-band, the low temperature properties are entirely determined by the p-band fermions, since the s-band is completely filled and remains inert while higher bands remain empty. The interaction between these atoms is usually weak at low temperatures because the Pauli exclusion principle only allows scattering in high partial-wave channels (p, f, *etc.*), which is however weak at low temperatures.

One way to reach the strongly-correlated regime in such a situation relies on deep optical lattice potentials, which often means experimentally inaccessible low temperature [87]. An alternative is to increase the p-wave elastic scattering cross section employing a Feshbach resonance (see, *e.g.*, [355–361]; for a review, see [295]). Typically, this is done by coupling channels in the electronic ground state through magnetic fields. For the case of p-waves, however, this method usually leads to significant atom losses through three-body inelastic collisions [355–358], because the scattering state is well localized by the angular-momentum barrier and has good Franck-Condon overlap with more deeply bound molecules [295].[2]

To circumvent this problem, recently Goyal, Reichenbach, and Deutsch considered enhanced p-wave interactions via an optical Feshbach resonance (OFR) [362, 363] between a scattering state and an electronically excited "purely-long-range" molecule. Such molecules have inner turning points at very large distances (*e.g.*, $> 50a_0$ in ^{171}Yb, where a_0 is the Bohr radius), well beyond the chemical binding region, and thus three-body recombination should be highly suppressed [364]. Differently form magnetic Feshbach resonances, OFRs have an additional loss mechanism due to spontaneous decay from the electronically excited state. However, Ciuryło and coworkers showed that in alkaline-earth-metal species, unlike in alkali-metal atoms, large changes of the scattering length should be possible while maintaining small atom losses, because the molecu-

[1] Such an effect can also occurs in the lowest band, for example due to positive hopping matrix elements (Chapter 3) or finite Peierls phases (Chapter 5).

[2] In strong three-dimensional optical lattices, with exactly one fermion per site and vanishing tunneling, these losses can be completely suppressed, as shown in the experiments of Günter and coworkers [358]. From a many-body perspective, however, such a state is a trivial insulator.

lar photoassociation transition associated to the OFR can have a very narrow linewidth [365]. Hence, using OFR opens the perspective of studying strongly-correlated many-body phases of ultracold, spinless fermions. What is more, it also provides for a high degree of control. For example, the width of the OFR can be tuned by the laser intensity [366–368], and, in our case, the interaction strength among different p-orbitals can be tuned differently, as we will show below.

Motivated by these developments, we investigate in this chapter the phase diagram of spinless fermions on a cubic lattice near an OFR. Starting from the microscopic scattering properties of ultracold atoms, we discuss in Sec. 6.1 the model describing their relevant physics at low temperatures, namely a three-color Fermi–Hubbard model with color-dependent interaction, a novel color-changing term, and spatially anisotropic and color-dependent tunneling. We describe how strong, color-dependent interactions can be induced by an optical Feshbach resonance [364]. In Sec. 6.2, we derive the orbital exchange constants at $1/3$ filling on the cubic optical lattice. Using this, we compute the phase diagram in a Gutzwiller *Ansatz* (as explained in Chapter 13.1). Besides a phase without tunneling and an "orbital Néel" phase where p_x and p_y orbitals alternate, we find novel phases with "axial orbital order" in which p_z and $p_x + ip_y$ (or $p_x - ip_y$) orbitals alternate, breaking spatial and time-reversal symmetry. In Sec. 6.3, finally, we demonstrate that the non-trivial Wannier envelope of the p-band fermions allows the observation of the different phases in experimentally straightforward time-of-flight (ToF) measurements. The results presented in this chapter have been published in Ref. [369].

6.1 Tunable interactions using an optical Feshbach resonance

At low temperatures, the spinless fermions on a cubic lattice near an OFR can be described by the following Hubbard-like model

$$\begin{aligned}\hat{\mathcal{H}} &= -\sum_{i=1}^{N}\sum_{\mu,\nu=x,y,z} t_\nu^\mu \left(\hat{f}_i^{\mu\,\dagger}\hat{f}_{i+\nu}^{\mu} + \text{h.c.}\right) \\ &+ \sum_{i=1}^{N}\left[V_1\hat{n}_i^x\hat{n}_i^y + V_2\left(\hat{n}_i^x\hat{n}_i^z + \hat{n}_i^y\hat{n}_i^z\right) + \left(iV_3\hat{f}_i^{x\,\dagger}\hat{f}_i^y\hat{n}_i^z + \text{h.c.}\right)\right].\end{aligned} \tag{6.1}$$

The number of lattice sites is N. The operators $\hat{f}_i^\mu$ and $\hat{f}_{i+\nu}^\mu$ destroy a fermion in the orbital $p_{\mu=x,y,z}$ at site i located at $\boldsymbol{r}_i$ and at site $i+\nu$ located at $\boldsymbol{r}_i + \boldsymbol{e}_\nu$,

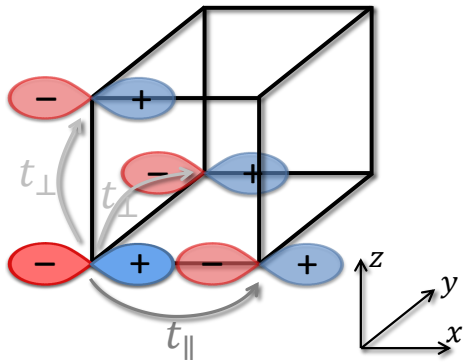

Figure 6.1: **Orbital tunneling,** exemplified for the p_x orbital. Due to the absence of orbital-changing hopping, a fermion in a p_x-orbital (blue and red dumbbell) can tunnel only into neighboring p_x-orbitals (semi-transparent dumbbells). The hopping amplitude is given by the overlap of the p_x-Wannier functions, so that under typical conditions $|t_\parallel| \gg |t_\perp|$, with $t_\parallel = t_x^x$ and $t_\perp = t_y^x = t_z^x$. Moreover, the Wannier functions change sign from one side of the lattice site to the other, as indicated by "−" (red) and "+" (blue), so that $\mathrm{sgn}(t_\perp) = -\mathrm{sgn}(t_\parallel)$.

respectively (with $\boldsymbol{e}_\nu$ the unit vector in direction $\nu = x, y, z$ and the lattice spacing set to 1). $\hat{n}_i^\mu = \hat{f}_i^{\mu\,\dagger} \hat{f}_i^\mu$ is the corresponding number operator. This model is a straightforward generalization of the Bose–Hubbard Hamiltonian (2.4) to the case of fermions and to a multi-orbital situation. To this, one has to expand the (fermionic) field operators appearing in the original free-space Hamiltonian (2.1) in terms of the p-orbital Wannier basis,

$$\hat{\Psi}(\boldsymbol{r}) = \sum_{i=1}^{N} \sum_{\mu=x,y,z} w_\mu(\boldsymbol{r} - \boldsymbol{r}_i)\, \hat{f}_i^\mu \,. \tag{6.2}$$

Note also that, due to the anisotropy of the p-orbital Wannier wave functions, the nearest-neighbor (NN) hopping amplitude $t_\nu^\mu = t_\parallel \delta_{\mu,\nu} + t_\perp (1 - \delta_{\mu,\nu})$, sketched in Fig. 6.1, is direction and orbital dependent [370–372]. This spatial dependence makes the case of three dimensions interesting (additionally to the larger number of available orbital states compared to 1D and 2D).

The interactions $V_{1,2,3}$ are induced by an OFR laser [364] that couples the electronic ground state of the atom to an excited state. The interaction can be expressed in terms of the (p-wave) pseudo-potential V_p^m for two particles with

mass $M_{\rm at}$ and relative angular momentum m,

$$V_p^m(\boldsymbol{r}) = \lim_{s\to 0} \frac{3\Re[\left(a_p^m\right)^3]}{2M_{\rm at}} \frac{\delta(r-s)}{s^3} \partial_r^3 r^2 \,. \tag{6.3}$$

The real part of the p-wave scattering volume, $\Re[\left(a_p^m\right)^3]$, can be tuned by the detuning and the intensity of the OFR laser (see Fig. 6.2).

The expansion (6.2) for the interaction term

$$\hat{\mathcal{H}}_{\rm int} = \int {\rm d}^3 r_1 \int {\rm d}^3 r_2 \hat{\Psi}^\dagger(\boldsymbol{r}_1)\hat{\Psi}^\dagger(\boldsymbol{r}_2) V_p^m(\boldsymbol{r}_1-\boldsymbol{r}_2)\hat{\Psi}(\boldsymbol{r}_1)\hat{\Psi}(\boldsymbol{r}_2) \tag{6.4}$$

leads to the on-site, inter-orbital interaction

$$\hat{\mathcal{H}}_{\rm int} = \sum_{i=1}^{N} \sum_{\mu,\nu,\mu',\nu'=x,y,z} V_{\mu,\nu,\mu',\nu'} \hat{f}_i^{\mu'\,\dagger} \hat{f}_i^{\nu'\,\dagger} \hat{f}_i^{\mu} \hat{f}_i^{\nu} \,, \tag{6.5}$$

where repeated indices are summed over. (As is standard, off-site interactions can be neglected to good approximation; see also the discussion after Eq. (2.6).)

The matrix elements

$$\begin{aligned} V_{\mu,\nu,\mu',\nu'} \;=\; & \sum_{m=-1,0,1} \int {\rm d}^3 r_1 \int {\rm d}^3 r_2\, w_{\mu'}(\boldsymbol{r}_1-\boldsymbol{r}_i)\, w_{\nu'}(\boldsymbol{r}_2-\boldsymbol{r}_i) \\ & \times V_p^m(\boldsymbol{r}_1-\boldsymbol{r}_2)\, w_\mu(\boldsymbol{r}_1-\boldsymbol{r}_i)\, w_\nu(\boldsymbol{r}_2-\boldsymbol{r}_i) \end{aligned} \tag{6.6}$$

can now be computed by separating the relative and center-of-mass coordinates. For the purpose of estimating on-site interactions, for deep lattices, the p-orbital Wannier functions are well approximated by the first excited states of harmonic oscillators (with the oscillator length ζ controlled by the lattice depth). Then, the only non-zero interaction terms are the ones given in Eq. (6.1), with

$$V_1 = \frac{1}{4}(U_1 + U_{-1}) \,, \tag{6.7a}$$

$$V_2 = \frac{1}{8}(U_1 + U_{-1} + 2U_0) \,, \tag{6.7b}$$

$$V_3 = \frac{1}{8}(U_{-1} - U_1) \,. \tag{6.7c}$$

Here, $U_m = 3\sqrt{2}\Re[\left(a_p^m\right)^3]/(\sqrt{\pi}\zeta^5 M_{\rm at})$ defines the interaction strength in the scattering channel with angular momentum $m = 1, 0, -1$. A Zeeman splitting, which may be introduced by a magnetic field, leads to different detuning of the

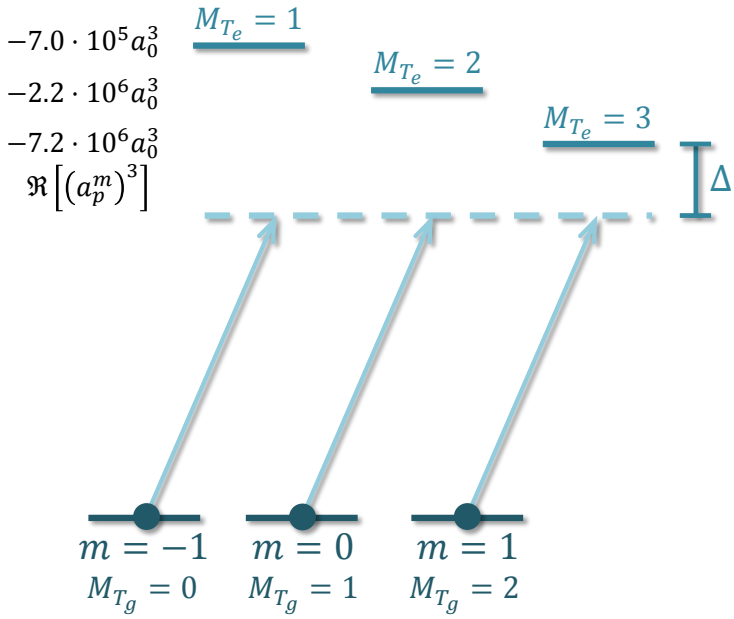

Figure 6.2: **Level scheme and coupling strengths of the optical Feshbach resonance (OFR).** In the OFR, σ^+-polarized light couples the scattering state of the ground-state potential (with the three different projections m of p-wave angular momentum) to the excited purely-long-range bound state. The σ^+-polarized light couples only transitions $M_{T_g} \to M_{T_e} + 1$, where M_{T_g} (M_{T_e}) is the projection onto the quantization axis of the total angular momentum of the ground (excited) state. This figure shows only the states permitted by selection rules. The values of the real part of the scattering volume, $\Re\left[(a_p)^3\right]$, depend on the detuning to each excited level. They are given in the figure for each of the three transitions of the ${}^1S_0 \to {}^3P_1$ intercombination line in ^{171}Yb in a 30-G magnetic field (creating an energy shift of the three excited levels), and for an intensity of 185W/cm^2 and detuning $\Delta = -3$ MHz below the resonance at -355 MHz. The figure is reproduced from the work by Goyal, Reichenbach, and Deutsch [364].

OFR laser for the three scattering channels (see Fig. 6.2). This makes the scattering length a_p^m dependent on m, and consequently the U_m's can be different in magnitude and even in sign. Thus, the relative strengths and signs of $V_{1,2,3}$ can be varied by changing the strength of the Zeeman splitting together with the detuning of the OFR laser. By contrast, in a standard magnetic Feshbach resonance, $U_{-1} = U_{+1}$. In our case, breaking the symmetry between U_{-1} and U_{+1} leads to the orbital-changing term V_3. Physically, it allows (p_x or p_y) particles to move on a 2D plane, instead of along a chain only, as is the case in typical situations where $t_\perp$ can be neglected [373]. Since the V_3 term explicitly breaks time-reversal symmetry (TRS), we can expect it to lead to novel phases reflecting that intriguing property. As discussed in Chapter 5.4, TRS breaking can produce topological insulators with the prospect of a wide range of applications.

Hamiltonian (6.1) generalizes the models of Refs. [373–378]. For $V_1 = V_2$, and $V_3 = 0$, it reduces to the SU(3) Hubbard model. One can visualize p-band fermions as particles carrying a color index representing the p_x, p_y, and p_z orbital state. Then, Hamiltonian (6.1) describes a three-color fermion model with color-dependent interaction $V_{1,2}$, a novel color-changing term V_3, and spatially anisotropic and color-dependent tunneling t_ν^μ.

We will show in the next section that this model hosts novel quantum phases. For this purpose, we study the strong-coupling limit for p-band filling $1/3$, and determine the orbital order using a Gutzwiller mean-field *Ansatz* (GMFA).

6.2 Phase diagram in the strong-coupling limit at 1/3 filling

An important limiting case of Hamiltonian (6.1) is the one where interactions dominate over tunneling terms, the so called strong-coupling limit. In Hubbard models of spinful s-band fermions, this limit leads to the emergence of Heisenberg and $t-J$ models, which are relevant for high-T_c superconductivity. Different from these situations, in our case three orbital instead of two spin states are involved.

In the strong-coupling limit of Hamiltonian (6.1),

$$\left|t_\parallel\right| \ll V_1, \quad \left|t_\parallel\right| \ll V_2 - V_3, \quad \text{and} \quad \left|t_\parallel\right| \ll V_2 + V_3\,, \tag{6.8}$$

double occupancy of the lattice sites is energetically suppressed. Therefore, at average filling of the p-band of 1/3, the low-energy manifold consists of states with one p-band particle per site, and density fluctuations are frozen. Since

$|t_\perp| \ll |t_\parallel|$, we can safely neglect perpendicular tunneling $t_\perp$ in this limit [373], and, for brevity, we write $t = t_\parallel$.

The low-energy states are coupled via virtual hopping that induces exchange interactions between NN orbitals (see Fig. 6.3). The resulting physics within the low-energy manifold is captured in an effective Hamiltonian that can be derived from second-order perturbation theory. For a general, pedagogic explanation of this procedure, see Appendix A of the review by Lewenstein *et al.* [379]. Following this approach and treating the tunneling t in (6.1) as a perturbation, we obtain the effective Hamiltonian for the low-energy manifold at 1/3 filling

$$\begin{aligned}\hat{\mathcal{H}}_{\text{eff}} \;=\; -\sum_i \Big\{ \sum_{\mu=x,y,z} J_\mu \hat{n}_i^\mu \left(2 - \hat{n}_{i+\mu}^\mu - \hat{n}_{i-\mu}^\mu\right) + \sum_{\mu=x,y} (J_2 - J_1)\, \hat{n}_i^\mu \left(\hat{n}_{i+\mu}^z + \hat{n}_{i-\mu}^z\right) \\ + J_3 \left[i \hat{f}_i^{y\,\dagger} \hat{f}_i^x \left(\hat{n}_{i+z}^z + \hat{n}_{i-z}^z\right) + \text{h.c.} \right] \Big\}. \end{aligned} \tag{6.9}$$

To write it more compactly, we have used $\hat{n}_i^x + \hat{n}_i^y + \hat{n}_i^z = 1$, and defined

$$J_1 \;\equiv\; t^2/V_1\,, \tag{6.10a}$$

$$J_2 \;\equiv\; t^2 V_2/(V_2^2 - V_3^2)\,, \tag{6.10b}$$

$$J_3 \;\equiv\; t^2 V_3/(V_2^2 - V_3^2)\,, \tag{6.10c}$$

and $J_x = J_y = J_1$, $J_z = J_2$. For $V_3 = 0$, $V_1 = V_2$, Hamiltonian (6.9) reduces to terms of the form $J_\mu \hat{n}_i^\mu \hat{n}_{i\pm\mu}^\mu$, a hallmark of the quantum 3-state Potts model.[3]

6.2.1 Preliminary considerations

To get insight into which orbital order is favored, we first discuss the simple case of $J_3 = 0$. For positive couplings $J_{1,2}$, the first term of Hamiltonian (6.9) favors any configuration where the orbitals at neighboring sites differ, while for negative $J_{1,2}$ it favors configurations where the orbitals at neighboring sites are equal. The second term favors an alternating pattern between p_z- and not-p_z-particles if $J_2 > J_1$, and an alternating pattern between p_x and p_y if $J_2 < J_1$. This leads to the appearance of three different phases:

(A) For $J_1 > \max(J_2, 0)$, the favored configuration is an alternating pattern between p_x- and p_y-particles in the xy-plane.

(B) For $J_2 > \max(J_1, 0)$, the (highly degenerate) ground state is any alternating pattern between p_z and not-p_z.

[3] Orbital order in a simpler model without OFR, and its relation to the Potts model were discussed by C. Wu in the unpublished version of the work of arXiv:0801.0888v1.

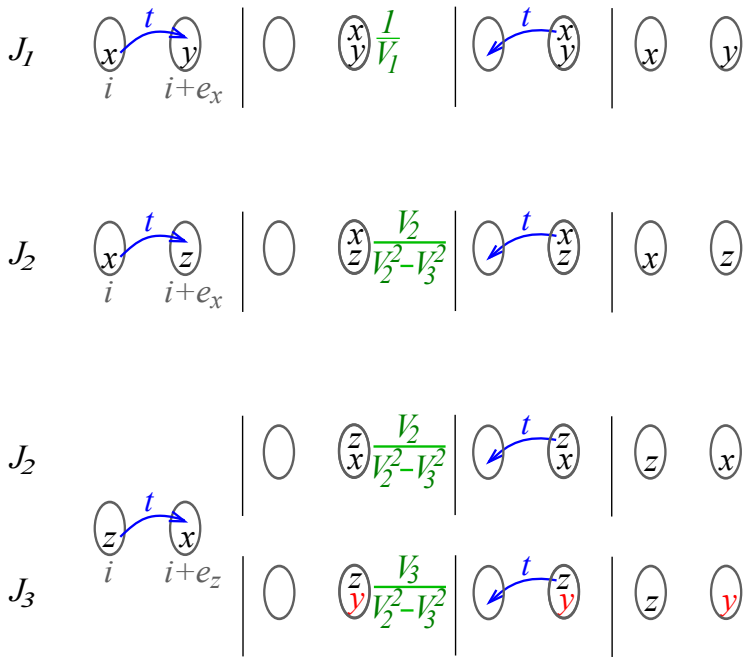

Figure 6.3: **Sketch of the virtual hopping processes at p-band filling one-third (one p-band particle per site) leading to the effective Hamiltonian** (6.9)**.** If neighboring particles are in different orbitals p_μ and p_ν (abbreviated by μ and ν, respectively), and if they are connected by a bond in μ or ν direction, a particle can tunnel with amplitude t (blue) to a neighboring site (leftmost column). There, it experiences on-site interaction (green processes, second column). Due to the anisotropic tunneling, only the same particle can tunnel back (third column). Rightmost row: for the processes J_1 and J_2, the final configuration is the same as the initial one, but in the orbital-changing process J_3 an x-particle has changed into a y-particle (bottom row). Neglecting $t_\perp$, the sketched processes – plus the ones obtained by interchanging x and y – are the only ones that can occur.

(C) For the case $J_1, J_2 < 0$, the best configuration is a homogeneously filled lattice. This case does not fulfill the strong-coupling requirements (6.8), however, and is therefore unstable.

Certain aspects of Hamiltonian (6.9) become clearer when we rewrite it in terms of the generators of the SU(3) group. Introducing the Gell-Mann matrices $\lambda^{(n)}$ and the so-called F-spin operators $Y_i = \frac{1}{\sqrt{3}} \hat{f}_i^{\mu\,\dagger} \lambda^{(8)}_{\mu,\nu} \hat{f}_i^{\nu}$ and $T_i^{(\alpha)} = \frac{1}{2} \hat{f}_i^{\mu\,\dagger} \lambda^{(\alpha)}_{\mu,\nu} \hat{f}_i^{\nu}$ $(\alpha = 1,2,3)$, $\hat{\mathcal{H}}_{\text{eff}}$ becomes

$$\hat{\mathcal{H}}_{\text{eff}} = \frac{4}{3} \sum_i \Big[(J_2 - J_1)\, Y_i - J_3 T_i^{(2)} + J_2 Y_i Y_{i+z} + J_3 T_i^{(2)} Y_{i+z} + J_3 Y_i T_{i+z}^{(2)} \Big] \tag{6.11}$$
$$+ 2 \sum_i \sum_{\mu=x,y} \left(J_1 T_i^{(3)} T_{i+\mu}^{(3)} + \frac{2J_2 - J_1}{4} Y_i Y_{i+\mu} + \frac{J_2}{2} T_i^{(3)} Y_{i+\mu} + \frac{J_2}{2} Y_i T_{i+\mu}^{(3)} \right),$$

where we neglected constant terms. In the basis (p_x, p_y, p_z), Y and $T^{(3)}$ are diagonal, making the terms $Y_i Y_j$, $Y_i T_j^{(3)}$, or $T_i^{(3)} T_j^{(3)}$ Ising-like. Additionally, the orbital-changing term V_3 involves $T^{(2)} = \frac{1}{2i} \left(T^{(+)} - T^{(-)} \right)$, where $T^{(\pm)}$ are ladder operators of the T-spin.

$T^{(3)}$ and $T^{(2)}$ do not commute with each other, but both do commute with Y. Therefore, we can replace Y by its eigenvalues $-\frac{2}{3}$ (for $|p_z\rangle$) and $\frac{1}{3}$ (for $|p_x\rangle$ and $|p_y\rangle$), which gives some insight into the physics of Hamiltonian (6.11). Following the previous qualitative discussion of the phases A-C, we assume that the ground state is bipartite with respect to the eigenvalue of Y.[4] Then, there are three different cases:

(A) at all sites the eigenvalue of Y is $\frac{1}{3}$,

(B) the eigenvalues $-\frac{2}{3}$ and $\frac{1}{3}$ alternate, and

(C) all sites have eigenvalue $-\frac{2}{3}$.

In the last case, there is a $|p_z\rangle$-particle on every site. Therefore, the Pauli exclusion principle prohibits all tunneling and the Hamiltonian equals zero. In the sectors A and B, it reads (neglecting constant terms)

$$\hat{\mathcal{H}}_{\text{eff}}^{(A)} = \frac{J_1}{2} \sum_i \sum_{\mu=x,y} \sigma_i^{(3)} \sigma_{i+\mu}^{(3)}\,; \tag{6.12a}$$

$$\hat{\mathcal{H}}_{\text{eff}}^{(B)} = -2J_3 \sum_{i \in \Omega} \sigma_i^{(2)}\,. \tag{6.12b}$$

[4] In principle, more complex (*i.e.*, non-bipartite) partitions are possible, but the numerical mean-field analysis (see below) shows that bipartite states are the only relevant ones.

Here, σ denotes the usual Pauli-matrices, which act on the subspace spanned by $|p_x\rangle$ and $|p_y\rangle$. Sector A is reduced to the Ising model on decoupled xy-planes, which favors an antiferromagnetic ground state. This is just the model found in the 2D-case treated in Refs. [373, 376]. In sector B, Ω denotes the partition where Y has eigenvalue $\frac{1}{3}$. On these sites, J_3 acts as a magnetic field in y-direction, lifting the degeneracy between $|p_x\rangle$ and $|p_y\rangle$ and leading to the ground state $(|p_x\rangle \pm i\,|p_y\rangle)/\sqrt{2}$ (for $J_3 \gtrless 0$).

6.2.2 Gutzwiller mean-field analysis

Having obtained a qualitative picture of the expected phases, we now analyze the phase diagram of Hamiltonian (6.11) quantitatively. To this, we assume that correlations between sites are small so that the ground state can be approximated by a product over sites. Accordingly, we employ a Gutzwiller variational wave function (see Chapter 13.1) for Hamiltonian (6.11), and minimize the energy of a cube with side length L under periodic boundary conditions. In principle, close to phase transitions, where fluctuations become important, such a mean-field *Ansatz* becomes problematic. In the present case of three dimensions, however, we can expect mean-field methods to provide an – at least qualitatively – reliable picture.

The energy per site for even L is smaller than for odd L, which shows that the ground state periodicity is indeed 2.[5] In agreement with the qualitative picture from the previous section, we find three classes of ground states with different orbital order (summarized in Fig. 6.4):

(A) For $J_1 > J_2 + |J_3|/2$ and $J_1 > 0$, we find an *antiferro-orbital* phase similar to, *e.g.*, the 2D-model of Zhao and Liu [373]: in each xy-plane, sites with p_x- and p_y-orbitals alternate, see Fig. 6.4, bottom right (similar to the AFM Néel state). Since p_x- and p_y-particles do not tunnel in z-direction, the xy-planes are decoupled, and within our approximation (*e.g.*, neglecting $t_\perp$), there is no LRO in z-direction. It is possible, however, that LRO among the planes develops at low temperature for finite $t_\perp$.

(B) For $J_1 < J_2 + |J_3|/2$ and $J_2 > -|J_3|/2$, the ground state shows *axial orbital order*. The state is bipartite with $|p_z\rangle$ on one sublattice and $(|p_x\rangle \pm i\,|p_y\rangle)/\sqrt{2}$ (for $J_3 \gtrless 0$, respectively) on the other sublattice (right panel of Fig. 6.4). The degeneracy between $|p_x\rangle$ and $|p_y\rangle$ is lifted by a finite

[5] Further, we checked that for even L the occurring phases do not depend on L, indicating that the ground-state periodicity is indeed 2.

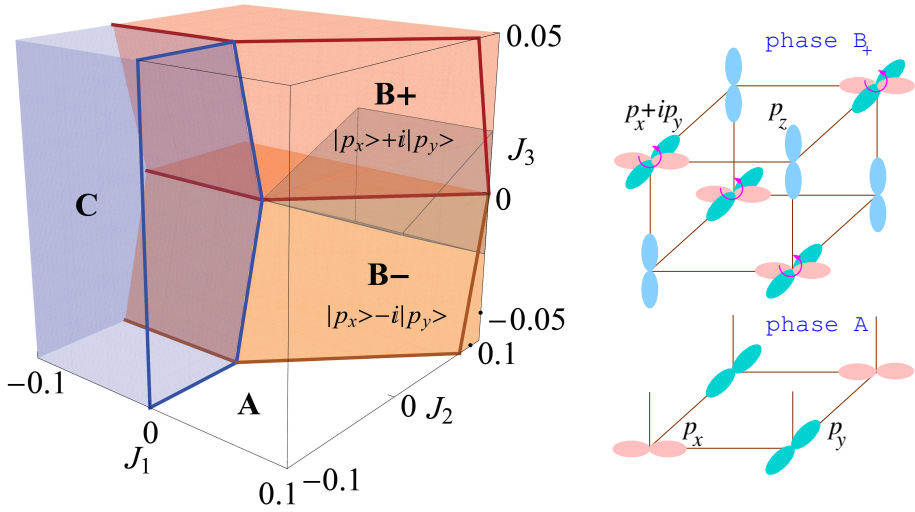

Figure 6.4: **Left: The phase diagram** of $\hat{\mathcal{H}}_{\text{eff}}$, Eq. (6.9), at 1/3 filling shows four phases: phase A with antiferro-orbital order (empty region), phases B_+ and B_- with axial orbital order (red/orange region and $J_3 > 0/< 0$, respectively), and finally phase C (blue region) with tunneling completely frozen. The gray wedge indicates the region satisfying the strong-coupling conditions (6.8), $0 \leq J_{1,2} \ll 1$, $J_3 \ll J_2$. **Right: sketch of phases A and B_+.** In phase B_+, $|p_z\rangle$ and $|p_x\rangle + i\,|p_y\rangle$ orbitals alternate. Phase B_- can be visualized from this by replacing $|p_x\rangle + i\,|p_y\rangle$ with $|p_x\rangle - i\,|p_y\rangle$.

J_3. The state $(|p_x\rangle \pm i\,|p_y\rangle)/\sqrt{2}$ has *finite angular momentum*, whence this novel phase breaks TRS.

(C) For $J_1 < 0$ and $J_2 < -|J_3|/2$, virtual tunneling is energetically disadvantageous. Then, the energetically most favorable situation is where Pauli exclusion prohibits all tunneling $t_\parallel$ (by filling $\alpha\beta$-planes uniformly with p_α or p_β, where $\alpha\beta = xy, xz, yz$). This state is unstable, however, because it cannot fulfill the strong-coupling requirements (6.8).

Interestingly, phases A and C preserve TRS, although V_3 in Hamiltonian (6.1) breaks it explicitly.

6.3 Experimental signatures of the orbital phases in ToF images

To distinguish the different phases experimentally, one can employ standard ToF imaging, similar to what is explained in Chapter 2.1. Generalizing Eq. (2.10) to multi-component Fermi-gases, the free-space density distribution after a time τ_{ToF} of free expansion relates to the in-trap momentum distribution via

$$\langle n(\boldsymbol{r})\rangle_{\tau_{\mathrm{tof}}} = L^3 \sum_{\mu,\nu} w_\mu^\star(\boldsymbol{k})\, w_\nu(\boldsymbol{k})\, \langle \hat{f}^{\mu\dagger}(\boldsymbol{k})\, \hat{f}^{\nu}(\boldsymbol{k})\rangle \,, \tag{6.13}$$

with $w_\mu(\boldsymbol{k})$ the Fourier transform of the Wannier orbital $w_\mu(\boldsymbol{r})$ of p-band state μ. (We assume translational invariance so that $w_\mu(\boldsymbol{r})$ is independent of site i.) Further,

$$\hat{f}^\mu(\boldsymbol{k}) = \frac{1}{L^{3/2}} \sum_i \mathrm{e}^{i\boldsymbol{k}\cdot\boldsymbol{r}_i} \hat{f}_i^\mu \,, \tag{6.14}$$

and $\boldsymbol{k} = M_{\mathrm{at}}\,\boldsymbol{r}/(\hbar\,\tau_{\mathrm{tof}})$. In the analysis of the previous sections, we only considered insulating states, which dominate in the strong-coupling limit at p-band filling 1/3. In such states, the ToF pictures will show no peaks associated to off-diagonal LRO. However, signatures of the distinct phases do appear in the momentum distribution due to the non-trivial p-orbital Wannier envelope. This allows to distinguish phases A and B by their column density (*i.e.*, the density integrated along one spatial direction), as shown in Fig. 6.5.

Observation of these novel phases requires that we simultaneously achieve strong interactions, $V \gg t$, and low temperatures, $k_B T \ll t^2/V$, for the characteristic tunneling rate t and interaction energy V. At experimentally feasible temperatures, this requires a significant enhancement of the real part of the

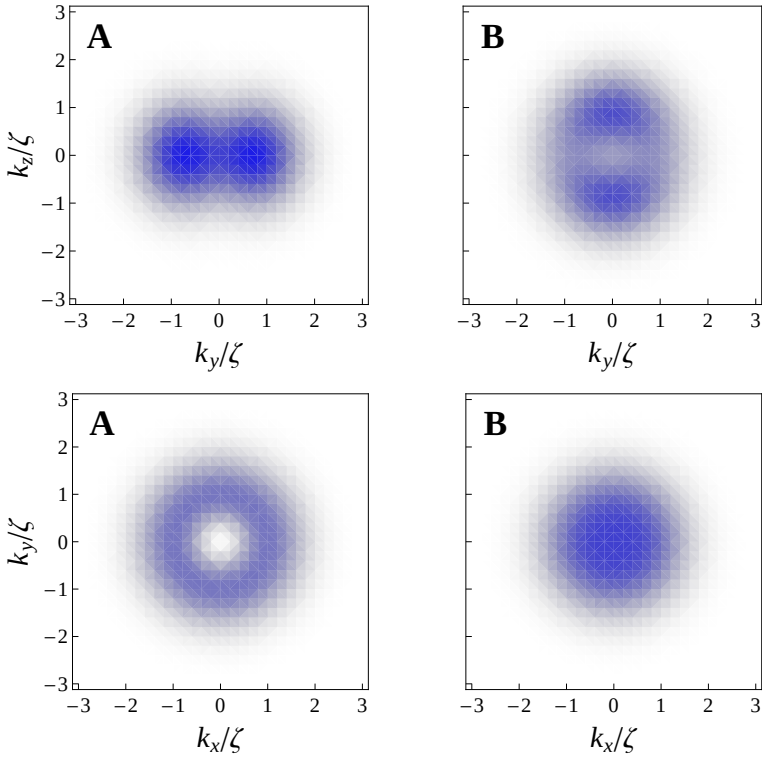

Figure 6.5: **Predicted time-of-flight density distributions,** which would allow to experimentally distinguish phases A and B. Lower (upper) row: $\langle n(\boldsymbol{r})\rangle_{t_{\mathrm{tof}}}$ integrated along z (x) in arbitrary scale. When viewed along the z-direction, phase A displays a doughnut form (lower left panel) because of an incoherent addition of p_x- and p_y-Wannier envelopes. In phase B, the sites occupied by $(|p_x\rangle \pm i\,|p_y\rangle)/\sqrt{2}$ give a similar doughnut structure, but the hole at $k_x = k_y = 0$ is filled by the other half of the sites which are occupied by p_z-particles (lower right). Viewing along the x-direction reveals the existence of p_z-particles in phase B (upper right), contrary to phase A (upper left), where only the dumbbell of p_y-particles is found.

p-wave scattering volume via the OFR. In practice, however, and in contrast to magnetic Feshbach resonances, this is limited by spontaneous emission, which broadens the resonance and also leads to recoil heating. For the example considered in the work by Goyal, Reichenbach, and Deutsch [364], based on the $^1S_0 \rightarrow {}^3P_1$ intercombination line in ^{171}Yb, the atomic linewidth is ≈180 kHz, which limits the useful OFR p-wave enhancement. Other species such as ^{87}Sr, where the same transition has a linewidth of ≈7.5 kHz, should result in a substantial OFR, with a reasonable linewidth. Experimental studies of OFRs in related isotopes are currently underway [380].

6.4 Summary

To summarize this chapter, we investigated the orbital order of spinless fermions in the p-band of a cubic lattice with interactions controlled by an OFR. Such a system can be realized with current technology.

We analyzed the orbital order in the strong-coupling limit at p-band filling 1/3. To this, we found an elegant expression of the model Hamiltonian in terms of Gell-Mann matrices, which gives qualitative insight into the expected phases. We computed the phase diagram quantitatively using a GMFA. Besides a phase where all tunneling is blocked and an antiferro-orbital phase where p_x- and p_y-orbitals alternate, we found a novel phase with axial orbital order which not only breaks translational symmetry but also has macroscopic orbital angular momentum.

We expect our results to stimulate future work on this subject. For example, it is interesting to investigate how quantum fluctuations affect the phase diagram: they might distort it [378] or even lead to disordered 'orbital liquid' states. Fluctuations may also lift the degeneracy between p_x- and p_y orbitals at $J_3 = 0$, and possibly lead to *spontaneous* TRS breaking. To treat fluctuations and correlations between sites in a more quantitative way, future studies could employ mean-field methods where interaction terms are not decoupled over sites but instead over bonds (see, *e.g.*, the work by Szirmai and Lewenstein [381]). Further, the limit of small interactions, where related models show non-trivial color-superfluidity [374, 375, 377], may also be of interest. More complex lattice geometries, such as the triangular or honeycomb lattices discussed in Chapters 3 and 4, may host other orbital-ordered phases or even disordered ones due to frustration effects. Finally, phase $B_\pm$ may have interesting topological properties. For example, at an interface of two domains with $p_x + ip_y$ and $p_x - ip_y$ order, chiral zero mode fermions may arise (similar to the edge states in spin-Hall

insulators discussed in Chapter 5.4).

Considering higher orbits for quantum simulation is a relatively new avenue in optical lattices. Traditionally, in the description of ultracold bosons in standard optical lattices, higher-orbit effects have been neglected, which is a good approximation at low temperatures and weak interactions; as we will show in Chapter 9, in the regime of strong interactions, however, orbital effects can become significant, and one has to consider them – if one wants to or not.

Chapter 7

Devil's staircases and quasi-supersolids: A trapped-ion quantum simulation of long-range interactions

Up to this point, the interactions in the considered models were of short range. However, long-range interactions can lead to many effects which are not present in such short-range systems [167]. Most strikingly, systems with *strong* long-range interactions (where the integral over the interactions does not converge) can exhibit counterintuitive thermodynamic behavior like super-extensive quantities or breaking of ergodicity [382].

But even for *weak* long-range interactions (which we will consider here) novel effects are expected. For instance, they lead to new ground states, such as insulating states similar to the Mott insulators of the Bose–Hubbard model but at fractional (instead of integer) filling factors. An example of such an insulating crystal state is the checkerboard state; there, the sites of a square lattice are alternately occupied and empty. At half filling, this state is the ground state at weak tunneling and strong nearest-neighbor (NN) repulsion. If repulsive interactions beyond NNs are present, many such insulating configurations

become possible, with filling factors other than 1/2. Since deforming one configuration into another costs a large amount of energy, these low-lying states are metastable and have large life times [383]. The large number of such metastable states might be useful for quantum-information storage [187, 188, 384, 385], but it also complicates finding the ground state.

Another example for the intriguing physics due to long-range interactions are supersolids, which are exotic quantum states with coexistence of crystal and superfluid (SF) long-range order (LRO). For instance, if the checkerboard crystal state is doped with holes, these can delocalize and develop long-range phase coherence on top of a checkerboard-like density background. For interactions with limited range, however, such a state does not form the ground state but is subject to phase separation [386–388]. Dipolar interactions, on the other hand, can stabilize such a supersolid phase [389]. This combination of novel physics with an increase in computational difficulty makes systems with long-range interactions interesting targets for QSs.

For such long-range quantum simulations, trapped ions seem more natural candidates than neutral atoms, since dipolar interactions can be achieved without additional experimental effort [175]. Ion setups have the additional peculiarity that, contrary to ultracold-atoms architectures, not only two-body (density–density) interactions, but also tunneling terms can be long ranged. Furhtermore, in the trapped-ion architecture, a high degree of control over state preparation, evolution, and readout can be achieved (see Chapter 2.2)

In this chapter, we describe how, combining trapped ions with a standing laser wave, one can realize a quantum simulation of a one-dimensional hard-core-boson model with dipolar off-site interaction and tunneling. This model is equivalent to a dipolar XXZ spin-1/2 chain. We explore its rich phase diagram in detail, employing (see Part IV for technical details) perturbative mean-field theory (PMFT), exact diagonalization (ED), and quasi-exact numerical techniques (DMRG and iTEBD). We find that the complete devil's staircase – an infinite sequence of crystal states existing at vanishing tunneling – spreads to a succession of lobes similar to the Mott-lobes found in NN Bose–Hubbard models. Further, we find *quasi-supersolid* behavior inside the insulating lobes: additionally to long-range density–density correlations, off-diagonal correlations are quasi-long-ranged [390], opposed to models with NN tunneling where they decay exponentially. This quasi-supersolid is exceptional, since normally systems with dipolar interactions in 1D can be described by Luttinger theory [391–393]. In that case, diagonal correlations decay with the Luttinger parameter K, and off-diagonal correlations with $1/K$. This means that a slow decay of the first implies a fast decay of the latter, and *vice versa*. In contrast, in our model with

long-range tunneling both diagonal and off-diagonal correlations decay slowly, and Luttinger theory is not a valid description. These findings for the 1D system have been published in Ref. [180]. We also present some results, derived with QMC, for an extension of the model to a 2D triangular lattice at finite temperature. There, we find that long-range tunneling can stabilize true supersolid phases (*i.e.*, LRO in diagonal and off-diagonal correlations). The results on the triangular lattice can be found in the arXiv preprint [204].

We organize this chapter as follows: First, we introduce the considered model Hamiltonian in Sec. 7.1, and explain in Sec. 7.2 how it can be implemented with trapped ions. Then, in Sec. 7.3, we outline our expectations by discussing previous, related results for the 1D case. The following sections are dedicated to a thorough investigation of the ground-state phase diagram in 1D. Our most accurate analysis comes from DMRG (Sec. 7.5). However, it is good to first form intuition via analytical approaches, even if approximate. We present mean-field and perturbative results in Sec. 7.4 to find the upper borders of the crystal lobes. Some limitations of DMRG can be overcome with other numerical techniques. For instance, we can study infinite systems (as opposed to finite sized) with the iTEBD algorithm (Sec. 7.6), and experimentally relevant small systems can be studied with ED (Sec. 7.7). At the end of this chapter (Sec. 7.8), we discuss the extension to the 2D triangular lattice, and in Sec. 7.9 we offer some final remarks.

7.1 A spin model with competing long-range interactions

In this chapter, we are interested in the interplay between long-range interactions and tunneling, such as given in a chain of dipolar XXZ spins, described by the Hamiltonian

$$\hat{\mathcal{H}} = J \sum_{i<j} \frac{1}{|i-j|^3} \left[\cos\theta S_i^z S_j^z + \sin\theta \left(S_i^x S_j^x + S_i^y S_j^y \right) \right] - \mu \sum_i S_i^z \,, \tag{7.1}$$

where the S_i^α are spin-1/2 operators at site i, and μ is the chemical potential (equivalent to an external magnetic field), adjusting the magnetization

$$\frac{\langle Z \rangle}{N} \equiv \sum_{i=1}^{N} \langle S_i^z \rangle \,, \tag{7.2}$$

where N is the chain length. Since the Hamiltonian (7.1) shows a symmetry of up-down spins, we consider in this chapter only negative magnetization.

In one dimension (which is the main subject of this chapter), standard analytical and numerical techniques typically suffice to reliably probe the phase diagram. Still, the 1D limit is not only important to gain intuition, it also allows to judge the reliability and performance of QSs. Even more relevant are studies of two or more dimensions (see Section 7.8) or dynamics (see also our discussion of the most relevant tasks for a QS on p. 12*f*).

By varying the angle θ, we can explore all ranges of relative strength of the interactions, *e.g.*, the XX chain in a transverse field ($\theta = \pi/2$), or the Ising model ($\theta = 0$) – but both with long-range interaction. Moreover, the model can be tuned from negative to positive XY interaction, with the latter leading to a deformation of the phase diagram due to frustration effects (for a discussion of phenomena due to strong frustration, see Chapter 3).

The problem can be mapped to a system of hard-core bosons using the standard Holstein–Primakoff transformation, Eq. (3.2). In the following, we will use the spin and boson pictures interchangeably, because some aspects are better described in terms of spins, while others are more familiar in the language of hard-core bosons. In the hard-core boson description, an up-spin corresponds to an occupied site and a down-spin to an empty one, the ZZ terms translate to dipolar off-site density–density interactions, and the XX and YY interactions become long-range tunneling terms. Since typically tunneling terms are short-ranged, this has to be seen as an important peculiarity of the trapped-ion model.

A similar model with short-range tunneling emerges in the context of ultracold polar molecules (or Rydberg atoms) [394, 395]. Placed in a one-dimensional optical lattice, in the limit of strong on-site interaction, the cloud of polar molecules is effectively described by Hamiltonian (7.1), but with NN instead of long-ranged tunneling (the derivation is similar to the standard Bose–Hubbard model, see Chapter 2.1). Hence, the quasi-supersolid phase (which, as we will discuss below, is entirely due to the long-range tunneling) cannot be observed in this system. Recently, ideas have been put forward how to achieve the long range of the tunneling terms also in a system of polar molecules [396]. Throughout this chapter, we draw comparisons between our model and the model with NN tunneling and dipolar interaction, as well as with a model with both NN tunneling and interaction (the NN-XXZ model, relevant for magnetic materials).

7.2 Experimental implementation

The Hamiltonian (7.1) can be simulated in an ion-trap experiment, as we explain now. For more details on ion-trap experiments, see also Sec. 2.2. We base the

discussion on the original work of Porras and Cirac [175] to which we refer for technical details. This scenario is conceptually straightforward, but relies on standing waves and intensity gradients. For technical reasons, however, actual implementations usually involve polarization gradients and walking waves. We will comment on this situation further below.

We consider a collection of N trapped ions at low temperatures, such as depicted in Fig. 2.3a or Fig. 2.4. In such a situation, the Coulomb repulsion (or the microtrap pattern) arranges the ions in a crystal and allows only small oscillations, centered at the equilibrium positions. The ion equilibrium positions will later mark the sites of the effective spin model. The Coulomb interaction further couples the small vibrations around equilibrium into collective modes (phonons), governed by the Hamiltonian

$$\hat{\mathcal{H}}_{\text{vib}} = \sum_{\alpha=x,y,z} \sum_{k=1}^{N} \hbar\omega_k^\alpha \hat{a}_k^{\alpha\dagger} \hat{a}_k^\alpha \,, \tag{7.3}$$

where $\hat{a}_k^\alpha$ and $\hat{a}_k^{\alpha\dagger}$ are the phonon annihilation and creation operators, respectively, of modes with energy $\hbar\omega_k^\alpha$.

The main idea is now to choose two electronic hyper-fine ground states of each ion, which act as a pseudo-spin 1/2, and mediate – in the spirit of the Cirac–Zoller gate [174] – an effective spin–spin interaction via the collective vibrational modes of the ion chain. To describe the pseudo-spins, we introduce the Pauli-sigma matrices σ_α, $\alpha = x, y, z$, and we denote the eigenstate with eigenvalue $1(-1)$ of σ_α by $|\uparrow(\downarrow)\rangle_\alpha$.

The chemical potential (*i.e.*, magnetic field) term of Hamiltonian (7.1) can be achieved rather easily in a number of ways. For example, one can couple the hyperfine states that constitute the effective spin 1/2 via a stimulated Raman transition [28, 29]. To do this, one can use one of the beams that induce the spin–spin coupling (see below) and beat it with an additional beam such that the detuning between them is resonant with the hyperfine transition between $\uparrow$ and $\downarrow$. Choosing the phase difference appropriately, one can generate terms like

$$\hat{\mathcal{H}}_{\text{mag}} = \sum_i B_\alpha \sigma_i^\alpha \,. \tag{7.4}$$

A similar effect can be achieved by resonantly driving the transition directly with a rf-frequency field [27]. This couplings generate a term proportional to σ_i^x, which can be mapped to the z component by an appropriate redefinition of the spin operators. Alternatively, an off-resonant microwave can be used to

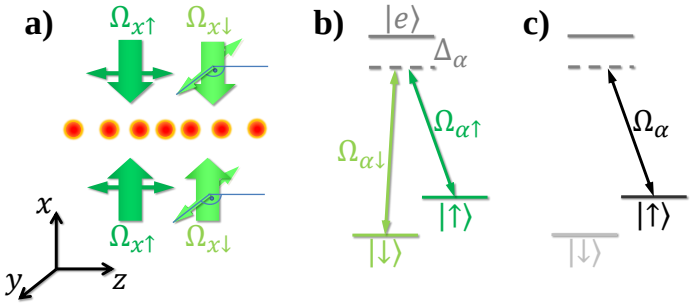

Figure 7.1: **Raman lasers generating the effective spin–spin interaction.** **(a)** Pairs of counterpropagating laser beams with Rabi frequencies $\Omega_{\alpha\uparrow,\downarrow}$ illuminate the ion chain in the three directions of space (shown are the beams in x direction). Their polarizations are chosen to avoid undesired interference effects. **(b)** The lasers couple the hyperfine-states constituting the pseudo-spin 1/2 to an auxiliary excited state. **(c)** For appropriately chosen phase differences, the $|\downarrow\rangle$ state is dark. If the Raman beams are standing waves, making the intensity and thus the light–spin coupling position-dependent, this scheme can generate a spin–spin interaction mediated by ion vibrations.

create a state-selective potential, leading to an energy difference between the hyperfine states, creating a term proportional to σ_i^z.

7.2.1 Porras–Cirac (2004) scenario

To achieve the effective coupling, one can use pairs of counterpropagating laser beams providing Rabi frequencies $\Omega_{\alpha\uparrow}$ and $\Omega_{\alpha\downarrow}$ (Fig. 7.1a). Here, $\alpha = x, y, z$ denotes the direction of propagation, and $\Omega_{\alpha\uparrow}$ ($\Omega_{\alpha\downarrow}$) couple the state $|\uparrow\rangle_z$ ($|\downarrow\rangle_z$) off-resonantly to an excited state $|e\rangle$ (see Fig. 7.1b).

For appropriate polarizations which avoid interferences [175], these couplings can be expressed as $\Omega_{\alpha\uparrow}|e\rangle\langle\uparrow|_z + \Omega_{\alpha\downarrow}|e\rangle\langle\downarrow|_z$. In z-direction, only the $\uparrow$ state is addressed, $\Omega_{z\downarrow} = 0$, while in x and y we choose the relative phases $\Omega_{x\downarrow} = \Omega_{x\uparrow}$ and $\Omega_{y\downarrow} = i\Omega_{y\uparrow}$. This way, one achieves the atom–light couplings

$$\hat{\mathcal{H}}_{\mathrm{a}-\ell,\alpha} = \hbar\Omega_{\alpha\uparrow}|e\rangle\langle\uparrow|_z + \Omega_{\alpha\downarrow}|e\rangle\langle\downarrow|_z = \hbar\Omega_\alpha|e\rangle\langle\uparrow|_\alpha\,, \tag{7.5}$$

i.e., the state $|\downarrow\rangle_\alpha$ is dark for the beams propagating in direction α (Fig. 7.1c). This choice is convenient for notation, but note that in principle we could, using the beam propagating in direction α, create this type of coupling for any

spin component α'. For strong detuning Δ_α, we can adiabatically eliminate the excited state $|e\rangle$. To this, one can insert the parameters depicted in Fig. 7.1b into the effective Hamiltonian (5) of the article by Brion, Pedersen, and Mølmer [397] (replacing from their notation $\delta = 0$, $\Omega_a = \Omega_{\alpha\uparrow}$, and $\Omega_b = \Omega_{\alpha\downarrow}$). This leaves us with the effective atom–light couplings

$$\hat{\mathcal{H}}^{\text{eff}}_{\text{a}-\ell,\alpha} = -\hbar \frac{|\Omega_\alpha|^2}{4\Delta(1+\delta_{\alpha,z})} \left(\sigma^\alpha + \mathbb{I}\right) . \tag{7.6}$$

Since in z-direction there is only one beam pair while in x and y there are two, we introduced the factor $(1+\delta_{\alpha,z})$.

Up to now, we only considered light forces acting on individual ions. Now, we want to show how these can couple hyperfine states of different ions, employing a mediation by the collective vibrational modes. To this, we assume that the counterpropagating beams form standing laser waves, so that

$$|\Omega_\alpha|^2 = |\Omega_{\alpha,0}|^2 \cos(k_{\ell,\alpha} x^\alpha)^2 , \tag{7.7}$$

with $x^\alpha = x, y, z$. We assume that the position of the intensity minima relative to the ion equilibrium positions $x_i^{\alpha,0}$ is fixed to $x_i^{\alpha,0} = (1+2m)\pi/(4k_{\ell,\alpha})$, with m integer numbers, and where i numbers the ions from 1 to N. We assume that the displacements of the ions from their equilibrium position, $q_i^\alpha = x_i^\alpha - x_i^{\alpha,0}$, is small compared to the light wavelength, *i.e.*, $k_{\ell,\alpha} q_i^\alpha \ll 1$. In this so called Lamb–Dicke regime, we can expand the cosine term (7.7) in the spin–light couplings (7.6), leading to the spin–position coupling

$$\hat{\mathcal{H}}_{\text{s-p}} = -\sum_{\alpha=x,y,z} \sum_{i=1}^{N} F_\alpha \, q_i^\alpha \frac{1}{2} \left(\sigma_i^\alpha + \mathbb{I}\right) . \tag{7.8}$$

Here, we defined the coupling strengths $F_\alpha = \hbar k_{\ell,\alpha} |\Omega_\alpha|^2 / (2\Delta(1+\delta_{\alpha,z}))$ and neglected terms that act only on the spin components. These are similar to a homogeneous magnetic field and can be compensated by the terms (7.4).

It is convenient to express the ion positions q_i^α in terms of the phonon modes,

$$q_i^\alpha = \sum_k \frac{\mathcal{M}^\alpha_{i,k}}{\sqrt{2 M_{\text{ion}} \omega_k^\alpha / \hbar}} \left(\hat{a}_k^\alpha + \hat{a}_k^{\alpha\,\dagger}\right) , \tag{7.9}$$

with M_{ion} the ion mass. The unitary matrices $\mathcal{M}^\alpha$ diagonalize the vibrational Hamiltonian, $\mathcal{M}^\alpha_{i,k} \mathcal{K}^\alpha_{i,j} \mathcal{M}^\alpha_{j,k'} = {\omega_k^\alpha}^2 \delta_{k,k'}$, where $\mathcal{K}$ is the elasticity matrix. The

elasticity matrix is determined by the energy it costs to elastically deform the ion crystal,

$$V_{\text{elast}} = \frac{1}{2} M_{\text{ion}} \sum_{\alpha,i,j} \mathcal{K}^{\alpha}_{i,j} x^{\alpha}_i x^{\alpha}_j \,. \tag{7.10}$$

This energy is given by the second derivatives of the Coulomb repulsion, so that for an ion chain along the z direction, we get

$$\mathcal{K}^{\alpha}_{ij} = \begin{cases} \omega^2_\alpha - c_\alpha \sum_{j'(\neq i)} \frac{e^2/M_{\text{ion}}}{\left|z^0_i - z^0_{j'}\right|^3} \,, & i = j \\ +c_\alpha \frac{e^2/M_{\text{ion}}}{\left|z^0_i - z^0_j\right|^3} \,, & i \neq j \end{cases} \tag{7.11}$$

Here, $c_{x,y} = 1$, $c_z = -2$, and the z^0_i denote the equilibrium positions ($x^0_i = y^0_i = 0$). Further, $\hbar\omega_\alpha$ is the vibrational energy of an individual ion (*i.e.*, given solely by the trap and without the influence of the Coulomb repulsion to other ions).

7.2.2 Effective spin–spin interaction

To arrive at the promised spin Hamiltonian it is convenient to apply the canonical transformation $U = e^{-A}$ with

$$A = \sum_{\alpha,i,k} \eta^{\alpha}_{i,k} \left(\sigma^{\alpha}_i + \mathbb{I}\right) \left(\hat{a}^{\alpha\,\dagger}_k - \hat{a}^{\alpha}_k\right) \,, \tag{7.12}$$

where

$$\eta^{\alpha}_{i,k} = F_\alpha \, \frac{\mathcal{M}^{\alpha}_{i,k}}{\hbar\omega_{\alpha,k}} \sqrt{\frac{\hbar}{2M_{\text{ion}}\omega_{\alpha,k}}} \tag{7.13}$$

parametrizes the laser-induced displacements of the ions compared to the ground-state size of the vibrational modes. In the new basis, the Hamiltonian includes an effective spin-spin interaction,

$$e^{-A}\left(\hat{\mathcal{H}}_{\text{vib}} + \hat{\mathcal{H}}_{\text{s-p}} + \hat{\mathcal{H}}_{\text{mag}}\right) e^{A} = \hat{\mathcal{H}}_{\text{vib}} + \frac{1}{2} \sum_{\alpha,i,j} J^{\alpha}_{i,j} \sigma^{\alpha}_i \sigma^{\alpha}_j + \sum_i B'_\alpha \sigma^{\alpha}_i + \hat{\mathcal{H}}_{\text{res}} \,. \tag{7.14}$$

The effective magnetic fields have been modified by $B'_\alpha = B_\alpha + F^2_\alpha/(M_{\text{ion}}\omega_\alpha)$. Further, the residual spin–phonon coupling $\hat{\mathcal{H}}_{\text{res}}$ can be neglected in the regime of small $\eta^{\alpha}_{i,k}$. Then, the spins are completely independent of the vibrational modes and one is left with an effective spin model that governs the dynamics of the two hyperfine states $|\uparrow\rangle$ and $|\downarrow\rangle$.

In this scenario, the effective spin–spin interaction between two sites i and j is

$$\begin{aligned} J_{i,j}^{\alpha} &= -\sum_k \frac{F_\alpha^2}{M_{\text{ion}}\omega_{\alpha,k}^2}\mathcal{M}_{i,k}^{\alpha}\mathcal{M}_{j,k}^{\alpha} = -2\sum_k \eta_{i,k}^{\alpha}\eta_{j,k}^{\alpha}\hbar\omega_{\alpha,k} \\ &= -\frac{F_\alpha^2}{M_{\text{ion}}}\left(\frac{1}{\mathcal{K}^{\alpha}}\right)_{ij} . \end{aligned} \tag{7.15}$$

This spin–spin coupling completes all terms in Hamiltonian (7.1).

Since the vibrational modes are due to the Coulomb interaction between the ions, the effective spin-model is long-ranged. The precise spatial form of the spin–spin interactions is determined by the ratio of the relevant energy scales, namely the Coulomb interaction between neighboring ions on the one side and the vibrational energy of an individual ion ω_α on the other side. Their ratio can be quantified by the dimensionless parameter $\beta_\alpha \equiv |c_\alpha| e^2/M_{\text{ion}}\omega_\alpha^2 d_0^3$, where we introduced the mean inter-ion distance d_0 and where we assume that the ion chain is homogeneous. In a realistic experimental situation, if an overall trapping potential is used, the inter-ion spacing becomes non-uniform. In the central region of a long ion chain, however, this inhomogeneity can be neglected. An equidistant ion chain could also be created by placing the ions in individual microtraps [181, 182]. For these reasons, we can assume in the following that the system is homogeneous. Then, in the stiff limit where $\beta_\alpha \ll 1$, an evaluation of the elasticity matrix (7.11) shows that the decay of the spin-spin interactions obeys a dipolar power law as promised.

Note that in a linear Paul trap $\beta_\alpha \ll 1$ can only be achieved for the radial modes, while in the axial direction, $\beta_\alpha \sim 1$ has to be fulfilled. Increasing the axial confinement increases the frequency ω_α, thus reducing β, but it also reduces the ion distances and can even lead to a deformation of the chain into a zig-zag structure [177]. In individual microtraps, however, the condition $\beta_\alpha \ll 1$ can be fulfilled also for axial modes.

By choosing to which ion modes the laser couples (axial or radial), one can change the sign of $J_{i,j}^{\alpha}$ and thus tune the spin–spin coupling to ferromagnetic (FM) or antiferromagnetic (AFM), as desired. To have all three couplings at the same time FM or AFM may be experimentally challenging, since this can only be achieved by coupling to the same types of modes (*i.e.*, either all axial or all radial). If, however, the pairs of laser beams acting on two different spin components σ^{α_1} and σ^{α_2} couple to the same set of modes, the transformation (7.14) generates the additional spin–spin interactions $\sigma_i^{\alpha_1}\sigma_j^{\alpha_2}$. This can be avoided by addressing individual modes. For this purpose, one can choose for each spin-

component the detuning between the laser beams detuned by a small amount δ to a specific vibrational mode. In the Lamb–Dicke regime, the trajectory in phase space of the addressed mode follows a circle that closes after time $1/\delta$, so that one can trace over the motional degree of freedom without errors. If other modes are close in energy, however, the system evolution follows also circles in their phase spaces. With increasing number of modes, it becomes more difficult to close all the circles simultaneously, so that entanglement between internal (spin) and external (motional) degrees of freedom remains. This leads to errors when tracing out the motional degree of freedom. Therefore, cross-talk between the different addressed modes has to be avoided, which becomes technically challenging for large ion crystals due to the increase of the number of modes with the ion number.

7.2.3 Scenario involving walking waves and polarization gradients

The standing laser waves considered above are actually nothing else than an optical lattice. Although these may be conceptually more straightforward, experiments typically employ "walking" laser waves [27–29], since they have the advantage over standing waves that one does not need to fix the position of the ions with respect to the intensity minima (only the relative distance between the ions) [184].

In a typical scenario, the walking waves are created by two beams almost counterpropagating along the axial direction of the ion chain. A relative angle between the beams allows to tune the effective wave length (*i.e.*, measured along the chain axis). Also, in typical experimental situations it has proven technically advantageous to obtain the position-dependent coupling not by spatial variations of the intensity but of the polarization. To this, the two laser beams creating the walking wave are perpendicularly polarized. Since the relative phase of the two beams varies along the chain, this generates a polarization gradient, and the polarization dependence of the hyperfine couplings, in turn, leads to a position-dependent force.

Further, the two beams have a small detuning ω_{w} between them, so that the resulting wave moves slowly ("walks") over the ion crystal. The spatial dependence of the coupling is then given by an exponential of the form $\exp(ik_{\ell,\alpha}x^{\alpha} + \omega_{\mathrm{w}}t)$. In the Lamb–Dicke limit, this can again be expanded in terms of the ion displacements. In the stiff-crystal limit, $\beta_{\alpha} \ll 1$, the ions are almost independent and the dispersion relation of the modes has a small band-width compared to ω_w. One can then tune the walking waves to the red sideband with respect

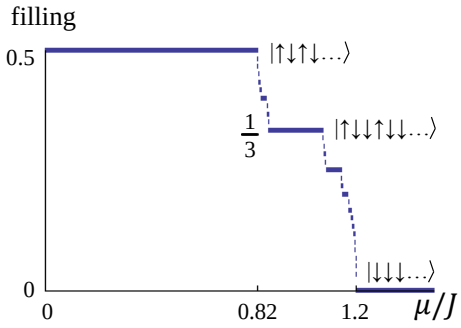

Figure 7.2: **Complete devil's staircase** for the trapped-ion Hamiltonian (7.1) at $\theta = 0$, consisting of steps of constant hard-core boson filling in dependence on the chemical potential μ. In principle, the devil's staircase is continuous and covers all rational fillings from 0 to 1, but for clarity we show only the most prominent steps (and only positive μ). For the largest steps (filling 1/2, 1/3, and 0), we give the ground-state wave function.

to all vibrational modes. This yields a term similar to Eq. (7.8), and following the same reasoning as above we obtain a state-dependent coupling similar to Eq. (7.15) [184].

Using this type of coupling, tunable spin–spin interactions of Ising type have been demonstrated in a number of proof-of-principle experiments [27–29]. From now on, we neglect the ion dynamics and only consider the effective Hamiltonian (7.1) governing the hyper-fine states. We will see that it hosts an extremely rich phase diagram worth exploring in such experiments.

7.3 Expected behavior of the model

Before proceeding to the detailed numerical analysis of the ground-state phase diagram of Hamiltonian (7.1), let us briefly sketch the expected behavior of the present model, starting from previous related results.

For $\theta = 0$, Hamiltonian (7.1) describes a long-range Ising model, or equivalently a 1D system of hard-core bosons with repulsive dipolar interaction. This is a classical model that can be solved analytically [398]. Due to the long-range nature of the interactions, for any given filling factor, the particles arrange in a periodic crystal pattern (a generalized Wigner lattice). For a given filling factor, these periodic patterns can be constructed by maximizing the mutual distance between the particles. Every rational filling factor $q = \frac{m}{n}$ occupies a finite extent in μ, thus giving rise to a plateau of fixed particle density, and these plateaux cover the entire range of μ. Similar to the model considered by Bak and Bruinsma [398], plotting the filling factor against the chemical potential μ yields a self-similar structure – a complete devil's staircase (Fig. 7.2). The name "devil's staircase" derives from its surprising mathematical properties, challenging naive

intuitions about continuity and measure: since all rational fillings are present (in an infinite chain), it is a continuous function; moreover, its derivate vanishes almost everywhere (*i.e.*, only on a set of measure zero is it non-zero, indeed, infinite) – and still it is not a constant, but goes over a finite range from 0 to 1. The devil's staircase is "complete," because it covers all values of μ.

The stair's steps have a width

$$\Delta\mu\left(\frac{m}{n}\right) = 2\frac{3n\pi^2\csc\left(\frac{\pi}{n}\right)^2 - n\pi^2 - 3\pi^3\cot\left(\frac{\pi}{n}\right)\csc\left(\frac{\pi}{n}\right)^2}{3n^3}\,. \tag{7.16}$$

This means that fillings with a large denominator – equivalent to a large crystal period – become the ground state only in a very small range of chemical potential.

A finite tunneling, $(\theta \bmod \pi) \neq 0$, makes the problem quantum mechanical. The tunneling allows particles to gain kinetic energy, which tends to destabilize the crystal. It melts at some critical tunneling strength into a SF phase where the particles are delocalized over the chain. Two possible scenarios for a transition from the crystal to the molten phase are thinkable: a direct crystal–SF transition, or an intervening supersolid phase. The latter has been predicted to occur in similar – but two-dimensional – hard-core boson systems [388, 399–403]. Until recently, there was only one claim of an experimental realization of a supersolid in ^{4}He [290, 291], which is still disputed [292, 293]. Therefore, it would be interesting to find other systems which show supersolid behavior and are easier to interpret. One such experiment has been carried out recently [14, 294], where an atom cloud in a cavity spontaneously breaks spatial symmetry while at the same time showing off-diagonal LRO.

At finite tunneling, the points $\theta = \pm\pi/2$ are special, since here the ZZ interaction term vanishes from Hamiltonian (7.1). The limit $\theta = -\pi/2$ describes a FM XY model. Here, the long-range tunneling can be subsumed in a renormalized NN interaction, since, first, all interactions work towards the same ordering, and, second, in one dimension the integral over dipolar interactions converges. For $\theta = +\pi/2$, the system is an AFM XY model, which displays frustration, and the behavior is less obvious. It turns out, however, that a similar renormalization to a NN interaction captures the main physics. Hence, analogies to a NN-XY model can help understanding the behavior of the system near $\theta = \pm\pi/2$.

7.4 Mean-field approximations

In the following, we study how the ground-state phase diagram of Hamiltonian (7.1) develops as a function of θ. We start with two approximative methods to obtain qualitative insights.

7.4.1 Perturbative mean-field theory

A first understanding of the crystal–SF transition can be obtained by a PMFT, valid for small tunneling. While not being very accurate in 1D, such a mean-field treatment is generally expected to become better for longer-ranged interactions. As explained in Sec. 13.2, the PMFT allows to compute a critical tunneling strength where the SF order parameter becomes finite, and the assumption that the ground state is localized is no longer valid. This gives an estimation for the upper border of the crystal lobes, corresponding to an instability under adding or removing a single particle. The main disadvantage of the PMFT is that there are potentially more complicated excitations, *e.g.*, the addition of a particle plus a relocation of the neighboring particles. Such a deformation of the crystal could decrease the potential energy. In the simple PMFT *Ansatz*, however, this type of excitations is not captured. Moreover, it is not the method of choice to extract information about precise values of observables. It does, however, allow the assessment of the appearance of meta-stable states.

For our calculations, we assumed an infinite system with the restriction that the states have a periodicity of 12 sites. Since the crystal phases with a large periodicity become very small in their extent in μ [by virtue of Eq. (7.16)], this is a reasonable restriction which still captures the most prominent features of the phase diagram.

In Fig. 7.3, we show the insulating-lobe structure that we obtain from PMFT. The thick line, which follows the breakdown of the ground state, gives an upper limit for the stability of crystal states. A dotted line marks the μ where the ground state magnetization changes, *i.e.*, where a different crystal structure becomes lower in energy. Frustration effects make the crystal lobes more stable for AFM ($\theta>0$) than for FM XY-interaction ($\theta<0$). Further, the data exhibit the rich structure of metastable states (delimited by thin lines), which – as proposed in the context of ultracold dipolar neutral atoms – could be useful as quantum memories [187, 188]. (For clarity, states that constitute the ground state only over a small region of the phase diagram are not displayed.)

We also computed the phase diagram within Gutzwiller mean-field theory (not shown; for technical details of this method, see Chapter 13.1). The qualita-

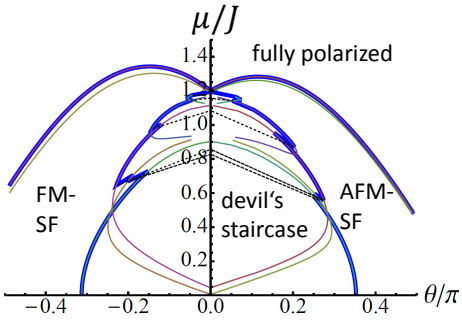

Figure 7.3: **Stability regions of the crystal states within PMFT,** exhibiting the large number of metastable states (delimited by thin lines). Dotted lines mark the μ where the crystal ground state changes periodicity. The thick line, tracing the melting of the crystal state to ferromagnetic or antiferromagnetic superfluids (FM-SF, AFM-SF), gives an upper limit for the stability of crystal states. Frustration effects lead to an asymmetry between the negative (FM) and positive (AFM) θ side.

tive behavior of the phase diagram is similar to PMFT, but the lobes are somewhat smaller because PMFT considers destabilization under single-particle or single-hole excitations, while Gutzwiller mean-field theory captures better more complicated excitations.

7.4.2 Wigner-crystal melting at low filling

For low magnetizations, we can draw an analogy to the melting of Wigner crystals [404, 405]. As described in Sec. 7.3, at $\theta = 0$, the hard-core bosons are perfectly localized, with an inter-particle distance given by the filling fraction. At finite tunneling, $\theta \neq 0$, the particles spread, but at small tunneling and low filling it is reasonable to assume that they remain spatially well separated.

Under this assumption, we can approximate the total wave-function by a product of Gaussians representing the individual particles,[1]

$$|\Psi\rangle_{\mathrm{CM}} = \bigotimes_{p=1}^{N_p} |\psi_p\rangle = \bigotimes_{p=1}^{N_p} \sum_{i=1}^{N} f_p(i)\, |d_0 p + i\rangle_p \,, \tag{7.17}$$

where the tensor product includes all particles numbered from 1 to N_p and the sum runs over all sites i. The Fock states $|d_0 p + i\rangle_p$ denote the particle p at site $d_0 p + i$, where site $d_0 p$ is the center of the wave packet. For simplicity, we assume that the wave packets as well as the distance d_0 between them are equal for all particles. Then, the particle distribution around the wave-packet center

[1] PMFT neglects coherence between different *sites*, while this *Ansatz* neglects coherence between different *particles*.

becomes particle-independent, $f_p(i) = f(i)$, and is symmetric, $f(-i) = f(i)$. Further, it obeys the normalization condition $\sum_i |f(i)|^2 = 1$.

In the Fock basis of the individual particles, we can rewrite Hamiltonian (7.1) as

$$\hat{\mathcal{H}} = J \sum_i \sum_{j \neq i} \frac{1}{|i-j|^3} \left(\sin\theta \sum_p |i\rangle_p \langle j|_p + \frac{1}{4} \cos\theta \sum_p \sum_{q \neq p} |i\rangle_p \langle i|_p \otimes |j\rangle_q \langle j|_q \right) . \quad (7.18)$$

Here, sums over indices q, p run over particles $1, ..., N_\mathrm{p}$ and sums over i, j over sites $1, ..., N$. Moreover, for now we fix the particle number N_p, equivalent to fixing the distance d_0.

We can arrive at the variational ground state by minimizing the energy expectation value. For the wave function (7.17), Hamiltonian (7.18) yields the energy

$$\frac{\langle \hat{\mathcal{H}} \rangle_{CM}}{N_\mathrm{p}} \equiv \frac{E_{CM}}{N_\mathrm{p}} = J \sum_{i,j;i \neq j} \frac{\sin\theta}{|i-j|^3} f(i)^* f(j) + \frac{J}{4} \sum_{p \neq 0} \sum_{i,j} \frac{\cos\theta}{|d_0 q + i - j|^3} |f(i)|^2 |f(j)|^2 . \quad (7.19)$$

The sums in the second term obey the condition $d_0 q + i - j \neq 0$.

Similar to the Gutzwiller *Ansatz* (Chapter 13.1), the energy can be minimized by using the Schrödinger equation [see Eq. (13.9)], followed by taking the functional derivative with respect to the $f(i)$.[2] This procedure gives a self-consistent equation for the $f(i)$,

$$\frac{1}{N_\mathrm{p}} \frac{\delta E_{CM}}{\delta f(l)^*} = i\dot{f}(l) = J \sum_{j \neq l} \frac{\sin\theta}{|l-j|^3} f(j) + \frac{J}{2} \sum_{p \neq 0} \sum_{j; j \neq d_0 q + l} \frac{\cos\theta}{|d_0 q + l - j|^3} |f(j)|^2 f(l) , \quad (7.20)$$

that can be solved by imaginary-time evolution.

The spread of the wave packets increases with θ until the initial assumption that the particles are well separated breaks down. In particular, the state $|\Psi\rangle_\mathrm{CM}$ contains double occupancies of sites, which is not allowed in the original spin Hamiltonian (7.1). For large particle separation and small wave-packet width, the contribution of such states is small, so that we can neglect them. For more spread-out wave-packets, however, their weight increases, and the description in terms of independent particles, $|\Psi\rangle_\mathrm{CM}$, is not valid any more. In such a situation of large overlap between particles, we consider the crystal as molten.

[2] Note, however, the different interpretation of the weights f in the Gutzwiller *Ansatz*. There, the weights describe the probability at each site of the spin being up or down. Here, they correspond to the distribution of a single up spin over a background of down spins.

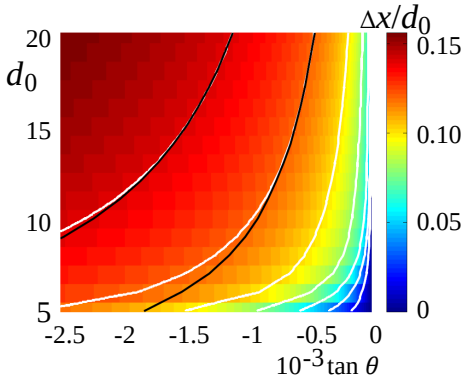

Figure 7.4: **The Lindemann parameter** $\mathcal{V} \equiv \frac{\Delta x}{d_0}$ describes the delocalization of hard-core bosons at large interparticle distances d_0. The white lines are contour lines at $\mathcal{V} = 0.02 \ldots 0.14$ in steps of 0.02. Comparison with the two black lines following the law $\tan\theta \propto d_0^{-1}$ shows that at large d_0, $\mathcal{V}$ behaves as in the continuum limit.

A measure for the particle spread is the normalized variance

$$\mathcal{V} \equiv \frac{\Delta x}{d_0} = \frac{1}{d_0}\sqrt{\langle x^2\rangle - \langle x\rangle^2} = \frac{1}{d_0}\sqrt{\sum_i |f(i)|^2\, i^2}\,, \tag{7.21}$$

the so called *Lindemann parameter* [406]. We show our results for the Lindemann parameter in Fig. 7.4, where we truncated the dipolar tunneling at NNs. This is a reasonable simplification for low filling, since here the melting occurs at small θ, so that the tunneling to larger distances than NN is extremely small. For large inter-particle spacing d_0, the system behaves similar to the continuum limit, where it is known [404] that there is a melting transition at

$$J\tan\theta_c = \text{const}/d_0\,. \tag{7.22}$$

We find that the contour lines of the Lindemann parameter in the lattice system follow this behavior well for d_0 much larger than the lattice spacing, The physical reason behind the behavior of the melting transition (7.22), is the weakness of the repulsive interactions at large inter-particle distances: the larger d_0, the smaller the gain in kinetic energy needed to destabilize the crystal.

At smaller inter-particle distances, the contour lines of $\mathcal{V}$ deviate from the const/d_0 law. In the lattice system, the particles cannot move over arbitrarily small distances, but have to jump at least an entire lattice spacing. For small d_0, a single jump can already mean a large increase of repulsive interaction, and the tunneling has to be stronger than in the continuum case to overcome this.

7.5 Density-matrix renormalization group

While mean-field theories can provide some physical understanding of the system, in 1D they are not very precise. Therefore, we now turn to a thorough numerical analysis of the phase diagram with the quasi-exact density-matrix renormalization group (DMRG) method [407–409] (see Chapter 12.2). We consider chains with open boundary conditions of up to $N = 102$ sites, and with a bond dimension of $D = 128$. We cut off the interaction range at half the length of the chain.

Figure 7.5 presents the mean polarization, $\langle Z \rangle / N$, Eq. (7.2). As with PMFT, due to the long-range nature of the hopping terms, the polarization is asymmetric with respect to $\pm\theta$, in contrast to the system with only NN tunneling [394]. For large enough field μ, or strong FM ZZ-interaction (corresponding to θ not too far from $\pm\pi$), the system is in a fully polarized state, similar to what we saw in the mean-field calculations. However, as expected, the general precision of the mean-field *Ansatz* in this one-dimensional system is low: the DMRG results indicate that the θ-range of the crystal lobes is up to an order of magnitude smaller than the upper bounds given by PMFT. In fact, in the global view given in the main panel of Fig. 7.5, only the plateau for 1/2 filling (polarization 0 in spin language) is discernible. Panel E of Fig. 7.5 shows the small region of the phase diagram where the 1/3-filling crystal lobe (polarization $-1/6$) is located.

For the finite systems used here, open boundary conditions play an important role. For example, in the center of the main panel of Fig. 7.5, there appears a broad plateau with $(1/2 - 1/N)$ filling (*i.e.*, with one spin flipped away from half filling). In the thermodynamic limit, this phase merges with the 1/2-filling plateau to a single lobe. This peculiarity is highly relevant for the correct interpretation of future experiments, which might be carried out with open boundary conditions for technical convenience. Moreover, boundary effects play an important role in the determination of the decay of correlations, which we now describe.

To find supersolid behavior, we now characterize the in-plane correlations $\left|\langle \sigma^+_{N/2} \sigma^-_{N/2+j} \rangle\right|$, where $\sigma^\pm$ are the usual Pauli matrices. In a supersolid phase, these correlations show LRO. The log–log plots in panels A to D show their decay at some selected points in the phase diagram (filled circles), and compare the result to the same system but with NN hopping (solid lines). In the SF phase (panels B and D), the decay is algebraic for both NN and dipolar hopping. Panels A and C lie inside the lobes corresponding to 1/2 and 1/3 filling,

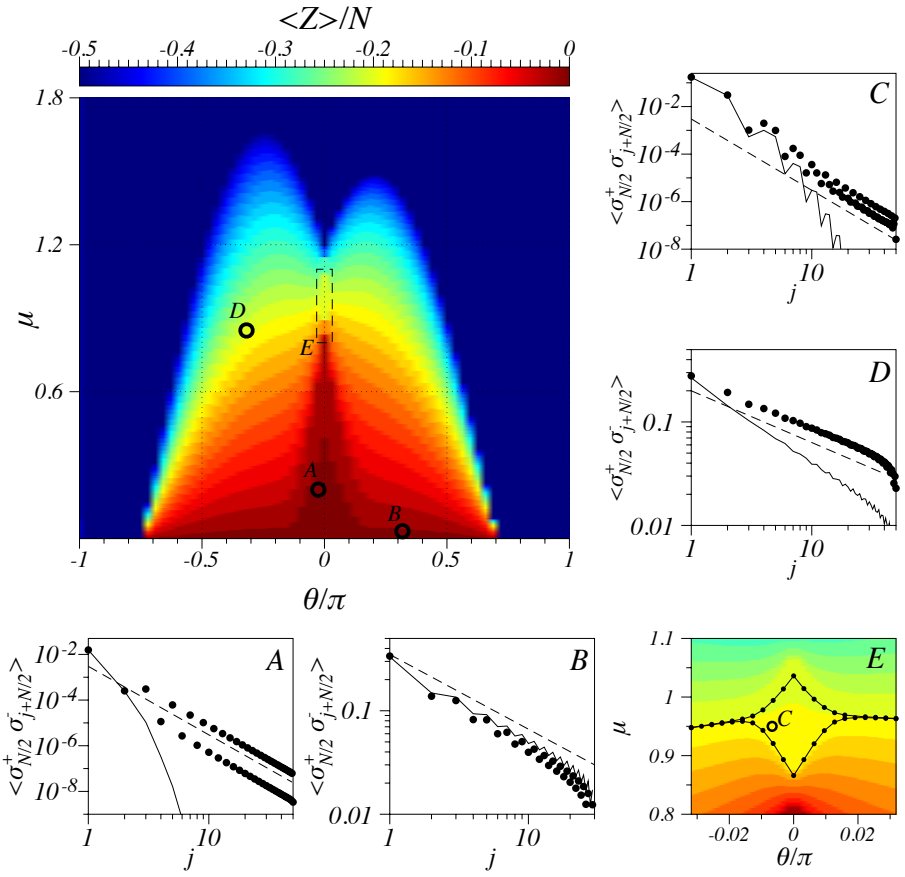

Figure 7.5: **Main panel: DMRG phase diagram** from the mean polarization $\langle Z \rangle / N$, for a system with dipolar hopping and $N = 60$. As in PMFT, frustration leads to an asymmetry between $\theta < 0$ and $\theta > 0$. **(A-D) Decay of off-diagonal correlations** at the marked points of the phase diagram, in log–log scale, for $N = 102$. For NN hopping (solid lines) the decay is exponential, while for dipolar hopping (points), the decay is algebraic everywhere, even within the lobes (A and C), where it follows the dipolar exponent $\alpha = 3$ (dashed lines provide guides to eye proportional to j^{-3}). (B) In the AFM-SF, the algebraic decay is faster than for NN hopping, and (D) in the FM-SF it is slower. **(E) The crystal lobe at 1/3 filling** from a finite-size-scaling analysis is much smaller than predicted from PMFT (the plotted area corresponds to the dashed section of the main panel).

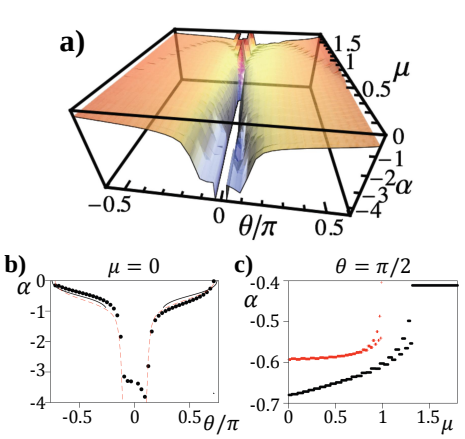

Figure 7.6: **(a) Exponents α of an algebraic fit** $c_0 j^{\alpha}$ to the correlations $\left|\langle \sigma^+_{N/2}\sigma^-_{N/2+j}\rangle\right|$, for $N = 60$. The panels show cuts at **(b)** $\mu = 0$ (1/2 filling) and **(c)** $\theta = \pi/2$ (XY model). The black lines in (b) are the exact results for the NN XXZ model, which can be solved using the Bethe *Ansatz* [74]. AFM interaction induces larger exponents compared to the NN XXZ model, while FM interaction leads to smaller exponents. Inside the insulating lobes, we find $\alpha = 3$ (deviations are due to finite-size effects). Results for NN tunneling are shown in red [dashed line in (b), filled circles in (c)].

respectively, which is visible through the oscillation of the correlation function superposed to the overall decay. For dipolar hopping, the decay is algebraic everywhere, even within the lobes, where for NN hopping the correlations decay exponentially. In the lobes, the decay for dipolar hopping follows the interactions with exponent $\alpha = 3$ [390]. A clear fit for this exponent can only be obtained for rather large chains with $N > 60$ spins. Moreover, although the strength of the XY-interactions decays rapidly with distance, the power-law decay of correlations inside the lobes can only be observed if the interaction is not truncated, because it decays exponentially after the truncation distance.

Since inside the lobes we have a crystal structure, the long-range decay of the transverse correlations is an anomaly when compared to other models with insulating phases. For this similarity to a supersolid, we call this phase a quasi-supersolid. In a true supersolid, a crystal structure coexists with LRO in the transverse correlations. However, in 1D, off-diagonal LRO cannot be spontaneously broken [229]. Hence, the closest analogue to a supersolid that can exist in 1D is a state as the present one – with diagonal LRO and algebraically decaying off-diagonal correlations.

A change in the behavior of the correlations marks the transition from a crystal state to the SF. For a quantitative evaluation, at each point in the phase diagram we fit an algebraic function $c_0 j^{-\alpha}$ to the off-diagonal correlations $\left|\langle \sigma^+_{N/2}\sigma^-_{N/2+j}\rangle\right|$. The value of α for a chain of $N = 60$ spins is shown in Fig. 7.6. The cuts of Fig. 7.6 at $\mu = 0$ [1/2 filling, (b)] and $\theta = \pi/2$ [XY model, (c)] show the wide range that the exponent of the correlations takes in this system. They

also demonstrate the influence of frustration: the correlations decay faster at the AFM side ($\theta > 0$) than at the FM side ($\theta < 0$). The exponents are similar to the NN XXZ model [black line in (b)], but cover a broader range. In particular, they are not independent of the filling for $\theta = \pi/2$ (c), where the NN XXZ model has $\alpha = -0.5$. The results for a system with dipolar ZZ-interaction but NN XY-interaction are shown in red [dashed line in (b), filled circles in (c)]. The main qualitative difference is that inside the insulating lobes the decay is no longer a power law, but follows an exponential.

In a finite system, finding the quantum phase transition (QPT) from the crystal state to the SF is not simple, because the finite number of spins prevents the system from assuming arbitrary polarizations. This results in a division of the phase diagram into stripes with different fixed integer number of up spins, which makes the crystal lobes difficult to discern. In infinite systems, however, one expects a step-like behavior of the polarization only in crystal phases, while in the SF the polarization should change smoothly with μ between $-1/2$ and $1/2$. This observation makes it possible to extrapolate the border between the crystal phases and the SF by the following finite-size scaling: At fixed θ and for a given polarization, compute the upper and lower limits of the polarization plateau, $\mu_a(N)$ and $\mu_b(N)$, for several chain lengths N. From these, one can extrapolate to $\mu_{a,b}(N = \infty)$. In the SF, where the polarization should be a continuum, $\mu_a(\infty)$ and $\mu_b(\infty)$ should be equal. However, in the crystal lobe there will be a finite distance between $\mu_a(\infty)$ and $\mu_b(\infty)$: the width of the lobe for that value of θ. A similar procedure is known to work well for the estimation of Mott-lobes from finite systems in the Bose–Hubbard model [410]. The main difference is that in our model there is in principle a lobe for any rational filling factor, instead of only for integer filling factors. Panel E of Fig. 7.5 shows the result of this approach for the 1/3-filling lobe, using chain lengths of up to 102 spins. The cusp structure is typical for one dimensional systems [411].

7.6 Infinite time evolving block decimation

To complement the results of the previous section, we study the phase diagram with the infinite time evolving block decimation (iTEBD) algorithm [412] (see also Chapter 12.2), in which infinite chains can be directly addressed without the need of finite-size extrapolations. Treating long-range interaction complicates the original formulation of the iTEBD algorithm and turns out to lead to convergence problems. Instead, we implement a variant of the original algorithm in which the translationally invariant character of the problem is kept in the state

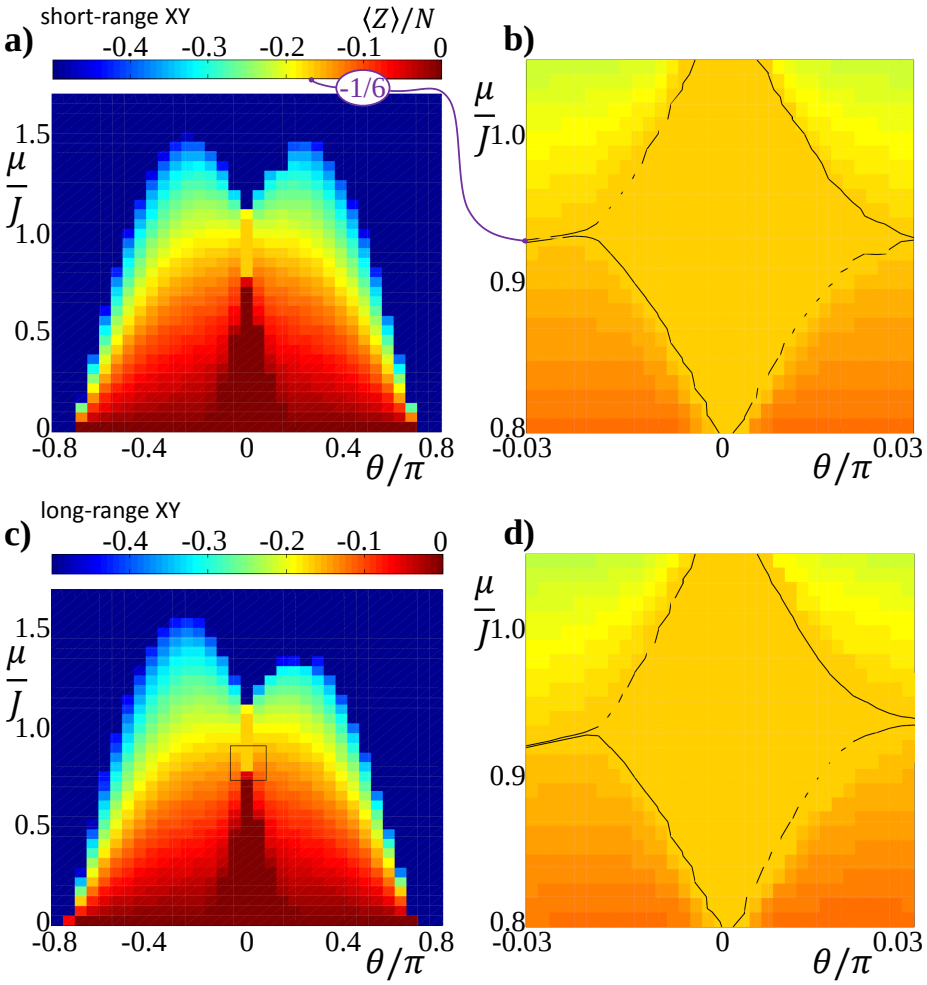

Figure 7.7: **iTEBD mean magnetization** for an infinite chain. **(a-b) Nearest-neighbor XY and next-nearest-neighbor ZZ interactions.** The phase diagram is symmetric with respect to $\theta \to -\theta$. **(c-d) Next-nearest-neighbor XY and ZZ interactions.** Due to frustration effects, the phase diagram becomes asymmetric. The right panels show a zoom on the insulating lobe at polarization $-1/6$ (1/3 filling), as indicated by the box in (c).

and the interactions, thanks to the use of matrix product operators [413]. In this way, we can include interaction terms ranging longer than NNs in a much simpler way.

By comparing the phase diagrams for different ranges of XY interactions, we may study the effect of the long-range hopping in the thermodynamic limit. The method still requires a truncation of the interaction range to some finite order, so that it will not be possible to reproduce the power-law decay of correlations within the crystal lobes. We truncate the ZZ interactions above next-to-NN (NNN) interactions and compare the cases of NN and NNN tunnelings. We observe that a small bond dimension, $D = 10$, provides already a good approximation to the overall phase diagram. To analyze the insulating lobe at 1/3 filling, we increase the bond dimension to $D = 20$.

As in the work by Burnell *et al.* [394] on dipolar molecules, the phase diagram is symmetric if XX and YY interactions range only to the NN (Fig. 7.7a). This is also seen in the zoom on the filling-1/3 crystal lobe (Fig. 7.7b). Including one more term in the XX-YY interactions already causes a clear asymmetry of the phase diagram with respect to $\theta \to -\theta$. This is clearly visible in the SF phases (Fig. 7.7c), and in the zoom on the insulating lobe at filling 1/3 (Fig. 7.7d). The size of the lobe is larger than predicted in the finite-size extrapolation from DMRG. Since here we are only including the first term further than the NN, we expect, however, that longer range terms correct the exact shape of the lobe, as they will give rise to lobes corresponding to other filling factors.

7.7 Exact diagonalization

In this section, we supplement the previous results by ED of chains of 18 spins with periodic boundary conditions, using the Lanczos method (see Chapter 12.1). Although ED only allows investigation of very small systems, from these one can often infer surprisingly much about the behavior of the model at larger sizes (see, *e.g.*, Chapter 3.2.3). Here, we show that ED results hold strong precursors of the crystal–SF transition. Moreover, an experimental implementation with a chain of trapped ions will have to start with short chain lengths. For such a case, ED provides a valuable validation of the trapped-ion QS.

Figure 7.8 displays the fidelity susceptibility,

$$\chi_F = \frac{1 - |\langle \psi(\theta) | \psi(\theta + \Delta\theta) \rangle|^2}{\Delta\theta^2} \tag{7.23}$$

for 1/3 filling. At a second-order quantum phase transition, χ_F diverges in

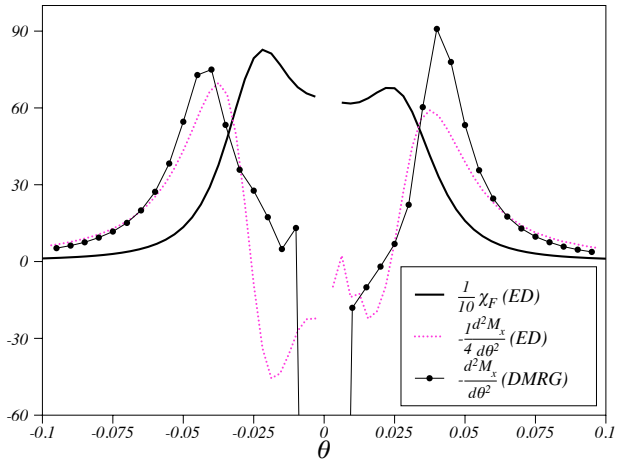

Figure 7.8: **Results for small chains** (ED, $N = 18$). Whereas χ_F shows only weak maxima, strong peaks appear in $\partial^2 M_x/\partial\theta^2$. These lie already at the location expected for large lattices (DMRG, $N = 60$). All quantities are rescaled to facilitate comparison of the peak locations.

the thermodynamic limit. The peaks in a finite system are precursors thereof. However, in the present system the divergence turns out to be relatively weak, which makes it difficult to extrapolate the exact critical point. The qualitative value, however, is consistent with the DMRG and iTEBD data for large systems. The second derivative of the energy has been proposed [414] as a substitute of the fidelity susceptibility to detect QPTs. In the present system, however, the energy is too smooth to indicate the crystal–SF transition well.

Instead, a convenient observable turns out to be the total magnetization. In Fig. 7.8, we compare χ_F to the second derivative of the total in-plane correlations

$$M_x \equiv \frac{2}{N\,(N-1)} \sum_{i \neq j} \left| \langle S_i^x S_j^x + S_i^y S_j^y \rangle \right| . \tag{7.24}$$

Here, we sum the absolute values of the correlations to account for the different staggered configurations occurring at different filling factors. $\partial^2 M_x/\partial\theta^2$ peaks at slightly larger absolute values of θ than χ_F, but the rough peak locations are consistent. We find that the second derivative of the total out-of-plane correlations $\sum_{i \neq j} \left| \langle S_i^z S_j^z \rangle \right|$ (not shown) peaks at θ's very similar to $\partial^2 M_x/\partial\theta^2$.

Finally, a comparison to the results from DMRG shows a very similar peak location, although in that case the peak is stronger due to the larger system size. This means that already at very small chains strong precursors of the QPT appearing in long chains can be observed.

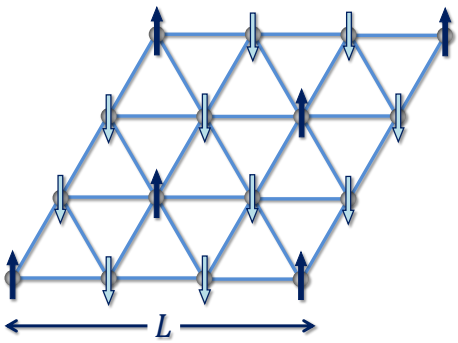

Figure 7.9: **Sketch of the triangular lattice** with the $\sqrt{3} \times \sqrt{3}$ Ising order associated to the crystal state at polarization $-1/6$ (1/3 filling). The state at polarization $+1/6$ can be visualized by interchanging $\uparrow$ and $\downarrow$ spins. These states are ground states at low tunneling.

7.8 Dipolar ions in 2D

In this section, we extend our analysis to dimensions larger than one. Concretely, we study Hamiltonian (7.1) on the two-dimensional triangular lattice (Fig. 7.9), since this is the natural configuration that trapped ions adopt in a Paul trap (see Fig. 2.3) with a strong planar asymmetry in the trapping potential [178].[3]

Studying higher dimensions is relevant for a variety of reasons. First, the influence of long-range interactions increases with dimensionality. As we saw, already in 1D dipolar terms strongly modify the phase diagrams of corresponding short-range models, potentially even leading to novel phases. We can assume that this is even more true in larger dimensions. For example, if long-range tunneling induces quasi-supersolids in 1D, we can expect that it may change dramatically the stability of two-dimensional supersolids. These appear, *e.g.*, in triangular lattices with NN tunneling at the transition between crystal and SF phases [399–402]. Moreover, 2D is computationally considerably more difficult than 1D (see our discussion on p. 12), making an experimental quantum simulation much more interesting. This is especially true if frustration comes into play, since it invalidates QMC, the method of choice for many 2D lattices. Above, we saw that already in 1D frustration has some effects; in 2D these should be strongly enhanced due to the increased number of interactions in higher dimensions. On the triangular lattice, which we are interested in this chapter, frustration is particularly strong due to the geometry (see also Chapter 3).

For experiments, an analysis of the finite-temperature behavior is especially important. First, this allows to judge the stability of the occurring phases

[3] But note also that in principle any geometry can be engineered in surface microtraps such as sketched in Fig. 2.4 [183].

towards thermal excitations that will be present in every realistic experimental realization. What is more, recently Peter and coworkers scanned the phase diagram of Hamiltonian (7.1) along the line $\mu = 0$ in a square lattice [415]; the authors found that above the SF on the FM side (*i.e.*, $\theta < 0$), the continuous U(1) symmetry of the off-diagonal correlations remains broken even at finite temperatures. Thus, the long-range nature of the tunneling leads to a phase that defies the Mermin–Wagner theorem [229].[4]

The computational method

To compute the phase diagram of Hamiltonian (7.1) on the triangular lattice, we use QMC codes from the ALPS library [407]. The algorithm works by sampling world lines in the path integral representation of the partition function in the grand canonical ensemble. Since the frustration of AFM XY interactions in the triangular lattice leads to a QMC sign problem, we can only access the FM side of the phase diagram. Here, we reproduce some of our results, focusing on a system of $N = L \times L = 6 \times 6$ sites, with L the linear dimension. All interactions are truncated at the fifth-nearest neighbor.[5] A more detailed analysis, including systems up to $L = 12$, can be found in Ref. [204].

We can expect a similar collection of quantum mechanical phases as in 1D, namely a SF at large tunneling and crystal states at low tunneling. Further, a supersolid phase is expected to occur in between them. To differentiate these phases, we analyze several order parameters for crystal and SF behavior. Crystal phases reveal themselves as plateaux in the polarization $\langle Z \rangle / N$, Eq. (7.2), and extensive peaks in the structure factor for diagonal (ZZ-) correlations,

$$S_{zz}(\boldsymbol{k}) = \frac{1}{N} \sum_{i,j} e^{-i\boldsymbol{k}\cdot(\boldsymbol{r}_i - \boldsymbol{r}_j)} \langle S_i^z S_j^z \rangle \ . \tag{7.25}$$

Here, we focus on the wave vector $\boldsymbol{k} = \boldsymbol{Q} = (4\pi/3, 0)$, which corresponds to the $\sqrt{3} \times \sqrt{3}$ order parameter that is associated with the crystal states at 1/3 and 2/3 filling (polarization $\pm 1/6$); see Fig. 7.9 for a sketch of this state. We compare $\langle Z \rangle / N$ and $S_{zz}(\boldsymbol{k})$ to the SF stiffness ρ_S, which is a measure for correlations in the XY plane. For hard-core bosons it is related to the spin stiffness of the corresponding spin model (see Chapter 3.2.5). In the QMC algorithm, it can be derived from the winding number of the world lines.

[4] The theorem remains valid, of course, as it applies only to short-range models.

[5] *I.e.*, not five lattice spacings in one direction but the fifth-nearest site in absolute distance.

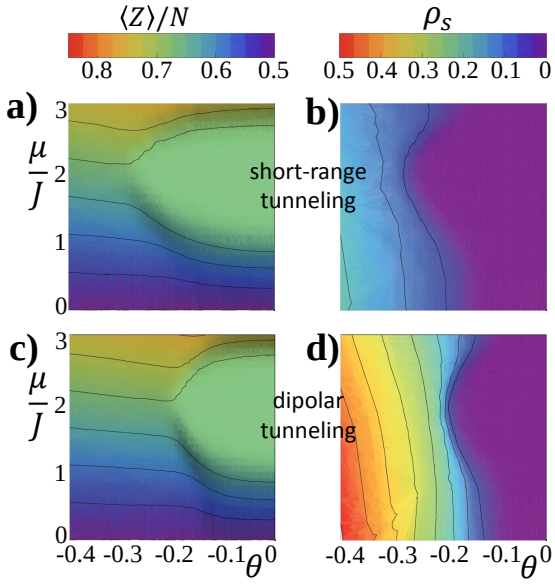

Figure 7.10: **Crystal lobes for the 2D triangular lattice** around polarization 1/6. **(a,c) Polarization** $\langle Z \rangle / N$, and **(b,d) SF stiffness** ρ_S. Dipolar XY interactions (c-d) destabilize the crystal phase compared to short-range XY interactions (a-b) (in both cases, the ZZ interactions are dipolar). The data are from QMC calculations for a $L \times L = 6 \times 6$ system.

The phase diagram

First, we consider the example of the FM 1/6-polarization crystal in the grand-canonical ensemble. We set $k_B T/J = 0.1$, which should be small enough to get an idea of the main ground-state characteristics. As Fig. 7.10 shows, compared to NN tunneling, dipolar tunneling destabilizes the crystal lobes of the devil's staircase. A comparison of different system sizes presented in Ref. [204] suggests that – compared to NN tunneling – this leaves more space for the supersolid phase that is known to exist next to the crystal lobe [399–402].

As emphasized in Chapter 1, a real-world QS always suffers from experimental imperfections. Particularly important are thermal excitations. To characterize the stability of the ground-state phases, we study how finite temperatures melt crystal and SF order [characterized by structure factor $S_{zz}(\boldsymbol{Q})$ and SF stiffness ρ_S, respectively]. Figure 7.11 shows cuts at θ fixed to around 80% of the tip of the crystal lobes. These cuts traverse all three important quantum phases, the SF (large μ; finite ρ_S), the crystal [intermediate μ; finite $S_{zz}(\boldsymbol{Q})$], and the supersolid [low μ; finite ρ_S and $S_{zz}(\boldsymbol{Q})$]. Both order parameters decrease more rapidly with T for short-range tunneling. This indicates that dipolar tunneling stabilizes all three kinds of ordered phases (SF, crystal, and supersolid).

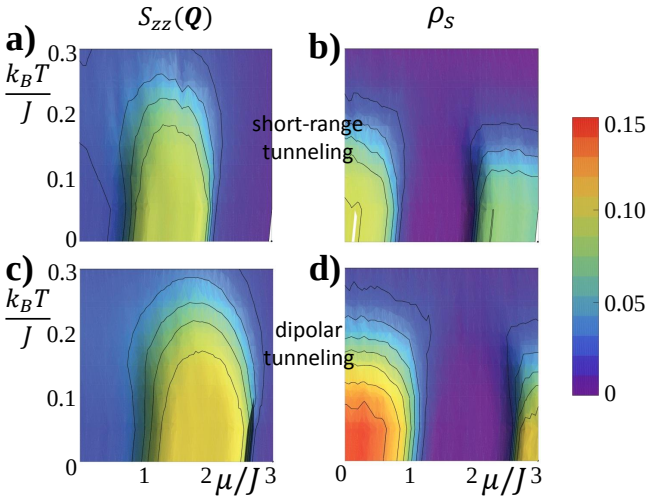

Figure 7.11: **Melting of SF-, crystal-, and supersolid order at finite temperature** k_BT/J. Data are from QMC calculations for a $L \times L = 6 \times 6$ system, comparing short-range (a-b) with dipolar (c-d) tunneling (in both cases, dipolar ZZ interactions). To facilitate comparison, the tunneling strength θ is chosen in both cases to lie at around 80% of the tip of the crystal lobes shown in Fig. 7.10 ($\theta = -0.23$ and -0.15, respectively). **(a,c) Structure factor of the $\sqrt{3} \times \sqrt{3}$ order,** $S_{zz}(\boldsymbol{Q})$, and **(b,d) SF stiffness** ρ_S**.** Dipolar XY interactions stabilize supersolid order compared to short-range XY interactions.

7.9 Summary

To summarize this chapter, we have studied a system of hard-core bosons where particles interact and tunnel at long distances with an algebraically decaying strength. We have discussed how the system can be mapped onto a spin Hamiltonian that can be simulated experimentally using trapped ions. Unlike other atomic QSs (such as dipolar ultracold atoms), trapped ions appear to be more flexible in the manipulation of some parameters – *e.g.*, the interactions and hoppings can be changed from negative to positive by addressing different vibrational modes of the ions.

In one dimension, the system we have studied has a rich phase diagram, with many insulating phases filled with (possibly long-lived) meta-stable states

and (quasi-)LRO in all correlations – two prominent features that are induced solely by the long-range nature of the interactions. The coexistence of diagonal LRO and off-diagonal quasi-LRO in the insulating lobes can be seen as a quasi-supersolid, the closest analogue to a supersolid that can be found in 1D.

Extending our results to a two-dimensional triangular lattice, QMC calculations indicate that the dipolar tunneling – compared to short-range tunneling – can stabilize true supersolids, in the ground state as well as at finite temperature. Long-range tunneling could therefore prove advantageous for an experimental realization of supersolidity in two-dimensional lattice systems.

Since calculations are more complicated for long-range interactions, one can consider the present model as a testbed for numerical tools. The accuracy of the standard PMFT proves insufficient, because it does not capture excitations beyond the single-particle level. ED, DMRG, and iTEBD, however, all deliver a consistent picture. Among these, DMRG is the method of choice for the model studied. However, it is restricted to finite systems. While iTEBD is less accurate and restricted to shorter range of interactions, it allows to investigate the thermodynamic limit directly. ED, finally, while being relevant only for small systems, can still serve for benchmarking other less accurate computational methods and near-future experiments. Despite the small sizes treatable in ED, it seems to correctly predict the location of quantum phase transitions.

In the future, it would be interesting to study other system properties that could be affected by the long-range nature of the interactions, such as response to excitations, dynamics of correlations, or possible changes in the universality class of the crystal–SF transition [416]. Further, in ion-trap experiments the precise decay exponent of the long-range interactions can be tuned (such that it differs from 3) [136]. A change of the exponent may drastically affect the ground-state phase diagram, in particular the frustration and supersolid effects it hosts. With decreasing decay exponent, one can expect a cross-over from weak long-range behavior to strong long-range physics.

Until now, we illustrated at several examples the variety of models that can be quantum simulated in trapped-ion and optical-lattice setups. In the next chapter, we will turn to a different issue. As we have seen at various places throughout this thesis, quantum phases (such as the supersolids encountered in this chapter) are fundamentally characterized by their correlations. Therefore, the ability to manipulate these correlations may be extremely useful for quantum simulation purposes. In the next chapter, we will present a possible scheme to engineer spin-correlation patterns in optical-lattice experiments.

Chapter 8

Quantum control of spin correlations in ultracold lattice gases

The preparation, manipulation, and detection of quantum correlations in strongly-correlated quantum many-body systems are fundamental to future applications of quantum physics, not only for quantum simulations, but also for quantum computation, communication, and metrology. As we have seen throughout this thesis, ultracold atomic gases trapped in optical lattices offer an unprecedented playground for studying such systems. In particular, quantum states of ultracold lattice gases with spin degrees of freedom may be used to simulate quantum magnetism (see Chapters 3 and 4), topological insulators (see Chapter 5), or quantum phases thought to be important in high-T_c superconductivity [4, 231, 417–419]. Considerable progress has been made towards engineering such systems, which is experimentally challenging because of the low temperatures involved [87]. Here, we propose an alternative, top-down approach to producing highly correlated quantum states using the tools of quantum spin polarization spectroscopy (SPS).

SPS has emerged as a promising technique for the *detection* of the quantum phases in lattice gases [420] via the coherent mapping of spin-correlations onto scattered light in a quantum non-demolition (QND) measurement. In particular, spatially-resolved SPS that employs standing-wave laser configurations [421] allows direct probing of magnetic structure factors and order parameters [153,

422–424].

In this chapter, we propose inverting the tools of spatially resolved SPS as a means of *preparing* strongly correlated states of lattice gases. For the manipulation of cold (and not-so-cold) atomic ensembles, SPS has proven to be an extremely successful tool. In particular, in recent years, spin-squeezing via SPS QND measurements has been demonstrated in several experiments [425–429]. These ideas where extended by Tóth and Mitchell [430], who proposed that such a spin squeezing can create macroscopic singlet states in clouds of ultracold atoms, which however, would be spatially featureless. Here, we suggest a simple modification of the detection scheme proposed by Eckert *et al.* [421] that would allow the preparation of quantum states with distinct correlation signatures. The proposed principle works in optical lattices with low particle number per site (such as filling-1 Mott-insulators), but – due to larger optical depths which allow stronger correlations – is especially suited to arrays of microtraps in which each trap holds a mesoscopic number of particles, such as in the experiments of G. Birkl's group in Darmstadt [431–433] or of T. Esslinger's group in Zürich [154].

Control over quantum correlations, and the order parameters associated with them, will be a central ingredient for a reliable performance of many-body quantum simulators. As seen in previous chapters, understanding the correlations of a strongly-correlated quantum system is crucial for mapping out its phase diagram and for tracking down exotic quantum phases.

In many situations, correlations decay exponentially – on a length scale given by the correlation length – towards a constant (the order parameter). Upon approaching a critical point, however, the correlation length diverges, and the decay becomes algebraic [434, 435]. Hence, distinguishing between exponential and algebraic decay allows to locate critical points, and studying *how* the correlation length diverges gives important insight about universal behavior close to them.

In this context, an especially interesting class of quantum phases are disordered ones where the order parameter vanishes and correlations decay to zero at large distances. In such a case, *algebraically decaying correlations* are related to gapless, and hence critical, systems, which are ubiquitous in 1D systems, but rare in 2D. *Exponentially decaying correlations*, on the other hand, signify completely disordered phases. In 2D spin systems, such phases are conjectured to appear in the vicinity of high-T_c superconducting phases [4, 231, 417–419]. These so called gapped spin-liquids have fractional excitations which could be useful as qubits for topological quantum computation [329]. As discussed in Chapter 3, there are paradigmatic magnetic models which might harbor such

exotic quantum phases, but it is far from clear under which general circumstances these states emerge in dimensions larger than one [231, 419]. Being able to manipulate the correlations in strongly-correlated quantum systems may allow the preparation of such interesting many-body states. These may then allow to directly study their properties or, by preparing correlations which closely resemble a desired final state, serve as a starting point to ramp into phases which are otherwise difficult to access. Further, a particular class of correlations, entanglement, is considered the fundamental resource in quantum computing [436].[1] Hence, manipulating correlations in the way proposed here may also offer a valuable tool for quantum information processing.

The rest of this chapter is organized as follows. In Sec. 8.1, we describe how the scheme can be implemented to create a desired spin correlation function. First, we show that a QND measurement with wavevector k_p induces spin squeezing in a single atomic mode with wavevector $2k_p$, while leaving the other modes almost unchanged (Sec. 8.1.1). Using this QND interaction, our strategy to imprint spin–spin correlations consists in letting a one-dimensional lattice gas interact with a series of such standing-wave light pulses that covers the first Brillouin zone (Sec. 8.1.2). We motivate that the outcome should be approximately given by the cosine Fourier transform of the atom–light couplings. These can be easily adjusted as demanded by altering the frequency or intensity of each probe pulse. We also derive formulas for decoherence due to spontaneous emission, indicating the robustness of the method (Sec. 8.1.3), and we introduce a witness appropriate for finding spatial patterns of entanglement (Sec. 8.1.4). Then, in Sec. 8.2, we compute the resulting spin correlations for several fundamental numerical examples that use the above strategy: First, we demonstrate that correlations with generic exponential or algebraic decay can be produced (Sec. 8.2.1). Then, in Sec. 8.2.2, we study two cases which are more specific, namely, correlations with the structure factor peaked at wave vectors $k = \pm 2\pi/3$ (similar to the critical phase of the bilinear-biquadratic Hamiltonian of a spin-1 chain), and correlations with a Gaussian peak at a predefined distance. These widely different examples show the flexibility of the proposed scheme. We finish the chapter in Sec. 8.3 with some summarizing remarks. The results presented here can be found in the preprint [444].

[1] But see also the very recent discussion about quantum discord [437, 438] that questions the essential role of entanglement [439, 440]. Some of the recent development is nicely reviewed in the Nature News Feature by Z. Meraly [441]. For some recent experiments, see [38, 442, 443].

8.1 Description of the scheme

To illustrate our proposed scheme, we consider the interaction of atoms, trapped in a one-dimensional optical-lattice potential, with a set of standing-wave pulses of near-resonant light with wave-numbers k_p. The atoms are described by collective variables

$$J_{\alpha,i} \equiv \sum_{m=1}^{N_\mathrm{a}} j_{\alpha,i}^{(m)} , \tag{8.1}$$

where the index m runs over the N_a atoms at lattice site i and $\alpha = x, y, z$ labels the components of the atomic spin operators with length j. For simplicity, we assume a fixed integer filling per site of N_a. Such a fixed filling is routinely produced by driving the atom–lattice system into the Mott-insulating phase as discussed in various examples of this thesis. With N_s lattice sites, the total number of atoms is $N_\mathrm{tot} = N_\mathrm{s} N_\mathrm{a}$. The photons are described by collective Stokes operators S_μ defined as

$$S_\mu \equiv \frac{1}{2} \left(\hat{a}_+^\dagger, \hat{a}_-^\dagger \right) \sigma_\mu \begin{pmatrix} \hat{a}_+ \\ \hat{a}_- \end{pmatrix} , \tag{8.2}$$

where the σ_μ are the Pauli matrices and $\hat{a}_\pm$ are annihilation operators for the spatial and temporal mode of the pulse with circular plus/minus polarization. We use the labels $\mu = 1, 2, 3$ to distinguish the Stokes operators from the atom spins, which are labeled with x, y, z.

8.1.1 Atom–light interaction, measurement, and feedback

The atom–light interaction for a single pulse is then described by the effective Hamiltonian [445, 446]

$$\hat{\mathcal{H}} = \Omega_p \sum_{i=1}^{N_\mathrm{s}} c_i(k_p) J_{z,i} S_3 , \tag{8.3}$$

where $c_i(k_p) = (1 + \cos(2k_p r_i))/2$ describes the standing-wave intensity profile and the coupling constants Ω_p are functions of the probe detuning and intensity (we work in units where $\hbar = 1$). Hamiltonian (8.3) describes a QND measurement that induces spin-squeezing of the J_z component of the collective atomic modes

$$J_\alpha(k) \equiv \frac{1}{\sqrt{N_\mathrm{s}}} \sum_{i=1}^{N_\mathrm{s}} J_{\alpha,i} \mathrm{e}^{ikr_i} \tag{8.4}$$

with $k = 0, \pm 2k_p$. For multi-level alkali atoms, this effective Hamiltonian can be synthesized using multicolor or dynamical-decoupling probing techniques [425, 447].

The aim of this chapter is to employ the interaction (8.3) to engineer spin–spin correlations in an ultracold lattice gas. We model the interaction using methods developed for treating the Gaussian dynamics of collective-variable systems [378, 448–450]. For this assumption to be valid, there has to be a large number of atoms in each mode.[2] The full system is then described by the operators $R_m(k) = \{J_x(k), J_y(k), J_z(k), S_1, S_2, S_3\}$ and the covariances

$$\Gamma_{mn}(k_1, k_2) \equiv \frac{1}{2}\langle R_m(k_1)R_n(k_2) + R_n(k_2)R_m(k_1)\rangle - \langle R_m(k_1)\rangle\langle R_n(k_2)\rangle\,. \quad (8.5)$$

(Under slight abuse of notation, the covariances involving the stokes operators S_μ drop the corresponding argument k.)

The dynamical equations for the covariances can be derived from the Heisenberg equation of motion for the operators, where, in the small-angle regime, an operator changes as

$$R_m(k)^{(\mathrm{out})} = R_m(k)^{(\mathrm{in})} - i\tau[R_m(k)^{(\mathrm{in})}, \hat{\mathcal{H}}]\,. \quad (8.6)$$

Here, τ is the photon transit time through the ensemble. We assume that the initial atomic state before the procedure is completely mixed, with covariances $\tilde{\Gamma}^{(0)}_{zz}(r_1, r_2) = \tilde{\Gamma}^{(0)}\delta_{r_1,r_2}$ where

$$\tilde{\Gamma}^{(0)} = \frac{N_\mathrm{a} j(j+1)}{3}\,. \quad (8.7)$$

(We distinguish covariances in the spatial domain with a tilde.) This also implies $\Gamma^{(0)}_{\alpha\beta}(k_1, k_2) = \tilde{\Gamma}^{(0)}\delta_{k_1,-k_2}\delta_{\alpha\beta}$, $\alpha, \beta = x, y, z$. Further, we assume that atomic and light variables are uncorrelated before the measurement. Then, for an input S_1-polarized pulse, the only covariances that change due to the pulse are

$$\Gamma^{(\mathrm{out})}_{z2}(k) = \frac{\kappa_p}{2\sqrt{j}}G^{(\mathrm{in})}_{zz}(k), \text{ and} \quad (8.8a)$$

$$\Gamma^{(\mathrm{out})}_{22} = \Gamma^{(\mathrm{in})}_{22} + \frac{\kappa_p^2}{8j}[2G^{(\mathrm{in})}_{zz}(0) + G^{(\mathrm{in})}_{zz}(2k_p) + G^{(\mathrm{in})}_{zz}(-2k_p)]\,, \quad (8.8b)$$

[2] This choice is for convenience of calculation. The scheme itself should also work outside of the Gaussian limit.

where we have introduced the coupling strength

$$\kappa_p = \tau\Omega_p S_1 \sqrt{\frac{N_s j}{S_0}}\,, \tag{8.9}$$

and where we have defined

$$G_{zz}(k) \equiv \Gamma_{zz}(0,k) + \frac{1}{2}\Gamma_{zz}(2k_p,k) + \frac{1}{2}\Gamma_{zz}(-2k_p,k)\,. \tag{8.10}$$

Detection of S_2 then transfers the correlations described in Eqs. (8.8) to the atoms. This can be modeled as a projection [430]

$$\Gamma^{(\mathrm{M})} = \Gamma^{(\mathrm{out})} - \Gamma^{(\mathrm{out})}(\Pi_2\Gamma^{(\mathrm{out})}\Pi_2)^{\mathrm{MP}}\Gamma^{(\mathrm{out})}\,, \tag{8.11}$$

where MP indicates the Moore–Penrose pseudoinverse and

$$\Pi_2 = \mathrm{diag}(0,0,0,0,1,0)\,. \tag{8.12}$$

After the measurement, the atomic covariances are

$$\Gamma^{(\mathrm{M})}_{\alpha\beta}(k_1,k_2) = \Gamma^{(\mathrm{out})}_{\alpha\beta}(k_1,k_2) - \frac{\Gamma^{(\mathrm{out})}_{\alpha 2}(k_1)\Gamma^{(\mathrm{out})}_{2\beta}(k_2)}{\Gamma^{(\mathrm{out})}_{22}}\,. \tag{8.13}$$

Since by virtue of Eq. (8.8a) only $\Gamma^{(\mathrm{out})}_{z2}(k)$ is finite, but not $\Gamma^{(\mathrm{out})}_{x2}(k)$ or $\Gamma^{(\mathrm{out})}_{y2}(k)$, the only atomic covariances changed by the interaction—measurement process are $\Gamma_{zz}(k_1,k_2)$. Further, the process is highly symmetric. In particular, it preserves the symmetries $\Gamma_{\alpha\alpha}(k,k') = \Gamma_{\alpha\alpha}(k,-k')$ for $k \neq k'$ and $\Gamma_{\alpha\alpha}(k,k') = \Gamma_{\alpha\alpha}(k',k)\ \forall k,k'$.

The orthogonal spin components $J_\alpha(2k_p)$ can be successively measured by coherently rotating the atomic spin between measurements. To allow the measurement-induced squeezing to be repeated for each spin component, we require $\langle J_\alpha(2k_p)\rangle = 0$, which allows us to avoid measurement-induced back-action due to the Heisenberg uncertainty relation

$$\Gamma_{\alpha\alpha}(k_1,k_1)\Gamma_{\beta\beta}(k_2,k_2) = (\Delta J_\alpha(k_1))^2(\Delta J_\beta(k_2))^2 \geq \varepsilon_{\alpha\beta\gamma}\tfrac{1}{4N_s}|\langle J_\gamma(k_1+k_2)\rangle|^2\,. \tag{8.14}$$

To obtain $\langle J_\alpha(2k_p)\rangle = 0$, the result of the measurement of S_2 can be used as the input to an optical pumping feedback process: a weak pulse of near-resonant light at wavevector k_p with an intensity proportional to $S_2^{(\mathrm{out})}$ will set

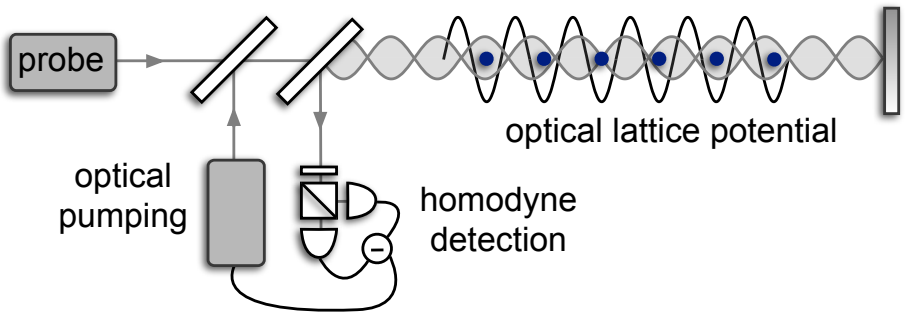

Figure 8.1: **Proposed experimental set-up.** Atoms (blue bullets) trapped in an optical lattice (black) are probed with a far-detuned, linearly-polarized standing-wave light pulse with wavevector k_p. Afterwards, the probe beam is outcoupled to a detector, where S_2 is recorded. A projection-noise-limited measurement induces spin squeezing, introducing quantum correlations among the atoms in spatial mode $k = 2k_p$. Feedback is applied via optical pumping with the same wavevector k_p to set the ensemble-average magnetization in that spatial mode to zero. Successive spin components J_α can then be separately measured by coherently rotating the atomic spin between measurements. The procedure is repeated for a set of wavevectors k_p, with interaction strengths weighted by the corresponding amplitude of the cosine Fourier transform of the desired spatial correlation signature.

$\langle J_z(2k_p) + J_z(-2k_p)\rangle = 0$, and a second pulse with a half-period phase shift sets $\langle J_z(2k_p) - J_z(-2k_p)\rangle = 0$, so that $\langle J_z(2k_p)\rangle = \langle J_z(-2k_p)\rangle = 0$. As shown by Tóth and Mitchell [378], and as discussed in Sec. 8.1.3 below, this feedback introduces spin noise that is negligible in the thermodynamic limit.[3]. We summarize this interaction—measurement—feedback procedure in Fig. 8.1.

[3] Alternatively, data with small $\langle J_\alpha(2k_p)\rangle$ $\forall k_p$ could be post-selected based on the measurement outcomes.

8.1.2 Strategy for quantum correlation engineering

Our aim is to use the interaction (8.3) to systematically manipulate the spin–spin correlation function

$$\begin{aligned}\tilde{\Gamma}_{\alpha\alpha}(r_1,r_2) &\equiv \langle J_\alpha(r_1)J_\alpha(r_2)\rangle - \langle J_\alpha(r_1)\rangle\langle J_\alpha(r_2)\rangle \\ &= \frac{1}{N_\mathrm{s}}\sum_{k_1,k_2=1}^{N_\mathrm{s}} \mathrm{e}^{ik_1r_1}\mathrm{e}^{ik_2r_2}\Gamma_{\alpha\alpha}(k_1,k_2)\,,\end{aligned} \tag{8.15}$$

where we label the k-vectors covering the first Brillouin zone $]-\pi,\pi]$ from 1 to N_s. Indeed, such a spatial dependence of the correlations can be transferred from the probe beams to the atoms due to the $c_i(k_p)$ term in the atom–light Hamiltonian (8.3). Equations (8.8) and (8.13) imply that the covariances of a given collective mode $J_\alpha(k)$ are only altered after a pulse with $k = 2k_p$ has been applied. This suggests that we can manipulate $\tilde{\Gamma}_{\alpha\alpha}(r_1,r_2)$ with a sequence of pulses with wavevectors $2k_p$ that cover the first Brillouin zone. Now, we show that this can be done by an appropriate choice of coupling constants κ_p.

From our assumption that the initial state is completely mixed, we have initially $\Gamma^{(0)}_{zz}(k_1,k_2) = \tilde{\Gamma}^{(0)}\delta_{k_1,-k_2}$. After the pulse with $2k_p$ has passed, Eqs. (8.8) and (8.13) create strong correlations for the mode $2k_p$ only for $\Gamma_{zz}(2k_p,0)$, $\Gamma_{zz}(2k_p,2k_p)$, and $\Gamma_{zz}(2k_p,-2k_p)$. The correlations to the zero mode will in later pulses also create correlations to other modes. These are small, however, and for the sake of deriving a suitable strategy, we can neglect all covariances $\Gamma_{\alpha\alpha}(k_1,k_2)$ with $k_2 \neq \pm k_1, 0$. Then, Eq. (8.15) becomes

$$\begin{aligned}\tilde{\Gamma}_{zz}(r_1,r_2) &\approx \frac{1}{N_\mathrm{s}}\Gamma_{zz}(0,0) + \frac{2}{N_\mathrm{s}}\sum_p \left[\cos(2k_pr_1)+\cos(2k_pr_2)\right]\Gamma_{zz}(2k_p,0) \\ &+ \frac{2}{N_\mathrm{s}}\sum_p\big[\cos(2k_p(r_1+r_2))\Gamma_{zz}(2k_p,2k_p) \\ &\qquad + \cos(2k_p(r_1-r_2))\Gamma_{zz}(2k_p,-2k_p)\big]\,.\end{aligned} \tag{8.16}$$

The spatial dependence is strongly dominated by the $\Gamma_{zz}(2k_p,-2k_p)$ term, which, after the pulse with k_p, becomes $\Gamma^{(\mathrm{out})}_{zz}(2k_p,-2k_p) = \tilde{\Gamma}^{(0)}(1-f_p/4)$, where we define the scaled coupling constants

$$f_p \equiv \frac{\kappa_p^2\tilde{\Gamma}^{(0)}}{4j\Gamma^{(\mathrm{out})}_{22}}\,. \tag{8.17}$$

Focusing only on the dominating $\Gamma_{zz}(2k_p, -2k_p)$ term, Eq. (8.16) becomes then

$$\tilde{\Gamma}_{zz}(r_1, r_2) \approx \frac{\Gamma_{zz}(0,0)}{N_\mathrm{s}} + \frac{2}{N_\mathrm{s}} \sum_p \cos(2k_p(r_1 - r_2))\tilde{\Gamma}^{(0)} \left(1 - \frac{f_p}{4}\right) \tag{8.18}$$

in which spatial dependence is given by the final term, which, if the k_p cover the first Brillouin zone, is the cosine Fourier transform of the f_p.

This suggests the following strategy for manipulating the spin–spin correlations $\tilde{\Gamma}_{zz}(r_1, r_2)$: Let

$$\tilde{\Gamma}_{zz}(r_1, r_1 + \delta r) = C_\mathrm{des}(\delta r) \tag{8.19}$$

be the desired output correlation signature. To determine the coupling strength κ_p that should be used for each wavevector k_p in order to create $C_\mathrm{des}(\delta r)$, we approximate f_p in Eq. (8.17) by the inverse cosine Fourier transform of $-4C_\mathrm{des}(\delta r)/\tilde{\Gamma}^{(0)}$, $f_p \to f_p(C_\mathrm{des})$. Further, in Eq. (8.17), in the expression for $\Gamma_{22}^{(\mathrm{out})}$, Eq. (8.8b), we replace the covariances $\Gamma_{zz}(k_1, k_2)$, with the completely mixed values $\tilde{\Gamma}^{(0)}$. *A posteriori*, we find that both approximations are valid for realistic experimental parameters. Now, we can solve Eq. (8.17) for κ_p, which yields

$$\kappa_p = 2\sqrt{j} \sqrt{\frac{\Gamma_{22}^{(\mathrm{in})} f_p(C_\mathrm{des})}{1 - g_p \tilde{\Gamma}^{(0)} f_p(C_\mathrm{des})}} \tag{8.20}$$

where $g_p = \frac{9}{2}$ for $k_p = 0$ and $g_p = \frac{3}{2}$ otherwise.

To create $C_\mathrm{des}(\delta r)$ in this way, the coupling strengths κ_p can be adjusted experimentally by choosing detuning Δ, intensity, and duration of the pulse appropriately. In fact, $\kappa_p = \sqrt{N_\mathrm{tot} N_\mathrm{ph} \sigma \gamma / A\Delta}$, where σ is the on-resonance cross section for the probe transition, γ the spontaneous decay rate, and A the cross section of the atomic ensemble illuminated by the probe. With a finite on-resonance optical depth d_op, κ_p is related to the probability of spontaneous emission η_p via $\kappa_p = \sqrt{d_\mathrm{op}\eta_p}$,[4] giving a trade-off between coupling strength and decoherence.

The approximations made for arriving at our strategy (8.20) apply for not too strong couplings. Below, we demonstrate that these are sufficient to create clearly distinguishable correlation patterns. The general idea remains valid also for larger couplings, but then, because one has to keep track of the changing

[4] This relationship is strictly true only for $j = 1/2$. For $j = 1$, if the near-resonant intermediate state has $j = 0$, one has to include a correction factor, $\kappa_p = \sqrt{\frac{9}{8} d_\mathrm{op}\eta_p}$ [451].

correlations over the course of the pulse sequence, the relation between the κ_p and $C_{\mathrm{des}}(\delta r)$ is less intuitive. Also, for given optical depth d_{op}, a larger coupling $\kappa_p = \sqrt{d_{\mathrm{op}}\eta_p}$ can only be achieved on the expense of an increased probability of resonant excitation η_p, hence increasing decoherence due to spontaneous emission. The balance between created correlations and decoherence sets the optimum detuning and intensity of the pulses to achieve maximum spin squeezing. We turn to discussing the influence of decoherence in the next section.

8.1.3 Influence of decoherence

In realistic experimental situations, the atoms will get partially excited by the off-resonant laser beam, which leads to decoherence due to spontaneous emission, thus reducing correlations. Following Refs. [430, 445, 449, 450], we consider this as the only decoherence mechanism.

Other decoherence processes include noise introduced by the feedback, which, however, can be neglected as shown by Tóth and Mitchell [430]. For setting $\langle J_\alpha(k)\rangle$ to zero, on the order of $\sim\sqrt{N_{\mathrm{tot}}}$ atoms are affected, introducing extra noise $(\Delta J_\alpha(k))^2 \sim \sqrt{N_{\mathrm{tot}}}$. In the limit of large total atom number N_{tot}, this is negligible relative to the initial noise of $\sim N_{\mathrm{tot}}$ [452]. One could also, instead of feedback, use post-selection to identify cases with low $\langle J_\alpha(k)\rangle$. Alternatively, since feedback introduces the same type of error due to spontaneous emission as the probe pulses, it could be taken into account effectively by renormalizing the probability of resonant excitation η.

To derive an approximate formula describing the effect of spontaneous emission on the covariances, we assume conservatively that, when an atom scatters a photon, the atom ends up in a completely mixed state. Decoherence is a Gaussian process, and, as shown by Giedke and Cirac [453], we can include the entire decoherence suffered during a pulse by simply applying its total effect to the output covariances $\Gamma_{\alpha\alpha}(k_1,k_2)$. After a single scattering event, their change can be written as

$$\begin{aligned}\Gamma_{\alpha\alpha}(k_1,k_2)^{\mathrm{sc}\,1} &= \left(1-\frac{2}{N_{\mathrm{tot}}}\right)\Gamma_{\alpha\alpha}(k_1,k_2) \\ &\quad + \frac{1}{N_{\mathrm{s}}}\gamma^{\mathrm{mix}}\delta_{k_1,-k_2} + \frac{1}{N_{\mathrm{s}}N_{\mathrm{tot}}}\sum_{l=1}^{N_{\mathrm{s}}}\sum_{m=1}^{N_{\mathrm{a}}} \mathrm{e}^{i(k_1+k_2)r_i}\gamma_{\alpha,l}^{(m)}\,.\end{aligned} \tag{8.21}$$

Here, $\gamma_{\alpha,l}^{(m)} = \langle (j_{\alpha,l}^{(m)})^2\rangle - \langle j_{\alpha,l}^{(m)}\rangle^2$ denotes the covariance of the α'th spin component of atom m at site l before the scattering event, and γ^{mix} is the correspond-

ing covariance in a completely mixed state. In Eq. (8.21), we took the mean over all atoms m residing at site l, as well as over all sites l.

The following equations are greatly simplified if we assume that the individual covariances before the scattering are close to the mixed ones, *i.e.*, $\gamma_{\alpha,l}^{(m)} \approx \gamma^{\mathrm{mix}}$. Then, Eq. (8.21) becomes

$$\Gamma_{\alpha\alpha}(k_1,k_2)^{\mathrm{sc}\,1} \approx \left(1-\frac{2}{N_{\mathrm{tot}}}\right)\Gamma_{\alpha\alpha}(k_1,k_2)+\frac{2}{N_{\mathrm{s}}}\gamma^{\mathrm{mix}}\delta_{k_1,-k_2}\,. \tag{8.22}$$

After n scattering events [*i.e.*, inserting Eq. (8.22) into itself $n-1$ times], the covariances read

$$\Gamma_{\alpha\alpha}(k_1,k_2)^{\mathrm{sc}\,n} \approx \left(1-\frac{2}{N_{\mathrm{tot}}}\right)^{n}\Gamma_{\alpha\alpha}(k_1,k_2)+\sum_{i=0}^{n-1}\left(1-\frac{2}{N_{\mathrm{tot}}}\right)^{i}\frac{2}{N_{\mathrm{s}}}\gamma^{\mathrm{mix}}\delta_{k_1,-k_2}\,. \tag{8.23}$$

Setting $n = \eta N_{\mathrm{tot}}$, *i.e.*, defining η as the fraction of excited atoms, and taking the limit $N_{\mathrm{tot}} \to \infty$, we arrive at

$$\Gamma_{\alpha\alpha}(k_1,k_2)^{\mathrm{sc}\,\eta N_{\mathrm{tot}}} \approx \mathrm{e}^{-2\eta}\Gamma_{\alpha\alpha}(k_1,k_2)+\left(1-\mathrm{e}^{-2\eta}\right)N_{\mathrm{a}}\gamma^{\mathrm{mix}}\delta_{k_1,-k_2}\,. \tag{8.24}$$

With $N_{\mathrm{a}}\gamma^{\mathrm{mix}} = \tilde{\Gamma}^{(0)}$, and in the limit of $\eta \to 0$, this becomes

$$\Gamma_{\alpha\alpha}(k_1,k_2)^{\mathrm{sc}\,\eta N_{\mathrm{tot}}} \approx (1-2\eta)\,\Gamma_{\alpha\alpha}(k_1,k_2)+2\eta\tilde{\Gamma}^{(0)}\delta_{k_1,-k_2}\,, \tag{8.25}$$

generalizing Eq. (20) from the work by Tóth and Mitchell [430] to a many-mode system with several atoms at each site.

One way to reduce decoherence would consist in increasing the total atom number. This increases the optical depth, thus allowing larger detuning which in turn reduces spontaneous emission. Alternatively, one could counteract decoherence by adjusting the coupling strengths κ_p, *e.g.*, by inducing stronger correlations at those k-components which suffer stronger decoherence.

8.1.4 Entanglement witness

A special kind of correlations, entanglement is considered an indispensable resource for quantum information processing [436] and is of great importance in quantum many-body systems [454–457]. To show that our proposal can create such quantum correlations, we now derive an entanglement witness for the multimode spatial correlations. For single spatial modes, spin squeezing is related to entanglement via spin squeezing inequalities [458–460], which have been generalized to treat unpolarized ensembles with $\langle J_\alpha\rangle = 0$ in Refs. [461–463].

Generalizing the strategy of Refs. [464, 465], we use the witness

$$\mathcal{W} \equiv \frac{w}{N_\mathrm{a}} - 1\,, \tag{8.26}$$

such that $\mathcal{W} < 0$ implies entanglement. Here, we define

$$w \equiv \sum_{\alpha=x,y,z} \sum_{i,j=1}^{N_\mathrm{s}} \langle J_{\alpha,i} J_{\alpha,j} \rangle f^*(r_i) f(r_j)\,, \tag{8.27}$$

where $f(r_i)$ is any normalized function

$$\sum_{i=1}^{N_\mathrm{s}} |f(r_i)|^2 = 1\,. \tag{8.28}$$

The feedback procedure sets $J_z(2k_p) = 0$ for all modes k_p, which ensures also $\langle J_{\alpha,i} \rangle = 0$, $\forall i$. Hence, we can replace $\langle J_{\alpha,i} J_{\alpha,j} \rangle$ by the covariances $\tilde{\Gamma}_{\alpha\alpha}(r_1, r_2)$, Eq. (8.15), so that $\mathcal{W}$ serves as an entanglement witness for multimode spatial correlations in our scheme. The definition of $\mathcal{W}$ encompasses and generalizes the plane waves described in Refs. [464, 465], and allows us to calculate the entanglement witness $\mathcal{W}$ as a function of spatial separation, which may be of general interest outside this particular example.

8.2 Numerical results

We illustrate our proposed technique for quantum correlation engineering by computing the mean spatial correlations for a 1D chain of spin $j = 1$ atoms with $N_\mathrm{s} = 200$ sites and $N_\mathrm{a} = 10$ atoms per site. Note that the same results generalize to a single atom per site, as long as we bin the chain into N_s bins with N_a atoms per bin, and redefine the coupling constant κ_p as an average over the N_a atoms in each bin.

This latter situation is relevant to the bilinear-biquadratic Hamiltonian, which has a rich phase diagram displaying ferromagnetic, critical, dimerized, and Haldane phases, each with distinctive spatial correlation signatures [466–473]. There have been ideas to quantum simulate this model with spin-1 bosons in an optical lattice [470, 472], and De Chiara, Romero-Isart, and Sanpera [424] proposed an interesting procedure to measure its phases using polarization spectroscopy. Its experimental realization remains still elusive, however, since it requires extremely low temperatures and a careful engineering of the many-body Hamiltonian. To prepare the phases appearing in the bilinear-biquadratic

Hamiltonian, it could prove advantageous to start from states which already have correlations close to the phase under consideration. These correlations could be prepared using our scheme.

While ferromagnetic phases are well-studied and -understood, a preparation of the other phases of the bilinear-biquadratic Hamiltonian seems much more interesting: the Haldane phase is a paradigmatic example of a topological phase [466], and the dimerized and critical phases have long eluded a clear classification of their phase boundaries and ground-state behavior [471, 473]. The Haldane and dimer phases are gapped, having exponentially decaying, antiferromagnetic spin–spin correlations. The critical phase, on the other hand, has an overall algebraic decay, with a structure factor peaked at $k = \pm 2\pi/3$ [468, 469], leading to characteristic period-three oscillations [467].

In the following, we want to compute mean correlations for cases which are of general interest but in particular relevant to this bilinear-biquadratic Hamiltonian. To probe the spatial dependence of the induced entanglement, we calculate the witness $\mathcal{W}$ between two sets of lattice bins $r_{s=1\ldots m}$ and $r_{w=1\ldots n}$ separated by a distance δr using the function

$$f(r_i) = \begin{cases} 1 & \text{if } r_i \in r_s, \\ \exp(i\phi) & \text{if } r_i \in r_w, \\ 0 & \text{otherwise.} \end{cases} \tag{8.29}$$

For given δr, $\mathcal{W}$ can then be minimized with respect to ϕ.

8.2.1 Generic examples: exponential and algebraic decay

First, we demonstrate the preparation of spin correlations $C_{\mathrm{des}}(\delta r)$ with:

(a) An exponential decay $\mathrm{e}^{-r/\xi}$ with a correlation length ξ, corresponding to gapped phases; these are, amongst others, relevant to gapped spin liquids (see Chapter 3).

(b) An algebraic decay $r^{-\zeta}$, corresponding to critical phases and quantum critical points.

We illustrate case (a) with $\xi = 5$ and case (b) with $\zeta = 0.7$. We compute the f_p corresponding to $C_{\mathrm{des}}(\delta r)$ as described in Eq. (8.20), apply the pulses in sequence to the atoms, and compute the resulting real-space spin-correlations after all pulses have been applied,

$$C(\delta r) = \frac{1}{N_{\mathrm{s}}/4} \sum_{i=1}^{N_{\mathrm{s}}/4} \sum_{\alpha=x,y,z} \frac{\tilde{\Gamma}_{\alpha\alpha}(r_i, r_i + \delta r)}{\tilde{\Gamma}^{(0)}} \,. \tag{8.30}$$

Since the correlations are symmetric with respect to the center of the lattice, we restrict the sum to $N_\mathrm{s}/4$. The only remaining free parameter is then the maximum coupling strength $\max_p\{\kappa_p\}$, which we set to ≈ 0.95, ensuring that the approximations suggesting the used coupling strengths (8.20) are valid. This is a conservative choice: we could increase κ_p and calculate the f_p taking into account the change in the covariances $\Gamma_{zz}(k_1, k_2)$ after each pulse in the sequence. We then calculate the correlations for $d_\mathrm{op} = 33, 99, 300$, varying the decoherence at fixed k_p, and compare this to the decoherence-free case with $d_\mathrm{op} = \infty$.

Since the pulses which are applied first suffer decoherence from subsequent pulses, the order of the pulses matters, although the overall behavior is relatively robust in this respect. We find that the optimal order can be different for different patterns of desired correlations. Here, we use for the exponential decay the sequences $k_p = \frac{p\pi}{N_\mathrm{s}}$, $p = 1, \ldots, \frac{N_\mathrm{s}}{2}$ and for the algebraic decay $k_p = \frac{\pi}{2} - \frac{(p-1)\pi}{N_\mathrm{s}}$, $p = 1, \ldots, \frac{N_\mathrm{s}}{2}$.[5] We consider only positive k_p, which is sufficient due to symmetry reasons. In all the cases we consider here, since squeezing the zero-mode only introduces a constant shift of the correlations but no spatial pattern, we exclude it from the k_p sequences. Furthermore, since many Fourier transforms are strongly peaked, in practice one could neglect k-modes with little weight.

The exponential and algebraic decay signatures produced this way are clearly distinguishable in Fig. 8.2, and, at large optical depths, fits to the desired correlation signature $C_\mathrm{des}(\delta r)$ (green dashed lines) coincide well with the data points (blue). For case (a), moreover, the exponential decay is maintained over several orders of magnitude. Here, fits to the short-range behavior yield the correlation lengths $\xi = 8.4, 6.9, 5.7, 5.1$ corresponding to $d_\mathrm{op} = \infty, 300, 99, 33$, which are sufficiently close to the desired value $\xi = 5$, considering the simplicity of our strategy. For case (b), a clear algebraic decay is seen with a fitted $\zeta \approx 0.4$. Deviations from the desired parameters induced by finite optical depths could be further compensated by adjusting the κ_p appropriately. For both cases (a) and (b), we checked that an exponential (algebraic) fit performs better for a desired exponential (algebraic) decay, demonstrating that the class of correlations can be engineered as desired. In the insets, we have subtracted the constant base line $b \equiv C(\delta r \to \infty)$ from the correlations, b, in order to exhibit the pure exponential and algebraic decay, respectively. In the corresponding log–linear and log–log plots, these should thus yield straight lines. The reason for the (seemingly)

[5] The chosen k_p-modes induce correlations which correspond to periodic boundary conditions of the chain. As implied by Weyl's theorem, the precise form of boundary conditions does not play any role in the limit of large lattices [474].

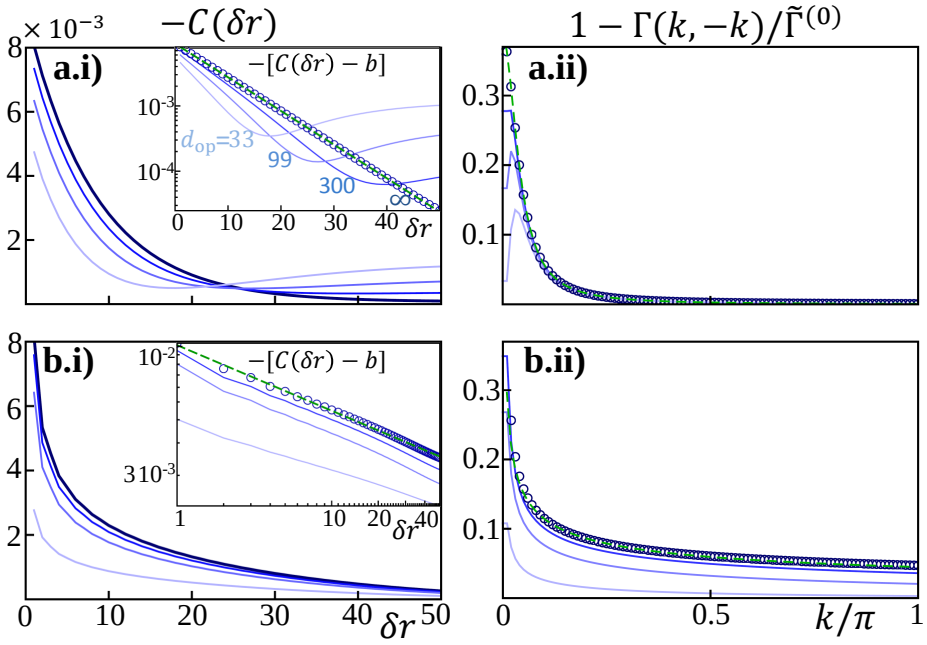

Figure 8.2: **Numerical results for two generic examples, (a) exponential decay, and (b) algebraic decay. (i) First column:** After the procedure, $C(\delta r)$ follows the desired pattern $C_{\rm des}(\delta r)$. The lines from darker to brighter shades of blue are for $d_{\rm op} = \infty$, 300, 99, and 33. In some cases, the $d_{\rm op} = \infty$ data is plotted as circles to facilitate comparison to fits (green dashed lines). The insets in (a.i) and in (b.i) are log-linear and log-log plots, respectively, where for clarity we subtracted $b \equiv C(\delta r \to \infty)$, extracted from a fit. For (a), without decoherence, the decay follows an exponential fit. For finite decoherence ($d_{\rm op} < \infty$), $C(\delta r \to \infty)$ cannot be reliably determined, yielding deviations from straight lines. For (b), the curves are straight lines for all values of $d_{\rm op}$, and algebraic fits are very accurate. **(ii) Second column:** The covariances $\Gamma(k,-k)$ follow the Fourier-transform of the desired correlation signature $C_{\rm des}(\delta r)$, even for small $d_{\rm op}$. Deviations occur primarily only at small k where the pulse strength κ_p is high.

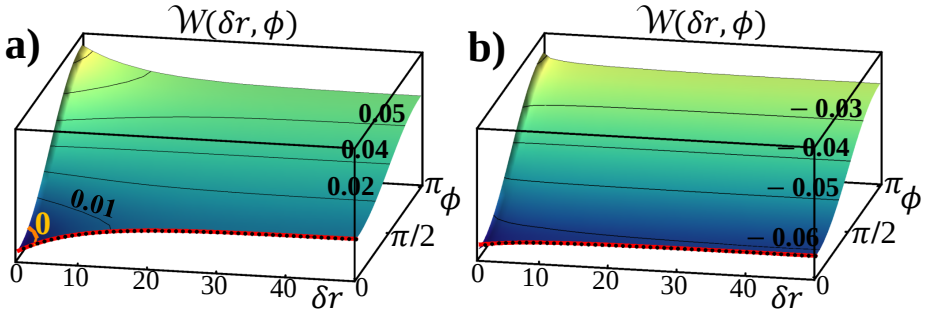

Figure 8.3: **Entanglement witness for (a) exponential decay, and (b) algebraic decay.** In both cases $\mathcal{W}(\delta r, \phi) < 0$ can be achieved, which witnesses non-classical correlations. In (a) and (b), the red lines are fits to $\mathcal{W}(\delta r, 0)$ [(a) exponential, (b) algebraic; data: black points], showing that the spatial decay of entanglement behaves as the total correlations. The orange contour line in (a) marks $\mathcal{W}(\delta r, \phi) = 0$.

non-monotonic curves in the inset of (a.i) is that finite decoherence deteriorates the correlations at large distances, which makes it difficult to reliably extract the extremely small base line b.

The real-space correlation signature can also be extracted by fitting the Fourier transform of $C_{\mathrm{des}}(\delta r)$ to the covariances $\Gamma(k, -k)$, which are the observables that are measured and manipulated in the experiment. This is illustrated in the second column of Fig. 8.2. The corresponding fits for $d_{\mathrm{op}} = \infty$ are shown as green lines, demonstrating that the data points follow the ideal cosine-Fourier functions of $C^{\mathrm{des}}(\delta r)$ closely. The parameters extracted from these fits are very close to those found in the spatial domain and to the desired results.

In Fig. 8.3, the entanglement witness $\mathcal{W}$, calculated for a single bin entangled with a chain of 106 bins, is shown for the two cases (a) and (b). In both cases, $\mathcal{W}$ is minimized for $\phi = 0$, where it decays exponentially (algebraically) with δr, thus following the spatial behavior of the total correlations. The entanglement is considerably stronger for algebraic decay.

8.2.2 Specific examples: period-three critical phase, Gaussian peak

So far, we discussed numerical results for two quite generic cases. Now, we demonstrate that our scheme also works in more specific situations. The case

(a) treated above can be easily extended to generate *antiferromagnetic* spin–spin correlations dressed with an overall exponential decay, as occurring in the Haldane and dimer phases of the bilinear-biquadratic Hamiltonian. To this, one has to simply use for the coupling strengths a Lorentzian centered at $k = \pi$ (or, to include algebraic corrections, the square-root of a Lorentzian).

Here, we are more interested in the critical phase of this Hamiltonian, with its overall algebraic decay and a structure factor which is peaked at $k = \pm 2\pi/3$ [468, 469], leading to characteristic period-three oscillations [467]. Heuristically, we model this structure factor using the functional form

$$f_p \propto \sqrt{\frac{2}{\pi}}\mathcal{E}(1-\zeta)\sin\left(\frac{\pi\zeta}{2}\right)\left(\left|2k_p - \frac{2\pi}{3}\right|^{-1+\zeta} + \left|2k_p - \frac{4\pi}{3}\right|^{-1+\zeta}\right). \tag{8.31}$$

Here, $\mathcal{E}$ is the Euler gamma function. The cosine Fourier transform of the function (8.31) has two parts, one decaying as $1/\delta r^2$ and one decaying as $\cos(2\pi\delta r/3)/\delta r^\zeta$. For $\zeta < 2$, this second term dominates at large distances δr and produces the desired algebraic decay with period-three oscillations. The form (8.31) is chosen to resemble the structure factor at the Lai–Sutherland point of the bilinear-biquadratic model [468, 469].

As seen in Fig. 8.4(a.i), the resulting real-space correlations (for the input value $\zeta = 1.1$) display the characteristic period-three oscillations as desired. To be more quantitative, we fit a function $\frac{a}{\delta r^2} + \frac{b\cos(p\delta r+\varphi)}{\delta r^\zeta} + c$ to the correlations $C(\delta r)$. The best fit (green dashed line) yields the desired values for the period ($p = \frac{2\pi}{3}$), the phase ($\varphi = 0$), and the exponent ($\zeta = 1.11$), thus perfectly reproducing the desired result. Similarly, after the procedure, $\Gamma(k, -k)$ reproduces the desired functional form of the structure factor, as displayed in Fig. 8.4(a.ii).

Finally, we want to show that our scheme can even produce exotic real-space correlations without known parallels in many-body systems. For example, we can create correlations which are peaked at a predefined distance. This might be useful for quantum information tasks such as state-preparation protocols or the creation of localizable entanglement between distant qubits [457], usable for teleportation. As an example, we shape the coupling strengths as the Fourier transform of a Gaussian $\frac{1}{\sqrt{\Delta r}}\exp\left(-[(\delta r - r_0)/\Delta r]^2\right)$ centered at a distance $r_0 = 20$ with a small variance ($\Delta r = 2$). The result, shown in Fig. 8.4b, is – besides the appearance of higher harmonics around $\delta r \approx 40$ – a Gaussian peak centered at $\delta r = 19.95$ with a width of $\Delta r = 2$, thus accurately reproducing the desired result.

For the examples considered in this section, we used $d_{\text{op}} = \infty$ with, for the algebraic period-three decay, the sequence $k_p = \frac{p\pi}{N_s}$, $p = 1, .., \frac{N_s}{2}$, and, for the Gaus-

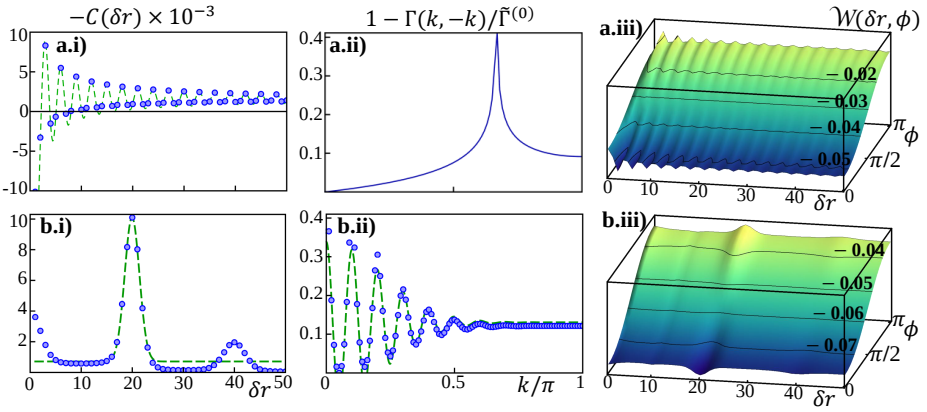

Figure 8.4: **Specific numerical examples, (a) period-three oscillations with algebraic decay, (b) Gaussian peak. (i) First column:** The real-space correlations reproduce the desired form. Fits (green dashed lines) yield (a) period-three oscillations with an overall algebraic decay, $(\cos(\frac{2\pi}{3}-\delta r))/\delta r^{\zeta}$, with $\zeta = 1.1$, and (b) a Gaussian at $\delta r = 19.95$ with width $\Delta r = 2$. **(ii) Second column:** The k-space correlations follow the desired pattern given by the coupling strengths. **(iii) Third column:** The witness $\mathcal{W}(\delta r,\phi)$ proofs entanglement. At $\phi = 0$, its spatial signature follows the total real-space correlations.

sian peak, interlaced rising and falling sequences, $\left\{\frac{\pi}{N_s}+\frac{2(p-1)\pi}{N_s},\frac{\pi}{2}-\frac{2(p-1)\pi}{N_s}\right\}$, $p = 1,..,\frac{N_s}{4}$. Here, we should note another subtlety which is relevant for these examples: the cosine-Fourier transform can attain negative values. Since a negative coupling κ_p is non-physical, we use in such cases a constant off-set which shifts all couplings κ_p to non-negative values. This does not change the correlation pattern, since the Fourier transform of a constant is a delta function at the origin, thus only influencing the correlations between atoms on the same site.

For both of these examples, the witness $\mathcal{W}(\delta r,\phi)$ proofs for all values of ϕ entanglement between the single bin and the 106 reference bins. The spatial signature again follows the total real-space correlations. The magnitude is comparable to the purely algebraic decay, case (b) from Sec. 8.2.1. Notably, the perhaps most exotic correlation pattern, the Gaussian peak, achieves the largest absolute values of $\mathcal{W}(\delta r,\phi)$.

8.3 Summary

In this chapter, we have shown that polarization spectroscopy is not only a powerful technique to measure correlations, but that – with a simple modification of the experimental scheme discussed by Eckert *et al.* [421] – it makes it possible to engineer a quantum lattice gas with an arbitrary spin correlation function. We have illustrated the flexibility of the procedure with several examples mimicking the quantum phases of the bilinear-biquadratic Hamiltonian. In particular, we have shown how to prepare exponentially- and algebraically-decaying correlations, as well as the correlation pattern pertaining to the critical phase of this Hamiltonian. We further considered the more exotic example of correlations which are peaked at a predefined distance.

In our calculations, we make conservative assumptions about the experimental parameters, leaving considerable scope for further optimization of the procedure. Further, we have shown that the procedure is fairly robust under the influence of decoherence. Moreover, we have generalized the entanglement witness proposed in Refs. [464, 465], which may be of independent interest outside this particular example. Using this witness, we have shown that the engineered spin-correlations entail multimode atomic entanglement.

Engineering correlations in such a way could be a valuable preparatory step for state preparation, which is important for both quantum computing and quantum simulation. There exist various schemes to reach interesting many-body ground states (which are typically characterized by high entanglement), *e.g.*, by cooling a sample [475], or by adiabatically ramping parameters from an easy-to-prepare initial state. If, however, the correlations in the initial state can be engineered to be close to the correlations of a desired state, one can hope that the probability to reach that desired state after the cooling/ ramping is increased. Notably, our procedure is readily extendible to higher dimensions and larger-spin systems, and does not depend on the fermionic or bosonic nature of the atoms.

In this chapter, we saw the detrimental effect of decoherence, and how it suppresses the correlations achievable. As discussed at various points of this thesis, such error sources will always be present in realistic quantum-simulation experiments. In the next part of this thesis, we will make an attempt at characterizing more generally how imperfections compromise the results of an analog quantum simulator.

Part III

Quantum Simulators – Robustness and Reliability

Already in the introductory Chapter 1, we saw that little is known about the robustness of analog quantum simulators (AQSs) under realistic experimental imperfections. This led us to the fundamental question: *Can we trust quantum simulators?* Since there are no known ways for quantum error correction in AQSs, the rigorous answer to this question should be "no;" yet in practice we do tend to trust them, at least to some extent.

One of the aims of this thesis is addressing the fundamental issue of reliability of AQSs and the relationship to the complexity/efficiency of the simulation [requirements (c) and (d) of our QS definition in Chapter 1.1]. For a reliable performance of a QS, it is indispensable to ensure that no terms in the fundamental equations describing its behavior have been forgotten, lest the QS simulate the wrong model. In Chapters 9 and 10, we will discuss two such cases where conventionally neglected effects change the phase diagrams of systems of ultracold atoms.

The core piece of the present part is Chapter 11, where we discuss the influence of imperfections on a generic AQS. To this purpose, we study a paradigmatic example, the quantum Ising chain, subject to quenched disorder. Our analysis demonstrates how disorder suppresses correlations, modifies universal behavior near a quantum phase transition, and changes the dynamical response of the system. In particular, it suggests that the reliability of an AQS and the efficiency of calculations are interrelated: precisely in those parameter regimes where classical calculations become less efficient, the AQS performs worse.

The analysis of disorder in an AQS may also inspire valuable ideas for the validation of such devices. We proposed such a test to certify the reliability of AQSs in Ref. [61] (see also Fig. 8.5 and Ref. [62]): This test consists of *purposefully* adding imperfections to the QS, such as static disorder or dynamical noise. Static disorder, *e.g.*, can be increased in a controlled manner in AQS implementations with trapped ions [189] or ultracold atoms [155]. This would then allow *(i)* to judge how strong the reaction of the QS with respect to these perturbations is and thus to bound possible errors, and *(ii)* to extrapolate interesting observables to the ideal, zero-disorder limit. The latter would be a workaround to the validation, assuring that imperfections are properly accounted for. These considerations can also be applied to DQSs, but are particularly relevant for AQSs since in that case standard error-correction schemes are not available.

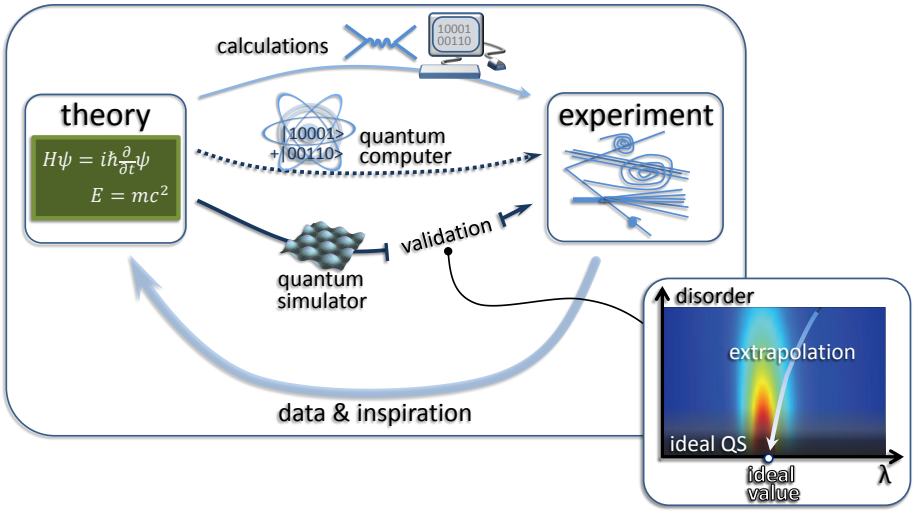

Figure 8.5: **Quantum simulators in the interplay of theory and experiment.** Experiments inspire the search for fundamental answers and show where theoretical models have to be improved to agree with nature. In turn, theorists derive simplified models, the solution of which should help explain experiments. However, even some of the most simple of such quantum models cannot be solved efficiently by analytical or numerical calculations on classical computers. Large-scale quantum computers could serve this purpose, but they are not yet available. Using existing technology, one could solve these models with analog quantum simulators (AQSs). Before these can work reliably, however, we must bridge a crucial link – their validation. **Lower right: Test for imperfections.** As proposed in Ref. [61], a strategy could be to test how the results of the AQS depend on purposefully introduced imperfections. Here, we show a paradigmatic case for the suppression of the correlation length in a 1D system along the phase diagram (spanned by the parameter λ) under varying the amount of disorder (from Chapter 11). This may allow to bound experimental errors. An extrapolation of the results obtained at finite imperfections to the case of the ideal model (arrow) – *e.g.*, to identify the location of a critical point in the phase diagram (white dot) – can constitute a workaround to the validation of AQSs.

Chapter 9

Bose–Hubbard model with occupation-dependent parameters

The general definition of a simulator given on p. 3 reminds us that — prior to any simulation — we have to derive a faithful model for the system we are planning to simulate. In the context of analog quantum simulation, we then desire to solve that simplified model by operating the analog quantum simulator (AQS) in a regime where its fundamental dynamics is described by the same equations. If, however, the effective equations governing the AQS are not derived with sufficient accuracy, we are actually simulating a different model, thus provoking systematic errors. In particular, if we neglect terms which in fact do play a role, the simulated phase diagram can change completely, and exotic effects may be ascribed to a certain model when in reality they are (maybe even trivially) due to overseen terms. On the other hand, besides being only a nuisance, such additional terms can also be a benefit, giving access to novel physics not contained in the original, more simple, model.[1]

[1] For example, in the spin models of Chapter 7 – derived in trapped-ion setups as an effective spin–spin interaction mediated by lattice vibrations – residual couplings between spins and lattice vibrations can compromise the desired spin model. On the other hand, engineering these spin–phonon interactions opens access, *e.g.*, to quantum simulations of the Jahn–Teller effect, which explains distortions and non-degenerate energy levels in molecular and solid-state physics [200].

In this and the following chapter, we will analyze regimes where such neglected terms in optical-lattice Hamiltonians become important. We will show how these terms modify phase diagrams that are conventionally assumed to describe these Hamiltonians, and how they lead to novel effects which are of fundamental interest on their own.

9.1 Bose–Hubbard physics at strong interactions

For many important strongly-correlated many-body states of ultracold atoms, possible realizations rely on strong interactions. However, when the interactions between the particles are strongly enhanced, *e.g.*, via a Feshbach resonance, the standard Bose–Hubbard model (2.4), which typically describes ultracold bosons in an optical lattice extremely accurately, has to be modified. Namely, such strong interactions make effects of higher bands important, invalidating the description in terms of the conventional single-band Bose–Hubbard model.

In the conventional scenario, for not too shallow lattices, the kinetics of the atoms is exhausted by single-particle tunneling processes between lattice minima. When the lattice is ramped up, an initially weak interparticle interaction eventually becomes important with respect to the kinetics. This conventional Bose–Hubbard model (2.4) has only two parameters, the on-site interaction energy U, and the nearest-neighbor (NN) tunneling matrix element t. As long as the interaction is weak compared to the lattice potential, the description in terms of the lowest-band single-particle Bloch or Wannier states as given in Eq. (2.3) is a good approximation. Then, U and t are given by the matrix elements (2.6) and (2.7), which are taken with respect to the single-particle Wannier states. This approximation corresponds to degenerate perturbation theory up to first order in the interaction, where couplings to higher bands are neglected.

However, if the interaction is stronger, higher-order corrections start to play a role. One may then still describe the system in terms of lattice-site occupation numbers n_j, but the occupied Wannier-like orbitals will have admixtures from higher bands which depend on the occupation number. The most significant effect of the repulsive interaction will be a broadening of the Wannier-like orbitals with increasing occupation, effectively enhancing t and decreasing U. At this place, we take this in terms of the Hubbard description into account by replacing t and U by functions $t_{\hat{n}_i,\hat{n}_j}$ and $U_{\hat{n}_i}$ of the number operators $\hat{n}_i$. At a theoretical level, several authors have studied quantitative consequences of this kind of modification to the plain bosonic Hubbard model [476–478]. For example, additional Mott-insulator (MI) phases have been predicted considering an

interaction-induced modification of the Wannier functions [479, 480]. Also, the effect on the Mott transition of the interaction-induced coupling to the first excited band has been considered [481], and the interaction-induced modification of Hubbard parameters has been predicted to lead to re-entrant behavior in the SF–MI transition [481, 482]. Finally, the effect of interaction on the tunneling dynamics in one-dimensional double-well and triple-well potentials have been studied in Refs. [483, 484], where the authors found enhanced correlated pair tunneling near the fermionization limit. On the experimental side, occupation-number-dependent on-site interaction has been observed in the coherent dynamics of an atomic ensemble [485]. Similar occupation-dependent effects have been measured in Bose–Bose [486] and Fermi–Bose mixtures [299, 300, 487], and – in the latter case – have been explained theoretically in terms of occupation-dependent parameters U and t [488].

Here, we show that – going beyond a mere quantitative change – even new quantum phases can arise in Hubbard models with number-dependent parameters. To do this, we first derive the effective single-band Hamiltonian for strong interactions (characterized by the s-wave scattering length a_s), including the effect of the site occupation (Sec. 9.2). For later comparison, we study in Sec. 9.3 the instability of the MI phase with respect to simple particle and hole excitations, leading to the usual single-particle SF. Then, in Sec. 9.4, we investigate the instability of the Mott phase with respect to the excitation of *bond-centered pairs* of particles (*i.e.*, pairs which are extended over neighboring lattice sites). We show that this mechanism becomes relevant when the s-wave scattering length is increased, and that it leads to a phase transition to a SF of extended pairs. This feature is novel, since the extended pairs emerge in a single-species repulsive bosonic system without the presence of any long-range interaction (for pair-SFs in systems with long-range interactions, see Chapter 10). In Sec. 9.5, proceeding to even stronger interactions, we find an instability of the Mott phase towards a SF of *site-centered* pairs. In this regime, the Mott phase with a filling of two particles per site can disappear completely. Finally, in Sec. 9.6, we focus on the regime where interaction effects are important not because of large scattering lengths, but rather because of large site occupations. In this limit, starting from the Bogoliubov approach for the homogeneous system, we find a phonon instability at a critical filling fraction. When exceeding that fraction, the new ground state is a Bose condensate where the particle density is localized along one spontaneously chosen spatial direction. The results presented in this chapter have been published in Ref. [489].

9.2 The occupation-dependent Bose–Hubbard model

In this section, we discuss how interaction-induced orbital effects can be captured in an effective single-band Bose–Hubbard model with occupation-dependent parameters. We will analyze the resulting model in the following sections.

As described in Eq. (2.1), the Hamiltonian of short-range-interacting ultracold bosonic atoms in the presence of a periodic lattice potential $V_{\mathrm{lat}}(\boldsymbol{r}) = V_0[\sin^2(\pi x/d) + \sin^2(\pi y/d) + \sin^2(\pi z/d)]$ with lattice constant d, can be written as

$$\hat{\mathcal{H}} = \int \mathrm{d}^3 r \hat{\Psi}^\dagger(\boldsymbol{r}) \left[-\frac{\hbar^2}{2M_{\mathrm{at}}} \nabla^2 + V_{\mathrm{lat}}(\boldsymbol{r}) + \frac{g}{2} |\hat{\Psi}(\boldsymbol{r})|^2 \right] \hat{\Psi}(\boldsymbol{r}) \,, \tag{9.1}$$

with bosonic field operators $\hat{\Psi}$, atom mass M_{at}, and interaction strength $g = 4\pi\hbar^2 a_s / M_{\mathrm{at}}$. Notably, for high interactions in the presence of an optical lattice, the pseudo-potential form of contact interaction can still be used when a modified scattering length instead of the bare scattering length is employed [490–493].

Similar to Eq. (2.3), to derive a Hubbard-type description, we expand the field operators $\hat{\Psi}(\boldsymbol{r})$ in terms of Wannier-like orbitals $w_i(\boldsymbol{r}; \hat{n}_i) = w(\boldsymbol{r} - \boldsymbol{R}_i; \hat{n}_i)$ localized at the lattice minima $\boldsymbol{R}_i$ (assuming translational invariance), so that

$$\hat{\Psi}(\boldsymbol{r}) = \sum_i \hat{b}_i w(\boldsymbol{r} - \boldsymbol{R}_i; \hat{n}_i) \,. \tag{9.2}$$

Here, $\hat{b}_i$ creates a boson at lattice minimum $\boldsymbol{R}_i$, and $\hat{n}_i = \hat{b}_i^\dagger \hat{b}_i$ is the corresponding number operator. In contrast to the expansion (2.3), here we take the interaction-induced occupation-dependent broadening explicitly into account, so that the Wannier orbitals w depend on the number operator $\hat{n}_i$. Keeping only on-site interactions, which we will justify *a posteriori* at the end of this section, we are led to the effective single-band Hamiltonian

$$\hat{\mathcal{H}} = -\sum_{\langle ij \rangle} t_{\hat{n}_i, \hat{n}_j} \hat{b}_i^\dagger \hat{b}_j + \frac{1}{2} \sum_i U_{\hat{n}_i} \hat{n}_i (\hat{n}_i - 1) - \sum_i \mu \hat{n}_i \,, \tag{9.3}$$

where the matrix elements (2.6) and (2.7) now read

$$\begin{aligned} t_{\hat{n}_i, \hat{n}_j} &= -\int \mathrm{d}^3 r w(\boldsymbol{r} - \boldsymbol{R}_i; \hat{n}_i) \Big[-\frac{\hbar^2}{2M_{\mathrm{at}}} \nabla^2 + V_{\mathrm{lat}}(\boldsymbol{r}) \Big] w(\boldsymbol{r} - \boldsymbol{R}_j; \hat{n}_j + 1) \,, \\ U_{\hat{n}_i} &= g \int \mathrm{d}^3 r w^2(\boldsymbol{r} - \boldsymbol{R}_i; \hat{n}_i) w^2(\boldsymbol{r} - \boldsymbol{R}_i; \hat{n}_i - 1) \,. \end{aligned} \tag{9.4}$$

In Hamiltonian (9.3), we have also introduced the chemical potential μ to control the particle number.

In order to estimate the occupation-number dependence in a mean-field approach, we make a Gaussian *Ansatz* for the Wannier-like wave functions,

$$w(\boldsymbol{r}-\boldsymbol{R}_i;n_i) = \mathrm{e}^{-(\boldsymbol{r}-\boldsymbol{R})^2/\Delta_w(n_i)^2}\,, \tag{9.5}$$

where the width $\Delta_w(n_i)$ is a variational parameter. For simplicity, we replaced the dependence on the particle *operator* $\hat{n}_i$ by a dependence on the particle *number* $n_i = \langle\hat{n}_i\rangle$. From this, we can minimize the Gross–Pitaevskii energy functional for the *Ansatz* (9.5). The idea to employ the width of the Wannier function as a variational parameter has also been used in Refs. [494–496]. Taking into account the full lattice potential (*i.e.*, not employing a quadratic approximation for the lattice minima), for a given n_i this leads to

$$\left(\frac{\Delta_w(n_i)}{\Delta_{w,0}}\right)^5 \exp\left(-\pi^2\frac{\Delta_w^2(n_i)}{d^2}\right) \;=\; \frac{\Delta_w(n_i)}{\Delta_{w,0}} + \sqrt{2\pi}\left(\frac{V_0}{E_R}\right)^{1/4}\frac{a_s}{d}(n_i-1)\,. \tag{9.6}$$

Here, we use $\Delta_{w,0}/d = (V_0/E_R)^{-1/4}/\pi$ to denote the width of w in the limit $V_0 \gg E_R$, where $E_R = \pi^2\hbar^2/(2M_{\mathrm{at}}d^2)$ is the recoil energy. Note that Eq. (9.6) has a solution only as long as $\sqrt{V_0/E_R} \gg \Delta_w^2(n_i)/\Delta_{w,0}^2$. Using the variational result, the tunneling parameter between two adjacent sites can be approximated by

$$\frac{t_{n_i,n_j}}{E_R} \approx \left(\frac{\pi^2}{4}-1\right)\frac{V_0}{E_R}\exp\left(-\frac{d^2}{2\left[\Delta_w^2(n_i+1)+\Delta_w^2(n_j)\right]}\right). \tag{9.7}$$

When calculating the tunneling strength, the Gaussian approximation (9.5) generally results in a lower value than the exact calculation; the exact Wannier orbital has an exponential tail which decays slower than a Gaussian. Nevertheless, our simple approximation provides us with reasonable numerical values and with a suitable model for the occupation dependence of tunneling in the regime under consideration. This allows us to get a qualitative understanding of the physics at work.

For the number-dependent on-site interaction strength, the variational result gives

$$\frac{U_{n_i}}{E_R} = \sqrt{\pi}\left(\frac{V_0}{E_R}\right)^{3/4}\left(\frac{4\Delta_{w,0}^2}{\Delta_w^2(n_i)+\Delta_w^2(n_i-1)}\right)^{3/2}\frac{a_s}{d}\,. \tag{9.8}$$

In principle, the expansion of the quartic interaction in Hamiltonian (9.1) in terms of Wannier functions, Eq. (9.2), gives additionally rise to terms proportional to $\hat{b}_i^\dagger \hat{n}_j \hat{b}_j$ (*occupation-induced single-particle tunneling*) and $\hat{b}_i^\dagger \hat{b}_i^\dagger \hat{b}_j \hat{b}_j$ (*pair tunneling*). However, these terms are exponentially smaller than $t(n_i, n_j)$, approximately by a factor of $\exp\left(-\pi^2\sqrt{V_0/E_R}/4\right) a_s/d$ for the occupation-induced single-particle tunneling and by $\exp\left(-\pi^2\sqrt{V_0/E_R}/2\right) a_s/d$ for the pair tunneling. Since we are in the limit of $V_0/E_R \gg 1$, we can neglect these terms in Hamiltonian (9.3). As shown in Chapter 10, however, if strong *long-range* interactions are present, such terms can become important.

9.3 Insulator to single-particle superfluid transition

Having derived a suitable model Hamiltonian describing the regime of strong interaction, we now study the instability of the MI (with occupation number $n_i = \overline{n}$ for all sites i) towards a SF of single particles/holes. In later sections, we will study its instability towards more exotic pair-SFs (PSFs), to which the present analysis is an important point of comparison.

For this purpose, we use a Gutzwiller-type product *Ansatz* $\prod_i |\Phi\rangle_i$ for the many-body state (see Chapter 13.1), with the variational coherent spin-representation state [497, 498]

$$|\Phi\rangle_i = \cos\theta|\overline{n}\rangle_i + \sin\theta\sin\psi|\overline{n}+1\rangle_i + \sin\theta\cos\psi|\overline{n}-1\rangle_i \tag{9.9}$$

at each site i. Here, $|n_i\rangle_i$ denote the occupation-number basis states. In this *Ansatz*, we assume that the state is translationally invariant, and we truncate the Fock-state representation at one additional particle or hole, which in the Mott phase and close to the transition to the SF, where particle fluctuations are small, is sufficient. Accordingly, the variational mean-field energy is given by

$$\frac{E_{\rm ss}}{N} = -\frac{zE_t}{4}\sin^2 2\theta + \left(\frac{E_U}{2} + \mu\cos 2\psi\right)\sin^2\theta\,, \tag{9.10}$$

where $z = 6$ is the coordination number for the cubic lattice and

$$E_t = \sqrt{\overline{n}^2+\overline{n}}\,t_{\overline{n},\overline{n}}\sin^2\psi/2 + (\overline{n}+1)t_{\overline{n}+1,\overline{n}}\sin^2\psi + \overline{n}\,t_{\overline{n},\overline{n}-1}\cos^2\psi, \tag{9.11a}$$

$$E_U = \overline{n}(\overline{n}-1)U_{\overline{n}}\cos^2\theta + \overline{n}(\overline{n}+1)U_{\overline{n}+1}\sin^2\theta\sin^2\psi + (\overline{n}-1)(\overline{n}-2)U_{\overline{n}-1}\sin^2\theta\cos^2\psi\,. \tag{9.11b}$$

Minimizing the energy (9.10) determines θ and ψ. The value $\theta = 0$ corresponds to an incompressible MI state, where the number of particles $\overline{n}$ per site is an integer that stays constant within a finite interval of the chemical potential μ. In contrast, for $\theta \neq 0$, the state is a SF with order parameter $\langle \hat{b}_i \rangle \sim \sin 2\theta$, and the average particle number per site depends smoothly on the chemical potential via the parameter ψ.

Thus, when $E_{\rm ss}$ minimizes for non-zero θ, the Mott state becomes unstable with respect to single particle and hole excitations, which is the usual scenario of instability of the MI. For interaction strength $a_s/d = 0.15$ and $\overline{n} = 1$, this happens at the black lines (solid or dotted) in the plane spanned by μ/V_0 and $t_{0,1}/V_0$ in Fig. 9.1. For small ψ, the transition to the SF occurs mainly via the creation of holes, while for ψ near $\pi/2$ the MI is destroyed mainly by the creation of particles. In the latter case, the MI becomes unstable when the energy cost of creating an additional particle at one site, namely $U_{n+1} n(n+1)/2 - \mu$, is overcome by the reduction in energy due to tunneling of that particle. This gain in tunneling energy is on the order of $z(\overline{n}+1)t_{\overline{n}+1,\overline{n}}$.

9.4 Superfluidity of extended (bond-centered) pairs

So far, we have described the usual scenario where the Mott phase becomes unstable with respect to single particle and hole delocalization, as it is also found for non-number-dependent Hubbard coupling t and U. We will now show that – as a consequence of occupation-dependent hopping and on-site interaction – the MI can also become unstable with respect to the creation of *pairs* of particles, and this already at smaller tunneling strengths than where the creation of single particles becomes favorable.

On top of a $\overline{n} = 1$ Mott background, consider a pair excitation with one additional particle at site i and another one at the neighboring site j, as sketched in the upper left corner of Fig. 9.2a. This situation corresponds to the state

$$|P_{\langle ij \rangle}\rangle \equiv \frac{1}{2} \hat{b}_i^\dagger \hat{b}_j^\dagger |\{n_i = 1\}\rangle \,. \tag{9.12}$$

Such a *bond-centered* or extended pair excitation at $\langle ij \rangle$ can tunnel coherently to a neighboring bond, say $\langle ik \rangle$, where $k \neq j$ is another neighbor of site i. (Generally, bonds are considered neighbors if they share a common site.) Such a pair tunneling process occurs in second order with respect to single-particle

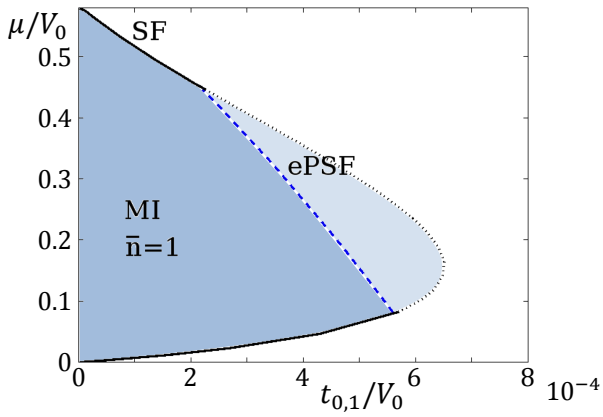

Figure 9.1: **MI–SF transition for** $a_s/d = 0.15$**.** Inside the darker shaded region (enclosed by the black solid and the blue dashed line), the system is a MI with $\overline{n} = 1$ particles per site. Leaving this region by crossing the black solid line, a simple SF of single particles or holes is formed. In contrast, crossing the blue dashed line into the lighter shaded region, one enters a SF phase of extended (bond-centered) pairs (ePSF), where no single-particle superfluidity is present. In technical terms of our variational approaches: outside the shaded regions (*i.e.*, the Mott lobe if only single-particle/hole excitations are present) the energy (9.10) is minimized by $\theta \neq 0$, and on the right of the blue dashed line expression (9.19) is minimized by $\theta_{\mathrm{ep}} \neq 0$.

tunneling via the virtual, site-centered pair state

$$|P_i\rangle \equiv \frac{1}{\sqrt{3!}} \hat{b}_i^\dagger \hat{b}_i^\dagger |\{n_i = 1\}\rangle \,, \tag{9.13}$$

which remains almost un-occupied due to its larger energy. According to second-order degenerate perturbation theory, the amplitude of the pair tunneling process is given by

$$t_{\mathrm{eff}} = 6t_{2,2}^2/(3U_3 - 2U_2) \,. \tag{9.14}$$

On the same footing, perturbation theory gives the binding energy of $-2t_{\mathrm{eff}}$ for the bond-centered pair due to number fluctuations within the pair (*i.e.*, processes where a particle tunnels on top of its partner particle (with which it is bound in a pair) and back to its initial site; such fluctuation processes do not change the state but can reduce the energy).

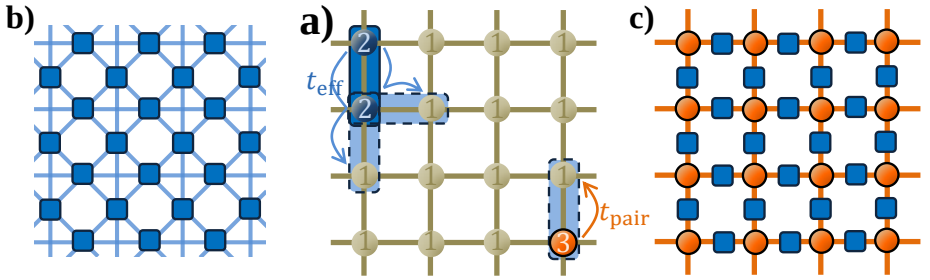

Figure 9.2: **Lattice geometries emerging due to different pair-hopping processes. (a) Original square lattice.** Excitations on top of a $\overline{n} = 1$ Mott background (olive bullets) can lead to double-occupied (upper left, dark blue bullets) and triple-occupied sites ("site-centered pairs;" lower right, orange bullet). At strong interactions, correlated hopping can bind double-occupied sites into bond-centered pairs (dark blue box). These move via second-order processes t_{eff} (upper left; faint blue boxes denote the final state after tunneling). This can give rise to **(b) a checkerboard lattice where the bond-centered pairs live.** The bonds of (a) constitute the sites of this effective lattice (blue boxes). Second-order tunneling connects the effective sites if the corresponding bonds in the original lattice (a) share a site. **(c) Effective lattice for bound pairs.** At even stronger interactions, bond-centered and site-centered pairs have similar energy, making them coexist. They can transform into one another via single-particle tunneling t_{pair}, as sketched in the lower right of (a). The pairs then move on the decorated square lattice (c), where sites are marked by blue boxes and orange bullets, and bonds by orange lines. (In this chapter we study the three-dimensional cubic lattice, but generalizing the figures to that case is straightforward.)

If the initial lattice of sites has cubic symmetry, the bond-centered pair excitations live on an exotic lattice of coordination number $z' = 10$ that is a generalization of the two-dimensional checkerboard (CB) lattice (see Fig. 9.2b) to three dimensions. This allows the pair to reduce its energy by $10t_{\mathrm{eff}}$ when delocalizing. Collecting these contributions, the bond-centered pair can gain an energy of $-(10+2)t_{\mathrm{eff}}$. In contrast, two particles that do not form a pair delocalize on the original cubic lattice (coordination number 6), which reduces their energy by $2 \times 6 \times 2t_{1,2}$.

Thus, according to perturbation theory, the formation of a bond-centered

pair is favorable if

$$-(10+2)t_{\text{eff}} < -24t_{1,2}\,, \tag{9.15}$$

or, equivalently,

$$t_{2,2}^2 > \frac{1}{3}t_{1,2}(3U_3 - 2U_2)\,. \tag{9.16}$$

For certain scattering lengths a_s, this condition can be fulfilled, since the Wannier-broadening with increasing scattering lengths leads to an increase of both U_2/U_3 (thus bringing $3U_3 - 2U_2$ closer) and $t_{2,2}/t_{1,2}$. Then, the creation of bond-centered pairs is energetically more favorable than the creation of single-particle excitations. If further the energy the pair excitations gain by delocalizing, $-10t_{\text{eff}}$, overcomes the cost to create them, $2(U_2 - \mu) - 2t_{\text{eff}}$, they destabilize the MI state. It is interesting to note that an equivalent scenario does not happen for hole excitations, since these decrease the occupation number and with that the tunneling amplitudes.

To evaluate the boundary of the $\overline{n} = 1$ MI phase, we construct a model for the bond-centered pair excitations, which we can solve within Gutzwiller mean-field theory (see Chapter 13.1). When the number of pairs is small compared to the number of sites, the Hamiltonian for the pairs living on top of a $\overline{n} = 1$ MI state can be written as

$$\hat{\mathcal{H}}_{\text{pair}} = -t_{\text{eff}} \sum_{\langle ll' \rangle} \hat{p}_l^\dagger \hat{p}_{l'} + 2(U_2 - \mu - t_{\text{eff}}) \sum_l \hat{n}_l^p\,. \tag{9.17}$$

Here, $l = \langle ij \rangle$ labels the bonds of the cubic lattice (olive lines in Fig. 9.2a and blue boxes in b), and $\langle ll' \rangle$ denotes pairs of NNs of these bonds (in Fig. 9.2b: the blue boxes connected by blue lines). In the effective Hamiltonian (9.17), we have defined the bosonic creation and destruction operators for bond-centered pair excitations, $\hat{p}_l^\dagger$ and $\hat{p}_l$, and the corresponding number operator $\hat{n}_l = \hat{p}_l^\dagger \hat{p}_l$. As a consequence of the diluteness assumption, we have neglected the interaction between pairs, which arises if pairs occupy neighboring bonds. Since the transition to a PSF will happen with the creation of a single pair, this approximation will not influence the phase boundary.

The energy of a condensate of bond-centered pairs can now be estimated in a similar fashion as Eq. (9.9) by making a Gutzwiller-type product *Ansatz* $\prod_l |\Phi_{\text{ep}}\rangle_l$, where we restrict the $|\Phi_{\text{ep}}\rangle_l$ to superpositions of zero and one pair at each bond,

$$|\Phi_{\text{ep}}\rangle_l = \cos\theta_{\text{ep}}|0\rangle_l + \sin\theta_{\text{ep}}|1\rangle_l\,. \tag{9.18}$$

The order parameter of the pair condensate for this wave function is $\langle \hat{p}_l \rangle = \frac{1}{2}\sin(2\theta_{\text{ep}})$. According to this *Ansatz*, the variational mean-field energy per site

is

$$\frac{E_{\rm ep}}{3N} = -\frac{z' t_{\rm eff}}{4} \sin^2 2\theta_{\rm ep} + 2(U_2 - t_{\rm eff} - \mu) \sin^2 \theta_{\rm ep} \,, \tag{9.19}$$

where $z' = 10$ is the coordination number of the three-dimensional CB lattice (see Fig. 9.2). The mean-field approach gives the same phase boundary for the appearance of a pair condensate as the perturbation-theory considerations of the previous paragraph. The equivalence of both approaches is generally given for an *Ansatz* like Eq. (9.18) which includes only two states per site.

In Figure 9.1, we plot the results of the minimizations of $E_{\rm ss}$ and $E_{\rm ep}$ with respect to θ and $\theta_{\rm ep}$, respectively, for $a_s/d = 0.15$. The part of the Mott phase which is stable with respect to single-particle and hole excitations (characterized by $\theta = 0$) is given by the interior of the black solid and dotted lines. On the right of the blue dashed line, one finds a region where $\min[E_{\rm ep}] < \min[E_{\rm ss}]$ and $\theta_{\rm ep} \neq 0$. Thus, here the system is characterized by $\langle \hat{p}_l \rangle \neq 0$ and $\langle \hat{b}_i \rangle = 0$, *i.e.*, the state is a SF of extended pairs (ePSF).

Condensates of extended pairs have also been proposed in the context of dimer models of reduced dimensions which describe frustrated magnets like $SrCu_2(BO_3)_2$ [499]. By approximating triplet excitations as hard-core bosons, Bendjama, Kumar, and Mila [500] argue that in the presence of correlated hopping these bosons can condense in pairs. Such pairing processes also bear resemblance to molecular condensation due to Feshbach resonances in an optical lattice [501].

At this point, we would like to point out that triple, quadruple, or higher-order excitations do not play any important role. The effective tunneling matrix element of such excitations will be very small since it appears in third- or higher-order perturbation theory. Therefore, inside a $\overline{n} = 1$ phase, triple and higher excitations cannot lower their energy efficiently by delocalization. We can, thus, exclude a SF of triples or higher-order objects.

However, there is another possible competitive scenario. Instead of exciting a triple or quadruple, one can create a large cluster of extra particles, *i.e.*, a big spatial domain with doubly occupied sites. In this case, within each cluster, the energy of the additional particles (on top of the $\overline{n} = 1$ Mott background) is not lowered by delocalization, but rather by the effective attractive interaction between them as it appears in second-order perturbation theory. In the bulk of such a cluster, this gives a binding energy of $-6t_{\rm eff}$ per extra particle. In comparison, in the PSF, each particle can lower its energy by $t_{\rm eff}$ because of binding and by another $5t_{\rm eff}$ because of delocalization (*i.e.*, Bose condensation), which in total gives the same energy gain of $-6t_{\rm eff}$. Accordingly, in leading order, a SF of bond-centered pairs on top of the $\overline{n} = 1$ MI is equally favorable as

a state that is phase separated into spatial domains hosting MIs of filling $\overline{n} = 1$ and MIs of filling $\overline{n} = 2$. As a consequence, we cannot reliably exclude phase separation by means of simple variational arguments.

Finally, let us briefly discuss another issue: in this chapter, we are working with a fixed chemical potential rather than with fixed particle number. This approach is suitable for the description of experiments with ultracold atoms, provided the atoms are trapped by a sufficiently shallow potential. In such a situation, the local-density approximation applies and different regions in the trap correspond to different values of the chemical potential. However, if the trap is too steep for the local-density approximation to hold, it might introduce new physics. Consider the following example. The phase-separated state described in the preceding paragraph might not be favored in the homogeneous system. But, because it is energetically very close to the PSF, it can be favored already when a slight potential difference is introduced, helping to form $\overline{n} = 2$ Mott domains in the region of slightly lower potential energy. Such a scenario can spoil the local-density approximation already for a very weak trapping potential.

9.5 Superfluidity of local (site-centered) pairs

Increasing a_s/d further, site-centered pair excitations on top of the $\overline{n} = 1$ Mott background, described by $|P_i\rangle$, Eq. (9.13), can become more favorable than the bond-centered excitations described by $|P_{\langle ij\rangle}\rangle$, Eq. (9.12). This occurs when the ratio U_3/U_2 is reduced enough, so that $3U_3 \leq 2U_2$, *i.e.*, the energy to create a pair of particles on the same site is smaller than the energy to create a pair of particles on neighboring sites. Equation (9.6) shows that such a situation is possible: in the limit of large $V_0 \gg E_R$ and a_s/d, we can write $\Delta_w(n)/\Delta_{w,0} \approx (gn_i)^{1/5}$, resulting in $3U_3 - 2U_2 \approx -0.02U_0$.

Particularly interesting is the regime where bond- and site-centered pairs have only a small energy difference, *i.e.*, where $|3U_3 - 2U_2|$ is comparable to or smaller than $t_{2,2}$. In that case, a bond-centered pair $|P_{\langle ij\rangle}\rangle$ can transform to a site-centered pair $|P_i\rangle$ by a single-particle tunneling process, given by the matrix element $t_{\mathrm{pair}} = \sqrt{6}t_{2,2}$. In this regime, the pairs occupy the lattice given by both the sites and the bonds of the cubic lattice, which forms a decorated square lattice (see Fig. 9.2c). By delocalizing on this lattice, a pair can reduce its kinetic energy by $12t_{\mathrm{pair}}$. The pair is stable towards breaking as long as this energy is greater than what two non-paired particles can gain by delocalization, which amounts to $24t_{1,2}$. Thus, the pair is stable for $t_{2,2} > \sqrt{3/2}t_{1,2}$. The binding

mechanism of the pair is based solely on the delocalization of its center of mass. The regime $|3U_3-2U_2| \approx 0$ is given, *e.g.*, for $a_s/d \approx 0.21$ when $V_0/E_R \approx 16$. In that case, the $\overline{n} = 1$ MI becomes unstable with respect to this type of pair creation when the delocalization energy $12t_{\mathrm{pair}}$ exceeds the energy $3U_3 - 2\mu$ needed for the pair creation.

If the scattering length is increased further, such that $2U_2 - 3U_3 \gg t_{2,2}$, site-centered pair excitations $|P_i\rangle$ will be created rather than bond-centered pairs $|P_{\langle ij\rangle}\rangle$. The site-centered pair excitations can then tunnel from site to site coherently via the occupation of a virtual bond-centered pair excitation. In second-order perturbation theory, the corresponding tunneling matrix element reads

$$t'_{\mathrm{eff}} = 6\frac{t_{2,2}^2}{2U_2 - 3U_3} = -t_{\mathrm{eff}} \,. \tag{9.20}$$

Additionally, the pair has a binding energy of $6t'_{\mathrm{eff}}$ (stemming from a small perturbative admixture of the 6 neighboring bond-centered pair states). Therefore, a site-centered pair is more favorable than two single-particle excitations if

$$3U_3 - 12t'_{\mathrm{eff}} < 2(U_2 - 12t_{1,2}) \,. \tag{9.21}$$

or, equivalently,

$$t_{2,2}^2 > \frac{1}{72}(2U_2 - 3U_3)\left[24t_{1,2} - (2U_2 - 3U_3)\right] \,. \tag{9.22}$$

If this condition is fulfilled, the MI becomes unstable towards the creation of site-centered pairs rather than to the creation of single particles. As in Sec. 9.4, a mean-field calculation leads to the same phase boundary. We plot the boundary of the $\overline{n} = 1$ Mott phase for $a_s/d = 0.3$ in Fig. 9.3. The instability towards the creation of single particles is hardly important. It is predominantly the creation of single holes or site-centered pairs of particles which destroys the Mott phase.

Similar site-centered pairs have been found in a variety of optical-lattice systems. For example, in the limit of $U_1 \gg t_{0,1}$, metastable repulsively-bound pairs of ultracold bosons have been observed [502, 503]. Also, two-species mixtures of bosons with inter-species attraction have been shown to give rise to pair superfluidity [504]. In the context of dipolar atoms in a two-leg ladder, when no tunneling is present between the two legs, pair superfluidity arises due to attraction between the dipolar atoms in different legs [505, 506]. Also, using a state-dependent optical lattice, a correlated tunneling of on-site pairs can be created, which gives rise to a PSF [507, 508]. In our present study, we find that

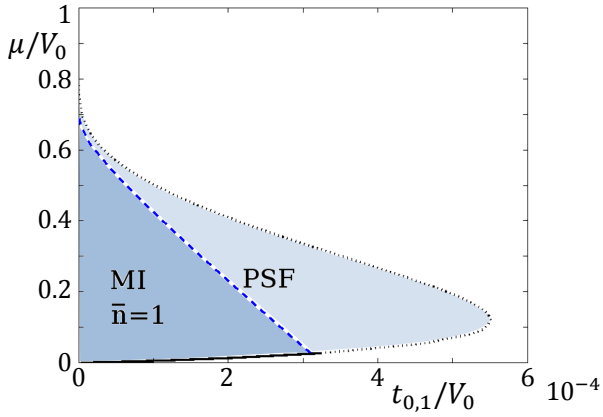

Figure 9.3: **MI–SF phase transition for** $a_s/d = 0.3$**.** Inside the darker shaded region (enclosed by the black solid and the blue dashed line), the system is a MI with $\overline{n} = 1$ particles per site. Crossing the blue dashed line, one enters a SF of local, site-centered pairs (PSF), and crossing the black solid line, a SF of single holes. The black dotted line delimits the instability towards single particle or hole excitations in the absence of occupation-dependent effects, and the shaded regions mark the corresponding Mott lobe.

such local pairing can emerge simply due to the strong occupation-dependence of tunneling and on-site interaction.

After having studied the phase boundaries of the $\overline{n} = 1$ Mott state, we now discuss the one with $\overline{n} = 2$. In the limit of vanishing tunneling, this state is favorable for $U_2 < \mu < 3U_3 - U_2$. The lower border of this interval is given by the energy difference between filling a site with 2 or with 1 particles, and the upper border by the energy difference between filling a site with 3 or 2 particles. However, the upper border can, in fact, become smaller than the lower one, which is the case if $3U_3 - 2U_2 < 0$. Then, the $\overline{n} = 2$ MI phase is never stable with respect to the creation of particle-hole pairs, irrespective of the tunneling strength; it ceases to exist. In the limit of vanishing tunneling, the disappearance of the $\overline{n} = 2$ MI coincides with the point where site-centered pair excitations become more favorable than bond-centered ones.

Note that within the Gaussian approximation 9.5 the MI phases with higher filling, $\overline{n} \geq 3$, do not disappear, even for large interaction a_s/d. These phases do not share the fate of the $\overline{n} = 2$ MI, because the broadening of the Wannier-like functions w in response to adding one particle to a site becomes less pronounced

with increasing occupation,

$$U_2/U_3 \geq U_3/U_4 \geq U_4/U_5 \geq \dots . \tag{9.23}$$

However, for strong interaction, sites occupied by three and more particles suffer strong dissipation due to three-body collisions [509, 510].

Since there is no $\overline{n} = 2$ Mott phase for $3U_3 - 2U_2 < 0$, one might wonder what else the system's ground state is at fixed filling $n = 2$. At vanishing tunneling, the ground state is highly degenerate; all Fock states are equal in energy where half of all sites have occupation $n_i = 1$ and the other half $n_i = 3$. Alternatively, one might say that on top of a $\overline{n} = 1$ MI, half of the sites are occupied by additional site-centered pairs in an arbitrary pattern. For small but finite hopping, this degeneracy will be lifted. One might think of three possible scenarios: *(i)* the pairs gather in one region in space; this corresponds to a phase segregation between the $\overline{n} = 1$ and the $\overline{n} = 3$ Mott phases; *(ii)* the pairs delocalize to form a SF; and *(iii)* the pairs form a CB-type insulator avoiding pairs on neighboring sites.

In order to decide which of these will be the ground state, we consider an effective Hamiltonian for the site-centered pairs,

$$\hat{\mathcal{H}}_{\text{pair}} = -t'_{\text{eff}} \sum_{\langle i,j \rangle} \hat{c}_i^\dagger \hat{c}_j + (t'_{\text{eff}} - D) \sum_{\langle ij \rangle} \hat{n}_i^c \hat{n}_j^c - \sum_i (2\mu - 6t'_{\text{eff}}) \hat{n}_i^c , \tag{9.24}$$

with bosonic pair annihilation and creation operators $\hat{c}_i$, $\hat{c}_i^\dagger$, and where we assume a hard-core constraint $(\hat{c}_i^\dagger)^2 = 0$. The NN repulsion described by the last term, where

$$D = 2 \frac{t_{3,3}^2}{6U_4 + U_2 - 6U_3} , \tag{9.25}$$

stems from super-exchange processes between neighboring pairs.

Since these are hard-core bosons, this model can be mapped to a spin-1/2 XXZ model using the standard Holstein–Primakoff transformation (3.2). In that case, the first term corresponds to the XX coupling, the second term to the ZZ coupling, and the last one to a magnetic field. The XXZ model is well studied (see, *e.g.*, the book by Th. Giamarchi [74]). It can be solved using Bethe *Ansatz* equations, from which we know that, since always $(t'_{\text{eff}} - D) \leq t'_{\text{eff}}$, the system will neither form the CB pattern *(iii)* (corresponding to an antiferromagnetic state of the XXZ magnet) nor show the phase segregation *(i)*. The system forms the SF of site centered pairs *(ii)*.

9.6 Weakly-interacting limit

Finally, we investigate the limit where interaction effects are important not because of a large scattering length but because of large site occupation; *i.e.*, $a_s/d \ll 1$, but the mean number of particles per site $n_0 \gg 1$. We assume small on-site number fluctuations $\delta n \ll n_0$, *i.e.*, $\sqrt{U_{n_0}/(n_0 t_{n_0})} \ll 1$. Expanding the occupation-dependent tunneling and on-site interactions (9.4) in that limit, we can rewrite the modified Hubbard Hamiltonian (9.3) as

$$\begin{aligned}\hat{\mathcal{H}} &= -t_{n_0} \sum_{\langle ij \rangle} \hat{b}_i^\dagger \left[1 + \alpha(\delta\hat{n}_i + \delta\hat{n}_j)\right] \hat{b}_j \\ &\quad + \frac{U_{n_0}}{2} \sum_i \hat{n}_i(\hat{n}_i - 1)\left[1 + \beta - 2\beta(\hat{n}_i - 1)\right] - \sum_i \mu\, \hat{n}_i \,, \end{aligned} \tag{9.26}$$

where $\delta\hat{n}_i = \hat{n}_i - n_0$,

$$\beta = \frac{3}{5}\sqrt{\frac{\pi}{2}} \left(\frac{V_0}{E_R}\right)^{1/4} \frac{a_s}{d}, \tag{9.27a}$$

$$\alpha = \frac{\pi^{5/2}}{10\sqrt{2}} \left(\frac{V_0}{E_R}\right)^{3/4} \frac{a_s}{d}, \qquad \text{and} \tag{9.27b}$$

$$\frac{t_{n_0}}{V_0} = \left(\frac{\pi^2}{4} - 1\right) \exp\left(-\frac{\pi^2}{4}\sqrt{\frac{V_0}{E_R}}\left[1 - \frac{2\sqrt{2\pi}}{5}\left(\frac{V_0}{E_R}\right)^{1/4} \frac{a_s}{d} n_0\right]\right). \tag{9.27c}$$

Notably, the Hamiltonian (9.26) shows some similarity to the quantum Ablowitz–Ladik model for q-deformed bosons [511], given by

$$\hat{\mathcal{H}}_{\mathrm{AL}} = -\sum_i [\hat{B}_i^\dagger \hat{B}_{i+1} + \hat{B}_{i+1}^\dagger \hat{B}_i + \frac{1}{2\gamma} \ln(1 - Q\hat{B}_i^\dagger \hat{B}_i)] \,, \tag{9.28}$$

where $Q = 1 - \exp(-2\gamma)$ and $\hat{B}_i$ ($\hat{B}_i^\dagger$) creates (annihilates) a particle at site i. These operators fulfill the deformed-boson commutation relation $[\hat{B}_i, \hat{B}_i^\dagger] = \exp\left(-2\gamma\hat{N}_i\right)$. In the limit of $\gamma \to 0$ and $\gamma\langle\hat{N}_i\rangle \ll 1$, the quantum Ablowitz–Ladik model (9.28) with the substitution $\hat{B}_i \to (1 - \gamma\delta\hat{n}_i)\hat{b}_i$ reduces in first order in γ to the occupation-dependent modified Hubbard model (9.26) with $\alpha = -\gamma$, $\mu = 1$, and $U_{n_0} = 0$. In one and higher dimension, the Ablowitz–Ladik model contains localized solutions [512, 513].

Inspired by this, we now investigate the possibility of localized solutions in Hamiltonian (9.26). To do so, we first find the ground state in the SF limit,

where one has the order parameter $\langle \hat{b}_i \rangle = \sqrt{n_0}$. To look for fluctuations around the ground state, we convert the Hamiltonian (9.26) to momentum space by defining

$$\hat{b}_i = \sum_k \hat{b}_k \mathrm{e}^{-i\boldsymbol{k}\cdot\boldsymbol{r}_i}, \tag{9.29a}$$

$$\epsilon_k = 4 \sum_{\nu=x,y,z} \sin^2 \frac{k_\nu d}{2}, \qquad \text{and} \tag{9.29b}$$

$$\gamma_k = 4 \sum_{\nu=x,y,z} \cos^2 \frac{k_\nu d}{2}. \tag{9.29c}$$

Neglecting correlations arising from the three-body interaction term Hamiltonian (9.26), one arrives at the equation

$$\begin{aligned} \hat{\mathcal{H}}_{\mathrm{mod}} &= -\frac{n_0^2 U_{n_0}}{2} + \sum_k t_{n_0} \epsilon_k \hat{b}_k^\dagger \hat{b}_k \\ &+ \sum_k \left\{ \frac{n_0 U_{n_0}}{2} \left[1 + \beta - 2\beta(n_0 - 1) \right] - \alpha t_{n_0} n_0 \gamma_k \right\} \left(2\hat{b}_k^\dagger \hat{b}_k + \hat{b}_k^\dagger \hat{b}_{-k}^\dagger + \hat{b}_k \hat{b}_{-k} \right). \end{aligned} \tag{9.30}$$

This quadratic Hamiltonian can be diagonalized via a Bogoliubov transformation, which gives the excitation spectrum ω_k of the SF,

$$\omega_k^2 = t_{n_0}^2 \epsilon_k^2 + 2 t_{n_0} U_{n_0} n_0 \left[1 + \beta - 2\beta(n_0 - 1) - 2\alpha \frac{t_{n_0}}{U_{n_0}} \gamma_k \right] \epsilon_k . \tag{9.31}$$

One can find dynamical instabilities by studying the normalized phonon velocity v_{ph}, which is obtained in the limit $k \to 0$ of ω_k via $\omega_k / \sqrt{2 t_{n_0} U_{n_0} n_0} = v_{\mathrm{ph}} |k| d$. In a cubic lattice,

$$v_{\mathrm{ph}} = \sqrt{\left[1 + \beta - 2\beta(n_0 - 1) \right] - 2\alpha \frac{t_{n_0}}{U_{n_0}} \gamma_0} . \tag{9.32}$$

In the non-interacting limit, this expression tends towards 1. In Fig. 9.4, we plot the phonon velocity v_{ph} as a function of the filling fraction n_0 for $a_s/d = 0.01$. Initially, the phonon velocity increases with increasing n_0. Due to the attractive effect of the occupation-dependent tunneling term, however, the phonon velocity starts decreasing for higher n_0, until it becomes imaginary for some critical n_0. This results in a dynamical instability of the SF [as long as we are within the limit $\frac{a_s}{d} n_0 < 1$, which was a crucial ingredient for deriving Hamiltonian (9.26)].

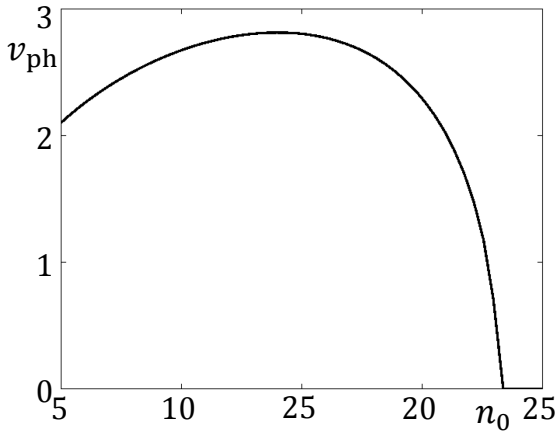

Figure 9.4: **Phonon velocity v_{ph} as a function of the SF occupation number n_0** (for $a_s/d = 0.01$ and $V_0/E_{\mathrm{rec}} = 10$). After a critical occupation number, the phonon velocity becomes imaginary, marking a dynamical instability.

To understand the nature of this instability, we make a transition from the discrete Hubbard model to a continuous model with a continuous field $\phi(r)$, applicable for $kd \ll 1$,

$$\hat{\mathcal{H}}_{\mathrm{cont}} = -\int \mathrm{d}^3 r \phi^*(r) \nabla^2 \phi(r) + \frac{U}{2} \int \mathrm{d}^3 r \, \mathrm{d}^3 r' V_{\mathrm{eff}}(r-r') |\phi(r)|^2 |\phi(r')|^2 \,. \quad (9.33)$$

Here, the distance is expressed with respect to the lattice constant d, and the effective interaction potential is given by

$$V_{\mathrm{eff}}(r-r') = \mathrm{FT}^{-1} \left[1 + \beta - \beta(n_0 - 1) - 2\alpha \frac{t_{n_0}}{U_{n_0}} \gamma_k \right] . \quad (9.34)$$

where FT^{-1} stands for the inverse Fourier transform.

Using an *Ansatz* wave-function that is Gaussian along one direction, say x, and uniform in the other directions, $\phi(r) = 1/\pi^{1/4} \Delta_s^{1/2} \exp(-x^2/2\Delta_s^2)$, the energy functional for the self-trapped state reads

$$E_{\mathrm{sol}} = \frac{1}{\Delta_s^2} + \frac{U_{n_0}}{t_{n_0}\sqrt{2\pi}} \left[1 + \beta - 2\beta(n_0 - 1) - \alpha \frac{2t_{n_0}}{U_0} \left(5 + \mathrm{e}^{-\frac{2}{\Delta_s^2}} \right) \right] \frac{1}{\Delta_s} \,. \quad (9.35)$$

When n_0 exceeds a critical density, E_{sol} is minimized for a finite width $\Delta_s \gg 1$ (instead of $\Delta_s = \infty$). Thus, the homogeneous SF becomes dynamically unstable towards a state which is localized only in one direction and uniform in the other two, forming a 2D slab.[2]

[2] We found that instabilities which are additionally localized in one or both of the other two

9.7 Summary

To summarize this chapter, we have analyzed how the results of an AQS for the Bose–Hubbard model, consisting of ultracold atoms in an optical lattice, are modified in the regime of strong interactions. In particular, to describe interaction-induced band mixing, we have derived a modified bosonic Hubbard model with occupation-dependent parameters. This model comprises an effective interaction-induced broadening of the Wannier-like single-particle orbitals, and, thus, captures also the situation when the s-wave scattering length becomes comparable to the lattice spacing, $a_s/d \to 1$.

Using this model, we have shown for specific, experimentally relevant parameter values that the $\overline{n} = 1$ MI state can become unstable towards a SF which consists of bond-centered pair excitations. This scenario is novel, since the pairs emerge due to the occupation dependence of tunneling strength and on-site interaction. For even higher interaction, the nature of the SF pair excitations that destroy the MI changes. The pairs can now occupy both the sites or bonds (*i.e.*, two neighboring sites) of the lattice; in that way, a decorated square lattice emerges. Increasing the interaction further, eventually the pairs live only on the sites of the lattice. In this regime, the entire $\overline{n} = 2$ Mott phase is destabilized by the site-centered pair fluctuations. It is fascinating to observe the emergence of exotic lattice geometries as a consequence of pair creation.

We have also investigated the regime where interaction-induced Wannier-broadening arises from large filling $\overline{n} \gg 1$ at small scattering lengths, $a_s \ll d$. In this limit, we found that the SF becomes dynamically unstable due to the attractive nature of the occupation-dependent tunneling. The system then transforms from a uniform SF state to an asymmetric state which is localized in one direction and extended in the other two.

To connect to experiment in a more quantitative fashion, one could consider extensions in various directions, such as a more accurate determination of the number dependence of the Hubbard parameters t_{n_i,n_j} and U_{n_i}. Further, it would also be worth studying in detail the role of a trapping potential as it is present in experiments. Finally, to judge the robustness of the ground-state phase diagram, it would be interesting to characterize the role of dissipation, which can be expected to be enhanced by strong interactions.

directions have a higher energy. They can only become lower in energy for (unrealistically) high interactions.

Chapter 10

Dipolar molecules in optical lattices revisited

In the previous chapter, we saw that the simple Bose–Hubbard model (2.4) describing ultracold atoms in optical lattices has to be modified in the regime of strong on-site interactions. In a similar vein, the presence of strong *dipolar* interactions between ultracold molecules makes it necessary to include novel occupation-dependent-tunneling and pair-tunneling processes, which have typically been neglected. As we show in this chapter, these terms can change the conventionally accepted phase diagram of dipolar bosonic molecules in optical lattices, and destroy for example checkerboard (CB) phases in favor of pair-superfluids (PSFs).

10.1 Description of the system

As discussed in Chapter 2.1, in the simplest case, ultracold atoms in optical lattices are well described by the Bose–Hubbard model (2.4), where the phase diagram is determined by the interplay of only two parameters: a tunneling t and an on-site interaction U. A natural extension of the Bose–Hubbard model comes from including long-range interactions between the particles, such as discussed in Chapter 7. In recent years, experiments on ultracold polar molecules have renewed interest in such extended Bose–Hubbard models [514–517]. Because of the strong electric dipole moment of polar molecules, long-range interactions play a crucial role in the collective behavior of the system, leading to the appearance

of novel ground states, such as various structured insulating states, supersolids, Wigner crystals, pair-supersolids, and more [167, 389, 505, 506, 518–520].

In this chapter, we study dipolar molecules in a 2D square optical lattice with a harmonic trapping along the polarization direction of the dipoles. We derive a modified Bose–Hubbard model which includes additional occupation-dependent nearest-neighbor (NN) hopping processes arising from long-range dipolar interactions in the lowest Bloch band. Usually, interaction-induced hopping terms are neglected when discussing dipolar bosonic molecules. Here, we show that these terms considerably change the physics of dipolar soft-core bosons. Such soft-core bosons in square and one-dimensional lattices have been discussed in the literature within the extended Hubbard model, focusing on the presence of stable supersolidity [387, 521]. In these systems, in the usual case with only NN interaction and at sufficient dipolar strength, the ground states at half- and unit-filling are CB insulating states. Here, we show that interaction-induced hopping can destroy these CB states at large dipole moments. To illustrate this, we study a one-dimensional extended Hubbard model including the novel occupation-dependent hopping processes, using exact diagonalization (ED) and the multiscale entanglement-renormalization *Ansatz* (MERA). We find that, with increasing dipolar interaction, the system enters from the CB phase to a novel state which has one-particle SF and PSF properties. In particular, we find a region where these coexists. In this region, the SF order parameter has alternating sign at consecutive sites.

The rest of this chapter is organized as follows. First, we derive the extended Hubbard model describing dipolar molecules in optical lattices, where we emphasize the appearance of two additional terms for large dipolar interactions (Sec. 10.2). Then, we discuss how these additional terms change the phase diagram of the extended Hubbard model (Sec. 10.3), using ED at fixed filling (Sec. 10.3.1), as well as MERA and ED in the grand-canonical ensemble (Sec. 10.3.2). For better contact to experiment, we discuss in Sec. 10.3.3 the phase diagram for the same model but with the full long-range part of dipolar interactions taken into account. In Sec. 10.4, finally, we give a summary of this chapter. The results presented in this chapter have been published in Ref. [522].

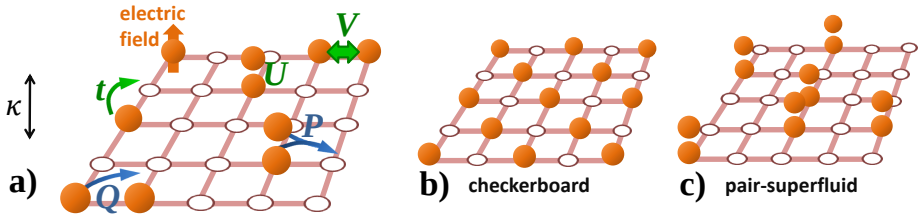

Figure 10.1: **The system.** Bosonic molecules (red bullets) with dipole moment p are polarized by an electric field (sketched in the upper-leftmost molecule). An external potential (characterized by the dimensionless parameter κ) confines the molecules to the xy plane, where they live on a square optical lattice. The effective Bose–Hubbard model consists of five terms, sketched in panel (a): well known are the terms of the extended Bose–Hubbard model, colored in green, the NN tunneling t, the on-site interaction U, and the NN repulsion V; for strong p, new terms become important (blue), namely, pair tunneling P and in particular correlated hopping Q. **(a-c) Illustrations of the states occurring from low to large** p (at approximately half filling and for the parameters given in the text). **(a)** At low p, single-particle tunneling t dominates, and the system has *superfluid* long-range order (LRO) and density short-range order. **(b)** Increasing p, the repulsion V suppresses tunneling and leads to density-LRO – the system is a *checkerboard* insulator. **(c)** At large p, V still suppresses single-particle hopping but the correlated hopping Q allows the particles to tunnel if they are bound into pairs – the system is a *pair-SF*. This phase is entirely due to the previously neglected term Q.

10.2 Bose–Hubbard physics for strong dipole moment

Our system consists of dipolar bosons polarized by an external electric field along the z direction and confined in a square optical lattice, as illustrated in Fig. 10.1. The corresponding Hamiltonian reads

$$\begin{aligned}\hat{\mathcal{H}} &= \int \mathrm{d}^3\boldsymbol{r}\ \hat{\Psi}^\dagger(\boldsymbol{r})\left[-\frac{\hbar^2}{2M_{\mathrm{mol}}}\nabla^2 + V_{\mathrm{lat}}(\boldsymbol{r})\right]\hat{\Psi}(\boldsymbol{r}) \\ &+ \frac{1}{2}\int\int \mathrm{d}^3\boldsymbol{r}\,\mathrm{d}^3\boldsymbol{r}'\hat{\Psi}^\dagger(\boldsymbol{r})\hat{\Psi}^\dagger(\boldsymbol{r}')V_{\mathrm{int}}(\boldsymbol{r}-\boldsymbol{r}')\hat{\Psi}(\boldsymbol{r})\hat{\Psi}(\boldsymbol{r}')\,, \qquad (10.1)\end{aligned}$$

where $\hat{\Psi}^\dagger(\boldsymbol{r})$ $\left(\hat{\Psi}(\boldsymbol{r})\right)$ are the creation (annihilation) field operators for bosonic molecules of mass M_{mol}. The external lattice potential

$$V_{\mathrm{lat}}(\boldsymbol{r}) = V_0\left(\sin^2\frac{2\pi}{\lambda}x + \sin^2\frac{2\pi}{\lambda}y\right) + M_{\mathrm{mol}}\Omega_z^2 z^2/2 \tag{10.2}$$

of lattice depth V_0 is generated by a laser field of wave-length λ, and an additional external harmonic potential in z direction, the strength of which is characterized by Ω_z. The dipole–dipole interaction is denoted by $V_{\mathrm{int}}(\boldsymbol{r})$. Throughout this chapter, we measure all lengths in units of the laser wave length λ and all energies in recoil energies $E_R = 2\pi^2\hbar^2/(M_{\mathrm{mol}}\lambda^2)$. Accordingly, we define the dimensionless parameter $\kappa = \hbar\Omega_z/2E_R$ characterizing the confinement in z direction.

Generalizing the derivations in Chapter 2.1 to strong dipolar interactions, we now compute the lowest-band extended Bose–Hubbard model effectively governing the physics at not too small lattice depths. For this purpose, we first find the lowest Bloch band for a single particle moving in the potential $V_{\mathrm{lat}}(\boldsymbol{r})$, and construct the (exact) corresponding Wannier functions $w_i^2(x,y)\mathrm{e}^{-\kappa z^2}$ localized at site i [523]. By expanding the field operator $\hat{\Psi}(\boldsymbol{r}) = \sum_i w_i(x,y)\mathrm{e}^{-\kappa z^2/2}\,\hat{b}_i$ in the corresponding basis, and by restricting ourselves to on-site and NN terms, we arrive at the extended Bose–Hubbard model

$$\hat{\mathcal{H}} = -t\sum_{\langle ij\rangle}\hat{b}_i^\dagger\hat{b}_j + \frac{U}{2}\sum_i\hat{n}_i(\hat{n}_i-1) + \sum_{\langle ij\rangle}\left[V\hat{n}_i\hat{n}_j - Q\hat{b}_i^\dagger\left(\hat{n}_i+\hat{n}_j\right)\hat{b}_j + \frac{P}{2}\hat{b}_i^\dagger\hat{b}_i^\dagger\hat{b}_j\hat{b}_j\right], \tag{10.3}$$

where $\hat{b}_i$ $(\hat{b}_i^\dagger)$ annihilates (creates) a particle on lattice site i, $\hat{n}_i = \hat{b}_i^\dagger\hat{b}_i$ is the corresponding density operator, and angle brackets denote NN bonds.

The standard tunneling coefficient is denoted by t, U is the on-site interaction, and V is the NN interaction arising from a truncation of the dipolar interactions to the dominating NN term. These are the terms which have been typically taken into account in the literature to describe molecules with permanent dipole moment in optical lattices (green terms in Fig. 10.1a).

Strong dipole moments render two additional terms in Hamiltonian (10.3) important which typically have been neglected (purple terms in Fig. 10.1a): The term proportional to Q describes one-particle tunneling induced by the occupation of a neighboring site, and the term proportional to P is responsible for NN pair tunneling [524–526]. Explicitly, the correlated hopping Q and the

pair-hopping P read

$$Q = \int\int \mathrm{d}^3\boldsymbol{r}\mathrm{d}^3\boldsymbol{r}' w_i^2(x,y)\mathrm{e}^{-\kappa z^2} V_{\mathrm{int}}(\boldsymbol{r}-\boldsymbol{r}')w_i(x',y')w_j(x',y')\mathrm{e}^{-\kappa z'^2}, \quad (10.4a)$$

$$P = \frac{1}{2}\int\int \mathrm{d}^3\boldsymbol{r}\mathrm{d}^3\boldsymbol{r}' w_i(x,y)w_j(x,y)\mathrm{e}^{-\kappa z^2} V_{\mathrm{int}}(\boldsymbol{r}-\boldsymbol{r}')w_i(x',y')w_j(x',y')\mathrm{e}^{-\kappa z'^2}. \quad (10.4b)$$

These terms can become important if $V_{\mathrm{int}}(\boldsymbol{r}-\boldsymbol{r}')$ is strong for NNs (and if there is a finite overlap of the Wannier functions).

The matrix elements U, V, Q, and P are given by a sum of dipolar and δ-like contact interactions,[1]

$$V_{\mathrm{int}}(\boldsymbol{r}-\boldsymbol{r}') = g\,\delta^{(3)}(\boldsymbol{r}-\boldsymbol{r}') + \gamma\left(\frac{1}{|\boldsymbol{r}-\boldsymbol{r}'|^3} - 3\frac{(z-z')^2}{|\boldsymbol{r}-\boldsymbol{r}'|^5}\right). \quad (10.5)$$

Here, we defined the dimensionless coupling constants describing contact and dipolar interaction, $g = 16\pi^2 a_s/\lambda$ and $\gamma = M_{\mathrm{mol}}p^2/(\hbar^2\varepsilon_0\lambda)$ (where a_s is the s-wave scattering length, ε_0 is the vacuum permittivity, and p is the electric dipole moment of the bosons).

10.3 The phase diagram at strong dipole moment

To compute the ground-state phase diagram for a concrete example, we consider ultracold dipolar molecules with a mass of $M_{\mathrm{mol}} = 220a.m.u$ and confined in an optical lattice of lattice depth $V_0 = 6E_R$ and wave length $\lambda = 790\,\mathrm{nm}$ (this is the value relevant for RbCs, which has a strong dipole moment [527]). For the s-wave scattering length of the molecules, we assume $a_s \approx 100a_0$, where a_0 is the Bohr radius. For these parameters, $g \approx 1.06$ is approximately constant. We consider dipole moments p up to $\sim 3\,\mathrm{D}$ (γ up to ~ 470), which can be achievable for molecules like bosonic RbCs or KLi [528].

To illustrate the relative strengths of the different parameters, we compare in Fig. 10.2 at fixed $\gamma = 52$ the tunneling t with the dipolar contribution to the parameters U, V, Q, and P (we denote the dipolar contribution by the subscript D).[2] The strength and sign of U_D can be tuned by changing κ: a small κ allows

[1] The contact interactions alone typically do not give rise to appreciable correlated tunneling due to the small Wannier overlap between neighboring sites, see also last paragraph of Chapter 9.2.

[2] The chosen γ corresponds to $p = 1\mathrm{D}$. Note that, by virtue of Eq. (10.5), the plotted dipolar contributions scale linearly with γ.

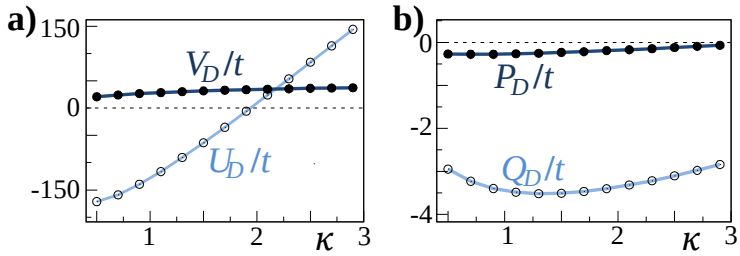

Figure 10.2: **Dependence of the model parameters on the z-confinement κ.** Plotted is (for $V_0 = 6E_R$ and $\gamma = 52$) the contribution of the dipolar interactions (subscript D) to **(a)** the usual terms of the extended Bose–Hubbard model U and V, and **(b)** the novel terms Q and P. For the chosen parameters, Q and P are one order of magnitude smaller than V, but they can dominate for large γ. The interaction-induced tunneling Q can have opposite sign to t, thus opening the possibility of counteracting the effect of t.

the molecules to explore the region within a lattice site where they are aligned on top of each other, where the dipolar interaction is attractive; a large κ does not permit this, and therefore the molecules predominantly feel the repulsive part of the dipolar interactions. For the parameters chosen, Q_D and P_D are one order of magnitude smaller than V_D. On the other hand, Q_D can dominate over t for large γ. In addition, Q_D and t can have opposite sign, as seen in Fig. 10.2.

For concreteness, we work in the following at the z-confinement parameter $\kappa = 1.95$, making (additionally to t) the on-site interaction U almost independent of the dipole moment ($U_D \approx 0$). In this case, for large enough γ, we expect that with increasing p the parameters V, Q, and P determine the system properties. In the following, we illustrate the effect of the novel terms on the example of a 1D chain of N lattice sites with periodic boundary conditions.

10.3.1 Exact diagonalization at half-filling

To get a first understanding of the system, we compute the ground state $|\psi(p)\rangle$ as a function of the dipole moment p using ED of a half-filled system with $N = 8$ sites. The results are presented in Fig. 10.3, along with calculations for $N = 12$ and 16 to check for system-size dependence.

Without the occupation-dependent tunneling terms Q and P, we observe the usual scenario with only two phases, a single-particle SF and a CB phase (as

sketched in Fig. 10.1a and b). The transition happens at $p \approx 0.4\,\mathrm{D}$. It is marked by an increase of the contribution of the checkerboard states to the ground state to almost 100% (dotted line in Fig. 10.3a). Also, the one-particle correlation function $\phi_i = \sum_{j\,\mathrm{NN\,of}\,i} \langle \hat{b}_j^\dagger \hat{b}_i \rangle$ almost vanishes, indicating the transition to an insulating state (dotted line in Fig. 10.3b). The transition occurs in the half-filled system because for large enough V the particles can decrease their energy by avoiding every second site. If we neglect Q and P, the situation will not change by further increasing p, since this only increases V even more.

However, the situation changes significantly when we take into account the density-induced tunneling Q and the pair tunneling P. In this case, for $p \approx 1.1\,\mathrm{D}$, a second phase transition occurs, destroying the CB order. Previous studies have completely neglected such a possible destruction of CB order at large p. At the transition, the contribution of the CB state to the ground state decreases rapidly (solid line in Fig. 10.3a), and the one-particle as well as the two-particle NN correlation function $\Phi_i = \sum_{j\,\mathrm{NN\,of}\,i} \langle \hat{b}_j^\dagger \hat{b}_j^\dagger \hat{b}_i \hat{b}_i \rangle$ (solid and dashed-dotted lines in Fig. 10.3b) attain finite positive values, indicating that the new phase shows single-particle as well as pair superfluidity. To understand which of the terms is responsible for this PSF, we also studied the effects of Q and P alone (not shown). From these artificial cases, we found that PSF is mainly generated due to the correlated tunneling term Q (in interplay with the NN interaction V), and not as one might expect due to the pair-tunneling term P. In this PSF region, we also find that the correlation function $\langle \hat{b}_j^\dagger \hat{b}_i \rangle$ for $|i-j| \leq 6$ decays slowly with alternating sign at consecutive sites. This suggests the appearance of some antiferromagnetic (AFM) order due to the positive hopping Q. For even larger electric moments ($p \approx 1.5\mathrm{D}$), a third phase transition occurs, where ϕ_i changes sign and Φ_i increases strongly, indicating another PSF phase.

The appearance of pair superfluidity has previously been predicted in bilayer dipolar systems where the particles are bound by an attractive interaction between the layers [505–507], although in these systems the state is a true PSF as $\Phi_i \neq 0$, whereas $\phi_i \equiv 0$. In the present system, the pairs are created due to the occupation-dependent tunneling terms in Hamiltonian (10.3) (similar to Chapter 9), in spite of *repulsive* interactions.

We also note that for very low dipolar strength Φ_i has a small nonzero value, irrespective of the presence of Q and P, as seen in Fig. 10.3b. This behavior can be traced back to second-order processes due to t, which can also give rise to pair correlations at small distances and with small magnitude.

To confirm that the observed transitions are indeed quantum phase transitions (QPTs), we compute – for different chain lengths N – the ground-state

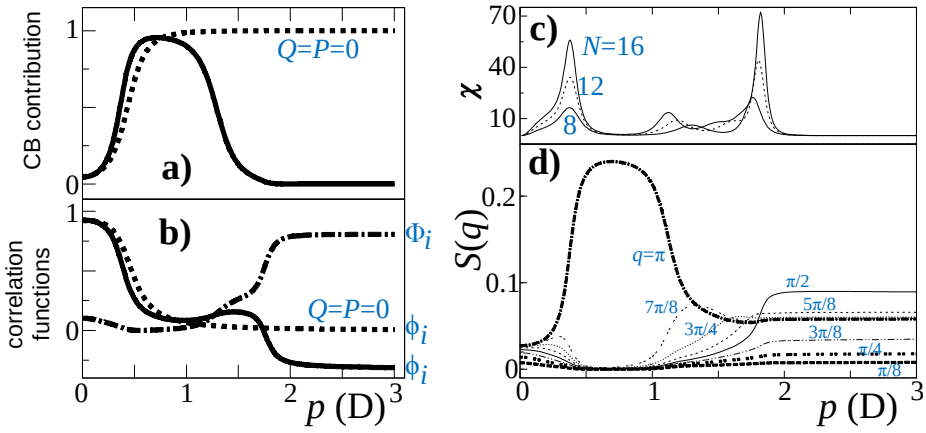

Figure 10.3: **ED for a half-filled system. (a) Contribution of the checkerboard (CB) states** to the ground state for $N = 8$. Finite Q and P destroy the CB state at large p (solid line), while neglecting Q and P predicts that the CB state remains the ground state (dotted line). **(b) One-particle and two-particle correlation functions** ϕ_i and Φ_i. Neglecting Q and P, ϕ_i goes to zero after the transition SF–CB (dotted line). When $Q, P \neq 0$, ϕ_i (solid line) and Φ_i (dash-dotted) attain finite values, indicating the coexistence of one- and two-particle superfluidity. The sign change of ϕ_i is a consequence of the dominance of the (positive) correlated hopping Q. **(c) Fidelity susceptibility** χ at half-filling. Three distinct peaks, increasing with system size, suggest QPTs, from SF to CB, from CB to an intermediate phase, and finally to a pair-SF. **(d) Structure-factor** $S(q)/N$ at half filling for $N = 16$. After the point where χ attains its first peak, the dominant structure factor is at the CB ordering vector $q = \pi$. Between the second and third peak of χ, the dominant q changes stepwise. It reaches $q = \pi/2$ at the third peak, indicating that the particles are in a structure with larger period than in the CB state. Large contributions from other ordering vectors suggest that the order is only over short range.

fidelity susceptibility [529–531]. It is defined equivalently to Eq. (7.23), but now with p as the control parameter,

$$\chi(p) = \frac{1 - |\langle \psi(p) | \psi(p + \delta p) \rangle|^2}{\delta p^2} . \tag{10.6}$$

Divergences in χ are efficient indicators of QPTs. In Fig. 10.3c, we present $\chi(p)$ for different chain sizes. There are three clear peaks located at the QPTs found from the correlation functions (as presented in Fig. 10.3b). The positions of the transition points do not significantly depend on the number of sites, especially for the first and third one, which correspond to the transition from single-particle SF to CB and the transition between the two types of PSF, respectively. The middle peak in Fig. 10.3c refers to the transition from the CB to the AFM SF. The magnitude of the fidelity susceptibility at all three transitions increases with chain length, which suggests that the transitions will survive in the thermodynamic limit.

Additional insight into the properties of the observed phases comes from the static structure factor, which in this context is defined as[3]

$$S(q) = \frac{1}{N} \sum_{j,k=1}^{N} \mathrm{e}^{iq(j-k)} \left(\langle \hat{n}_j \hat{n}_k \rangle - \langle \hat{n}_j \rangle \langle \hat{n}_k \rangle \right) , \tag{10.7}$$

with $q = 2\pi m/N$, and $0 \leq m \leq N-1$ integer. A peak in the structure factor at finite momentum points towards the presence of periodic density modulation in the system.

In Fig. 10.3d, we present $S(q)/N$ for a half-filled system with $N = 16$ sites. In the CB phase (between the first and second peak of the fidelity susceptibility χ), the dominant peak of $S(q)$ is at $q = \pi$, and its magnitude is almost independent of system size. Above the third peak of χ, the system is in a phase where ϕ_i has an inverted sign and Φ_i is large. Here, states dominate where bosons occur in pairs (their contribution to the ground state is about 95%). Since, due to the dipolar interactions, boson pairs do not occupy neighboring sites, the system has some local structure, leading to a predominant structure-factor peak at $q = \frac{\pi}{2}$. The intermediate phase (between the second and third peak of χ) has interesting properties: the ground state of the finite system deforms its structure stepwise, changing the dominant q from π to $\pi/2$ by one quantum $\Delta q = 2\pi/N$ at a time. For $N = 16$, this leads to three changes in the dominant q. Since in an infinite system q can take every value between 0 and 2π, we expect in large chains a continuous change from the CB ($q = \pi$) to the two-particle SF ($q = \pi/2$).

[3] See also Eq. (7.25), where we introduced it for hard-core bosons in terms of spin language.

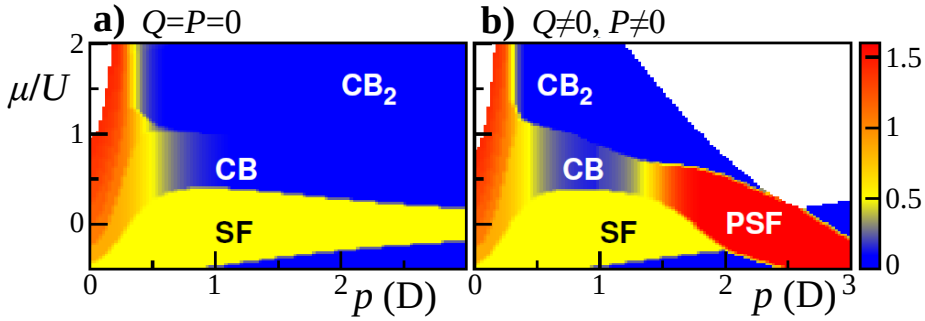

Figure 10.4: **ED phase diagram (a) without and (b) with additional terms** Q and P. To visualize the phase diagram, the color scale encodes a weighted sum of the correlations ϕ_i and Φ_i. **(a)** Neglecting Q and P, at large p and μ the system is always in an insulating phase and the average number of particles is a multiple of 1/2. CB (CB_2) denotes the checkerboard phase where sites with 0 and 1 (2) particles alternate. **(b)** Including the new terms, the insulating phases are replaced by a PSF for large enough p. We truncate the Hilbert space at a maximal occupation of 4 particles per site, and exclude data points where the occupation becomes too high (white region).

10.3.2 Grand-canonical phase diagram

In a realistic ultracold atom QS, a trapping potential is used to confine the atoms, resulting in a changing atom density across the trap. If the trapping potential changes slowly, one can invoke the local-density approximation, which assigns to each site a local chemical potential. Then, one can directly translate results obtained in the grand-canonical ensemble to the in-trap situation: a radial cut through the trapping potential corresponds to a line of varying chemical potential in the grand-canonical phase diagram.

In Fig. 10.4, we present the grand-canonical phase diagram for ED calculations of 4 sites with occupation truncated at 4 particles per site.[4] In the conventional phase diagram which occurs if one sets $Q = P = 0$ (Fig. 10.4a), the system is SF at small μ/U and at low p, while it is always insulating at large p. When the additional terms Q and P are included, a large p destroys the CB phase, making place for a PSF (Fig. 10.4b). These three main phases –SF, CB, PSF – are sketched in Fig. 10.1.

[4] This cut-off can be justified by the non-linear increase of interaction energy with site-occupation, see Chapter 12.1.

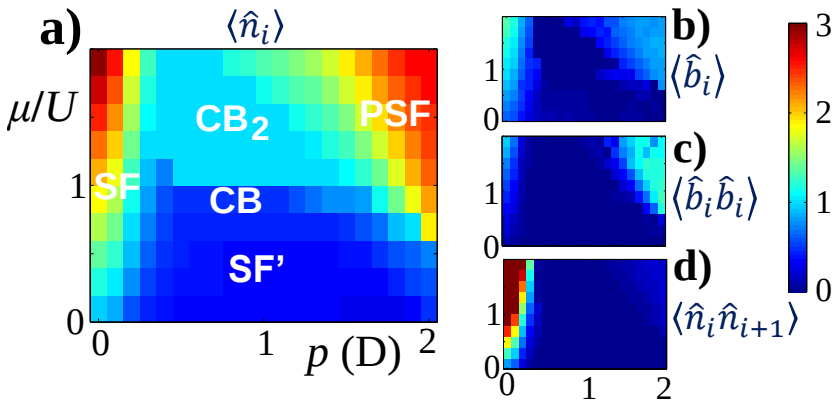

Figure 10.5: **MERA phase diagram including the additional terms** Q and P. **(a) Occupation,** constant in CB phases. **(b) SF order parameter. (c) PSF order parameter. (d) NN density correlations.** The MERA data (averaged over the chain) with refinement parameter $m_r = 8$ for $N = 128$ reveal that checkerboard (CB and CB$_2$) order is replaced, due to the novel terms, by a pair-superfluid (PSF). SF denotes a normal superfluid also found in the model with $Q = P = 0$. SF' is a superfluid with very small NN density correlations, implying that it has supersolid-like properties.

ED can only solve small systems. To get information about large systems, we compute the phase diagram within MERA [532, 533]. The MERA is a quasi-exact variational method that consists in postulating a specific, layered tensor-network structure for the low-energy states of a given Hamiltonian, which in particular yields good results in critical phases, where other methods such as DMRG are very costly [532, 533]. In Chapter 12.2, we explain the method and the particular tensor-network structure that we used.

Our results are presented in Figs. 10.5a-d, where we show, averaged over the chain, the occupation $\langle \hat{n}_i \rangle$, the SF order parameter $\langle \hat{b}_i \rangle$, the PSF order parameter $\langle \hat{b}_i \hat{b}_i \rangle$, and NN density–density correlations $\langle \hat{n}_i \hat{n}_{i+1} \rangle$. The phase diagram extracted from these observables is indicated in Fig. 10.5a. At low p, there is a single-particle SF, which for not too small μ gives way to CB phases at increasing p. For higher μ, we get a CB with two particles in the filled site (CB$_2$ phase), which is possible due to the low on-site repulsion U. Increasing p further, the system undergoes a transition to another SF phase, where initially (for a range of ≈ 0.2D) one-particle superfluidity dominates (similar to the ED results), and

afterwards pair superfluidity. At a few points in the PSF region, we also checked that the SF correlations have an alternating sign as a function of distance, as seen in the ED calculations. This reinforces the assumption that the PSF phase has AFM behavior due to the positive sign of Q. As our numerical calculations are carried out in one dimension, the various SF correlations decay as a power law with distance.

Additionally, at low μ, we find a phase (SF') which has SF order (*i.e.*, a finite $\langle \hat{b}_i \rangle$) but where NN density–density correlations almost vanish. Hence, it has a local structure where sites with high and low occupation alternate, reminding of CB order. We checked that this phase is not due to phase separation. Such a coexistence of a finite SF order parameter with CB order (if it is of long range) implies supersolidity. This is remarkable, because in the usual extended Bose–Hubbard model with soft-core interactions stable supersolidity appears only at the particle-doped region of the CB phase [387, 521].

The main result of this analysis is that – as already indicated by ED – the new terms Q and P drastically change the phase diagram, destroying CB order in favor of PSF phases. Hence, these terms cannot be neglected when describing QS experiments of ultracold molecules with strong dipole moments.

10.3.3 ED at half-filling for full long-range interactions

To make better contact with experiment, we now examine the disappearance of the CB pattern when the full dipolar interactions are taken into account, *i.e.*, we replace the NN interaction term in Hamiltonian (10.3) with

$$\sum_{\langle ij \rangle} V \hat{n}_i \hat{n}_j \to \sum_{i \neq j} \frac{V}{|i-j|^3} \hat{n}_i \hat{n}_j \,, \tag{10.8}$$

where now we sum over all pairs of sites i and j.

Using ED at half-filling for $N = 16$ (see Fig. 10.6), we find that qualitatively the phase diagram does not change much with respect to our previous calculations with the simplified Hamiltonian (10.3) (see Fig. 10.3b). When the occupation-induced tunneling terms Q and P are neglected, the CB phase remains stable for arbitrarily large p (Fig. 10.6a). In contrast, when taking into account the tunneling terms Q and P, it disappears, making way for a PSF phase (Fig. 10.6b). This happens even at smaller p than when truncating the interactions at NNs. Namely, the PSF phase appears for $p \geq 0.7$D. Also in this situation, we have checked that counter-intuitively PSF arises predominantly due to the correlated tunneling Q, not the pair-tunneling P as one might ex-

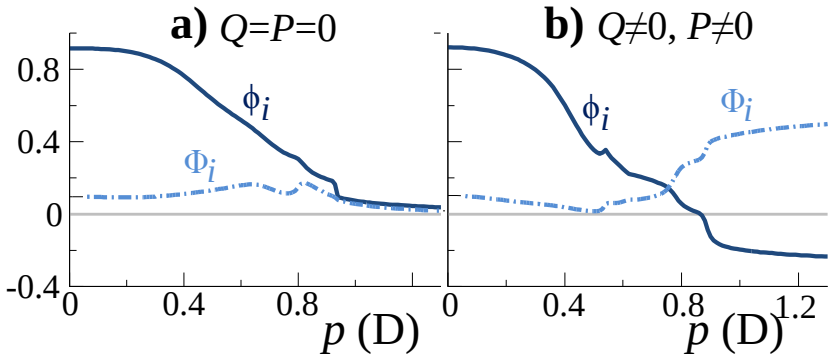

Figure 10.6: **Half-filled system with full dipolar interactions** (ED with $N = 16$). The one-particle and two-particle correlation functions ϕ_i (solid line) and Φ_i (dotted line) behave qualitatively similar to a system with interactions truncated at NNs (Fig. 10.3). **(a) Neglecting Q and P,** the system is always in a CB phase for large enough p ($\phi_i = \Phi_i = 0$). **(b) Including Q and P,** the large Φ_i and negative ϕ_i indicate the break down of the CB phase to a PSF.

pect. Without this term, the PSF phase can not be reached for reasonable electric moments.

We also note that in Fig. 10.6b there is a kink in ϕ_i around $p \sim 0.5$D. This kink corresponds to the appearance of a crystal-like phase with modulation $|\ldots 200100200100\ldots\rangle$, which may be an indication for a novel phase.

10.4 Summary

In summary, we have shown how the extended Bose–Hubbard model describing ultracold polar molecules in an optical lattice has to be modified at strong dipolar interactions.

In that regime, occupation-dependent- and pair-tunneling terms can no longer be neglected. Based on ED and MERA, we calculated for a specific choice of optical-lattice parameters how these additional terms destroy insulating CB phases for sufficiently large electric moments p, leading to a novel pair-SF phase. MERA results suggest also that a supersolid phase could appear for 1/2 filling even in the hole-doped case. Our calculations are based on realistic parameters, experimentally achievable in the near future. Hence, these modifications to the extended Bose–Hubbard model have to be taken into account

in future quantum-simulation experiments using ultracold polar molecules, and they may even allow to access novel phases.

Chapter 11

Robustness of quantum simulators against disorder

In the previous two chapters, we discussed terms in model Hamiltonians that have typically been disregarded but which can change the response of an analog quantum simulator (AQS) in certain parameter regimes. In this chapter, we turn to another type of error that can compromise the results of an AQS, namely statistical errors. This analysis serves to substantiate our discussion from Chapter 1 concerning the reliability of AQSs and its relationship to the complexity/efficiency of the simulation.

For this, we study the statics and dynamics of a generic example, the quantum Ising chain, where for simplicity we assume quenched disorder as the only possible imperfection. In the future, it will be in particular interesting to also investigate the effects of dynamical noise, and the decoherence and relaxation that occurs due to coupling with an environment. Concerning statics, we explore how disorder affects the universal behavior around the second-order quantum phase transition (QPT) of the transverse Ising model. In general, the regions around QPTs are both the most interesting and most sensitive parts of quantum phase diagrams. Here, we show that the expectation values of certain local observables appear fairly robust under disorder, while this need not be true for the global many-body state of the AQS. In particular, disorder can have a significant effect on relevant quantities describing the behavior of the model near the QPT, such as critical points and exponents [534], or – if the system is described by a conformal field theory – its central charge [434]. Further, we

briefly address the relationship between robustness and complexity by studying the dynamics of different thermal states after a quench of the Hamiltonian. Our results suggest that AQSs appear to work better in regimes that are classically easier to solve or simulate (high-temperature states, large distance to QPTs), thus hinting at a connection between the amount of quantum correlations and the robustness of an AQS.

The rest of this chapter is organized as follows. In Sec. 11.1, we introduce the model system, which we analyze in detail in the rest of the chapter. Section 11.2 is concerned with its static ground-state properties, while we discuss its dynamical behavior in Sec. 11.3. The presented results, together with the general considerations of Chapter 1, have been published in Ref. [61] (see also Ref. [62]).

11.1 The transverse Ising model – an exactly solvable model

To illustrate the influence of disorder on an AQS, we study the example of a paradigmatic model, the transverse Ising chain

$$\hat{\mathcal{H}} = -\sum_{\langle ij \rangle} J_{ij}\sigma_i^x\sigma_j^x - \sum_i h_i\sigma_i^z\,, \tag{11.1}$$

where $\sigma_i^{x,z}$ are the usual Pauli spin matrices and $\sum_{\langle ij \rangle}$ means sum over nearest neighbors (NNs). The system is subject to quenched disorder in both the interaction and field terms. We denote the NN spin coupling and the transverse field by $J_{ij} = J(1 + r\,\delta J_{ij})$ and $h_i = h(1 + r\,\delta h_i)$, respectively, where δJ_{ij} and δh_i are independent random variables with a Gaussian distribution of mean zero and variance r.

The transverse Ising model, even under the presence of disorder, is efficiently solvable – by which we mean that the eigenstates and eigenenergies of the system can be found using a classical computer, and that the cost of the algorithms (in time and hardware) is polynomial with the size (number of particles) of the system. The transverse Ising model, in particular, can be solved by using a Jordan–Wigner transformation to a system of non-interacting fermions – and the cost of solving the non-interacting fermion system is the cost of diagonalizing a matrix with rank equal to twice the number of spins in the chain [535] (see Chapter 12.3). While such a solvable model, *per se*, is not of interest for quantum simulation, it can be expected that general properties, such as the influence of

disorder on second-order phase transitions, are valid in a broader class of models that share the main characteristics of the transverse Ising model, such as being integrable or having a QPT of second order.

The transverse Ising model is well studied, since as early as the 1960's [536]. For low fields, the ground state is a ferromagnet, while for large fields it is a paramagnet. At zero temperature and disorder, the system undergoes a QPT when the dimensionless control parameter $\lambda = h/J$ approaches the critical value, $\lambda_c = 1$, *i.e.*, when the field intensity equals the interaction strength.

The influence of disorder can have dramatic effects on this phase diagram: imperfections can create new phases, or even destroy the ones we want to investigate. Indeed, in the transverse Ising model when the disorder strength is comparable with the interactions, the critical point disappears and is replaced by a so called Griffiths phase [103], which extends across a region of size proportional to the disorder strength. Even more, in this Griffiths phase observables become non-self-averaging, *i.e.*, fluctuations increase with system size, and hence dominate the thermodynamic limit. In this study, we consider small disorder strengths, which allows us to ignore the Griffiths phase, especially in finite-size systems. Moreover, a state-of-the-art AQS can achieve very low levels of disorder, whence this is the experimentally relevant regime. Note that while the transverse Ising model has been studied extensively in the limit of large disorder [537] there are few studies addressing directly the influence of small disorder on the universal properties near QPTs. However, it is well known that even small disorder can lead to novel quantum phases such as Bose [538] or Fermi [539] glasses (see also the section on disorder in the review by Lewenstein *et al.* [379] and references therein). In the following, we analyze the robustness of relevant observables to disorder in static and dynamic situations.

11.2 Influence of disorder on quantum simulation of statics

First, we investigate static properties of the AQS and their robustness to disorder, where we focus especially on the interesting region around the QPT. A description for solving the transverse Ising model using the Jordan–Wigner transform and a derivation of the observables can be found in Chapter 12.3. As is usual in the presence of statistical errors, we average all analyzed quantities over many realizations of disorder.

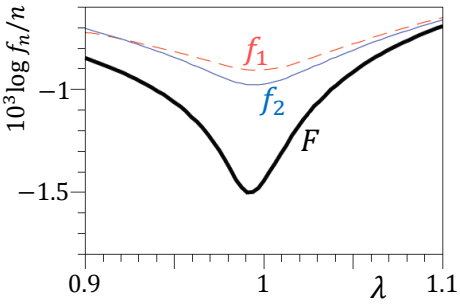

Figure 11.1: **Influence of quenched disorder on the static simulator fidelity,** for a chain of 400 spins and disorder level $r = 0.1$ (averaged over 5000 realizations of disorder). Local fidelities (f_1 and f_2) are more robust than the total simulator fidelity F, which gives hope that local quantities can be reliable even if disorder deteriorates the overall ground state. As expected, disorder has more severe effects close to the QPT.

11.2.1 Simulator fidelities

One can quantify how the results of the AQS degrade due to disorder using the *simulator fidelity*, see Eq. (12.12). For pure states, we define it as the overlap between the state obtained with a perturbed simulator, $|\Psi_r(\lambda)\rangle$, and the ideal state $|\Psi_0(\lambda)\rangle$,

$$F(r,\lambda) = |\langle\Psi_0(\lambda)|\Psi_r(\lambda)\rangle|\,. \tag{11.2}$$

Although we define the simulator fidelity for any possible target state, we focus on the ground state.

As Fig. 11.1 shows, this overlap is considerably suppressed near the QPT, reaching values as low as 55% (for $r = 0.1$ in a chain of $L = 400$ sites). When scaling to larger systems, $F(r,\lambda)$ will typically vanish exponentially fast, simply due to the exponential growth of the dimension of the Hilbert space (a kind of "orthogonality catastrophe"). In a universal quantum computation, the fidelity would have to be very close to 1 for the quantum computer to work fault-tolerantly. However, QSs have the advantage that we do not necessarily demand of the entire state to be robust. Often, it is enough if we can distinguish the relevant phases by measuring faithfully *local* observables (local in the quantum information sense that few sites are involved, although they may be physically far apart).

To quantify the robustness of local observables, we investigate the single-site fidelity $f_1(r,\lambda)$ and the NN two-site simulator fidelity $f_2(r,\lambda)$, as defined in Eqs. (12.13) and (12.14), respectively. As the one- and two-particle density matrices will generally be mixed when the overall pure many-body state is entangled, these are defined as the Uhlmann fidelity [540] between the single- or two-site reduced density matrices of the ideal state and the one at disorder strength r, $f \equiv \mathrm{Tr}\sqrt{\sqrt{\hat\rho^{(0)}}\hat\rho^{(r)}\sqrt{\hat\rho^{(0)}}}$. It can be assumed that fidelities of the

reduced system decrease more or less monotonically with the number of sites involved. As seen in Fig. 11.1, the reduced simulator fidelities are much more robust to disorder than the global one. Near the phase transition, $f_2(r,\lambda)$ decreases to approximately 0.998, and $f_1(r,\lambda)$ remains above 0.999. This gives optimism that local quantities are robust enough to allow a faithful distinction between different quantum phases.

11.2.2 Correlations, gap, and critical point

From the discussion in the previous paragraph, it seems that local quantities are relatively robust in the presence of disorder. However, one is often more interested in extracting non-local properties from the AQS that characterize the critical point and quantify its universality class.

One step beyond local properties of the ground state are the *correlation lengths* dictating the exponential decay of long-distance correlation functions. We investigate the correlation length extracted from the correlation function

$$C(i,j) = \langle\Psi_r|\sigma_z^{(i)}\sigma_z^{(j)}|\Psi_r\rangle - \langle\Psi_r|\sigma_z^{(i)}|\Psi_r\rangle\langle\Psi_r|\sigma_z^{(j)}|\Psi_r\rangle\,, \tag{11.3}$$

which can be computed exactly via Eq. (12.10). Away from criticality, the correlations decay as $C(i,j) \propto \exp(-|i-j|/\xi)$ with correlation length ξ. At the critical point, in the absence of disorder and for infinite systems, ξ diverges, because at criticality collective phenomena emerge that involve infinite degrees of freedom at all length scales. In practice, we can only deal with finite systems so that we cannot observe real criticality but only smoothed out signatures of it, a phenomenon called "pseudo-criticality." For example, the correlation length ξ is bounded by the system size. Still, its peak gives a reliable signature for the location of the critical point. In Fig. 11.2 we show ξ computed from fits to part of the wings of $C(i,j)$. The data are for $L = 400$ and 10000 realizations of disorder of variable strength. As this figure shows, disorder suppresses correlations and broadens the peak of ξ, thus making an extraction of the critical point much less reliable.

Another criterion to locate the QPT is provided by the *energy gap* Δ between ground and first excited state. It is intrinsically connected to the correlations (*e.g.*, in harmonic-lattice systems with gap, the correlations decay necessarily exponentially [247]). At criticality, the low-energy spectrum of the Hamiltonian is gapless in the thermodynamic limit. In finite systems, it presents non-vanishing gaps that decrease in a systematic way with increasing system size. Due to this characteristic scaling of physical observables such as the gap Δ as a function

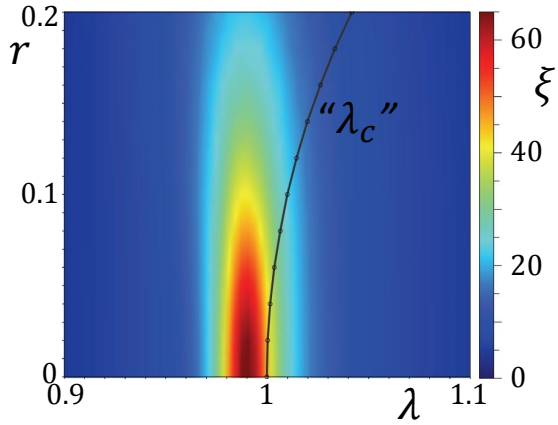

Figure 11.2: **Influence of quenched disorder on the statics of an AQS.** The correlation length ξ decreases with disorder r, and its peak broadens (shown for a chain of 400 spins). The critical point (as extracted from a finite-size scaling of the energy gap Δ, labeled "λ_c") shifts to larger λ with increasing disorder (black line). However, the change begins relatively smoothly.

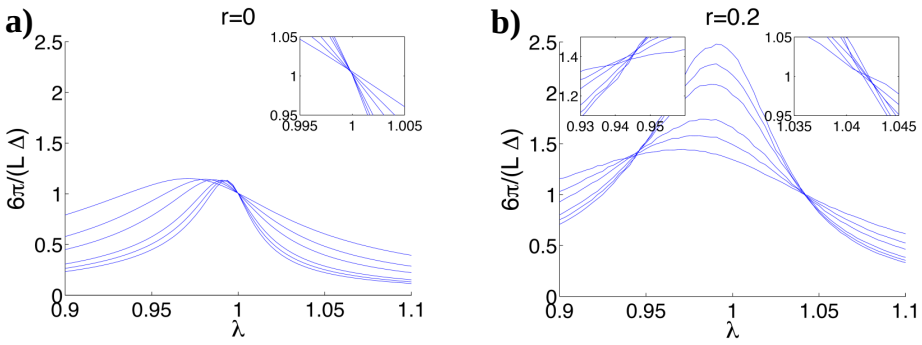

Figure 11.3: **Inverse gaps for different chain lengths. (a)** For low disorder ($r = 0$), the scaled curves $1/(L\Delta(L))$ cross perfectly at the location of the critical point, $\lambda = 1$. **(b)** With increasing disorder ($r = 0.2$), the crossing point moves to larger values of λ and becomes less well defined. At large disorder there appears a second crossing point below $\lambda = 1$. The insets show zooms on the crossing points.

of system size, criticality can be detected by studying sequences of increasingly large but finite systems, a technique called *finite-size scaling* [541]. For the example of the gap: for close-by chain lengths L the rescaled curves $1/(L^{\zeta}\Delta(L))$ (where ζ is the dynamical critical exponent) cross at a series of pseudo-critical points. With increasing L, this series tends rapidly to the real critical point of the thermodynamic limit [542]. Assuming that the dynamical critical exponent ζ does not change much from the disorder-free value 1, we use the scaling of the disorder-free case also for finite disorder. Accordingly, we approximate the critical point as the mean of the points where the rescaled curves $1/(L\Delta(L))$ cross. For this analysis, we use $L = 100, 150, 200, 300, 350, 400$ with 10000 realizations of disorder each.

As displayed in Fig. 11.3 for two examples of disorder strength, the crossing point moves to larger values of λ with increasing disorder. This analysis implies that computing the location of the QPT in a real-world AQS without correcting for disorder can yield erroneous results. On the other hand, as can be appreciated in the black line of Fig. 11.2), which includes more values of disorder strength, the change sets in smoothly at small disorder. We also note that the crossing points show more scatter with increasing disorder, showing the effect of the neglected change of ζ.

Finally, at large disorder, a second crossing point appears at $\lambda < 1$. The two crossing points open up to a V-like structure with increasing disorder. This could be interpreted as an indication of the Griffiths phase (the crossing points are qualitatively consistent with the extent of the Griffiths phase found by Jacobson *et al.* [543]). For a more quantitative analysis, however, one would need to account for a change of ζ with increasing disorder.

11.2.3 Universal quantities: Critical exponents and central charge

Perhaps of more fundamental interest than the exact location of a critical point is its universality class. All models within a given universality class give rise to the same collective behavior at large distances, irrespective of their microscopic details [434]. In fact, all relevant thermodynamic quantities for all models within a class are characterized by the same small set of *critical exponents*. These describe the power-law decay of the correlation functions of local observables in the large-distance regime, a property that allows to differentiate among different emerging collective behaviors.

To characterize the robustness of the universal behavior, we investigate as an example the critical exponent for the correlation length, ν. It can be extracted

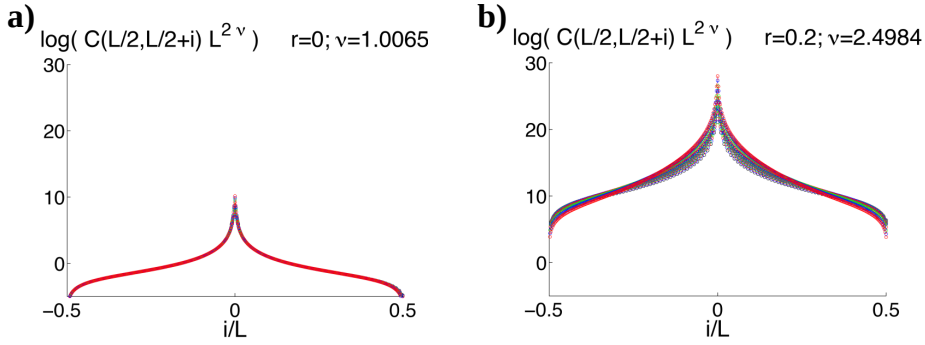

Figure 11.4: **Spin–spin correlations for different chain lengths. (a)** For low disorder ($r = 0$), the curves $C(i,j)L^{2\nu}$ for different L, plotted as functions of $|i-j|/L$, collapse perfectly for the physically correct value of the critical exponent, $\nu = 1$ (dots of different color correspond to different L). **(b)** With increasing disorder ($r = 0.2$), the collapse worsens, and the best collapse is obtained for some $\nu > 1$.

from a collapse of the correlations, taking advantage of another scaling law: without disorder, the correlations follow the law

$$C(i,j)L^{2\nu} \propto f(|i-j|/L) \tag{11.4}$$

with some universal function f [434], as can be seen in Fig. 11.4a.

Hence, we can find ν as the value for which the correlations scaled as in Eq. (11.4) collapse best onto a single curve. The ν resulting from this analysis is shown in Fig. 11.5. Here, we used the following lengths: $L = 100$ to 190 in steps of 10 (10^6 disorder realizations), $L = 200$, 250, 300 (5×10^5 realizations), and $L = 350$, 400 (10^5 realizations). Already for a few percent of disorder, ν increases strongly from its ideal value 1. Hence, using the scaling (11.4) on a disordered AQS yields a too large critical exponent compared to the ideal model. Moreover, the quality of the collapse worsens with increasing disorder (see Fig. 11.4b), demonstrating that a naive application of the scaling (11.4) is unjustified if disorder is large. Therefore, if one simply neglects the influence of disorder, the extraction of critical exponents yields wrong results.

As another fundamental quantity, we analyze the *central charge* c, which characterizes the QPT if it is described by a conformal field theory (a specific subclass of one-dimensional critical systems). In these systems, the central charge appears ubiquitously [544]. It, *e.g.*, governs the temperature dependence

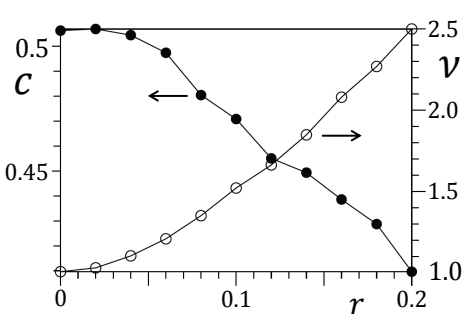

Figure 11.5: **Influence of quenched disorder on universal quantities of an AQS.** Left axis, full circles: central charge c, extracted from the part-chain entropy. Right axis, open circles: critical exponent ν, extracted from a collapse of the correlations for different chain lengths. Both c and ν change with disorder, which can lead to erroneously assigning the QPT to an incorrect universality class. However, the change begins smoothly.

of the free energy (Stefan–Boltzmann law), the Casimir effect in finite geometries, but also the scaling of the entanglement entropy of sub-regions of the ground state of the corresponding quantum models. Models with different central charge have different emerging collective behavior. For example, models whose collective behavior is that of a free Majorana fermion (as in the disorder-free transverse Ising model) have central charge $c = 1/2$, while models whose collective behavior is that of a free boson have central charge $c = 1$.

Strictly speaking, the transverse Ising model has an underlying conformal field theory only in the disorder-free case, but there have been efforts to extract an effective central charge also for the disordered model [537], *e.g.*, from the von Neumann entropy $\mathcal{S}$ of the reduced density matrix of a part of the chain of size l. At criticality, this entropy scales (for open boundary conditions) as [456, 545, 546]

$$\mathcal{S} = \frac{c}{6} \log\left(\frac{L}{\pi} \sin\left(\frac{l\pi}{L}\right)\right) + A\,, \tag{11.5}$$

where A is a constant that is not important for our purposes. Using this scaling, we extract c by fitting $\mathcal{S}$ for several subchain lengths l in a chain of size $L = 300$. We exclude small l to avoid boundary effects, and we use 10000 disorder realizations. As seen in Fig. 11.5, an increase of disorder suppresses the effective central charge, indicating the decrease of entanglement (this is also reflected in the decrease of correlations, see Fig. 11.2). Again, applying the analysis that is correct in the disorder-free case without adjustments to the disordered system yields results which deviate from the desired ideal case. Already a small deviation of the central charge would indicate a completely different universality class.

Fortunately, for all the extracted static quantities (except the global simulator fidelity), the levels of disorder for appreciable changes to occur are at least

a few percent. If the AQS can be operated below such a value, its results seem to be robust, at least in this simple model system. In many experimental situations, one can hope to reach such low levels of disorder. Frequently, however, changing parameters from the regime where validation via classical simulation is possible to the regime of *terra incognita* might lead to uncontrolled disorder or noise.

11.3 Influence of disorder on quantum simulation of dynamics

As described in the list of possible tasks for a QS on p. 11*ff.*, efficient classical algorithms for computing static properties of quantum systems are more developed than for computing dynamics (the difficulty arises mainly because entropy and correlations grow rapidly with simulated time). Therefore, one can assume that in the absence of disorder, a quantum simulation of dynamics can much more easily outperform classical computers. Indeed, in a recent experiment based on ultracold bosonic atoms, the controlled dynamics ran for longer times than present classical algorithms based on MPS could efficiently keep track of [19]. We thus turn to the issue of how disorder affects the reliability of quantum simulations of dynamics. Again, the dynamical behavior can be computed with the Jordan–Wigner transform, as explained in Chapter 12.3. As with statics, we investigate the behavior of the simulator fidelity, but now also as a function of time, initial state, and external driving.

Typically, we expect that the simulator fidelity will decay with time, and eventually reach an asymptotic finite value. The effect of disorder in both the decay rate and the asymptotic saturation value can, in general, be understood from established techniques such as Fermi's Golden rule, and random matrices [547]. On the other hand, the effect of the initial state and the external driving is known to be nontrivial and of particular interest for our purposes. For example, it is known that numerical techniques such as the time-dependent density-matrix renormalization group (tDMRG) can simulate efficiently the dynamics after a sudden quench of the field h, as long as the quench is restricted to a few sites on the chain. However, if the quench is global, it has been shown that the computational resources needed to keep a fixed amount of error grow exponentially with time [548, 549]. Generically, solving for the dynamics of a quantum many-body system is a hard problem for classical algorithms. Our model is special because it can be solved exactly for all cases, although it remains

hard for the tDMRG algorithm. We use this to our advantage to study how this class of classical algorithms behaves when solving for quantum dynamics.

We studied the behavior of the full simulator fidelity under the following driving. As initial state we prepare the ground state of the Hamiltonian for a given value of the external field. At time zero, the field is quenched instantaneously to a larger strength, and the system is allowed to evolve. In Fig. 11.6a-b, we compare the short- and long-time behavior of the fidelity for the case of a global and a local (single-site) quench. The AQS keeps a high fidelity in the case of a local quench, while it performs poorly for the global quench, with fidelities reaching lows of 0.8 even for small systems of 50 spins. We also observe that the AQS performs worse when the quench crosses the critical point, as shown in Fig. 11.6c, where we fix the strength of the quench and vary the initial field value.

The initial state can also have an effect on the efficiency of classical algorithms. Using the same setup with a global quench, but starting from a thermal initial state, tDMRG becomes efficient for high temperatures [548] where the state and its correlations are almost classical. However, it becomes exponentially inefficient with time for low-temperature initial states. For initial thermal states, we can still compute the dynamics exactly, although computationally it becomes too expensive to calculate the full many-body fidelity between the evolved states. In this case, therefore, we focus on the reduced simulator fidelity. For the regimes of disorder that we studied, we observe that the time dependent fidelity decays with a rate roughly proportional to the strength of the disorder squared (typical of a Fermi golden rule [547]). For this reason, we show in Fig. 11.6a a rescaled form of the fidelity, $(1-f_1)/r^2$, that exemplifies the typical behavior for all disorder strengths, as a function of time and temperature of the initial state.

As with the classical algorithms [548], the AQS remains faithful when the state is almost classical (high temperatures). The simulator fidelity decreases rapidly for low temperatures, although it saturates at a fairly high value. In terms of distinguishability, the values we find imply that a fair observer would have only a 4% chance of distinguishing the 1-spin reduced state of the AQS from the ideal state. In the inset of the top panel we show the average asymptotic fidelity as a function of temperature of the initial state. Again, for low temperatures fidelity worsens, but it saturates to a few percent. For high temperatures, it is simple to perform an expansion of the fidelity which shows that $f_1 \simeq 1 - T^{-2}$.

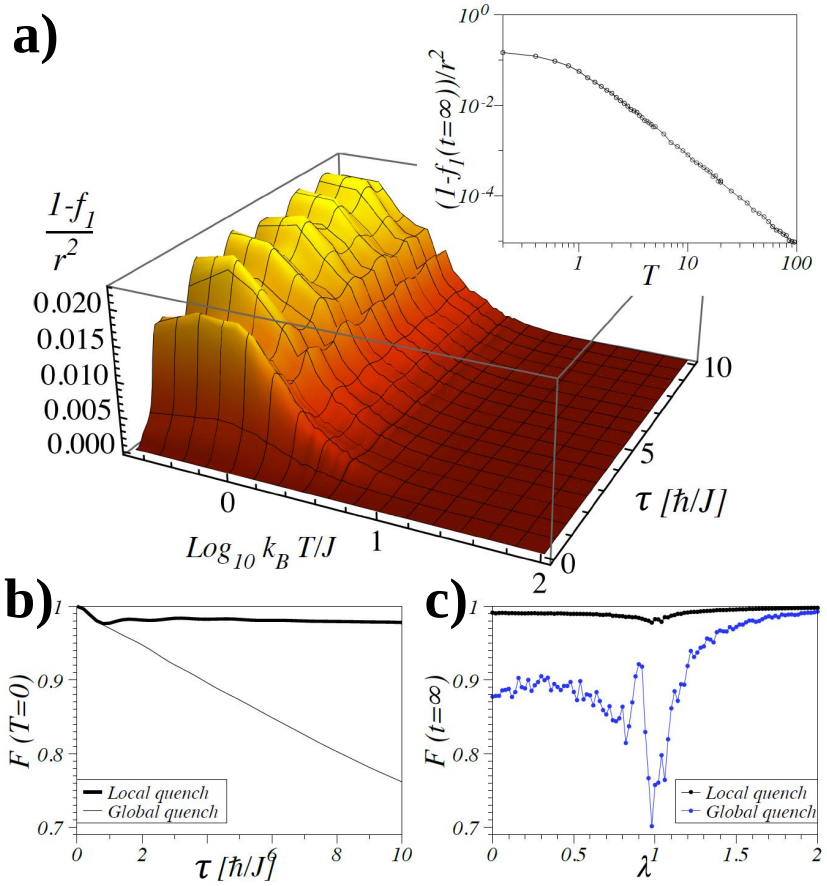

Figure 11.6: **Simulator fidelities for dynamics of a disorder-affected AQS. (a)** Evolution in time τ of the average reduced simulator fidelity as a function of the temperature of the initial state. The system is an Ising spin chain of length 50, the initial state is a thermal state at criticality ($\lambda = 1$), and at time zero the field is suddenly quenched to $\lambda = 2$. In the vertical axis, we show the infidelity (one minus fidelity) normalized by the disorder strength r squared. For larger temperatures (where there are less correlations), the state is more robust. In the inset, we show the average asymptotic infidelity as a function of temperature. For large temperatures it decays as $1/T^2$. **(b)** Evolution of the full simulator fidelity for an initial state equal to the ground state at $\lambda = 0.75$ after a sudden quench to $\lambda = 1.25$. For a local quench in a single site, fidelity saturates rapidly at large values, but decreases strongly for a global quench. **(c)** Asymptotic value of the total simulator fidelity as a function of the initial value of the field λ, with a fixed quench strength of $\delta\lambda = 0.25$. The system is much less robust for global quenches and near criticality ($\lambda = 1$).

11.4 Discussion and Outlook

A key issue for future investigation is the relationship between the robustness of an AQS and its computational power. For the model we have considered here, the physically relevant correlation functions are robust for a reasonable degree of disorder. This suggests that such an AQS could perform well in a laboratory demonstration. But, the transverse Ising model that we considered here is simulatable on a classical computer. Is this connection between robustness and classical simulatability coincidental, or does it reflect a deeper relationship?

Disorder reduces the correlation length of the spin chain. Because less-correlated quantum states can be described with fewer parameters, there is reason to suspect that certain aspects of weakly disordered quantum many-body systems could actually be *easier* to simulate on classical computers than their clean idealized versions. This happens, for example, in the realm of digital quantum computation, where a quantum circuit becomes classically simulatable for noise above the level where quantum gates lose their entangling power [550–552]. In the context of many-body physics, the success of DMRG in, *e.g.*, 1D spin chains, is rigorously related to the existence of efficient MPS representations [456]. These take advantage of the small amount of quantum correlations in such systems, thus compressing the $O(\exp(n))$ parameters needed to describe a general n-particle state to $O(n)$ finite-dimensional matrices (see also Chapter 12.2). In higher-dimensional lattices, states which obey the so-called "area law" [101, 553], where quantum correlations are smaller than in generic states, may still be amenable to a classical simulation using state-of-the-art techniques such as tensor networks [77, 79, 80, 409, 554], density-functional theory [84], or quantum Monte Carlo [73].

We thus arrive at the fundamental question: *Do the finite imperfections of an analog quantum simulator reduce the correlations, and thus the number of parameters needed to describe the system, so as to render the device simulatable by classical means*? We know that for noise above certain levels a digital quantum circuit is classically simulatable and for levels below a certain threshold it can be rendered fault tolerant. Is there an *intermediate regime* for which noise is too great to allow fault-tolerant universal quantum computation, but small enough that an AQS accesses physics beyond classical simulation? The existence of an intermediate regime would imply that there exists a whole class of problems outside P that we can access in the near future, even without a fully functioning quantum computer.

The results we present here, in particular those for dynamics, are an initial attempt – albeit in a trivial model – at understanding the above problem. We

can see how an AQS works well when a classical solution is efficient, and worsens (but only in a limited way) when the problem becomes classically hard to simulate. Even though the underlying model is actually solvable, this may be positive evidence for the existence of an intermediate regime of noise, and the efficiency of AQSs in more complex situations.

Our main discussion focused on AQSs, but similar issues pertain to DQSs. Since to date there exists no known way to fault-tolerantly error-correct AQSs, there is a natural tendency to explore the advantages of DQSs, where error correction is possible. The above discussion shows, however, that a digital implementation of a quantum simulation does not, in itself, guarantee an efficient and more powerful simulation than one that is carried out classically. As in any quantum algorithm, initialization, evolution of the state, and measurement must be performed efficiently, *i.e.*, with a polynomial use of physical resources (space and time). Digital quantum simulation is no exception. Indeed, as discussed in Chapter 1.2, a fault-tolerant implementation of the standard approach based on the Trotter expansion [106] comes at the cost of an overhead in the number of gates and time required that grows exponentially with the degree of precision [68], possibly letting the time needed for fault-tolerant, digital quantum simulation explode [124]. If we can guarantee the reliability of AQSs while avoiding such exponential costs, many open problems from all areas of physics could suddenly come into the reach of being solved.

Finally, we can turn the problem of quantum simulation on its head and ask, what does Nature do? For any real material, like a high-T_c cuprate, has imperfections. Does Nature access highly correlated states that cannot be efficiently simulated on a classical computer? Certainly, in some cases we believe it does, as for example in high-T_c superconductors [5] or in certain ground states of frustrated quantum antiferromagnets which are believed to carry topological order [419]. If noise is low enough, does Nature protect quantum correlations to a degree that classical methods cannot efficiently represent the physically interesting quantities? And, can we exploit this capability with a quantum simulator? If Nature does it, we should take advantage of it!

Part IV

Analytical and numerical methods

In the preceding parts of this PhD thesis, we have theoretically analyzed possibilities as well as limitations for quantum simulation of selected many-body models. To a large extent, the relevance for quantum simulation of systems as these derives from the computational complexity of their many-body ground states, preventing exact and efficient classical calculations in many important cases. From circumstances where such calculations can be carried out, we can hope to derive universal features that can be carried over to more difficult cases. But even in cases where the results are only approximative, calculations allow us to shape the expectations that we can have towards the quantum-simulated systems: How will they most probably behave? Is it likely that they will host fundamentally important properties?

To be useful, such theoretical analyses require accurate techniques. This is the subject of the following chapters, where we describe methods that are especially useful in the context of (but not restricted to) trapped ions and ultracold atoms in optical lattices. Instead of going into technical detail, we will motivate the advantages and limitations of the methods used in the preceding chapters. For a concise discussion of the possible tasks demanded from a quantum simulator and how the different methods perform therein, see also pages 11*ff*.

We start in Chapter 12 by explaining some techniques that are (quasi-)exact, but which have their own restrictions (be it due to the small system sizes treatable, due to being restricted to low dimensions, or due to biases towards slightly-entangled states). In Chapter 13, we review mean-field methods which are more approximative, but which can, *e.g.*, treat very large systems and are not restricted to low dimensions. In this sense, they have properties complementary to the (quasi-)exact techniques. For another approach that falls into the category of mean-field methods, Takahashi's modified spin-wave theory [224], we devote the separate Chapter 14. In that chapter, we also show the validity of this method by computing ground-state phase diagrams of frustrated quantum models relevant to magnetic compounds, and we discuss exotic quantum states of matter that may be found in such materials.

Chapter 12

(Quasi-)Exact methods

In this chapter, we review some of the most common (quasi-)exact methods used to analyze phase diagrams of quantum many-body systems. We discuss first in Sec. 12.1 exact diagonalization (ED), which allows to find the ground state exactly but is restricted to very small systems. In Sec. 12.2 we review shortly the quasi-exact density-matrix renormalization group (DMRG) methods, which are a powerful tool to describe approximate ground states and dynamics in 1D (and since recently also in 2D) with polynomial instead of exponential resources. In Sec. 12.3, we sketch the Jordan–Wigner transformation, which allows to map a certain class of one-dimensional spin models to free-fermion systems, which can then be solved analytically.

12.1 Exact diagonalization

Naively, one might think that the best way to find the ground state of a many-body system is to simply diagonalize its Hamiltonian. However, normally this can be done only for very small systems. The problem results from the exponential scaling of Hilbert space. For example, for a spin-1/2 Hamiltonian of N lattice sites, counting all possible states, the Hilbert space dimension is given by

$$D_H(N) = 2^N \,. \tag{12.1}$$

This exponential scaling leads to drastic demands in terms of computational memory capacities.

To illustrate what this means: for $N = 16$ spins of length 1/2, a matrix with $D_H \times D_H = 2^{16} \times 2^{16} = 4,294,967,296$ complex entries has to be diagonalized. This corresponds to 16Gb of RAM (assuming double precision), which may easily be stored in a modern computer. With only a couple of spins more, only powerful supercomputers can offer the required memory capacities. For example, for 20 spins, $2^{20} \times 2^{20} = 1,099,511,627,776$ complex entries require already 4Tb of RAM. Hence, if no additional tricks are employed already, systems with only around 20 lattice sites are too big for practical systematic investigations. And with another few spins more, even the most powerful computers cannot store the full Hamiltonian matrices into memory. (For example, with $N = 24$ one arrives already in the petabyte range.) In many cases, we would, however, like to characterize the behavior of models relevant for realistic solid state systems. These can have on the order of 10^{23} degrees of freedom, which is essentially the limit of an infinite number particles, *i.e.*, the thermodynamic limit. Even if the exponential growth of computer resources from previous decades (the famous Moore's law [555]) persists, the resulting improvement in terms of simulatable system sizes is only incremental. It is therefore extremely unlikely that a simple improvement of computer power can lead to ED of systems that are sufficiently large so that its observables are close to the thermodynamic limit.

To overcome these limitations at least to some extent, several improvements have been devised. A simple one is to take advantage of the sparse nature of the Hamiltonian matrix (for short-range interactions) and only store non-zero matrix elements, which considerably reduces memory requirements. Second, one can often reduce the effective Hilbert space by introducing a suitable cut-off. In the Bose–Hubbard model (2.4), *e.g.*, one typically restricts the maximally allowed occupation of each site.[1] This cut-off can be justified by the quadratic growth of the interaction energy $Un(n+1)$ with the site occupation n. For example, in the calculations of Chapter 10, we employed this cut-off to reduce the Hilbert space of an ensemble of bosons with on-site and dipolar interactions to tractable sizes. The improvement achieved this way is, however, rather small.

More memory can be economized when the system Hamiltonian has some symmetry, *i.e.*, when there exists some operator $\hat{O}$ which commutes with the Hamiltonian. In this situation, one can find a basis which consists of simultaneous eigenstates of the Hamiltonian and the operator $\hat{O}$, and the Hamiltonian matrix can be written in the form of independent blocks, each corresponding to a subspace with definite eigenvalue of $\hat{O}$. The problem then reduces to the sepa-

[1] Such a cut-off is used in many numerical and analytical techniques, such as DMRG and quantum Monte Carlo schemes, or the Gutzwiller mean-field *Ansatz* (see Chapter. 13.1).

rate diagonalization of each block. This is especially convenient if it is known in which sector one has to search for the ground state. We used this simplification for the spin models of Chapters 3, 7.7, and 14, where the system Hamiltonians contain only terms of the form $S_i^z S_j^z$ and $S_i^x S_j^x + S_i^y S_j^y = (S_i^+ S_j^- + S_i^- S_j^+)/2$. Both types of terms commute with the total magnetization, $\hat{O} = \sum_i S_i^z$, so that our calculations could profit from working at fixed polarization. (Similarly, for the calculations in Chapter 10.3.1, we worked at fixed filling, $\hat{O} = \sum_i \hat{n}_i$, of an extended Bose–Hubbard model.) Even more, separating the eigenstates of the Hamiltonian $\hat{\mathcal{H}}$ with regard to such a symmetry $\left[\hat{O}, \hat{\mathcal{H}}\right]$ has additional advantages. A good example can be found in Chapter 3.2.3, where we classified the excitation spectrum of a frustrated spin Hamiltonian with respect to the magnetization. This allowed to estimate the order properties that the system will attain at *large* sizes.

Another huge reduction of memory cost can be realized by never actually storing the Hamiltonian matrix in memory. This can be done because of the way the most efficient ED algorithms, such as the Lanczos method [226], work. In general, to find the largest eigenvalue of a matrix $\mathcal{A}$, these algorithms iteratively apply the action of $\mathcal{A}$ to a set of vectors. This procedure allows to extract the (practically) exact eigenvectors of $\mathcal{A}$ with largest eigenvalues (except in pathological cases, which can, however, be taken care of by careful implementation of the algorithm). In our case, to find the ground state ψ (the state with largest *negative* eigenvalue) of a quantum mechanical Hamiltonian $\hat{\mathcal{H}}$, one simply uses $\mathcal{A} = -\hat{\mathcal{H}}$ (if the spectrum crosses the zero, a constant energy offset may be necessary to really arrive at the ground state and not the highest excited state). Now, to find the ground state in these algorithms, all one needs is the action of $\hat{\mathcal{H}}$ on the vectors $\boldsymbol{x}$ of the Hilbert space, *i.e.*, $\boldsymbol{x}' = \hat{\mathcal{H}}\boldsymbol{x}$, but not actually $\hat{\mathcal{H}}$ itself. For this, however, it is not necessary to actually store $\hat{\mathcal{H}}$ into memory. Rather, one can implement the action of $\hat{\mathcal{H}}$ onto a wave-function by, *e.g.*, using if- and while-loops. Instead of a D_H-dimensional matrix with $D_H \times D_H$ entries, one then only needs to store the D_H entries of the wave function. Although this method only allows to extract the few lowest-lying states, this is often sufficient, as one often is only interested in the low-energy properties of a Hamiltonian. On the down-side, the required loops can considerably increase the run times of the algorithm. The starting vectors can be completely random, but substantial speed-up of the convergence procedure can be achieved if one can use prior knowledge. For example, if the ground state $\psi(\lambda)$ at some point λ of the phase diagram of $\hat{\mathcal{H}}$ is known, one can obtain the ground state at a near-by point $\lambda+\delta\lambda$ by using $\psi(\lambda)$ as the starting vector of the Lanczos optimization. This assumes

that the state does not change much when proceeding from λ to $\lambda + \delta\lambda$, which is a good assumption far away from quantum phase transitions (QPTs). Using these improvements, modern ED can reach up to 40 lattice sites in spin-1/2 systems (see, *e.g.*, the work by Richter and Schulenburg [556]).

From ED of such small systems, one can often learn surprisingly much about the bulk behavior of a model Hamiltonian. This is especially true, if an adequate finite-size scaling is employed, which can allow to extract a wealth of information about the thermodynamic limit [541]. Further, it is particularly valuable as a complementary method to techniques as mean-field theory, which treat large systems, but often under un-controlled approximations. This makes ED, despite its limitations, an extremely valuable tool. Nowadays, sophisticated ED algorithms are readily available based on open-source packages such as ARPACK [557].

12.2 Density-matrix renormalization group (DMRG) methods

As discussed in the previous section, ED is limited to very small systems, because it essentially considers *all* possible states of the Hilbert space. New ideas – inspired from quantum-information theory – have, however, in recent years led to the understanding that actually physical states occupy only a small "corner" of Hilbert space [75]. If one can find an efficient representation of these physically accessible states, then the computational resources needed for finding ground-states or describing time-evolution of strongly-correlated systems can decrease drastically.

12.2.1 Matrix-product states (MPS) and DMRG

An efficient representation of quantum many-body states can be derived by considering the *matrix-product states* (MPS) formulation. For a system of N lattice sites, any wave function can be written as

$$|\psi\rangle = \sum_{\sigma_1,\ldots,\sigma_N} A^{\sigma_1} A^{\sigma_2} \ldots A^{\sigma_{N-1}} A^{\sigma_N} |\sigma_1,\ldots,\sigma_N\rangle \,, \tag{12.2}$$

where the A^{σ_i} are matrices ($A^{\sigma_{1,N}}$ are vectors) encoding the information of the d_{loc}-dimensional local state spaces σ_i (for a spin-1/2 system: $d_{\mathrm{loc}} = 2$ and

$\sigma_i = \uparrow, \downarrow$). In all generality, the maximal dimension of the A^{σ_i} is $d_{\mathrm{loc}}^{N/2-1} \times d_{\mathrm{loc}}^{N/2}$,[2] so that in principle the matrices A blow up exponentially with the system size N, which is the same problem as faced in ED. However, it turns out that in several physically relevant Hamiltonians the exact ground state is a MPS with small dimension, such as in the AKLT model [558] or the Majumdar–Ghosh chain [559]. In other cases, as long as the system fulfills the so-called *area laws* [101, 553], the singular values of the A^{σ_i} decay exponentially [101, 560]. Therefore, one can retain only the D largest singular values (the so-called *bond dimension*) while assuring exponential precision, thus allowing to efficiently represent ground states within well controlled error bounds.

In general, the accuracy of this representation is connected to the eigenvalue spectra of reduced density operators, implying that a decrease of D limits the amount of entanglement present in the system, which means that good knowledge of the entanglement properties of quantum many-body states is necessary. In this light, insights from the quantum-information perspective have shown that standard MPS methods are less efficient at QPTs and in critical phases, where correlations decay algebraically, and that in two dimensions unrealistically large bond dimensions become necessary. Therefore, MPS methods are particularly successful in one dimensional gapped systems, where already relatively small values of D are sufficient for extremely good accuracy. To give an example (described in Chapter 7), we used this representation to compute the ground state of a long-range interacting spin chain with over a hundred sites.

To find the ground state within the MPS representation, one typically uses iterative algorithms which start from a random MPS, apply the action of the Hamiltonian on it, and then truncate the new MPS again to bond dimension D. This procedure is, in fact, closely connected to the DMRG method [561–565]. In these renormalization methods, one starts from a small 1D chain that can be exactly diagonalized. Then, a new lattice site is added, the Hamiltonian that couples the new site to the chain is renormalized by disregarding all physically irrelevant couplings, and the resulting Hamiltonian is diagonalized. This is repeated iteratively until convergence [409, 566]. Östlund and Rommer demonstrated that, if the renormalization converges to a fixed point, the attained quantum states in the thermodynamic limit (with periodic boundary conditions) can be represented by a MPS [561]. Due to this connection, the names MPS and DMRG are often used interchangeably for these techniques. The current body of knowledge concerning the use of these techniques has reached very

[2] Which A^{σ_i} attains the maximal dimension depends on the decomposition used to reach the matrix-product representation.

sophisticated levels. For a recent pedagogical review, see, *e.g.*, the article by U. Schollwöck [75].

Renormalization group methods have also been generalized to infinite systems, as for example in the infinite time-evolving block-decimation (iTEBD) method [412]. This method exploits the translational invariance of most quantum many-body models and the possibility to parallelize the local updates of the renormalization procedure (instead of sweeping through the chain, as is done in conventional DMRG algorithms). This allows the treatment of quantum many-body models directly in the thermodynamic limit. An example where we used the iTEBD method can be found in Chapter 7.

12.2.2 Limitations of MPS in 2D and their extension to PEPS

In dimensions larger than one, the DMRG algorithm is unpractical, as the bond dimension D needed to accurately represent the ground state can become extremely large. This can be understood from the area law [101, 553], which states that – under quite general circumstances – the entanglement between a block of spins and its environment scales as the boundary of the block. In one dimension, this boundary is a single site, while in two dimensions it is a chain of spins. The number of relevant degrees of freedom D that have to be retained grows exponentially with this boundary, so that calculation in two dimensions become much more problematic. Despite this restriction, recent years have seen spectacular progress in applying DMRG methods to 2D (see especially the works by S. White and coworkers [78, 238, 567, 568]). This is mainly possible by computing the ground states in quasi-one-dimensional ladder geometries followed by a finite-size scaling. Still, the restrictions in memory are considerable, since such a procedure forces the method to work outside of its natural "habitat."

A more natural representation to overcome these restrictions has been developed in recent years, the so called projected entangled-pair states (PEPS) [554, 569–572]. These can be understood as a natural extension of MPS to arbitrary dimensions, which are therefore – even in 2D – quite accurate already at small bond dimension D. Examples can be found in Chapters 3.2 and 14.2, where we used the PEPS algorithm to characterize the ground-state phase diagram of strongly frustrated spin systems. For such frustrated systems, PEPS are particularly suited as the standard method of choice for 2D, QMC, fails due to the famous sign problem [73].

12.2.3 Limitations of MPS at criticality and MERA

Another weak point of standard MPS algorithms are QPTs or critical phases, where correlation lengths diverge [435]. This implies that entanglement at large distances is important [457], and the truncation in the MPS has to be done at high levels. This means that MPS methods perform worst precisely at the most interesting points of a phase diagram.

To overcome this limitation, in recent years the multiscale entanglement-renormalization *Ansatz* (MERA) has been developed [532, 533]. This is a quasi-exact variational method which in particular yields especially good results in critical phases. It consists in postulating a layered tensor-network structure for the low-energy states of the studied Hamiltonian. (MPS methods can be understood as such a tensor network with a single layer.) The tensor network $\mathcal{T}$ has the following properties. (i) It is built from elementary tensors belonging to two different families, isometries $\mathcal{I}_i$ and disentanglers $\mathcal{D}_i$ that are isometric,

$$\mathcal{I}_i\mathcal{I}_i^\dagger = \mathbb{I}, \quad \mathcal{D}_i\mathcal{D}_i^\dagger = \mathbb{I}\,. \tag{12.3}$$

(ii) The tensor network $\mathcal{T}$ has a layered structure, $\mathcal{T} = \prod_i \mathcal{T}_i$, such that each layer $\mathcal{T}_i$ performs an entanglement-renormalization transformation [573, 574] from a lattice $\mathcal{L}_i$ with lattice spacing d_i to a lattice $\mathcal{L}_{i+1}$ with spacing $d_{i+1} = nd_i$, where n is an integer. Property (ii) is at the origin of the ability of the MERA to describe infinite critical states with finite computational resources. Symmetries of the Hamiltonian can be encoded in the structure of the tensors. For example, in order to encode translational invariant states of chains with periodic boundary conditions, one uses inside each layer the same isometry and disentangler as many times as required to complete the entanglement-renormalization transformation from the lattice $\mathcal{L}_i$ to the lattice $\mathcal{L}_{i+1}$. When all the isometries and disentanglers inside a given layer are chosen to be the same, the factor n not only characterizes the blocking factor of the entanglement-renormalization procedure (we call this an *n to 1* MERA) but it also defines the size of the unit cell of the state.

In particular, we used MERA to study modifications of extended Hubbard models by strong dipolar interactions, as presented in Chapter 10.3.2 . In that model, ED indicates the presence of checkerboard (CB) patterns in some parts of the phase diagram, which suggests that we need an *Ansatz* that can naturally encode at least a unit cell of two sites. This can be accomplished by a *2 to 1* MERA, *i.e.*, by blocking two sites into one at each step of the entanglement-renormalization procedure. However, this MERA is computationally more expensive than the *3 to 1* MERA. Unfortunately, the translationally invariant *3*

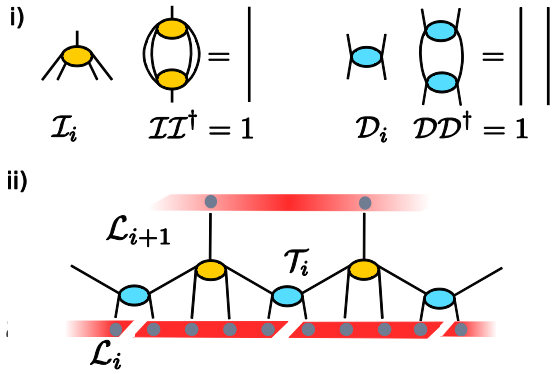

Figure 12.1: **4 to 1 MERA.** Tensors $\mathcal{I}_i$ (isometries) and $\mathcal{D}_i$ (disentanglers) are represented by circles with trailing legs representing their indices. Lines connecting two tensors represent tensor contractions over the involved indices. **(i)** The tensors are chosen such as to fulfill the isometry constraints (12.3). **(ii)** A layer $\mathcal{T}_i$ of the *4 to 1* MERA tensor network $\mathcal{T}$ that maps operators and states defined on a lattice $\mathcal{L}_i$ with lattice spacing d_i to operators and states defined on a lattice $\mathcal{L}_{i+1}$ with lattice spacing $4d_i$ [532].

to 1 MERA does not easily accommodate a CB pattern, whence we choose a *4 to 1* MERA that both naturally accommodates the two-site unit cell of a CB phase and reduces the computational cost of the *2 to 1* MERA [533]. In Fig. 12.1ii, we show a layer of the TN structure for the *4 to 1* MERA that we used in our calculations. Similarly to DMRG methods, MERA has a refinement parameter m_r, larger values of which provide more accurate results but imply larger simulation time, because the complexity of the algorithm is $\mathcal{O}(m_r^5)$ in memory and $\mathcal{O}(m_r^8)$ in the number of operations per iteration [533]. However, modest values of m_r, such as $m_r = 8$, are often enough to acquire qualitatively correct results.

This results in an exponential speed-up compared to ED, combined with excellent accuracy. This advantage makes MERA and related methods such as TEBD and MPS, as well as their extension to 2D, PEPS, enormously useful tools for the analysis of strongly-correlated quantum systems.

12.3 The Jordan–Wigner transformation

In some particular cases, exact analytical results exist to solve the ground- and even excited-state behavior of a quantum many-body system. Whereas these are rare exceptions (and typically only work in 1D), they often serve to benchmark numerical techniques, and one can hope that insights derived from such analytical solutions carry over to a larger family of similar models.

One example of such an exact analytical solution is given by the celebrated Jordan–Wigner transformation. It allows to solve a particular class of 1D spin systems, the nearest-neighbor (NN) XY model in a transverse field, and works even if the model is disordered [435]. This XY model is described by

$$\hat{\mathcal{H}} = -\sum_{j=1}^{N} J_j \left[\frac{1+\gamma}{2} \sigma_j^x \sigma_{j+1}^x + \frac{1-\gamma}{2} \sigma_j^y \sigma_{j+1}^y \right) + \sum_{j=1}^{N} \lambda_j \sigma_j^z \,, \tag{12.4}$$

where σ are the usual spin-1/2 Pauli matrices, and γ interpolates between XX and Ising couplings. Via the Holstein–Primakoff transformation (3.2), the XX model (which is often equally called XY model) is equivalent to a system of hard-core bosons, such as bosonic atoms in optical lattices with strong contact interactions.

The main idea of the Jordan–Wigner transformation is to map the spin degrees of freedom to a system of free fermions, which can then be solved analytically (meaning in this context that a matrix has to be diagonalized, the size of which grows at most polynomially with the chain length).

The mapping to fermionic operators is inspired by the fact that spins fulfill fermionic commutation relations on site, *i.e.*, $\left\{\sigma_j^+, \sigma_j^-\right\} = 1$ and $\left\{\sigma_j^+, \sigma_j^+\right\} = \left\{\sigma_j^-, \sigma_j^-\right\} = 0$. For different sites, however, this is not true, since one has $\left[\sigma_j^+, \sigma_j^-\right] = \left[\sigma_j^+, \sigma_j^+\right] = \left[\sigma_j^-, \sigma_j^-\right] = 0$. Hence, a simple identification of spin operators with fermionic operators is not possible. The basic insight of Jordan and Wigner [575] was that such a mapping between spins and Fermions can be achieved if the non-local operator $\prod_{m<j} \mathrm{e}^{i\pi\sigma_i^+\sigma_i^-}$ is included. The correct transformation that retains the spin commutation relation is then defined by

$$\hat{f}_j = \prod_{m<j} \mathrm{e}^{i\pi\sigma_m^+\sigma_m^-} \sigma_j^- \tag{12.5a}$$

$$\hat{f}_j^\dagger = \sigma_j^+ \prod_{m<j} \mathrm{e}^{i\pi\sigma_m^+\sigma_m^-} \,, \tag{12.5b}$$

where the $\hat{f}_j$ are now spinless fermion operators. Inserting the inverse relations

$$\sigma_j^+ = \hat{f}_j^\dagger \prod_{m=1}^{j-1} \left(1 - 2\hat{f}_m^\dagger \hat{f}_m\right) , \tag{12.6a}$$

$$\sigma_j^- = \prod_{m=1}^{j-1} \left(1 - 2\hat{f}_m^\dagger \hat{f}_m\right) \hat{f}_j , \tag{12.6b}$$

$$\sigma_j^z = 2\hat{f}_j^\dagger \hat{f}_j - 1 \tag{12.6c}$$

(where we have used $e^{i\pi\sigma_m^+\sigma_m^-} = 1 - 2\hat{f}_m^\dagger \hat{f}_m$) into Hamiltonian (12.4), one arrives at the NN, free-fermion (*i.e.*, quadratic in fermion operators) Hamiltonian

$$\hat{\mathcal{H}} = \sum_{ij} \left[\hat{f}_i^\dagger A_{ij} \hat{f}_j + \left(\hat{f}_i^\dagger B_{ij} \hat{f}_j^\dagger + \text{h.c.}\right)\right] - \frac{1}{2}\sum_j A_{jj} , \tag{12.7}$$

where

$$A_{ij} = -J_j \left(\delta_{j,i+1} + \delta_{j,i-1}\right) - 2\lambda_i \delta_{j,i} , \tag{12.8a}$$

$$B_{ij} = -J_j \gamma \left(\delta_{j,i+1} - \delta_{j,i-1}\right) . \tag{12.8b}$$

Here, the relationship $\left(1 - 2\hat{f}_m^\dagger \hat{f}_m\right)\left(1 - 2\hat{f}_m^\dagger \hat{f}_m\right) = 1$ has canceled all non-local terms (to see this, use the fermionic commutation relations together with $\hat{f}_m \hat{f}_m = \hat{f}_m^\dagger \hat{f}_m^\dagger = 1$).

Hamiltonian (12.7) can now be diagonalized to

$$\hat{\mathcal{H}} = \sum_{k=1}^{N} \Lambda_k \hat{\eta}_k^\dagger \hat{\eta}_k + E_0 , \tag{12.9}$$

where $\Lambda = \Phi\left(A - B\right)\Psi^\top$ is diagonal, and where $E_0 = -\text{Tr}\left(\Lambda\right)/2$ is a constant energy offset. Λ, Φ, and Ψ can be obtained from the singular value decomposition of $Z \equiv A - B$. The normal modes are $\hat{\eta}_k = \sum_{j=1}^{N}\left(g_{k,j}\hat{f}_j + h_{k,j}\hat{f}_j^\dagger\right)$, where $g = \left(\Phi + \Psi\right)/2$, and $h = \left(\Phi - \Psi\right)/2$. From this, one can in principle compute all observables of interest.

For example, the excitation spectrum, including the gap Δ to the first excited state, is simply contained in the normal mode spectrum Λ_k. Other important observables, such as ground-state expectation values, can be computed using the fact that the ground state $|\psi\rangle$ of Hamiltonian (12.9) is the vacuum of the normal modes (*i.e.*, $\hat{\eta}_k |\psi\rangle = 0$, $\forall k$). For the ZZ-correlations, for instance, this

yields

$$\begin{aligned} C(i,j) &\equiv \langle\psi_r|\sigma_z^{(i)}\sigma_z^{(j)}|\psi_r\rangle - \langle\psi_r|\sigma_z^{(i)}|\psi_r\rangle\langle\psi_r|\sigma_z^{(j)}|\psi_r\rangle \\ &= 4\langle\psi_r|\hat{f}_i^\dagger\hat{f}_i\hat{f}_j^\dagger\hat{f}_j|\psi_r\rangle - 4\langle\psi_r|\hat{f}_i^\dagger\hat{f}_i|\psi_r\rangle\langle\psi_r|\hat{f}_j^\dagger\hat{f}_j|\psi_r\rangle \\ &= 4\left(h^\top h\right)_{ij}\left(g^\top g\right)_{ij} - 4\left(h^\top g\right)_{ij}\left(g^\top h\right)_{ij} . \end{aligned} \tag{12.10}$$

Unfortunately, the Jordan–Wigner transformation allows only the exact solution of a very restricted class of spin models. For one, the non-local operators $\prod_{m=1}^{j-1}\left(1-2\hat{f}_m^\dagger\hat{f}_m\right)$ only cancel for NN spin–spin interactions. Including next NN interactions leads to a system of *interacting* fermions (*i.e.*, the Hamiltonian includes terms quartic in the fermion operators), which cannot be solved analytically. Similarly, the standard Jordan–Wigner transformation fails in dimension higher than one, although there are many efforts to generalize it to higher dimensions (see, *e.g.*, the work by Verstraete and Cirac [576]; for a brief review of other such attempts, see also Chapter 19 in A. Tsvelik's book [577]). Still, the specialized class of models the Jordan–Wigner transform *can* solve is quite fundamental, and one hopes that results derived for them are of universal nature.

Interestingly, the Jordan–Wigner and Holstein–Primakoff transformations, Eqs. (12.6) and (3.2), imply that, in 1D, there is no fundamental difference between spins, fermions, and hard-core bosons. The crossover from bosonic to fermionic behavior upon increasing repulsion has been nicely shown – more than 40 years after the theoretical analysis by M. Girardeau [578] – in the recent ultracold-atoms experiments in I. Bloch's group [579].

In this thesis, we applied the Jordan–Wigner transformation to compare the results of an ideal AQS simulating the XY model (12.4) to the performance of a real-world, disorder-affected AQS (Chapter 11). Meaningful observables for this purpose are the global simulator fidelity F (the overlap to the disorder-free ground state) and reduced simulator fidelities.

Ground-state fidelities. In general, the overlap between the ground states of two realizations of Hamiltonian (12.7), parametrized by Z and $\widetilde{Z}$, is [530]

$$F\left(Z,\widetilde{Z}\right) = \sqrt{\det\frac{1+T^{-1}\widetilde{T}}{2}}\,, \tag{12.11}$$

with $T = \left(\Phi^{-1}\Lambda\Phi\right)^{-1} Z$. We define the simulator fidelity F as the overlap at fixed λ between the ideal, disorder-free state and the state at disorder strength

r,

$$F(r,\lambda) \equiv F\left(Z(\lambda)_r, Z(\lambda)_0\right) . \tag{12.12}$$

This is a global quantity. In our analysis of the disorder-affected QS, one can expect that local observables are more robust. A measure for the change of local quantities is the *single-site simulator fidelity*

$$f_1(r,\lambda) = \sum_{i=1}^{L} \mathrm{tr}\sqrt{\sqrt{\hat{\rho}_i^{(0)}(\lambda)}\hat{\rho}_i^{(r)}(\lambda)\sqrt{\hat{\rho}_i^{(0)}(\lambda)}}\,, \tag{12.13}$$

where $\hat{\rho}_i^{(r)} = \mathrm{tr}_{\mathcal{C}\setminus\{i\}}\hat{\rho}$ is the reduced density matrix of site i under disorder r, and $\hat{\rho}_i^{(0)}$ is the one in the disorder-free case. Here, $\mathcal{C}\setminus\{i\}$ denotes the chain without spin i. Since one can expand $\hat{\rho}_i = \frac{1}{2}\left(\mathbb{I} + \sum_{\mu=x,y,z}\langle\sigma_i^\mu\rangle\,\sigma^\mu\right)$, the single-site reduced density matrix is completely determined by the expectation values of σ_i^μ. In Chapter 11, we also analyzed the NN *two-site simulator fidelity*

$$f_2 = \sum_{i=1}^{L} \mathrm{tr}\sqrt{\sqrt{\hat{\rho}_{i,i+1}^{(0)}(\lambda)}\hat{\rho}_{i,i+1}^{(r)}(\lambda)\sqrt{\hat{\rho}_{i,i+1}^{(0)}(\lambda)}}\,. \tag{12.14}$$

Here, $\hat{\rho}_{i,i+1}^{(r)} = \mathrm{tr}_{\mathcal{C}\setminus\{i,i+1\}}\hat{\rho}$ is the reduced density matrix of sites $(i,i+1)$ under disorder r, and $\hat{\rho}_{i,i+1}^{(0)}$ is the one in the disorder-free case.

Time dependent fidelities. For time evolution, we distinguish between the zero- and finite-temperature fidelities, although the underlying technique is the same. We start by rewriting the fermionic Hamiltonian (12.7) as

$$\hat{\mathcal{H}} = \frac{1}{2}\vec{\hat{\Psi}}^\dagger \cdot \mathrm{H} \cdot \vec{\hat{\Psi}}, \tag{12.15}$$

where $\vec{\hat{\Psi}}^\dagger = (\hat{f}_1^\dagger, ..., \hat{f}_N^\dagger, \hat{f}_1, ..., \hat{f}_N)$ is a length-$2N$ vector composed of all creation and annihilation operators present in $\hat{\mathcal{H}}$, and $\mathrm{H} = A\otimes\sigma_z + iB\otimes\sigma_y$ is a $2N\times 2N$ matrix with complex coefficients.

For computing fidelities, we use the convenient Levitov's formula [580, 581], which relates traces of operators in the Hilbert space of the fermions to determinants of much smaller matrices (like H). For example, let $\hat{P} = \vec{\hat{\Psi}}^\dagger \cdot \mathrm{P} \cdot \vec{\hat{\Psi}}$ and $\hat{Q} = \vec{\hat{\Psi}}^\dagger \cdot \mathrm{Q} \cdot \vec{\hat{\Psi}}$ be two operators in the space of fermions, with P and Q complex-valued $2N\times 2N$ matrices. Then,

$$\mathrm{Tr}\left(e^{\hat{P}}e^{\hat{Q}}\right) = \det\left(1 + e^{\mathrm{P}}e^{\mathrm{Q}}\right). \tag{12.16}$$

Similar formulas hold for a larger or smaller number of operators.

In the zero-temperature case, when the initial state remains pure after evolution, the fidelity takes the form of an overlap

$$F = |\langle\psi_0(t)|\psi_r(t)\rangle|, \tag{12.17}$$

where $|\psi_0(t)\rangle = e^{-i\hat{\mathcal{H}}_0 t}|\psi_0\rangle$ is the initial state evolved with the target Hamiltonian of the simulation, $\hat{\mathcal{H}}_0$, and $|\psi_r(t)\rangle = e^{-i\hat{\mathcal{H}}_r t}|\psi_0\rangle$ is the same state evolved with an imperfect Hamiltonian $\hat{\mathcal{H}}_r = \hat{\mathcal{H}}_0 + r\hat{V}$. Rewriting the fidelity,

$$F = \mathrm{Tr}\ \hat{\rho}_0 e^{i\hat{\mathcal{H}}_r t} e^{-i\hat{\mathcal{H}}_0 t}, \tag{12.18}$$

with $\hat{\rho}_0 = |\psi_0\rangle\langle\psi_0|$, we can use Levitov's formula and obtain

$$F = \det\left(1 - G_0 + G_0 e^{i\mathrm{H}_r t} e^{-i\mathrm{H}_0 t}\right), \tag{12.19}$$

with $G_0 = \langle\psi_0|\hat{G}|\psi_0\rangle$, and $\hat{G}$ the correlation matrix of the original fermionic operators, $\hat{G}_{i,j} = \hat{\Psi}_i^\dagger \hat{\Psi}_j$.

If the initial state is not pure but a thermal state, the state remains mixed even if the evolution is unitary. In this case, we cannot compute the fidelity for the full many-body state, but only the fidelity of the reduced density matrix for a few spins. For this we must evaluate the correlation functions of the Pauli operators at different sites of the chain. For the case of a single spin, the symmetry of the system ensures that at all times the reduced density matrix can be written as $\hat{\rho} = (1 + \langle\sigma_x^i\rangle\sigma_x^i)/2$. Since $\langle\sigma_x^i\rangle = \langle\hat{f}_i^\dagger \hat{f}_i\rangle$, we only need to compute the evolution of the diagonal terms in the G correlation matrix.

Chapter 13

Mean-field methods

Nowadays, a large variety of approximative analytical methods exists that are complementary to (quasi-)exact methods. Many of these analytical techniques have reached excellent levels of refinement, allowing to not only form intuition but also to obtain quantitatively reliable predictions at strongly reduced cost in terms of numerical resources. In this respect, mean-field approaches are particularly widely used, because they give – despite their simple implementation – good qualitative and even quantitative results.

The unifying concept behind mean-field theories is to neglect some kind of correlations, thus typically decoupling higher-order expectation values into products of lower order. A simple example is the first mean-field theory, the one of magnetism introduced by P. E. Weiss. It treats Hamiltonians of the form

$$\hat{\mathcal{H}} = J \sum_{\langle ij \rangle} \boldsymbol{S}_i \boldsymbol{S}_j + h \sum_i \boldsymbol{S}_i \,, \tag{13.1}$$

where J denotes the coupling between spins $\boldsymbol{S}_i$ and $\boldsymbol{S}_j$ occupying neighboring sites i and j, and h is an external magnetic field. To find an approximation to the ground state, one decouples interaction terms between spins as

$$\sum_{\langle ij \rangle} \langle \boldsymbol{S}_i \boldsymbol{S}_j \rangle \to \sum_{\langle ij \rangle} \langle \boldsymbol{S}_i \rangle \langle \boldsymbol{S}_j \rangle \,. \tag{13.2}$$

The energy

$$E \equiv \langle \hat{\mathcal{H}} \rangle = \sum_i \langle \boldsymbol{S}_i \rangle \left(h + J \sum_{j \,\mathrm{NN}\, i} \langle \boldsymbol{S}_j \rangle \right) \tag{13.3}$$

can now be minimized in a self-consistent way. As the expression for E shows, the decoupling (13.2) amounts to regarding spin $\boldsymbol{S}_i$ as sitting in a magnetic field generated by the external field h plus a NN contribution, the "mean field" $\sum_{j\,\mathrm{NN}\,i} \langle \boldsymbol{S}_j \rangle$ (also called "molecular field"). Historically, mean-field theory was for a long time the *only* theory of phase transitions. Since its beginnings, it has been generalized to a great number of applications, and even today mean-field theory is typically the first tool to sort out the essential physics when confronted with an unexplored many-body problem.

The reliability of mean-field theory increases with the dimensionality of the system (in four dimensions, it gets exact for conventional systems with short-range interactions), but many refinements have been devised to improve its performance also in low dimensions. As a big advantage, many formulations of mean-field theory work naturally in the thermodynamic limit so that one can nicely confront their approximate results on large systems to, *e.g.*, ED results on small systems. It is tempting to accept features that appear in both limits as the true behavior of the model under consideration.

In this chapter, we discuss several mean-field methods which are useful for treating ultracold atoms in optical lattices. First, in Sec. 13.1, we discuss the Gutzwiller mean-field *Ansatz* (GMFA), which is one of the most simple mean-field methods, entirely neglecting correlations between sites. Despite its simplicity, this *Ansatz* exactly solves the Bose–Hubbard model (2.4) at integer filling in the limit of infinite interactions $U/t \to \infty$, where the system is perfectly Mott-insulating. A related method is to start from the insulating ground state of $U/t \to \infty$ and take tunneling terms t into account perturbatively (the so called strong-coupling expansion). As a simplification, the tunneling terms can then be treated – in the so called perturbative mean-field theory (PMFT), discussed in Sec. 13.2 – at a mean-field level. This technique allows to trace an upper limit for the insulating phase, and also allows to find meta-stable insulating states in a straightforward fashion. Finally, we discuss a method valid in the opposite limit of weak interactions, namely an expansion in the fluctuations of a Bose–Einstein-(quasi-)condensate due to Mora and Castin [262] (Sec. 13.3). Contrary to GMFA and PMFT, this method is valid if correlations do not decay too rapidly, which in 2D is the case at low temperatures and weak interactions. For another mean-field *Ansatz*, the modified spin-wave theory, which we used extensively for our calculations presented Chapter 3, we reserve the separate Chapter 14.

13.1 The Gutzwiller mean-field *Ansatz*

Maybe the simplest mean-field method, the Gutzwiller mean-field *Ansatz* (GMFA) [582, 583], is – despite its conceptual and numerical simplicity – a reliable tool to get a qualitative picture of ground-state phase diagrams of many-body systems. In particular, it predicts quite correctly the quantum critical points separating the Mott phase from the SF phase in the Bose–Hubbard model in 3D, or even in 2D. Its accuracy, however, decreases dramatically for 1D systems.

13.1.1 General formalism

A relatively general model amenable to a treatment with the GMFA is the extended Bose–Hubbard Hamiltonian,

$$\hat{\mathcal{H}} = -\sum_{ij} t_{ij}\hat{b}_i^\dagger\hat{b}_j + \sum_i \frac{U_i}{2}\hat{n}_i\left(\hat{n}_i - 1\right) + \sum_{ij} V_{ij}\hat{n}_i\hat{n}_j + \sum_i \mu\,\hat{n}_i\,. \tag{13.4}$$

Here, $\hat{b}_i$ ($\hat{b}_i^\dagger$) annihilates (creates) a boson at site i, and $\hat{n}_i = \hat{b}_i^\dagger\hat{b}_i$ is the corresponding number operator; t_{ij} denotes the tunneling amplitude between sites i and j, μ_i is the chemical potential controlling the filling, U_i the on-site interaction, and V_{ij} an off-site interaction. The GMFA can be applied in a straightforward manner to systems with long-range interactions V_{ij} or tunnelings t_{ij}, where other methods such as DMRG become considerably more complex. Such models are relevant to, *e.g.*, dipolar atoms in optical lattices (Chapter 10) or trapped-ion quantum simulations of spin systems (Chapter 7).

In its simplest version, the GMFA is based on neglecting correlations between different sites, *i.e.*, it approximates the many-body wave function by a product over single-site contributions

$$|\psi_{\mathrm{GMFA}}\rangle = \bigotimes_i \sum_{n=0}^{n_{\max}} f_n^{(i)}\,|n\rangle_i\,. \tag{13.5}$$

Here, $|n\rangle_i$ denotes the Fock state of n atoms in the i-th lattice site with its corresponding amplitude $f_n^{(i)}$; $n_{\max}$ is a (system-size independent) cut-off for the number of atoms per site. The amplitudes are normalized to $\sum_n \left|f_n^{(i)}\right|^2 = 1$. One can find the variational ground state of Hamiltonian (13.4) within this

Ansatz by minimizing its energy expectation value,

$$E \equiv \langle \hat{\mathcal{H}} \rangle = -\sum_{ij} t_{ij} \langle \hat{b}_i^\dagger \rangle \langle \hat{b}_j \rangle + \sum_i \frac{U_i}{2} \langle \hat{n}_i (\hat{n}_i - 1) \rangle + \sum_{ij} V_{ij} \langle \hat{n}_i \rangle \langle \hat{n}_j \rangle + \sum_i \mu \langle \hat{n}_i \rangle \ . \tag{13.6}$$

Inserting the expectation values

$$\langle \hat{b}_i \rangle = \sum_{n=0}^{n_{\max}-1} \sqrt{n+1} f_i^{(n)*} f_i^{(n+1)} \ , \quad \text{and} \tag{13.7a}$$

$$\langle \hat{n}_i^q \rangle = \sum_{n=0}^{n_{\max}} n^q \left| f_i^{(n)} \right|^2 \ , \tag{13.7b}$$

we obtain

$$\begin{aligned} E = & -\sum_{ij} t_{ij} \sum_{n,n'=0}^{n_{\max}-1} \sqrt{n+1}\sqrt{n'+1} f_i^{(n)*} f_i^{(n+1)} f_j^{(n')*} f_j^{(n'+1)} \\ & + \sum_i \sum_{n=0}^{n_{\max}} \left[\frac{U_i}{2} (n-1) + \mu \right] n \left| f_i^{(n)} \right|^2 + \sum_{ij} V_{ij} \sum_{n,n'=0}^{n_{\max}} n\, n' \left| f_i^{(n)} \right|^2 \left| f_j^{(n')} \right|^2 \ . \end{aligned} \tag{13.8}$$

The variational ground state can now be found by minimizing E with respect to the $f_i^{(n)}$. A convenient way to do this is via the Schrödinger equation,

$$\hat{\mathcal{H}} |\Psi\rangle = i \frac{\partial}{\partial t} |\Psi\rangle \ . \tag{13.9}$$

Multiplying from the left by $\langle\Psi|$, we can rewrite it in the form

$$E = i \langle \Psi | \frac{\partial}{\partial t} |\Psi\rangle = i \bigotimes_i \sum_n f_i^{(n)*} \langle n|_i \sum_l \bigotimes_{j \neq l} \sum_{n'} f_j^{(n')} |n'\rangle_j \otimes \sum_{n''} \dot{f}_l^{(n'')} |n''\rangle_l \ . \tag{13.10}$$

Invoking $\langle n|_i |n'\rangle_i = \delta_{n,n'}$ and the normalization of the $f_i^{(n)}$, this yields

$$E = i \sum_l \sum_n f_l^{(n)*} \dot{f}_l^{(n)} \ , \tag{13.11}$$

and therefore, taking the functional derivative of E,

$$\frac{\delta E}{\delta f_l^{(n)*}} = i \dot{f}_l^{(n)} \ . \tag{13.12}$$

Finally, expressing the left-hand side in terms of the $f_i^{(n)}$, using the expectation value of the energy (13.8), gives a self-consistent equation for the amplitudes $f_i^{(n)}$. This equation can be solved by imaginary-time evolution, leading to the Gutzwiller variational ground state.

13.1.2 Example: standard Bose–Hubbard model

As an example, let us consider the homogeneous NN Bose–Hubbard model, corresponding to Eq. (13.4) with $t_{ij} = 0 \ \forall \, |i-j| > 1$, $U_i \equiv U$, and $V_{ij} \equiv 0$. At an integer number of particles per site n_0, this model undergoes the SF to MI transition. In the GMFA, this is identified as the point $t/U = (t/U)_c$ where the SF order parameter $\langle \hat{b}_i \rangle$ becomes finite. For $t/U < (t/U)_c$, the amplitudes are $f_n^{(i)} = \delta_{n,n_0}$ (resulting in $\langle \hat{b}_i \rangle = 0$), implying that the wave function is a single Fock state, $|\psi_{\mathrm{GMFA}}\rangle = |n_0, n_0, ...\rangle$. Hence, the Gutzwiller wave function reproduces the exact behavior in the limit $t/U \to 0$. It is also possible to argue that the differences between the exact result and the GMFA (13.5) are negligible in the limit of a large lattice and $t/U \to \infty$ [584]. Therefore, one may hope that the GMFA also reasonably interpolates between these two extreme limits and gives a qualitatively reliable overview of the entire phase diagram.

To quantitatively evaluate the reliability of the GMFA, we compare its predictions for the SF–MI transition to other, more sophisticated methods. According to the GMFA, the critical point $(t/U)_c$ for the $n_0 = 1$ MI–SF transition is located at $1/(5.8z)$ [584]. Here, the dimensionality of the system only enters via the coordination number z (*i.e.*, the number of NNs). A comparison of the critical tunneling with precise predictions from state-of-the-art-methods is displayed in Table 13.1a. In 3D, the agreement is satisfactory (considering the simplicity of the GMFA), but in 1D there are huge discrepancies.

This is mainly due to the fact that mean-field lobes such as predicted by the GMFA are always rounded off at their tip, as can be seen in the color data of Fig. 13.1b. In 2D and 3D, this behavior is correct, but in 1D the true lobes have strongly pointed cusps, as can be seen in the data from Freericks and Monien (black lines and dots in the foreground of Fig. 13.1b) [411]. Due to this property, the tip of the lobe actually extends to much larger values than predicted by the GMFA.

13.1.3 Advantages and limitations

Despite its limitations, the Gutzwiller *Ansatz* is attractive for a number of reasons. First, the numerical demand is quite low and convergence is achieved easily as long as the system is reasonably homogeneous and metastable states do not hinder reaching the ground state (these can become problematic, *e.g.*, in extended Bose–Hubbard models such as encountered in Chapter 7). In homogeneous situations, since the Gutzwiller *Ansatz* does not host any correlations between sites, there is no length scale in the system and calculations for a single

a)

	z	GMFA	benchmark value
3D	6	0.0287	0.034
2D	4	0.0431	0.061
1D	2	0.0862	0.29

b)

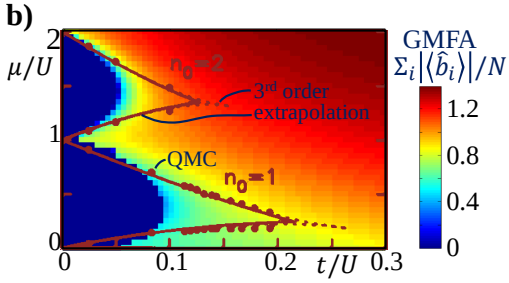

Figure 13.1: **Benchmarking GMFA. Table (a) Comparison of GMFA predictions to state-of-the-art results,** for the critical point of the $n_0 = 1$ SF–MI transition on a cubic lattice (coordination number z). In 3D GMFA performs satisfactorily, while in 1D huge discrepancies become apparent. The reference results are as follows. 3D: perturbative expansions [411] and QMC [585], 2D: QMC [586], 1D: DMRG [587]. **Figure (b) Mott lobes with $n_0 = 1$ and 2 for the 1D Bose–Hubbard model.** The GMFA (color data) traces reliably the boundaries of the Mott lobes for low tunneling t/U, but at their tips the lobes are rounded off. The true lobes are pointy as shown by the green data in the foreground, taken from Freericks and Monien [411] (dashed and solid lines: 3rd order strong-coupling expansion and extrapolation to infinite order; dots: QMC from Batrouni and Scalettar [588]).

site correspond already to the thermodynamic limit (*i.e.*, if there are no density waves, in which case one has to take as many sites as needed to accommodate the periodicity of the ground state). For inhomogeneous situations, the simplicity of the GMFA still allows to treat extremely large lattices. For instance, calculations in experimentally realistic three-dimensional systems of ultracold atoms, including trapping potentials, have been done for up to 65^3 lattice sites [589]. Second, the Gutzwiller approach can be easily extended to a variety of systems, such as Bose–Bose [590, 591] or Bose–Fermi mixtures [592–594], systems with long-range interactions (see Chapters 7 and 10), or occupation-dependent terms (Chapters 9 and 10). It even allows to treat time-dependent problems [590].

However, the simplicity of the GMFA also leads to a variety of problems. For example, only in the limit $t/U = 0$ is the Mott insulator really given by a single Fock state $|\psi\rangle = |n_0, n_0, ...\rangle$. At finite $t/U \neq 0$, there are correlations between sites, and the Mott insulator acquires small occupation-number fluctuations. Another drawback of the *Ansatz* (13.5) is the missing distance-dependence of correlations. This implies a vanishing correlation length, which should, however, diverge close to a QPT. This consideration shows that one cannot expect quantitatively reliable results close to such quantum critical points. In fact, being a mean-field theory, the GMFA always predicts mean-field exponents for the universal critical behavior of the system. Related to this, the Gutzwiller approach in general underestimates finite-size effects. For instance, it predicts QPTs in systems of any size, while these can – strictly speaking – only occur in the thermodynamic limit. Also, GMFA is usually formulated in the grand-canonical ensemble, because it is not simple to apply it in the canonical ensemble with fixed number of particles. This problem can be solved by a projection of the Gutzwiller wave function (13.5) onto the subspace of fixed atom number [583, 590], but the subsequent calculations become more complicated. Finally, while the ground-state phase diagram can be obtained easily, the calculation of excited states is not possible in the standard Gutzwiller formalism.

While there exist various improvements over the GMFA, for the purpose of quickly reaching an intuitive understanding, it proved to be sufficient in a variety of systems treated in this thesis (see Chapters 4, 6, 7, and 9).

13.2 Perturbative mean-field theory

Another mean-field method that works well at small tunneling is the perturbative mean-field theory (PMFT). It is a relatively simple analytical tool which can give upper bounds for critical points between insulating and SF phases.

However, it is not the method of choice to predict further properties of the involved phases, such as correlations or the precise values of order parameters.

Let us exemplify how this *Ansatz* works at the example of the extended XXZ model,

$$\hat{\mathcal{H}} = \sum_{i<j} J_{ij} \left[S_i^z S_j^z + \lambda \left(S_i^x S_j^x + S_i^y S_j^y \right) \right] - h \sum_i S_i^z \,, \tag{13.13}$$

where h is a magnetic field, and the S_i^α are spin-operators at site i. We have analyzed this Hamiltonian in detail in Chapter 7 (where $J_{ij} = \cos\theta / |i-j|^3$, $\lambda = \tan\theta$, $h = \mu / \cos\theta$).

Within PMFT, one decomposes the Hamiltonian into an interaction part $\hat{\mathcal{H}}_0$ and a tunneling part $\hat{\mathcal{H}}_{\rm per}$, such that $\hat{\mathcal{H}} = \hat{\mathcal{H}}_0 + \hat{\mathcal{H}}_{\rm per}$. Typically, the ground state of $\hat{\mathcal{H}}_0$ is an insulating state that is known exactly, to which $\hat{\mathcal{H}}_{\rm per}$ is then introduced as a perturbation.

For Hamiltonian (13.13), we choose

$$\hat{\mathcal{H}}_0 = \sum_{i<j} J_{ij} S_i^z S_j^z - h \sum_i S_i^z \,. \tag{13.14}$$

The ground states of this Hamiltonian are insulating states with a filling depending on h (see Chapter 7.3). To this, we introduce the perturbation

$$\hat{\mathcal{H}}_{\rm per} = \sum_{i<j} J_{ij} \lambda \left(S_i^x S_j^x + S_i^y S_j^y \right) = \sum_{i<j} J_{ij} \lambda S_i^+ S_j^- \,. \tag{13.15}$$

The aim is now to find the tunneling strength λ where the expectation value of the SF order parameter becomes finite. That point provides an estimation of the upper bound for the break down of the insulating phase. In general, the SF order parameter of site i is

$$\langle S_i^- \rangle = {\rm Tr} \left(\hat{\rho} S_i^- \right) \,, \tag{13.16}$$

where S_i^- is the spin lowering operator at site i and $\hat{\rho}$ is the density matrix of the system, given by

$$\hat{\rho} = {\rm e}^{-\beta \hat{\mathcal{H}}} / Z \,, \tag{13.17}$$

with Z the partition function and $\beta = 1/(k_B T)$ the inverse temperature.

For small tunneling, *i.e.*, small $\hat{\mathcal{H}}_{\rm per}$, we can approximate $\hat{\rho}$ using the Dyson expansion

$${\rm e}^{-\beta \hat{\mathcal{H}}} \simeq {\rm e}^{-\beta \hat{\mathcal{H}}_0} - {\rm e}^{-\beta \hat{\mathcal{H}}_0} \int_0^\beta {\rm d}\tau {\rm e}^{\tau \hat{\mathcal{H}}_0} \hat{\mathcal{H}}_{\rm per} {\rm e}^{-\tau \hat{\mathcal{H}}_0} \,. \tag{13.18}$$

Now, we make a convenient simplification, namely we treat $\hat{\mathcal{H}}_{\rm per}$ in a mean-field approximation,

$$\hat{\mathcal{H}}_{\rm per} \simeq \sum_{i<j} J_{ij}\lambda\left(S_i^+\langle S_j^-\rangle + \langle S_i^+\rangle S_j^- - \langle S_i^+\rangle\langle S_j^-\rangle\right). \tag{13.19}$$

We insert this together with Eqs. (13.17) and (13.18) into the expectation value (13.16). Further, since we are interested in ground-state properties, we take the limit $\beta\to\infty$. Then, the partition function goes to $Z\to \mathrm{e}^{-\beta E_0}$, where E_0 is the ground-state energy. These steps yield a self-consistent equation for the SF order parameter,

$$\langle S_l^-\rangle = -\mathrm{e}^{\beta E_0}\int_0^\beta \mathrm{d}\tau \mathrm{Tr}\left\{S_l^-\mathrm{e}^{-(\beta-\tau)\hat{\mathcal{H}}_0}\left(-\frac{\lambda}{2}\sum_i S_i^+\overline{\langle S_i^-\rangle}\right)\mathrm{e}^{-\tau\hat{\mathcal{H}}_0}\right\}, \tag{13.20}$$

where we introduced the abbreviation

$$\overline{\langle S_i^-\rangle} \equiv \sum_{j,j\neq i} J_{ij}\langle S_j^-\rangle. \tag{13.21}$$

One finds that in the trace appearing in Eq. (13.20) only one-hole excited states and the ground state yield finite contributions.

For small λ, Eq. (13.20) has only the trivial solution $\langle S_i^-\rangle = 0$. At some critical tunneling, however, SF order develops, *i.e.*, $\langle S_i^-\rangle \neq 0$. An easy way to compute the critical tunneling for finite systems of size N, is to write the self-consistent equation (13.20) in matrix form, *i.e.*,

$$\overrightarrow{\langle S^-\rangle} = \mathcal{A}\cdot\overrightarrow{\langle S^-\rangle}, \tag{13.22}$$

where $\overrightarrow{\langle S^-\rangle} = (\langle S_1^-\rangle, \langle S_2^-\rangle, \ldots, \langle S_N^-\rangle)^\top$. When $\det\mathcal{A}\neq 0$, the self-consistent equation (13.20) admits a non-trivial solution $\overrightarrow{\langle S^-\rangle}\neq 0$. Within second-order perturbation theory, the tunneling term for this solution contributes a non-vanishing, negative amount to the energy of the Mott-insulating state, contrary to the trivial solution $\overrightarrow{\langle S^-\rangle} = 0$, where the tunneling contribution vanishes. Therefore, without having to know its precise form, we are assured that the solution $\overrightarrow{\langle S^-\rangle}\neq 0$ forms the new ground state, and the λ at which $\det\mathcal{A}$ becomes finite identifies the QPT to the SF phase.

Remarkably, the properties of PMFT and the GMFA (discussed in Sec. 13.1) complement each other. For example, within PMFT, the mechanism for the break down of the insulating phase is an instability under adding or removing

a single particle. Potentially, there are, however, more complicated excitations than that. For instance, in extended Bose–Hubbard models with interactions which go beyond on site, the addition of a particle plus a relocation of neighboring particles can be a relevant excitation for insulating crystals. In the simple PMFT, this type of excitations is not captured, which is an important disadvantage compared to the GMFA. Also, PMFT is more easily implemented to compute the transition between SF and insulating phases, but not their precise properties. An important advantage of PMFT is, however, that it allows to find the extent of metastable insulating states in a straightforward manner. To this, one simply perturbs around a different insulating state than the actual ground state. We used this property of PMFT in Chapter 7 to characterize the manifold of metastable states that Hamiltonian (13.13) with long-range J_{ij} accommodates at small tunneling.

In the opposite limit of weak interactions, LRO develops, and a mean-field *Ansatz* that neglects correlations between sites is no longer valid. In the next section, we discuss a method that poses a convenient alternative in such a regime.

13.3 Mora–Castin expansion in fluctuations of a BEC

For typical scenarios in the Bose–Hubbard model (2.4), the bosons become superfluid at small interactions U. They then transmit long-range correlations, and the ground state is characterized by LRO of density as well as phase. In that case, a description in terms of a Bogolioubov–deGennes expansion of the condensate wave function gives a good quantitative description of the ground-state behavior. Here, field operators are replaced by mean values dressed with small fluctuations around them. However, at increasing interactions such ordering tendencies are suppressed, leading in the large-U limit to the MI state without long-range correlations. This disruption of order is strongly enhanced by geometrical frustration, as described in Chapters 3.2 or 3.4. It can be expected that frustration reduces order also in the weakly-interacting regime, at least for the condensate phase $\hat{\varphi}$, which is subject to stronger fluctuations than the density. Since the standard Bogolioubov–deGennes expansion assumes the smallness of long-range phase fluctuations, it is in such a situation not an adequate approach.

This problem is overcome by the expansion due to Mora and Castin [262], which relies on the much less stringent assumption that not long-range but only

NN phase fluctuations are small. This *Ansatz*, in particular, also allows the description of quasi-condensates.

In the Mora–Castin formalism, the bosonic operators in the Bose–Hubbard Hamiltonian (2.4) are rewritten as

$$\hat{b}_i \to \mathrm{e}^{i\hat{\varphi}_i}\sqrt{\hat{n}_i}\,, \tag{13.23}$$

with the phase $\hat{\varphi}_i$, and where one assumes $\hat{\varphi}_i \approx \hat{\varphi}_i^\dagger$. The site-dependence of phase and density is due to the AFM nature of the couplings t_{ij}; in a FM system it would be energetically favorable to have at all sites the same phase and density (see introduction to Chapter 3). Now, one divides

$$\hat{n}_i \;\to\; n_i + \delta\hat{n}_i \quad \text{and} \tag{13.24a}$$

$$\hat{\varphi}_i \;\to\; \varphi_i + \delta\hat{\varphi}_i \tag{13.24b}$$

in local mean values (quantities without hat) and fluctuations around them ($\delta\hat{n}_i$, $\delta\hat{\varphi}_i$). Relative density fluctuations $\delta\hat{n}_i/n_i$ are typically small, as are fluctuations $\delta\hat{\varphi}_{ij}$ of NN phase differences $\hat{\varphi}_i - \hat{\varphi}_j \to \Delta\varphi_{ij} + \delta\hat{\varphi}_{ij}$, even in quasi-condensates. Their smallness justifies an expansion of Hamiltonian (2.4) in $\delta\hat{n}_i/n_i$ and $\delta\hat{\varphi}_{ij}$.

For the calculations presented in Chapter 3.6, we applied this method to the spatially anisotropic triangular lattice (SATL), where it is particularly suited due to the strong frustration and low dimensionality of that model. In their original paper [262], Mora and Castin considered a BEC in free space, which they had to discretize by hand to avoid divergences due to commutations of the field operators. In our case, this discretization is given naturally by the optical lattice.

Also, Mora and Castin conducted the expansion in the fluctuations only up to second order. Here, we also include fourth-order terms, which in the frustrated SATL, where the influence of quantum fluctuations is strongly enhanced, proves to be a straightforward but essential improvement. In fact, in the quantum limit of the SATL (Chapter 3.2), quantum fluctuations considerably shift the critical point between spiral and square-lattice Néel order from the classical value $\alpha_{\mathrm{cl}} = 2$ to $\alpha \approx 1.4$. Interestingly, the on-site interaction U in the Bose–Hubbard Hamiltonian interpolates between these two limits, where the classical spin model is reached at $U = 0$ and the quantum spin-1/2 model at $U \to \infty$. Hence, we can expect that an increasing U smoothly shifts α_{cl} from 2 to 1.4. We find, however, that an expansion only up to second order in the fluctuations does not describe any shift of α_{cl} – optimizing the type of order immediately renders the expansion instable. An expansion up to fourth order, where interactions

are treated in a self-consistent mean-field *Ansatz*, however, does describe such a shift.[1] In the rest of this section, we explain – for a general Bose–Hubbard Hamiltonian as given by Eq. (2.4) – how the approximate ground state can be extracted from such a fourth-order expansion.

13.3.1 Expansion in phase and density fluctuations

In the following, we will assume a constant mean density $n_i = n$, since under short-range interactions density waves are not to be expected. In this case, expanding the interaction term of Hamiltonian (2.4) in terms of mean values with small fluctuations, Eq. (13.24), yields

$$\hat{\mathcal{H}}_{\text{int}} \equiv \frac{U}{2}\sum_i \hat{n}_i\left(\hat{n}_i - 1\right) = \frac{U}{2}\sum_i n^2\left[1 + 2\frac{\delta\hat{n}_i}{n} + \left(\frac{\delta\hat{n}_i}{n}\right)^2 - \frac{1}{n} - \frac{1}{n}\frac{\delta\hat{n}_i}{n}\right]. \tag{13.25}$$

Similarly, for the tunneling term, we get

$$\begin{aligned}\hat{\mathcal{H}}_{\text{tun}} &\equiv \frac{1}{2}\sum_{i,j} t_{ij}\hat{b}_i^\dagger\hat{b}_j \qquad (13.26)\\ &= \frac{1}{2}\sum_{i,j} t_{ij}\sqrt{n}\mathrm{e}^{-i\varphi_i}\sqrt{n}\mathrm{e}^{i\varphi_j}\left(1 - i\delta\hat{\varphi}_{ij} - \frac{1}{2}\delta\hat{\varphi}_{ij}^2 + \frac{i}{6}\delta\hat{\varphi}_{ij}^3 + \frac{1}{24}\delta\hat{\varphi}_{ij}^4 + O\left(\delta\hat{\varphi}_{ij}^5\right)\right)\\ &\quad\times\left[1 + \frac{1}{2}\frac{\delta\hat{n}_i}{n} - \frac{1}{8}\left(\frac{\delta\hat{n}_i}{n}\right)^2 + \frac{1}{16}\left(\frac{\delta\hat{n}_i}{n}\right)^3 - \frac{5}{128}\left(\frac{\delta\hat{n}_i}{n}\right)^4 + O\left(\left(\frac{\delta\hat{n}_i}{n}\right)^5\right)\right]\\ &\quad\times\left[1 + \frac{1}{2}\frac{\delta\hat{n}_j}{n} - \frac{1}{8}\left(\frac{\delta\hat{n}_j}{n}\right)^2 + \frac{1}{16}\left(\frac{\delta\hat{n}_j}{n}\right)^3 - \frac{5}{128}\left(\frac{\delta\hat{n}_j}{n}\right)^4 + O\left(\left(\frac{\delta\hat{n}_j}{n}\right)^5\right)\right],\end{aligned}$$

where we Taylor-expanded the square roots and exponentials in Eq. (13.23) up to fourth order in $\delta\hat{n}_i/n_i$ and $\delta\hat{\varphi}_{ij}$.

The fluctuations fulfill the commutation relation $[\delta\hat{n}_i, \delta\hat{\varphi}_i] = i$, but it is more convenient to work with modes which have bosonic commutation relations. To arrive at such a description, we introduce the bosonic annihilation and creation operators

$$\hat{d}_i = \sqrt{n}\left(\frac{1}{2}\frac{\delta\hat{n}_j}{n} + i\delta\hat{\varphi}_i\right), \tag{13.27a}$$

$$\hat{d}_i^\dagger = \sqrt{n}\left(\frac{1}{2}\frac{\delta\hat{n}_j}{n} - i\delta\hat{\varphi}_i\right), \tag{13.27b}$$

[1] Similarly, in spin-wave theory, second-order expansions cannot describe such a shift of the order properties, while self-consistent fourth-order expansions do (see further Ref. [595] and Chapter 14).

yielding

$$\hat{\mathcal{H}}_{\rm int} = \frac{U}{2}\sum_i \left[n(n-1) + 2n^{3/2}\hat{d}_i + 2n^{3/2}\hat{d}_i^\dagger + n\,\hat{d}_i\hat{d}_i + n\,\hat{d}_i^\dagger\hat{d}_i + n\,\hat{d}_i\hat{d}_i^\dagger + n\,\hat{d}_i^\dagger\hat{d}_i^\dagger\right], \tag{13.28}$$

$$\hat{\mathcal{H}}_{\rm tun} = \frac{1}{2}\sum_{i,j} t_{ij} n\, \mathrm{e}^{-i\Delta\varphi_{ij}}\left[1 + \frac{\hat{d}_j}{\sqrt{n}} + \frac{\hat{d}_i^\dagger}{\sqrt{n}} - \frac{\hat{d}_i\hat{d}_i}{4n} + \frac{\hat{d}_j\hat{d}_j}{4n} - \frac{\hat{d}_i^\dagger\hat{d}_i}{2n} + \frac{\hat{d}_i^\dagger\hat{d}_j}{n} - \frac{\hat{d}_j^\dagger\hat{d}_j}{2n} + \frac{\hat{d}_i^\dagger\hat{d}_i^\dagger}{4n} - \frac{\hat{d}_j^\dagger\hat{d}_j^\dagger}{4n} + O\left(\left(\frac{\hat{d}}{\sqrt{n}}\right)^4\right)\right]. \tag{13.29}$$

At this moment, we only show terms up to second order in the fluctuations, since the generalization to fourth order is straightforward but the formulas become very unhandy. The final results can be written more compactly, and we will state them including fourth-order terms.

13.3.2 Minimization of free energy

Our aim is to find the ground state of Hamiltonian (2.4), which is attained at the minimum of the free energy $\mathcal{F} = E - T\mathcal{S}$, where $E = \langle\hat{\mathcal{H}}\rangle$ is the energy expectation value and $\mathcal{S} = \frac{1}{N}\sum_{\boldsymbol{k}}(n_{\boldsymbol{k}}^{(\alpha)}+1)\ln(n_{\boldsymbol{k}}^{(\alpha)}+1) - n_{\boldsymbol{k}}^{(\alpha)}\ln n_{\boldsymbol{k}}^{(\alpha)}$ the entropy.[2]

This is best done via subsequent Fourier and Bogolioubov transforms, *i.e.*, $\hat{a}_{\boldsymbol{k}} = \frac{1}{N}\sum_i \mathrm{e}^{i\boldsymbol{k}\boldsymbol{r}_i}\hat{d}_i$, where N is the number of sites, and

$$\hat{\alpha}_{\boldsymbol{k}} = \cosh\theta_{\boldsymbol{k}}\hat{a}_{\boldsymbol{k}} + \sinh\theta_{\boldsymbol{k}}\hat{a}_{-\boldsymbol{k}}^\dagger \tag{13.30a}$$

$$\hat{\alpha}_{-\boldsymbol{k}}^\dagger = \cosh\theta_{-\boldsymbol{k}}\hat{a}_{-\boldsymbol{k}}^\dagger + \sinh\theta_{-\boldsymbol{k}}\hat{a}_{\boldsymbol{k}}\,, \tag{13.30b}$$

where *a priori,* modes $\boldsymbol{k}$ and $-\boldsymbol{k}$ can be different. To treat the fourth-order terms, we restrict the variational manifold to Gaussian states. Then, we can apply Wick's theorem, which allows to decouple fourth-order terms into products of second-order terms [596],

$$\langle\hat{d}_{\boldsymbol{k}_1}\hat{d}_{\boldsymbol{k}_2}\hat{d}_{\boldsymbol{k}_3}\hat{d}_{\boldsymbol{k}_4}\rangle \to \langle\hat{d}_{\boldsymbol{k}_1}\hat{d}_{\boldsymbol{k}_2}\rangle\langle\hat{d}_{\boldsymbol{k}_3}\hat{d}_{\boldsymbol{k}_4}\rangle + \langle\hat{d}_{\boldsymbol{k}_1}\hat{d}_{\boldsymbol{k}_3}\rangle\langle\hat{d}_{\boldsymbol{k}_2}\hat{d}_{\boldsymbol{k}_4}\rangle + \langle\hat{d}_{\boldsymbol{k}_1}\hat{d}_{\boldsymbol{k}_4}\rangle\langle\hat{d}_{\boldsymbol{k}_2}\hat{d}_{\boldsymbol{k}_3}\rangle\,, \tag{13.31}$$

[2] The following treatment is very similar to MSWT explained in Chapter 14, only that in that case the bosonic modes describe quantum fluctuations of spin degrees of freedom, while here they describe fluctuations of density and phase of a bosonic SF.

and similarly for any combination of four $\hat{d}$ and $\hat{d}^\dagger$ operators. With this simplification, the minimum of the free energy can be found as the self-consistent solution of a quadratic theory.

Using Wick's theorem, Eq. (13.31), we obtain the energy expectation values[3]

$$\begin{aligned}\langle\hat{\mathcal{H}}_{\text{int}}\rangle &= \frac{U}{2}\sum_i\Bigg\{n(n-1)+n\frac{1}{N}\sum_{\boldsymbol{k}}\Big[\Big(1+2n_{\boldsymbol{k}}^{(\alpha)}\Big)\cosh\theta_{\boldsymbol{k}}^2 \\ &\quad -2\Big(1+2n_{\boldsymbol{k}}^{(\alpha)}\Big)\cosh\theta_{\boldsymbol{k}}\sinh\theta_{-\boldsymbol{k}}+\Big(1+2n_{-\boldsymbol{k}}^{(\alpha)}\Big)\sinh\theta_{\boldsymbol{k}}^2\Big]\Bigg\}, \qquad (13.32)\end{aligned}$$

$$\begin{aligned}\langle\hat{\mathcal{H}}_{\text{tun}}\rangle &= \frac{1}{2}\sum_{i,j}t_{ij}n\mathrm{e}^{-i\Delta\varphi_{ij}}\Bigg\{1+\frac{1}{N}\sum_{\boldsymbol{k}}\frac{1}{n}\Big[n_{\boldsymbol{k}}^{(\alpha)}\cosh\theta_{\boldsymbol{k}}^2\left(\mathrm{e}^{i(\boldsymbol{r}_i-\boldsymbol{r}_j)\boldsymbol{k}}-1\right) \\ &\quad +\left(\mathrm{e}^{i(\boldsymbol{r}_i-\boldsymbol{r}_j)\boldsymbol{k}}-1\right)\Big(1+n_{-\boldsymbol{k}}^{(\alpha)}\Big)\sinh\theta_{\boldsymbol{k}}^2\Big]\Bigg\}+O\left(\left(\frac{\hat{d}}{\sqrt{n}}\right)^4\right) \qquad (13.33)\end{aligned}$$

where we introduced the occupation number of Bogolioubov particles $n_{\boldsymbol{k}}^{(\alpha)} \equiv \langle\hat{\alpha}_{\boldsymbol{k}}^\dagger\hat{\alpha}_{\boldsymbol{k}}\rangle = 1/\left(\exp(\omega_{\boldsymbol{k}}/T)-1\right)$. Here, T is the temperature and $\omega_{\boldsymbol{k}}$ the dispersion relation of the Bogolioubov particles. Later, we will put T to 0, since we are only concerned with the ground state. This will give $n_{\boldsymbol{k}}^{(\alpha)}=0$. At this point, however, we keep the T dependence because this gives a convenient way to minimize the system's energy E with respect to $\omega_{\boldsymbol{k}}$, because $\omega_{\boldsymbol{k}}/T$ enters in E through $n_{\boldsymbol{k}}^{(\alpha)}$.

Now, we make the assumption that the mean value of the phase is given by an ordering vector $\boldsymbol{Q}$, *i.e.*,

$$\varphi_i = \boldsymbol{Q}\cdot\boldsymbol{r}_i\,. \qquad (13.34)$$

Classically, if the underlying lattice is a Bravais lattice, the ground state can always be described by such an ordering vector. In that case, $\boldsymbol{Q}$ is just the wave vector which minimizes the classical dispersion relation $\sum_{\boldsymbol{\delta}} t_{\boldsymbol{\delta}}\mathrm{e}^{i\boldsymbol{k}\cdot\boldsymbol{\delta}}$, where $\boldsymbol{\delta}$ are

[3] Here, only even-order terms play a role. The reason is that all odd-order terms can, by virtue of Wick's theorem, be decoupled in products of second-order and first-order expectation values, and the first-order terms vanish at the free-energy minimum. In principle, third order terms should be reintroduced via second-order perturbation theory, since these are of order $O(n^0)$ [the product of two third order terms gives $O(\sqrt{n}^2)$, these are divided by an energy difference of $O(n^2)$, and summing over all states which are coupled by the third-order terms gives another $O(n)$]. These terms are of the same order in $1/n$ as the direct fourth-order terms which we did keep, so that in principle we would have to account for them. However, this treatment is extremely involved and beyond the scope of this thesis.

the vectors connecting NN sites.[4] Since we are working in the limit of small U, we can assume that the quantum-mechanical ground state is close to a classical state, and that therefore the ordering-vector concept is applicable. Then

$$\begin{aligned} E = {} & \frac{U}{2} n(n-1) + n \sum_{\boldsymbol{\delta}} t_{\boldsymbol{\delta}} \cos(\boldsymbol{Q}\cdot\boldsymbol{\delta}) \\ & + \frac{1}{2}\frac{1}{N} \sum_{\boldsymbol{k}} \Big\{ nU(1+2n_{\boldsymbol{k}}^{(\alpha)}) \left(\cosh\theta_{\boldsymbol{k}}^2 - 2\cosh\theta_{\boldsymbol{k}} \sinh\theta_{-\boldsymbol{k}} + \sinh\theta_{\boldsymbol{k}}^2\right) \\ & -2\sum_{\boldsymbol{\delta}} t_{\boldsymbol{\delta}} \left[\cos(\boldsymbol{Q}\cdot\boldsymbol{\delta}) - \cos((\boldsymbol{Q}+\boldsymbol{k})\cdot\boldsymbol{\delta})\right] \left(n_{\boldsymbol{k}}^{(\alpha)} \cosh\theta_{\boldsymbol{k}}^2 + \sinh\theta_{\boldsymbol{k}}^2 + n_{-\boldsymbol{k}}^{(\alpha)} \sinh\theta_{\boldsymbol{k}}^2\right) \Big\} \\ & + O\left(\left(\frac{\hat{d}}{\sqrt{n}}\right)^4\right). \end{aligned} \tag{13.35}$$

The fourth-order terms, which are not given here, involve double sums over $\boldsymbol{k}$ and $\boldsymbol{k}'$.

To find the ground state, we now minimize $\mathcal{F}$ with respect to $\theta_{\boldsymbol{k}}$, $\omega_{\boldsymbol{k}}$, and $\boldsymbol{Q}$. This yields a set of self-consistent equations. The first of these minimizations, $d\mathcal{F}/d\theta_{\boldsymbol{k}} = 2\left(A_{\boldsymbol{k}}\ \cosh(2\theta_{\boldsymbol{k}}) + B_{\boldsymbol{k}} \sinh(2\theta_{\boldsymbol{k}})\right) = 0$, yields

$$\tanh(2\theta_{\boldsymbol{k}}) = -A_{\boldsymbol{k}}/B_{\boldsymbol{k}}\,, \tag{13.36}$$

where we defined, now including the fourth-order terms,

$$\begin{aligned} A_{\boldsymbol{k}} \quad \equiv \quad & -nU + \frac{1}{4n} \sum_{\boldsymbol{\delta}} t_{\boldsymbol{\delta}} \Big\{ \left[\cos((\boldsymbol{Q}-\boldsymbol{k})\cdot\boldsymbol{\delta}) + \cos((\boldsymbol{Q}+\boldsymbol{k})\cdot\boldsymbol{\delta})\right] \left[1 - F(0) + G(0)\right] \\ & -2\cos(\boldsymbol{Q}\cdot\boldsymbol{\delta}) \left[1 - 2F(0) + F(\boldsymbol{\delta}) + 2G(0) - G(\boldsymbol{\delta})\right] \Big\} \end{aligned} \tag{13.37a}$$

$$\begin{aligned} B_{\boldsymbol{k}} \quad \equiv \quad & \frac{b_{\boldsymbol{k}} + b_{-\boldsymbol{k}}}{2} \\ = \quad & nU + \frac{1}{4n} \sum_{\boldsymbol{\delta}} t_{\boldsymbol{\delta}} \Big\{ \left[\cos((\boldsymbol{Q}-\boldsymbol{k})\cdot\boldsymbol{\delta}) + \cos((\boldsymbol{Q}+\boldsymbol{k})\cdot\boldsymbol{\delta})\right] \left[2n + F(\boldsymbol{\delta}) - G(0)\right] \\ & -2\cos(\boldsymbol{Q}\cdot\boldsymbol{\delta}) \left[2n + F(0) - 2G(0) + G(\boldsymbol{\delta})\right] \Big\}, \end{aligned} \tag{13.37b}$$

[4] In the particular case of the SATL, $\boldsymbol{\delta} = \pm\boldsymbol{\tau}_{1,2,3}$ with $\boldsymbol{\tau}_1 = \boldsymbol{e}_x$, $\boldsymbol{\tau}_2 = \left(\boldsymbol{e}_x + \sqrt{3}\boldsymbol{e}_y\right)/2$, and $\boldsymbol{\tau}_3 = \left(\boldsymbol{e}_x - \sqrt{3}\boldsymbol{e}_y\right)/2$, as defined in Fig. 3.1b. The associated couplings are $t_{\pm\boldsymbol{\tau}_1} \equiv t_1$, $t_{\pm\boldsymbol{\tau}_{2,3}} \equiv t_2$.

with

$$b_{\boldsymbol{k}} \equiv nU + \frac{1}{2n}\sum_{\boldsymbol{\delta}} t_{\boldsymbol{\delta}} \Big\{ \cos((\boldsymbol{Q}+\boldsymbol{k})\cdot\boldsymbol{\delta})\,[2n + F(\boldsymbol{\delta}) - G(0)] - \cos(\boldsymbol{Q}\cdot\boldsymbol{\delta})\,[2n + F(0) - 2G(0) + G(\boldsymbol{\delta})] \Big\} \quad (13.38)$$

and the correlators (defined using translational invariance)

$$F(\boldsymbol{r}) \equiv 2\langle d^\dagger_{\boldsymbol{r}_i} d_{\boldsymbol{r}_i+\boldsymbol{r}}\rangle + \delta(\boldsymbol{r}) \quad (13.39a)$$

$$= 2\frac{1}{N}\sum_{\boldsymbol{k}} \mathrm{e}^{i\boldsymbol{k}\boldsymbol{r}} \cosh(2\theta_{\boldsymbol{k}}) \left(n^{(\alpha)}_{\boldsymbol{k}} + \frac{1}{2}\right) = 2\frac{1}{N}\sum_{\boldsymbol{k}} \mathrm{e}^{i\boldsymbol{k}\boldsymbol{r}} \frac{B_{\boldsymbol{k}}}{\sqrt{B^2_{\boldsymbol{k}} - A^2_{\boldsymbol{k}}}} \left(n^{(\alpha)}_{\boldsymbol{k}} + \frac{1}{2}\right),$$

$$G(\boldsymbol{r}) \equiv -2\langle d^\dagger_{\boldsymbol{r}_i} d^\dagger_{\boldsymbol{r}_i+\boldsymbol{r}}\rangle = -2\langle d_{\boldsymbol{r}_i} d_{\boldsymbol{r}_i+\boldsymbol{r}}\rangle \quad (13.39b)$$

$$= 2\frac{1}{N}\sum_{\boldsymbol{k}} \mathrm{e}^{i\boldsymbol{k}\boldsymbol{r}} \sinh(2\theta_{\boldsymbol{k}}) \left(n^{(\alpha)}_{\boldsymbol{k}} + \frac{1}{2}\right) = 2\frac{1}{N}\sum_{\boldsymbol{k}} \mathrm{e}^{i\boldsymbol{k}\boldsymbol{r}} \frac{-A_{\boldsymbol{k}}}{\sqrt{B^2_{\boldsymbol{k}} - A^2_{\boldsymbol{k}}}} \left(n^{(\alpha)}_{\boldsymbol{k}} + \frac{1}{2}\right).$$

By virtue of Wick's theorem (13.31), all expectation values can be represented by these correlators.

The spectrum $\omega_{\boldsymbol{k}}$ is determined by the derivate $d\mathcal{F}/d\omega_{\boldsymbol{k}} = 0$,

$$\omega_{\boldsymbol{k}} = \frac{b_{\boldsymbol{k}} - b_{-\boldsymbol{k}}}{2} + \sqrt{B^2_{\boldsymbol{k}} - A^2_{\boldsymbol{k}}}. \quad (13.40)$$

One can show easily that at $\boldsymbol{k} = 0$ (where $\boldsymbol{k}$ is the wave vector relative to the ordering vector $\boldsymbol{Q}$) the gap vanishes, as it should in a quasi-condensed phase.[5] Now, since we are only interested in the ground state, we can put $T = 0$ (and therefore $n^{(\alpha)}_{\boldsymbol{k}} = 0$).

In the Bose–Hubbard model, quantum fluctuations are driven by the interaction U. Therefore, at $U = 0$, the classical results should be recovered. Indeed, in this case $\sinh\theta_{\boldsymbol{k}} = 0$, and Eq. (13.39) becomes $F(\boldsymbol{r}) = \delta(\boldsymbol{r})$ and $G(\boldsymbol{r}) = 0$. Hence, the expectation values of the fluctuations vanish. In that case, the ordering vector takes the classical value, which in the SATL is given by Eq. (3.29). To describe a change of the ordering vector $\boldsymbol{Q} = (Q_x, Q_y)$ compared to the classical value, we have to include its optimization, $d\mathcal{F}/dQ_x = 0$ and $d\mathcal{F}/dQ_y = 0$ in the

[5] This is also the case if terms only up to second order are included, both in the Mora–Castin formulation as well as in the usual Bogolioubov expansion (in fact, at second order the spectrum coincides for both). In the latter, however, the spectrum acquires a gap when including fourth-order terms. This artifact is due to the neglect of third-order contributions. Notably, in the expansion due to Mora and Castin the gaplessness is preserved, indicating that the division in third- and fourth-order terms is better behaved.

self-consistent iteration. In the special case of the SATL, these equations are solved by $Q_y = 0$ and

$$Q_x = \pm 2 \arccos\left(-\frac{t_2}{2t_1}\frac{R(\boldsymbol{\tau_2})}{R(\boldsymbol{\tau_1})}\right), \tag{13.41}$$

where we defined

$$\begin{aligned} R(\boldsymbol{\delta}) = {} & 4n\left[2n + 1 - F(0) + F(\boldsymbol{\delta})\right] + \left[1 - F(0) + G(0)\right]\left[F(0) - 2G(0) + 2G(\boldsymbol{\delta})\right] \\ & + G(0)\left[F(0) - 2F(\boldsymbol{\delta})\right] + F(\boldsymbol{\delta})^2 - F(0), \end{aligned} \tag{13.42}$$

and where we used $G(\boldsymbol{\delta}_2) = G(\boldsymbol{\delta}_3)$ and $F(\boldsymbol{\delta}_2) = F(\boldsymbol{\delta}_3)$. One could, in principle, apply the optimization of the ordering vector also to second-order expansions. However, in that case a shift of the ordering vector leads to imaginary modes in the dispersion relation $\omega_{\boldsymbol{k}}$, meaning that the state becomes unstable. At fourth order, these instabilities are usually not present. We expect them to possibly occur only close to quantum disordered phases (see Chapter 3.2).

Now, the knowledge of the correlators F and G – as obtained by solving self-consistently Eqs. (13.37-13.39), and (13.41) – allows, in principle, to compute the ground-state expectation value of any desired observable. For example, for the calculations of Chapter 3.6, we used the variance of the phase and the condensate fraction to quantify the degree of order of weakly-interacting ultracold bosons loaded into an optical lattice. Where the phase fluctuations are large or the condensate fraction is small, the initial expansion in small condensate fluctuations is no longer justified. This fundamental consistency check also identifies regimes where quantum-disordered behavior may be expected. The NN phase fluctuations read

$$\begin{aligned} \Delta_\varphi(\boldsymbol{\delta}) &\equiv \sqrt{\langle(\delta\varphi_{\boldsymbol{i}+\boldsymbol{\delta}} - \delta\varphi_{\boldsymbol{i}})^2\rangle - \langle(\delta\varphi_{\boldsymbol{i}+\boldsymbol{\delta}} - \delta\varphi_{\boldsymbol{i}}^2\rangle} \\ &= \sqrt{\frac{1}{2n}\left[F(0) + G(0) - F(\boldsymbol{\delta}) - G(\boldsymbol{\delta})\right]}. \end{aligned} \tag{13.43}$$

The condensate fraction n_c, on the other hand, can be computed from the long-distance behavior of the correlations. These read

$$\langle \hat{b}_i^\dagger \hat{b}_j \rangle = \psi_i^* \psi_j \exp\left[-\frac{1}{n} I_3(\boldsymbol{r}_i - \boldsymbol{r}_j)\right], \tag{13.44}$$

where

$$I_3(\boldsymbol{r}) = \frac{1}{N}\sum_{\boldsymbol{k}\neq\boldsymbol{k}_0} (1 - \cos\boldsymbol{k}\cdot\boldsymbol{r})\left[\left(\cosh\theta_{\boldsymbol{k}}^2 + \sinh\theta_{\boldsymbol{k}}^2\right) n_{\boldsymbol{k}}^{(\alpha)} + \sinh\theta_{\boldsymbol{k}}^2\right]. \tag{13.45}$$

Here, we defined $\psi_i \equiv \sqrt{n}\mathrm{e}^{i\varphi_i}$. In the limit of large distances the correlations tend towards the condensate fraction,

$$n_c \equiv \lim_{\boldsymbol{r}\to\infty} \left|\langle \hat{b}_i^\dagger \hat{b}_{\boldsymbol{i}+\boldsymbol{r}}\rangle\right| / n = \exp\left(-\frac{1}{n}\frac{1}{N}\sum_{\boldsymbol{k}\neq\boldsymbol{k}_0}\frac{A_{\boldsymbol{k}}^2}{B_{\boldsymbol{k}}^2 - A_{\boldsymbol{k}}^2}\right). \tag{13.46}$$

Chapter 14

Formalism of the modified spin-wave theory with ordering-vector optimization

Spin-wave theories are typically the first method applied to spin Hamiltonians because of their low numerical cost and because they are easily generalizable to a huge class of magnetic models. These theories generally take a classical, ordered state as a starting point, which they dress with quantum fluctuations in a perturbative manner. Spin-wave theories often give a good qualitative overview over occurring ordered phases, but they are not adequate to describe the properties of disordered ones. Still, often a breakdown of the theory, or a weakening of magnetic order, can announce at least the *appearance* of quantum disordered phases in the true ground-state phase diagram.

An especially versatile variant is Takahashi's modified spin-wave theory (MSWT) [224] as it not only satisfactorily describes systems with LRO but also such with quasi-LRO, making it especially suited to describe low-dimensional or frustrated models. Compared to the classical reference states, such systems generally present strong quantum corrections to the predominant type of order. To account for these quantum corrections, we extended the MSWT by an optimization of the ordering vector [597], as we will describe below. This improvement allows to satisfactorily describe the most salient features of the phase diagrams of various frustrated quantum models.

Such frustrated systems are prime targets for QSs, because they may display

exotic quantum-disordered behavior, and because it is difficult to find accurate theoretical descriptions of disordered quantum lattice models. On the other hand, this difficulty makes it hard to tell *a priori* which systems will present interesting phases in an experiment. Therefore, it would be highly desirable to dispose of a fast tool that can outline quantum-mechanical phase diagrams, point out candidate regions for disordered phases, and thus classify model Hamiltonians according to their potential relevance for experimental quantum simulation. We propose that MSWT with ordering-vector optimization will serve this very purpose. We have seen the good performance of MSWT in our calculations in Chapter 3, where we treated models with XY interactions, which are relevant in the context of QSs consisting of ultracold hard-core atoms in optical lattices.

In this chapter, we first review the MSWT formalism for general XXZ interactions. After that, we will illustrate the possibilities of the MSWT on selected examples of frustrated Heisenberg models.

14.1 The formalism

Our aim is to determine the phase diagrams of several incarnations of the following general Hamiltonian that describes a large variety of spin systems,

$$\hat{\mathcal{H}}_{\mathrm{S}} = \sum_{\langle ij \rangle} t_{ij} \left(S_i^x S_j^x + S_i^y S_j^y + \lambda S_i^z S_j^z \right) . \tag{14.1}$$

Here, S_i^μ is the μ'th component of the spin-operator at site i, and spins on sites i and j interact with a strength of t_{ij}. We denote the length of the spins by S and use throughout this chapter units where $\hbar$, the reduced Planck constant, as well as the lattice spacing equal unity. At $\lambda = 0$, this Hamiltonian describes XY interactions, while at $\lambda = 1$, it describes a Heisenberg magnet, so that it comprises both the models of Chapter 3.2 that arise in the context of hard-core bosonic atoms in optical lattices and the models of Chapter 14.2 that are relevant to magnetic materials.

In the following, we discuss the formalism of the MSWT for calculating ground-state and finite-temperature properties of Hamiltonian (14.1). For more details, see my Diploma thesis [595]. The MSWT has been introduced by Takahashi about 20 years ago to describe low-dimensional Heisenberg magnets [224]. Here, we extend the formulas to encompass both Heisenberg and XY interactions. It can be expected that the validity of the spin-wave approach is even better justified for XY interactions, since here quantum fluctuations are reduced by the anisotropy in the spin–spin coupling.

14.1.1 Expansion around classical reference state

A fundamental assumption of spin-wave theory is that the ground state is well approximated by a classical state, which shows long-range order (LRO), dressed with quantum fluctuations. Without restriction of generality, we can assume that in the classical reference state the spins lie in the xy-plane.[1] For a translationally invariant system, like the ones under investigation, the ordered ground state is then characterized by a well-defined ordering vector $\boldsymbol{Q}$ [see also Eq. (13.34)]. Under this assumption, it is convenient to rotate the local reference system of each spin from (x, y, z) to (η, ζ, ξ) so that the ground state in the new reference frame has all spins aligned in the same direction. This is achieved by the following transformation:

$$S_i^x = -\sin(\boldsymbol{Q}\cdot\boldsymbol{r}_i)\, S_i^\eta + \cos(\boldsymbol{Q}\cdot\boldsymbol{r}_i)\, S_i^\zeta\,, \tag{14.2a}$$

$$S_i^y = \cos(\boldsymbol{Q}\cdot\boldsymbol{r}_i)\, S_i^\eta + \sin(\boldsymbol{Q}\cdot\boldsymbol{r}_i)\, S_i^\zeta\,, \tag{14.2b}$$

$$S_i^z = -S_i^\xi\,. \tag{14.2c}$$

Then S_i^ζ, which will be the quantization axis, lies parallel to the classical spin $\boldsymbol{S}_i = (\cos(\boldsymbol{Q}\cdot\boldsymbol{r}_i), \sin(\boldsymbol{Q}\cdot\boldsymbol{r}_i), 0)$. Unlike in ordinary spin-wave theories, we do not make any assumption on the ordering vector $\boldsymbol{Q}$. In particular, it may well differ from the one exhibited by the system in the classical limit $S \to \infty$, $\boldsymbol{Q}^{\mathrm{cl}}$.

Spin waves around the classical reference state can be described via the Dyson–Maleev transformation [598, 599], which maps the physical spins to interacting bosons,

$$S_i^- \to \frac{1}{\sqrt{2S}}\left(2S - \hat{a}_i^\dagger \hat{a}_i\right)\hat{a}_i\,, \tag{14.3a}$$

$$S_i^+ \to \sqrt{2S}\,\hat{a}_i^\dagger, \tag{14.3b}$$

$$S_i^\zeta \to -S + \hat{a}_i^\dagger \hat{a}_i\,, \tag{14.3c}$$

where $S_i^\pm \equiv S_i^\xi \pm i S_i^\eta$. The Dyson–Maleev transformation is an exact mapping between spins and bosons as long as projectors are retained which keep the system in the physical subspace, *i.e.*, the subspace where at each site only $2S$ Dyson–Maleev bosons are present at most. It can be shown that these projectors have the form $\mathcal{P} = \mathbb{1} + \mathcal{O}[n/(2S)]^3$ where n is the Dyson–Maleev boson density [600]. Hence, under the assumption of diluteness of the Dyson–Maleev boson

[1] Without magnetic field, this is trivially true for XY interactions; and for Heisenberg interactions one can, in great generality, find classical ground states which fulfill this condition.

gas, $n/(2S) < 1$ (in fact $\langle n \rangle = S$, see Sec. 14.1.3), we can safely neglect the $\mathcal{P}$ projectors.

14.1.2 Mean-field approximation

Applying Eqs. (14.2) and (14.3) to Hamiltonian (14.1) one arrives at the bosonic Hamiltonian

$$\begin{aligned}\hat{\mathcal{H}} \;=\; \frac{1}{4}\sum_{\langle ij\rangle} t_{ij}\Big\{ \quad & \left[2S\left(\hat{a}_i^\dagger\hat{a}_j + \hat{a}_i\hat{a}_j^\dagger\right) - \hat{a}_i^\dagger\hat{a}_j^\dagger\hat{a}_j\hat{a}_j - \hat{a}_i^\dagger\hat{a}_i\hat{a}_i\hat{a}_j^\dagger\right](\lambda + \cos(\boldsymbol{Q}\cdot\boldsymbol{r}_{ij})) \\ & + \left[2S\left(\hat{a}_i^\dagger\hat{a}_j^\dagger + \hat{a}_i\hat{a}_j\right) - \hat{a}_i\hat{a}_j^\dagger\hat{a}_j\hat{a}_j - \hat{a}_i^\dagger\hat{a}_i\hat{a}_i\hat{a}_j\right](\lambda - \cos(\boldsymbol{Q}\cdot\boldsymbol{r}_{ij})) \\ & + 4\left[S^2 - S\left(\hat{a}_i^\dagger\hat{a}_i + \hat{a}_j^\dagger\hat{a}_j\right) + \hat{a}_i^\dagger\hat{a}_i\hat{a}_j^\dagger\hat{a}_j\right]\cos(\boldsymbol{Q}\cdot\boldsymbol{r}_{ij}) \quad \Big\}\,. \end{aligned} \tag{14.4}$$

Here, we have dropped the terms with six boson operators, which are of order $\mathcal{O}[n/(2S)^3]$ and are negligible for $n/(2S) < 1$. Moreover the truncation of the Hamiltonian to this order is consistent with neglecting the the projectors $\mathcal{P}$ which amounts to discarding terms of the same order.

MSWT relies on the minimization of the free energy $\mathcal{F} = E - T\mathcal{S}$, where

$$\mathcal{S} = \sum_{\boldsymbol{k}} \left[(n_{\boldsymbol{k}} + 1)\ln(n_{\boldsymbol{k}} + 1) - n_{\boldsymbol{k}}\ln n_{\boldsymbol{k}}\right] \tag{14.5}$$

is the entropy of a set of harmonic oscillators.[2] To compute the expectation value $E \equiv \langle\hat{\mathcal{H}}\rangle$, we make the assumption that the ground state is Gaussian. This approximation allows to make use of Wick's theorem, Eq. (13.31), to decouple the boson–boson interaction terms, *i.e.*, the terms consisting of four boson operators. The energy expectation value can then be written as

$$\begin{aligned} E = \langle\hat{\mathcal{H}}\rangle \;=\; \frac{1}{2}\sum_{\langle ij\rangle} t_{ij}\Bigg\{ & \left[S + \frac{1}{2} - F(0) + F(\boldsymbol{r}_i - \boldsymbol{r}_j)\right]^2(\lambda + \cos(\boldsymbol{Q}\cdot\boldsymbol{r}_{ij})) \\ & - \left[S + \frac{1}{2} - F(0) + G(\boldsymbol{r}_i - \boldsymbol{r}_j)\right]^2(\lambda - \cos(\boldsymbol{Q}\cdot\boldsymbol{r}_{ij}))\Bigg\}\,. \end{aligned} \tag{14.6}$$

[2] This treatment is formally very similar to the self-consistent fourth-order Mora–Castin expansion explained in 13.3.2.

Here, we have defined the correlators

$$\langle \hat{a}_i^\dagger \hat{a}_j \rangle = F(\boldsymbol{r}_{ij}) - \frac{1}{2}\delta_{ij}, \tag{14.7a}$$

$$\langle \hat{a}_i \hat{a}_j \rangle = \langle \hat{a}_i^\dagger \hat{a}_j^\dagger \rangle = G(\boldsymbol{r}_{ij}). \tag{14.7b}$$

These correlators can be rewritten in terms of independent particles by first Fourier transforming $\hat{a}_{\boldsymbol{k}} = \frac{1}{\sqrt{N}} \sum_i \hat{a}_i \mathrm{e}^{-i\boldsymbol{k}\cdot\boldsymbol{r}_i}$, where N is the number of sites, and then applying a Bogoliubov transformation

$$\hat{\alpha}_{\boldsymbol{k}} = \cosh\theta_{\boldsymbol{k}}\, \hat{a}_{\boldsymbol{k}} - \sinh\theta_{\boldsymbol{k}}\, \hat{a}_{-\boldsymbol{k}}^\dagger, \tag{14.8a}$$

$$\hat{\alpha}_{-\boldsymbol{k}}^\dagger = -\sinh\theta_{\boldsymbol{k}}\, \hat{a}_{\boldsymbol{k}} + \cosh\theta_{\boldsymbol{k}}\, \hat{a}_{-\boldsymbol{k}}^\dagger. \tag{14.8b}$$

Requiring that the Bogoliubov particles be non-interacting imposes $\langle \hat{\alpha}_{\boldsymbol{k}} \hat{\alpha}_{\boldsymbol{k}'} \rangle = \langle \hat{\alpha}_{\boldsymbol{k}}^\dagger \hat{\alpha}_{\boldsymbol{k}'}^\dagger \rangle = 0$. This condition also removes the anti-Hermitian part of the Hamiltonian that has been introduced by the Dyson–Maleev transformation (14.3).

The correlators are then

$$F(\boldsymbol{r}) = \frac{1}{N} \sum_{\boldsymbol{k}} \cosh(2\theta_{\boldsymbol{k}})\, e^{-i\boldsymbol{k}\cdot\boldsymbol{r}} \left(n_{\boldsymbol{k}} + \frac{1}{2} \right), \tag{14.9a}$$

$$G(\boldsymbol{r}) = \frac{1}{N} \sum_{\boldsymbol{k}} \sinh(2\theta_{\boldsymbol{k}})\, e^{-i\boldsymbol{k}\cdot\boldsymbol{r}} \left(n_{\boldsymbol{k}} + \frac{1}{2} \right), \tag{14.9b}$$

with $n_{\boldsymbol{k}} = \langle \hat{\alpha}_{\boldsymbol{k}}^\dagger \hat{\alpha}_{\boldsymbol{k}} \rangle = 1/(\exp(\omega_{\boldsymbol{k}}/T) - 1)$ being the occupation number of Bogoliubov mode $\boldsymbol{k}$ at temperature T (with the Boltzmann constant k_{B} set to unity). The dispersion relation $\omega_{\boldsymbol{k}}$ is determined self-consistently in the section after the next one.

14.1.3 Takahashi's constraint

So far, we have essentially formulated a standard Hartree–Fock theory for the gas of interacting Dyson–Maleev bosons. A very important modification to this theory, due to Takahashi [224], is the constraint of zero magnetization at each site,

$$\langle S_i^\zeta \rangle = -S + \langle \hat{a}_i^\dagger \hat{a}_i \rangle = -S - \frac{1}{2} + F(0) = 0. \tag{14.10}$$

This constraint effectively reduces the Hilbert space dimension available to the Dyson–Maleev bosons by fixing their average density to the spin length S. For $S = 1/2$-spins in a bipartite lattice, one can in fact show a reduction of the

Hilbert space dimension from ∞ (linear spin-wave theory) to $\frac{4}{\pi}\frac{2^N}{N}$ (MSWT) which restores, up to logarithmic accuracy, the physical value of 2^N [601].

Takahashi's constraint imposes that $\langle n\rangle/(2S) < 1$, and it guarantees the correctness of the truncations of high powers of $n/(2S)$. Finally, if the Hamiltonian is $Z_2 \times U(1)$ symmetric because of a uniaxial anisotropy, as in the case of interest in this work, one expects $\langle S_i^\zeta \rangle = 0$. The constraint (14.10) elegantly restores this reflection symmetry of the ground state with respect to the quantization axis.

If the spin Hamiltonian (14.1) with $\lambda = 0$ is obtained as the hardcore limit of the Bose–Hubbard Hamiltonian (2.4), it is important to distinguish the Dyson–Maleev bosons $\hat{a}$ from the physical $\hat{b}$-bosons from which the effective spin Hamiltonian originated. The Dyson–Maleev bosons at a site i quantify the deviation of the i^{th} spin from the local direction in the xy plane set by the ordering vector $\boldsymbol{Q}$. On the other hand, the physical bosons correspond to the spin deviations with respect to full alignment of the spin along the z axis. The particle-hole symmetry of the bosonic Hamiltonian (2.4) in the hardcore limit leads to half filling of the physical bosons, which accidentally coincides with the average filling imposed by Takahashi's constraint on the Dyson–Maleev bosons for $S = 1/2$. Yet, all other properties are in general quite different. In Chapter 3.2.5, one can find an instruction to translate spin observables to hard-core boson observables.

14.1.4 The self-consistent equations

The correct spin-wave description is found by minimizing the free energy $\mathcal{F}$ with respect to $\theta_{\boldsymbol{k}}$ and $\omega_{\boldsymbol{k}}$ under the constraint (14.10). This leads to a set of self-consistent equations,

$$\tanh 2\theta_{\boldsymbol{k}} = \frac{A_{\boldsymbol{k}}}{B_{\boldsymbol{k}}} \tag{14.11}$$

with

$$A_{\boldsymbol{k}} = \frac{1}{N}\sum_{\langle ij\rangle} t_{ij}\left(\lambda - \cos\left(\boldsymbol{Q}\cdot\boldsymbol{r}_{ij}\right)\right) G_{ij}\, \mathrm{e}^{i\boldsymbol{k}\cdot\boldsymbol{r}_{ij}}\,, \tag{14.12a}$$

$$B_{\boldsymbol{k}} = \frac{1}{N}\sum_{\langle ij\rangle} t_{ij}\left[\left(\lambda - \cos\left(\boldsymbol{Q}\cdot\boldsymbol{r}_{ij}\right)\right) G_{ij} - \left(\lambda + \cos\left(\boldsymbol{Q}\cdot\boldsymbol{r}_{ij}\right)\right) F_{ij}\left(1 - \mathrm{e}^{i\boldsymbol{k}\cdot\boldsymbol{r}_{ij}}\right)\right] - \mu\,, \tag{14.12b}$$

where μ is the Lagrange multiplier for the constraint (14.10) corresponding to the chemical potential for changing the total magnetization.

In Eqs. (14.12), we have abbreviated $F_{ij} = F(\boldsymbol{r}_{ij})$, and $G_{ij} = G(\boldsymbol{r}_{ij})$. The spin-wave spectrum reads

$$\omega_{\boldsymbol{k}} = \sqrt{B_{\boldsymbol{k}}^2 - A_{\boldsymbol{k}}^2}\,, \tag{14.13}$$

and the correlators at the minimum of the free energy take the form

$$F_{ij} = \frac{1}{N}\sum_{\boldsymbol{k}} \frac{B_{\boldsymbol{k}}}{\omega_{\boldsymbol{k}}} \cos(\boldsymbol{k}\cdot\boldsymbol{r}_{ij}) \left(n_{\boldsymbol{k}} + \frac{1}{2}\right), \tag{14.14a}$$

$$G_{ij} = \frac{1}{N}\sum_{\boldsymbol{k}} \frac{A_{\boldsymbol{k}}}{\omega_{\boldsymbol{k}}} \cos(\boldsymbol{k}\cdot\boldsymbol{r}_{ij}) \left(n_{\boldsymbol{k}} + \frac{1}{2}\right). \tag{14.14b}$$

Note that in the classical limit $S \to \infty$ one gets $G_{ij}, F_{ij} \approx S$, and Eqs. (14.12) become analogous to their linear spin-wave theory (LSWT) counterparts.

Inserting Eq. (14.12) into the dispersion relation (14.13) shows that a finite μ entails a gap at $\boldsymbol{k} = 0$. This is in contrast to LSWT where the spectrum always has a gapless Goldstone mode at $\boldsymbol{k} = 0$. At $T = 0$, one finds $n_{\boldsymbol{k}} = 0\ \forall \boldsymbol{k} \neq 0$ and a vanishing μ. This implies also the disappearance of the gap at $\boldsymbol{k} = 0$, which is a necessary requirement for the appearance of the Goldstone mode associated with magnetic LRO, and it enables Bose condensation of the Dyson–Maleev bosons in the $\boldsymbol{k} = 0$ mode. This condensate is depleted by interactions of the Dyson–Maleev bosons. The larger this depletion, the more Dyson–Maleev bosons reside at momenta different from zero, thus decreasing magnetic LRO. Because of this special role, it is convenient to separate out the contribution of the zero mode,

$$\langle \hat{a}^\dagger_{\boldsymbol{k}=0} \hat{a}_{\boldsymbol{k}=0} \rangle / N = \langle \hat{a}_{\boldsymbol{k}=0} \hat{a}_{\boldsymbol{k}=0} \rangle / N \equiv M_0\,. \tag{14.15}$$

M_0 corresponds to the order parameter measuring the total spiraling magnetization for the quantization axes given by the ordering vector $\boldsymbol{Q}$. Then, one arrives at the zero-temperature equations

$$F_{ij} = M_0 + \frac{1}{2N}\sum_{\boldsymbol{k}\neq 0} \frac{B_{\boldsymbol{k}}}{\omega_{\boldsymbol{k}}} \cos(\boldsymbol{k}\cdot\boldsymbol{r}_{ij})\,, \tag{14.16a}$$

$$G_{ij} = M_0 + \frac{1}{2N}\sum_{\boldsymbol{k}\neq 0} \frac{A_{\boldsymbol{k}}}{\omega_{\boldsymbol{k}}} \cos(\boldsymbol{k}\cdot\boldsymbol{r}_{ij})\,, \tag{14.16b}$$

and the constraint (14.10) becomes

$$S + \frac{1}{2} = M_0 + \frac{1}{2N}\sum_{\boldsymbol{k}\neq 0} \frac{B_{\boldsymbol{k}}}{\omega_{\boldsymbol{k}}}. \tag{14.17}$$

14.1.5 Optimization of the ordering vector

It is not *a priori* clear that the classical ordering vector $\boldsymbol{Q}^{\mathrm{cl}}$ correctly describes the LRO in the quantum system. To account for the competition between states with LRO at different ordering vectors $\boldsymbol{Q}$, we extend the MSWT procedure by optimizing the free energy with respect to this quantity. This procedure, first introduced by Xu and Ting [597], significantly improves the predictions of MSWT. It amounts to finding the best ordered reference state with in-plane ordering vector $\boldsymbol{Q}$ (spiral state) whose free energy is minimized not at the classical level, but including the effect of quantum fluctuations self-consistently within MSWT.

The minimization of $\mathcal{F}$ with respect to Q_x and Q_y yields two additional equations

$$\frac{\partial}{\partial Q_x}\mathcal{F} = -\frac{1}{2}\sum_{\langle ij\rangle} t_{ij}\sin\left(\boldsymbol{Q}\cdot\boldsymbol{r}_{ij}\right) r_{ij}^{x}\left[F_{ij}^2 + G_{ij}^2\right] = 0\,, \tag{14.18a}$$

$$\frac{\partial}{\partial Q_y}\mathcal{F} = -\frac{1}{2}\sum_{\langle ij\rangle} t_{ij}\sin\left(\boldsymbol{Q}\cdot\boldsymbol{r}_{ij}\right) r_{ij}^{y}\left[F_{ij}^2 + G_{ij}^2\right] = 0\,. \tag{14.18b}$$

In the SATL (treated in Chapters 3.2 and 14.2.1), one finds $Q_y = 0$ and

$$Q_x = 2\arccos\left(-\frac{\alpha}{2}\frac{F_{\boldsymbol{\tau}_2}^2 + G_{\boldsymbol{\tau}_2}^2}{F_{\boldsymbol{\tau}_1}^2 + G_{\boldsymbol{\tau}_1}^2}\right). \tag{14.19}$$

Here, $\boldsymbol{\tau}_1 = (1,0)$ and $\boldsymbol{\tau}_2 = \left(1/2, \sqrt{3}/2\right)$ are the primitive lattice vectors, as defined in Fig. 3.1b, with associated interactions t_1 and t_2. For $F_{ij} = G_{ij} = S$, attained when $S \to \infty$, this reduces to the classical ordering vector, $Q_x^{\mathrm{cl}} = 2\arccos\left(-\alpha/2\right)$, $Q_y^{\mathrm{cl}} = 0$.

The values of F_{ij} and G_{ij} can now be calculated by solving self-consistently Eq. (14.18) together with Eqs. (14.10, 14.11–14.14). At zero temperature, Eqs. (14.10) and (14.14) have to be replaced by Eqs. (14.17) and (14.16), respectively. Through Wick's theorem the knowledge of the quantities F_{ij} and G_{ij} allows for the computation of the expectation value of any observable. For example, the in-plane two-point correlation function reads

$$C_{ij} \equiv \langle S_i^x S_j^x + S_i^y S_j^y\rangle \,/\, \cos\left(\boldsymbol{Q}\cdot\boldsymbol{r_{ij}}\right) = \frac{1}{2}\left(F_{ij}^2 + G_{ij}^2\right). \tag{14.20}$$

14.1.6 Spin stiffness

The optimization of the ordering vector allows for a straightforward calculation of the spin stiffness. This additional information, complementary to the order

parameter, helps us in identifying candidate regions for spin-liquid behavior.

MSWT always returns a single ordering vector $\boldsymbol{Q}^0$, the optimal one. However, if the true ground state is only short-range ordered, we might expect the $\boldsymbol{Q}$-minimum to be relatively shallow, and that a slight change of the ordering vector barely affects the free energy $\mathcal{F}$. This means that the order is not very stable against twists of the spin configuration, which can be quantified by the *spin stiffness* tensor

$$\rho_{\alpha\beta} = \frac{1}{N} \left. \frac{\mathrm{d}^2\mathcal{F}}{\mathrm{d}Q_\alpha \mathrm{d}Q_\beta} \right|_{\boldsymbol{Q}=\boldsymbol{Q}^0} . \tag{14.21}$$

Particular important are two coordination-system-independent quantities, the *parallel spin stiffness* $\rho_\parallel \equiv \frac{1}{2}\operatorname{Tr}\rho = \frac{1}{2}(\rho_{xx} + \rho_{yy})$ and the *Gaussian spin stiffness*

$$\Upsilon = \det \rho \,. \tag{14.22}$$

The spin stiffness not only yields deeper insight into the order properties of the system, it also provides a fundamental self-consistency check of our approach. In fact, a small spin stiffness casts doubt on the reliability of the spin-wave approach in describing such a strongly fluctuating state, and hence suggests that the true ground state might be quantum disordered.

Since a change in $\boldsymbol{Q}$ affects the correlators F_{ij} and G_{ij}, we must compute Υ self-consistently. After finding the optimal $\boldsymbol{Q}^0$, we calculate $\frac{1}{N}\mathcal{F}(Q_x, Q_y)$ self-consistently for several fixed ordering vectors $\boldsymbol{Q} = \boldsymbol{Q}^0 + \Delta\boldsymbol{Q}$ and fit a quadratic form to the results. Since the minimum in the free energy can be very shallow, this procedure can be affected by numerical noise. As an approximation to the true spin stiffness, the *partial spin stiffness* $\rho_{\alpha\beta}^{\mathrm{partial}}$ can be computed via the partial derivatives, *i.e.*, without recalculating the self-consistent equations. It reads

$$\rho_{\alpha\beta}^{\mathrm{partial}} \equiv \frac{1}{N} \frac{\partial^2}{\partial Q_\alpha \partial Q_\beta} \mathcal{F} = -\frac{1}{2N} \sum_{\langle ij \rangle} t_{ij} \cos(\boldsymbol{Q}\cdot\boldsymbol{r}_{ij})\, r_{ij}^\alpha r_{ij}^\beta \left[F_{ij}^2 + G_{ij}^2\right] . \tag{14.23}$$

We define $\Upsilon^{\mathrm{partial}}$ analogously to Υ [Eq. (14.22)] as the determinant of the partial spin-stiffness tensor. The system can lower its energy by adjusting F_{ij} and G_{ij} to the new ordering vector, and therefore $\Upsilon^{\mathrm{partial}}$ is an upper bound to Υ. In some cases, the partial spin stiffness $\Upsilon^{\mathrm{partial}}$ gives a good estimate of the total spin stiffness Υ, but there are cases where it is considerably larger. We find that the partial spin stiffness is sufficient to extract the location of disordered phases, but it may not be able to distinguish gapped from gapless spin liquids (see Chapter 14.2.1).

In the following, we present the zero-temperature phase diagram of several frustrated Heisenberg models, relevant to experiments on magnetic organic salts. These examples will show the surprisingly good performance of MSWT with ordering-vector optimization in describing order properties of strongly frustrated systems. Hereby, an advantage of MSWT theory is that it allows computation in the thermodynamic limit, simply by replacing finite sums over the first Brillouin zone with integrals.

14.2 Example: MSWT on frustrated Heisenberg magnets

Low-dimensional frustrated quantum spin systems can display an intriguing interplay between order and disorder (see Chapter 3): classical order has been shown to be quite resilient in two or three dimensions [419, 602–604]; frustration, however, can lead to the melting of magnetic LRO and the emergence of quantum-disordered states like valence-bond solids or resonating valence-bond states [605, 606]. Understanding such magnetically-disordered quantum phases is important for the search for fractionalized excitations in two dimensions [605], as well as for the understanding of the behavior of layered magnetic insulators/metals in which magnetism is disrupted by charge doping, leading to dramatic phenomena such as superconductivity at high critical temperature [4, 607, 608]. Since such quantum-disordered states in strongly-correlated lattice systems are notoriously difficult to describe theoretically, it is hoped that QSs can help to further our understanding of magnetic quantum phases.

A large variety of magnetic materials can be described by the Heisenberg Hamiltonian

$$\hat{\mathcal{H}}_{\mathrm{S}} = \sum_{\langle ij \rangle} J_{ij}\ \boldsymbol{S}_i \cdot \boldsymbol{S}_j, \tag{14.24}$$

where $\boldsymbol{S}_i$ is a quantum spin-S operator at site i. The Heisenberg Hamiltonian is the special case with $\lambda = 1$ of the more general XXZ Hamiltonian (14.1). Note that in the general derivations in Sec. 14.1 we denoted the couplings by t's, but in this section we use J's to be more consistent with the language of magnetism.

In this section, we will focus on the antiferromagnetic (AFM) case for $S = 1/2$ in two-dimensional frustrated lattices. These are relevant to a variety of compounds, realizing the spatially anisotropic triangular lattice (SATL) (*e.g.*, in Cs_2CuCl_4 [609] and κ-(BEDT-TTF)$_2$Cu$_2$(CN)$_3$ [610, 611]), or the frustrated ($J_1 J_2$) square lattice (*e.g.*, in $Li_2VOSi(Ge)O_4$, $VOMoO_4$ [612], $BaCdVO(PO_4)_2$

[613]). For both lattice geometries, the Heisenberg model is expected to display spin-liquid phases for particular values of the frustrated couplings, although the extent and nature of these spin-liquid phases is still under theoretical debate, both for the SATL [237–242, 614–618] and for the frustrated square lattice [619–627].

In the following, we investigate – using MSWT with ordering-vector optimization – the Heisenberg SATL and its generalization, the spatially completely anisotropic triangular lattice (SCATL), as well as the square lattice with nearest, next-to-nearest, and next-to-next-to-nearest neighbor (NN, NNN, NNNN) couplings (the $J_1J_2J_3$ model [624, 628–630]). We find that these models feature a very complex $T = 0$ phase diagram, with spirally and collinearly ordered regions, whose ordering vector is subject to strong quantum corrections with respect to the classical ($S \to \infty$) limit. They also feature extended breakdown regions for MSWT, pointing at the possible spin-liquid nature of the true ground state of the system. Comparison with numerical results coming from ED and PEPS calculations show that MSWT correctly accounts for some of the most salient features of the quantum phase diagram of these systems, and that it hence represents a very versatile tool to probe the robustness (or the breakdown) of a semi-classical description of the ground state of frustrated quantum magnets. As such, it requires a relatively low effort to find parameter regions which might harbor exotic quantum phases, and which are therefore good candidates for a useful application of a quantum simulator. The results presented in this chapter also give important insight into the location of quantum-disordered phases. In fact, similar to what we have seen in the XY models treated in Chapter 3, in all considered models disordered phases do not occur at strongest frustration, but intervene in transitions between different types of (quasi-)order. We propose that this might be a general behavior, which could facilitate the search for spin-liquid ground states.

The remainder of this chapter is organized as follows: Section 14.2.1 presents the ground-state phase diagram of the SATL with NN Heisenberg interactions. Motivated by recent works that point out the insufficiency of the SATL to describe some magnetic compounds, we consider its generalization to the SCATL in Sec. 14.2.2. In Sec. 14.2.3, we calculate the ground-state phase diagram of the $J_1J_2J_3$ model. Finally, in Sec. 14.2.4 we present a short summary of our findings. The results presented in this chapter can be found in the published article [241] and in the preprint [631].

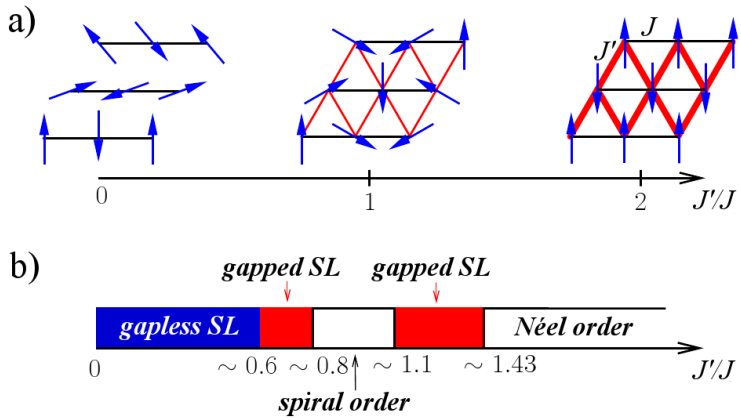

Figure 14.1: **(a) Classical ground-state phase diagram of the Heisenberg SATL** with a sketch of the 1D state at $\alpha = 0$, the spiral state at $\alpha = 1$, and the 2D-Néel state for $\alpha \geq 2$. (The horizontal black bonds have strength J, and the diagonal red bonds have strength J'.) **(b) The quantum-mechanical phase diagram** changes considerably due to order-by-disorder effects and the appearance of spin liquids (from [239, 614]).

14.2.1 MSWT on the SATL

The triangular lattice with Heisenberg interactions has been considered as one of the first candidate systems for quantum-disordered behavior in the ground state [605]. It is defined in Fig. 14.1a, where the interaction strength J is associated to bonds along the $\boldsymbol{e}_x$ coordinate vector, and J' to bonds along the $1/2\boldsymbol{e}_x \pm \sqrt{3}/2\boldsymbol{e}_y$ vectors, and we define $\alpha = J'/J$.

There are a few well-established limiting cases of the quantum SATL. For $\alpha \gg 1$, one recovers the square lattice limit, where Néel order at the classical ordering vector persists also in the quantum case [632]. Similarly, in the isotropic triangular lattice, $\alpha = 1$, spiral LRO survives quantum fluctuations [633]. The limit $\alpha \to 0$ corresponds to ensembles of decoupled, critical Heisenberg chains, with algebraic correlations along individual chains but no correlations between them.

In the classical limit of $S \to \infty$ (Fig. 14.1a), the spiral phase spans the entire region from $\alpha > 0$ to $\alpha = 2$, where the transition to the Néel phase happens. Quantum effects change this classical phase diagram considerably, possibly even

giving rise to disordered spin liquids. At the low-α side of the spiral phase, many previous works predict such a disordered phase, which could extend to as large α as $\approx 0.8 - 0.9$ [239, 240, 242, 615]. In the following, we term this predicted disordered region "small-α spin liquid." It is associated to a spread of the gapless spin-liquid phase of the isolated chains ($J' = 0$) to finite coupling [239–242], possibly followed by a gapped spin liquid [239–241]. This double-nature of the disordered region is still under debate, since some works only find a gapless spin liquid [242]. Consistently, however, all these methods predict that quantum fluctuations disrupt ordering tendencies between the chains even for relatively large inter-chain couplings, leading to an extended quasi-1D critical phase. But consent about the physics in this region seems far from reached. For example, recent DMRG studies entirely question the existence of the small-α spin liquid(s) [238]. And a recent renormalization-group analysis [237] found collinear AFM long-range order in the region $\alpha \leq 0.3$ (see also [618]), and at larger α spiral order. The extreme weakness of the latter leaves the possibility of observing a disordered phase in the true ground state in the parameter range $0.3 - 0.5$.

Coming from the large-α limit, it is commonly accepted that order-by-disorder effects due to quantum fluctuations stabilize the Néel phase considerably compared to the classical model, moving the point where Néel order disappears downwards from the classical value $\alpha = 2$ to values between $\alpha \approx 1.1$ to 1.67, depending on the method used [238, 241, 242, 614, 634, 635]. Further, several methods predict that quantum fluctuations spread the transition point between the Néel and the spiral phase into a quantum-disordered phase [241, 614, 615, 634]. In the following, we term this predicted disordered region "large-α spin liquid." The classical phase diagram is contrasted with the quantum mechanical one (composed from Refs. [614] and [239]) in Fig. 14.1. It is interesting to notice that it is qualitatively very similar to the one on the SATL with XY interactions, as described in Chapter 3.2 (see also Refs. [202, 225]).

A variety of experiments have been carried out on magnetic compounds described by the Heisenberg model on the SATL, with results that are still controversial. For instance neutron scattering experiments of Coldea and coworkers [609] on Cs_2CuCl_4, where $\alpha \approx 1/3$, claimed evidence that the low-energy physics is governed by spinons, fractionalized excitations with $S = 1/2$ which represent the elementary excitations in the case of uncoupled chains. Yet, Kohno, Starykh, and Balents [617] showed that, for a finite inter-chain coupling, spinons tunnel between chains in bound pairs with $S = 1$ (so-called triplons), so that the fractionalization in two dimensions is strictly speaking not present. Kohno, Starykh, and Balents [617] argue that the spinons in Cs_2CuCl_4 are descendants

of the excitations of the individual 1D chains and not characteristic of any exotic 2D state. This further reinforces the idea of a quasi one-dimensional behavior up to relatively high inter-chain interactions mentioned in the previous paragraph.

In the following, we discuss the ground-state phase diagram of the $S = 1/2$ SATL with NN Heisenberg interactions. We apply the MSWT in the thermodynamic limit, and, in order to assess its validity, compare its predictions with ED, for which we compute (using the Lanczos method) the ground state of small clusters of 14, 24, and 30 spins. The considered geometry for the 30-spin system can be found in Fig. 3.2c. The 24-spin system can be obtained from it by removing the top and bottom rows. The 14-spin cluster is an equivalent system with rows of 2, 3, 4, 3, and 2 spins. The clusters are chosen for their symmetry with respect to reflection along the coordinate axis, and for their ratio of the number of J'-bonds (red) to the number of J-bonds (black), which lies close to the bulk value of 2. We use open boundary conditions to allow for the accommodation of incommensurate spiral order.

MSWT ground-state energy in comparison with previous results

As a first step in our analysis, we compare the energy from MSWT to other methods. We find quite good agreement to data that were obtained by Yunoki and Sorella by variational QMC methods [239], shown in Fig. 14.2. This agreement suggests that MSWT yields reliable predictions despite its simplicity. For comparison, we also show in Fig. 14.2 the data that Yunoki and Sorella obtained with a projected-BCS (p-BCS) wave-function [239]. To further judge the quality of the MSWT predictions, we now compare them to ground-state energies derived with various other methods, focusing on a few special values of α. The corresponding data can be found in Table 14.1.

In the isotropic triangular lattice, the MSWT energy compares favorably to the data from the Green's function Monte Carlo method with stochastic reconfiguration (GFMCSR) by Capriotti, Trumper, and Sorella [633], but both energy and order parameter lie closest to the variational QMC calculation from Weber *et al.* [636], who used a mixture of a BCS wave-function and a wave function with spiral order as their starting point (BCS+spiral). MSWT predicts a smaller energy than LSWT as well as 1/S expansion [228, 640], but since neither of these methods is variational this does not rigorously mean that the MSWT ground state is better.

At $\alpha = 0$, the MSWT value $E_0(\alpha = 0) = -0.4647$ is relatively close to the exact result of the one-dimensional case, $-(\ln 2 - 1/4) = -0.44315$. However, it is located *below* the exact value. Again, this is due to the non-variational nature

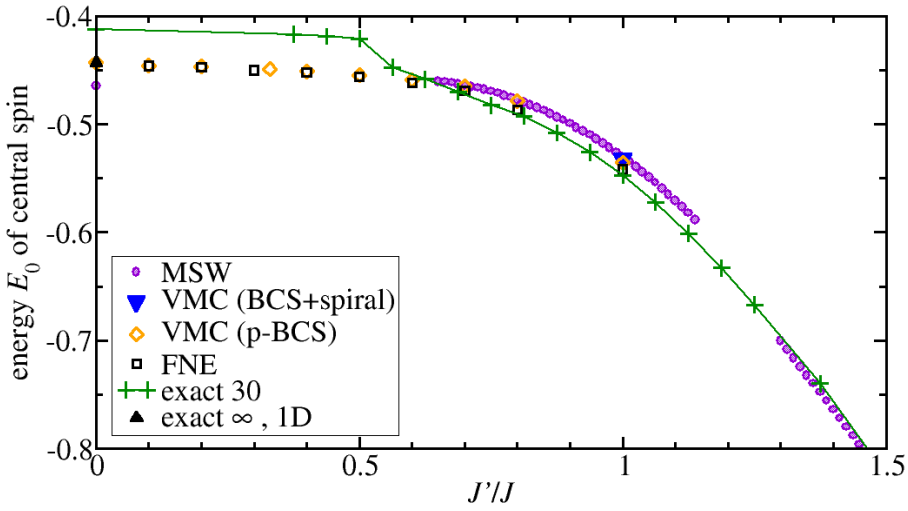

Figure 14.2: **Ground-state energy for the quantum Heisenberg SATL.** MSWT results lie close to those from previous studies. Shown are the data due to Yunoki and Sorella [239] of a variational QMC (VMC) *Ansatz* with a projected BCS wave-function (p-BCS) and the improved FN effective Hamiltonian method (FNE); the value obtained for $\alpha = 1$ by Weber *et al.* [636] using a VMC method with a mixture of a BCS and a spiral ordered wave-function (BCS+spiral); and the exact result of the 1D limit. The numbers in the labels are the respective system sizes.

Method	$\alpha = 0$	$\alpha = 0.7$	$\alpha = 0.8$	$\alpha = 1$	$\alpha = \infty$	M at $\alpha = 1$
exact, thermodynamic limit	−0.443147					
exact, $N = 30$ (present study)	−0.4127			−0.5471		0.1314
exact, $N = 40$, extrapolated [632]					−0.6701	
VMC (RVB) [239]				−0.5123(1)		0.0
VMC (RVB with $\mu = 0$) [239]				−0.5291(1)		0.0
VMC (BCS+spiral) [636]				−0.532(1)		0.36
VMC (p-BCS) [239]	−0.442991	−0.46467	−0.47840	−0.5357(1)		0.0
FN [239]		−0.47051	−0.48521	−0.53989(3)		0.1625(30)
FNE [239]		−0.47171	−0.48691	−0.54187(6)		0.1765(35)
GFMCSR [633, 637]				−0.545(2)		0.205(10)
DMRG [568]						0.205(15)
QMC [638]					−0.669437(5)	
series expansion [637] [1]					−0.6696(3)	
series expansion [639] [1]				−0.5502(4)		0.19(2)
LSWT [239, 637][1]				−0.538(2)		0.2387
1/S expansion [640][1]						0.266
1/S expansion [228][1]				−0.5468		0.24974
SBMFT [641][1]				−0.5697		0.275
MSWT (present study)[1]	−0.4647	−0.4639	−0.4775	−0.5303	−0.6699	0.3426

[1] These methods do not provide a rigorous upper bound for the ground-state energy.

Table 14.1: **Comparison of the ground-state energy** per spin derived by various methods, for some values of α. Abbreviations are as follows. VMC: variational QMC (with the underlying wave function in brackets); FN (FNE): (improved) lattice fixed node effective Hamiltonian method; SBMFT: Schwinger-boson mean-field theory; GFMCSR: Green's function Monte Carlo with stochastic reconfiguration. Also included are the exact result for $\alpha = 0$ in the thermodynamic limit (which can be computed via the Jordan–Wigner transform, see Chapter 12.3), the ED results for the 30-spin cluster, and ED results from finite-size extrapolations of calculations on clusters of up to 40 spins [632]. Given the simplicity and flexibility of MSWT, the quantitative agreement is satisfactory. The last column gives the order parameter for the staggered magnetization.

of MSWT. We also notice that the ground-state energies derived from ED of the 30-site system lie close to the predictions from other methods except in the 1D-like phase, $\alpha \lesssim 0.5$. This could be attributed to the small system size: if for small α the Heisenberg SATL is in a 1D-like phase with algebraic correlations, finite-size effects naturally play an important role in that region. This would explain the strong deviation of the ED energy in that parameter region.

On the square lattice ($\alpha \to \infty$), Takahashi showed already twenty years ago the extremely good performance of MSWT [224]; its ground-state energy per spin is -0.6699, which is in excellent agreement with the QMC result $-0.669437(5)$ [638].

Parameter regions where MSWT fails to converge

Convergence in the self-consistent equations of MSWT with ordering-vector optimization, Eqs. (14.11–14.17, 14.19), cannot be achieved in selected regions of the ground-state phase diagram, namely for $\alpha \lesssim 0.65$ and for $1.14 \lesssim \alpha \lesssim 1.3$. (Interestingly, convergence is restored in the pure 1D limit, $\alpha = 0$, for which the theory formulates surprisingly good predictions.) This breakdown of convergence corresponds to the appearance of an imaginary part in the spin-wave frequencies (14.13), signaling an instability of the ordered ground state.

As discussed in Chapter 3.2, the breakdown of a self-consistent description of the system in terms of an ordered ground state is strongly suggestive of the presence of a quantum-disordered ground state in the exact behavior of the system. Hence, one can interpret these parameter regions as candidates for the spin-liquids predicted from Refs. [239, 614] (see Fig. 14.1b). The breakdown regions of MSWT appear to be fully contained within the regions of spin-liquid behavior estimated in Refs. [239, 614]. Hence, MSWT is seen to possibly underestimate the width of the quantum-disordered regions in the phase diagram, which is to be expected due to the partial account of quantum fluctuations given by MSWT.

Order parameter and spin stiffness from MSWT

Our next, complementary step is to determine the regions where the presence of a finite order parameter M_0 and spin stiffness Υ reveal magnetic LRO. Even when these are finite, a caveat is still in order: a finite order parameter with a very small stiffness might suggest that taking quantum fluctuations more completely into account than in MSWT could lead to a completely disordered state.

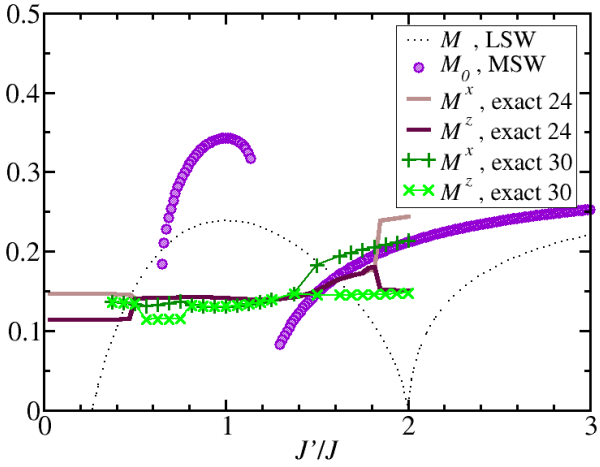

Figure 14.3: **The order parameter** from MSWT decreases towards $\alpha \to 0.65^+$, $\alpha \to 1.14^-$, and $\alpha \to 1.3^+$ indicating the destabilization of magnetic order. For comparison, results from LSWT and ED are also included. The numbers in the labels give the respective system sizes.

A finite order parameter M_0 (Fig. 14.3) and spin stiffness (Fig. 14.4) show that magnetic LRO is present in the intervals $0.65 < \alpha < 1.14$ and $\alpha > 1.3$. Both order parameter and spin stiffness decrease upon approaching the regions $1.14 \lesssim \alpha \lesssim 1.3$ and $\alpha \lesssim 0.65$, which are the parameter regimes where the self-consistent description breaks down. This finding further corroborates the assumption that in these regions magnetic LRO disappears in the true quantum ground state. This is to be contrasted with LSWT, which predicts the breakdown of magnetic order only for $\alpha \lesssim 0.3$ [642]. Further, the vanishing ρ_{xx} at $\alpha \to 0.65^+$ is not consistent with a gapless spin liquid, since in such a critical phase, the spin stiffness along the chains remains finite. This gives support to the assumption that the quantum ground state hosts a gapped spin liquid in this region (see Fig. 14.1b).

In the square lattice limit, $\alpha \to \infty$, on the other hand, MSWT attains a finite staggered magnetization of 0.303 (coinciding with the LSWT value), which compares favorably with the most recent estimates $M_0 = 0.30743(1)$ from QMC calculations [643]. For the spin stiffness, MSWT gives in this limit $\rho_\parallel/\alpha = 0.216$, somewhat overestimating the value from QMC $\rho_\parallel/\alpha = 0.175(2)$ [638].

In the isotropic case, $\alpha = 1$, the spin stiffness from MSWT is $\rho_\parallel/\alpha = 0.113$. This value falls between the LSWT prediction, $\rho_\parallel/\alpha = 0.122$ [644], and the estimate obtained from ED calculations after finite-size extrapolation, $\rho_\parallel/\alpha = 0.075$ [644]. The large-S expansion result, $\rho_\parallel/\alpha = 0.070$ [640], on the other hand,

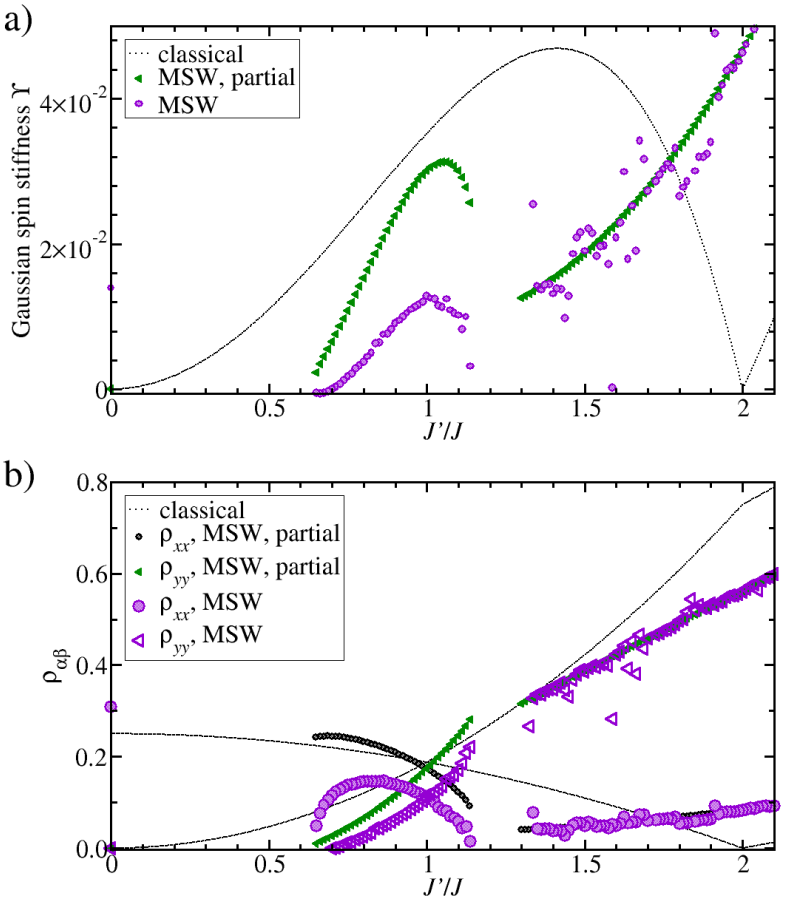

Figure 14.4: **(a) The Gaussian spin stiffness** Υ vanishes at $\alpha = 0.65^+$ and it drops significantly when approaching $\alpha = 1.14$ from below, suggesting the weakening of magnetic order. **(b) Components of the spin stiffness tensor.** ρ_{yy} vanishes at $\alpha = 0$ and when reaching $\alpha = 0.65$ from above. ρ_{xx} decreases strongly when approaching $\alpha = 0.65^+$ and $\alpha = 1.14^-$, suggesting the onset of gapped spin-liquid phases. The mixed second derivative ρ_{xy} vanishes for symmetry reasons. The curves labeled 'partial' were obtained via Eq. (14.23).

is closer to the ED result than the MSWT value. Notably, at this value of α, the MSWT order parameter is considerably higher than what is predicted by LSWT. Comparison to the best numerical estimates, which are presented in Table 14.1, shows that in this respect MSWT performs worse than other analytical methods, like Schwinger-boson mean-field theory (SBMFT) [641] or 1/S expansion [228, 640]. Nonetheless we notice that among all analytical predictions surprisingly LSWT gives the one which is the closest to the more recent numerical estimates. This strongly suggests that an adequate account of quantum corrections to the magnetization is a hard task for theories accounting for spin-wave interactions at a perturbative or mean-field level, and that non-perturbative approaches or approaches beyond mean-field theory would be necessary. Another explanation of this discrepancy could lie in corrections to the spin-wave expansion of third-order in the boson operators. These are neglected in our approach, but they can become important in spiral configurations [228].

In the limit of decoupled chains, $\alpha = 0$, MSWT achieves convergence (which was lost in the interval $0 < \alpha < 0.65$) and provides a spin stiffness $\rho_{xx}/\alpha = 0.309$ in the thermodynamic limit. As for the ground-state energy, this value lies relatively close to the exact result in the thermodynamic limit, $\rho_{xx}/\alpha = 1/4$ [230].

Ordering vector and chirality correlations from MSWT

Now, we describe the ordered phases found by MSWT for the Heisenberg SATL in more detail. To this end, we analyze the the ordering vector $\boldsymbol{Q}$, given by Eq. (14.19), and the chiral order parameter Ψ^-, defined in Eq. (3.33). The chiral order parameter is finite in spiral phases. For the ordering vector, three limiting values are known. For $\alpha = 0$, intra-chain AFM (Néel) order is described by $\boldsymbol{Q} = \pi \boldsymbol{e}_x$. For $\alpha \to \infty$, square-lattice Néel order is described by $\boldsymbol{Q} = 2\pi \boldsymbol{e}_x$. In the isotropic lattice ($\alpha = 1$), the threefold symmetry forces the ordering vector to $\boldsymbol{Q} = \frac{4\pi}{3} \boldsymbol{e}_x$.

A comparison of these quantities (Figs. 14.5 and 14.6) shows a spiral phase at around $0.65 \lesssim \alpha \lesssim 1.14$ and a 2D-Néel ordered phase for $\alpha \gtrsim 1.3$. Moreover, when approaching $\alpha \approx 0.65$ from above, the spin–spin correlations (not shown), the ordering vector, and the ground-state energy approach their respective 1D values. This is an indication that below $\alpha \approx 0.65$ the true ground state of the system may enter a 1D-like spin-liquid phase. Nonetheless, as mentioned before, the vanishing of the spin stiffness ρ_{xx} for $\alpha \to 0.65^+$ is not consistent with the onset of a *gapless* 1D spin-liquid phase, for which the spin stiffness should remain finite. Hence, the MSWT results rather suggest that the phase appearing below

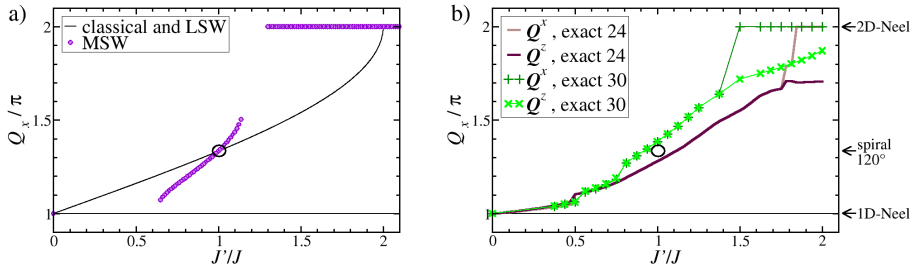

Figure 14.5: **Ordering vector.** **(a)** Q_x from MSWT [Eq. (14.19)] shows a considerable shift with respect to the the classical and the LSWT results. The black circle marks the order vector $Q_x = 120°$ of the isotropic triangular lattice. **(b)** For ED, Q_x depends strongly on whether it is derived from M^x or from M^z. Also, the difference between the 24 and the 30 site cluster is significant.

$\alpha = 0.65$ is a *gapped* spin liquid, and that the gapless 1D spin-liquid phase, connected continuously with the limit $\alpha = 0$, is only attained for even smaller α. This seems consistent with the prediction of Yunoki and Sorella [239] that a gapped spin-liquid phase separates the spirally ordered phase from the 1D-like gapless one.

Order parameter and correlations in comparison with ED

In the case of ED, the static structure factor

$$S_{\mu\mu}(\boldsymbol{k}) = \frac{1}{N}\sum_{i,j}\langle S_i^\mu S_j^\mu\rangle\, e^{-i\boldsymbol{k}\cdot\boldsymbol{r}_{ij}} \qquad (\mu = x,y,z) \tag{14.25}$$

allows to extract the order parameter $M^\mu = \sqrt{S_{\mu\mu}(\boldsymbol{Q})/N}$, where $\boldsymbol{Q}$ is the ordering vector associated with a peak in $S_{\mu\mu}(\boldsymbol{k})$. In the thermodynamic limit, this is equivalent to M_0 from MSWT. A comparison of both quantities can be found in Fig. 14.3. We find that, due to the peculiar geometries chosen, there exist parameter ranges where the ED ground state falls into the threefold degenerate triplet with total spin equal to unity. Nonetheless, we restrict our calculations to the $M_z^{\text{total}} = 0$ subspace (with M_z^{total} being the z component of the total spin), and the $M_z^{\text{total}} = \pm 1$ states are excluded. This results in an apparent breaking of the x–z symmetry (the x–y symmetry is preserved). This symmetry would be recovered by averaging over the whole triplet subspace. The reason for such an apparent symmetry breaking resides in the particular

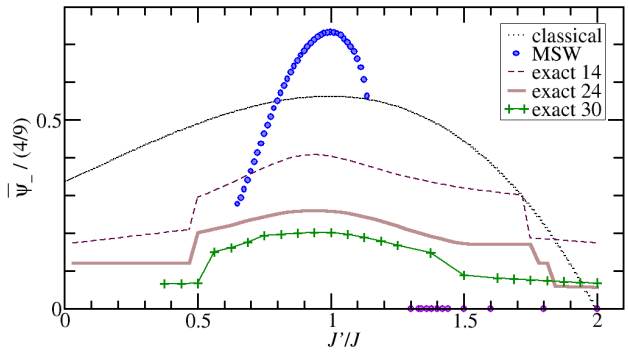

Figure 14.6: **Chiral correlations,** normalized to the theoretical maximum of 4/9. MSWT and ED results suggest the survival of chiral correlations in a range around $\alpha = 1$, but their breakdown for $\alpha \lesssim 0.6$.

geometry of the clusters considered, which complicates the comparison between different system sizes. This triplet physics might play an important role for bigger systems, although we cannot draw conclusions about the thermodynamic limit from the small clusters considered. A non-trivial triplet physics could be especially an issue for variational methods restricting their focus to the singlet subspace.

Discontinuous jumps in the ED magnetizations are due to the change of the spin sector hosting the ground state, going from the singlet sector (characterized by $M^x = M^z$) to the triplet sector (characterized by $M^x \neq M^z$). We observe severe deviations between the ED data on the one side and the predictions from LSWT and MSWT on the other side. In particular, apart from the deviations between M^x and M^z, the ED data appears to be almost constant over a large α interval. The strong difference between ED results on the one hand and MSWT/LSWT predictions on the other can also be attributed to significant finite-size corrections to the ED data, which are particularly pronounced here, due to the open boundary conditions of the ED clusters. Nonetheless, for $\alpha = 1$ the magnetization of the 30-site cluster gives $M^x = M^z \approx 0.13$, lying close to recent Monte Carlo estimates [240].

From the location of the peak of the structure factor one can extract the vector of predominant ordering, $\boldsymbol{Q}$, the x-component of which is plotted in Fig. 14.5. For MSWT, we observe a significant shift with respect to the classical and LSWT results (Fig. 14.5a). Remarkably, for ED of the 30-site cluster, the ordering vector corresponding to M^x (labeled $\boldsymbol{Q}^x$ in the figure) indicates a transition from spiral to Néel order at around $\alpha \approx 1.4$, which lies well below the classical threshold $\alpha = 2$ (Fig. 14.5b). On the contrary, the ordering vector

corresponding to M^z (labeled $\boldsymbol{Q}^z$) increases smoothly up to $\alpha \approx 2$, where it undergoes a discontinuous transition to the square-lattice Néel value. However, increasing the system size from 24 to 30 spins shifts significantly the curves of $\boldsymbol{Q}^x$ and $\boldsymbol{Q}^z$ to the left, suggesting that for even larger sizes both curves might exhibit a discontinuous transition to the Néel ordering vector for a value of α close to the transition indicated by MSWT, $\alpha \approx 1.3$. Finally, we notice that at $\alpha = 1$ the ED results deviate from the isotropic value $Q_x = 120°$ because the threefold symmetry is broken by the shape of the simulation cluster, Fig. 3.2c.

Finally, we focus on the chirality correlations. Comparing such correlations for the 14, 24, and 30 spin clusters shows that they are strongly suppressed for $\alpha \lesssim 0.5$ and for $\alpha \gtrsim 1.4$ when going to larger lattice sites. This indicates that a non-spiral phase appears in this region in the thermodynamic limit, in agreement with our MSWT calculations. The persistence of significant correlations in the region $0.5 \lesssim \alpha \lesssim 1.4$ indicates that spiral order in the ground state might persist in a portion of this parameter range.

In summary, despite the significant deviations in the magnitude of the order parameter, both ED and MSWT give a coherent picture, both qualitatively and quantitatively, of the evolution of the nature of spin-spin correlations upon increasing α, going from quasi-1D to spiral to Néel.

Discussion

Despite its limitations, MSWT with ordering-vector optimization reproduces faithfully the main characteristics of the phase diagram of the quantum SATL as sketched in Fig. 14.1b, and thus remarkably improves on the results that were previously obtained for this model with conventional spin-wave theories. A breakdown of magnetic order – along with a variety of observables like the ordering vector or NN spin–spin correlations – indicates that a 1D-like spin liquid might be attained below $\alpha \approx 0.65$. Due to the partial account of quantum fluctuations provided by MSWT, we can safely take this as a lower bound for a spin liquid in the true ground state. Furthermore, we find a relatively small region with spiral LRO between $0.65 \lesssim \alpha \lesssim 1.14$. For $\alpha \gtrsim 1.30$ the system is ordered at the 2D-Néel wave-vector. Between $1.14 \lesssim \alpha \lesssim 1.30$ the breakdown of convergence suggests another candidate region for spin-liquid behavior.

14.2.2 MSWT on the spatially completely anisotropic triangular lattice (SCATL)

As seen in the last section, there are strong indications that the AFM Heisenberg SATL harbors spin-liquid phases. Initially, these were assumed to appear at strongest frustration, but they seem to actually occur at transitions between two different types of order. To identify if this is more general, we here analyze – again using Takahashi's MSWT complemented by ED – a generalization of the SATL, the spatially *completely* anisotropic triangular lattice (SCATL).[3]

In the SCATL, the NN couplings J_{ij} along *all three* lattice directions are different, see left side of Fig. 3.15 (with t's replaced by J's). For simplicity, we will work throughout this section in the associated square lattice (right side of Fig. 3.15), where the vectors connecting NN sites are $\boldsymbol{\tau}_1 \equiv (1,1)$, $\boldsymbol{\tau}_2 \equiv (0,1)$, and $\boldsymbol{\tau}_3 \equiv (-1,0)$, and define $J_{\boldsymbol{\tau}_1} \equiv J$, $J_{\boldsymbol{\tau}_2} \equiv J'$, and $J_{\boldsymbol{\tau}_3} \equiv J''$. An advantage of the SCATL geometry is the possibility, given by the additional anisotropy, to approach the putative spin-liquid phases from different angles, possibly revealing crucial information not only about their location in parameter space, but also about their nature. Indeed, the results presented in this section suggest that the gapped spin liquids of the SATL, apparently two distinct phases, might actually be continuously connected via the additional anisotropy of the SCATL. Studying the persistence and characteristics of the putative spin-liquid phases with respect to this additional anisotropy is the first main aim of the present section.

The second main aim is related to experimental findings in magnetic materials. While the SATL has found considerable attention in recent years, to our knowledge the ground-state phase diagram of the Heisenberg SCATL has never been thoroughly investigated. Recent first-principles calculations, however, show that some magnetic materials that are well described by weakly-coupled 2D triangular lattices, such as the organic salts $\mathrm{Me}_{4-n}\mathrm{Et}_n Pn[\mathrm{Pd(dmit)}_2]_2$ (abbreviated $Pn-n$) [645], TMTTF [646], or $\mathrm{BaAg_2Cu[VO_4]_2}$ [647] can have considerable anisotropies between all three intra-plane couplings.[4] Typically, to locate the material within the well-studied SATL model, the two closer bond strengths have been averaged. However, this places materials such as Sb-0 and As-2, which are experimentally found to be AFM ordered, into a region of the phase diagram, where according to many theoretical studies [239–242, 615] no

[3] The $S = 1/2$ AFM SCATL with XY interactions, motivated by recent experiments with frustrated bosonic atoms in optical lattices, is treated in a similar way in Chapter 3.4.

[4] Although in the last material the physics is dominated by a superposition of antiferromagnetic and ferromagnetic 1D chains.

LRO should exist. The second aim of this section, therefore, is to show that the additional anisotropy between the couplings could explain this discrepancy naturally, since it shifts the parameter values corresponding to these materials into an ordered phase. This also suggests that the spin-liquid state is quite sensitive to this additional anisotropy, which therefore has to be taken into account when interpreting experiments.

Known limiting cases

Before proceeding to the computation of the phase diagram of the quantum Heisenberg SCATL, let us first discuss briefly some well-known limiting cases. This helps us to assess which phases and quantum effects are to be expected in the phase diagram of the SCATL.

For $(J'/J, J''/J) = (1,0)$, $(J'/J, J''/J) = (0,1)$, and $J'/J, J''/J \gg 1$, one recovers the square lattice limit. Here, Néel order at the classical ordering vector persists also in the quantum case [632]. Similarly, in the isotropic triangular lattice, $J' = J'' = J$, spiral long-range order survives quantum fluctuations [633]. The limits ($J' = J'' = 0$), ($J' \to \infty$ with $J'' = \text{const}$), and ($J'' \to \infty$ with $J' = \text{const}$) correspond to ensembles of decoupled Heisenberg chains. In this limit, each chain is critical with algebraic decay of correlations along the chains but no correlations between different chains. For $J' = J'' \equiv \alpha J$ (or, equivalently, $J' = J$ or $J'' = J$), one recovers the SATL discussed in the previous section (see Fig. 14.1 for its phase diagram).

The classical phase diagram (equivalent to $S \to \infty$) can give some further intuition about possible ordered phases. For Heisenberg interactions, it is equivalent to the solution for XY spins (3.37a) as obtained in Chapter 3.4.1, if (without loss of generality) we focus on the classical solution where the spins are oriented in the xy-plane. The classical phase diagram can be found in Fig. 3.16. The Néel phases spread around the square-lattice limits [$(J'/J, J''/J) = (1,0)$ with $\boldsymbol{Q}^{\text{cl}} = (0,\pi)$, $[(J'/J, J''/J) = (0,1)$ with $\boldsymbol{Q}^{\text{cl}} = (\pi,0)$, and $J'/J, J''/J \gg 1$ with $\boldsymbol{Q}^{\text{cl}} = (\pi,\pi)$]. The spiral phase, with continuously varying ordering vector connects smoothly to the Néel phases, and occupies the extended region between them. In particular, it extends down to $J'/J = J''/J = 0$ [and, symmetrically, to ($J'/J = 1$, $J''/J \to \infty$) and ($J''/J = 1$, $J'/J \to \infty$)], where the system decouples into an ensemble of 1D chains.

From our experience with the frustrated spin systems treated in this thesis, we can expect appreciable changes to the classical phase diagram due to quantum fluctuations. To compute the quantum phase diagram, we again make use of Takahashi's MSWT (in the thermodynamic limit). We compare these

approximate results to ED of a 15-site lattice, as depicted in Fig. 3.15. Again, we leave the boundaries open to account for incommensurate ordering vectors.

MSWT and ED results – ordering vector and order parameter

We obtain an overview of the quantum-mechanical phase diagram of the SCATL from the ordering vector $\boldsymbol{Q}$ and the order parameter M. Afterwards, we will analyze complementary observables. For Heisenberg interactions, we define the magnetization for ED as

$$M^{\mathrm{ED}} \equiv \sqrt{S(\boldsymbol{Q}^{\mathrm{ED}})/N} = \sqrt{\sum_{\alpha=x,y,z} S^{\alpha}(\boldsymbol{Q}^{\mathrm{ED}})/N}\,, \tag{14.26}$$

where the ED ordering vector $\boldsymbol{Q}^{\mathrm{ED}}$ is located at the peak of the structure factor $S(\boldsymbol{k})$, as defined in Eq. (14.25). As seen in the MSWT and ED ordering vectors, presented in Fig. 14.7, quantum fluctuations stabilize the Néel phases compared to the classical case, as already observed in the SATL. In the central region around $J' \sim J'' \sim J$, the ordering vector indicates spiral order with a broad range of incommensurate ordering vectors. The finite MSWT order parameter (Fig. 14.8, left panel) suggests that in these phases indeed long-range order survives quantum fluctuations. (Note that the self-consistent MSWT calculations become relatively unstable for small order parameters, which results in the ragged boundary lines of the ordered phases.)

In the Néel phases, the ED order parameter (Fig. 14.8, right panel) is maximal, giving support to the assumption that here LRO persists. However, it is much smaller in the spiral phase than the MSWT value, a discrepancy already found in the SATL, Sec. 14.2.1, and the XY models treated in Chapter 3.

Between the ordered regions, we find a broad region where the MSWT theory breaks down, indicating as usual that these regions do not allow a description in terms of an ordered, semi-classical state. This, in turn, hints at quantum spin-liquid phases. Therefore, it appears that it is a quite universal feature of frustrated quantum antiferromagnets that spiral- and collinearly-ordered phases are always separated by quantum disordered phases. This is the first main result of this section.

We obtain further support to this interpretation (which we will further corroborate in the next two sections) from the strong decrease of the MSWT and ED order parameters upon approaching the breakdown region (Fig. 14.8). Note also that both the ED and MSWT order parameter seem to disappear smoothly when approaching the putative 1D-like spin liquid (consider, *e.g.*, in the range

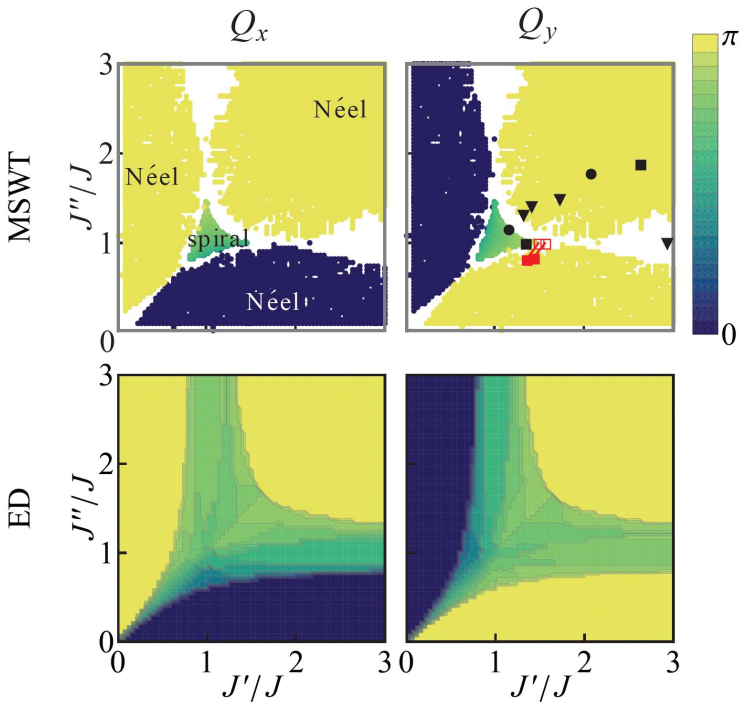

Figure 14.7: **Phase diagram of the quantum Heisenberg SCATL, ordering vector. Upper row: MSWT data.** Quantum fluctuations stabilize the Néel phase. Around $J' = J''$, a part of the classical spiral phase survives quantum fluctuations. Labels for the ordered phases can be found in the upper left panel. The solid symbols (upper right panel) denote some experimental materials (see Table 14.2). (For clarity, we show only symbols in the lower right part of the figure, excluding points which are connected by symmetry between J, J', and J''.) ▲: magnetically disordered; ●: charge-ordered; ■: AFM LRO. Note especially the two ■ at $(J'/J, J''/J) = (1.44, 0.84)$ and $(J'/J, J''/J) = (1.36, 0.82)$ marking the materials As-2 and Sb-0, which lie well inside a Néel ordered phase. Neglecting the asymmetry between the couplings would put As-2 into the supposedly disordered region and Sb-0 just at its boundary (□). **Lower row: ED data** for $N = 15$ sites. Already at this small system size, it can be appreciated that the Néel phase grows at the expense of spiral order.

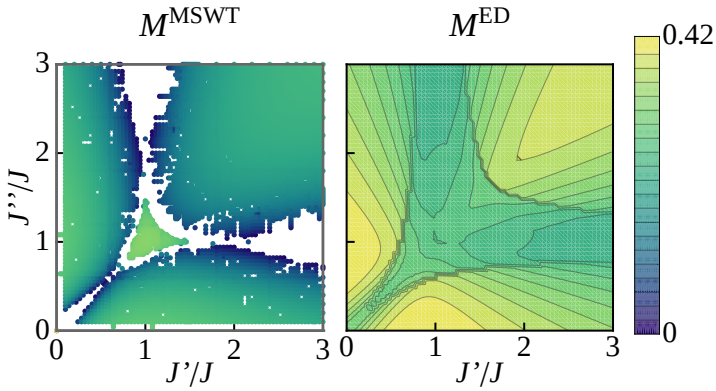

Figure 14.8: **Phase diagram of the quantum Heisenberg SCATL, order parameter.** ED results qualitatively confirm the MSWT phase diagram. In particular, the order parameter for both methods decreases rapidly upon approaching the MSWT breakdown regions.

$2 \lesssim J'/J \lesssim 3$, $J''/J \to 1^-$). Upon approaching the putative large-α spin liquid dividing spiral from Néel LRO, on the other hand, for ED the order parameter decreases sharply (consider, *e.g.*, the line $J'/J = 1$, $J''/J \to 1^-$), and for MSWT the breakdown occurs abruptly at finite order parameters. This points at a difference in the type of phase transition upon approaching the large-α spin liquid and the spin liquid at the decoupled-chains limit.

The second main result of this section concerns experimental measurements of ground-state behavior of some materials, taken from the article by Scriven and Powell [645] (see also the reviews [648, 649]), as well as from the works by Coldea *et al.* [650] (Cs_2CuCl_4) and by Ono *el al.* [651] (Cs_2CuBr_4). For reference, the corresponding data are presented in Table 14.2, and included as solid symbols in the upper right panel of Fig. 14.7. We mark magnetically disordered materials (spin liquids, resonating valence-bond states, or valence-bond solids) with triangles, charge-ordered materials with bullets, and antiferromagnetically ordered materials with squares. Including the full anisotropy of the triangular lattice, all ordered materials lie within the ordered phases from MSWT theory.[5] In particular, the AFM ordered materials As-2 and Sb-0 [at $(J'/J, J''/J) = (1.44, 0.84)$ and

[5]Some magnetically disordered materials are erroneously found in ordered regions of the MSWT phase diagram. However, it is known that MSWT overestimates ordered phases.

material	$(J'/J, J''/J)$	state
N-3	(10, 9.1)	AFM
P-2	(2.63, 1.89)	AFM
Sb-2	(2.08, 1.79)	CO
Sb-1	(1.72, 1.49)	SL
κ-CN	(1.41, 1.41)	SL
P-1	(1.32, 1.32)	VBS
Cs	(1.16, 1.16)	CO
Sb-0	(0.74, 0.60)	AFM
Cs_2CuBr_4	(0.74, 0.74)	AFM
As-2	(0.69, 0.58)	AFM
Cs_2CuCl_4	(0.34, 0.34)	RVB

Table 14.2: **Some relevant materials** for which the ground state has been measured in experiment, together with the coupling strengths, and the state they are found to be in (from Refs. [645, 650, 651] and references therein). AFM stands for antiferromagnetic LRO, CO for charge ordered, SL for spin liquid, VBS for valence-bond solid, and RVB for resonating valence-bond state.

$(J'/J, J''/J) = (1.36, 0.82)$] lie well inside a Néel ordered phase. If one neglects the anisotropy between J' and J'', taking the mean of both couplings as is usually done, they would lie at the position of the empty squares at $(J'/J, J''/J) = (1.57, 1)$ [equivalent to $(J'/J, J''/J) = (0.64, 0.64)$] and $(J'/J, J''/J) = (1.50, 1)$ [equivalent to $(J'/J, J''/J) = (0.67, 0.67)$] – inside a phase where many methods [239, 240, 242, 615] predict disorder; specifically, within MSWT, symmetrizing the couplings puts Sb-0 just at the border to the breakdown region (which should be a lower limit for disorder in the true ground state) and As-2 within it. The appearance of AFM Néel LRO in these experiments might find, therefore, a simple explanation in the full anisotropy of the SCATL. This second main result of this section shows how crucial the full anisotropy is for the interpretation of experimental data. The rest of this section is devoted to fleshing these main findings out.

Supporting observables from MSWT – spin stiffness and spin-wave velocities

In Chapters 3 and 14.2.1, the spin-stiffness tensor has proven a valuable consistency check of our MSWT calculations, because it characterizes how stiff the magnetic order is under change of the ordering vector. Since for our purposes it is enough to extract an upper bound for the spin stiffness, we here use the partial derivative (14.23). While it may not be able to distinguish gapped from gapless spin liquids, it still seems adequate to capture the location of disordered regions. In Fig. 14.9, we show the determinant of the spin-stiffness tensor,

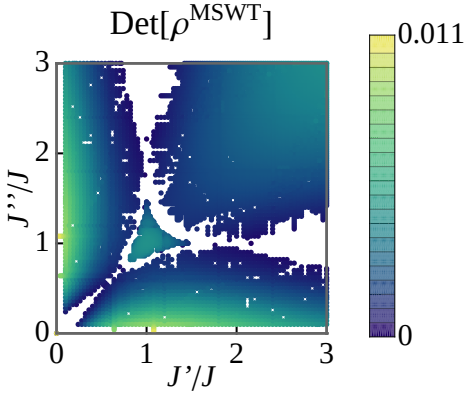

Figure 14.9: **The partial spin stiffness** (normalized to the coupling strengths $1 + J' + J''$) decreases upon approaching the MSWT breakdown region, suggesting the disruption of magnetic LRO.

$\det(\rho)$, normalized to the coupling strengths $1 + J' + J''$. As we should expect [258], $\det(\rho)$ decreases upon approaching the phase transitions, especially from the Néel-ordered side. At large J' (J''), this decrease is due to a softening of the stiffness in x (y) direction, and at small ($J'/J, J''/J$) in the direction perpendicular to $\boldsymbol{\tau}_1$, *i.e.*, perpendicular to the dominating coupling strength (as can also be seen in the SATL, Chapter 14.2.1).

Another indicator for approaching disordered phases is given by the spin-wave velocities $v_{x,y}$, as defined in Eqs. (3.38). Since they can be measured directly from the spin-wave dispersion, they allow an experimental check of our findings. As seen in Fig. 14.10, close to the 1D breakdown region they, too, soften in the direction perpendicular to the dominating coupling. On the other hand, when approaching the putative large-α spin liquid dividing the spiral from the Néel phase, both spin-wave velocities remain finite. This is another (besides the different behavior of the order parameter) indication that the large-α spin liquid is qualitatively different from the spin liquid found in the limit of decoupled chains.

Supporting observables from ED – energy derivative, gap, and chiral correlations

The ED observables investigated above, order parameter and ordering vector, allowed to interpret the predominant ordering behavior, but did not yield clear evidence if within ED really quantum phase transitions (QPTs) exist, and if yes, where their boundaries lie. The second derivatives of the ED ground-state

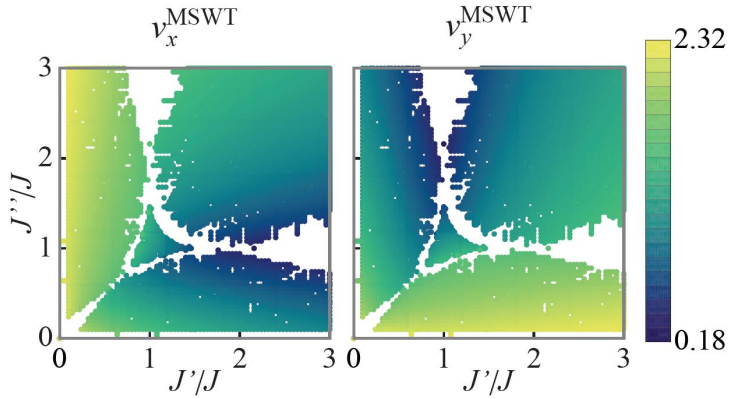

Figure 14.10: **The spin-wave velocities** (normalized to the coupling strengths $1 + J' + J''$) soften in the 1D limits in the direction perpendicular to the dominating coupling strength. Differences in the spin-wave velocities might allow to measure the anisotropy of the SCATL.

energy, which we plot in Fig. 14.11, can provide such an indicator. In fact, in the thermodynamic limit, it should diverge at a QPT.

Indeed, there are clear peaks along lines similar to where in MSWT the Néel order breaks down. Also, a peak appears around $(J', J'') = (1, 1)$. This might be interpreted as the precursor of a QPT away from the spiral state, and to an intermediate phase, possibly the spin liquid that is supposed to exist in this system.

From the ED energy gap between ground and first excited state, Fig. 14.12, we get further support for the phase diagram that has emerged so far. In the well-known limiting cases of the SCATL, it behaves as expected: There is no gap close to the decoupled-chains limits, since the system is then in a critical phase. In the Néel-ordered phases, there is a large gap which separates the ground state from closely-spaced excitations, which in larger lattices become the spin waves, collapsing slowly towards the ground state [231]. This is consistent with the considerable size dependence found in our calculations, as can be seen in the right panels of Fig. 14.12, where we plot cuts of ΔE^{ED} at fixed $J''/J = 1, 2, 3$ for triangular systems (similar to the one in Fig. 3.15) with $N = 6, 10, 15$.

On the contrary, there is no gap in the spiral-ordered phase, because the

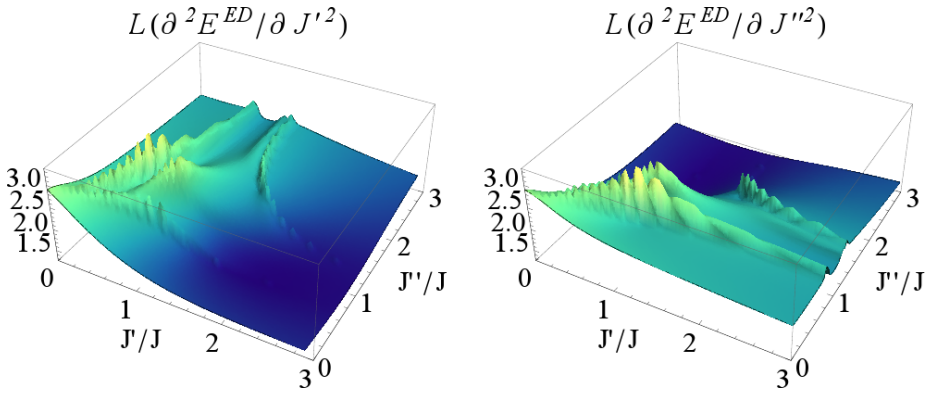

Figure 14.11: **Second derivative of ED ground-state energy** for the $N = 15$ system. For clarity, we plot the logarithm after a shift to positive values larger than one, $L(\partial^2(E/N)/\partial J^{\gamma 2})$, where J^γ is J' or J'', and $L(x) = \log(1+\max(x)-x)$. Strong peaks clearly mark the phase transitions from the Néel phases. An additional peak around $(J', J'') = (1, 1)$ might be an indication of an additional phase separating the Néel phases from the spiral one.

ambiguity in the choice of chirality leads to a ground-state degeneracy.[6] We find that the vanishing of the gap depends strongly on the system geometry, but it occurs consistently for all triangular systems considered.

Interestingly, the gapless spiral phase is surrounded by a region where the gap attains considerable values. The very small dependence on system size indicates that here it may be stable towards the thermodynamic limit. A finite gap is not consistent with a spiral-ordered phase. On the other hand, the predominant order in this region is at incommensurate wave-vectors. Hence, the finite gap is clearly not due to square-lattice Néel-like physics. Optimistically, these findings could therefore be interpreted as the precursors of a gapped spin-liquid phase. This gapped region completely encircles the spiral phase, suggesting that the low- and large-α gapped spin liquids found in the SATL could actually be continuously connected via the additional anisotropy of the SCATL.

Upon approaching the Néel phases, the gap closes, indicating a QPT.

Comparing the left and right panels of Fig. 14.8, the lateral extent of the putative spin liquid is qualitatively different between MSWT and ED. Scanning

[6] We checked that in the spiral phase there is a gap, similar to the spin-wave gap found in the Néel phases, between the *second* and the *third* energy level.

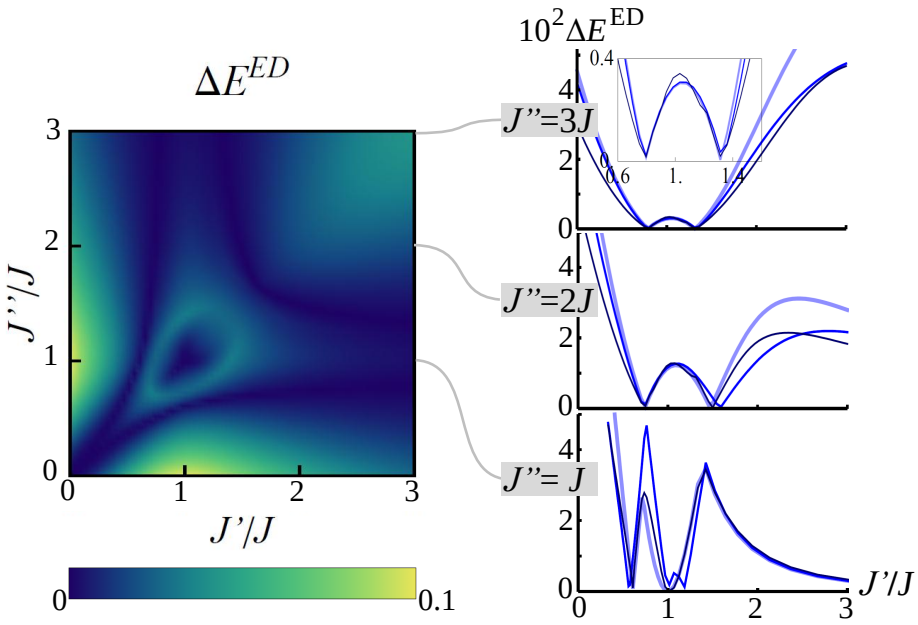

Figure 14.12: **Left panel: The singlet gap from ED** gives support to the MSWT phase diagram. A finite gap separates in the Néel phases spin-wave excitations from the ground state. In the spiral phase, the ground state is doubly degenerate due to the ambiguity in choice of chirality. The finite gap surrounding the degenerate region could be a precursor of a gapped, disordered phase. At the QPTs to the Néel phases, the gap closes again. **Right panels: cuts** at fixed $J''/J = 1, 2, 3$ for triangles with increasing N (from light to dark and thick to thin: 6,10,15). There is little size dependence in the central gapped phase ($J'' = 2, 3J$ with $J' \approx J$, as well as $J'' = J$ and $J'/J \gtrsim 1.5$). Also, for $J' = 3J$ the transition points do not show any appreciable size dependence, while for $J' = 2J$ the one around $J'/J = 1.5$ does.

along $J' = J$, within MSWT it is smallest around $J'' = 2J$, while for ED it decreases monotonously with increasing J''. As the right panels in Fig. 14.12 indicate, this discrepancy could be due to finite-size effect. Indeed, we find in ED that for $J'/J = 2$ the transition point at $J''/J \approx 1.5$ shows an appreciable size dependence, while the transition points for $J'/J = 3$ do not. This leaves the possibility open that the lateral extent of the putative spin liquid at around $J'/J = 2$ decreases with N, making the MSWT and ED pictures consistent.

From the gap, it seems that there is support for the assumption of an extended gapped phase separating spiral and Néel LRO. Still, it would be desirable to be able to exclude for this region spiral LRO in the thermodynamic limit. To do this, we now study where chiral correlations persist. The chiral correlations generalized for the small systems used in our ED have been defined in Eq. (3.39).

As can be seen from the ED results of the $N = 15$ lattice (Fig. 14.13, left panel), the chirality is relatively small in the Néel phases. However, at this lattice size, there are still appreciable chiral correlations in the rest of the parameter regime. In particular, in the 1D limit, the chiral correlations are only a little smaller than in the spiral phase around $(J'/J, J''/J) = (1, 1)$. Therefore, we also plot in Fig. 14.13, right panel, an extrapolation to large lattices by $\Psi_-(N) = \Psi_-(N = \infty) + \frac{c_1}{\sqrt{N}} + \frac{c_2}{N} + \frac{c_3}{N^{3/2}}$, where we use the known form for the leading finite-size behavior [260] but also include subleading corrections due to the small systems under consideration (our data comes from lattices with $N = 7, 10, 12, 15, 18$, all chosen to have the same number of J, J', and J'' bonds, as sketched at the bottom of Fig. 14.13). While this can not be seen as a rigorous finite-size analysis, which is difficult for the small systems studied, it shows a clear trend, namely that the chiral correlations only survive in a small region around $(J'/J, J''/J) = (1, 1)$, which roughly corresponds to the region where the vanishing gap indicated the spiral phase.[7] If further studies can confirm this analysis, it means that outside of this region, there is no spiral LRO.

With this, we have several independent observations from ED indicating the existence of a magnetically disordered phase surrounding the spiral phase: the increase of the gap when leaving the central region around $(J'/J, J''/J) = (1, 1)$ and the disappearance of chiral LRO when extrapolating to large lattices both suggest that there is no spiral LRO in this region. On the other hand, the predominant order is at incommensurate ordering vectors, indicating that this phase is also not Néel ordered. Therefore, it seems natural to assume that this

[7] The smaller peaks around $(J'/J, J''/J) = (3, 1)$ and $(J'/J, J''/J) = (1, 3)$ are results of the strong geometry dependence of observables for the small lattices used. It can be understood that these peaks are artifacts of the extrapolation, because it is highly implausible that the chiral LRO first disappears when increasing the one-dimensionality and then finds a revival.

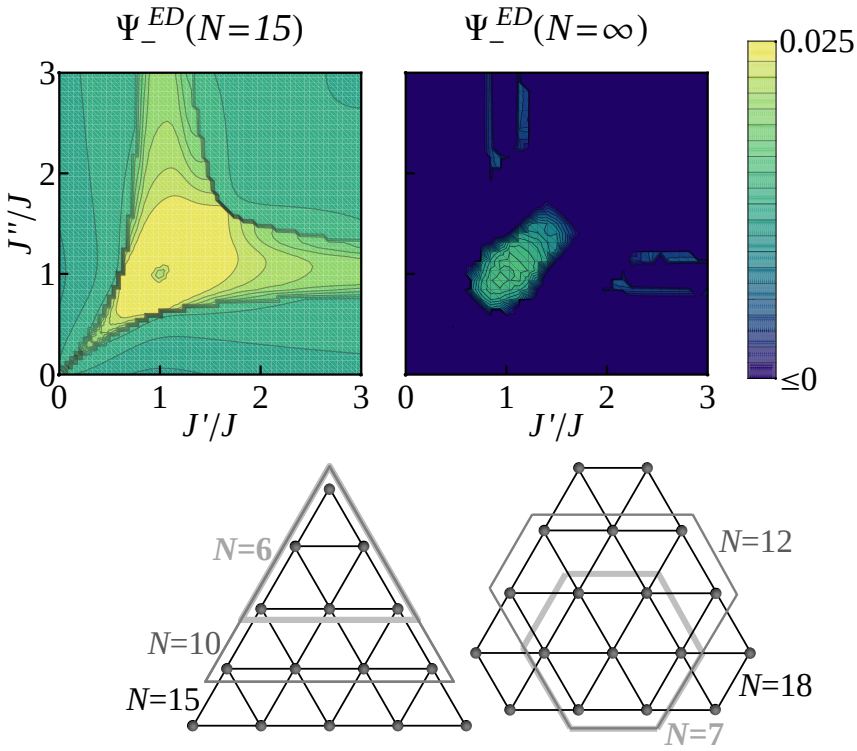

Figure 14.13: **Chiral correlations from ED. Upper left:** Already for small systems ($N = 15$), the chiral correlations are appreciably smaller in the Néel phases than in the rest of the phase diagram. **Upper right:** From an extrapolation to large lattices, it appears that chiral LRO only survives in a small central region around $(J'/J, J''/J) = (1, 1)$, lending support to an extended disordered phase surrounding a spiral phase. **Below:** The geometries used in the extrapolation are chosen for symmetry upon rotation by 60° and equal number of J, J', and J'' bonds.

region could host a spin-liquid phase, possibly gapped far away from the 1D limit and gapless close to it.

MSWT spin-wave dispersion relations

Finally, we present the spin-wave dispersion relations $\omega_{\boldsymbol{k}}$, which can be measured by inelastic neutron scattering [652], thus providing another experimental probe of the physics associated to the additional anisotropy.

In Fig. 14.14, we show the dispersion relation as computed from MSWT, Eq. (14.13), for parameters corresponding to a point from the spiral phase and the magnetically ordered materials listed in Table 14.2. We provide (where applicable) a comparison to the dispersion relation which would result if two of the couplings were equal. These comparisons can be seen more quantitatively in the cuts (c.i-iii) shown in the lowest row of Fig. 14.14. For the point from the spiral phase (a.i), the symmetrization (b.i) does not significantly change the dispersion relation, but for P-2 and, especially, for Sb-0, the differences are considerable. The latter in particular changes even qualitatively since a symmetrization would put it instead of into a Néel phase into a spiral phase. These differences seem significant enough to be measurable in experiment. Such a measurement could allow to quantify the actual magnitude of coupling anisotropies.

Summary of the SCATL

To summarize this section, we have provided a thorough analysis of the ground-state phase diagram of the quantum Heisenberg SCATL, which has to the best of our knowledge not been considered before – despite its relevance to experiments on magnetic compounds.

Using various observables from MSWT, supported by ED, we have found this model to behave qualitatively similar to its XY counterpart (Chapter 3.4). In particular, quantum fluctuations stabilize Néel order with respect to the classical phase diagram. Further, they reduce the extent of the spiral phase, which seems to be entirely surrounded by a quantum disordered region. This result, which constitutes our first main finding, is supported by the breakdown of MSWT, together with the strong decrease of the order parameter and the spin stiffness. It is further corroborated by ED data, where a finite gap and a vanishing chiral correlation make spiral LRO seem unlikely, while the location of the structure-factor peak at incommensurate wave vectors seems to preclude Néel LRO. Also, the strong decrease of the ED structure-factor peak appears to support this interpretation.

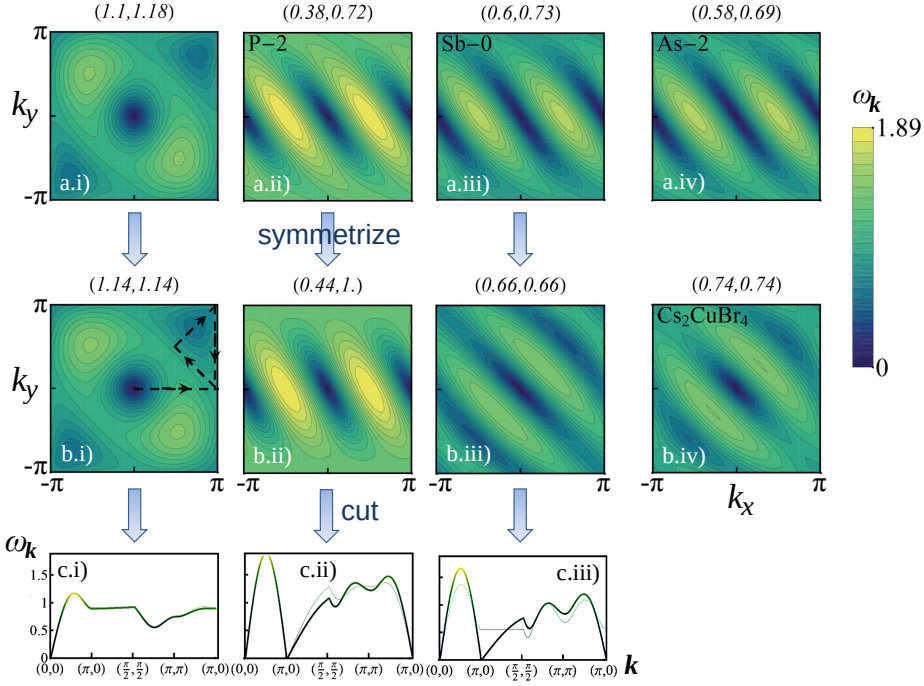

Figure 14.14: **Spin-wave dispersion from MSWT,** normalized to the coupling strengths $1 + J' + J''$. **Top row:** Parameters corresponding to **(a.i)** a completely anisotropic point in the spiral phase, and **(a.ii-iv)** the magnetically ordered materials cited by Scriven and Powell [645]. **Middle row: (b.i-iii)** Symmetrizing the two closer couplings can change the dispersion relations. **(b.iv)** Dispersion relation for Cs_2CuBr_4. **Bottom row:** Cuts along the path indicated in (b.i). In (c.ii-iii) the dispersion relation taken from (a.ii-iii), thick line, differs considerably from the corresponding symmetrized one taken from (b.ii-iii), thin line.

A complete encircling of the spiral phase by disordered phases could naturally explain the succession of a gapped and a gapless spin liquid at the low-α limit of the SATL. The gapless spin liquid would be continuously connected to the limit of decoupled chains, while the additional anisotropy of the SCATL would adiabatically connect the gapped spin liquids at small and large α. This consideration shows the great potential of the additional anisotropy to deliver new insights into the nature of these phases. Further, it allows to approach the small-α spin liquids not only from the spiral phase, but also from the Néel phase. We found, indeed, some indications that very close to the 1D limit the transition from the Néel phase to the putative disordered region could be qualitatively different from what happens at larger α.

Our second main finding is connected to experimental results: measurements find magnetic LRO in materials which theoretical analyses on the SATL predict to be magnetically disordered. We show that this discrepancy finds a simple explanation in the additional anisotropy of the SCATL, which is neglected in the SATL. Taking it into account, we predict these material to lie in magnetically ordered phases, in accordance to experiment. These findings show the importance of the complete lattice anisotropy for the explanation of recent experiments.

Finally, we provided spin-wave dispersion relations, a comparison to which might allow to probe the additional anisotropy experimentally.

14.2.3 MSWT on the $J_1J_2J_3$ model

In the SATL and its generalization, the SCATL, commensurate and incommensurate order seem to be never directly connected, but spin-liquid phases appear to separate them. To see if this is a more universal feature, we investigate in this section another paradigmatic frustrated spin model, the $J_1J_2J_3$ model on the square lattice. It involves couplings between nearest-neighbors (NN), J_1, next-nearest-neighbors (NNN), J_2, and next-next-nearest-neighbors (NNNN), J_3. A sketch of the geometry of the system may be found in Fig. 14.15a. This model allows to continuously tune the Hamiltonian from an unfrustrated AFM square lattice to a highly frustrated magnet.

Classical and quantum mechanical phase diagram of the $J_1J_2J_3$ model at $T = 0$

The classical phase diagram of the $J_1J_2J_3$ model [630, 653–655] can provide valuable intuition about the expected ordered phases. It is sketched in Fig. 14.15b. One identifies:

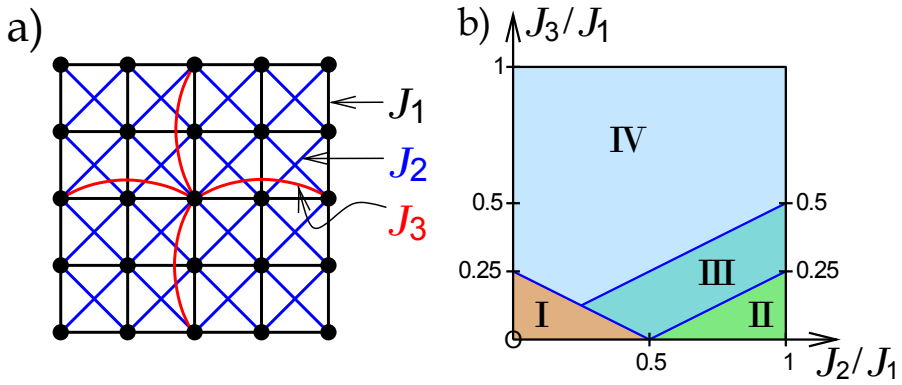

Figure 14.15: **(a) Geometry** of the $J_1J_2J_3$ model on a square lattice. NNs are coupled with bonds of strength J_1 (black), NNNs (along the diagonals) with J_2 (blue) and NNNNs with J_3 (red). **(b) The classical phase diagram** of the $J_1J_2J_3$ model shows four ordered phases. Phase I is characterized by Néel order on the square lattice. In phase II the system decouples into two independently Néel ordered sublattices with a doubled unit cell each. Phases III and IV are spirally ordered with $\boldsymbol{Q} = (q, \pi)$ and $\boldsymbol{Q} = (q, q)$, respectively.

I) A 2D-Néel phase with $\boldsymbol{Q} = (\pi, \pi)$ just as in the unfrustrated square lattice. It is delimited by the classical critical line $(J_2 + 2J_3)/J_1 = 1/2$;

II) A phase where the system decouples into two independent J_2–sublattices with a doubled unit cell. Both sublattices are Néel ordered individually. This phase is infinitely degenerate because the relative spin orientation between the two sublattices can be rotated without affecting the energy;

III) A spiral phase with ordering vector $\boldsymbol{Q} = (q, \pi)$, where q varies continuously over the phase diagram;

IV) A second spiral phase, with $\boldsymbol{Q} = (q, q)$; $q \to \pi/2$ for $J_3 \to \infty$, attaining the limit of two decoupled, Néel-ordered J_3–sublattices.

This phase diagram is believed to change considerably in the quantum limit [624, 628–630]: In phase II quantum fluctuations select the columnar ordered states with $\boldsymbol{Q} = (\pi, 0)$ or $\boldsymbol{Q} = (0, \pi)$ from all the possible classical states. Furthermore, the Néel phase I increases in size considerably and Néel order persists up to near the line $(J_2 + J_3)/J_1 = 1/2$. In the vicinity of this line, the classical

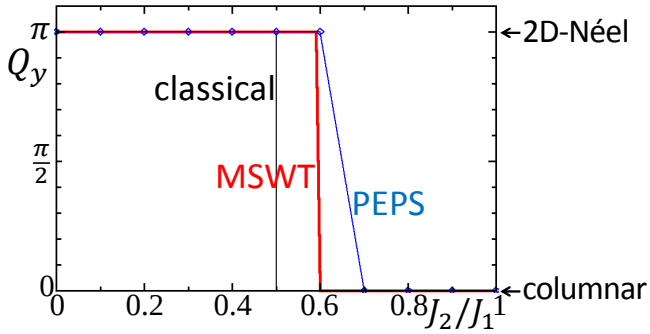

Figure 14.16: **The y-component of the ordering vector in the J_1J_2 lattice** shows a considerable shift in the quantum model with respect to the classical value.

order is believed to be destabilized and to be replaced by a non-magnetic state. The controversy about the exact nature of the ground state in this highly frustrated region, however, is still not settled. In particular, it has been suggested that it could have the nature of a *columnar valence-bond crystal* [656] with both translational and rotational broken symmetries, of a *plaquette state* with no broken rotational symmetry [624], or of a *spin liquid* with all symmetries restored [567, 657–660].

In the following, we investigate the quantum model using MSWT with a lattice size of $N = 32\times32$. In most of parameter space, this is essentially already converged to the infinite lattice, except close to quantum critical points. We compare the MSWT data to recent results from PEPS calculations from V. Murg and coworkers [661]. We focus on the extrapolations to the thermodynamic limit contained in that work, except if stated otherwise.

We first discuss in more detail the special cases of the J_1J_2 model (*i.e.*, $J_3 = 0$) and the J_1J_3 model (*i.e.*, $J_2 = 0$). Both models have been studied before within MSWT [597, 601, 662–666]. On the one hand, we confirm existing results on the J_1J_2 case, for which the optimization of the ordering wave-vector returns only two possible values (corresponding to Néel order [$\boldsymbol{Q} = (\pi,\pi)$] or columnar order [$\boldsymbol{Q} = (\pi,0)$ or $\boldsymbol{Q} = (0,\pi)$]), and we give further insight into the spin stiffness and the dimer–dimer correlation functions. On the other hand, we analyze the J_1J_3 model with optimization of the ordering wavevector, which proves crucial to correctly capture the quantum effects on the classical spiraling phases appearing in this case [597]. Finally, we give an overview of the entire quantum ground-state phase diagram of the $J_1J_2J_3$ model.

Ground state properties of the J_1J_2 model

Figure 14.16 reports the ordering vector for the J_1J_2 model from MSWT as well as from PEPS calculations. For the PEPS results, we extract the wave vector of dominant spin correlations $\boldsymbol{Q}^{\mathrm{PEPS}}$ from the location of the peak of the static structure factor, analogous to Eq. (14.26). Up to $J_2/J_1 = 0.6$, $\boldsymbol{Q}^{\mathrm{PEPS}}$ is located at the Néel value (π, π), while above this it lies at the value of columnar order $(\pi, 0)$. In agreement with PEPS and other methods, *e.g.*, ED [632, 667, 668] or Schwinger bosons [669], MSWT finds Néel order with $\boldsymbol{Q} = (\pi, \pi)$ at small J_2/J_1 and columnar order with $\boldsymbol{Q} = (\pi, 0)$ or $\boldsymbol{Q} = (0, \pi)$ at large J_2/J_1.

As is well known from previous studies, there is a region between $0.56 \lesssim J_2/J_1 \lesssim 0.62$ where the 2D-Néel ordered and the columnar state are both stable solutions within MSWT. The starting point of the self-consistent calculations determines which type of order is returned as the solution. However, the solutions differ in energy and therefore one of them is only a local free-energy minimum of the self-consistent equations. As can be seen from the energies, Fig. 14.17a, the transition from 2D-Néel to columnar order takes place at $J_2/J_1 \simeq 0.6$.

For comparison, we also plot the values for the energy and magnetization that where obtained by Schulenburg and Richter [632] from diagonalization of small clusters. We find a remarkable correspondence of the ground-state energy per spin between the MSWT prediction and these ED results [632], as well as with the PEPS results, both extrapolated to the infinite-lattice limit. Especially the noticeable kink associated at $J_2/J_1 \simeq 0.6$, marking clearly a transition point, is exhibited by all three methods.

For the magnetization, MSWT delivers extremely reliable predictions deep in the Néel phase. As shown in Fig. 14.17b, at small J_2/J_1, the finite size extrapolation of the ED staggered magnetization from Schulenburg and Richter [632] lies very close to the MSWT results, and, as already mentioned in the context of the S(C)ATL, in the unfrustrated square lattice limit ($J_2 = 0$) the MSWT value $M_0 = 0.303$ [224] is very similar to QMC results, for which the most recent estimates give $M_0 = 0.30743(1)$ [643]. For the PEPS calculations a quantity analogous to the magnetization can – similar to Sec. 14.2.1 – be derived from the peak height of the static structure factor, Eq. (14.26). We show its finite size extrapolation in Fig. 14.17b. In the Néel phase PEPS agrees very well with MSWT, considerably better than ED, which decreases faster towards the strongly frustrated region.

In the other limit, deep in the columnar phase, MSWT seems to overestimate the order parameter as compared to ED and PEPS. In comparison to ED, this remains true also close to the transition, but in that region agreement to PEPS

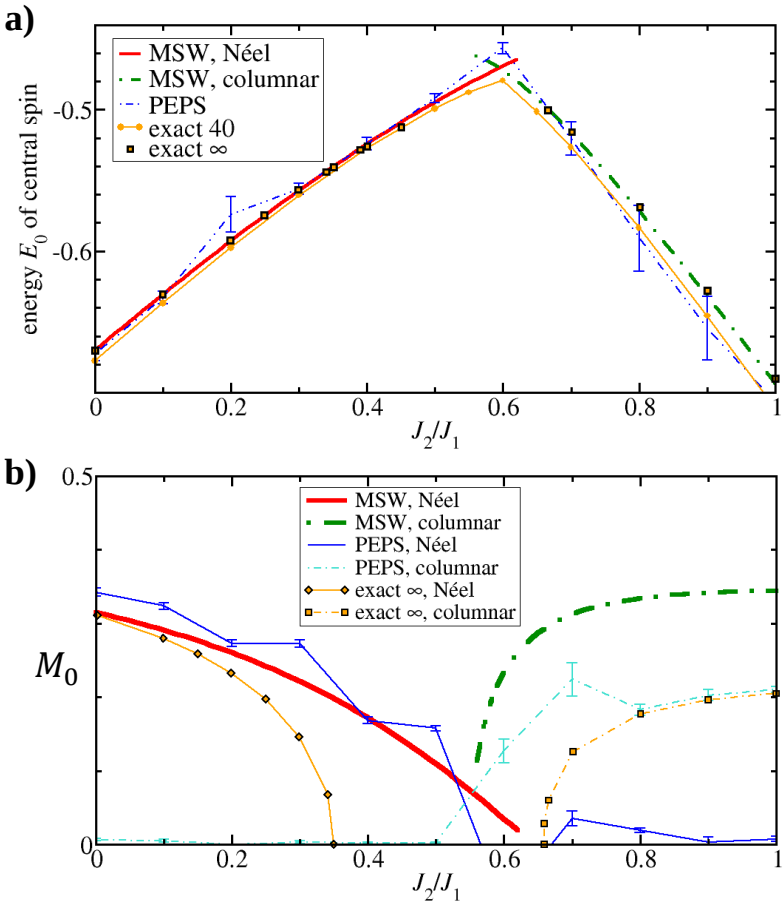

Figure 14.17: **For the $J_1 J_2$ model, MSWT data compares favorably to other methods.** We show PEPS data extrapolated to the thermodynamic limit and ED by Schulenburg and Richter [632] for a 40-spin cluster ('exact 40') and extrapolated to the thermodynamic limit ('exact ∞'). **(a) Ground-state energy** of the central spin. **(b) Order parameter from MSWT,** compared to ED results and the PEPS magnetizations $M(\pi,\pi)$ (Néel) and $M(\pi,0)$ (columnar). For MSWT, the curves obtained when starting the self-consistent iteration from a Néel state (thick red line) and from a columnar ordered state (thick dot-dashed green line) are both included. Magnetic order weakens at the transition from the Néel to the columnar phase, and the ED data even suggest an extended quantum-disordered region.

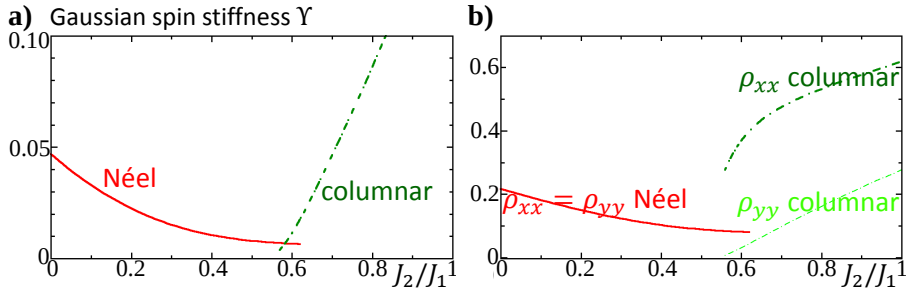

Figure 14.18: **For the J_1J_2 model, the MSWT spin stiffness** indicates a weakening of magnetic order close to the transition between the Néel and the columnar phase. **(a) Gaussian spin stiffness. (b) Components of the spin stiffness tensor.** In the Néel phase $\rho_{xx} = \rho_{yy}$ by symmetry. The partial spin stiffnesses $\rho_{\alpha\beta}^{\text{partial}}$ equal the total ones, $\rho_{\alpha\beta}$. For MSWT, the curves obtained when starting the self-consistent iteration from a Néel state (thick red line) and from a columnar ordered state (thick dot-dashed green line) are both included.

becomes better.

Although upon approaching the Néel-to-columnar transition the order parameter decreases for both MSWT and PEPS, neither method finds a quantum-disordered region. This contradicts the ED data, which predicts a magnetically disordered region in the range $0.35 \lesssim J_2/J_1 \lesssim 0.66$ [632]. Recent results based on tensor product states [626] and DMRG [627] seem to prove without doubt that the region around $0.4 - 0.5 \lesssim J_2/J_1 \lesssim 0.6$ hosts a quantum-disordered ground state without magnetic nor valence-bond-solid order.

For MSWT, this discrepancy is not surprising: since it is based on an ordered classical reference state, it often overestimates magnetic order. In the previous Chapters 3.2, 3.4, 14.2.1, and 14.2.2, however, the spin stiffness (see Sec. 14.1.6), has proven a valuable tool to find regions where this magnetic order softens. It can be assumed that in such regions quantum fluctuations may overcome all ordering tendencies, leading to spin-liquid behavior in the true ground state. Such a suppression of the spin stiffness has been observed in previous results coming from ED of finite clusters [667] or from the Schwinger-boson approach [669, 670]. In Fig. 14.18, we plot for our MSWT calculations the Gaussian spin stiffness Υ as well as the individual components of the spin-stiffness tensor, Eq. (14.21). Although the spin stiffness remains finite for any considered value of J_2/J_1, it is strongly suppressed in the region $0.3 \lesssim J_2/J_1 \lesssim 0.6$. As a consequence,

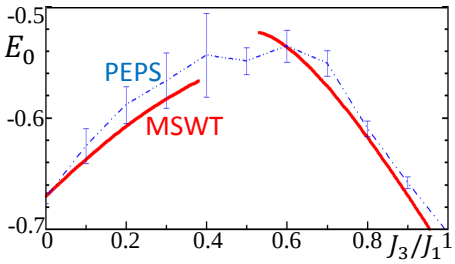

Figure 14.19: **For the J_1J_3 model, the MSWT ground-state energy compares well to PEPS results.** (For PEPS we show the energy of the central spin extrapolated to the thermodynamic limit.)

even though MSWT admits a stable solution with magnetic order for any J_2/J_1 value, for $J_2/J_1 = 0.6$ it exhibits a clear transition from *soft* Néel order to a *stiff* columnar order, suggesting that this transition could actually separate the columnar state from a quantum disordered phase.

We further investigated the nature of the state in the transition region between Néel and columnar order, where magnetic order is strongly reduced, through the study of the dimer–dimer correlations (the results can be found in Ref. [241]). Remarkably, around $J_2/J_1 \approx 0.7$, MSWT shows a short-range modulation in the dimer correlations whose structure is compatible with that of a valence-bond crystal. Although MSWT is not appropriate to characterize such non-magnetic states, it is remarkable that it identifies a columnar valence-bond structure as the dominant form of dimer correlations at short range. This indication is consistent with, *e.g.*, PEPS results [661], which point towards columnar valence-bond order in the non-magnetic region of the J_1J_2 model. The short-range nature of this dominant dimer–dimer correlations is consistent with the recent results from Refs. [626, 627], which predict the absence of long-range valence-bond-solid order.

Ground state properties of the J_1J_3 model

We now turn to the J_1J_3 model. As a first check, we compare the ground-state energy from MSWT to PEPS results (Fig. 14.19). We find extremely good agreement in the entire range of J_3/J_1 where MSWT converges.

To analyze the phase diagram of the J_1J_3 model, we first study its ordering vector (Fig. 14.20a), comparing again MSWT to PEPS as well as to the classical results. Classically, this model has a transition from Néel to spiral order at $J_3 = 0.25J_1$. For $S = 1/2$, recent PEPS calculations show that Néel order persists up to approximately $J_3/J_1 = 0.3$ [661]. Above this point the peak of the structure factor is still at the Néel ordering vector (π, π) but its height appears to vanish

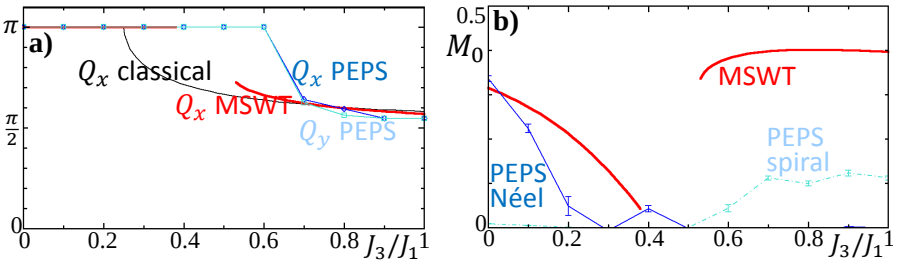

Figure 14.20: **Comparison of MSWT and PEPS results for the J_1J_3 model. (a) Ordering vector.** Quantum fluctuations stabilize Néel order, as compared to the classical result. For MSWT and classically, $Q_x = Q_y$. **(b) The order parameter** decreases towards the MSWT breakdown region. For PEPS we show in (a) the position (Q_x, Q_y) of the structure-factor peak, and in (b) its height at $\boldsymbol{Q} = (\pi, \pi)$ (Néel) and $\boldsymbol{Q} = (q, q)$ (spiral).

in the thermodynamic limit, which suggests a complete loss of magnetic LRO. A different type of LRO arises anew at approximately $J_3/J_1 = 0.6$ with an ordering vector $\boldsymbol{Q} = (q, q)$ that tends to $(\pi/2, \pi/2)$ in the limit of large J_3. For large enough J_3, the nature of the ordered phase becomes similar to that of the classical limit. Within MSWT with ordering-vector optimization, coming from small J_3/J_1, quantum fluctuations stabilize Néel against spiral order, so that Néel order persists up to $J_3/J_1 = 0.39$. Coming from the opposite limit of $J_3 \sim J_1$, we observe a spiral phase with continuously varying pitch vector $\boldsymbol{Q} = (q, q)$, where q approaches $\pi/2$ for $J_3/J_1 \to \infty$, and increases up to $q \approx 0.7\pi$ for $J_3/J_1 \to 0.52^+$. In the region $0.39 < J_3/J_1 < 0.52$, convergence of the MSWT calculations breaks down, which points at a possible spin-liquid phase, in agreement with the predictions from PEPS.

This indication of a disordered phase is further corroborated by the MSWT order parameter M_0 (Fig. 14.20b), which decreases strongly for $J_3/J_1 \to 0.39^-$ and for $J_3/J_1 \to 0.52^+$. Again, the PEPS order parameter deep in the Néel phase is similar to the MSWT data, but in the spiral phase the MSWT order parameter lies well above the PEPS result. Despite quantitative differences, the PEPS order parameter vanishes in the range $0.3 \lesssim J_3/J_1 \lesssim 0.5$ and thus confirms the destabilization of magnetic order.

The MSWT spin stiffness (Fig. 14.21) gives additional credibility to the assumption of a disordered phase in the J_1J_3 model: it is drastically reduced when approaching $J_3/J_1 = 0.39$ from below and $J_3/J_1 = 0.52$ from above. The

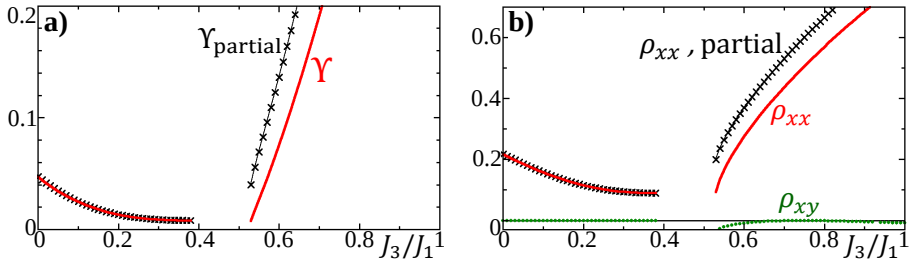

Figure 14.21: **For the J_1J_3 model, the MSWT spin stiffness** softens towards the region between Néel and spiral order. **(a) Gaussian spin stiffness. (b) Components of the spin-stiffness tensor.** (By symmetry, $\rho_{xx} = \rho_{yy}$ and $\rho_{xy}^{\text{partial}} \equiv 0$.)

Gaussian spin stiffness is extremely small already for $J_3/J_1 \gtrsim 0.3$ (Fig. 14.21a), which corresponds to the value where PEPS predicts a vanishing magnetization. Our results are also consistent with the ED of a system of 20 sites by Bonča *et al.* [671], where it was found that the spin stiffness vanishes at $J_3/J_1 = 0.35$.

The precise nature of the state in the candidate region for quantum-disordered behavior cannot be determined reliably by the use of MSWT. From an analysis of the dimer–dimer correlations in the convergence regions, we can find no indications of any exotic disordered quantum state. On the contrary, PEPS results indicate a plaquette state in the region of maximal frustration $J_3 \approx J_1/2$ [661].

As a final remark, we note that in our calculations, despite using the same equations as Xu and Ting [597], we find a considerably larger breakdown region. However, the region where our calculations do not yield a result is very stable, *i.e.*, it does not depend much on system size nor on the exact algorithm for solving the self-consistent MSWT equations.

MSWT phase diagram of the $J_1J_2J_3$ model

After having investigated the two limiting cases of the J_1J_2 and the J_1J_3 models, we now consider the more general $J_1J_2J_3$ model. We first present the MSWT data, and compare them afterwards to PEPS predictions.

As already seen in the case of the J_1J_3 model, we observe a sizable parameter range over which the convergence of MSWT breaks down, and which is then pointed out as a candidate region for non-magnetic behavior (see Fig. 14.22). We notice that, while convergence is achieved for any J_2/J_1 ratio at $J_3 = 0$, a region of convergence breakdown opens up by adding a small J_3 component

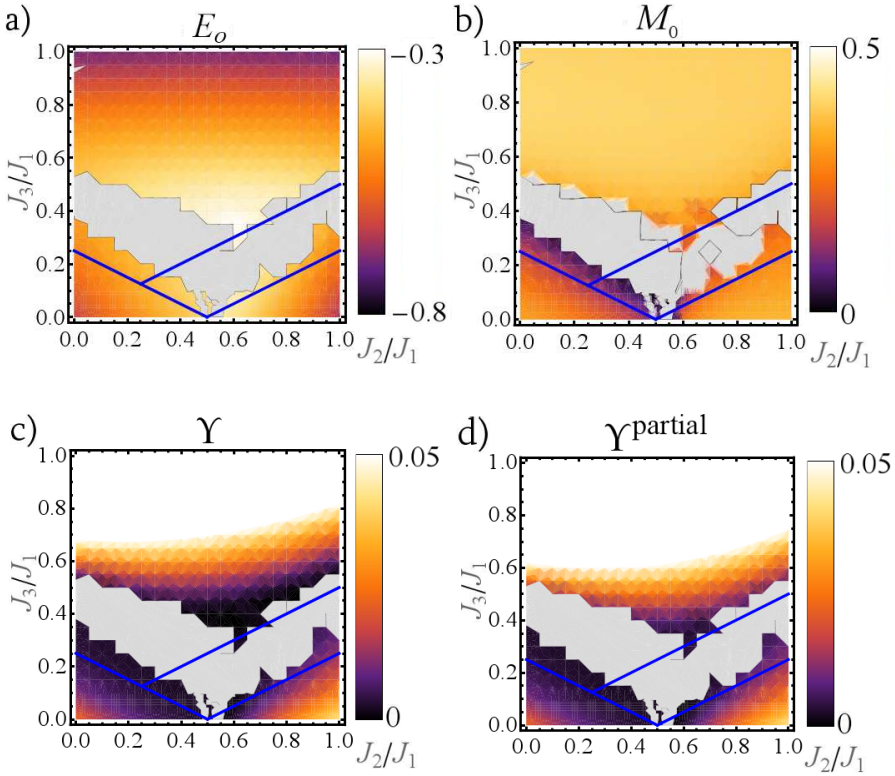

Figure 14.22: **MSWT phase diagram of the quantum $J_1J_2J_3$ model. (a) Ground state energy** per spin E_0, **(b) order parameter** M_0, **(c) Gaussian spin stiffness** Υ, and **(d) partial Gaussian spin stiffness** $\Upsilon^{\text{partial}}$ calculated via Eq. (14.23). Note that Υ and $\Upsilon^{\text{partial}}$ rise beyond the linear scale in the upper half of the plot. The blue lines are the classical phase boundaries, and in the gray areas convergence of the self-consistent equations could not be reached, suggesting disordered behavior in the true quantum ground state.

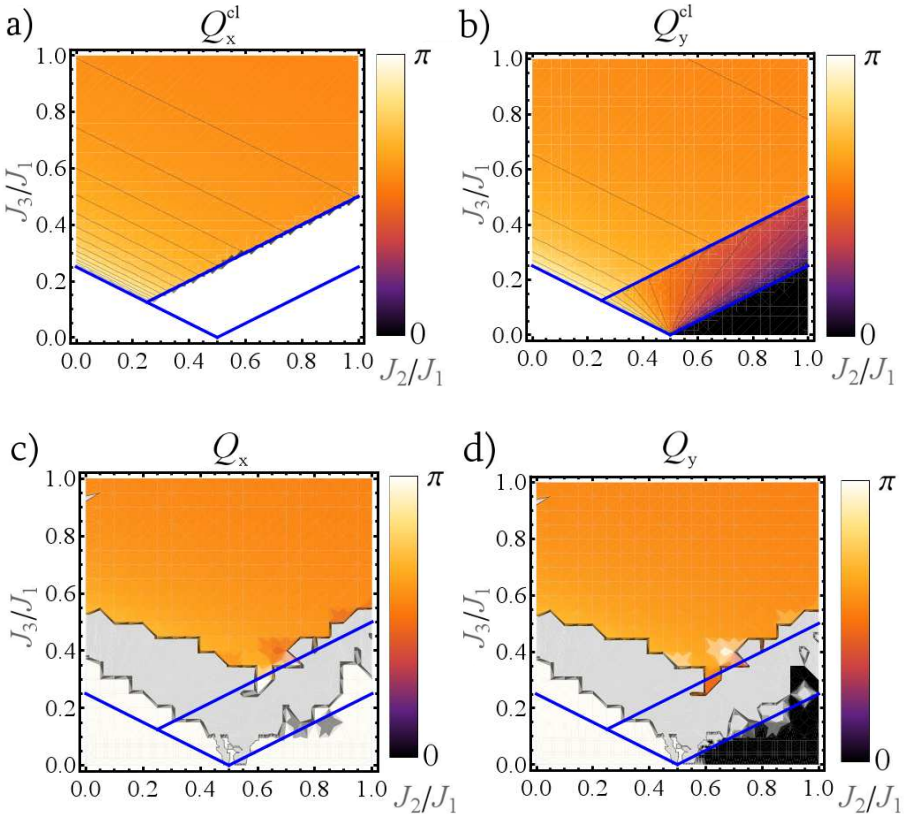

Figure 14.23: **Ordering vector for the $J_1J_2J_3$ model** in linear color scale. In the gray area convergence of the self-consistent equations could not be reached. **(a)** x-component and **(b)** y-component of the classical ordering vector, differentiating four classical phases (blue lines are the classical phase boundaries); **(c)** x-component and **(d)** y-component of the quantum mechanical MSWT ordering vector, identifying only three ordered quantum phases.

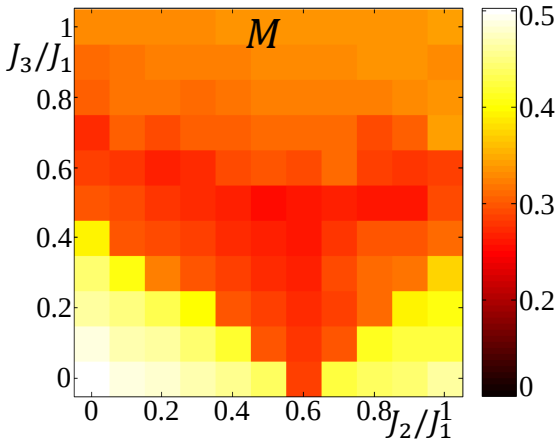

Figure 14.24: **The PEPS order parameter** M suggests a destabilization of magnetic LRO in a broad asymmetric v-shaped region, marked by low values (calculations for a 8×8 lattice with auxiliary dimension $D = 3$).

around $J_2/J_1 \approx 0.5$. The energy per spin increases when approaching this region, showing the increased influence of frustration (Fig. 14.22a). The indications for a quantum disordered phase in the breakdown region is corroborated by the decrease of the order parameter (Fig. 14.22b) and the spin stiffness (Fig. 14.22c and d) when approaching the breakdown region.

The nature of the phases where MSWT reaches convergence can be seen in the ordering vector, which we display in Fig. 14.23 in comparison with the classical one. We find three ordered phases. (1) For small J_3/J_1 and J_2/J_1 we find a Néel ordered phase. Its boundary is pushed upwards to higher values of J_3/J_1 with respect to the classical limit. (2) A columnar phase is found at small J_3/J_1 but larger $J_2/J_1 \gtrsim 0.6$. (3) For large J_3/J_1, a spiral phase arises with an ordering vector $\boldsymbol{Q} = (q, q)$ that approaches $\boldsymbol{Q} = (\pi/2, \pi/2)$ for large J_3/J_1. As a consequence, a dramatic effect of quantum fluctuations seems to be the disappearance of phase III of the classical phase diagram, characterized by magnetic order at a pitch vector $\boldsymbol{Q}_{cl} = (q, \pi)$ with continuously varying q, in favor of the columnar phase and of a potentially quantum-disordered phase.

Comparison to PEPS calculations

To validate the MSWT results with a complementary approach, we now compare its predictions to data coming from PEPS calculations on a 8×8 lattice with auxiliary dimension $D = 3$.

In Fig. 14.24, we display the PEPS order parameter as extracted from the peak height of the static structure factor [see Eq. (14.26)]. We observe a broad

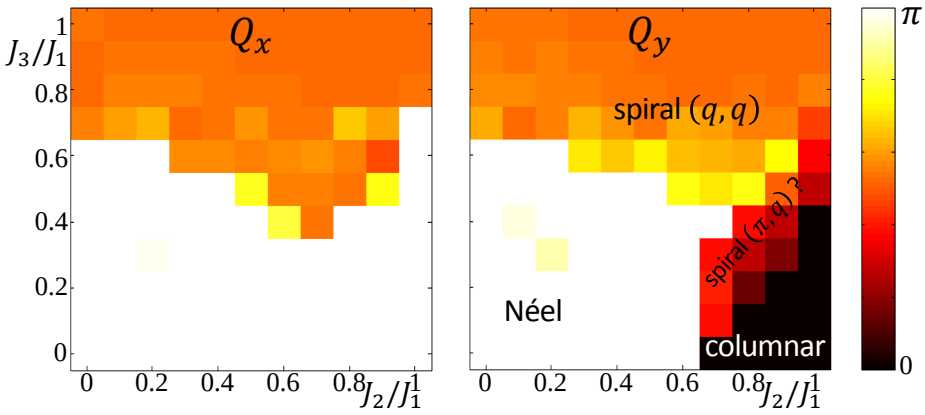

Figure 14.25: **The PEPS ordering vector** shows three phases, Néel (π,π), columnar $(\pi,0)$, and spiral (q,q) order. From this data, it is not clear if the classical phase with (π,q), found in between the columnar and spiral phases, survives quantum fluctuations. (Calculations for a 8×8 lattice with $D=3$.)

asymmetric v-shaped region in which the magnetic order, quantified by the height of the peak in the structure factor, is strongly suppressed. This region is strongly reminiscent of (albeit broader than) the breakdown region of MSWT. In particular, the asymmetry is due to the fact that the bottom of the "v" lies at $J_2/J_1 > 0.5$, a characteristic which is shared with the MSWT phase diagram.

While a thorough finite-size scaling analysis of the PEPS data would be necessary to determine the precise boundaries of the possible magnetically disordered regions, a quantitative information can be extracted even from the finite-size PEPS data concerning the location of the pitch vector of the dominant magnetic correlations. As seen in Fig. 14.25, similarly to what happens in the above spin-wave calculations, a pronounced peak at the Néel ordering vector (π,π) appears if both J_2/J_1 and J_3/J_1 are small, while at large J_2/J_1 but small J_3/J_1 the structure factor is peaked at the columnar ordering vector $(\pi,0)$. For large J_3/J_1, the peak is located at (q,q), where q tends to $\pi/2$. From the ordering vector, we find in between the columnar and spiral phases remainders of the second classical spiral phase with $\boldsymbol{Q}=(\pi,q)$. This phase, however, lies in the region where the PEPS order parameter is small. Therefore, the associated LRO may possibly not survive quantum fluctuations in the thermodynamic limit.

In summary, in the $J_1J_2J_3$ lattice a large region with weak order properties separates the Néel-ordered region for small J_2 and J_3, from the columnar-

ordered region for $J_2 > J_1/2$ and small J_3, and from the spiral phase at large J_3. Further, quantum fluctuations stabilize Néel order while they possibly suppress one of the two spiral phases of the classical phase diagram. These features are confirmed in the calculations of Reuther *et al.*, who used three different methods (dynamical functional renormalization group, high-order coupled cluster calculations, and series expansion) [672].

14.2.4 Summary

In this chapter, we illustrated the performance of Takahashi's MSWT with ordering-vector optimization. For this purpose, we studied the ground-state phase diagram of the AFM $S = 1/2$ Heisenberg model on several two-dimensional frustrated geometries, the SATL, its generalization to the SCATL, and the $J_1J_2J_3$ lattice. Quantitative comparisons with more accurate methods (ED, variational *Ansätze* based on projected BCS states, PEPS) reveal that MSWT with ordering wave-vector optimization goes well beyond LSWT in dealing with quantum effects. It correctly accounts for the quantum correction to the ordering wave-vector of the ordered phases, and for the strong suppression (or total cancellation) of magnetic order in correspondence with the candidate regions for quantum-disordered behavior. Given its flexibility and its modest numerical cost, MSWT serves therefore as a unique tool for the identification of novel quantum phases in strongly frustrated quantum antiferromagnets.

In all studied models, we find two general trends. *(i)* Collinearly ordered states (Néel or columnar order, 1D-like quasi-order) are promoted against spiraling ones. *(ii)* Two phases with different (quasi-)order properties (spiral *vs.* collinear) are always separated by extended quantum-disordered spin liquids. We propose that this is a universal feature of frustrated quantum magnets, which may have far-reaching consequences for the search of spin-liquid phases. Interestingly, from our results in the SCATL it seems that two such gapped spin-liquids, which appear as distinct in the SATL, are actually adiabatically connected by an additional anisotropy in the couplings.

Finally, our findings may have important implications for experiment. In general, since our calculations give strong suggestions for candidate regions of spin-liquid behavior, experiments can focus on the most relevant parameter regimes. Further, our results on the SCATL may have great relevance for magnetic organic salts hosting triangular spin lattices. If there exists an anisotropy in all three coupling directions, previous studies typically averaged the two closer coupling strengths. The resulting parameters can then be compared to theoretical predictions from the SATL. There are, however, examples where this

procedure locates magnetically ordered materials in regions of the SATL phase diagram that are magnetically disordered. In contrast, we find that the parameter values that take the additional anisotropy into account are located in ordered regions of the SCATL phase diagram, so that the experimental observations find a natural explanation in the threefold anisotropy.

Conclusion

In this thesis, we considered quantum simulators (QSs) on a theoretical level. In an attempt to put this field onto more stable theoretical foundations, we identified a definition consisting in its core of four requirements: relevance, control, reliability, and efficiency. We emphasized the lack of careful studies of the reliability and efficiency, and their interplay, in particular for analog QSs,. As a first step in this direction, we characterized the influence of disorder on the static and dynamic behavior of a paradigmatic quantum model. We also studied quantum-simulation architectures where the models that are commonly accepted as describing their fundamental behavior have to be modified in certain, experimentally relevant parameter regimes.

Studying possibilities to improve control over QSs, we presented several feasible proposals for the analog quantum simulation of important phenomena, covering so widely different situations as orbital order of fermions, supersolids in systems with long-range interactions, spin liquids in frustrated quantum spin models, or quantum phase transitions, topological insulators, and non-Abelian gauge fields in exotic lattice geometries. To compute the expected behavior of these models, we employed a variety of theoretical techniques, some of which we had to adapt and extend to make them applicable to the theoretically challenging situations posed by these complex many-body models. We also presented a scheme to control quantum spin correlations in optical lattices with a mesoscopic number of particles at each lattice site. These examples were selected to provide a kaleidoscope of the multifaceted physics amenable to quantum simulation in non-standard optical lattices.

If we can guarantee that analog quantum simulators fulfill all four requirements of our definition, including above all the reliability of their results, we can expect them to deliver, in the medium term, valuable insights into a variety of outstanding quantum problems, such as quark confinement, high-T_c superconductivity, protein design, nano-material engineering, and much more.

Used acronyms

– in alphabetical order

ACT:	AC-induced tunneling
AFM:	antiferromagnetic
AQS:	analog quantum simulator
BEC:	Bose-Einstein condensate
BKT:	Berezinskii–Kosterlitz–Thouless
CB:	checkerboard
CQED:	circuit quantum electrodynamics
DFT:	density-functional theory
DMFT:	dynamical mean-field theory
DMRG:	density-matrix renormalization group
DQS:	digital quantum simulator
ED:	exact diagonalization
FM:	ferromagnetic
iTEBD:	infinite time evolving block decimation
LRO:	long-range order
MERA:	multiscale entanglement-renormalization *Ansatz*
MI:	Mott-insulator
MSWT:	modified spin-wave theory
NMR:	nuclear magnetic resonance
NN:	nearest neighbor
NNN:	next-to-nearest neighbor
NNNN:	next-to-next-to-nearest neighbor
nUAQS:	non-universal analog quantum simulator
nUDQS:	non-universal digital quantum simulator
OSAQS:	open-system analog quantum simulator
OSDQS:	open-system digital quantum simulator
PEPS:	projected entangled-pairs states
PMFT:	perturbative mean-field theory
PSF:	pair superfluid
OFR:	optical Feshbach resonance
QPT:	quantum phase transition
SATL:	spatially anisotropic triangular lattice
SCATL:	spatially completely anisotropic triangular lattice
SF:	superfluid
SPS:	spin polarization spectroscopy
tDMRG:	time-dependent density-matrix renormalization group
TNS:	tensor-network states
ToF:	time of flight
TTN:	tree tensor network states
UDQS:	universal digital quantum simulator
UAQS:	universal analog quantum simulator
QMC:	quantum Monte-Carlo
QND:	quantum non-demolition
QS:	quantum simulator

Bibliography

[1] R. D. Smith, *Encyclopedia of Computer Science, 4th Edition*, chapter Simulation Article, Grove's Dictionaries New York, 2000.

[2] The ATLAS Collaboration, *arXiv:1207.7214v1 [hep-ex]* (2012).

[3] The CMS Collaboration, *arXiv:1207.7235v1 [hep-ex]* (2012).

[4] P. A. Lee, N. Nagaosa, and X.-G. Wen, *Rev. Mod. Phys.* **78**, 17 (2006).

[5] P. A. Lee, *Rep. Prog. Phys.* **71**, 012501 (2008).

[6] R. P. Feynman, *Int. J. Theor. Phys.* **21**, 467 (1982).

[7] I. Buluta and F. Nori, *Science* **326**, 108 (2009).

[8] M. Lewenstein, A. Sanpera, and V. Ahufinger, *Ultracold Atoms in Optical Lattices: Simulating Quantum Many-Body Systems*, Oxford University Press, Oxford, 2012.

[9] *Science* **330**, 1605 (2010).

[10] Y.-J. Lin, R. L. Compton, K. Jiménez-García, J. V. Porto, and I. B. Spielman, *Nature* **462**, 628 (2009).

[11] W. S. Bakr, A. Peng, M. E. Tai, R. Ma, J. Simon, J. I. Gillen, S. Fölling, L. Pollet, and M. Greiner, *Science* **329**, 547 (2010).

[12] S. Trotzky, L. Pollet, F. Gerbier, U. Schnorrberger, I. Bloch, N. V. Prokof'ev, B. Svistunov, and M. Troyer, *Nat. Phys.* **6**, 998 (2010).

[13] R. Jördens, L. Tarruell, D. Greif, T. Uehlinger, N. Strohmaier, H. Moritz, T. Esslinger, L. D. Leo, C. Kollath, A. Georges, V. Scarola, L. Pollet, E. Burovski, E. Kozik, and M. Troyer, *Phys. Rev. Lett.* **104**, 180401 (2010).

[14] K. Baumann, C. Guerlin, F. Brennecke, and T. Esslinger, *Nature* **464**, 1301 (2010).

[15] Y. Liao, A. S. C. Rittner, T. Paprotta, W. Li, G. B. Partridge, R. G. Hulet, S. K. Baur, and E. J. Mueller, *Nature* **467**, 567 (2010).

[16] J. Simon, W. S. Bakr, R. Ma, M. E. Tai, P. M. Preiss, and M. Greiner, *Nature* **472**, 307 (2011).

[17] J. Struck, C. Ölschläger, R. Le Targat, P. Soltan-Panahi, A. Eckardt, M. Lewenstein, P. Windpassinger, and K. Sengstock, *Science* **333**, 996 (2011).

[18] K. Van Houcke, F. Werner, E. Kozik, N. Prokof'ev, B. Svistunov, M. J. H. Ku, A. T. Sommer, L. W. Cheuk, A. Schirotzek, and M. W. Zwierlein, *Nat.*

Phys. **8**, 366 (2012).

[19] S. Trotzky, Y.-A. Chen, A. Flesch, I. P. McCulloch, U. Schollwöck, J. Eisert, and I. Bloch, *Nat. Phys.* **8**, 325 (2012).

[20] M. Aidelsburger, M. Atala, S. Nascimbène, S. Trotzky, Y.-A. Chen, and I. Bloch, *Phys. Rev. Lett.* **107**, 255301 (2011).

[21] M. Cheneau, P. Barmettler, D. Poletti, M. Endres, P. Schausz, T. Fukuhara, C. G. Christian, I. Bloch, C. Kollath, and S. Kuhr, *Nature* **481**, 484 (2012).

[22] J. Struck, C. Ölschläger, M. Weinberg, P. Hauke, J. Simonet, A. Eckardt, M. Lewenstein, K. Sengstock, and P. Windpassinger, *Phys. Rev. Lett.* **108**, 225304 (2012).

[23] K. Jiménez-García, L. J. LeBlanc, R. A. Williams, M. C. Beeler, A. R. Perry, and I. B. Spielman, *Phys. Rev. Lett.* **108**, 225303 (2012).

[24] I. Bloch, J. Dalibard, and W. Zwerger, *Rev. Mod. Phys.* **80**, 885 (2008).

[25] A. Niederberger, S. Braungardt, U. Ebling, T. Grass, P. Hauke, A. Kubasiak, A. Zamora, R. Augusiak, O. Dutta, E. Szirmai, M. Ciappina, F. M. Cucchietti, A. Eckardt, J. K. Korbicz, G. J. Lapeyre, G. Szirmai, L. Tagliacozzo, M. Rodríguez, P. Massignan, and M. Lewenstein, *Opt. Pura Apl.* **44**, 333 (2011).

[26] I. Bloch, J. Dalibard, and S. Nascimbène, *Nat. Phys.* **8**, 267 (2012).

[27] A. Friedenauer, H. Schmitz, J. T. Glueckert, D. Porras, and T. Schaetz, *Nat. Phys.* **4**, 757 (2008).

[28] K. Kim, M.-S. Chang, S. Korenblit, R. Islam, E. E. Edwards, J. K. Freericks, G.-D. Lin, L.-M. Duan, and C. Monroe, *Nature* **465**, 590 (2010).

[29] R. Islam, E. Edwards, K. Kim, S. Korenblit, C. Noh, H. Carmichael, G.-D. Lin, L.-M. Duan, C.-C. J. Wang, J. Freericks, and C. Monroe, *Nat. Commun.* **2**, 377 (2011).

[30] B. P. Lanyon, C. Hempel, D. Nigg, M. Müller, R. Gerritsma, F. Zähringer, P. Schindler, J. T. Barreiro, M. Rambach, G. Kirchmair, M. Hennrich, P. Zoller, R. Blatt, and C. F. Roos, *Science* **7**, 57 (2011).

[31] J. T. Barreiro, M. Müller, P. Schindler, D. Nigg, T. Monz, M. Chwalla, M. Hennrich, C. F. Roos, P. Zoller, and R. Blatt, *Nature* **470**, 486 (2011).

[32] R. Gerritsma, G. Kirchmair, F. Zähringer, E. Solano, R. Blatt, and C. F. Roos, *Nature* **463**, 68 (2010).

[33] R. Gerritsma, B. Lanyon, G. Kirchmair, F. Zähringer, C. Hempel, J. Casanova, J. J. García-Ripoll, E. Solano, R. Blatt, and C. F. Roos, *Phys. Rev. Lett.* **106**, 060503 (2011).

[34] M. Johanning, A. F. Varón, and C. Wunderlich, *J. Phys. B* **42**, 154009 (2009).

[35] C. Schneider, D. Porras, and T. Schaetz, *Rep. Prog. Phys.* **75**, 024401 (2012).

[36] R. Blatt and C. F. Roos, *Nat. Phys.* **8**, 277 (2012).

[37] B. P. Lanyon, T. J. Weinhold, N. K. Langford, M. Barbieri, D. F. V. James, A. Gilchrist, and A. G. White, *Phys. Rev. Lett.* **99**, 250505 (2007).

[38] B. P. Lanyon, M. Barbieri, M. P. Almeida, and A. G. White, *Phys. Rev. Lett.* **101**, 200501 (2008).

[39] F. Belgiorno, S. L. Cacciatori, M. Clerici, V. Gorini, G. Ortenzi, L. Rizzi, E. Rubino, V. G. Sala, and D. Faccio, *Phys. Rev. Lett.* **105**, 203901 (2010).

[40] T. Kitagawa, M. Broome, A. Fedrizzi, M. Rudner, E. Berg, I. Kassal, A. Aspuru-Guzik, E. Demler, and A. G. White, *Nat. Commun.* **3**, 882 (2012).

[41] X. Ma, B. Dakic, W. Naylor, A. Zeilinger, and P. Walther, *Nat. Phys.* **7**, 399 (2011).

[42] A. Aspuru-Guzik and P. Walther, *Nat. Phys.* **8**, 285 (2012).

[43] A. D. Greentree, C. Tahan, J. H. Cole, and L. C. L. Hollenberg, *Nat. Phys.* **2**, 856 (2006).

[44] M. J. Hartmann, F. G. S. L. Brandão, and M. B. Plenio, *Nat. Phys.* **2**, 849 (2006).

[45] D. G. Angelakis, M. F. Santos, and S. Bose, *Phys. Rev. A* **76**, 031805(R) (2007).

[46] Z. Wang, Y. Chong, J. D. Joannopoulos, and M. Soljačić, *Nature (London)* **461**, 772 (2009).

[47] J. Koch, A. A. Houck, K. L. Hur, and S. M. Girvin, *Phys. Rev. A* **82**, 043811 (2010).

[48] D.G. Angelakis *et al.*, *in preparation* (2012).

[49] A. Singha, M. Gibertini, B. Karmakar, S. Yuan, M. Polini, G. Vignale, M. Katsnelson, A. Pinczuk, L. Pfeiffer, K. West, and V. Pellegrini, *Science* **332**, 1176 (2011).

[50] S. Somaroo, C. H. Tseng, T. F. Havel, R. Laflamme, and D. G. Cory, *Phys. Rev. Lett.* **82**, 5381 (1999).

[51] C. H. Tseng, S. Somaroo, Y. Sharf, E. Knill, R. Laflamme, T. F. Havel, and D. G. Cory, *Phys. Rev. A* **61**, 012302 (1999).

[52] J. Du, N. Xu, X. Peng, P. Wang, S. Wu, and D. Lu, *Phys. Rev. Lett.* **104**, 030502 (2010).

[53] G. Álvarez and D. Suter, *Phys. Rev. Lett.* **104**, 230403 (2010).

[54] E. J. Pritchett, C. Benjamin, A. Galiautdinov, M. R. Geller, A. T. Sornborger, P. C. Stancil, and J. M. Martinis, *arXiv:1008.0701v1 [quant-ph]* (2010).

[55] M. D. Reed, L. DiCarlo, S. E. Nigg, L. Sun, L. Frunzio, S. M. Girvin, and R. J. Schoelkopf, *Nature* **482**, 382 (2012).

[56] Y. Makhlin, G. Schön, and A. Shnirman, *Rev. Mod. Phys.* **73**, 357 (2001).

[57] M. Devoret, A. Wallraff, and J. Martinis, *arXiv:cond-mat/0411174* (2004).

[58] J. You and F. Nori, *Physics Today* **58**, 42 (2005).

[59] S. M. Girvin, M. H. Devoret, and R. J. Schoelkopf, *Phys. Scr. T* **137**, 014012 (2009), Proceedings of Nobel Symposium 141: Qubits for Future Quantum.

[60] P. Zoller *et al.*, *Eur. Phys. J. D* **36**, 203 (2005).

[61] P. Hauke, F. M. Cucchietti, L. Tagliacozzo, I. Deutsch, and M. Lewenstein, *Rep. Prog. Phys.* **75**, 082401 (2012).

[62] P. Hauke, L. Tagliacozzo, and M. Lewenstein, *Science* **336**, 1122 (2012).

[63] V. Kendon, K. Nemoto, and W. Munro, *Phil. Trans. R. Soc. A* **368**, 3609 (2010).

[64] R. Landauer, *Phys. Lett. A* **217**, 188 (1996).

[65] D. Deutsch, *Proc. R. Soc. Lond. A* **400**, 97 (1985).

[66] E. Knill and R. Laflamme, *Phys. Rev. A* **55**, 900 (1997).

[67] J. Preskill, *Introduction to Quantum Computation*, chapter Fault Tolerant Quantum

Computation, World Scientific, 1998.

[68] K. R. Brown, R. J. Clark, and I. L. Chuang, *Phys. Rev. Lett.* **97**, 050504 (2006).

[69] D. P. DiVincenzo, *Fort. Phys.* **48**, 771 (2000).

[70] D. Jaksch, C. Bruder, J. I. Cirac, C. W. Gardiner, and P. Zoller, *Phys. Rev. Lett.* **81**, 3108 (1998).

[71] M. Greiner, I. Bloch, O. Mandel, T. W. Hänsch, and T. Esslinger, *Phys. Rev. Lett.* **87**, 160405 (2001).

[72] M. Greiner, O. Mandel, T. Esslinger, T. W. Hänsch, and I. Bloch, *Nature* **415**, 39 (2002).

[73] A. Sandvik, *AIP Conf. Proc.* **1297**, 135 (2010).

[74] T. Giamarchi, *Quantum Physics in One Dimension*, Oxford Science Publications, 2004.

[75] U. Schollwöck, *Annals of Physics* **326**, 96 (2011).

[76] V. Alba, L. Tagliacozzo, and P. Calabrese, *J. Stat. Mech.* **1106**, P06012 (2011).

[77] G. Evenbly and G. Vidal, *arXiv:1109.5334v1 [quant-ph]* (2011).

[78] E. Stoudenmire and S. White, *Annual Review of Condensed Matter Physics* **3**, 111 (2011).

[79] L. Tagliacozzo, G. Evenbly, and G. Vidal, *Phys. Rev. B* **80**, 235127 (2009).

[80] L. Tagliacozzo and G. Vidal, *Phys. Rev. B* **83**, 115127 (2011).

[81] P. Corboz, S. White, G. Vidal, and M. Troyer, *Phys. Rev. B* **84**, 041108 (2011).

[82] L. Wang, Z. Gu, X. Wen, and F. Verstraete, *arXiv:1112.3331v2 [cond-mat.str-el]* (2011).

[83] J. J. Binney, N. J. Dowrick, A. J. Fisher, and M. E. J. Newman, *The theory of critical phenomena : an introduction to the renormalization group*, Clarendon Press (Oxford), 1992.

[84] R. Martin, *Electronic structure: Basic theory and practical methods*, Cambridge University Press, 2004.

[85] E. Stoudenmire, L. O. Wagner, S. R. White, and K. Burke, *arXiv:1107.2394v2 [cond-mat.str-el]* (2011).

[86] A. Georges, G. Kotliar, W. Krauth, and M. Rozenberg, *Rev. Mod. Phys.* **68**, 13 (1996).

[87] T. Esslinger, *Annu. Rev. Cond. Mat. Phys.* **1**, 129 (2010).

[88] A. Das and B. K. Chakrabarti, *Rev. Mod. Phys.* **80**, 1061 (2008).

[89] S. Sorella and F. Becca, *http://people.sissa.it/sorella/Simulazioni.pdf* (2011).

[90] C. Pineda, T. Barthel, and J. Eisert, *Phys. Rev. A* **81**, 050303(R) (2010).

[91] P. Corboz and G. Vidal, *Phys. Rev. B* **80**, 165129 (2009).

[92] T. Barthel, C. Pineda, and J. Eisert, *Phys. Rev. A* **80**, 042333 (2009).

[93] Q. Shi, S. Li, J. Zhao, and H. Zhou, *arXiv:0907.5520* (2009).

[94] P. Corboz, R. Orús, B. Bauer, and G. Vidal, *Phys. Rev. B* **81**, 165104 (2010).

[95] E. Lieb and D. Robinson, *Commun. Math. Phys.* **28**, 251 (1972).

[96] S. Bravyi, M. B. Hastings, and F. Verstraete, *Phys. Rev. Lett.* **97**, 050401 (2006).

[97] P. Calabrese and J. Cardy, *Phys. Rev. Lett.* **96**, 136801 (2006).

[98] J. Eisert and T. Osborne, *Phys. Rev. Lett.* **97**, 150404 (2006).

[99] B. Nachtergaele, Y. Ogata, and R. Sims, *J. Stat. Phys.* **124**, 1 (2006).

[100] N. Schuch, M. Wolf, K. Vollbrecht, and J. Cirac, *New J. Phys.* **10**, 033032 (2008).

[101] J. Eisert, M. Cramer, and M. B. Plenio, *Rev. Mod. Phys.* **82**, 277 (2010).

[102] D. Leibfried, *Nature* **463**, 608 (2010).

[103] R. Griffiths, *Phys. Rev. Lett.* **23**, 17 (1969).

[104] J. A. H. Fawaz Hrahsheh and and T. Vojta, *arXiv:1208.0471v1 [cond-mat.str-el]* (2012).

[105] Z. Hadzibabic, *private communication* (2011).

[106] S. Lloyd, *Science* **273**, 1073 (1996).

[107] H. Weimer, M. Müller, I. Lesanovsky, P. Zoller, and H. P. Büchler, *Nat. Phys.* **6**, 382 (2010).

[108] A. A. Houck, H. E. Türeci, and J. Koch, *Nat. Phys.* **8**, 292 (2012).

[109] E. Jane, G. Vidal, W. Dür, P. Zoller, and J. Cirac, *Quant. Comp. Inf.* **3**, 15 (2003).

[110] N. Wiebe, D. Berry, P. Hoyer, and B. Sanders, *J. Phys. A: Math. Theor.* **44**, 445308 (2011).

[111] S. P. Jordan, K. S. Lee, and J. Preskill, *Science* **336**, 1130 (2012).

[112] S. P. Jordan, K. S. Lee, and J. Preskill, *arXiv:1112.4833v1* (2011).

[113] P. W. Shor, *Phys. Rev. A* **52**, 2493(R) (1995).

[114] M. A. Nielsen and I. L. Chuang, *Quantum Computation and Quantum Information*, Cambridge University Press, 2000.

[115] D. G. Cory, M. D. Price, W. Maas, E. Knill, R. Laflamme, W. H. Zurek, T. F. Havel, and S. S. Somaroo, *Phys. Rev. Lett.* **81**, 2152 (1998).

[116] J. Chiaverini, D. Leibfried, T. Schaetz, M. D. Barrett, R. B. Blakestad, J. Britton, W. M. Itano, J. D. Jost, E. Knill, C. Langer, R. Ozeri, and D. J. Wineland, *Nature* **432**, 602 (2004).

[117] T. B. Pittman, B. C. Jacobs, and J. D. Franson, *Phys. Rev. A* **71**, 052332 (2005).

[118] M. Lassen, M. Sabuncu, A. Huck, J. Niset, G. Leuchs, N. J. Cerf, and U. L. Andersen, *Nature Photon.* **4**, 700 (2010).

[119] P. Schindler, J. T. Barreiro, T. Monz, V. Nebendahl, D. Nigg, M. Chwalla, M. Hennrich, and R. Blatt, *Science* **332**, 1059 (2011).

[120] D. Aharonov and A. Ta-Shma, Adiabatic quantum state generation and statistical zero knowledge, in *Proc. 35th STOC*, edited by N. Y. ACM, p. 20, 2003.

[121] D. Berry, G. Ahokas, R. Cleve, and B. Sanders, *Commun. Math. Phys.* **270**, 359 (2007).

[122] A. Childs and R. Kothari, *Theory of Quantum Computation, Communication, and Cryptography (TQC 2010), Lecture Notes in Computer Science* **6519**, 94 (2011).

[123] K. Brown, W. Munro, and V. Kendon, *Entropy* **12**, 2268 (2010).

[124] C. Clark, T. Metodi, S. Gasster, and K. Brown, *Phys. Rev. A* **79**, 062314 (2009).

[125] D. Abrams and S. Lloyd, *Phys. Rev. Lett.* **83**, 5162 (1999).

[126] U. Haeberlen and J. S. Waugh, *Phys. Rev.* **175**, 453 (1968).

[127] J. Waugh, *Average Hamiltonian Theory*, Encyclopedia of Magnetic Resonance, 2007.

[128] S. Diehl, A. Micheli, A. Kantian, B. Kraus, H. P. Büchler, and P. Zoller, *Nat. Phys.* **4**, 878 (2008).

[129] B. Kraus, H. P. Büchler, S. Diehl, A. Kantian, A. Micheli, and P. Zoller, *Phys. Rev. A* **78**, 042307 (2008).

[130] F. Verstraete, M. Wolf, and I. Cirac, *Nat. Phys.* **5**, 633 (2009).

[131] R. Wu, A. Pechen, C. Brif, and H. Rabitz, *J. Phys. A: Math. Theor.* **40**, 5681 (2007).

[132] F. M. Cucchietti, J.-F. Zhang, F. C. Lombardo, P. I. Villar, and R. Laflamme, *Phys. Rev. Lett.* **105**, 240406 (2010).

[133] J. Dodd, M. Nielsen, M. Bremner, and R. Thew, *Phys. Rev. A* **65**, 040301 (2002).

[134] P. Wocjan, M. Roetteler, D. Janzing, and T. Beth, *Quant. Inf. Comp.* **2**, 133 (2002).

[135] W. Dür, M. J. Bremner, and H. J. Briegel, *Phys. Rev. A* **78**, 052325 (2008).

[136] J. W. Britton, B. C. Sawyer, A. C. Keith, C.-C. J. Wang, J. K. Freericks, H. Uys, M. J. Biercuk, and J. J. Bollinger, *Nature* **484**, 489 (2012).

[137] M. Polini, R. Fazio, A. H. MacDonald, and M. P. Tosi, *Phys. Rev. Lett.* **95**, 010401 (2005).

[138] N. Schuch, M. Wolf, F. Verstraete, and J. Cirac, *Phys. Rev. Lett.* **100**, 030504 (2008).

[139] N. Schuch, J. Cirac, and F. Verstraete, *Phys. Rev. Lett.* **100**, 250501 (2008).

[140] M. Hastings, *Phys. Rev. Lett.* **103**, 050502 (2009).

[141] H. Quan, Z. Song, X. Liu, P. Zanardi, and C. P. Sun, *Phys. Rev. Lett.* **96**, 140604 (2006).

[142] P. Zanardi and N. Paunkovic, *Phys. Rev. E* **74**, 031123 (2006).

[143] B. Georgeot and D. L. Shepelyansky, *Phys. Ref. E* **62**, 3504 (2000).

[144] K. M. Frahm, R. Fleckinger, and D. L. Shepelyansky, *Eur. Phys. J. D* **29**, 139 (2004).

[145] P. W. Shor, *SIAM J. Comput.* **26**, 1484 (1997).

[146] H. Pichler, A. J. Daley, and P. Zoller, *Phys. Rev. A* **82**, 063605 (2010).

[147] H. Pichler, J. Schachenmayer, J. Simon, P. Zoller, and A. J. Daley, *arXiv:1205.6189v1 [cond-mat.quant-gas]* (2012).

[148] J. Hubbard, *Proceedings of the Royal Society of London* **276**, 238 (1963).

[149] P. Pedri, L. Pitaevskii, S. Stringari, C. Fort, S. Burger, F. S. Cataliotti, P. Maddaloni, F. Minardi, and M. Inguscio, *Phys. Rev. Lett.* **87**, 220401 (2001).

[150] V. A. Kashurnikov, N. V. Prokof'ev, and B. V. Svistunov, *Phys. Rev. A* **66**, 031601(R) (2002).

[151] M. Greiner, *Ultracold quantum gases in three-dimensional optical lattice*, PhD thesis, Ludwig-Maximilians-Universität München, 2003.

[152] W. S. Bakr, J. Gillen, A. Peng, S. Foelling, and M. Greiner, *Nature* **462**, 74 (2009).

[153] C. Weitenberg, M. Endres, J. F. Sherson, M. Cheneau, P. Schauss, T. Fukuhara, I. Bloch, and S. Kuhr, *Nature* **471**, 319 (2011).

[154] B. Zimmermann, T. Müller, J. Meineke, T. Esslinger, and H. Moritz, *New J. Phys.* **13**, 043007 (2011).

[155] L. Sanchez-Palencia and M. Lewenstein, *Nat. Phys.* **6**, 87 (2010).

[156] J. Billy, V. Josse, Z. Zuo, A. Bernard, B. Hambrecht, P. Lugan, D. Clement, L. Sanchez-Palencia, P. Bouyer, and A. Aspect, *Nature* **453**, 891 (2008).

[157] G. Roati, C. D'Errico, L. Fallani, M. Fattori, C. Fort, M. Zaccanti, G. Modugno, M. Modugno, and M. Inguscio, *Nature* **453**, 895 (2008).

[158] S. S. Kondov, W. R. McGehee, J. J. Zirbel, and B. DeMarco, *Science* **334**, 66 (2011).

[159] P. W. Anderson, *Phys. Rev.* **124**, 41 (1961).

[160] C. Becker, P. Soltan-Panahi, J. Kronjäger, S. Dörscher, K. Bongs, and K. Sengstock, *New J. Phys.* **12**, 065025 (2010).

[161] P. Soltan-Panahi, J. Struck, P. Hauke, A. Bick, W. Plenkers, G. Meineke, C. Becker, P. Windpassinger, M. Lewenstein, and K. Sengstock, *Nat. Phys.* **7**, 434 (2011).

[162] L. Tarruell, D. Greif, T. Uehlinger, G. Jotzu, and T. Esslinger, *Nature* **483**, 302 (2012).

[163] G.-B. Jo, J. Guzman, C. K. Thomas, P. Hosur, A. Vishwanath, and D. M. Stamper-Kurn, *Phys. Rev. Lett.* **108**, 045305 (2012).

[164] A. Eckardt, P. Hauke, P. Soltan-Panahi, C. Becker, K. Sengstock, and M. Lewenstein, *Europhys. Lett.* **89**, 10010 (2010).

[165] J. Struck, C. Ölschläger, R. Le Targat, P. Soltan-Panahi, A. Eckardt, M. Lewenstein, P. Windpassinger, and K. Sengstock, *Science* **333**, 996 (2011).

[166] M. Lewenstein and W. V. Liu, *Nat. Phys.* **7**, 101 (2011).

[167] T. Lahaye, C. Menotti, L. Santos, M. Lewenstein, and T. Pfau, *Rep. Prog. Phys.* **72**, 126401 (2009).

[168] R. Jördens, N. Strohmaier, K. Günter, H. Moritz, and T. Esslinger, *Nature* **455**, 204 (2008).

[169] U. Schneider, L. Hackermüller, S. Will, T. Best, I. Bloch, T. A. Costi, R. W. Helmes, D. Rasch, and A. Rosch, *Science* **322**, 1520 (2008).

[170] L. Hackermüller, U. Schneider, M. Moreno-Cardoner, T. Kitagawa, T. Best, S. Will, E. Demler, E. Altman, I. Bloch, and B. Paredes, *Science* **327**, 1621 (2010).

[171] D. Greif, L. Tarruell, T. Uehlinger, R. Jördens, and T. Esslinger, *Phys. Rev. Lett.* **106**, 145302 (2011).

[172] U. Schneider, L. Hackermüller, J. P. Ronzheimer, S. Will, S. Braun, T. Best, I. Bloch, E. Demler, S. Mandt, D. Rasch, and A. Rosch, *Nat. Phys.* **8**, 213 (2012).

[173] D. Chen, M. White, C. Borries, and B. DeMarco, *Phys. Rev. Lett.* **106**, 235304 (2011).

[174] J. I. Cirac and P. Zoller, *Phys. Rev. Lett.* **74**, 4091 (1995).

[175] D. Porras and J. I. Cirac, *Phys. Rev. Lett.* **92**, 207901 (2004).

[176] F. Mintert and C. Wunderlich, *Phys. Rev. Lett.* **87**, 257904 (2001).

[177] S. Fishman, G. De Chiara, T. Calarco, and G. Morigi, *Phys. Rev. B* **77**, 064111 (2008).

[178] J. P. Schiffer, *Phys. Rev. Lett.* **70**, 818 (1993).

[179] A. Dantan, M. Albert, J. Marler, P. F. Herskind, and M. Drewsen, *Phys Rev. A* **80**, 041802(R) (2009).

[180] P. Hauke, F. M. Cucchietti, A. Müller-Hermes, M.-C. Bañuls, J. I. Cirac, and M. Lewenstein, *New J. Phys.* **12**, 113037 (2010).

[181] R. Schmied, J. H. Wesenberg, and D. Leibfried, *New J. Phys.* **13**, 115011 (2011).

[182] J. Chiaverini and W. E. Lybarger, Jr., *Phys. Rev. A* **77**, 022324 (2008).

[183] R. Schmied, J. H. Wesenberg, and D. Leibfried, *Phys. Rev. Lett.* **102**, 233002 (2009).

[184] D. Porras and J. Cirac, *Phys. Rev. Lett.* **96**, 250501 (2006).

[185] C. Schneider, M. Enderlein, T. Huber, and T. Schaetz, *Nature Photon.* **4**, 772 (2010).

[186] M. Enderlein, T. Huber, C. Schneider, and T. Schaetz, *arXiv:1208.3329v1 [physics.atom-ph]* (2012).

[187] M. Pons, V. Ahufinger, C. Wunderlich, A. Sanpera, S. Braungardt, A. Sen(De), U. Sen, and M. Lewenstein, *Phys. Rev. Lett.* **98**, 023003 (2007).

[188] S. Braungardt, A. Sen(De), U. Sen, and M. Lewenstein, *Phys. Rev. A* **76**, 042307 (2007).

[189] A. Bermudez, M. Martin-Delgado, and D. Porras, *New J. Phys.* **12**, 123016 (2010).

[190] I. García-Mata, O. V. Zhirov, and D. L. Shepelyansky, *Eur. Phys. J. D* **41**, 325 (2007).

[191] A. del Campo, G. D. Chiara, G. Morigi, M. B. Plenio, and A. Retzker, *Phys. Rev. Lett.* **105**, 075701 (2010).

[192] L. Lamata, J. León, T. Schätz, and E. Solano, *Phys. Rev. Lett.* **98**, 253005 (2007).

[193] A. Bermudez, M. A. Martin-Delgado, and E. Solano, *Phys. Rev. A* **76**, 041801 (2007).

[194] B. Horstmann, B. Reznik, S. Fagnocchi, and J. Cirac, *Phys. Rev. Lett.* **104**, 250403 (2010).

[195] B. Horstmann, R. Schützhold, B. Reznik, S. Fagnocchi, and J. Cirac, *New J. Phys.* **13**, 045008 (2011).

[196] H. Schmitz, R. Matjeschk, C. Schneider, J. Glueckert, M. Enderlein, T. Huber, and T. Schaetz, *Phys. Rev. Lett.* **103**, 090504 (2009).

[197] D. Porras and J. I. Cirac, *Phys. Rev. Lett.* **93**, 263602 (2004).

[198] X.-L. Deng, D. Porras, and J. I. Cirac, *Phys. Rev. A* **77**, 033403 (2008).

[199] A. Bermudez, T. Schaetz, and D. Porras, *New J. Phys.* **14**, 053049 (2012).

[200] D. Porras, P. A. Ivanov, and F. Schmidt-Kaler, *Phys. Rev. Lett.* **108**, 235701 (2012).

[201] P. A. Ivanov and F. Schmidt-Kaler, *New J. Phys.* **13**, 125008 (2011).

[202] R. Schmied, T. Roscilde, V. Murg, D. Porras, and J. I. Cirac, *New J. Phys.* **10**, 045017 (2008).

[203] A. Bermudez, J. Almeida, F. Schmidt-Kaler, A. Retzker, and M. B. Plenio, *Phys. Rev. Lett.* **107**, 207209 (2011).

[204] M. Maik, P. Hauke, O. Dutta, J. Zakrzewski, and M. Lewenstein, *arXiv:1206.1752v1 [cond-mat.quant-gas]* (2012).

[205] D. Jaksch and P. Zoller, *New J. Phys.* **5**, 56 (2003).

[206] A. S. Sørensen, E. Demler, and M. D. Lukin, *Phys. Rev. Lett.* **94**, 086803 (2005).

[207] D. S. Goldbaum and E. J. Mueller, *Phys. Rev. A* **77**, 033629 (2008).

[208] J. J. Garcia-Ripoll and J. K. Pachos, *New J. Phys.* **9**, 139 (2007).

[209] A. Eckardt, P. Hauke, P. Soltan-Panahi, C. Becker, K. Sengstock, and M. Lewenstein, *Europhys. Lett.* **89**, 10010 (2010).

[210] K. Sacha, K. Targonska, and J. Zakrzewski, *Phys. Rev. A* **85**, 053613 (2012).

[211] P. Hauke, O. Tielemann, A. Celi, C. Ölschläger, J. Simonet, J. Struck, M. Weinberg, P. Windpassinger, K. Sengstock, M. Lewenstein, and A. Eckardt, *Phys. Rev. Lett.* **109**, 145301 (2012).

[212] H. T. Diep, editor, *Frustrated Spin Systems*, World Scientific, Singapore, 2004.

[213] R. Fazio and H. van der Zant, *Phys. Rep.* **355**, 235 (2001).

[214] P. Hauke, M. Lewenstein, and A. Eckardt, *in preparation* .

[215] K. Madison, M. C. Fischer, R. B. Diener, Q. Niu, and M. G. Raizen, *Phys. Rev. Lett.* **81**, 5093.

[216] H. Lignier, C. Sias, D. Ciampini, Y. Singh, A. Zenesini, O. Morsch, and E. Arimondo, *Phys. Rev. Lett.* **99**, 220403 (2007).

[217] D. H. Dunlap and V. M. Kenkre, *Phys. Rev. B* **34**, 3625 (1986).

[218] F. Grossmann, P. Jung, T. Dittrich, and P. Hänggi, *Z. Phys. B* **84**, 315 (1991).

[219] M. Holthaus, *Phys. Rev. Lett.* **69**, 351 (1992).

[220] A. Eckardt, C. Weiss, and M. Holthaus, *Phys. Rev. Lett.* **95**, 260404 (2005).

[221] A. Eckardt and M. Holthaus, *Phys. Rev. Lett.* **101**, 245302 (2008).

[222] E. Kierig, U. Schnorrberger, A. Schietinger, J. Tomkovic, and M. Oberthaler, *Phys. Rev. Lett.* **100**, 190405 (2008).

[223] H. Lignier, A. Zenesini, D. Ciampini, O. Morsch, E. Arimondo, S. Montangero, G. Pupillo, and R. Fazio, *Phys. Rev. A* **79**, 041601(R) (2009).

[224] M. Takahashi, *Phys. Rev. B* **40**, 2494 (1989).

[225] P. Hauke, T. Roscilde, V. Murg, J. I. Cirac, and R. Schmied, *New J. Phys.* **12**, 053036 (2010).

[226] C. Lanczos, *J. Res. Natl. Bur. Stand.* **45**, 255 (1950).

[227] A. W. Sandvik and C. J. Hamer, *Phys. Rev. B* **60**, 6588 (1999).

[228] A. L. Chernyshev and M. E. Zhitomirsky, *Phys. Rev. B* **79**, 144416 (2009).

[229] N. D. Mermin and H. Wagner, *Phys. Rev. Lett.* **17**, 1133 (1966).

[230] B. S. Shastry and B. Sutherland, *Phys. Rev. Lett.* **65**, 243 (1990).

[231] C. Lhuillier, *arXiv:cond-mat/0502464v1* (2005).

[232] P. Lecheminant, B. Bernu, C. Lhuillier, L. Pierre, and P. Sindzingre, *Phys. Rev. B* **56**, 2521 (1997).

[233] H. Kawamura, *arXiv:cond-mat/0202109v1* (2002).

[234] J. Richter, C. Gros, and W. Weber, *Phys. Rev. B* **44**, 906 (1991).

[235] C. L. Henley, *Phys. Rev. Lett.* **62**, 2056 (1989).

[236] S. E. Krüger, J. Richter, J. Schulenburg, D. J. J. Farnell, and R. F. Bishop, *Phys. Rev. B* **61**, 14607 (2000).

[237] S. Ghamari, C. Kallin, S.-S. Lee, and E. S. Sørensen, *Phys. Rev. B* **84**, 174415 (2011).

[238] A. Weichselbaum and S. R. White, *Phys. Rev. B* **84**, 245130 (2011).

[239] S. Yunoki and S. Sorella, *Phys. Rev. B* **74**, 014408 (2006).

[240] D. Heidarian, S. Sorella, and F. Becca, *Phys. Rev. B* **80**, 012404 (2009).

[241] P. Hauke, T. Roscilde, V. Murg, J. Cirac, and R. Schmied, *New J. Phys.* **13**, 075017 (2011).

[242] J. Reuther and R. Thomale, *Phys. Rev. B* **83**, 024402 (2011).

[243] P. C. Hohenberg, *Phys. Rev.* **158**, 383 (1967).

[244] V. L. Berezinskii, *Sov. Phys. JETP* **32**, 493 (1971).

[245] V. L. Berezinskii, *Sov. Phys. JETP* **34**, 610 (1972).

[246] J. M. Kosterlitz and D. J. Thouless, *J. Phys. C* **6**, 1181 (1973), Journal of Physics C: Solid State Physics.

[247] M. Cramer and J. Eisert, *New J. Phys.* **8**, 71 (2006).

[248] D. H. Lee, J. D. Joannopoulos, J. W. Negele, and D. P. Landau, *Phys. Rev. Lett.* **52**, 433 (1984).

[249] L. Capriotti, A. Cuccoli, V. Tognetti, P. Verrucchi, and R. Vaia, *Phys. Rev. B* **60**, 7299 (1999).

[250] A. Cuccoli, V. Tognetti, and R. Vaia, *Phys. Rev. B* **52**, 10221 (1995).

[251] H.-Q. Ding and M. S. Makivić, *Phys. Rev. B* **42**, 6827 (1990).

[252] K. Harada and N. Kawashima, *Phys. Rev. B* **55**, R11949 (1997).

[253] J. Stephenson, *Can. J. Phys.* **47**, 2621 (1969).

[254] J. Stephenson, *Can. J. Phys.* **48**, 1724 (1970).

[255] J. Stephenson, *Can. J. Phys.* **48**, 2118 (1970).

[256] J. Stephenson, *J. Math. Phys.* **11**, 420 (1970).

[257] P. Hauke, *arXiv:1205.1958v1 [cond-mat.quant-gas]* (2012).

[258] A. V. Chubukov, S. Sachdev, and J. Ye, *Phys. Rev. B* **49**, 11919 (1994).

[259] B. I. Halperin and P. C. Hohenberg, *Phys. Rev.* **188**, 898 (1969).

[260] T. Momoi, *J. Stat. Phys.* **75**, 707 (1994).

[261] C. N. Varney, K. Sun, V. Galitski, and M. Rigol, *Phys. Rev. Lett.* **107**, 077201 (2011).

[262] C. Mora and Y. Castin, *Phys. Rev. A* **67**, 053615 (2003).

[263] M. Snoek and W. Hofstetter, *Phys. Rev. A* **76**, 051603 (2007).

[264] C. Wu, D. Bergman, L. Balents, and S. Das Sarma, *Phys. Rev. Lett.* **99**, 070401 (2007).

[265] C. Wu and S. Das Sarma, *Phys. Rev. B* **77**, 235107 (2008).

[266] K. L. Lee, B. Grémaud, R. Han, B.-G. Englert, and C. Miniatura, *Phys. Rev. A* **80**, 043411 (2009).

[267] E. Alba, X. Fernandez-Gonzalvo, J. Mur-Petit, J. K. Pachos, , and J. J. Garcia-Ripoll, *Phys. Rev. Lett.* **107**, 235301 (2011).

[268] A. Geim and K. Novoselov, *Nature Mater.* **6**, 183 (2007).

[269] M. Lemme, T. Echtermeyer, M. Baus, and H. Kurz, *Electron Device Letters* **28**, 282 (2007).

[270] F. Schedin, A. K. Geim, S. V. Morozov, E. W. Hill, P. Blake, M. I. Katsnelson, and K. S. Novoselov, *Nature Mater.* **6**, 652 (2007).

[271] A. Vakil and N. Engheta, *Science* **332**, 1291 (2011).

[272] F. Bonaccorso, Z. Sun, T. Hasan, and A. C. Ferrari, *Nature Photon.* **4**, 611 (2012).

[273] D. E. Chang, A. S. Sørensen, P. R. Hemmer, and M. D. Lukin, *Phys. Rev. Lett.* **97**, 053002 (2006).

[274] F. H. Koppens, D. E. Chang, and F. J. G. de Abajo, *Nano Lett.* **11**, 3370 (2011).

[275] T. Echtermeyer, L. Britnell, P. Jasnos, A. Lombardo, R. Gorbachev, A. Grigorenko, A. Geim, A. Ferrari, and K. Novoselov, *Nat. Commun.* **2**, 458 (2011).

[276] Y. Liu, R. Cheng, L. Liao, H. Zhou, J. Bai, G. Liu, L. Liu, Y. Huang, and X. Duan, *Nat. Commun.* **2**, 579 (2011).

[277] J. Chen, M. Badioli, P. Alonso-González, S. Thongrattanasiri, F. Huth, J. Osmond, M. Spasenović, A. Centeno, A. Pesquera, P. Godignon, A. Z. Elorza, N. Camara, F. J. G. de Abajo, R. Hillenbrand, and F. H. L. Koppens, *Nature* **487**, 77 (2012).

[278] Z. Fei, A. S. Rodin, G. O. Andreev, W. Bao, A. S. McLeod, M. Wagner, L. M. Zhang, Z. Zhao, M. Thiemens, G. Dominguez, M. M. Fogler, A. H. C. Neto, C. N. Lau, F. Keilmann, and D. N. Basov, *Nature* **487**, 82 (2012).

[279] S. Iijima, *Nature* **354**, 56 (1991).

[280] X. Du, I. Skachko, F. Duerr, A. Luican, and E. Y. Andrei, *Nature* **462**, 192 (2009).

[281] M. Z. Hasan and C. L. Kane, *Rev. Mod. Phys.* **82**, 3045 (2010).

[282] D. Jaksch, H. J. Briegel, J. I. Cirac, C. W. Gardiner, and P. Zoller, *Phys. Rev. Lett.* **82**, 1975 (1999).

[283] O. Mandel, M. Greiner, A. Widera, T. Rom, T. W. Hänsch, and I. Bloch, *Nature* **425**, 937 (2003).

[284] P. J. Lee, M. Anderlini, B. L. Brown, J. Sebb-Strabley, W. D. Phillips, and J. V. Porto, *Phys. Rev. Lett.* **99**, 020402 (2007).

[285] Y.-J. Lin, R. L. Compton, A. R. Perry, W. D. Phillips, J. V. Porto, and I. B. Spielman, *Phys. Rev. Lett.* **102**, 130401 (2009).

[286] D. McKay and B. DeMarco, *New J. Phys.* **12**, 055013 (2010).

[287] R. Grimm, W. M., and O. Y. B., *Adv. At. Mol. Opt. Phys.* **42**, 95 (2000).

[288] H. P. Büchler and G. Blatter, *Phys. Rev. Lett.* **91**, 130404 (2003).

[289] I. Titvinidze, M. Snoek, and W. Hofstetter, *Phys. Rev. Lett.* **100**, 100401 (2008).

[290] E. Kim and M. H. W. Chan, *Nature* **427**, 225 (2004).

[291] E. Kim and M. H. W. Chan, *Science* **305**, 1941 (2004).

[292] A. S. C. Rittner and J. D. Reppy, *Phys. Rev. Lett.* **97**, 165301 (2006).

[293] A. S. C. Rittner and J. D. Reppy, *Phys. Rev. Lett.* **98**, 175302 (2007).

[294] K. Baumann, R. Mottl, F. Brennecke, and T. Esslinger, *Phys. Rev. Lett.* **107**, 140402 (2011).

[295] C. Chin, R. Grimm, P. Julienne, and E. Tiesinga, *Rev. Mod. Phys.* **82**, 1225 (2010).

[296] S. Inouye, M. R. Andrews, J. Stenger, H.-J. Miesner, D. M. Stamper-Kurn, and W. Ketterle, *Nature* **392**, 151 (1998).

[297] S. Doniach, *Phys. Rev. B* **24**, 5063 (1981).

[298] R. A. Pepino, J. Cooper, D. Z. Anderson, and M. J. Holland, *Phys. Rev. Lett.* **103**, 140405 (2009).

[299] K. Günter, T. Stöferle, H. Moritz, M. Köhl, and T. Esslinger, *Phys. Rev. Lett.* **96**, 180402 (2006).

[300] S. Ospelkaus, C. Ospelkaus, O. Wille, M. Succo, P. Ernst, K. Sengstock, and K. Bongs, *Phys. Rev. Lett.* **96**, 180403 (2006).

[301] J. Catani, G. Barontini, G. Lamporesi, F. Rabatti, G. Thalhammer, F. Minardi, S. Stringari, and M. Inguscio, *Phys. Rev. Lett.* **103**, 140401 (2009).

[302] P. Soltan-Panahi, D.-S. Lühmann, J. Struck, P. Windpassinger, and K. Sengstock, *Nature Physics* **8**, 71 (2012).

[303] J. Dalibard, F. Gerbier, G. Juzeliunas, and P. Öhberg, *Rev. Mod. Phys.* **83**, 1523 (2011).

[304] Y.-J. Lin, K. Jiménez-García, and I. B. Spielman, *Nature* **471**, 83 (2011).

[305] L.-K. Lim, C. Morais Smith, and A. Hemmerich, *Phys. Rev. Lett.* **100**, 130402 (2008).

[306] L.-K. Lim, A. Lazarides, A. Hemmerich, and C. Morais Smith, *Phys. Rev. A* **82**, 013616 (2010).

[307] A. Bermudez, N. Goldman, A. Kubasiak, M. Lewenstein, and M. Martin-Delgado, *New J. Phys.* **12**, 033041 (2010).

[308] C. Nayak, S. H. Simon, A. Stern, M. Freedman, and S. D. Sarma, *Rev. Mod. Phys.* **80**, 1083 (2008).

[309] A. L. Fetter, *Rev. Mod. Phys.* **81**, 647 (2009).

[310] K. Osterloh, M. Baig, L. Santos, P. Zoller, and M. Lewenstein, *Phys. Rev. Lett.* **95**, 010403 (2005).

[311] L. Mazza, A. Bermudez, N. Goldman, M. Rizzi, M. A. Martin-Delgado, and M. Lewenstein, *New J. Phys.* **14**, 015007 (2012).

[312] A. Zenesini, H. Lignier, C. Sias, O. Morsch, D. Ciampini, and E. Arimondo, *Laser Physics* **20**, 1182 (2009).

[313] S. Koghee, L.-K. Lim, M. O. Goerbig, and C. M. Smith, *Phys. Rev. A* **85**, 023637.

[314] V. Kalmeyer and R.-B. Laughlin, *Phys. Rev. Lett.* **59**, 2095 (1987).

[315] N. Goldman, A. Kubasiak, P. Gaspard, and M. Lewenstein, *Phys. Rev. A* **79**, 023624 (2009).

[316] A. Eckardt and M. Holthaus, *EPL* **80**, 50004 (2007).

[317] C. Sias, H. Lignier, Y. Singh, A. Zenesini, D. Ciampini, O. Morsch, and E. Arimondo, *Phys. Rev. Lett.* **100**, 040404 (2008).

[318] A. Alberti, V. V. Ivanov, G. M., Tino, and G. Ferrari, *Nat. Phys.* **5**, 547 (2009).

[319] E. Haller, R. Hart, M. J. Mark, J. G. Danzl, L. Reichsöllner, , and H.-C.

Nägerl, *Phys. Rev. Lett.* **104**, 200403 (2010).

[320] A. R. Kolovsky, *Euro. Phys. Lett.* **93**, 20003 (2011).

[321] S. D. Huber and E. Altman, *Phys. Rev. B* **82**, 184502 (2010).

[322] L. Messio, B. Bernu, and C. Lhuillier, *Phys. Rev. Lett.* **108**, 207204 (2012).

[323] L. Messio, O. Cepas, and C. Lhuillier, *Phys. Rev. B* **81**, 064428 (2010).

[324] C. L. Kane and E. J. Mele, *Phys. Rev. Lett.* **95**, 226801 (2005).

[325] F. D. M. Haldane, *Phys. Rev. Lett.* **61**, 2015 (1988).

[326] M. Levin and A. Stern, *Phys. Rev. Lett.* **103**, 196803 (2009).

[327] Z. Wang, X.-L. Qi, and S.-C. Zhang, *Phys. Rev. Lett.* **105**, 256803 (2010).

[328] W. Wu, S. Rachel, W.-M. Liu, and K. L. Hur, *Phys. Rev. B* **85**, 205102 (2012).

[329] G. P. Collins, *Scientific American* **294**, 56 (2006).

[330] J. Ruseckas, G. Juzeliūnas, P. Öhberg, and M. Fleischhauer, *Phys. Rev. Lett.* **95**, 010404 (2005).

[331] A. Jacob, P. Ohberg, G. Juzeliunas, and L. Santos, *Appl. Phys. B* **89**, 439 (2007).

[332] G. Juzeliūnas, J. Ruseckas, A. Jacob, L. Santos, and P. Öhberg, *Phys. Rev. Lett.* **100**, 200405 (2008).

[333] N. Goldman, A. Kubasiak, A. Bermudez, P. Gaspard, M. Lewenstein, and M. A. Martin-Delgado, *Phys. Rev. Lett.* **103**, 035301 (2009).

[334] F. Gerbier and J. Dalibard, *New J. Phys.* **12**, 033007 (2010).

[335] M. Burrello and A. Trombettoni, *Phys. Rev. Lett.* **105**, 125304 (2010).

[336] M. Burrello and A. Trombettoni, *Phys. Rev. A* **84**, 043625 (2011).

[337] A. Zamora, G. Szirmai, and M. Lewenstein, *Phys. Rev. A* **84**, 053620 (2011).

[338] A. Hemmerich and T. W. Hänsch, *Phys. Rev. Lett.* **70**, 410 (1993).

[339] X.-J. Liu, X. Liu, C. Wu, and J. Sinova, *Phys. Rev. A* **81**, 033622 (2010).

[340] T. D. Stanescu, V. Galitski, and S. D. Sarma, *Phys. Rev. A* **82**, 013608 (2010).

[341] N. Goldman, I. Satija, P. Nikolic, A. Bermudez, M. A. Martin-Delgado, M. Lewenstein, and I. B. Spielman, *Phys. Rev. Lett.* **105**, 255302 (2010).

[342] M. Buchhold, D. Cocks, and W. Hofstetter, *arXiv:1204.0016v1* (2012).

[343] N. Goldman, J. Beugnon, and F. Gerbier, *Phys. Rev. Lett.* **108**, 255303 (2012).

[344] E. Zhao, N. Bray-Ali, C. J. Williams, I. B. Spielman, and I. I. Satija, *Phys. Rev. A* **84**, 063629 (2011).

[345] H. M. Price and N. R. Cooper, *Phys. Rev. A* **85**, 033620 (2012).

[346] H. P. Breuer and M. Holthaus, *Phys. Rev. Lett.* **140**, 507 (1989).

[347] Y. Tokura and N. Nagaosa, *Science* **288**, 462 (2000).

[348] K. I. Kugel and D. I. Khomskii, *Sov. Phys. Usp.* **25**, 231 (1982).

[349] G. Khaliullin, *Prog. Theor. Phys. Supplement* **160**, 155 (2005).

[350] A. Browaeys, H. Häffner, C. McKenzie, S. L. Rolston, K. Helmerson, and W. D. Phillips, *Phys. Rev. A* **72**, 053605 (2005).

[351] M. Köhl, H. Moritz, T. Stöferle, K. Günter, and T. Esslinger, *Phys. Rev. Lett.* **94**, 080403 (2005).

[352] T. Müller, S. Fölling, A. Widera, and . I. Bloch *Phys. Rev. Lett.* **99**, *Phys. Rev. Lett.* **99**, 200405 (2007).

[353] M. Anderlini, P. J. Lee, B. L. Brown, J. Sebby-Strabley, W. D. Phillips, and J. V. Porto, *Nature* **448**, 452 (2007).

[354] G. Wirth, M. Ölschläger, and A. Hemmerich, *Nat. Phys.* **7**, 147 (2011).

[355] C. A. Regal, C. Ticknor, J. L. Bohn, and D. S. Jin, *Phys. Rev. Lett.* **90**, 053201 (2003).

[356] J. Zhang, E. G. M. van Kempen, T. Bourdel, L. Khaykovich, J. Cubizolles, F. Chevy, M. Teichmann, L. Tarruell, S. J. J. M. F. Kokkelmans, and C. Salomon, *Phys. Rev. A* **70**, 030702(R) (2004).

[357] C. H. Schunck, M. W. Zwierlein, C. A. Stan, S. M. F. Raupach, W. Ketterle, A. Simoni, E. Tiesinga, C. J. Williams, and P. S. Julienne, *Phys. Rev. A* **71**, 045601 (2005).

[358] K. Günter, T. Stöferle, H. Moritz, M. Köhl, and T. Esslinger, *Phys. Rev. Lett.* **95**, 230401 (2005).

[359] H. Moritz, T. Stöferle, K. Günter, M. Köhl, and T. Esslinger, *Phys. Rev. Lett.* **94**, 210401 (2005).

[360] T. Stöferle, H. Moritz, K. Günter, M. Köhl, and T. Esslinger, *Phys. Rev. Lett.* **96**, 030401 (2006).

[361] J. P. Gaebler, J. T. Stewart, J. L. Bohn, and D. S. Jin, *Phys. Rev. Lett.* **98**, 200403 (2007).

[362] M. Theis, G. Thalhammer, K. Winkler, M. Hellwig, G. Ruff, R. Grimm, and J. H. Denschlag, *Phys. Rev. Lett.* **93**, 123001 (2004).

[363] G. Thalhammer, M. Theis, K. Winkler, R. Grimm, and J. H. Denschlag, *Phys. Rev. A* **71**, 033403 (2005).

[364] K. Goyal, I. Reichenbach, and I. Deutsch, *Phys. Rev. A* **82**, 062704 (2010).

[365] R. Ciuryło, E. Tiesinga, and P. S. Julienne, *Phys. Rev. A* **71**, 030701(R) (2005).

[366] P. O. Fedichev, Y. Kagan, G. V. Shlyapnikov, and J. T. M. Walraven, *Phys. Rev. Lett.* **77**, 2913 (1996).

[367] J. L. Bohn and P. S. Julienne, *Phys. Rev. A* **54**, R4637 (1996).

[368] J. L. Bohn and P. S. Julienne, *Phys. Rev. A* **60**, 414 (1999).

[369] P. Hauke, E. Zhao, K. Goyal, I. H. Deutsch, W. V. Liu, and M. Lewenstein, *Phys. Rev. A* **84**, 051603(R) (2011).

[370] A. Isacsson and S. M. Girvin, *Phys. Rev. A* **72**, 053604 (2005).

[371] A. B. Kuklov, *Phys. Rev. Lett.* **97**, 110405 (2006).

[372] W. V. Liu and C. Wu, *Phys. Rev. A* **74**, 013607 (2006).

[373] E. Zhao and W. Liu, *Phys. Rev. Lett.* **100**, 160403 (2008).

[374] Ákos Rapp, G. Zaránd, C. Honerkamp, and W. Hofstetter, *Phys. Rev. Lett.* **98**, 160405 (2007).

[375] Ákos Rapp, W. Hofstetter, and G. Zaránd, *Phys. Rev. B* **77**, 144520 (2008).

[376] C. Wu, *Phys. Rev. Lett.* **100**, 200406 (2008).

[377] S. Miyatake, K. Inaba, and S. ichiro Suga, *Physica C* **470**, S916 (2009).

[378] T. A. Tóth, A. M. Läuchli, F. Mila, and K. Penc, *Phys. Rev. Lett.* **105**, 265301 (2010).

[379] M. Lewenstein, A. Sanpera, V. Ahufinger, B. Damski, A. Sen, and U. Sen, *Adv.*

Phys. **56**, 243 (2007).

[380] S. Blatt, T. L. Nicholson, B. J. Bloom, J. R. Williams, J. W. Thomsen, P. S. Julienne, and J. Ye, *Phys. Rev. Lett.* **107**, 073202 (2011).

[381] E. Szirmai and M. Lewenstein, *Europhys. Lett.* **93**, 66005 (2011).

[382] D. Mukamel, *arXiv:0905.1457v1* (2009).

[383] C. Menotti, C. Trefzger, and M. Lewenstein, *Phys. Rev. Lett.* **98**, 235301 (2007).

[384] P. Rabl and P. Zoller, *Phys. Rev. A* **76**, 042308 (2007).

[385] C. Trefzger, C. Menotti, and M. Lewenstein, *Phys. Rev. A* **78**, 043604 (2008).

[386] G. G. Batrouni, R. T. Scalettar, G. T. Zimanyi, and A. P. Kampf, *Phys. Rev. Lett.* **74**, 2527 (1995).

[387] P. Sengupta, L. P. Pryadko, F. Alet, M. Troyer, , and G. Schmid, *Phys. Rev. Lett.* **94**, 207202 (2005).

[388] L. Dang, M. Boninsegni, and L. Pollet, *Phys. Rev. B* **78**, 132512 (2008).

[389] B. Capogrosso-Sansone, C. Trefzger, M. Lewenstein, P. Zoller, and G. Pupillo, *Phys. Rev. Lett.* **104**, 125301 (2010).

[390] X.-L. Deng, D. Porras, and J. I. Cirac, *Phys. Rev. A* **72**, 063407 (2005).

[391] R. Citro, E. Orignac, S. De Palo, and M. L. Chiofalo, *Phys. Rev. A* **75**, 051602(R) (2007).

[392] R. Citro, S. De Palo, E. Orignac, P. Pedri, and M. L. Chiofalo, *New J. Phys.* **10**, 045011 (2008).

[393] M. Dalmonte, G. Pupillo, and P. Zoller, *Phys. Rev. Lett.* **105**, 140401 (2010).

[394] F. J. Burnell, M. M. Parish, N. R. Cooper, and S. L. Sondhi, *Phys. Rev. B* **80**, 174519 (2009).

[395] V. Nebendahl and W. Dür, *arXiv:1205.2674v1 [quant-ph]* (2012).

[396] A. V. Gorshkov, S. R. Manmana, G. Chen, J. Ye, E. Demler, M. D. Lukin, and A. M. Rey, *Phys. Rev. Lett.* **107**, 115301 (2011).

[397] E. Brion, L. H. Pedersen, and K. Mølmer, *J. Phys. A: Math. Theor.* **40**, 1033 (2007).

[398] P. Bak and R. Bruinsma, *Phys. Rev. Lett.* **49**, 249 (1982).

[399] S. Wessel and M. Troyer, *Phys. Rev. Lett.* **95**, 127205 (2005).

[400] M. Boninsegni and N. Prokof'ev, *Phys. Rev. Lett.* **95**, 237204 (2005).

[401] D. Heidarian and K. Damle, *Phys. Rev. Lett.* **95**, 127206 (2005).

[402] R. G. Melko, A. Paramekanti, A. A. Burkov, A. Vishwanath, D. N. Sheng, and L. Balents, *Phys. Rev. Lett.* **95**, 127207 (2005).

[403] L. Pollet, J. D. Picon, H. P. Büchler, and M. Troyer, *Phys. Rev. Lett.* **104**, 125302 (2010).

[404] A. S. Arkhipov, G. E. Astrakharchik, A. V. Belikov, and Y. E. Lozovik, *JETP Lett.* **82**, 39 (2005).

[405] H. P. Büchler, E. Demler, M. Lukin, A. Micheli, N. Prokof'ev, G. Pupillo, and P. Zoller, *Phys. Rev. Lett.* **98**, 060404 (2007).

[406] F. A. Lindemann, *Z. Phys.* **11**, 609 (1910).

[407] A. Albuquerque, F. Alet, P. Corboz, P. Dayal, A. Feiguin, S. Fuchs, L. Gamper, E. Gull, S. Gürtler, A. Honecker, R. Igarashi, M. Körner,

A. Kozhevnikov, A. Läuchli, S. Manmana, M. Matsumoto, I. McCulloch, F. Michel, R. Noack, G. Pawlowski, L. Pollet, T. Pruschke, U. Schollwöck, S. Todo, S. Trebst, M. Troyer, P. Werner, and S. Wessel, *J. Magn. Magn. Mater.* **310**, 1187 (2007).

[408] S. R. White, *Phys. Rev. Lett.* **69**, 2863 (1992).

[409] U. Schollwöck, *Rev. Mod. Phys.* **77**, 259 (2005).

[410] A. Eckardt, *private communication* (2010).

[411] J. Freericks and H. Monien, *Phys. Rev. B* **53**, 2691 (1996).

[412] G. Vidal, *Phys. Rev. Lett.* **98**, 070201 (2007).

[413] V. Murg, J. I. Cirac, B. Pirvu, and F. Verstraete, *New J. Phys.* **12**, 025012 (2010).

[414] S. Chen, L. Wang, Y. Hao, and Y. Wang, *Phys. Rev. A* **77**, 032111 (2008).

[415] D. Peter, S. Müller, S. Wessel, and H. P. Büchler, *Phys. Rev. Lett.* **109**, 025303 (2012).

[416] T. Koffel, M. Lewenstein, and L. Tagliacozzo, *arXiv:1207.3957v1 [cond-mat.str-el]* (2012).

[417] P. W. Anderson, *Science* **235**, 1196 (1987).

[418] G. Kotliar, *Phys. Rev. B* **37**, 3664 (1988).

[419] G. Misguich and C. Lhuillier, *Frustrated Spin Systems*, p. 229, World Scientific, Singapore, 2004.

[420] K. Eckert, O. Romero-Isart, M. Rodriguez, M. Lewenstein, E. S. Polzik, and A. Sanpera, *Nat. Phys.* **4**, 50 (2007).

[421] K. Eckert, O. Romero-Isart, M. Rodriguez, M. Lewenstein, E. S. Polzik, and A. Sanpera, *Nat. Phys.* **4**, 50 (2008).

[422] T. Roscilde, M. Rodríguez, K. Eckert, O. Romero-Isart, M. Lewenstein, E. Polzik, and A. Sanpera, *New J. Phys.* **11**, 055041 (2009).

[423] G. De Chiara and A. Sanpera, *J. Low Temp. Phys.* **165**, 292 (2011).

[424] G. De Chiara, O. Romero-Isart, and A. Sanpera, *Phys. Rev. A* **83**, 021604 (2011).

[425] J. Appel, P. J. Windpassinger, D. Oblak, U. B. Hoff, N. Kjærgaard, and E. S. Polzik, *Proc. Natl. Acad. Sci. U.S.A.* **106**, 10960 (2009).

[426] T. Takano, M. Fuyama, R. Namiki, and Y. Takahashi, *Phys. Rev. Lett.* **102**, 033601 (2009).

[427] M. H. Schleier-Smith, I. D. Leroux, and V. Vuletić, *Phys. Rev. A* **81**, 021804 (2010).

[428] Z. Chen, J. G. Bohnet, S. R. Sankar, J. Dai, and J. K. Thompson, *Phys. Rev. Lett.* **106**, 133601 (2011).

[429] R. J. Sewell, M. Koschorreck, M. Napolitano, B. Dubost, N. Behbood, and M. W. Mitchell, *Quantum Electronics and Laser Science Conference (QELS) San Jose, California, arXiv:1111.6969 [quant-ph]* (2012).

[430] G. Tóth and M. W. Mitchell, *New J. Phys.* **12**, 053007 (2010).

[431] R. Dumke, M. Volk, T. Müther, F. B. J. Buchkremer, G. Birkl, and W. Ertmer, *Phys. Rev. Lett.* **89**, 097903 (2002).

[432] J. Kruse, C. Gierl, M. Schlosser, and G. Birkl, *Phys. Rev. A* **81**, 060308(R)

(2010).

[433] M. Schlosser, S. Tichelmann, J. Kruse, and G. Birkl, *Quantum Inf. Process.* **10**, 907 (2011).

[434] J. Cardy, *Scaling and Renormalization in Statistical Physics*, Number 5, Cambridge Lecture Notes in Physics, 1996.

[435] S. Sachdev, *Quantum Phase Transitions*, Cambridge University Press, 1999.

[436] R. Jozsa and N. Linden, *Proc. R. Soc. Lond. A* **459**, 2011 (2003).

[437] H. Olliver and W. H. Zurek, *Phys. Rev. Lett.* **88**, 017901 (2001).

[438] L. Henderson and V. Vedral, *J. Phys. A* **34**, 6899 (2001).

[439] A. Datta, A. Shaji, and C. M. Caves, *Phys. Rev. Lett.* **100**, 050502 (2008).

[440] A. Ferraro, L. Aolita, D. Cavalcanti, F. M. Cucchietti, and A. Acín, *Phys. Rev. A* **81**, 052318 (2010).

[441] Z. Merali, *Nature* **474**, 24 (2011).

[442] M. Gu, H. M. Chrzanowski, S. M. Assad, T. Symul, K. Modi, T. C. Ralph, V. Vedral, and P. K. Lam, *Nat. Phys.* (2012).

[443] B. Dakić, Y. O. Lipp, X. Ma, M. Ringbauer, S. Kropatschek, S. Barz, T. Paterek, V. Vedral, A. Zeilinger, Č. Brukner, and P. Walther, *Nat. Phys.* (2012).

[444] P. Hauke, R. J. Sewell, M. W. Mitchell, and M. Lewenstein, *arXiv:1208.1861v1 [quant-ph]* (2012).

[445] K. Hammerer, K. Mølmer, E. S. Polzik, and J. I. Cirac, *Phys. Rev. A* **70**, 044304 (2004).

[446] S. R. de Echaniz, M. Koschorreck, M. Napolitano, M. Kubasik, and M. W. Mitchell, *Phys. Rev. A* **77**, 032316 (2008).

[447] M. Koschorreck, M. Napolitano, B. Dubost, and M. W. Mitchell, *Phys. Rev. Lett.* **105**, 093602 (2010).

[448] K. Mølmer and L. B. Madsen, *Phys. Rev. A* **70**, 052102 (2004).

[449] L. B. Madsen and K. Mølmer, *Phys. Rev. A* **70**, 052324 (2004).

[450] M. Koschorreck and M. W. Mitchell, *J. Phys. B* **42**, 195502 (2009).

[451] W. Demtrŏder, *Laser Spectroscopy*, Berlin: Springer, 2002.

[452] D. J. Wineland, J. J. Bollinger, W. M. Itano, and D. J. Heinzen, *Phys. Rev. A* **50**, 67 (1994).

[453] G. Giedke and J. I. Cirac, *Phys. Rev. A* **66**, 032316 (2002).

[454] T. J. Osborne and M. A. Nielsen, *Phys. Rev. A* **66**, 032110 (2002).

[455] A. Osterloh, L. Amico, G. Falci, and R. Fazio, *Nature* **416**, 608 (2002).

[456] G. Vidal, J. I. Latorre, E. Rico, and A. Kitaev, *Phys. Rev. Lett.* **90**, 227902 (2003).

[457] F. Verstraete, M. Popp, and J. I. Cirac, *Phys. Rev. Lett.* **92**, 027901 (2004).

[458] D. J. Wineland, J. J. Bollinger, W. M. Itano, F. L. Moore, and D. J. Heinzen, *Phys. Rev. A* **46**, R6797 (1992).

[459] A. S. Sørensen and K. Mølmer, *Phys. Rev. Lett.* **86**, 4431 (2001).

[460] J. K. Korbicz, J. Cirac, and M. Lewenstein, *Phys. Rev. Lett.* **95**, 120502 (2005).

[461] G. Tóth, C. Knapp, O. Gühne, and H. J. Briegel, *Phys. Rev. Lett.* **99**, 250405

(2007).

[462] G. Tóth, C. Knapp, O. Gühne, and H. J. Briegel, *Phys. Rev. A* **79**, 042334 (2009).

[463] G. Vitagliano, P. Hyllus, I. L. Egusquiza, and G. Tóth, *Phys. Rev. Lett.* **107**, 240502 (2011).

[464] P. Krammer, H. Kampermann, D. Bruss, R. A. Bertlmann, L. C. Kwek, and C. Macchiavello, *Phys. Rev. Lett.* **103**, 100502 (2009).

[465] M. Cramer, M. B. Plenio, and H. Wunderlich, *Phys. Rev. Lett.* **106**, 020401 (2011).

[466] F. D. Haldane, *Phys. Lett. A* **93**, 464 (1983).

[467] G. Fáth and J. Sólyom, *Phys. Rev. B* **44**, 11836 (1991).

[468] R. Bursill, T. Xiang, and G. Gehring, *J. Phys. A* **28**, 2109 (1995).

[469] U. Schollwöck, T. Jolicoeur, and T. Garel, *Phys. Rev. B* **53**, 3304 (1996).

[470] A. Imambekov, M. Lukin, and E. Demler, *Phys. Rev. A* **68**, 063602 (2003).

[471] K. Buchta, G. Fáth, Ö. Legeza, and J. Sølyom, *Phys. Rev. B* **72**, 054433 (2005).

[472] M. Rizzi, D. Rossini, G. De Chiara, S. Montangero, and R. Fazio, *Phys. Rev. Lett.* **95**, 240404 (2005).

[473] A. Läuchli, G. Schmid, and S. Trebst, *Phys. Rev. B* **74**, 144426 (2006).

[474] M. Kac, *Am. Math. Monthly* **73**, 1 (1966).

[475] D. Kafri and J. M. Taylor, *arXiv:1207.7111v1 [quant-ph]* (2012).

[476] P. R. Johnson, E. Tiesinga, J. V. Porto, and C. J. Williams, *New J. Phys.* **11**, 093022 (2009).

[477] J. Li, Y. Yu, A. M. Dudarev, and Q. Niu, *New J. Phys.* **8**, 154 (2006).

[478] K. R. A. Hazzard and E. J. Mueller, *Phys. Rev. A* **81**, 031602 (2010).

[479] O. E. Alon, A. I. Streltsov, and L. S. Cederbaum, *Phys. Rev. Lett.* **95** (2005).

[480] K. Sakmann, A. I. Streltsov, O. E. Alon, and L. S. Cederbaum, *New J. Phys.* **13**, 043003 (2011).

[481] J. Larson, A. Collin, and J.-P. Martikainen, *Phys. Rev. A* **79**, 033603 (2009).

[482] A. Cetoli and E. Lundh, *Euro. Phys. Lett.* **90**, 46001 (2010).

[483] S. Zöllner, H.-D. Meyer, and P. Schmelcher, *Phys. Rev. Lett.* **100**, 040401 (2008).

[484] L. Cao, I. Brouzos, S. Zöllner, and P. Schmelcher, *New J. Phys.* **13**, 033032 (2011).

[485] S. Will, T. Best, U. Schneider, L. Hackermüller, D. Lühmann, and I. Bloch, *Nature* **465**, 197 (2010).

[486] J. Catani, L. D. Sarlo, G. Barontini, F. Minardi, and M. Inguscio, *Phys. Rev. A* **77**, 011603(R) (2008).

[487] S. Will, T. Best, S. Braun, U. Schneider, and I. Bloch, *Phys. Rev. Lett.* **106**, 115305 (2011).

[488] D.-S. Lühmann, K. Bongs, K. Sengstock, and D. Pfannkuche, *Phys. Rev. Lett.* **101**, 050402 (2008).

[489] O. Dutta, A. Eckardt, P. Hauke, B. Malomed, and M. Lewenstein, *New J. Phys.* **13**, 023019 (2011).

[490] T. Busch, B.-G. Englert, K. Rzazewski, and M. Wilkens, *Found. Phys.* **28**, 549

(1998).

[491] P. O. Fedichev, M. J. Bijlsma, and P. Zoller, *Phys. Rev. Lett.* **92**, 080401 (2004).

[492] X. Cui, Y. Wang, and F. Zhou, *Phys. Rev. Lett.* **104**, 153201 (2010).

[493] H. P. Büchler, *Phys. Rev. Lett.* **104**, 090402 (2010).

[494] M. Chiofalo, M. Polini, and M. Tosi, *Eur. Phys. J. D* **11**, 371 (2000).

[495] P. Vignolo, Z. Akdeniz, and M. P. Tosi, *J. Phys. B* **36**, 4535 (2003).

[496] J.-F. Schaff, Z. Akdeniz, and P. Vignolo, *Phys. Rev. A* **81**, 041604(R) (2010).

[497] E. Altman and A. Auerbach, *Phys. Rev. Lett.* **89**, 250404 (2002).

[498] S. D. Huber, E. Altman, H. P. Büchler, and G. Blatter, *Phys. Rev. B* **75**, 085106 (2007).

[499] F. Mila and K. Schmidt, *Introduction to Frustrated Magnetism, Chapter 20*, volume 164, Springer Series in Solid-State Sciences, 2010.

[500] R. Bendjama, B. Kumar, and F. Mila, *Phys. Rev. Lett.* **95**, 110406 (2005).

[501] M. W. H. Romans, R. A. Duine, S. Sachdev, and H. T. C. Stoof, *Phys. Rev. Lett.* **93**, 020405 (2004).

[502] K. Winkler, G. Thalhammer, F. Lang, R. Grimm, J. Hecker Denschlag, A. J. Daley, A. Kantian, H. P. Büchler, and P. Zoller, *Nature* **441**, 853 (2006).

[503] D. Petrosyan, B. Schmidt, J. R. Anglin, and M. Fleischhauer, *Phys. Rev. A* **76**, 033606 (2007).

[504] A. Kuklov, N. Prokof'ev, and B. Svistunov, *Phys. Rev. Lett.* **92**, 050402 (2004).

[505] A. Argüelles and L. Santos, *Phys. Rev. A* **75**, 053613 (2007).

[506] C. Trefzger, C. Menotti, and M. Lewenstein, *Phys. Rev. Lett.* **103**, 035304 (2009).

[507] M. Eckholt and J. J. García-Ripoll, *Phys. Rev. A* **77**, 063603 (2008).

[508] L. Mazza, M. Rizzi, M. Lewenstein, and J. I. Cirac, *Phys. Rev. A* **82**, 043629 (2010).

[509] N. Syassen, D. M. Bauer, M. Lettner, T. Volz, D. Dietze, J. J. García-Ripoll, J. I. Cirac, G. Rempe, and S. Dürr, *Science* **6**, 1329 (2008).

[510] A. J. Daley, J. M. Taylor, S. Diehl, M. Baranov, and P. Zoller, *Phys. Rev. Lett.* **102**, 040402 (2009).

[511] M. J. Ablowitz and J. F. Ladik, *J. Math. Phys.* **17**, 1011 (1976).

[512] D. Cai, A. R. Bishop, and N. Grønbech-Jensen, *Phys. Rev. Lett.* **72**, 591 (1994).

[513] P. Kevrekidis, G. Herring, S. Lafortune, and Q. Hoq, *Phys. Lett. A* **376**, 982 (2012).

[514] K.-K. Ni, S. Ospelkaus, M. H. G. de Miranda, A. Pe'er, B. Neyenhuis, J. J. Zirbel, S. Kotochigova, P. S. Julienne, D. S. Jin, and J. Ye, *Science* **322**, 231 (2008).

[515] S. Ospelkaus, K.-K. Ni, M. H. G. de Miranda, B. Neyenhuis, D. Wang, S. Kotochigova, P. S. Julienne, D. S. Jin, and J. Ye, *Faraday Discuss.* **142**, 351 (2009).

[516] K. Aikawa, D. Akamatsu, J. Kobayashi, M. Ueda, T. Kishimoto, and S. Inouye, *New J. Phys.* **11**, 055035 (2009).

[517] J. Deiglmayr, A. Grochola, M. Repp, K. Mörtlbauer, C. Glück, J. Lange, O. Dulieu, R. Wester, and M. Weidemüller, *Phys. Rev. Lett.* **101**, 133004.

[518] K. Goral, L. Santos, and M. Lewenstein, *Phys. Rev. Lett.* **88**, 170406 (2002).

[519] G. Pupillo, A. Griessner, A. Micheli, M. Ortner, D. Wang, and P. Zoller, *Phys. Rev. Lett.* **100**, 050402 (2008).

[520] D. Wang, M. Lukin, and E. Demler, *Phys. Rev. Lett.* **97**, 180413 (2006).

[521] G. Batrouni, F. Hébert, and R. Scalettar, *Phys. Rev. Lett.* **97**, 087209 (2006).

[522] T. Sowiński, O. Dutta, P. Hauke, L. Tagliacozzo, and M. Lewenstein, *Phys. Rev. Lett.* **108**, 115301 (2012).

[523] W. Kohn, *Phys. Rev.* **115**, 809 (1959).

[524] A. V. Gorshkov, M. Hermele, V. Gurarie, C. Xu, P. S. Julienne, J. Ye, P. Zoller, E. Demler, M. D. Lukin, and A. M. Rey, *Nat. Phys.* **6**, 289 (2010).

[525] G. Mazzarella, S. M. Giampaolo, and F. Illuminati, *Phys. Rev. A* **73**, 013625 (2006).

[526] P. Bader and U. R. Fischer, *Phys. Rev. Lett.* **103**, 060402 (2009).

[527] S. Kotochigova and E. Tiesinga, *Phys. Rev. A* **73**, 041405(R) (2006).

[528] A.-C. Voigt, M. Taglieber, L. Costa, T. Aoki, W. Wieser, T. W. Hänsch, and K. Dieckmann, *Phys. Rev. Lett.* **102**, 020405 (2009).

[529] P. Buonsante and A. Vezzani, *Phys. Rev. Lett.* **98**, 110601 (2007).

[530] M. Cozzini, P. Giorda, and P. Zanardi, *Phys. Rev. B* **75**, 014439 (2007).

[531] W. L. You, Y. W. Li, and S. J. Gu, *Phys. Rev. E* **76**, 022101 (2007).

[532] G. Vidal, *Phys. Rev. Lett.* **101**, 110501 (2008).

[533] G. Evenbly and G. Vidal, *Phys. Rev. B* **79**, 144108 (2009).

[534] S. Sachdev, *Quantum Phase Transitions*, Cambridge University Press, Cambridge, 1999.

[535] A. De Martino, M. Thorwart, R. Egger, and R. Graham, *Phys. Rev. Lett.* **94**, 060402 (2005).

[536] E. Lieb, T. Schultz, and D. Mattis, *Annals of Phys.* **16**, 407 (1961).

[537] G. Refael and J. Moore, *Phys. Rev. Lett.* **93**, 260602 (2004).

[538] M. P. Fisher, P. B. Weichmann, G. Grinstein, and D. S. Fisher, *Phys. Rev. B* **40**, 546 (1989).

[539] R. Freedman and J. A. Hertz, *Phys. Rev. B* **15**, 2384 (1977).

[540] A. Uhlmann, *Rep. Math. Phys.* **9**, 273 (1976).

[541] M. N. Barber, *Phase Transitions and Critical Phenomena*, volume 8, Academic Press, 1983.

[542] M. Nightingale, *Physica A* **83**, 561 (1975).

[543] N. T. Jacobson, S. Garnerone, S. Haas, and P. Zanardi, *Phys. Rev. B* **79**, 184427 (2009).

[544] J. Cardy, *Boltzmann Medal Lecture, StatPhys24, Cairns, http://www-thphys.physics.ox.ac.uk/people/JohnCardy/seminars/statphys24.pdf* (2010).

[545] C. Holzhey, F. Larsen, and F. Wilczek, *Nucl. Phys. B* **424**, 443 (1994).

[546] P. Calabrese and J. Cardy, *J. Stat. Mech.* , P06002 (2004).

[547] T. Gorin, T. Prosen, T. Seligman, and M. Znidaric, *Phys. Rep.* **435**, 33 (2006).

[548] T. Prosen and M. Znidaric, *Phys. Rev. E* **75**, 015202 (2007).

[549] A. Perales and G. Vidal, *Phys. Rev. A* **78**, 042337 (2008).

[550] D. Aharonov and M. Ben-Or, *arXiv:quant-ph/9611029v1* , Proceedings of 37th Conference on Foundations of Computer Science (1996).

[551] A. Harrow and M. Nielsen, *Phys. Rev. A* **68**, 012308 (2003).

[552] S. Virmani, S. F. Huelga, and M. B. Plenio, *Phys. Rev. A* **71**, 042328 (2005).

[553] M. M. Wolf, F. Verstraete, M. B. Hastings, and J. I. Cirac, *Phys. Rev. Lett.* **100**, 070502 (2008).

[554] F. Verstraete and J. I. Cirac, *arXiv:cond-mat/0407066v1* (2004).

[555] G. E. Moore, *Electronics* **38** (1965).

[556] J. Richter and J. Schulenburg, *Eur. Phys. J. B* **73**, 117 (2009).

[557] http://www.caam.rice.edu/software/ARPACK/.

[558] I. Affleck, T. Kennedy, E. H. Lieb, and H. Tasaki, *Phys. Rev. Lett.* **59**, 799 (1987).

[559] C. K. Majumdar and D. Ghosh, *J. Math. Phys.* **10**, 1388 (1969).

[560] M. Hastings, *J. Stat. Mech. Theory and Exp.* , P08024 (2007).

[561] S. Östlund and S. Rommer, *Phys. Rev. Lett.* **75**, 3537 (1995).

[562] S. Rommer and S. Östlund, *Phys. Rev. B* **55**, 2164 (1997).

[563] J. Dukelsky, M. A. Martin-Delgado, T. Nishino, and G. Sierra, *Europhys. Lett.* **43**, 457 (1998).

[564] F. Verstraete, D. Porras, and J. I. Cirac, *Phys. Rev. Lett.* **93**, 227205 (2004).

[565] A. Weichselbaum, F. Verstraete, U. Schollwöck, J. I. Cirac, and J. von Delft, *Phys. Rev. B* **80**, 165117 (2009).

[566] S. R. White, *Phys. Rev. B* **48**, 10345 (1992).

[567] L. Capriotti, D. J. Scalapino, and S. R. White, *Phys. Rev. Lett.* **93**, 177004 (2004).

[568] S. R. White and A. L. Chernyshev, *Phys. Rev. Lett.* **99**, 127004 (2007).

[569] F. Verstraete, M. M. Wolf, D. Perez-Garcia, and J. I. Cirac, *Phys. Rev. Lett.* **96**, 220601 (2006).

[570] V. Murg, F. Verstraete, and J. I. Cirac, *Phys. Rev. A* **75**, 033605 (2007).

[571] N. Schuch, M. M. Wolf, F. Verstraete, and J. I. Cirac, *Phys. Rev. Lett.* **98**, 140506 (2007).

[572] F. Verstraete, J. I. Cirac, and V. Murg, *Adv. Phys.* **57 (2)**, 143 (2008).

[573] G. Vidal, *Phys. Rev. Lett.* **99**, 220405 (2007).

[574] G. Vidal, *Understanding Quantum Phase Transitions*, Taylor & Francis, Boca Raton, 2010.

[575] P. Jordan and E. Wigner, *Z. Phys.* **47**, 631 (1928).

[576] F. Verstraete and J. Cirac, *J. Stat. Mech.* **0509**, P012 (2005).

[577] A. Tsvelik, *Quantum Field Theory in Condensed Matter Physics*, Cambridge University Press, Cambridge, 2003.

[578] M. Girardeau, *J. Math. Phys.* **1**, 516 (1960).

[579] B. Paredes, A. Widera, V. Murg, O. Mandel, S. Fölling, J. I. Cirac, G. V. Shlyapnikov, T. W. Hänsch, and I. Bloch, *Nature* **429**, 277 (2004).

[580] L. Levitov, H. Lee, and G. Lesovik, *J. Math. Phys.* **37**, 4845 (1996).

[581] I. Klich, *Quantum Noise in Mesoscopic Systems*, Kluwer, 2003.

[582] D. S. Rokhsar and B. G. Kotliar, *Phys. Rev. B* **44**, 10328 (1991).

[583] W. Krauth, M. Caffarel, and J.-P. Bouchaud, *Phys. Rev. B* **45**, 3137 (1992).

[584] W. Zwerger, *J. Opt. B* **5**, S9 (2003).

[585] B. Capogrosso-Sansone, N. V. Prokof'ev, and B. V. Svistunov, *Phys. Rev. B* **75**, 134302 (2007).

[586] S. Wessel, F. Alet, M. Troyer, and G. Batrouni, *Phys. Rev. A* **70**, 053615 (2004).

[587] T. D. Kühner, S. R. White, and H. Monien, *Phys. Rev. B* **61**, 12474 (2000).

[588] G. G. Batrouni and R. T. Scalettar, *Phys. Rev. B* **46**, 9051 (1992).

[589] J. Zakrzewski, *Phys. Rev. A* **71**, 043601 (2005).

[590] D. Jaksch, V. Venturi, J. I. Cirac, C. J. Williams, and P. Zoller, *Phys. Rev. Lett.* **89**, 040402 (2002).

[591] B. Damski, L. Santos, E. Tiemann, M. Lewenstein, S. Kotochigova, P. Julienne, and P. Zoller, *Phys. Rev. Lett.* **90**, 110401 (2003).

[592] H. Fehrmann, M. A. Baranov, B. Damski, M. Lewenstein, and L. Santos, *Opt. Comm.* **243**, 23 (2004).

[593] H. Fehrmann, M. Baranov, M. Lewenstein, and L. Santos, *Opt. Express* **12**, 55 (2004).

[594] V. Ahufinger, L. Sanchez-Palencia, A. Kantian, A. Sanpera, and M. Lewenstein, *Phys. Rev. A* **72**, 063616 (2005).

[595] P. Hauke, Classical and Quantum Simulations of Frustrated Spin Models, Master's thesis, Technical University of Munich and Max-Planck Institute of Quantum Optics, Garching, 2009.

[596] A. Fetter and J. Walecka, *Quantum Theory of Many-Particle Systems*, McGraw Hill, New York, 1971.

[597] J. H. Xu and C. S. Ting, *Phys. Rev. B* **43**, 6177 (1991).

[598] F. J. Dyson, *Phys. Rev.* **102**, 1217 (1956).

[599] S. V. Maleev, *Zh. Eksp. Teor. Fiz.* **30**, 1010 (1957), see also Sov. Phys. JETP 6, 776 (1958).

[600] A. I. Akhiezer, V. G. Bariakhtar, and S. V. Peletminskii, *Spin waves*, North-Holland Pub. Co., 1968.

[601] A. V. Dotsenko and O. P. Sushkov, *Phys. Rev. B* **50**, 13821 (1994).

[602] F. J. Dyson, E. H. Lieb, and B. Simon, *J. Stat. Phys.* **18**, 335 (1978).

[603] T. Kennedy, E. H. Lieb, and B. S. Shastry, *J. Stat. Phys.* **53**, 1019 (1988).

[604] E. Manousakis, *Rev. Mod. Phys.* **63**, 1 (1991).

[605] P. Anderson, *Materials Research Bulletin* **8**, 153 (1973).

[606] P. Fazekas and P. W. Anderson, *Philosophical Magazine* **30**, 423 (1974).

[607] M. A. Kastner, R. J. Birgeneau, G. Shirane, and Y. Endoh, *Rev. Mod. Phys.* **70**, 897 (1998).

[608] C. de la Cruz, Q. Huang, J. W. Lynn, J. Li, W. Ratcliff II, J. L. Zarestky, H. A. Mook, G. F. Chen, J. L. Luo, N. L. Wang, and P. Dai, *Nature* **453**, 899 (2008).

[609] R. Coldea, D. A. Tennant, A. M. Tsvelik, and T. Tylczynski, *Phys. Rev. Lett.*

86, 1335 (2001).

[610] Y. Shimizu, K. Miyagawa, K. Kanoda, M. Maesato, and G. Saito, *Phys. Rev. Lett.* **91**, 107001 (2003).

[611] S. Yamashita, Y. Nakazawa, M. Oguni, Y. Oshima, H. Nojiri, Y. Shimizu, K. Miyagawa, and K. Kanoda, *Nat. Phys.* **4**, 459 (2008).

[612] P. Carretta, N. Papinutto, R. Melzi, P. Millet, S. Gonthier, P. Mendels, and P. Wzietek, *J. Phys.: Condens. Matter* **16**, S849 (2004).

[613] R. Nath, A. A. Tsirlin, H. Rosner, and C. Geibel, *Phys. Rev. B* **78**, 064422 (2008).

[614] Z. Weihong, R. H. McKenzie, and R. R. P. Singh, *Phys. Rev. B* **59**, 14367 (1999).

[615] M. Q. Weng, D. N. Sheng, Z. Y. Weng, and R. J. Bursill, *Phys. Rev. B* **74**, 012407 (2006).

[616] J. O. Fjaerestad, W. Zheng, R. R. P. Singh, R. H. McKenzie, and R. Coldea, *Phys. Rev. B* **75**, 174447 (2007).

[617] M. Kohno, O. A. Starykh, and L. Balents, *Nat. Phys.* **3**, 790 (2007).

[618] O. A. Starykh and L. Balents, *Phys. Rev. Lett.* **98**, 077205 (2007).

[619] R. R. P. Singh, Z. Weihong, C. J. Hamer, and J. Oitmaa, *Phys. Rev. B* **60**, 7278 (1999).

[620] L. Capriotti, F. Becca, A. Parola, and S. Sorella, *Phys. Rev. Lett.* **87**, 097201 (2001).

[621] O. P. Sushkov, J. Oitmaa, and Z. Weihong, *Phys. Rev. B* **63**, 104420 (2001).

[622] P. Sindzingre, *Phys. Rev. B* **69**, 094418 (2004).

[623] J. Sirker, Z. Weihong, O. P. Sushkov, and J. Oitmaa, *Phys. Rev. B* **73**, 184420 (2006).

[624] M. Mambrini, A. Läuchli, D. Poilblanc, and F. Mila, *Phys. Rev. B* **74**, 144422 (2006).

[625] R. Darradi, O. Derzhko, R. Zinke, J. Schulenburg, S. E. Krueger, and J. Richter, *Phys. Rev. B* **78**, 214415 (2008).

[626] L. Wang, Z.-C. Gu, F. Verstraete, and X.-G. Wen, *arXiv:1112.3331v2 [cond-mat.str-el]* (2011).

[627] H.-C. Jiang, H. Yao, and L. Balents, *Phys. Rev. B* **86**, 024424 (2012).

[628] F. Figueirido, A. Karlhede, S. Kivelson, S. Sondhi, M. Rocek, and D. S. Rokhsar, *Phys. Rev. B* **41**, 4619 (1989).

[629] N. Read and S. Sachdev, *Phys. Rev. Lett.* **66**, 1773 (1991).

[630] J. Ferrer, *Phys. Rev. B* **47**, 8769 (1993).

[631] P. Hauke, *arXiv:1205.1955v1 [cond-mat.str-el]* (2012).

[632] J. Schulenburg and J. Richter, *Eur. Phys. J. B* **73**, 117 (2010).

[633] L. Capriotti, A. E. Trumper, and S. Sorella, *Phys. Rev. Lett.* **82**, 3899 (1999).

[634] L. O. Manuel and H. A. Ceccatto, *Phys. Rev. B* **60**, 9489 (1999).

[635] R. L. Doretto and M. Vojta, *Phys. Rev. B* **85**, 104416 (2012).

[636] C. Weber, A. Läuchli, F. Mila, and T. Giamarchi, *Phys. Rev. B* **73**, 014519 (2006).

[637] R. R. P. Singh, *Phys. Rev. B* **39**, 9760 (1989).

[638] A. Sandvik, *Phys. Rev. B* **56**, 11678 (1997).

[639] W. Zheng, J. O. Fjaerestad, R. R. P. Singh, R. H. McKenzie, and R. Coldea, *Phys. Rev. B* **74**, 224420 (2006).

[640] A. V. Chubukov, S. Sachdev, and T. Senthil, *J. Phys.: Condens. Matter* **6**, 8891 (1994).

[641] C. J. Gazza and H. A. Ceccatto, *J. Phys.: Condens. Matter* **5**, L135 (1993).

[642] A. E. Trumper, *Phys. Rev. B* **60**, 2987 (1999).

[643] A. W. Sandvik and H. G. Evertz, *Phys. Rev. B* **82**, 024407 (2010).

[644] P. Lecheminant, B. Bernu, C. Lhuillier, and L. Pierre, *Phys. Rev. B* **52**, 9162 (1995).

[645] E. P. Scriven and B. J. Powell, *Phys. Rev. Lett.* **109**, 097206 (2012).

[646] K. Yoshimi, H. Seo, S. Ishibashi, and S. E. Brown, *Physica B: Condensed Matter* **407**, 1783 (2012).

[647] A. A. Tsirlin, A. Moeller, B. Lorenz, Y. Skourski, and H. Rosner, *Phys. Rev. B* **85**, 014401 (2012).

[648] K. Kanoda and R. Kato, *Annu. Rev. Condens. Matter Phys.* **2**, 167 (2011).

[649] B. J. Powell and R. H. McKenzie, *Rep. Prog. Phys.* **74**, 056501 (2011).

[650] R. Coldea, D. A. Tennant, K. Habicht, P. Smeibidl, C. Wolters, and Z.Tylczynski, *Phys. Rev. Lett.* **88**, 137203 (2002).

[651] T. Ono, H. Tanaka, T. Nakagomi, O. Kolomiyets, H. Mitamura, F. Ishikawa, T. Goto, K. Nakajima, A. Oosawa, Y. Koike, K. Kakurai, J.Klenke, P. Smeibidle, M. Meissner, and H. A. Katori, *J. Phys. Soc. Jpn. Suppl.* **74**, 135 (2005).

[652] G. Gasparovic, *Physics of frustrated systems: A neutron scattering study*, PhD thesis, The Johns Hopkins University, 2005.

[653] M. P. Gelfand, R. R. Singh, and D. A. Huse, *Phys. Rev. B* **40**, 10801 (1989).

[654] A. Moreo, E. Dagotto, T. Jolicoeur, and J. Riera, *Phys. Rev. B* **42**, 6283 (1990).

[655] A. Chubukov, *Phys. Rev. B* **44**, 392 (1991).

[656] P. W. Leung and N. Lam, *Phys. Rev. B* **53**, 2213 (1996).

[657] P. Chandra and B. Doucot, *Phys. Rev. B* **38**, 9335 (1988).

[658] P. Locher, *Phys. Rev. B* **41**, 2537 (1990).

[659] Q. F. Zhong and S. Sorella, *Europhys. Lett.* **21**, 629 (1993).

[660] L. Capriotti and S. Sachdev, *Phys. Rev. Lett.* **93**, 257206 (2004).

[661] V. Murg, F. Verstraete, and J. I. Cirac, *Phys. Rev. B* **79**, 195119 (2009).

[662] H. Nishimori and Y. Saika, *J. Phys. Soc. Jpn.* **59**, 4454 (1990).

[663] A. F. Barabanov and O. A. Starykh, *JETP Lett.* **51**, 311 (1990).

[664] J. H. Xu and C. S. Ting, *Phys. Rev. B* **42**, 6861 (1990).

[665] N. B. Ivanov and P. C. Ivanov, *Phys. Rev. B* **46**, 8206 (1992).

[666] I. G. Gochev, *Phys. Rev. B* **49**, 9594 (1994).

[667] T. Einarsson and H. J. Schulz, *Phys. Rev. B* **51**, 6151 (1995).

[668] H. Schulz, T. Ziman, and D. Poilblanc, *J. Phys. I France* **6**, 675 (1996).

[669] A. E. Trumper, L. O. Manuel, C. J. Gazza, and H. A. Ceccatto, *Phys. Rev.*

Lett. **78**, 2216 (1997).

[670] L. O. Manuel, A. E. Trumper, and H. A. Ceccatto, *Phys. Rev. B* **57**, 8348 (1998).

[671] J. Bonča, J. P. Rodriguez, J. Ferrer, and K. S. Bedell, *Phys. Rev. B* **50**, 3415 (1994).

[672] J. Reuther, P. Wölfle, R. Darradi, W. Brenig, M. Arlego, and J. Richter, *Phys. Rev. B* **83**, 064416 (2011).